Bangor University

DOCTOR OF PHILOSOPHY

The migration of large scale bed forms in the Dee Estuary

Way, Oliver

Award date:
2013

Awarding institution:
Bangor University

[Link to publication](#)

PRIFYSGOL
BANGOR
UNIVERSITY

The migration of large scale bed forms in the Dee Estuary

Oliver Way

A thesis submitted in accordance with the requirements of
Bangor University for the degree of Doctor of Philosophy

Bangor University

School of Ocean Sciences

Menai Bridge, Anglesey

LL59 5AB

January 2013

Abstract

The Dee Estuary, located on the southern side of Liverpool Bay, in the Eastern Irish Sea, is macrotidal with a peak spring tidal range in excess of 10m. The large tidal range and associated strong currents make the estuary a very dynamic system with large fluxes of sediment. River canalisation and land reclamation between 1700 and early 1900 has significantly altered the hydrodynamic and sedimentological conditions. This caused the main navigation channel to migrate from the eastern side to the western shore of the estuary. Large bed forms are visible in the intertidal zones of the mouth of the estuary in aerial photographs. These features can be seen to be migrating into the estuary from X-band radar images. Dune migration can lead to residual sand transport rates, depending of the direction and magnitude of the dune characteristics. It is therefore important to monitor the movement of these large scale bed forms to determine the stability of the complex area of sand banks and channels in the Dee Estuary. Understanding the patterns of dune migration and associated sediment transport is fundamental for effective sediment management of an estuary, as well as an important consideration for offshore construction. Monitoring the migration patterns of large scale bed forms in the mouth of the Dee Estuary will show if they correlate with the transport of sediment into the estuary and how much they contribute to the sediment budget of the estuary. The driving forces behind large scale bed form migration are investigated to determine whether it is the action of waves, tidal currents or a combination of the two which are important. ADCP deployments on West Kirby Sands show a strong flood dominant tide which could be indicative of a flood dominant residual sediment transport. A 'three pronged' approach is taken to understand the migration of large scale bed forms in the mouth of the Dee Estuary. This includes remote sensing with X-band radar data, field measurements using DGPS surveying and numerical modelling techniques. Modelling of the estuary using TELEMAC, validated with ADCP measurements at West Kirby Sands, shows flood dominant sediment transport over a tidal cycle. A 'model chaining' approach is taken to simulate tides, waves, wave generated currents and sediment transport. Developments are made to include a variable bed roughness feedback method into TELEMAC. This has the effect of increasing the shear stress, which in turn causes increased rates of sediment transport. DGPS surveys conducted on West Kirby Sands show how the

morphology of this intertidal area changes over short timescales of days to weeks. The sediment transport calculated from a 1D sediment continuity equation applied to paired profiles through the DGPS survey data showed sediment accumulation at West Kirby Sands during times of increased wave activity. X-band radar analysis shows increased onshore migration of large scale bed forms during winter months, during times of increased wave heights, where the largest monthly mean wave height was 1.8m. West Hoyle Bank experiences up to 50% larger migrations than West Kirby Sands during periods of increased activity due to its greater exposure to waves entering the estuary. Yearly average dune migration rates were greater at West Kirby Sands in 2006 and 2007, but greater at West Hoyle Bank in 2008. Total migration rates are significantly larger for 2007 with West Kirby Sands experiencing a cumulative migration of 83m, whereas 2006 shows total migration rates of 57m for jpg data and 58m for mat data, while 2008 experienced 37m. Total migration at West Hoyle Bank was significantly larger than West Kirby Sands, with greatest migration seen during 2007 at 98m, however considerable migration also occurred during 2008 with 83m, while 2006 experienced 67m total migration using the jpg data and 73m from the mat data. A comparison of simulated wave heights and sediment transport in the mouth of the estuary shows greatest onshore transport to occur during times of greatest wave heights. Migration rates obtained from cross correlation analysis of X-band radar images are an order of magnitude smaller than the simulated total transport. This suggests that the bed load component of sediment transport associated with large scale bed form migration in the mouth of the estuary is moving sediment into the estuary via West Kirby Sands. The sediment transport pathways seen in the modelling of the estuary show that sediment is transported over West Kirby Sands and West Hoyle Bank, in a southerly direction, entering the estuary. Sediment transport vectors for peak transport show similar onshore transport to the X-band radar motion tracking vectors. All three techniques used here (remote sensing, field measurements and numerical modelling) show a strong correlation between larger wave heights and higher rates of bed form migration. This suggests that it is the increased shear stress associated with larger waves that is the driving factor for bed form migration into the estuary. There is a close relationship between the maximum current related bottom shear stress and the maximum bed load transport rates when waves are included in model simulations. Larger depth average currents under the influence of wave generated currents than under the influence of waves and tides alone result in greater sediment transport occurring around the areas of interest in the mouth of the estuary. This adds strength to the conclusion that waves are an important driving force for the migration of large scale bed forms and the transport of sediment into the estuary. The waves have the effect of resuspending sediment, therefore increasing the amount of sand available to be transported by the mean current.

Acknowledgements

Contents

List of Figures

List of Tables

List of Symbols

A	Wave amplitude	m
A_d	Dune cross sectional area	m^2
A_r	Radar effective aperture	-
A_0	Orbital excursion amplitude	m
a	Tidal constituent amplitude	m
a_m	Dune shape and porosity coefficient	-
b	Bijker's parameter	-
c	Phase speed	-
c_{ref}	Reference concentration	-
c_z	Suspended sediment concentration	-
$\bar{c}$	Depth averaged concentration	-
C_D	Quadratic current drag coefficient	-
C_g	Wave group velocity	ms^{-1}
C_h	Chezy coefficient	-
C_{hp}	Skin friction Chezy coefficient	-
C_1	Bed load flux not included in downstream migration of bed form	m^2s^{-1}
D_{br}	Breaking wave dissipation	-
D_f	Deposition flux	ms^{-1}
D_{50}	Median grain diameter	m
D_{90}	90% grain diameter	m
D_*	Dimensionless gain diameter	-
E_f	Erosion flux	ms^{-1}
E_r	Energy of surface roller	-
f	Frequency	s
f_a	Absolute frequency	s
f_s	Granular coefficient	-
f_w	Wave friction factor	-
F	Wave direction spectrum variance	-
Fr	Froude number	-
g	Gravity	m^2s^{-1}
G	Tidal phase	-
G_t	Radar transmitter gain	-
h	Water depth	m
H_s	Significant wave height	m
H_{rms}	Root mean square wave height	m

i	Current directed coordinate	m
I	Einstein's integral factor	-
j	Current perpendicular coordinate	m
k	Wave number	-
k_s	Total bed roughness	m
$k_{s,d}$	Bed roughness due to dunes	m
$k_{s,m}$	Bed roughness due to mega ripples	m
$k_{s,r}$	Bed roughness due to ripples	m
K_1	Principal lunar diurnal tidal period	s
K_2	Lunisolar semidiurnal tidal period	s
L	Macro turbulent path length	m
L_d	Dune migration distance per month	$m\,month^{-1}$
m	Magnitude of migration vector	m
M	Underwater weight of sand	kg
M_2	Principal lunar semidiurnal tidal period	s
M_4	Principal lunar shallow water tidal period	s
O_1	Lunar diurnal tidal period	s
P	Pixel greyscale intensity	-
P_r	Radar return power	-
P_s	Wave component performance indicator	-
P_t	Radar transmitter power	-
P_1	Solar diurnal tidal period	s
q_b	Volumetric bed load transport rate	$m^2 s^{-1}$
$q_{b,dune}$	Volumetric transport rate associated with bed form celerity	$m^2 s^{-1}$
q_s	Volumetric suspended load transport rate	$m^2 s^{-1}$
q_t	Volumetric total load transport rate	$m^2 s^{-1}$
q_R	Volumetric transport rate from the right	$m^2 s^{-1}$
q_L	Volumetric transport rate from the left	$m^2 s^{-1}$
Q_1	Large lunar elliptic diurnal tidal period	s
r	Normalised cross correlation coefficient	-
ref	Height of reference concentration	m
R	Rouse number	-
R_r	Range to radar target	-
s	Sediment relative density to seawater	-
S	Source/sink terms	-
S_{lw}	Surface area at LW	m^2

S_{hw}	Surface area at HW	m^2
S_r	Radar pattern propagation factor	-
S_2	Principal solar semidiurnal tidal period	s
t	Time	s
T	Transport stage parameter	-
T_r	Non buoyant tracer	-
T_p	Wave period	s
T_z	Peak wave period	s
u	Velocity in x direction	ms^{-1}
$\bar{u}$	Depth averaged velocity in x direction	ms^{-1}
U	Flow velocity	ms^{-1}
u_*	Shear velocity	ms^{-1}
u'_*	Skin friction velocity term	ms^{-1}
u_{*c}	Critical bed shear velocity for currents	ms^{-1}
u_{*cr}	Critical bed shear velocity	ms^{-1}
u_{*cw}	Critical bed shear velocity for currents and waves	ms^{-1}
u_0	Wave velocity amplitude	ms^{-1}
u_w	Horizontal oscillating velocity	ms^{-1}
$\bar{u}$	Depth averaged velocity	ms^{-1}
v	Velocity in y direction	ms^{-1}
$\bar{v}$	Depth averaged velocity in y direction	ms^{-1}
v_t	Momentum coefficient	-
v_T	Tracer coefficient	-
v_i	Bed form volume	m^3
V_{ip}	Total eroded volume	m^3
V_{mig}	Dune migration speed	ms^{-1}
W	Width of tunnel	m
w_s	Settling velocity	ms^{-1}
$zmig$	Identical X-Band radar image migration	m
z	Near bed reference height	m
z_s	Free surface elevation	m
z_0	Bed roughness length	m
Z_E	Surface elevation	m
Z_b	Bed elevation	m
α	Gradient of fitted peaks	-
α_s	Depth dependent suspension parameters	-
β	Bed form coefficient	-
β_r	Radar cross section	-

β_s	Slope coefficient	-
β_{sp}	Suspended load constant	-
β_w	Wave front slope	-
δ	Angle between motion vector and the vertical	Deg
δ_w	Wave boundary layer thickness	m
ε	Porosity	-
η	Bed form height	m
η_d	Dune height	m
η_r	Ripple height	m
γ	Tidal asymmetry ratio	-
γ_s	Suspension constant	-
κ	Von Karman's constant	-
λ	Bed form wavelength	m
λ_w	Surface wavelength	m
λ_d	Dune wavelength	m
λ_r	Ripple wavelength	m
λ_R	Wavelength of incident radar energy	-
μ	Ripple factor	-
v	Kinematic viscosity	$m^2 s^{-1}$
ω	Angular frequency	-
Ω_0	Macro turbulent spectral maximum	-
ψ	Mobility parameter	-
Φ	Non dimensional bed load transport rate	-
ρ	Density of sea water	kgm^{-3}
ρ_s	Density of sediment	kgm^{-3}
ρ_w	Density of water	kgm^{-3}
σ	Tidal frequency	s
τ	Shear stress	Nm^{-2}
τ_0	Bed shear stress	Nm^{-2}
τ_0'	Bed shear stress due to skin friction	Nm^{-2}
τ_c	Current related bed shear stress	Nm^{-2}
τ_w	Wave related bed shear stress	Nm^{-2}
τ_{cw}	Wave and current bed shear stress	Nm^{-2}
θ	Shields parameter	-
θ_{cr}	Critical Shields parameter	-
θ_c	Current alone nondimensional shear stress	-
θ_{cw}	Wave and current nondimensional shear stress	-
θ_R	Radar grazing angle	-
θ_w	Wave direction	-
$\bar{\theta}$	Mean wave angle	-
ε	Calculated position on maximum r	-

Chapter 1

Introduction

Understanding the morphological behaviour of sandy coasts is important, as the mobility of sea bed sediments can significantly impact the increasing number of people living and working in close proximity to coastal environments. The increasing number of people interacting with this dynamic system has increased the need for reliable monitoring and predictions of coastal morphological change. Historically, mariners have had a great interest in the stability of navigation channels. With the modern day use of large container vessels in shallow coastal regions an increased interest in channel and sea bed mobility has developed due to the navigational hazards. Repeated surveying of navigational channels is an expensive but necessary procedure. This process could be greatly aided with the use of remote sensing techniques to monitor the movement of the sea bed in and around shallow coastal environments.

A changing coastal environment is affected by the complex interactions of waves, currents and sediment transport which produces the resulting morphological change. An improved understanding of the dynamic coastal environment and an increased computer efficiency has allowed the use of numerical models to quantitatively describe coastal morphological processes. The Dee Estuary experiences a large tidal range of approximately 9m due to its position within Liverpool Bay. The fast tidal streams and short flood times which occur in the Dee make it a region of intensive sediment transport. Figure 1.1 shows the migration of a navigation channel in the Dee Estuary moving between 30 and 70m in one year.
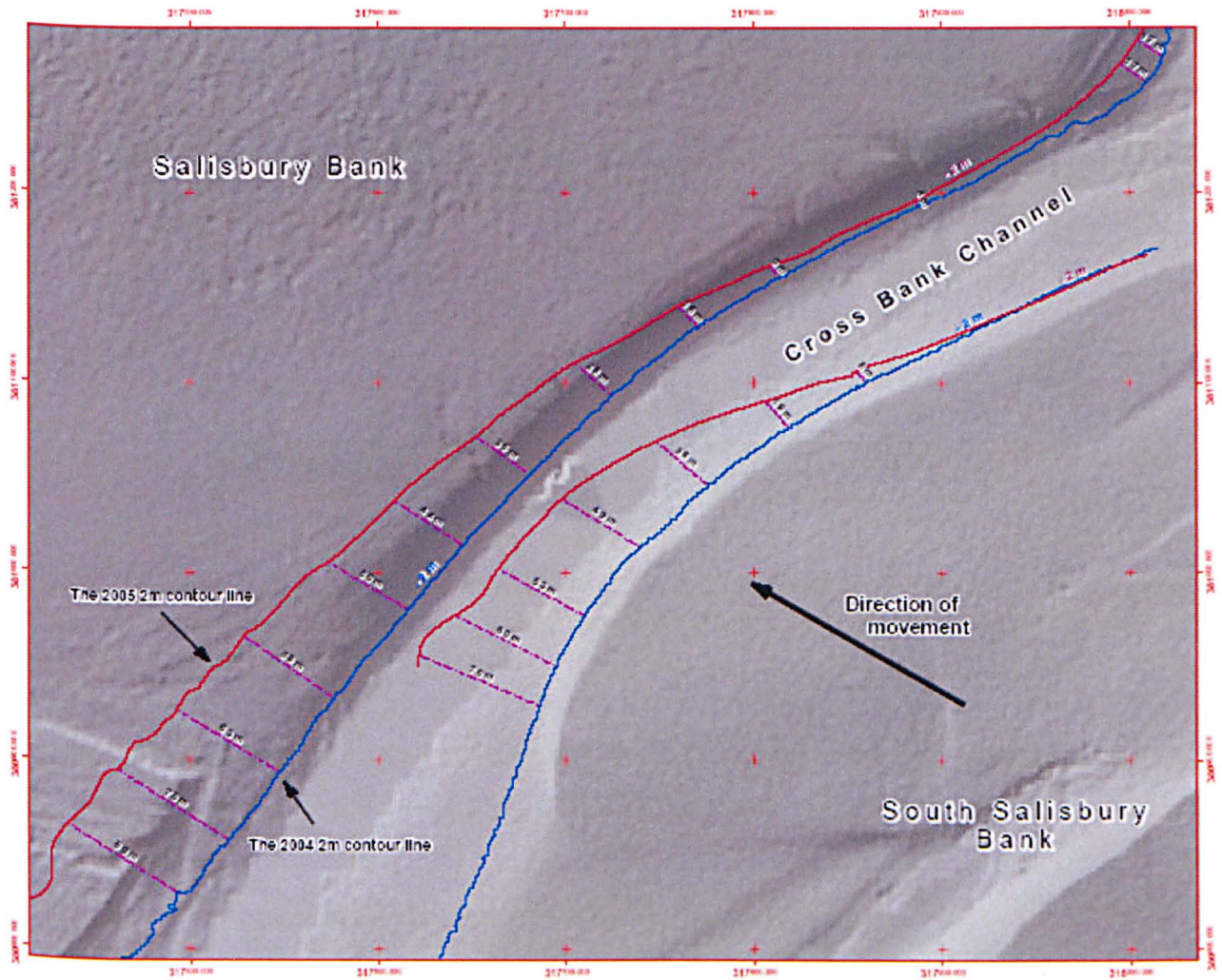
Figure 1.1: The migration of a cross-bank channel between 2004 and 2005 which is located to the north east of Mostyn Docks in the Dee Estuary. The 2004 base map is from Lidar data while the 2005 contour is from GPS survey data. The channel migration is between 30 and 70m in one year, shown by the pink lines. From Environment Agency (2005).

The migration of navigational marker buoys in the mouth of the Dee Estuary during energetic events is recorded by the Dee Conservancy Notice to Mariners which is supplied by the Environment Agency. One such event was recorded on 1st April 2010 when the HE 4 marker buoy moved 100m from its mooring location in the mouth of the Dee (Figure 1.2).
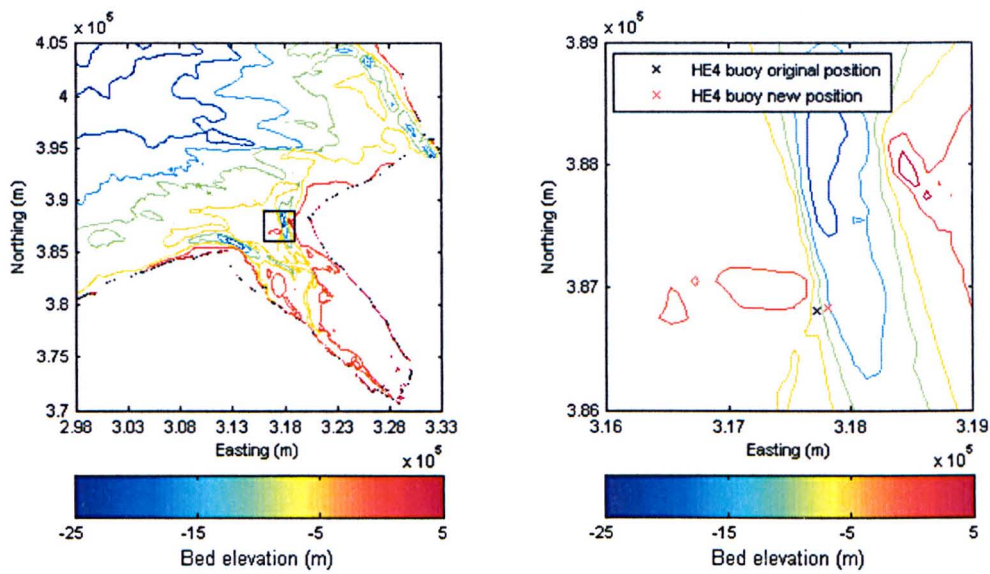
Figure 1.2: The migration of a navigation buoy in the mouth of the Dee Estuary as recorded by the Dee Conservancy Notice to Mariners supplied by the Environment Agency. The panel on the right is the subsection shown in the left hand panel.

Large bed forms are present on many of the sand flats in the mouth of the Dee. Figure 1.3 shows large scale bed forms present on the intertidal sand flats in the mouth of the estuary visible from an aerial photograph taken at low water.
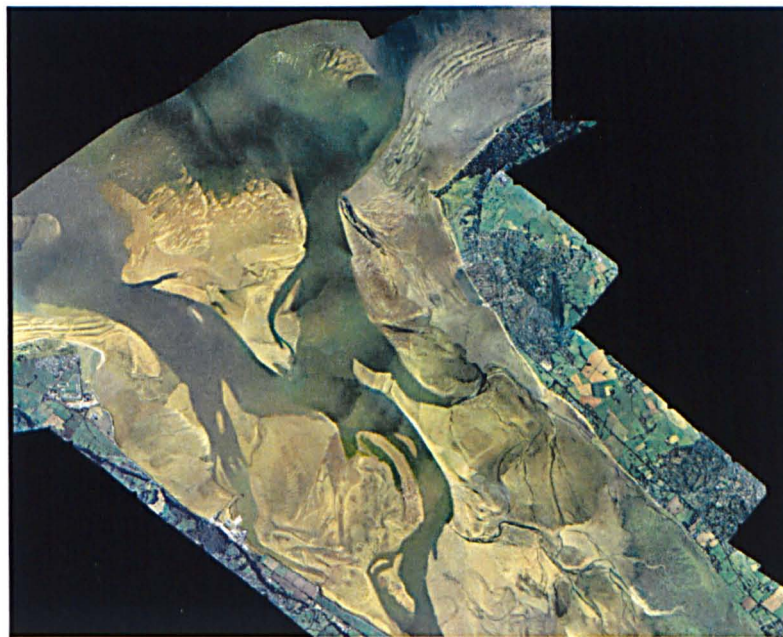
Figure 1.3: An aerial photograph of large scale bed forms on the intertidal sand flats in the mouth of the Dee Estuary.

McCann (2007) studied the migration of large, intertidal sand dunes on West Kirby Sands, in the mouth of the Dee, using the X-band radar facility on Hilbre Island for an MSc thesis project at

Bangor University, School of Ocean Sciences in 2007. The work of McCann (2007) can be seen as a feasibility study to determine the effectiveness of the Hilbre Island radar facility at detecting the migration of large scale bed forms. The work presented here by the author will continue this area of research, using the Hilbre Island radar facility to detect the migration of sand dunes over a wider area and longer time scales than that presented by McCann (2007).

1.1 Research aims

Dune migration can lead to residual sand transport rates, depending on the direction and magnitude of the dune characteristics. It is therefore important to monitor the movement of these large scale bed forms to determine the stability of the complex area of sand banks and channels in the Dee Estuary. Understanding the patterns of dune migration and associated sediment transport is fundamental for effective sediment management of an estuary, as well as an important consideration for offshore construction. Monitoring the migration patterns of large scale bed forms in the mouth of the Dee Estuary will aim to show if they correlate with the transport of sediment into the estuary and how much they contribute to the sediment budget of the estuary. The main aim of this research is to investigate the migration of large scale bed forms in the mouth of the Dee Estuary, primarily using remote sensing techniques, 2-dimensional numerical modelling and ground surveying. The research questions addressed herein include:

Are large scale bed forms migrating into the Dee Estuary?

Is the X-band radar installation on Hilbre Island in the mouth of the Dee Estuary an effective tool for remotely sensing the migration of large scale bed forms?

Do the intertidal sand flats in the estuary mouth act as pathways for sediment transport into the estuary?

Can the hydrodynamics and sediment dynamics of the Dee Estuary be accurately represented using numerical modelling techniques?

What are the driving forces behind large scale bed form migration in the mouth of the Dee Estuary? Is the action of waves, tidal currents or a combination of the two important?

Can field surveys of intertidal dune fields in the mouth of the Dee Estuary determine the mobility of sediment in these regions?

1.2 Thesis overview

The research is introduced in Chapter 1, setting the scene and outlining the research goals. Chapter 2 details the background information in the form of a literature review. This concentrates on the physics of sediment transport and the methods used to simulate transport rates in the coastal domain. Remote sensing techniques for monitoring the migration of large scale bed forms are discussed, before introducing the Dee Estuary.

Chapter 3 introduces data and observations obtained from the Dee Estuary during a field campaign between January to March 2011. This provides an initial look at the bed forms present in the mouth of the estuary and supplies model validation data. Chapter 4 presents the TELEMAC hydrodynamic and wave simulations and shows the model validation.

The TELEMAC sediment transport module is presented in Chapter 5, showing Bijker's (1992) sand transport model which is supplied as standard within TELEMAC. A technique for predicting bed roughness is also presented here as a modification by the author to the TELEMAC sediment transport subroutine.

Chapter 6 describes the methods employed for remotely sensing large scale bed forms in the mouth of the Dee Estuary using an X-band radar system. The results of X-band radar analysis are then presented in Chapter 7. The bed forms which are identified in the survey data from the field campaign, described in Chapter 3, are analysed in Chapter 8. Chapter 9 acts as a synthesis, bringing together field observations, remote sensing and modelling to show the migration of large scale bed forms in the mouth of the Dee Estuary.

A general discussion of the results is presented in Chapter 10, before final conclusions are made in Chapter 11 where research goals presented in Chapter 1 are answered. Following on from the conclusions, further work is proposed to extend the research already achieved in this study.

Chapter 2

Background information

2.1 Hydrodynamics

When a current flows over the sea bed it experiences friction, causing a turbulent boundary layer to develop. Boundary layers can form due to the action of currents, waves and combined current-wave conditions (Soulsby, 1983; Nielsen, 1992; Soulsby, 1997). The current velocity increases from zero at the bed to a maximum at the top of the boundary layer, with the greatest increase with height occurring near to the bed. For a steady current the velocity profile in the bottom few metres above the bed takes the form of a logarithmic velocity profile. The flow speed U at a specified height above the bed z is calculated by

$$U(z) = \frac{u_*}{\kappa} \ln \left(\frac{z}{z_0} \right) \qquad (2.1)$$

where u_* is the shear velocity, z_0 is the bed roughness length and κ is von Karman's constant (0.40). The shear velocity is a measure of the bed shear stress in relation to the velocity

$$u_* = \sqrt{\frac{\tau}{\rho}} \qquad (2.2)$$

where τ is the bed shear stress and ρ is the density of sea water. The bed roughness length z_0, included in Equation 2.1, is the height above the bed at which the velocity tends to zero, caused by friction between the flow and the bed that creates shear stress τ. The roughness length z_0 can be defined as a Nikuradse roughness k_s which can be calculated as $z_0 = k_s/30$ (Soulsby, 1997).

Waves make a significant contribution to stirring up sediment from the sea bed, whilst also generating steady current flows such as longshore currents which also transport sediment. Waves are

formed by either a locally wind generated sea caused by the effect of local wind blowing over the sea for a known distance (fetch) and time (duration) or as swell which originates from distant storms and comprises of longer period waves than a locally generated sea (Soulsby, 1997). Wave induced sediment motion will occur in shallow water regions, where the water depth h is less than half the wavelength λ_w. The motion beneath swell waves is usually modelled using linear wave theory, which describes the surface elevation Z_E of a surface wave travelling in the positive x_w direction given by

$$Z_E = A\cos(\omega t - kx_w) \tag{2.3}$$

where A is the wave surface amplitude, ω is the angular frequency ($\omega = 2\pi/T_p$) with T_p as the wave period, t is the time in seconds and k is the wave number ($k = 2\pi/\lambda_w$) with λ_w as the surface wavelength. The horizontal oscillating velocity at the bed is then given by

$$u_w = u_0 \cos(\omega t - kx_w) \tag{2.4}$$

where the velocity amplitude u_0 is given by

$$u_0 = \frac{A\omega}{\sinh(kh)} \tag{2.5}$$

An important length scale when considering the near bed flow and sediment transport due to waves is the orbital excursion amplitude A_0. This is defined in terms of the near bed velocity amplitude and wave frequency as

$$A_0 = \frac{u_0}{\omega} \tag{2.6}$$

The orbital excursion amplitude A_0 represents the maximum displacement of near bed fluid particles about their mean position during half of a wave cycle. The oscillatory boundary layer is typically 2-4% of the water depth for rough turbulent flow, and is thinner and more intense than the current boundary layer. This is due to the reversal of flow twice within each wave cycle which stops the growth of the boundary layer from the sea bed so that the process starts again.

2.2 Bed shear stress

The bed shear stress, or bottom friction, is the frictional force exerted by the flow on a unit area of the sea bed. It is the main hydrodynamic parameter in the erosion, transport and deposition of sediment in estuaries and coastal waters (Soulsby, 1997). Significant contributions to the bed shear stress are

made by the currents and waves, with the resulting shear stress consisting of a steady component due to the current and an oscillatory component due to the waves.

2.2.1 Bed shear stress due to currents

For currents the relationship between the bed shear stress τ_c and the depth average current $\bar{u}$ is expressed by the quadratic friction law

$$\tau_c = \rho C_D \bar{u}^2 \tag{2.7}$$

where C_D is the drag coefficient given by

$$C_D \left[\frac{0.4}{\ln(h/z_0) - 1} \right]^2 \tag{2.8}$$

2.2.2 Bed shear stress due to waves

The turbulence generated by the wave only component of flow is contained within a relatively small boundary layer on a scale of centimetres. The interaction of the flow with the bed within this small boundary layer produces larger velocity shear in comparison with the larger current alone boundary layer, which is on a scale of metres. This results in much greater bed shear stress produced by wave only oscillatory flow compared with that produced by a steady flow of similar magnitude (Nielsen, 1992; van Rijn, 1993; Soulsby, 1997). A similar quadratic friction law to that used to determine bed shear stress in steady flow (Equation 2.7) is applied to calculate bed shear stress for oscillatory flow τ_w

$$\tau_w = \frac{1}{2} \rho f_w u_0^2 \tag{2.9}$$

where f_w is the wave friction factor and u_0 is the peak orbital velocity during the wave cycle. The wave friction factor depends on the hydrodynamic regime, which is classified as laminar, smooth turbulent or rough turbulent. Soulsby (1997) related the wave friction factor f_w to the Nikuradse roughness k_s with the formula

$$f_w = 1.39 \left(\frac{A_0}{z_0} \right)^{-0.52} \quad \text{for all} \quad \frac{A_0}{k_s} \tag{2.10}$$

2.2.3 Bed shear stress due to currents and waves

The interaction of current and wave boundary layers is a non-linear process, due to the fact that they are turbulent regions and turbulence is a non-linear phenomenon. The quadratic friction law applied to calculate bed shear for currents and waves (Equations 2.7 & 2.9) shows shear stress to be proportional to the square of the velocity. Therefore the turbulence generated by the waves affects the currents and vice versa, enhancing both components of shear stress (Grant and Madsen, 1979; Soulsby et al., 1993).

Many theories and models have been proposed to describe the process of wave-current interaction over the years, which can be used to determine the wave-current bed shear stress. Soulsby et al. (1993) reviewed eight state of the art methods for boundary layer dynamics under combined wave-current flow, discussing the processes which affect the vertical profiles of current and wave kinematics and the bed shear stresses. The models reviewed include: the time-invariant eddy viscosity analytical models of Grant and Madsen (1979) and Christofferson and Jonsson (1985), the analytical mixing-length models of Bijker (1967) and Van Kesteren and Bakker (1984), the momentum-defect model of Fredsoe (1984), the similarity model of Myrhaug and Slaatelid (1989), and the fully numerical, turbulent-energy closure models of Davies et al. (1988) and Huynh-Thanh and Temperville (1992). Figure 2.1 shows a comparison between the eight model predictions for mean bed shear stress (τ_m) and maximum bed shear stress (τ_{max}) during a wave cycle.
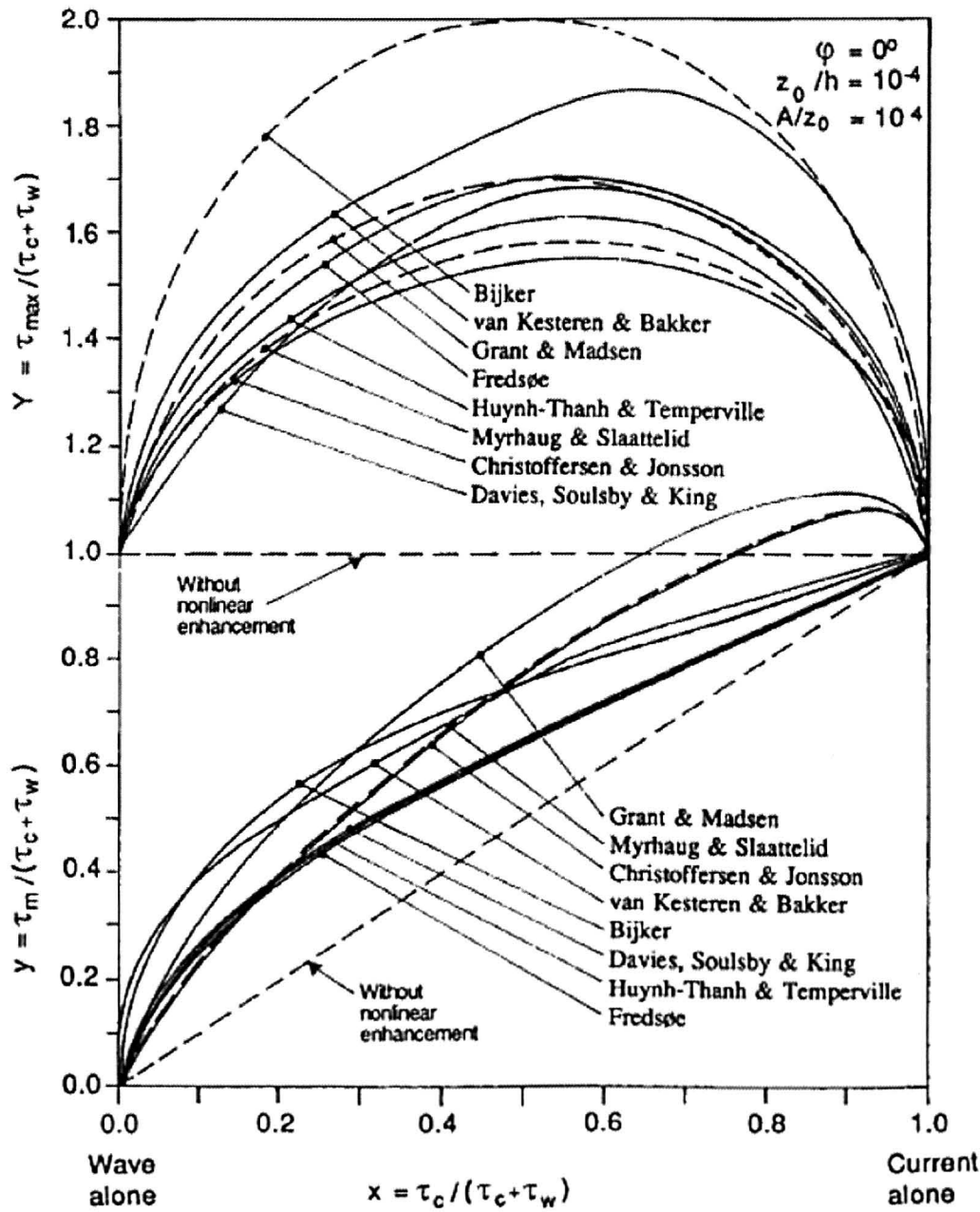
Figure 2.1: Intercomparison of eight models showing wave-current interaction for the prediction of mean and maximum bed shear stress (τ_m and τ_{max}). From Soulsby et al. (1993).

Differences between the mean and maximum bed shear stress during a wave cycle, τ_m and τ_{max} respectively are plotted with non-dimensional axes in Figure 2.1. This shows the variability in the degree of non-linear enhancement across the model outputs for the example shown, with differences commonly between 30-40% but also up to a factor of 4 for non-dimensional maximum stress during wave dominated conditions. The greatest level of non-linearity is shown by the Bijker (1967) model, while the models of Grant and Madsen (1979), Christofferson and Jonsson (1985), Myrhaug and Slaatelid (1989) exhibit different behaviour for non-dimensional mean stress in current dominated

conditions when compared to the others. Soulsby and Whitehouse (1997) found when examining a large data set that a two coefficient optimisation of the compiled data gave almost as good a fit as the best performing of the above listed theoretical models, when compared with measured data. This is referred to as DATA2 and is reduced to these simple equations

$$\tau_m = \tau_c \left[1 + 1.2 \left(\frac{\tau_w}{\tau_c + \tau_w} \right)^{3.2} \right] \tag{2.11}$$

$$\tau_{max} = [(\tau_m + \tau_w \cos \theta_{wc})^2 + (\tau_w \sin \theta_{wc})^2]^{0.5} \tag{2.12}$$

where θ_{wc} is the angle between the waves and the current, and τ_c and τ_w are the current and wave components of bed shear stress calculated using Equations 2.7 and 2.9, respectively.

2.3 Bed forms and bed roughness

2.3.1 Bed features

It is a common trait for flows over a sandy bed in rivers, estuaries and the sea, which exceed the threshold of motion, to form into one of a variety of types of regular bed features. These bed forms, which are created as a result of the interaction between the flow and the bed, occur at various spatial scales (Soulsby, 1997). Bed forms scale in relation to water depth h, with wavelength λ, measured from crest to crest, ranging from ripples ($\lambda << h$), to mega-ripples ($\lambda \leq h$) and then dunes ($\lambda \geq h$). Different types of flow, either tidal currents, waves or a combination of waves and currents, will result in the development of different bed forms (Figure 2.2). Tidal currents in estuaries are known to form small scale ripples, large scale dunes and also ripples superimposed on to the backs of dunes.
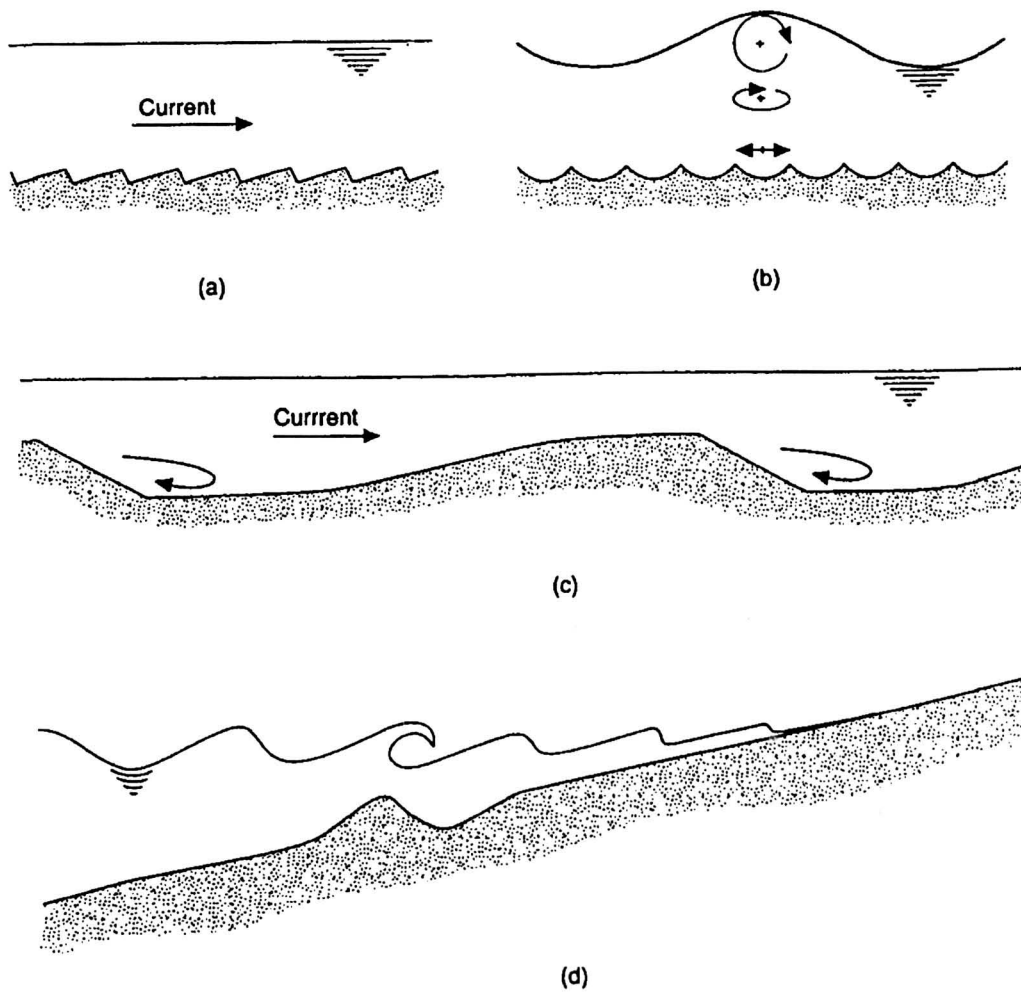
Figure 2.2: Some of the types of bed forms found in the coastal zone a) current ripples, b) wave ripples c) sand dunes d) breaker bar. From Soulsby (1997).

Current generated ripples are asymmetrical in cross section with the steeper 'lee' slope on the downstream side of the crest. The ripples move downstream in the direction of the current. Raudkivi (1997) analysed data on ripple dimensions, stating that initial ripple features migrate at speeds inversely proportional to their height. The ripple dimensions in the sand range ($62 < d_{50} < 2000\mu m$) can be expressed as ripple height $\eta_r = 18(d_{50})^{0.1}$ and ripple length $\lambda_r = 245(d_{50})^{0.35}$. When waves are the dominant hydrodynamic force, the wave generated ripples are generally more symmetrical in form caused by the oscillatory nature of the flow. Ripple configurations in combined wave and current flow were described by van Rijn and Havinga (1995) (Figure 2.3). It should be noted that Figure 2.3 is valid for perpendicular wave and flow directions. 2D patterns with straight crests perpendicular to the wave direction were observed in wave only conditions, 2.5D patterns with wavy crests were described for combined oscillatory and weak steady flows, while 3D honeycomb patterns were observed for combined oscillatory and relatively strong steady flows. Mega-ripples are ripples with a length

scale of the order of the water depth ($\lambda \approx h$).
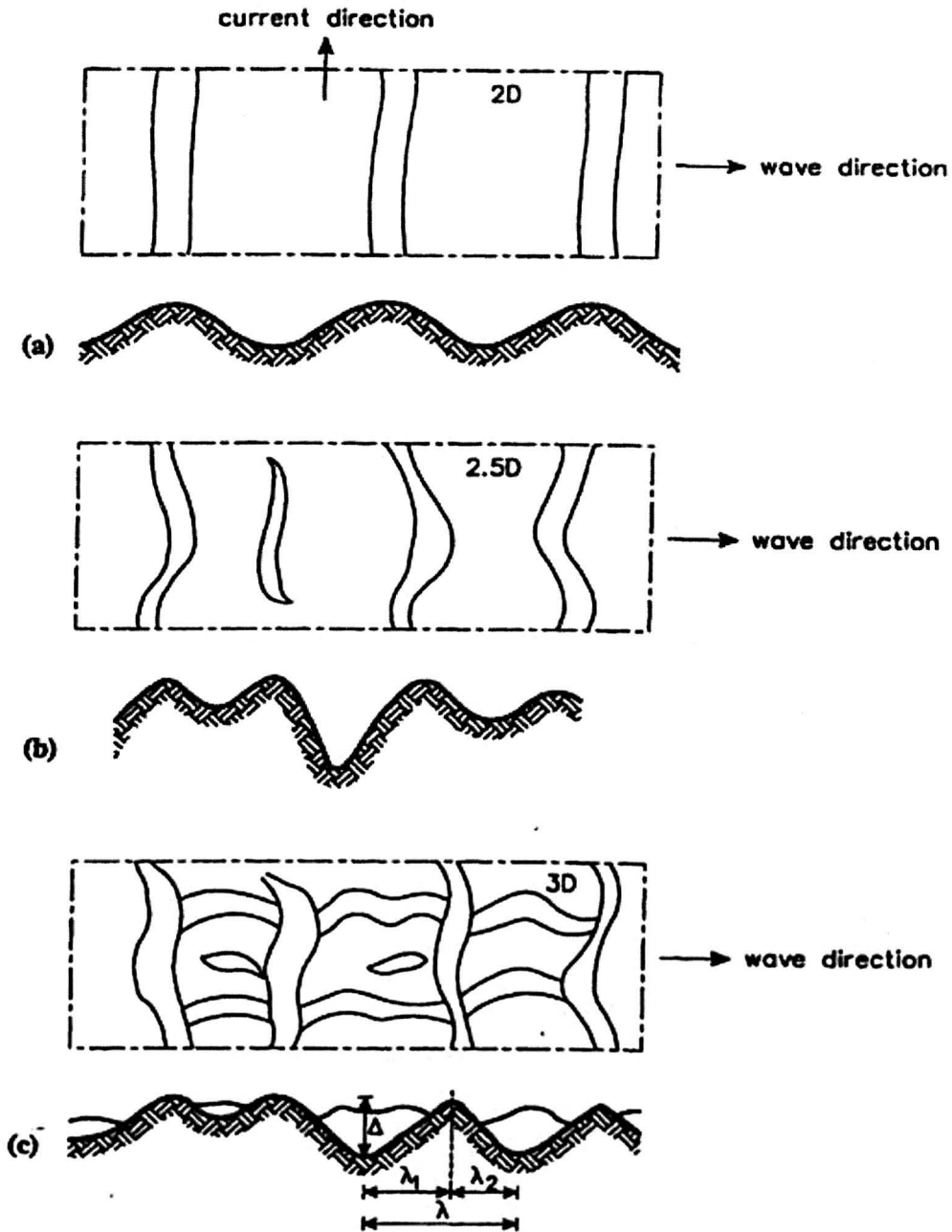
Figure 2.3: Ripple patterns in combined oscillatory flows and steady flows. From van Rijn and Havinga (1995).

The nomenclature for larger bed forms is slightly ambiguous, with large transverse sedimentary features being referred to as both sand waves and sand dunes in the literature. Herein the term sand dune will be used when referring to large scale bed forms. Large bed forms are commonly found in sandy environments with water depths greater than 1m, sediment sizes coarser than 0.15mm (very fine sand), and mean current velocities greater than 0.4ms^{-1} (Ashley, 1990). Dunes are here defined as statistically regular bed perturbations, which have crests orientated normal to the mean flow and

with a wavelength λ greater than the water depth h, therefore occurring in shallow flow (Figure 2.4).
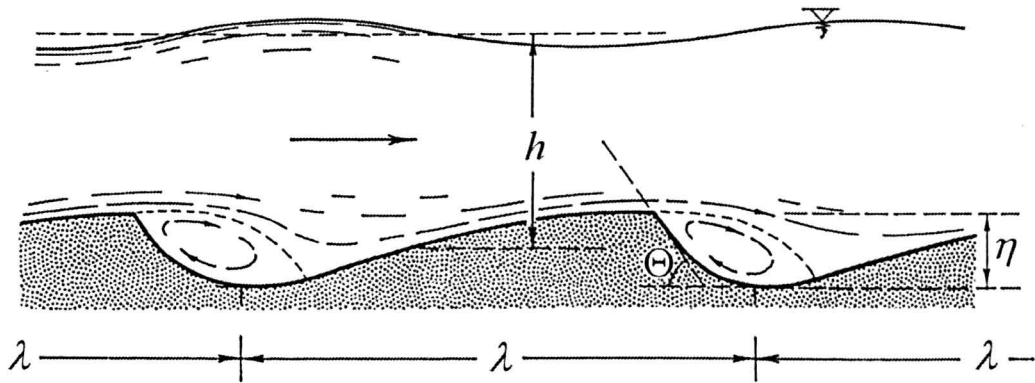
Figure 2.4: A typical asymmetrical sand dune under a steady current. From Yalin (1997).

As such, the dune wavelength has a strong dependence on flow depth. A number of relationships have been quoted in previous literature, most notably $\lambda_d = 2\pi h$ (Yalin, 1997) and λ_d is in the range of 3-15 h (van Rijn, 2007b). Dunes are often asymmetrical in cross-section with long, shallow sloping upstream (stoss) slopes and shorter, steeper downstream (lee) slopes (Figure 2.4). The asymmetry is caused by the presence of large lee slope eddies formed due to a separation of flow over the dune crest, resulting in a steeper lee slope angle Θ which is often close to the angle of repose.

Several classification schemes have been proposed for large scale bed forms, which has created a confusing terminology. Yalin (1997) simplified this nomenclature by regarding any sand wave generated by the flow as, either, a ripple, a sand dune or an anti-dune. These are defined by the free surface of the flow, which is quantified by the Froude number Fr, given by

$$Fr = \frac{\bar{u}}{\sqrt{gh}} \tag{2.13}$$

where $\bar{u}$ is the depth-averaged velocity, g is gravity, and h is the local water depth. Depending on the value of Fr, the flow may be characterised by one of three regimes: for values less than 1, the flow is subcritical; equal to 1, the flow is critical; and greater than 1, the flow is supercritical. If the flow is subcritical (Fr<1) then the two types of bed forms which will be present are ripples and dunes. Upper plane bed flow (sheet flow) is stable between Fr=0.84 and 1.16, while antidunes are stable at Fr>1.16. The field conditions at the sandflats in the mouth of the Dee Estuary will be strictly subcritical.

2.3.2 Dune formation

Yalin (1997) stated that the formation of dunes does not only depend on water depth, but also requires

the presence of large scale turbulent eddies. This turbulence may be primarily responsible for the formation of large scale bed forms, particularly the formation of dunes. According to Yalin (1997) a rough turbulent flow of depth h will display random fluctuations in flow speed U in horizontal space x and time t. The 'birth' and 'death' of a turbulent eddy, where the distance between is the path length L, is said to be a regenerative process, where the 'birth' of one eddy coincides with the 'death' of another. This means that the path of an eddy will end on the downstream side of where the next eddy begins. Therefore the longitudinal disturbances caused by these macro-turbulent eddies can be detected up to a distance of one path length L away from its source, where L is the average macro-turbulent path length. Therefore, a disturbance of the bed, such as a ridge at $x = x_0$ should be detectable in the flow up to a distance of $x_0 + L$. According to the theory of stability of parallel flow, the wavelength of a 'neutral distance' L, which is steady in time, is given by Narahari et al. (1971) as

$$\frac{L}{h} = 2\pi \tag{2.14}$$

Comparing this with the length of bed disturbances caused by the passage of the macroturbulent eddies λ, then an assumption can be made that the average length of λ scales on L. If the lengths of the bed disturbances are comparable with each other, and the random turbulent fluctuations in U are treated as a spectrum, then the corresponding bandwidth must be relatively narrow, as λ, L and U are inter-related. The frequency Ω_0 of the spectral maximum in U is assumed to be not significantly different to the average frequency in L, so that

$$\Omega_0 \approx \frac{2\pi}{L} = \frac{2\pi}{2\pi h} \approx \frac{1}{h} \tag{2.15}$$

If the spectrum of the frequency follows a Gaussian distribution, with a peak at Ω_0, then the autocorrelation function $K(x)$ can be written as

$$K(x) \approx e^{-2\pi x} \cos\left(\frac{x}{h}\right) \tag{2.16}$$

This implies that any change in the velocity profile at $x = 0$ will positively correlate with profiles separated by even multiples of πh, and negatively with odd multiples. The 'signal' generated at $x = 0$ will be damped by the function $e^{-2\pi x}$ at this distance from the source. Yalin (1997) then considered this signal as a deviation from the mean (logarithmic) velocity profile, generated by an unconformity on an otherwise flat bed. Taking the volumetric sediment transport rate q_b, and assuming a continuity of sediment volume, then the change in sediment volume which enters an area centred on a line $x =$ constant is equal to $q_b(x)$ per unit width. The volume of sediment that leaves this line is therefore

equal to

$$q_b(x) + \frac{dq_b}{dx}dx \tag{2.17}$$

and so the change in volume of sediment per unit time is given by

$$-\frac{dq_b}{dx}dx \tag{2.18}$$

assuming an insignificant contribution of suspended sediment. Taking ε as the porosity of naturally settled sand grains and z_b as the bed level then the continuity of sediment volume can be expressed as (Nielsen, 1992)

$$(1-\varepsilon)\frac{dz_b}{dt} = -\frac{dq_b}{dt} \tag{2.19}$$

If q_b is proportional to the flow speed, then the alternating changes in the mean flow profile with x will result in alternating patterns of sediment transport, with areas of accretion and erosion (Figure 2.5). Regions of accretion, such as $x = 2\pi h$ in Figure 2.5 can then act as the initial discontinuity for dune creation further downstream.
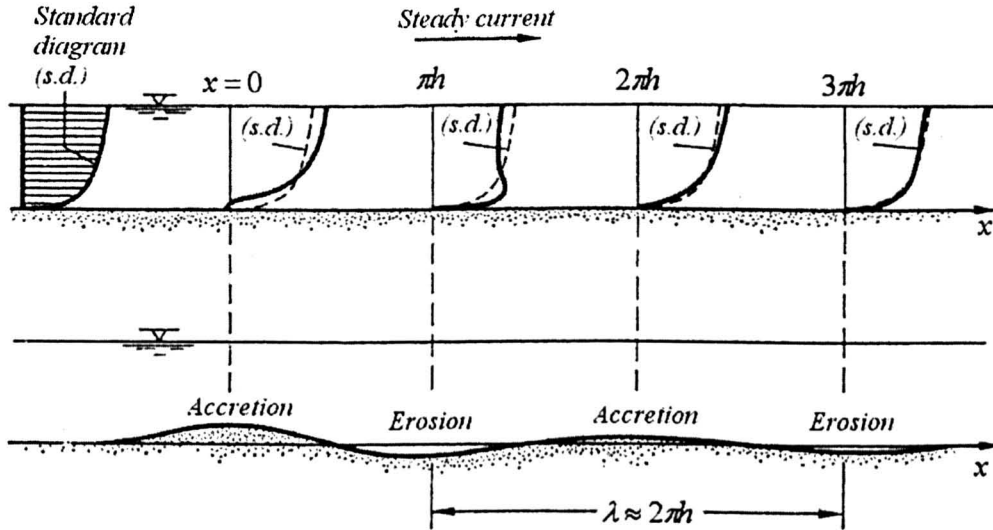
Figure 2.5: Deviations from the mean velocity profile resulting from disturbances in the structure of turbulence can lead to the formation of regular bed forms. From Yalin (1997).

While this accounts for the initiation of a dune field from a plane bed, it does not explain the eventual stability of the dunes with the associated finite amplitude effects. This can be addressed by considering the sediment flux along a dune, which is proportional to the bed shear stress τ_0. The inclusion of a phase lag by Kennedy (1963) between the steady mean flow and τ_0 shows how a bed form may grow

or decay. However, this does not take into account the frictional effects which will damp growing disturbances in nature. Engelund (1970) addressed this problem by adding frictional effects in the form of the turbulent eddy viscosity. However, this results in a maximum in τ_0 being calculated upstream of the crest.

McLean (1990) introduced a phase lag between the local bed shear stress and the sediment flux using the bed load transport formula of Meyer-Peter and Muller (1948). The non-dimensional growth rate for an unstable bed perturbation was derived using a continuity argument and taking the surface elevation of the bed form. McLean (1990) suggested that the phase lag could be the result of inertial 'hops' and saltations of the sediment which move the point of maximum flux downstream from the point of maximum shear stress. Therefore, if the length scales of these saltations downstream is equal to the upstream shift in maximum bed shear stress then the bed form may remain stable. Engelund (1970) included suspended load transport to determine the possible stabilising effects for dune growth. As the suspended load in a flow is significantly influenced by turbulence, then the downstream lag between maximum bed shear stress and sediment flux could be considerably increased by macroturbulent eddies which scale on the flow depth.

The asymmetric shape of dunes observed in nature is caused by large scale flow separation and eddy formation downstream of the dune crest. Flow separation is the result of a large relative difference in local fluid pressure on the upstream and downstream sides of the crest. If the crest is steep enough, and the flow fast enough, then this relative change in pressure is large and rapid. As the change is a relative drop in pressure, fluid flowing over the crest is effectively pulled down towards the bed. This leads to the formation of the characteristic lee slope eddy. Figure 2.6 shows the results of experiments conducted at Delft Hydraulics (1988), measuring the flow field over an artificial dune.
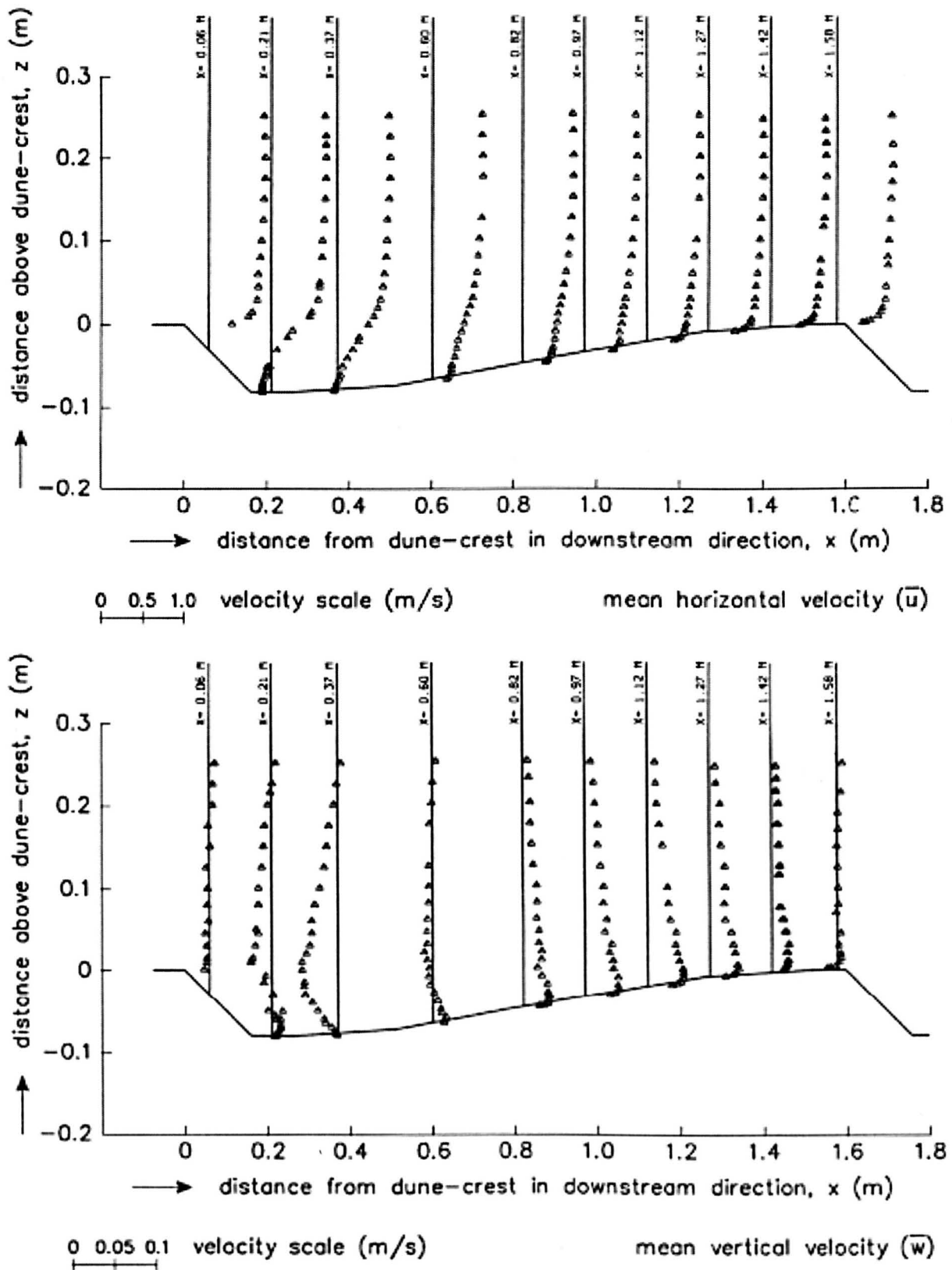
Figure 2.6: Vertical profiles of horizontal and vertical fluid velocity over an asymmetric dune shape. From van Rijn (1993).

Figure 2.6 shows a dune with a height of 80cm, a wavelength of 1.6m and a mean flow velocity of $0.51ms^{-1}$ with a Froude number of 0.29. A recirculation of the flow can be seen just after the dune crest, where separated fluid will be flowing down towards the bed, before turning back towards the crest. A point of zero fluid velocity, or stagnation point, can be seen to occur close to the bed at approximately 0.4m from the crest. Flow reattachment and acceleration can be seen on the lee slope of the next dune. Sediment moving in continuous contact with the bed, as bed load, will be transported in accordance with this flow field. This is an important consideration when determining the migration of large scale bed forms in the mouth of the Dee Estuary. One could expect a jet of sediment being 'blown' over the crest at high speed, circulated in the lee slope eddy, before possibly being deposited at the separation zone (stagnation point). From the continuity of sediment mass the high flux of sediment will result in erosion of the stoss slope and crest, and when coupled with deposition at the separation zone could result in a migration of the dune shape downstream.

2.3.3 Occurrence of dunes

The occurrence of dunes has been shown to be a function of the sediment properties and hydrodynamics by van Rijn (1984c), based on the dimensionless grain size D_* and the transport stage parameter T

$$D_* = D_{50} \left[\frac{(s-1)g}{v^2} \right]^{1/3} \tag{2.20}$$

$$T = \frac{\tau_0' - \tau_{0,cr}}{\tau_{0,cr}} \tag{2.21}$$

where D_{50} is the median grain size, s is the sediment density relative to seawater, v is the kinematic viscosity, τ_0' is the skin friction component of the bed shear stress and $\tau_{0,cr}$ is the critical bed shear stress for the initiation of sediment motion. Data collected from laboratory flume and field experiments allowed van Rijn (1984c) to create a bed form stability diagram (Figure 2.7). This shows that dunes occur for $0 \leq T \leq 10$ if $D_* > 10$ and for all grain sizes if $10 < T \leq 15$. Anti-dunes occur in super-critical flows where $Fr > 1:16$ and are in phase with water surface waves. Mini-ripples are defined as bed forms where $\lambda < h$, therefore they are independent of water depth, while mega-ripples are defined by van Rijn (1984c) as bed forms with $\lambda = h$.
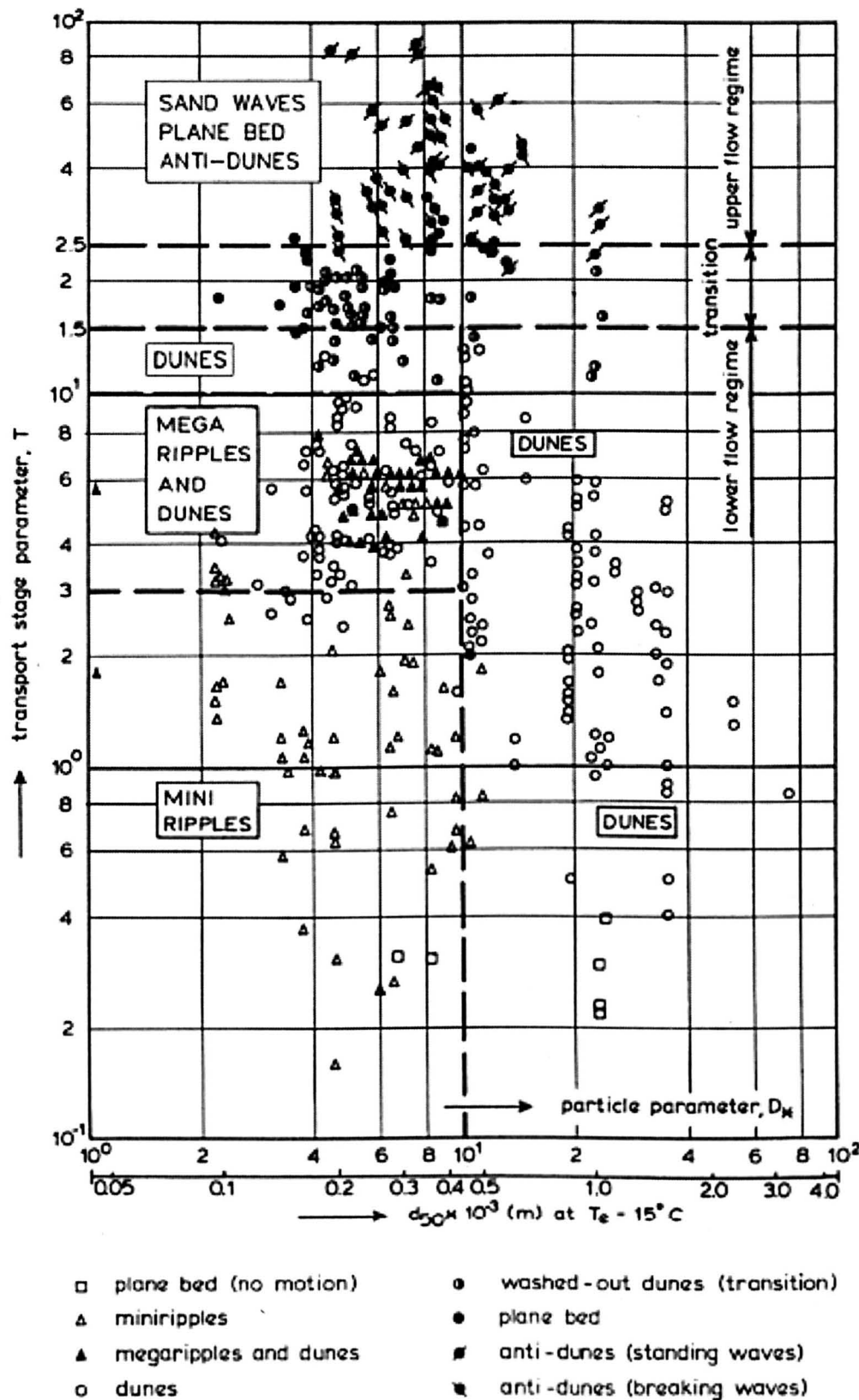
Figure 2.7: van Rijn's bed form classification plot, partitioning different types of bed form with regards to the relative excess stress and dimensionless grain size. From van Rijn (1993).

2.3.4 Bed forms in waves

Wave ripples are formed once the oscillatory motion is of sufficient strength to cause movement of the surface sediment grains (van Rijn, 1993). Wave generated ripples display an almost symmetrical and rounded profile. Kleinhans (2005) proposed a general classification diagram for bed forms in waves (Figure 2.8).
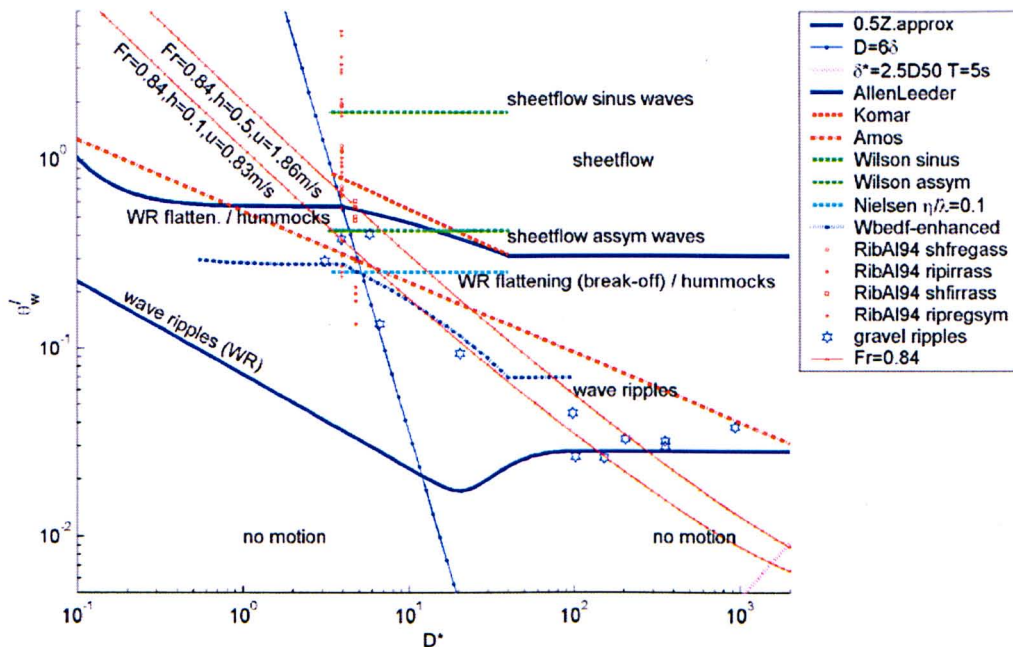
Figure 2.8: Bed form classification diagram for waves. From Kleinhans (2005).

The bed state of sheet flow in waves is assumed to be similar to that of upper plane bed in a current. When the wave ripple stability field is entered from the sheet flow regime, hummocks (large scale, bulge type bed forms of the order of mega-ripples, but without a clear lee side slope) are predicted. Two types of wave generated ripples have been distinguished. Smaller ripples, which encompass the well known relatively steep, small ripples and are known as short wave ripples, with heights of the order of 0.01 to 0.05m and lengths of the order of 0.2 to 0.5m. Larger size ripples are known as large wave ripples with heights of the order of 0.01 to 0.02m and lengths of the order of 0.5 to 2.0m. These are generally low amplitude, gently sloping long wavelength features and are usually associated with large wave orbital excursions.

2.3.5 Bed forms in currents and waves

Bed forms generated by the combined action of waves and currents display features of both hydraulic effects. If the wave component dominates then the bed forms are similar to fully developed wave

related bed forms. As the current component gains in strength, the bed forms become more asymmetrical and larger in height and length, especially in the case of an opposing current (van Rijn, 1993). The large wavelength of dunes, should mean, in theory that they would be unaffected by wave action. However, the oscillatory motion of waves does make the sediment more mobile than might otherwise be the case, which can have an effect on dune geometry (Sleath, 1984). In combined waves and currents the suspended load can be dominant even at small current velocities. As the suspended load increases the sand dune height decreases and the length increases, causing the sand dune steepness to drop rapidly with increasing current velocity (Fredsoe and Deigaard, 1992). Kleinhans (2005) has evaluated existing bed classification diagrams and proposed a new general classification diagram for wave and current generated bed forms (Figure 2.9). This is based on non-dimensional grain-related Shields parameters for currents (θ'_c) and waves (θ'_w) based on a D_{50} of $210\mu m$.
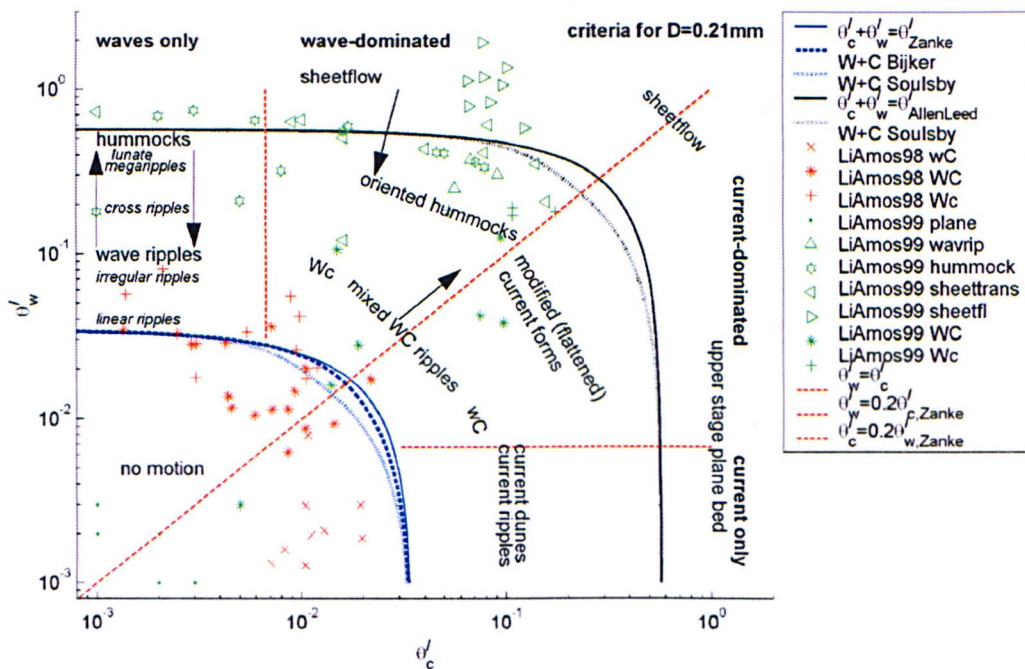
Figure 2.9: Bed form classification diagram for waves and currents. From Kleinhans (2005).

Kleinhans (2005) definitions of bed form type are given in Figure 2.10. For combined waves and currents, three bed state stability fields and a number of transient bed states are defined by two functions: incipient motion and the transition to upper plane bed or sheet flow. Figure 2.9 is essentially three dimensional, however the grain size influence is limited and the diagram is plotted for an average grain size of $210\mu m$. Regions of dominant waves, currents or waves plus currents are indicated by the ratios of wave and current Shields values. The influence of waves or currents is assessed by the ratios of wave or current Shields values with the critical current or wave Shields values, respectively (Kleinhans, 2005). van Rijn (1993) stated that sand dunes can be either symmetrical with an almost

trochoidal shape or slightly asymmetrical with a gentle stoss slope and a steeper lee slope. Symmetrical sand dunes are thought to occur under symmetrical tidal conditions and are not expected to migrate significantly, whereas asymmetrical sand dunes are associated with net sediment transport in the direction of the largest tidal velocity. Mega ripples can often be found migrating over the sand dunes and wave induced ripples can be present on the mega ripples during rough weather conditions.

Bed state name	Tentative bed state definition
Lower stage plane bed	plane bed with maximum roughness lengths of $O(d_{50})$, (excluding biogenic features), no or marginal motion of sediment
Upper stage plane bed	plane bed with maximum roughness lengths of $O(d_{50})$; much sediment suspension and a sediment layer of several d_{50} thick in motion by the flow, associated with large orbital and/or current flow velocities but subcritical flow (Fr~0.8), containing parallel lamination
Upper flow regime, antidunes	plane or undulating bed with undulations moving against the flow direction, associated with critical flow (plane bed, Fr~0.84) or supercritical flow (Fr~1)
Current ripples	linguoid bedforms with maximum length $O(0.4$ m) and height $O(0.02$ m), equilibrium dimensions are independent of flow conditions, non-equilibrium form may be straight-crested, associated with hydraulic smooth flow (Re•<11.6) or d_{50}<0.7 mm, containing small-scale cross-stratification
Current dunes	approximately triangular cross-sections but often convex-upward stoss sides; lee sides commonly at angle of repose and vortex shedding; observed height and length from smaller than current ripple sizes to $O(1$ m) high and $O(100$ m) long, equilibrium dimensions depend on flow conditions, e.g. dune height is 0.15-0.35 of water depth, associated with hydraulic rough flow (Re•>11.6) or d_{50}>0.7 mm, containing large-scale cross-stratification.
3D vs 2D dunes	2D dunes are straight or wavy-crested with small variations in dune top height and trough scour depth, whereas 3D dunes are lunate, cuspate or linguoid with much variation in dune top height and trough scour depth; transition 2D to 3D is associated with sediment mobility or, alternatively, 2D dunes are not in equilibrium with the flow
Wave ripples	concave-upwards, two-sided (or more) slip faces; may be straight-crested in sand of d_{50}<0.5 mm and calm conditions, but otherwise highly irregular; when sharp-crested with top angles approximating the angle of repose, there is also vortex shedding from the tops
Hummocks	convex-upwards, semi-spherical forms in an irregular spatial pattern; observed heights $O(0.1$ m) and lengths $O(1-10$ m), with much sediment suspension but no strong vortex shedding; associated with large orbital flows possibly combined with small currents but origin is unclear; containing Hummocky Cross-Stratification (HCS); semi-parallel lamination in undulating bands
Mixed flow ripples	bedforms with characteristics of both flow and current bedforms, e.g., weak current action on wave bedforms in following or opposing current causes skewness in the current direction; perpendicular small currents and waves give current ripples in the troughs of wave ripples; weak wave action on current bedforms causes rounding; equal current and wave action commonly causes irregular bedforms
Long wave ripples	wave ripples larger than commonly found wave ripples while both are simultaneously active and stable; origin is unclear but possibly related to short wave ripples or similar to skewed hummocks
Megaripples	in currents probably equal to dunes; in waves origin is unclear but possibly similar to skewed hummocks in deeper water

Figure 2.10: Bed state definitions for waves and currents. From Kleinhans (2005).

2.3.6 Bed form roughness

Bed forms are a principal cause of hydraulic roughness for flow over sedimentary beds and can drastically affect the flow field in the near bed region (van Rijn and Walstra, 2003), due to the form drag they generate from the pattern of dynamic pressure distribution over the bed form surface (Soulsby, 1997). These features will impact on transport rates by increasing the amount of turbulence in the lower layers of flow, which will enhance suspended sediment transport (Dyer, 1986; King, 1959; Nielsen, 1992). The scale of the bed form is directly related to the effect on the flow (Nielsen, 1981). For current generated ripples the total stress is usually obtained from the Nikuradse roughness k_s. Larger features such as mega-ripples and dunes create turbulent vortices which will affect the distribution of total bed shear stress and the mean flow velocity (Yalin, 1997). Depending on the height above the bed a different roughness element impacts on the flow, whether that is from ripples, mega-ripples or

dunes. However the total bed shear stress and the mean flow are affected by a total roughness of all the roughness elements combined. Accurate prediction of sand transport rates in the coastal zone is reliant on the methods used to calculate the bed roughness (Davies and Villaret, 2002, 2003*a,b*; van Rijn, 1984*c*).

van Rijn (2007*b*) proposed formulae to predict bed roughness directly from the hydrodynamic forcing. The roughness length is predicted for ripples ($k_{s,r}$), mega-ripples ($k_{s,m}$) and dunes ($k_{s,d}$) separately and then combined to form a total bed roughness. The formulae used are dependent on the mobility parameter ψ where

$$\psi = \frac{\bar{u}}{gsD_{50}} \tag{2.22}$$

and a granular coefficient f_s to reduce k_s at large grain sizes, where

$$f_s = 0.25(D_{gravel}/D_{50})^{1.5} \text{ for } D_{50} > 0.25D_{gravel} \tag{2.23}$$

and

$$f_s = 1 \text{ for} D_{50} \leq 0.25D_{gravel} \text{ where } D_{gravel} = 2mm \tag{2.24}$$

Ripples are assumed to be fully formed in the low flow regime ($\psi \leq 50$) and washed out in the high flow regime ($\psi > 250$) with the only contribution to k_s coming from moving grains in the sheet flow layer. In the transitional regime ($50 < \psi \leq 250$) a linear decay curve is assumed so that

$$
\begin{aligned}
k_{s,r} &= 150f_sD_{50} & \psi \leq 50 \\
k_{s,r} &= (182.5 - 0.652\psi)f_sD_{50} & 50 < \psi \leq 250 \\
k_{s,r} &= 20f_sD_{50} & \psi > 250 \\
k_{s,r} &= 20D_{silt} & D_{50} < D_{silt}
\end{aligned}
\tag{2.25}
$$

The contribution of mega-ripples, as well as dunes, to the bed roughness $k_{s,m}$ is not calculated from bed form dimensions but estimated directly from empirical experiments, related to ψ and h so that

$$k_{s,m} = 0.0002 f_s \psi h \qquad\qquad \psi \leq 50$$
$$k_{s,m} = (0.011 - 0.00002\psi) f_s h \qquad 50 < \psi \leq 550 \qquad (2.26)$$
$$k_{s,m} = 0.02 \qquad\qquad \psi > 550 \text{ and } D_{50} \geq 1.5 D_{sand}$$

Dunes produce the greatest contribution to the total hydraulic roughness of the bed. Dunes have a significant influence on current speeds due to their ability to cause flow separation and increasing turbulence downstream of the dune crest.

$$k_{s,d} = 0.0004 f_s \psi h \qquad\qquad \psi \leq 100$$
$$k_{s,d} = (0.048 - 0.00008\psi) f_s h \qquad 100 < \psi \leq 600 \qquad (2.27)$$
$$k_{s,d} = 0 \qquad\qquad \psi > 600$$

2.4 Sediment transport

There are two main modes of sediment transport, referred to as bed load and suspended load. Bed load can be defined as sediment which travels in more or less continuous contact with the bed, supported by inter-granular collisions and fluid lift forces, rather than fluid turbulence (Wilson, 1966; Fredsoe and Deigaard, 1992). Suspended load can be considered as the transported sediment which is predominantly supported by the upward components of fluid turbulence.

2.4.1 Bed load transport

Bed load transport occurs when the bed-shear velocity just exceeds the threshold of motion. During bed load transport sediment grains will be sliding, rolling and saltating along the bed (van Rijn, 1984a). This mode of transport is dominated by gravitational forces, as the grains are supported by inter-granular collisions and fluid lift forces (Bagnold, 1973). Bed load is the dominant mode of transport for low flow rates or large grain sizes (Soulsby, 1997). The bed load transport rate can be described by two dimensionless parameters, namely the dimensionless grain size D_* and a transport parameter T

$$D_* = D_{50} \left[\frac{(s-1)g}{v^2} \right]^{1/3} \qquad (2.28)$$

$$T = \frac{(u'_*)^2 - (u_{*cr})^2}{(u_{*cr})^2} \qquad (2.29)$$

where D_{50} is the median grain size, s is the specific density (ρ_s/ρ), g is the gravitational acceleration, ν is kinematic viscosity, u'_* is a skin friction velocity term and u_{*cr} is the critical bed shear velocity derived from the Shields parameter. Bed load transport will still occur in stronger flows which exceed the threshold for suspension, but a greater quantity of sand will be carried into suspension, especially for finer grains. A small change in flow velocity or bed roughness can cause a dramatic change in the bed load transport rate, due to the sensitivity to the variation in the shear velocity. Sediment grains are immediately deposited when the flow becomes too weak to sustain transport. Bed evolution may depend more strongly on the bed load component of transport even when suspension is dominant, due to the immediate response of the bed load transport to flow conditions (Soulsby and Damgaard, 2005).

2.4.2 Suspended load transport

Suspended load transport occurs when the bed-shear velocity exceeds the particle fall velocity (van Rijn, 1984b). The suspension of sand by waves, which is a non-linear process, is dependent on many factors, including the wave height, grain size and presence of bed forms (Vincent and Hanes, 2002). The proportion of sediment carried in suspension is generally much larger than the bed load transport, making the suspended load an important contribution to the total load sediment transport rate (Soulsby, 1997).

A reference concentration and concentration profile are required for computations of flow conditions involving suspended load transport. There is a rapid increase in concentration near to the bed, therefore the reference concentration is taken from where suspension joins the bed load layer (Dyer, 1986; van Rijn, 1984b). The Rouse concentration profile can be used to obtain the vertical distribution of sediment concentration in unidirectional flows. Under combined wave-current conditions the following modified Rouse equations can be used (Li et al., 1996)

$$c_z = c_{\delta w}(z/\delta_w)^{-\alpha_s} \text{ for } z > \delta_w$$

$$c_z = c_{ref}(z/z_0)^{-\alpha_s} \text{ for } z < \delta_w \qquad (2.30)$$

where c_z is the mean suspended sediment concentration at a height z above the bed, δw is the depth of the wave boundary layer, c_{δ_w} is the mean suspended sediment concentration at the top of the wave

boundary layer, c_{ref} is the reference concentration at a height ref, z_0 is the bottom roughness and α_s is the depth dependent suspension parameter

$$\alpha_s = \gamma_s w_{s1}/\kappa u_{*c} \text{ for } z > \delta_w$$

$$\alpha_s = \gamma_s w_{s2}/\kappa u_{*cw} \text{ for } z < \delta_w \tag{2.31}$$

in which γ_s is an empirical constant set to 0.74, w_{s1} and w_{s2} are the sediment grain settling velocities above and below the wave boundary layer respectively, κ is von Karman's constant (0.40), u_{*c} is the current shear velocity and u_{*cw} is the wave-current shear velocity.

The suspended load is mainly controlled by the settling velocity and the sediment diffusion coefficient (Fredsoe and Deigaard, 1992; van Rijn, 1984b). Hindered settling and turbulence damping is caused by grain interactions and occurs at high sediment concentrations (Nielsen, 1992; Soulsby, 1997; van Rijn, 1993). Near-bed concentrations are increased by up to two orders of magnitude through wave motion, experiencing maximum values when the direction of propagation is normal to that of the current flow (Davies, 1992; van Rijn and Kroon, 1992). The rate of suspended load transport q_s is calculated from the integral

$$q_s = \int_{ref}^{h} c(z)U(z) \tag{2.32}$$

where $c(z)$ is the concentration profile, $U(z)$ is the velocity profile, h is the water depth and z is the near-bed reference height (Soulsby, 1997).

2.4.3 Bijker's total load transport model

The total transport rate can be determined from an empirical formula or as the summation of bed load and suspended load transport rates, after both modes of transport have been calculated (Soulsby, 1997). The Bijker (1992) total transport model is widely used for waves and currents. Bijker's (1992) model was developed from classical transport concepts of bed load and suspended load for use offshore in combined current and wave conditions. Initially Bijker's model considered the bed load transport component q_b in steady flow (Equation 2.33). The skin friction component of the bed shear stress was used to calculate the bed load transport rate (q_b) based on the equivalent roughness ($k_s = D_{90}$ where 90% of the sediment by volume has a grain size smaller than D_{90}). Further consideration of wave-current interaction and the associated bed shear stress is given in Section 5.1.

$$q_b = bD_{50}\bar{u}\frac{\bar{u}}{C_h}\sqrt{\mu g}\exp\left[-0.27\frac{sD_{50}C_h^2}{\mu\bar{u}}\right] \tag{2.33}$$

where b is an exponentially derived coefficient, D_{50} is the median grain size, $\bar{u}$ is the depth averaged velocity, C_h is the Chezy coefficient, μ is a ripple factor, s is the relative density $(\rho_s/\rho - 1)$ and g is acceleration due to gravity. This bed load transport calculation is scaled by an experimentally derived coefficient 'b', normally taken as $b = 5$. As with other practical transport formulations, the presence of ripples is accounted for through the use of k_s, where the total bed shear stress is calculated using $k_s = \max(D_{90}, \eta)$ in which the ripple height (η) determination is left to the user (Davies and Villaret, 2002). The associated suspended transport component q_s is based on a reference concentration derived from the bed load transport q_b and implemented at height $z = k_s$. A standard Rouse concentration profile is applied above this level, with Rouse number

$$R = \frac{w_s}{(\beta_{sp}\kappa u_*)} \tag{2.34}$$

where u_* is the friction velocity based on the total bed shear stress, w_s is the sediment settling velocity, β_{sp} is a constant and κ is the Von Karman's constant (0.4). The suspended transport q_s is calculated by

$$q_s = 11.6\sqrt{\frac{\tau_c}{\rho}}rc_aI \quad \text{where } I = I_1\ln\left(\frac{33h}{r}\right) + I_2 \tag{2.35}$$

where r is height above the bed of the current boundary layer, h is depth, τ_c is the current shear stress, ρ is the fluid density and I_1, I_2 are Einstein's integrals. The Einstein's integral factor I can be calculated using numerical integration, but is also tabulated by Bijker. The values of r for Bijker's model are taken to be equal to the thickness of the bed load layer which, as shown earlier, is set equal to the bed roughness k_s. The influence of waves are included by modelling the bed shear stress with a quadratic friction law (Section 2.2.2). The presence of waves will generate turbulence which will affect the currents and vice versa, enhancing both components of shear stress (Section 2.2.3).

The wave influence also increases the values in Einstein's integrals which leads on from Equation 2.35 so that

$$q_s = 1.83Iq_b \tag{2.36}$$

where suspended load q_s is directly proportional to the bed load q_b. Finally, the total sediment transport q_t is calculated as the summation of bed load q_b and suspended load q_s transport (Bijker, 1992)

$$q_t = q_s + q_b = q_b(1 + 1.83I) \tag{2.37}$$

This formula has been used in many models to compute sediment transport rates in engineering problems. However, one difficulty with the formulation of Bijker is that the mean shear stress for currents and waves combined is highly non-linear, particularly for waves superimposed on a weak current. This has the effect of causing the reference concentration to increase whilst decreasing the Rouse number at the same time, causing significant consequences for transport predictions (Davies and Villaret, 2000a). Figure 2.11 shows the non-linear behaviour of Bijker's mode, represented by a significant spread in the transport curves, with respect to waves. The total transport rates for current alone and current combined with four different wave cases are denoted by their respective symbols. The tendency for Bijker's model to under-predict transport rates in the current alone case is evident (Davies and Villaret, 2002).
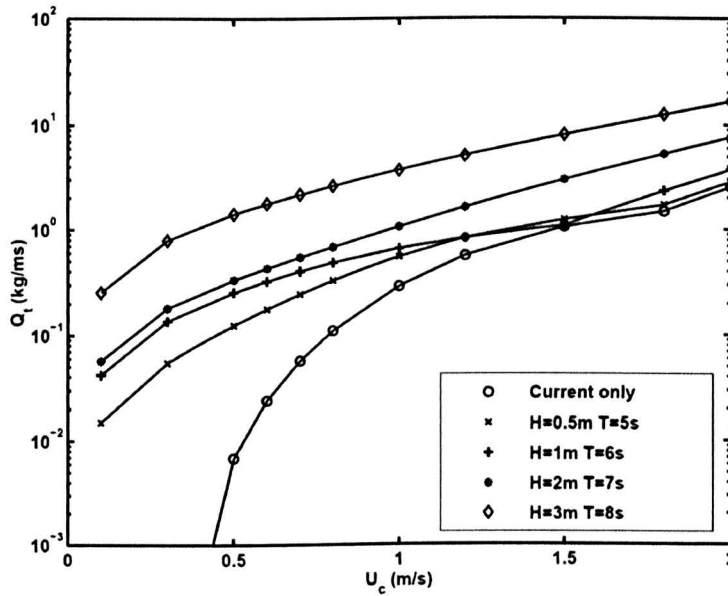
Figure 2.11: Total sediment transport rates predicted by the Bijker model (Davies and Villaret, 2002). The transport rate increases with the current speed until it causes the bed ripples to flatten out, at which point the increase in transport rates is reduced. For different wave cases this point occurs at different current strengths causing the lines to cross.

2.4.4 Dune migration

Migrating bed forms can offer a good estimation of bed load transport in the marine environment (Hoekstra et al., 2004), therefore tracking dune migration may be used to deduce bed load transport rates and directions. This has previously been done in riverine (Engel and Lam Lau, 1980, 1981; Ten Brinke et al., 1999) and tidal environments (Van Den Berg, 1987; Hoekstra et al., 2004; Masselink

et al., 2009).

Applying dune tracking techniques to marine systems will be significantly different to similar techniques applied to fluvial systems. This is especially true for intertidal conditions. Sediment transport under tidal conditions is not uni-directional, it will be either bi-directional due to a flat tidal ellipse or commonly multi-directional due to the tidal ellipse. Tidal flow is also, by definition, of a non-steady nature due to the continuously changing flow velocities and water depths. This will significantly affect bed form generation and growth while also causing lag effects (Dalrymple and Rhodes, 1995). Flow conditions can even change before a new equilibrium is reached for large scale bed forms (Allen, 1984). As a result dunes and ripples of varying sizes formed at different times may be observed together (Dalrymple and Rhodes, 1995). Another important factor is the presence of waves in open marine environments. Waves will act to modify or even dominate the flow field near to the bed. The interaction of waves and currents can generate more complex bed forms than those generated under current alone conditions. The influence of waves will be most pronounced when waves are superimposed on and obliquely orientated to a steady current (Hoekstra et al., 2004).

The theory that bed load transport rate could be reliably estimated from the bed form height and celerity was tested by Van Den Berg (1987). Bed form migration and hydraulic conditions were recorded simultaneously from sites in some of the larger Dutch and Belgian rivers, as well as the tidal channels of the Oostershelde and Ossenisse Shoal. Echogram surveys showed individual dunes, with wavelengths between 20 and 70m, which were easily identified migrating along a profile on consecutive daily surveys (Figure 2.12).
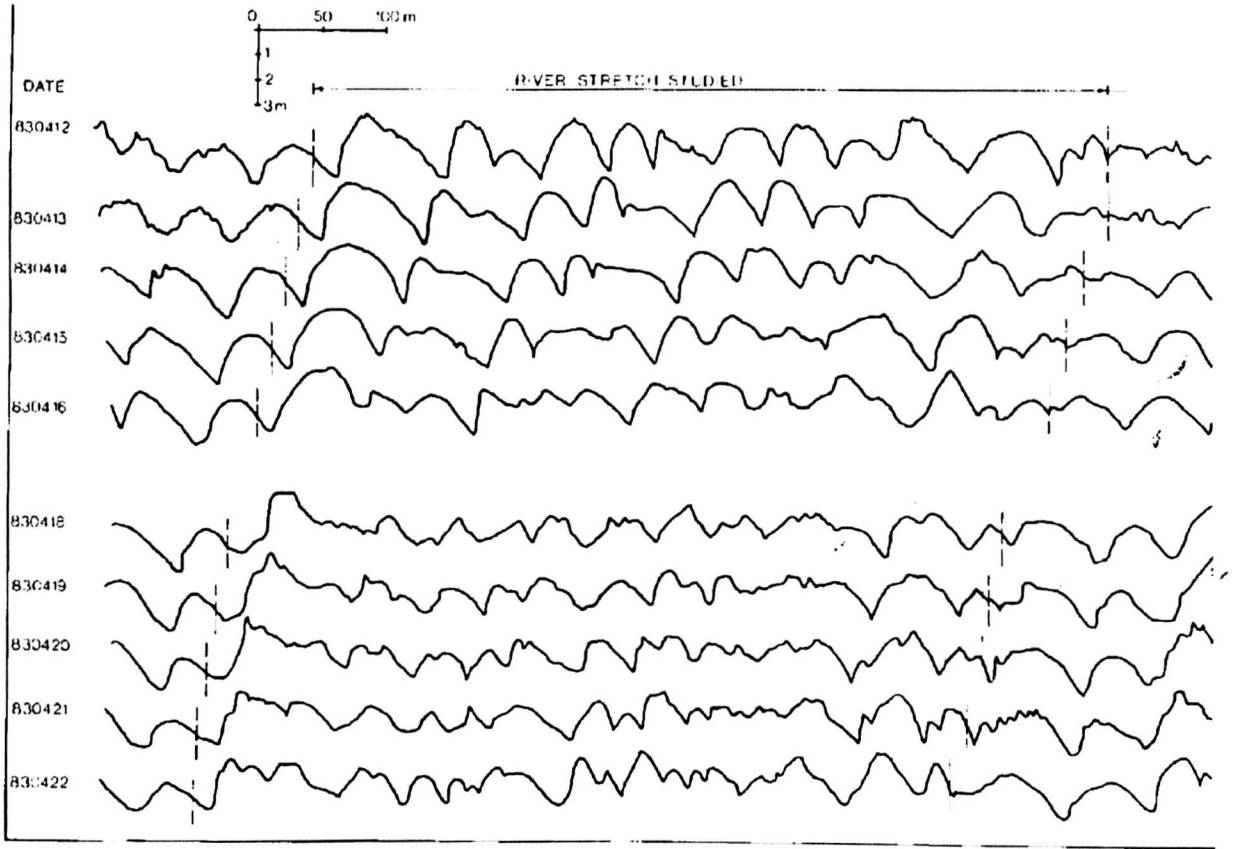
Figure 2.12: Dune migration shown on daily echograms from the River Waal, The Netherlands. From Van Den Berg (1987).

Bed load transport rates inferred from dune heights and migration rates were compared with two bed load prediction formulae. The simple formula to estimate bed load transport q_b from dune migration was

$$q_b = \rho_s(1-\varepsilon)\beta V_{mig}\eta \qquad (2.38)$$

where β is a bed form coefficient (0.6), ε is the porosity (0.4), V_{mig} is the dune migration speed and η is the bed form height. The two bed load formulae used for comparison are (van Rijn, 1984c)

$$q_b = 0.0351\rho D_{50}D_*^{-0.3}T^{1.5}u_*$$
$$\left\{ g + 2.6\log D_* - 8\left(\frac{\theta_{cr}}{\theta}\right)^{0.5} \right\} \qquad (2.39)$$

in which u_* is the bed shear velocity related to the sediment grains, and θ and θ_{cr} are the Shields

and critical Shields parameters, respectively. The second formula used by Van Den Berg (1987) was a modified version of the Kalinske-Frijlink (1951) bed load equation adapted for use in tidal environments

$$q_b = 5\rho_s D_{50} \sqrt{D_{50}g\Delta\theta} e^{-0.27/\theta} \tag{2.40}$$

The comparison of the two bed load transport formulae showed a relatively good correlation between predicted and observed transport as deduced from bed form parameters (Figure 2.13). However, the van Rijn (1984c) formula was shown to overestimate bed load transport at high transport stages and underestimate it at low transport stages. This trend was not observed when using the Kalinske-Frijlink (1951) formula, which predicted bed load transport within 0.5 to 2 times the measured rates for over 86% of the 43 sets of river data used. It should also be noted that measurements of bed load transport rate from bed form migration may be underestimated, as some grains do not come rest in the bed form trough, but either continue to roll along the bed, or are carried into suspension (Soulsby, 1997). This method does, however, give a reasonable estimate of the total bed load transport, as accurately measuring the bed load layer with bed load samplers, which is commonly 10 particle diameters in thickness, is significantly less reliable (van Rijn, 1984c).
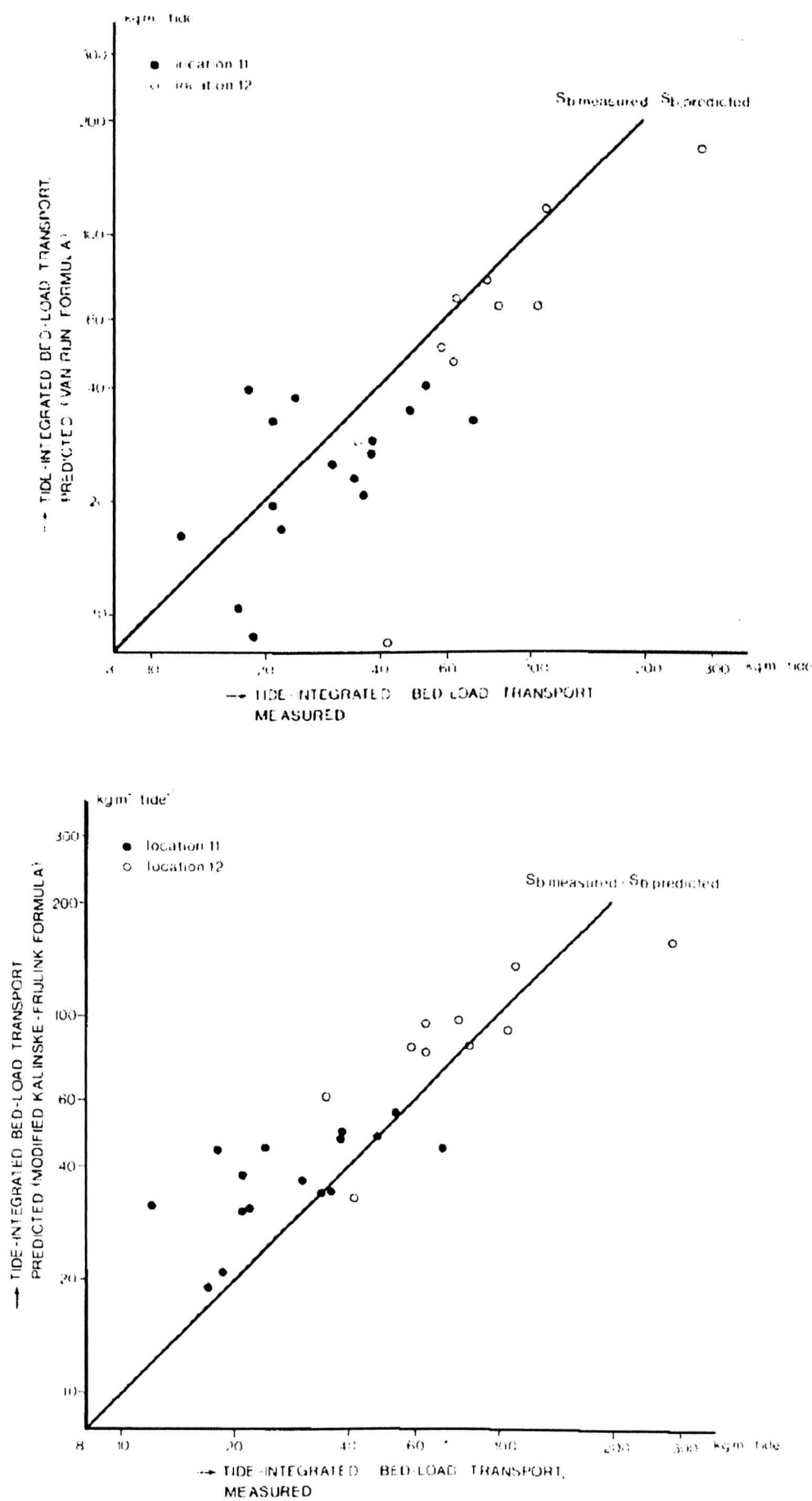
Figure 2.13: Comparison of tide integrated bed load transport measured by dune migration and predicted using bed load transport equations of Van Rijn (top) and Kalinske-Frijlink (bottom). From Van Den Berg (1987).

A similar study by Hoekstra et al. (2004) used dune tracking techniques to estimate bed load transport in the intertidal shoal in the mouth of the Teign estuary, Devon. The bed load transport formula of Ribberink (1998) was applied to field data from a ripple field and compared with bed load transport derived from dune migration. Encouraging results were achieved using the Ribberink (1998) formula, with a maximum difference between measurements and bed load calculations of 2, or 0.5 (Figure 2.14).
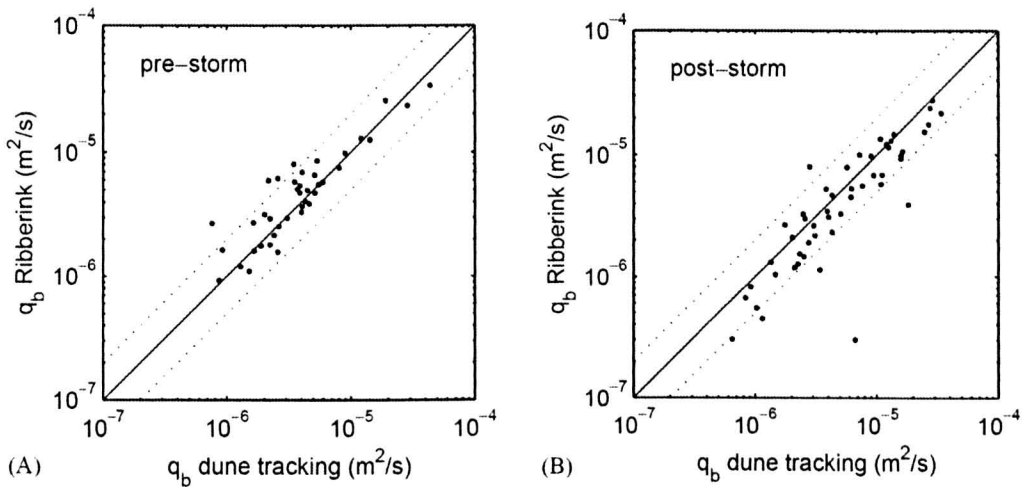
Figure 2.14: Comparison of bed load transport rates calculated using the Ribberink (1998) bed load transport formula and bed load transport rates based on dune migration in pre-storm (A) and post-storm (B) conditions. The solid line represents a 1:1 correlation and the dotted lines show 1:0.5 and 1:2 agreements From Hoekstra et al. (2004).

Hoekstra et al. (2004) stated that the presence of waves is a critical factor to the applicability of the dune tracking technique. Dunes were observed to start to migrate when wave orbital velocities exceeded 0.3ms^{-1}. Bed load transport increased by a factor of 2 when the wave orbital velocities reached $0.8-0.9 \text{ms}^{-1}$. The increase in bed load transport was the result of increased bed shear in the presence of waves.

Masselink et al. (2009) investigated the migration of subaqueous dunes over a 3 month period on an intertidal shoal near the mouth of the shallow mixed wave/tide dominated Avon Estuary on the English Channel coast of south west Britain. The dunes were surveyed every two weeks between 13/07/07-12/10/07. Dunes were characterised with heights of 0.05-0.2m and lengths of 5-10m. The repeat surveys of the dunes showed them to be migrating into the estuary, mainly during spring tides, with a total migration distance of 10-20m over the 3 month period. A comparison between volumetric transport rates, derived from dune migration rates and dimensions, and bed load equations shows that the theory significantly under-predicts the observations. Masselink et al. (2009) attributed this

to the modest flow velocities measured, stating that bed load predictors do no perform well near the threshold of motion. The importance of suspended load transport is shown with the application of the 'simplified' sediment transport model of van Rijn (1993) giving a ratio between suspended load and bed load transport of 3.5. The main conclusion of the Masselink et al. (2009) study was that accurate and well designed process measurements of dune dynamics and tidal currents can provide useful information for long term evolution of shallow, flood dominant estuaries.

2.4.5   Estimating bed load transport from paired bed elevation profiles

Gaeuman and Jacobson (2007) developed alternative algorithms for estimating bed load transport from paired longitudinal profiles of bed topography. Dune morphology and migration data were obtained from bed profiles extracted from survey data in the Missouri River, USA. Initially, bed load transport is estimated from bed form migration velocity and bed form dimensions using

$$q_b = 0.5(1 - \varepsilon)\eta\frac{dx}{dt} + C_1 \tag{2.41}$$

where ε is the porosity of the sediment composing the bed forms, η is the crest to trough amplitude of the bed form and dx is the down-stream propagation distance of the bed form during the time interval dt. The numerical coefficient 0.5 implies that the bed forms are migrating with a constant triangular form. Subsequent authors (Kostaschuk et al., 1989; Villard and Church, 2003) replaced 0.5 with a coefficient β which accounts for deviations of bed form shape from an idealised triangle. C_1 represents the portion of the bed load flux which does not contribute to the downstream translation of the bed form, as would be the case for particles which are transported from one bed form crest to the next bed form downstream with no residence time on the intervening slipface (Gaeuman and Jacobson, 2007). Field and laboratory experiments, as well as modelling results, suggest that C_1 may commonly account for more than half of q_b (Mohrig and Smith, 1996).

As a development of this method, Gaeuman and Jacobson (2007) estimate the bed form volume directly from the bed profiles, rather than on the basis of maximum height and assumed shape factor. An algorithm defined a datum representing the base of the mobile part of the bed by connecting successive bed form trough points along each profile with a straight line. The area between the datum and the bed surface is numerically integrated, and a division by length gives a mean height for each bed form. The time average of these mean heights η_m is calculated for use in a modified version of

Equation 2.41, in which no shape parameter is required

$$q_b = (1 - \varepsilon)\eta_m \frac{dx}{dt} \qquad (2.42)$$

A final method was developed to eliminate the need to identify and correlate individual dunes. Instead, only the positions of the most upstream and most downstream troughs in a section of paired profiles were required (Figure 2.15). This method implements a budgeting approach where the local volumetric bed load flux per unit width at any point along the profile is related to upstream volumes of erosion and downstream volumes of deposition. At each point along the paired profile the bed elevation at time $t_2(z_{x,2})$ is subtracted from the bed elevation at time $t_1(z_{x,1})$ to give dz_x. Erosion is recorded where dz_x is positive and deposition is recorded where dz_x is negative. Gaeuman and Jacobson (2007) found more accurate results to be obtained when calculating bed form volumes numerically, without the need for a shape factor. Eliminating the need to identify individual bed forms when calculating local sediment flux on the basis of local erosion and deposition and the principle of mass continuity was found to generally agree with transport derived from individual bed form identification.
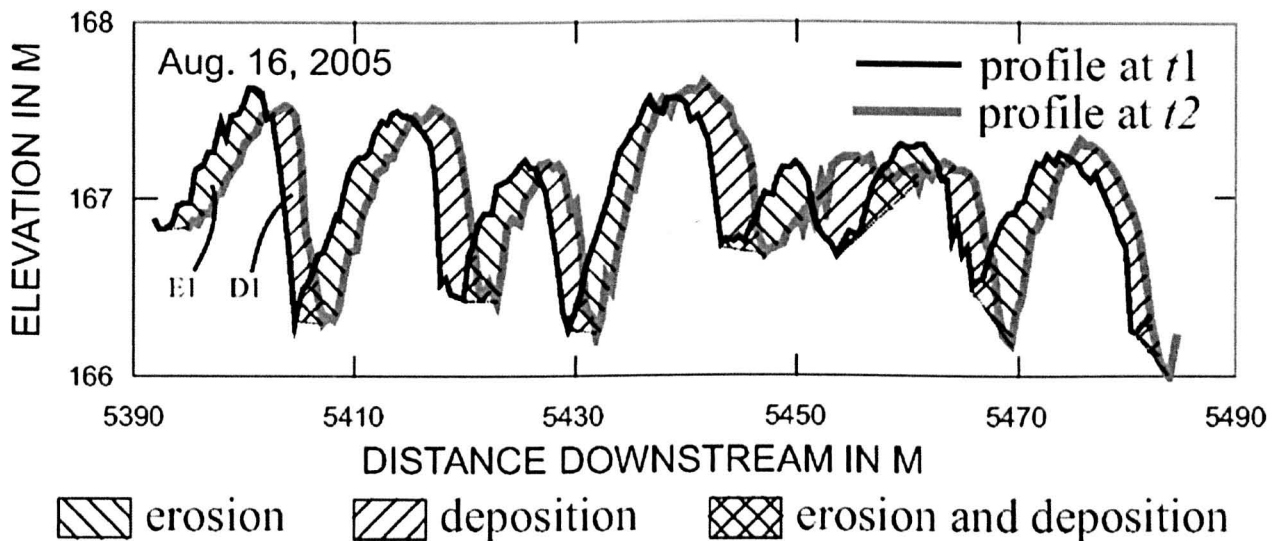
Figure 2.15: Erosion and deposition shown along paired bathymetric profiles. From Gaeuman and Jacobson (2007).

2.4.6 Mass conservation

Cloin (1998) applied a mass conservation technique to calculate the total net sediment transport along an experimental test section. The bed elevation was measured with a bed profiling system before and after experimental runs in the Large Oscillating Water Tunnel (LOWT) of Delft Hydraulics. Sand traps were installed in the experimental set up so that the weight of trapped sand can be used to solve

the mass conservation equation. Sand traps were installed at both ends of the LOWT so that the sediment continuity equation can be solved from the right and the left side, resulting in two net sediment transport rates for each experimental run. In principle the following equations were used:

measured porosity

$$1 - \varepsilon = \frac{M_{TOT}}{\rho_s \Delta V_{ip}} \frac{\rho_s}{\rho_s - \rho_w} \tag{2.43}$$

left trap estimation

$$q_L = \frac{\Delta V_{lip}(1 - \varepsilon)}{\Delta t} - \frac{M_L}{\rho_s \Delta t W} \frac{\rho_s}{\rho_s - \rho_w} \tag{2.44}$$

right trap estimation

$$q_R = \frac{\Delta V_{rip}(1 - \varepsilon_0)}{\Delta t} - \frac{M_R}{\rho_s \Delta t W} \frac{\rho_s}{\rho_s - \rho_w} \tag{2.45}$$

where M is the under water weight of sand collected in the total $(_{TOT})$, right $(_R)$ and left $(_L)$ sand traps, ρ_s is the density of sand, ρ_w is the density of water, Δt is the test duration, W is the width of the tunnel, ΔV_{ip} is the total eroded volume including pores from the left $(_{lip})$ or the right $(_{rip})$. This method gives two estimates of the actual occurring transport rate in the middle of the tunnel for a specific experimental run. Ideally, the left and right estimate should be of equal magnitude. However, measuring inaccuracies can cause differences to occur, therefore an average of the two estimates is taken.

2.5 Morphological modelling

2.5.1 The TELEMAC modelling system

TELEMAC is a computer modelling software system launched by the research and development department of Electricite de France (EDF) in 1987. A variety of modules are included within the modelling software which numerically simulate the hydrodynamics, sedimentology and water quality in two or three dimensions (Hervouet, 2007). For combined wave-current environments the three modules necessary are TELEMAC-2D, TOMAWAC and SISYPHE. These modules are written in Fortran-90 and operate in a PC or Unix environment. All modules are based on finite element techniques which utilise an unstructured flexible mesh of triangles to discretise space through the computational domain. This allows the user to model large domains with no restriction on resolution,

including complex coastlines, with computational effort concentrated where it is required.

The hydrodynamic variables are simulated using TELEMAC-2D, which solves the depth averaged Saint-Venant shallow water equations in two dimensions (Galland et al., 1991; Hervouet and Bates, 2000). This model has been used with considerable success and is widely regarded as an appropriate model for application to estuarine environments (Hervouet and Bates, 2000). The hydrodynamic equations computed by TELEMAC-2D, including the continuity equation (Equation 2.46), momentum equations (Equations 2.47 & 2.48) and tracer conservation (Equation 2.49) are as follows

$$\frac{\delta h}{\delta t} + u.\vec{\nabla}(h) + h\mathrm{div}(\vec{u}) = S_h \tag{2.46}$$

$$\frac{\delta u}{\delta t} + \vec{u}.\vec{\nabla}(u) = -g\frac{\delta Z_b}{\delta x} + S_x + \frac{1}{h}\mathrm{div}(h\nu_t\vec{\nabla}u) \tag{2.47}$$

$$\frac{\delta v}{\delta t} + \vec{u}.\vec{\nabla}(v) = -g\frac{\delta Z_b}{\delta y} + S_y + \frac{1}{h}\mathrm{div}(h\nu_t\vec{\nabla}v) \tag{2.48}$$

$$\frac{\delta T_r}{\delta t} + \vec{u}.\vec{\nabla}(T_r) = S_T + \frac{1}{h}\mathrm{div}(h\nu_T\vec{\nabla}T_r) \tag{2.49}$$

where h is water depth, u and v are velocity components, T_r is the non-buoyant tracer, g is gravity, ν_t and ν_T are the momentum and tracer coefficients, Z_b is the bed elevation, t is time, x and y are horizontal space coordinates, S_h is the source or sink of fluid, S_T is the source or sink of tracer and S_x and S_y are the source or sink terms of momentum in the dynamic equations. Within these equations h, u, v and T_r are unknown parameters which are solved for. The coriolis effect, turbulence and wetting and drying of tidal flats are some of the important features included in the model code (Hervouet, 2007).

Waves are simulated by TOMAWAC; a third generation spectral wave model. This solves the evolution equation for the directional spectrum of wave action to simulate wave propagation in the coastal zone (Hervouet, 2007). To do this TOMAWAC directly solves the general equation for the conservation of the directional spectrum of wave action by expressing it as a function of the directional spectrum variance, $F(x,y,\theta,f_a)$. Using Cartesian coordinates the directional spectrum of variance becomes a function of the x and y coordinates, the wave propagation (θ) and its absolute frequency (f_a)

$$\frac{\delta(BF)}{\delta t} + x\frac{\delta(BF)}{\delta x} + y\frac{\delta(BF)}{\delta y} + \theta\frac{\delta(BF)}{\delta \theta} + f_a\frac{\delta(BF)}{\delta f_a} = BS(x,y,\theta,f_a,t) \qquad (2.50)$$

where $B = C_g/\omega k$, with C_g being the wave group velocity, ω is the angular frequency, k is the wave number and S represents the source terms in the spectrum, which include wind input, white capping and bottom friction. TOMAWAC allows many interactions to be simulated, of importance for this research is the interaction of waves and tides/currents. Other features included are; wave shoaling, refraction of the wave field due to bathymetry and wind generated effects on wave growth.

The module SISYPHE calculates sediment transport magnitudes and directions by combining the previous simulations of TELEMAC-2D and TOMAWAC. SISYPHE can be run in an internally coupled mode so that the simulation runs alongside a simultaneous TELEMAC-2D simulation. SISYPHE calculates sediment transport as bed load or total transport, in an equilibrium, sediment continuity mode, using a choice of seven transport formulae. Suspended load is determined by the implicit calculation of a suspended sediment concentration profile and the use of an advection-diffusion transport algorithm.

Running SISYPHE and TELEMAC-2D in a coupled mode allows morphological change to be simulated by passing data between each module at a time step set by the user. Tidal and river flow data from TELEMAC-2D are passed to SISYPHE where they are used to calculate sediment transport magnitudes and directions, with the resulting local convergence or divergence of sediment flux causing bed accretion or erosion. This updated bed level is then passed back to TELEMAC-2D to be used for the next hydrodynamic computation, allowing the sea bed to evolve dynamically with a feedback between the bed morphology and the flow. SISYPHE uses two morphological models; an equilibrium local bed evolution model and an advection-diffusion model where suspended sediment can bypass grid cells and contribute to non-local morphological evolution. The equilibrium evolution model is a local sediment continuity equation (Exner's equation) so that the bed level results from a balance between solid matter entering and leaving an elementary volume (Hervouet, 2007)

$$(1-\varepsilon)\frac{\delta z_b}{\delta t} + \nabla(\vec{q}_s) = 0 \qquad (2.51)$$

where $\vec{q}_s$ is the sediment flux vector (m^2s^{-1}), Z_b is the bed level, t is time and ε is the bed porosity. When suspended sediment transport is enabled, SISYPHE calculates the suspended sediment concentration using an advection-diffusion scheme, based on semi-empirical expressions to account for non-equilibrium transport

$$\frac{\delta \bar{c}}{\delta t} + \bar{u}\frac{\delta \bar{c}}{\delta x} + \bar{v}\frac{\delta \bar{c}}{\delta y} = \frac{1}{h}\left[\frac{\delta}{\delta x}\left(hD_z\frac{\delta \bar{c}}{\delta x}\right) + \frac{\delta}{\delta y}\left(hD_z\frac{\delta}{\delta y}\right)\right] + \frac{(E_f - D_f)_{z=a}}{h} \qquad (2.52)$$

where h is the water depth, $\bar{u}$ and $\bar{v}$ are the depth-averaged flow velocities in the x and y directions, $\bar{c}$ is the depth-averaged sediment concentration, D_z is the sediment diffusivity coefficient, $E_f - D_f$ is the difference in net erosion (E_f) and net deposition (D_f) sediment flux, calculated at the interface between the suspended and bed load layer ($z = a$)

2.6 Remote sensing of coastal areas

The morphological behaviour of the coastal environment is becoming increasingly important due to human activities and changing environmental conditions. Therefore the development of a remote sensing technique to determine accurate bathymetric maps of the nearshore area, on a regular basis is of great interest for coastal engineers. A remote sensing technique can be conducted over a much larger area and is not as time consuming or expensive as ship borne methods. As this research project is interested in tracking the movement of large scale bed forms, it is possible to use proxy signals generated by these morphological features to monitor them remotely. For example waves will break over the shallower bathymetry of sand bars or dunes and will therefore allow the visualisation of the nearshore morphology. As waves break over underlying large scale bed forms a sharp contrast between bed form crest and trough results.

2.6.1 Video remote sensing

A technique commonly applied to detect the sharp contrast generated by breaking waves is by means of digital video cameras (Holland et al., 1997; Lippmann and Holman, 1989). Automated image collection, as in the ARGUS video system, allows high spatial and temporal data to be collected. Additionally, the use of wave breaking as an indirect measure for bed form morphology extends the applicability of the technique to more energetic conditions than possible with direct measurements of bed level. Van Enckevort and Ruessink (2001) found the cross-shore location of maximum video intensity to correspond well with underlying bar crest location, particularly when the crest location is defined as the location of maximum perturbation from a smooth underlying bed profile (Figure 2.16).
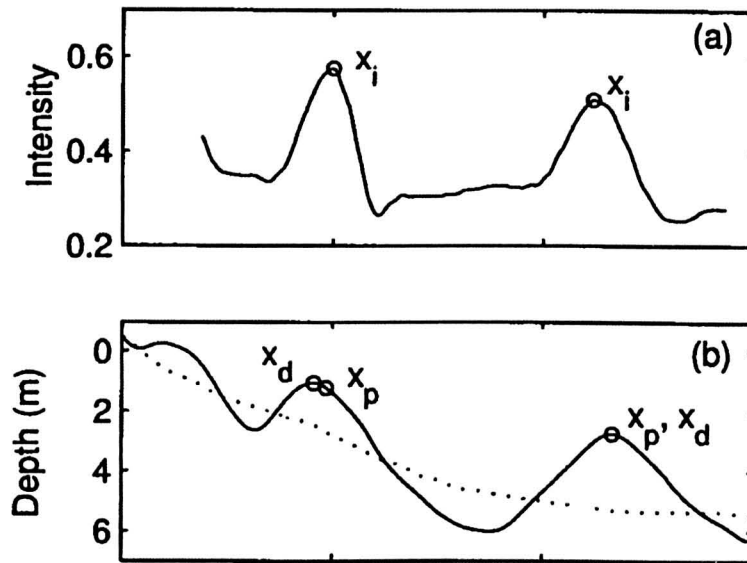
Figure 2.16: Example of ARGUS image intensity (a) and depth (b) with respect to cross shore distance. The crest positions of image intensity x_i and bed level x_p, x_d are shown (Van Enckevort and Ruessink, 2001).

Lippmann and Kannan (2003) and Worley et al. (1997) applied video techniques to map sand bars at high resolution and wide spatial coverage. Lippmann and Holman (1989) first demonstrated the capability of averaged video frames to locate and map a nearshore bar structure using foam produced by wave dissipation, producing high visual intensity, where waves break over submerged sand bars. Video techniques were initially used for morphology observations of shoreline and bar changes, before being expanded to characterise swash, particularly run up spectra, swash velocity and extreme run up (McNinch, 2007). There are, however, limitations to video based remote sensing techniques, most notably; requiring operation during day light, spatial coverage that is a function of camera elevation above the beach and impairment of video images by fog and rain. Also, during storm conditions, relict foam not directly associated with a breaking wave can cause complications for video imaging to identify the bar location.

2.6.2 Marine X-band radar

The use of radio detection and ranging (RADAR) for oceanographic remote sensing is also a well established technique for mapping nearshore bathymetry. The understanding and application of radar significantly advanced during the early part of World War II due to its military applications. Radar is an active imaging system, which is distinct from other passive imaging techniques such as digital cameras, that rely on reflected optical energy, and radiometers, which detect emitted energy. Radar systems emit an electromagnetic wave from the radar antenna, which propagates towards a target

where it is either reflected or absorbed and re-emitted (scattered).

Synthetic aperture radar (SAR) has been used to measure large scale intertidal bathymetry (Koopmans and Wang, 1994; Mason et al., 1998; Joo-Hyung et al., 2002), however as this is a satellite flown technique it is prohibitively expensive and impractical for routine monitoring. SAR images can provide high resolution images over wide areas, but they cannot create the dynamic information obtained from a sequence of images. Traditional in situ profiling techniques and video remote sensing designed for measuring the migration of bed forms are not practical during storm events (McNinch, 2007). An alternative technique, which is well developed although not extensively employed, is the use of marine X-band radar to remotely sense the nearshore environment (Ruessink et al., 2002).

Band designation	Nominal frequency range	Frequencies reserved for radar use
HF	3-30MHz	
VHF	30-300MHz	138-144MHz, 216-225MHz
UHF	300-1000MHz	420-450MHz, 890-942MHz
L	1-2GHz	1.215-1.400GHz
S	2-4GHz	2.3-2.5GHz, 2.7-3.7GHz
C	4-8GHz	5.250-5.925GHz
X	8-12GHz	8.50-10.68GHz
K_u	12-18GHz	13.4-14.0GHz, 15.7-17.7GHz
K	18-27GHz	24.05-24.25GHz
K_a	27-40GHz	33.4-36.0GHz
mm	40-300GHz	24GHz, 77GHz

Figure 2.17: Standard radar frequency band designations from Bell (2005).

Radar systems are classified by the wavelength of their emitted frequency (Figure 2.17). X-band radar operates in the radio frequency range of 8-12.5 GHz and with wavelengths between 2.5-3.75cm, which corresponds to a 'centimetric' wave designation (IEEE, 1984). The importance of the X-band radar wavelength for remote sensing sea surface parameters through 'Bragg scattering' effects is dis-

cussed in further detail in Section 6.1.1. Due to the accuracy at detecting small objects, X-band radar is traditionally used for military weapon guidance as well as civil marine radar applications. The use of X-band radar to remotely sense ocean waves is based on a well documented relationship between scattering mechanisms generating radar sea spikes and breaking waves (Henderson and Lewis, 1998; Trizna and Carlson, 1996). Haller and Lyzenga (2003) state the most influential wave scattering mechanism as quasi-specular scattering from the face of steep waves, edge diffraction from wave crests, and Bragg scattering from the sea surface roughness. Recent studies have shown the capability of X-band radar to remotely measure nearshore wave characteristics (Bell, 1999; Haller and Lyzenga, 2003), infer bathymetry (Bell, 1999; Greidanus, 1997) and measure the position and morphology of nearshore bars from time-averaged images (Ruessink et al., 2002). The benefit of using X-band radar for monitoring coastal processes is that it is not limited by the time of day and has the capacity to record data through moderate levels of fog and precipitation. Haller and Lyzenga (2003) compared video and X-band data, finding that the radar was less sensitive to relict foam on the sea surface and required less tuning to determine breaking and non-breaking waves. Another advantage of X-band radar over video based techniques is that the radar does not require an elevated platform, or an airborne vehicle, which video does require. Also, due to the fact that the radar system outputs the azimuth and range, the deployment and morphology mapping is substantially simpler than video based systems, which require precise knowledge of its geometry, such as location, orientation, camera/lens distortion and focal length, to accurately determine coastal features of interest, such as the shoreline and bed forms (McNinch, 2007).

2.6.3 The WaMoS II system

The wave and surface current monitoring system, WaMoS II, was developed at the German GKSS Research Centre in 1995 and is commonly used on fixed offshore platforms and moving vessels, especially under extreme conditions (Young et al., 1985; Nieto-Borge et al., 1999; Hessner et al., 2001). WaMoS II digitally records successive radar images to obtain wave field information in space and time. The mean intensity of the sea clutter can then be removed from the images to minimize the static spatial and temporal contributions to the spectrum (Nieto-Borge et al., 1999). The standard WaMoS II software delivers unambiguous directional wave spectra and time series of the integrated standard wave parameters; significant wave height (H_s), peak wave period (T_p) and peak wave direction (θ_p) in real time (Hessner et al., 2008). These data can then be displayed at the PC which operates the WaMoS II system or it can be potentially transferred to other stations via the internet, LAN or other networking device.

2.6.4   Nearshore bathymetry from X-band radar

Ruessink et al. (2002) used time exposure images of X-band radar snapshots to determine the positions of sandbar crests, in a similar technique to that of Lippmann and Holman (1989), who applied analysed time lapse digital images from the ARGUS system. This method used the high intensity return from spray created by waves breaking over sandbar crests. When images are averaged over a long time exposure only the high intensity areas of consistently high backscatter remain visible, which allows bar crest locations to be estimated.
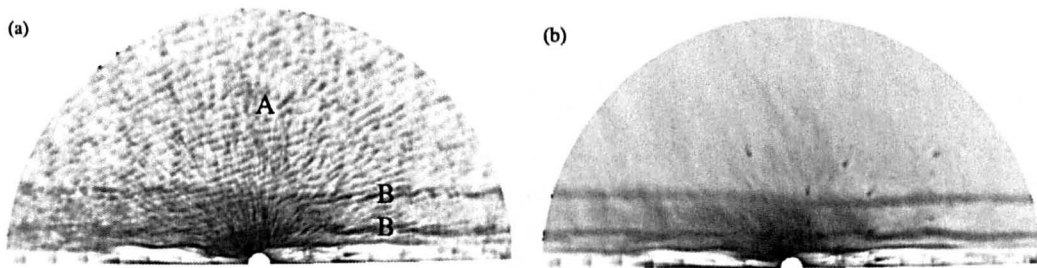
Figure 2.18: Snapshot radar image (a) showing Bragg scattering on the front faces of non breaking waves and mean radar image (b) using breaking waves to show the position of two sand bars. From Ruessink et al. (2002).

The dark, high intensity regions in the snapshot image (Figure 2.18 a) correspond to areas of resonant Bragg scattering from the front faces of capillary waves with respect to the radar. When a sequence of snapshot images are averaged over time, the backscattering signal from the capillary waves is averaged out, leaving a mean backscatter image, where areas of consistently high backscatter, such as breaking waves are more pronounced from areas of non-breaking waves. This can be seen in Figure 2.18 b where two sandbars are clearly visible. At successive alongshore coordinates Ruessink et al. (2002) use the cross-shore location of maximum radar intensity across a bar as the maximum intensity of that bar (Figure 2.19).
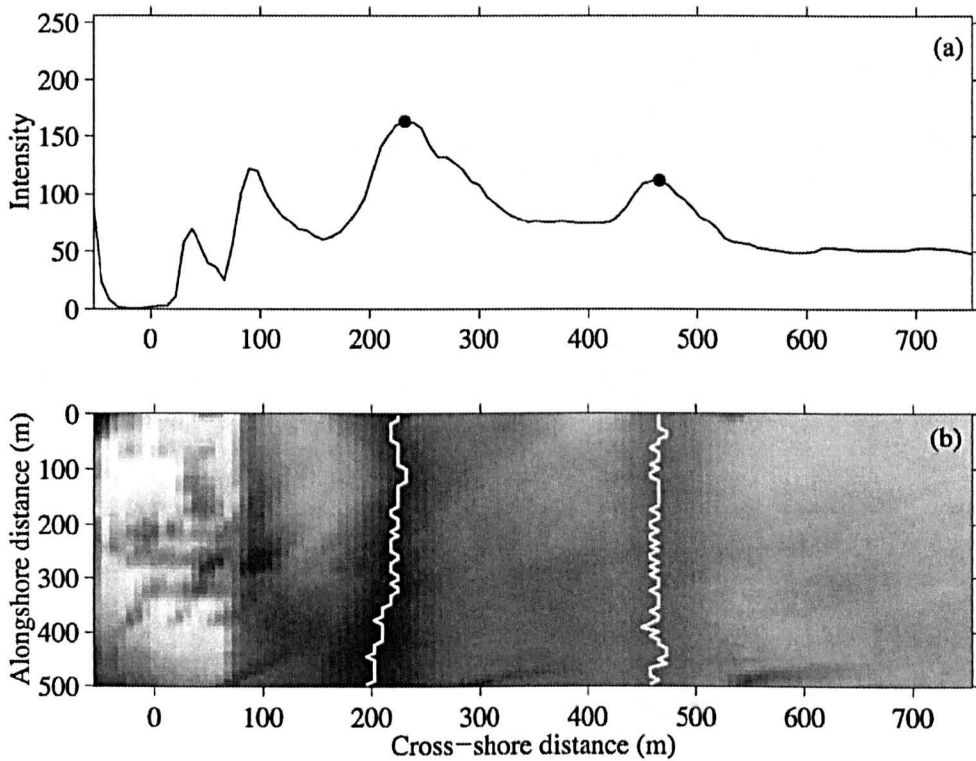
Figure 2.19: An example of cross-shore patterns in radar intensity (a), the black dots show the locations of maximum radar intensity which represent positions of the inner and outer sand bars. The time-averaged radar image is also shown with the inner and outer bar crest lines (b). From Ruessink et al. (2002).

Although this allows the position of bed forms to be identified it is limited to bed forms which induce waves to break, therefore limiting them to a specific depth or height. This technique also does not allow the height of the bed forms to be determined, which is essential when determining the bed load transport rate associated with the bed form migration. McLeish et al. (1981) used airborne radar observations to detect bed forms, created by the convergence and divergence of water currents flowing across changes in bottom depth. As water flows over large scale sea bed topography, the water surface experiences an acceleration and the wave energy is decreased, causing a change in radar reflectivity.

Takewaka (2005) use an X-band radar system installed on a research pier to determine shoreline positions and intertidal foreslopes over a 1.9km area in the longshore direction in Hasaki, Japan. Time averaged radar images (Figure 2.20) were analysed to estimate the horizontal position of shorelines. The water surface level is simultaneously measured at the pier and at a nearby fishery port to determine the elevation of the shoreline.
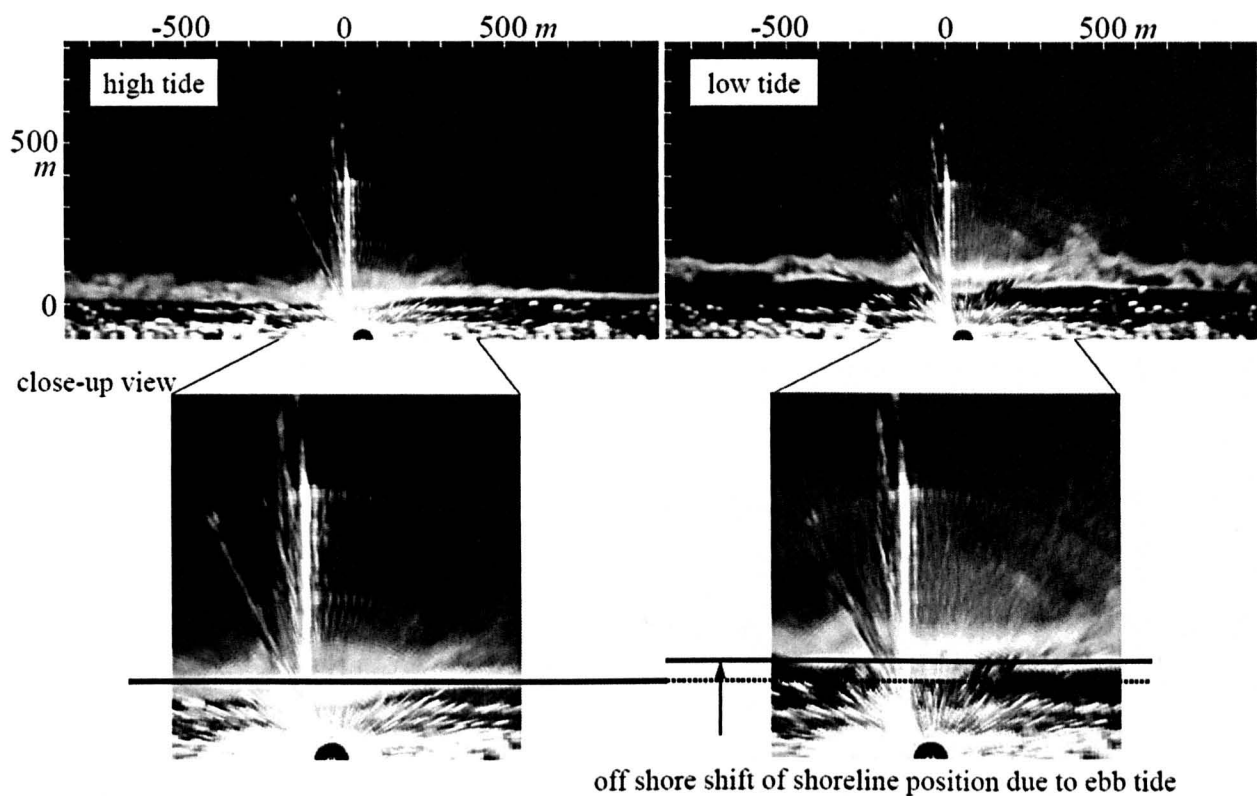
Figure 2.20: Time averaged X-band radar images at high tide (left, 06:00) and low tide (right, 10:00). From Takewaka (2005).

The horizontal water's edge in the time averaged radar images can be seen to correspond to the tide level (Figure 2.20). Takewaka (2005) extracted pixel intensities along a cross-shore line from the time averaged images to compare with the mean water level and the bottom profile (Figure 2.21).
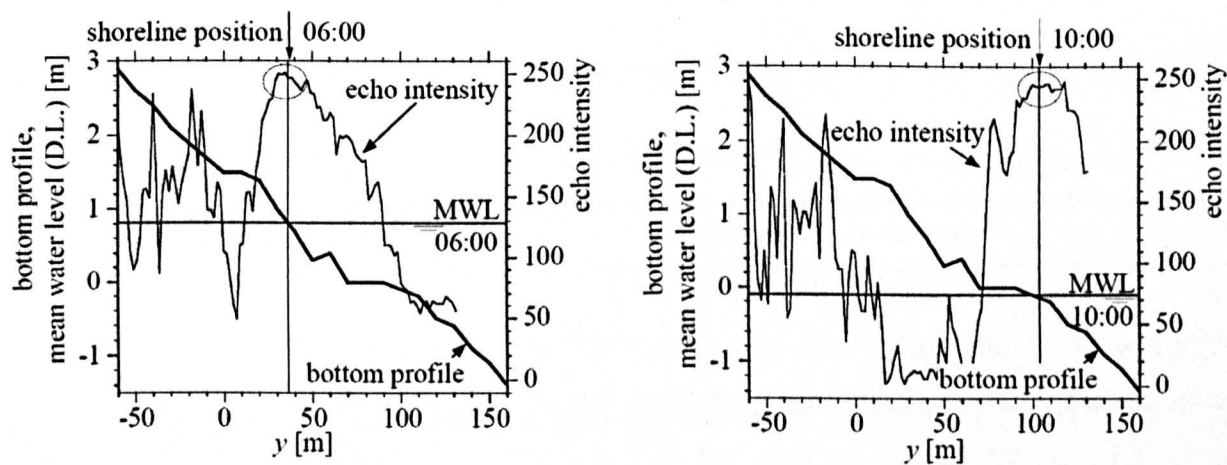
Figure 2.21: Cross shore pixel intensities extracted from time averaged radar images at high tide (left) and low tide (right). From Takewaka (2005).

46

The location of the peak in radar echo intensity can be seen to coincide with the intersection of the mean water level and the bottom profile. Takewaka (2005) determines the location of the shoreline by locating the peaks in the cross shore pixel intensity distributions. Local fittings of parabolic curves were then applied to the intensity distributions to determine the peak intensity locations. The mean foreshore slope of the concave beach profile is then defined as the slope given by the linear regression of the radar derived shoreline positions from high to low water.
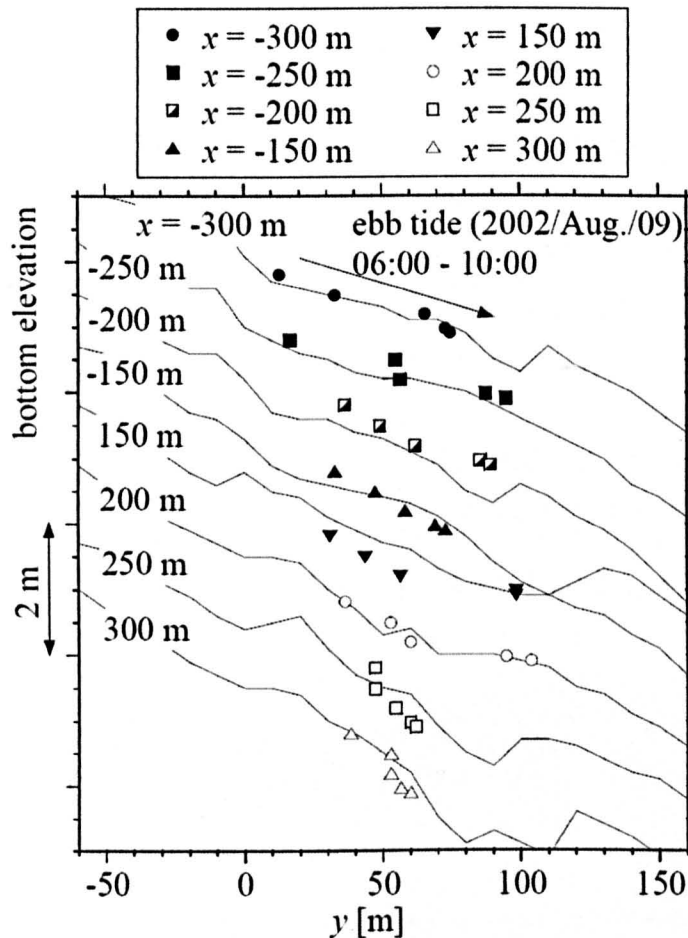
Figure 2.22: Comparison between radar measurements and surveyed results at different longshore positions. From Takewaka (2005).

Takewaka (2005) compares the intertidal morphology derived from radar measurements at high and low tide (Figure 2.20) with surveyed bathymetry profiles (Figure 2.22). The radar derived shoreline locations can be seen to follow reasonably well with the surveyed bottom profile, with horizontal shoreline positions reported to be measured within an error of 10m.

X-band radar has been used for many years to measure surface wave parameters (Heathershaw et al.,

1980; Nieto-Borge et al., 1999; Wolf and Bell, 2001). The principle behind this technique is to apply a three dimensional Fast Fourier Transform (FFT) to the individual pixels through time in a sequence of radar images, producing a wave number frequency spectrum. This information has then been used to determine coastal bathymetry (Bell, 1999; Bell et al., 2006; Ruessink et al., 2002; Hessner and Bell, 2009). A discrete 2-D Fourier transform technique is applied to the area imaged by the radar, to produce a three dimensional wavenumber (k) spectrum. A wave dispersion equation is then applied to this wavenumber spectrum so that the water depth (h) and 2D currents (U), which caused that wave behaviour, can be determined (Bell, 2005). The dispersion equation used is based on linear theory but also includes a modification for amplitude dispersion. This is to correct for the non-linear behaviour of waves with a large amplitude in shallow water which travel faster than linear theory alone can predict (Hedges, 1976). Trizna (2001) demonstrated that linear wave theory led to an over estimate of water depth in shallow water with high wave conditions, and that a non-linear approach would be more suitable. Bell (2001) also showed that non-linear behaviour of waves in shallow water due to amplitude dispersion was creating errors when calculating the water depth using depth inversion algorithms. There is also a correction for currents to account for the effect of Doppler shift on the waves, as waves travelling in a current will experience a shift to higher frequencies, while waves travelling against the current will experience a shift to lower frequencies. Once the wavelength, period and height of the waves have been determined from images of the sea surface, it is then possible to determine the water depth which caused that wave behaviour using

$$h = \frac{1}{k}\left(\tanh^{-1}\frac{(\omega - kU)^2}{gk}\right) - z \tag{2.53}$$

where k is the wave number defined as

$$k = \frac{2\pi}{\lambda} \tag{2.54}$$

and ω is the angular frequency

$$\omega = 2\pi f \tag{2.55}$$

for monochromatic waves

$$z = 0.5 H_s \quad \text{(Booij, 1981)} \tag{2.56}$$

for spectral waves

$$z = 0.35H_s \quad \text{(Bell, 1999)} \qquad\qquad (2.57)$$

The tidal level is then subtracted from the water depth derived from the X-band image so that bathymetry is referenced to chart datum. Bell (2008) used the depth inversion algorithm described above to determine water depth in the Dee Estuary from X-Band images collected using the marine radar deployed on Hilbre Island (Figure 2.23). Water depths are obtained from a tide gauge located in the mouth of the estuary and wave heights are obtained from a wave buoy located approximately 15km offshore. The radar derived bathymetric map is generally within +/- 1m of the survey data where the water depth is less than 15m (Bell, 2008).
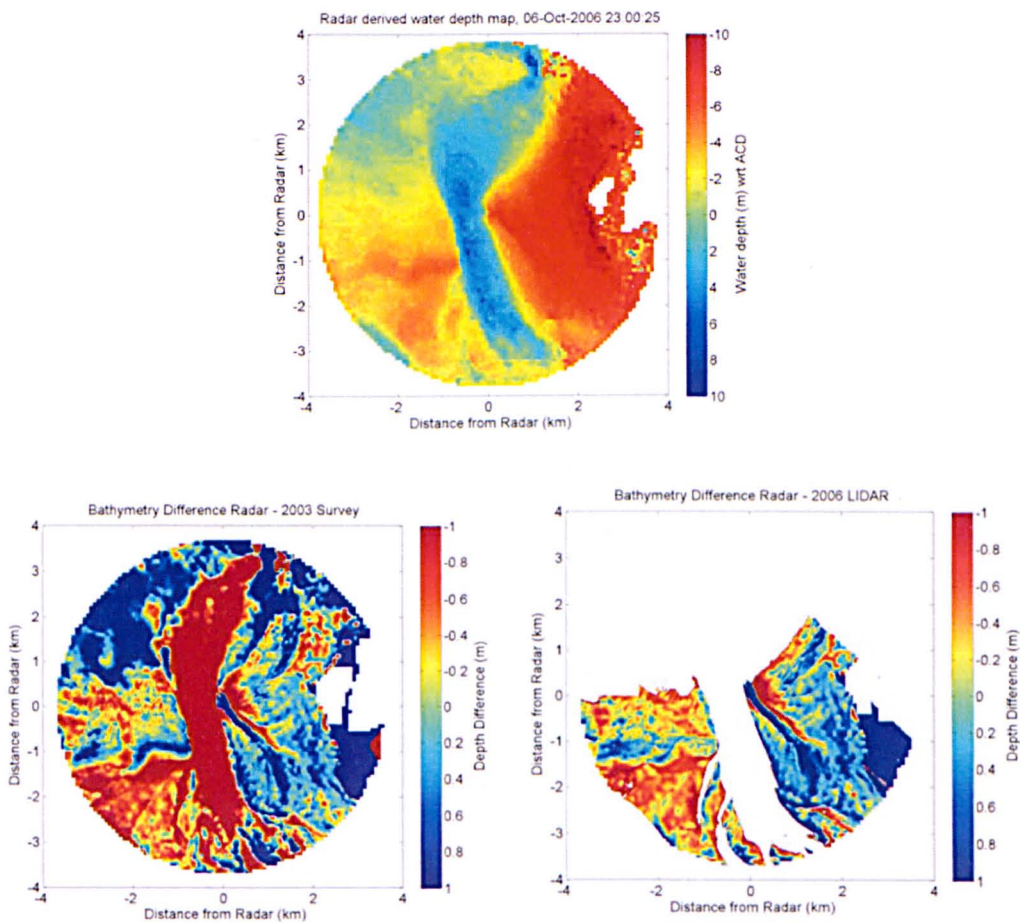
Figure 2.23: Bathymetry in the Dee Estuary derived from X-band radar images. The difference between the radar derived bathymetry and the combined 2003 survey data (left sub-figure) and the 2006 LIDAR survey (right sub-figure). From Bell (2008).

2.6.5 Waterline method

The waterline method combines remote sensing and accurate local water level data to construct a digital elevation model (DEM) of the imaged area (Koopmans and Wang, 1994; Mason et al., 1998). This involves using the water's edge (the waterline) with known tidal elevations at the waterline which are superimposed on its position. Therefore the waterline is a quasi-contour of the bathymetry, with elevation equal to the water height along the land sea boundary (Scott and Mason, 2007). This allows a DEM covering a large area to be created from multiple images obtained over a range of tidal conditions. Mason et al. (1999) used satellite synthetic aperture radar data and a hydrodynamic tide-surge model to construct a DEM of Morecambe Bay using the waterline method (Figure 2.24). These DEMs were created over an area of approximately $350km^2$ with a spatial resolution of about 50m and a vertical accuracy of about 40cm.
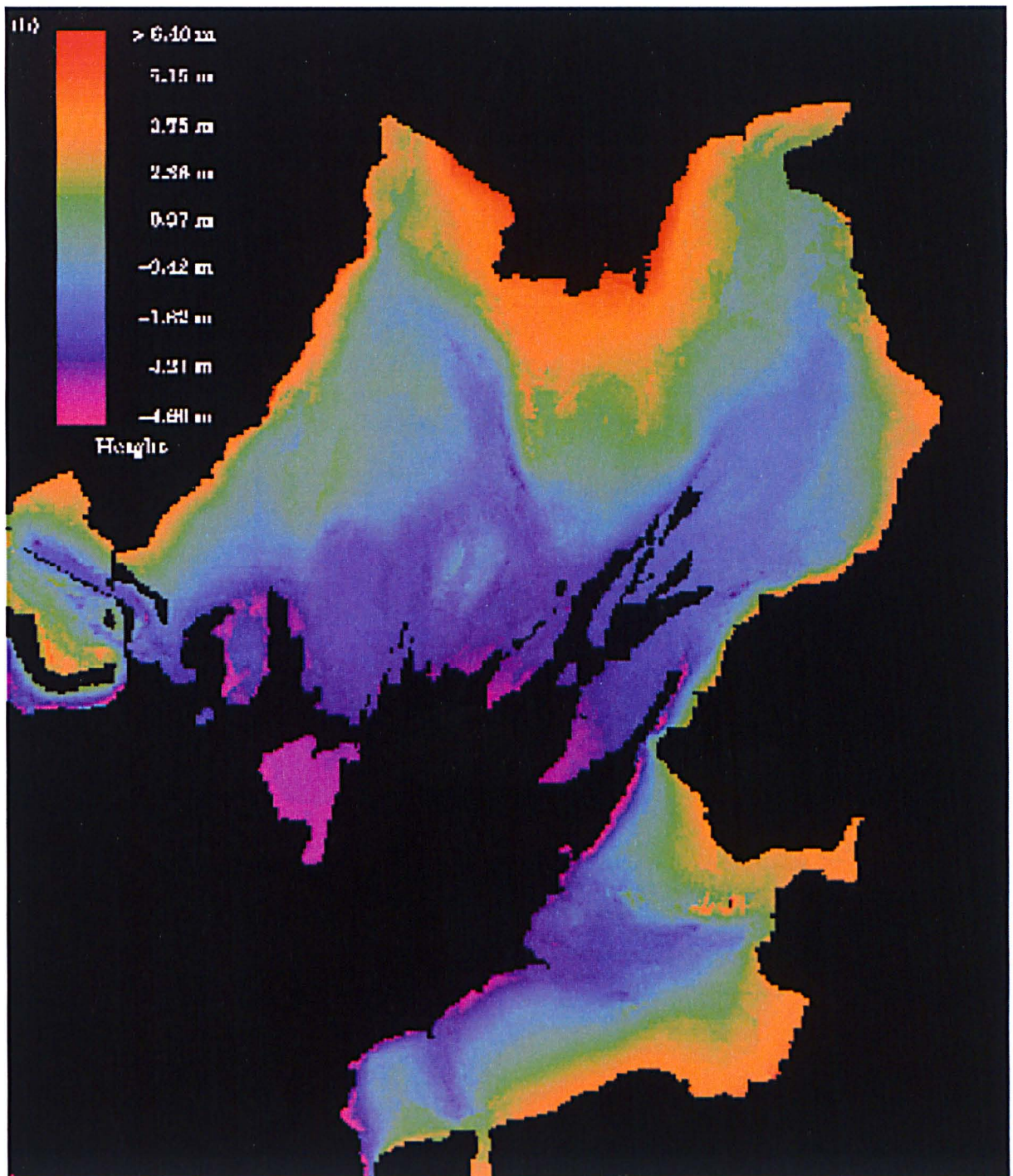
Figure 2.24: A digital elevation model of Morcambe Bay created using the waterline method for 1992-1994. The colour scale ranges from >6.10m (red) to -1.64m (purple). From Mason et al. (1999).

It is possible to detect changes over time in a series of DEMs to show sediment mass transfer within the inter-tidal zone, changes to the volume of sand banks and display areas of erosion and sedimentation (Mason et al., 1999). However, the accuracy of the DEM is shown to be limited by the accuracy of the hydrodynamic model used to calculate the total tide plus surge height (Mason et al., 1995). Ap-

plying the 'waterline method' to X-band radar data relies on the radar backscatter signal at the water's edge. This is a similar application to the method of Takewaka (2005) who determine intertidal beach morphology using the water edge radar backscatter signal, as detailed previously (Figure 2.22). The 'waterline method' will be applied in this research with the view to resolving large scale bed forms over the intertidal dune fields at West Kirby Sands and West Hoyle Bank, so that bed form dimensions can be extracted. McCann (2007) applied a variation of the 'waterline method' to X-band radar data from the Hilbre Island radar installation to create a vertical cross section through West Kirby Sands intertidal sandflats (Figure 2.25).
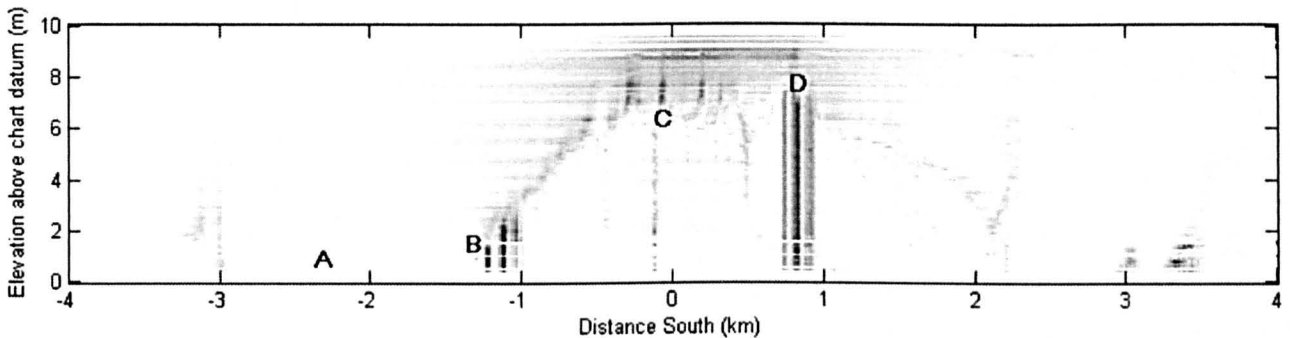
Figure 2.25: A cross section of the sand banks located on West Kirby Sands at the mouth of the Dee Estuary using the 'waterline method'. From McCann (2007).

From Figure 2.25 it is possible to identify the beginning of the shoreline (B), undulating bed forms (C) and the location of Little Hilbre Island (D). Unfortunately McCann (2007) was unable to resolve the large scale bed forms at West Kirby Sands with any accuracy using this method. Further development of this method will be undertaken in this research, while also creating vertical cross section images of the intertidal sandflats of West Hoyle Bank.

2.7 Dynamics of estuaries

The term 'estuary' is derived from the Latin 'aestus' meaning tide and refers to an extension of the sea reaching inland (Woodroffe, 2002). An estuary can be defined as a semi-enclosed coastal body of water having a free connection with the open sea and within which the saline water is measurably diluted with fresh water derived from land drainage (Cameron and Pritchard, 1963). Estuaries have typically developed since the last post-glacial rise in sea level, which inundated coastlines and drowned river mouths (Dyer, 1997). The changing relative intensities of the river, wave and tidal influence are considered to be the determining factors for the morphological development of estuaries (Prandle, 1992).

2.7.1 Tidal asymmetry in estuaries

A tide is classified as being symmetric when the ebb and flood are of equal durations, with maximum velocities of equal magnitudes, resulting in no overall net sediment transport. When the ebb and flood durations are of different lengths then this is classified as asymmetrical and is caused by tidal wave distortion during propagation into shoaling water, along the coastal shelf and on entry into estuaries (Dronkers, 1986). This is caused by the effect of non-linear tidal propagation, the principal sources of which are: quadratic friction, time varying water depth and time varying cross section (Friedrichs and Madsen, 1992). Estuaries are normally areas of significant human activity where morphological changes can cause a large impact on the environment, both in the short term if the velocity changes abruptly and over longer timescales, of years, through sediment redistribution (Robins and Davies, 2010).

As the shallow water tidal wave propagates up the estuary, greater frictional resistance at low tide slows the propagation of water level changes relative to high tide (Dronkers, 1986). Therefore, the time difference between low tide at the mouth and at the head of the estuary is greater than the equivalent time difference in relation to high tide. This results in a longer, weaker ebb tide and a shorter, stronger flood tide, due to the conservation of mass. If the flood flow is stronger than the threshold for sediment motion then this will cause a flood dominance in net sediment transport.

A significant number of researchers (Aubrey and Speer, 1985; Speer and Aubrey, 1985; Friedrichs and Aubrey, 1988; Friedrichs and Madsen, 1992; Stanev, Wolff, Burchard, Bolding and Floeser, 2003; Stanev, Floeser and Wolff, 2003) have shown that flood asymmetry is generated by shallow water and tidal flats, while deeper channels generate ebb asymmetry. This is due to low velocities over the intertidal sand flats at high tide, whereas at low tide, the tidal flats are dry and the channels are relatively deep, allowing a faster exchange of water which results in an overall ebb asymmetry (Friedrichs and Aubrey, 1988).

Sediment deposited in the estuary from offshore will reduce the mean, width-averaged, depth. Over time a central deep channel bound by high intertidal flats will typically develop, with river flow modifying the position of the main channel or producing multiple channels. In this situation, the mean low water (LW) depth, where the flow is constrained to the channels, exceeds the mean high water (HW) depth, due to the inundation of the extensive shallow sand flats. This reversal in mean depth at extreme tidal elevations causes ebb asymmetry, involving ebb dominant sediment transport (Pethick,

1994; Townend, 2003). The net sediment loss from the estuary increases the average depth (Dronkers, 1986), which leads to flood asymmetry and a return to flood dominance in net sediment transport. Estuaries are believed to alternate between erosional and depositional phases over long timescales, of perhaps 100 years (Pethick, 1994). Dronkers (1986) developed an asymmetry ratio γ to determine the flood/ebb asymmetry in duration of an estuary system

$$\gamma = \left(\frac{h+a}{h-a}\right)^2 \frac{S_{lw}}{S_{hw}} \tag{2.58}$$

where h is the mean water depth of the estuary, a is the tidal amplitude at the mouth, S_{lw} is the surface area at LW and S_{hw} is the surface area at HW. Equation 2.58 states that if the flood duration is shortened then the peak velocities will increase, leading to flood asymmetry. If $\gamma \approx 1$ then the tide is symmetrical, $\gamma > 1$ corresponds to flood asymmetry and $\gamma < 1$ corresponds to ebb asymmetry. Dronkers (1998) infers that the net coarse sediment transport is in the direction of the dominant tidal phase. Dronkers (1986) classifies estuaries according to the asymmetry ratio, where Type 1 estuaries consist of a wide deep rectangular channel (Figure 2.26).
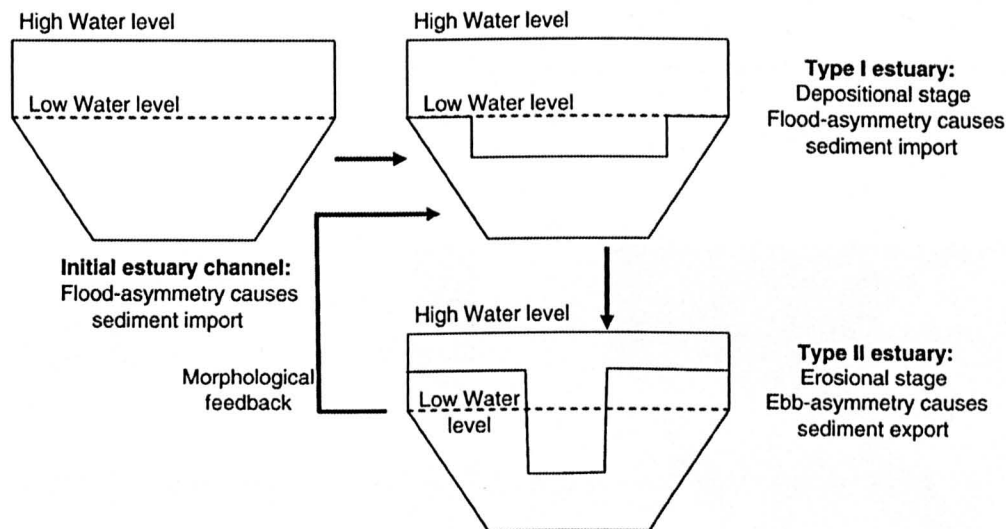
Figure 2.26: Typical stages of estuarine development (Townend, 2003), showing the oscillating dynamic equilibrium between Type I and Type II estuaries.

Low intertidal sand flats will promote flood asymmetry. Deposition of fine sediment fractions will occur at HW over the intertidal sand flats. Sediment deposited at LW slack, when the water is restricted to the deep water channels, will be re-suspended during the subsequent peak flood flow. This causes sediment to accumulate on the intertidal flats, causing the initially wide deep channel to become a central narrow channel with relatively high bounding sand and mudflats, forming a Type II estuary shown as the third schematic in Figure 2.26. The elevated sandflats cause a reduction in the

width-averaged depth at flood tide, resulting in ebb asymmetry and a net export of sediment from the estuary (Brown and Davies, 2010). These two estuary types (Type I & II) represent the successive temporal stages in estuarine development, with tidal flat extent determined by slack water asymmetry (Dronkers, 2005). The erosion of the intertidal sandflats in the Type II estuary is believed to revert the estuary back to a Type I classification, where this morphological feedback will keep the estuary in a dynamic equilibrium oscillating between Type I and II classifications (Pethick, 1994). In reality estuary systems are more complex than the relatively simplistic classifications of Dronkers (1998) and Pethick (1994) to determine whether an estuary is a net sink or source for sediment.

Tidal asymmetry can be represented by tidal harmonics and is commonly described as the distortion of the dominant lunar semi-diurnal M_2 tide by the higher frequency overtides (Wang et al., 2002). The dominant tidal constituent in Liverpool Bay is the M_2 tide, while the M_4 constituent is the most important harmonic overtide (Pingree and Griffiths, 1979) and is the first order harmonic overtide of the M_2 constituent. It is largely generated by non-linear interactions. The M_4 tide, along with other higher order harmonics, has been found to be the main contributor to tidal asymmetry in coastal areas (Friedrichs and Aubrey, 1988). Comparing the M_2 and M_4 tidal constituents is a useful indicator of the degree of tidal distortion and asymmetry. Figure 2.27 shows the amplitudes of the M_2 and M_4 tidal constituents in the Dee Estuary.
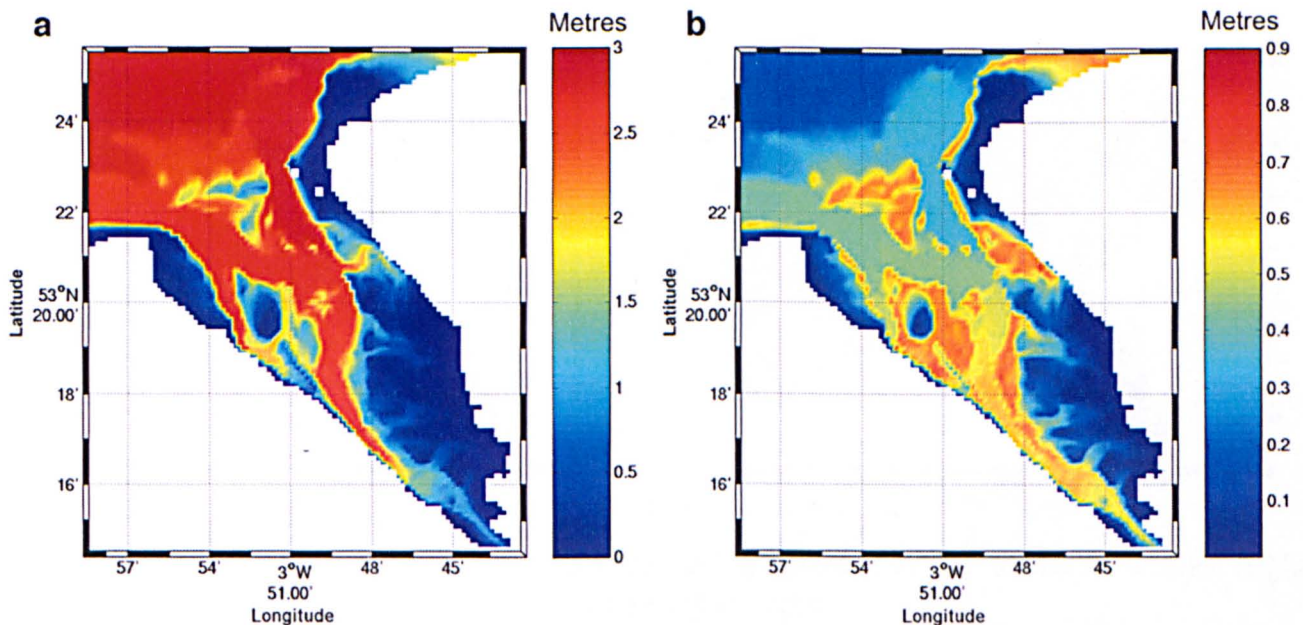
Figure 2.27: Tidal constituent amplitudes in the Dee Estuary for M_2 (a) and M_4 (b). From Moore et al. (2009).

Friedrichs and Aubrey (1988) performed least-squares analyses of the water surface elevation in 26

estuaries along the US Atlantic coast. They found that the interaction of the primary M_2 harmonic with the locally generated M_4 harmonic, together with the local bathymetry, produced non-linear asymmetry of the free surface. The tidal distortion and dominance equations proposed by Friedrichs and Aubrey (1988) (Equations 2.59 & 2.60) describe the tide as

$$M_{4_{amp}}/M_{2_{amp}} > 0.01 \text{ significant distortion of the tidal wave} \tag{2.59}$$

$$2M_{2\theta} - M_{4\theta} : \begin{cases} 0° - 180° = \text{flood dominant} \\ 180° - 360° = \text{ebb dominant} \end{cases} \tag{2.60}$$

The subscripts *amp* and θ represent the tidal constituent amplitude and phase, respectively. Figure 2.28 shows the tidal distortion and tidal dominance for the Dee Estuary as calculated by Moore et al. (2009). The tide outside of the estuary can be seen to be relatively undistorted and symmetrical (Figure 2.28 (left panel)), but becomes highly distorted on entering the estuary, especially in the shallower regions of the estuary. The highly distorted regions of the Dee Estuary can be seen to coincide with areas of high M_4 amplitude (Figure 2.27). Figure 2.28 (right panel) shows tidal asymmetry by phase difference, indicating that the shallow regions which are highly tidally distorted, tend to be flood dominant, with phase differences less than 180°. This explains why these regions are prone to accretion as sediment is transported into an estuary due to flood dominance (Moore et al., 2009).
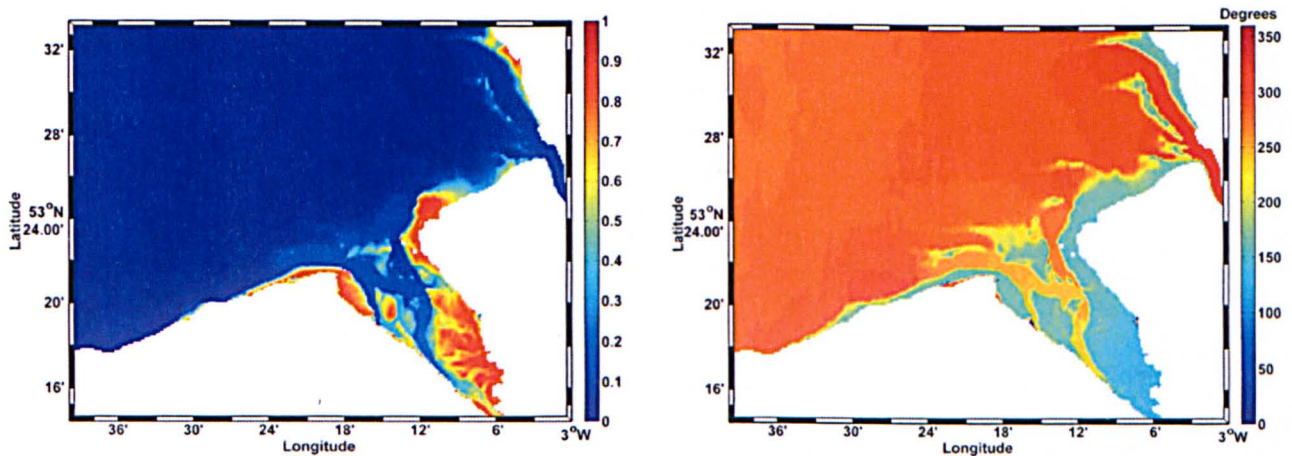
Figure 2.28: Tidal distortion (left panel) calculated using Equation 2.59 and tidal dominance (right panel) calculated using Equation 2.60. From Moore et al. (2009).

However, it is often impractical to use the phase comparison of Friedrichs and Aubrey (1988) in shallow estuaries as the surface wave is distorted by the tidal flats and the least squares analysis cannot be performed on the tidal signal. Friedrichs and Aubrey (1988) use the 1D model of Speer

and Aubrey (1985) to classify the tidal asymmetry of an estuary using the barotropic parameters A_0/h, which is equivalent to the offshore M_2 tidal amplitude over the average estuary depth below mean sea level, and also using V_s/V_c, which is the volume of the intertidal storage over the estuary volume below mean sea level. Friedrichs and Aubrey (1988) state that ebb asymmetry occurs when $A_0/h < 0.2$ while flood asymmetry occurs when $A_0/h > 0.3$. However, the research of Friedrichs and Aubrey (1988) suffers from several limitations; it was based on sea surface elevations and not the associated velocities, sediment transport was not included in their model, and their classification is based on averages over the whole estuary. In reality, some regions of the estuary may experience flood asymmetry while others will experience ebb asymmetry. Robins and Davies (2010) apply a locally varying ratio of a/h (local tidal amplitude over local depth at mean sea level) to investigate and categorise flood and ebb dominance, in relation to sea level rise, in the Dyfi Estuary, Cardigan Bay, Wales. The simulated net sediment flux by Robins and Davies (2010), in an idealised gently sloping estuary with no tidal flats, changes from ebb dominance in the outer (deeper) estuary to flood dominance in the inner estuary. This change occurs where a/h is in the range of 0.8-1.2, depending on the mean sea level. An increase in mean sea level was observed to decrease the critical value of a/h, as well as the gross and net sediment transport. The presence of a deep central channel in the model grid generated greater ebb transport in the channel and less flood transport on the surrounding sandflats.

2.8   The Dee Estuary

2.8.1   An introduction to the Dee Estuary

The Dee Estuary is a funnel shaped, macrotidal estuary in Liverpool Bay, which itself is an embayment of the Eastern Irish Sea (Figure 2.29).The estuary is situated between England and Wales, lying between the Wirral Peninsula and the North Wales coast.
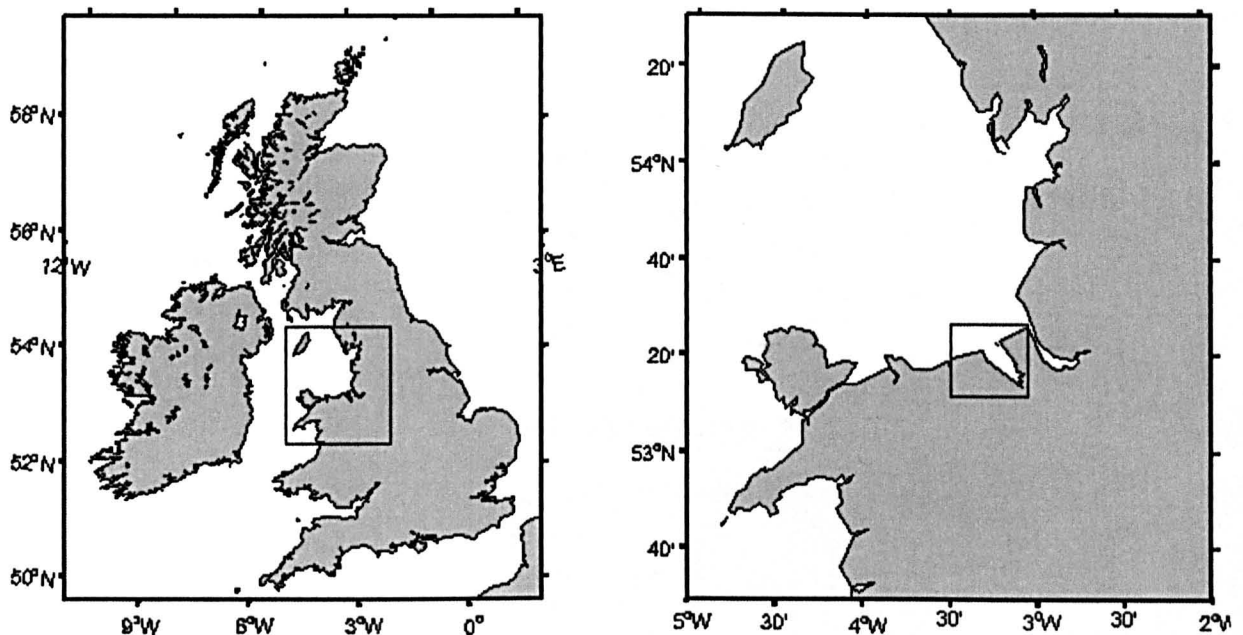
Figure 2.29: The location of the Dee Estuary within Liverpool Bay.

The Dee Estuary evolved during the last glacial maximum, approximately 18,000 years ago (Fairbanks, 1989). During the Pleistocene glaciations the Irish Sea was subjected to severe ice congestion due to its central position between the highlands of Scotland, Ireland and Wales (Charlesworth, 1957). Forced to divide, the glacial ice escaped from the Irish Sea basin flowing to the west of the Welsh ice sheet, where it moved south over the Wirral and into the Cheshire-Shropshire plain (Wills, 1912). This resulted in a deep channel being carved in the Carboniferous and Triassic rocks between the Welsh hills and the Wirral. Since glaciations, extensive deposits of mud, silt and sand from the River Dee, Liverpool Bay and the Irish Sea have accumulated in the estuary and are still accreting (Fahy et al., 1993).

The natural estuary extended as far inland as the Roman city of Chester (2000 BP), with a total length of 35-40km. Canalisation at the head of the estuary during the 18th Century, coupled with associated

land reclamation, has dramatically changed the hydrodynamic regime and reduced the estuary length (Moore, 2009). The present day Dee Estuary has a total length of 30km, with a 12km canalised channel extending from Queensferry to Chester, and a maximum width of 8.5km at the mouth. The canalisation of the River Dee had the effect of creating hydrodynamically calmer conditions on the eastern shore of the estuary. Marker (1967) suggested that the infilling of the Dee Estuary has been accentuated by the trapping of sediment which has been transported northward along Liverpool Bay by longshore currents to the mouth of the Dee where flood dominant currents act to retain the sediment in the estuary.
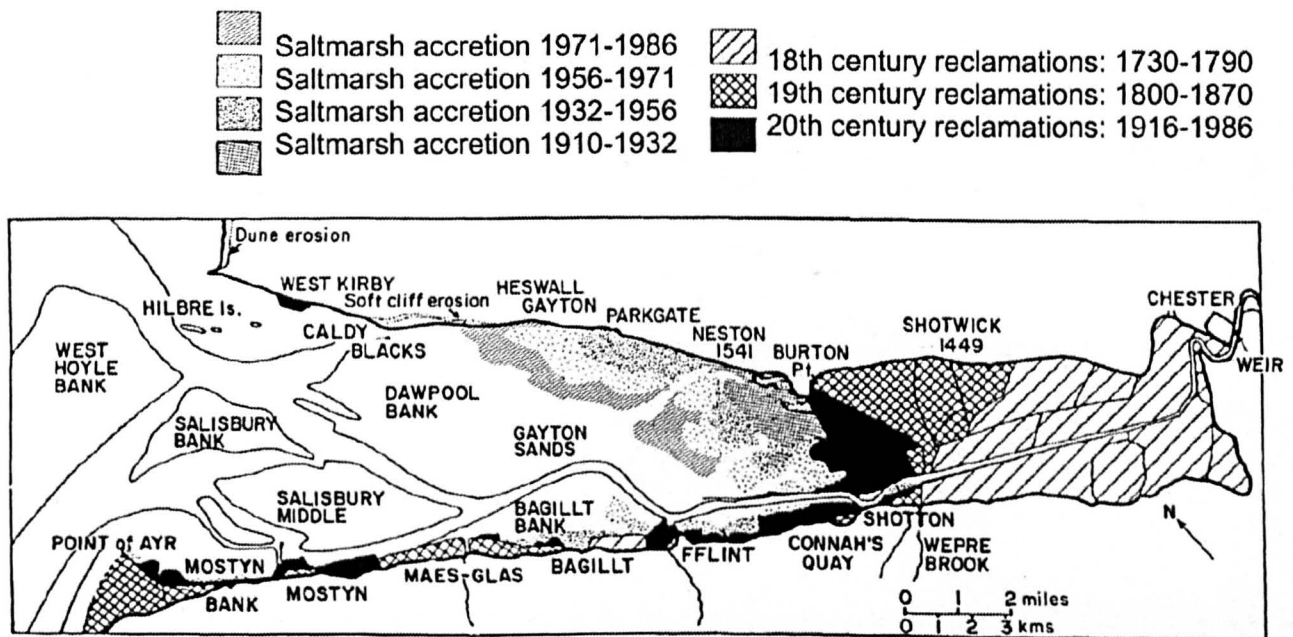
Figure 2.30: Dee Estuary land reclamation and salt marsh expansion between 1730-1986. From Moore (2009).

Figure 2.30 shows the progressive land reclamation and saltmarsh expansion in the Dee Estuary in the 18th, 19th and 20th centuries. Increased levels of siltation, leading to the development of mud and sand bank systems, which in turn became colonised by saltmarsh has led to further loss of area for the estuary. The locations of specific points of interest for this research can be seen in Figure 2.30, namely West Hoyle Bank, Hilbre Island and West Kirby. The present day Dee Estuary contains a main channel which bifurcates 12 km seaward of the canalised river at the head of the estuary, resulting in two deep channels which extend out into Liverpool Bay: the Welsh Channel, to the west, and the Hilbre Channel, to the east (Figure 2.31)

Bed elevation (m)
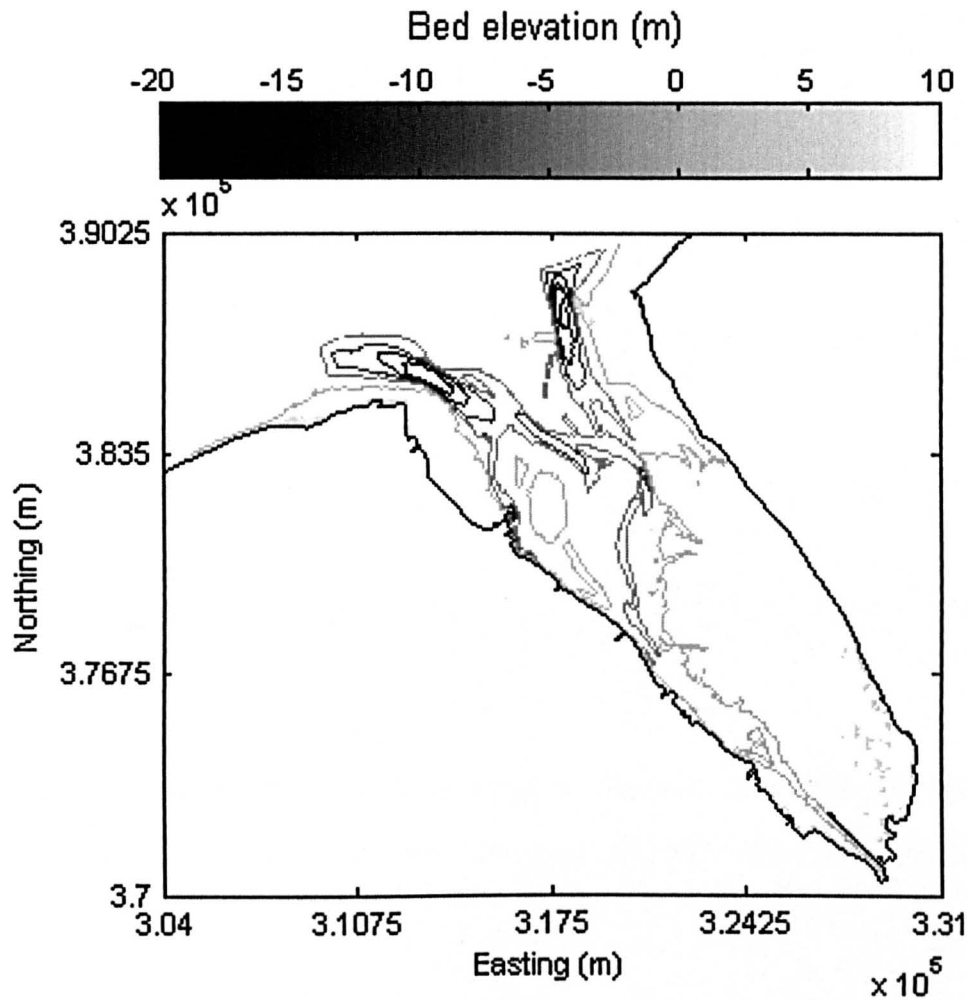
Figure 2.31: The present day Dee Estuary with the two main deep water channels visible in the mouth of the estuary.

2.8.2 Hydrodynamic processes in the Dee Estuary

The Dee Estuary is an active and dynamic estuary with a large tidal range and a variety of physical features such as channels, banks and tidal flats (Fahy et al., 1993). The estuary is characterised by the presence of waves at its outer margins and strong tidal flows in its channels (Moore, 2009). In the Dee the average tidal prism is $4\times10^8\mathrm{m}^3$, representing a volumetric increase of over 80% between mean low water and mean high water (Moore, 2009). The annual mean river discharge is small in comparison, in the order of $31\mathrm{ms}^{-1}$ (data from the UK National River Flow Archive from a gauging station run by the Environment Agency on the River Dee at Manley Hall). Lanzoni and Seminara (2009) state that a tidally-dominated estuary will typically have a river discharge significantly smaller than the tidal prism. This can be seen to be the case in the Dee, where the river discharge is 0.35% of the tidal prism over a tidal cycle, making the Dee a strongly tidally dominated estuary (Bolanos and

Souza, 2010).

2.8.3   Wave and wind climate in the Dee Estuary

The Irish Sea is subject to severe winter storms, where wind speeds can be in excess of $20ms^{-1}$, however waves within Liverpool Bay are mainly locally generated with little effect of long period ground swell (Wolf et al., 2011). Significant wave heights are less than 5.5m, the peak period is less than 12s and the mean wave period is less than 8s (Wolf, 2008a; Brown et al., 2009, 2010). The largest waves are associated with wind from the west or north west where the fetch is greatest. These winds correspond with the right rear quadrant of mid-latitude depressions, which track across the UK from the North Atlantic (Brown et al., 2009). Figure 2.32 shows wind data for 2004 to 2005. The wind rose displays a bimodal distribution in terms of the direction, with the strongest and most frequent winds from the west but with a secondary peak from the south east.
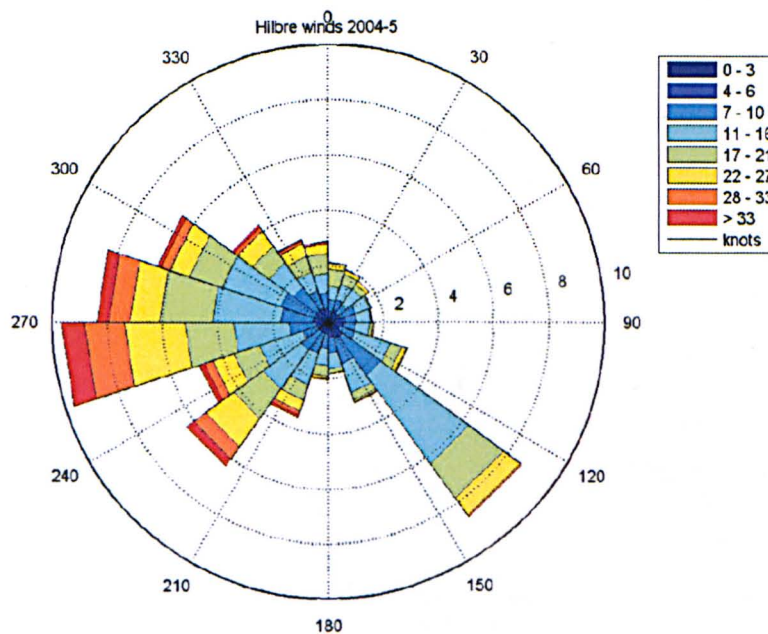
Figure 2.32: Wind rose for 2004-5 at Hilbre Island. From Wolf (2008b).

The WaveNet system of nearshore wave buoys has been deployed around the coast of England and Wales since 2002, and is maintained for the Environment Agency and DEFRA by CEFAS (Centre for Environment, Fisheries and Aquaculture Science). A WaveNet buoy is located in Liverpool Bay in 22m water depth and a Triaxys wave buoy is located in the mouth of the Dee Estuary, in a relatively sheltered position in approximately 10m water depth (Figure 2.33).
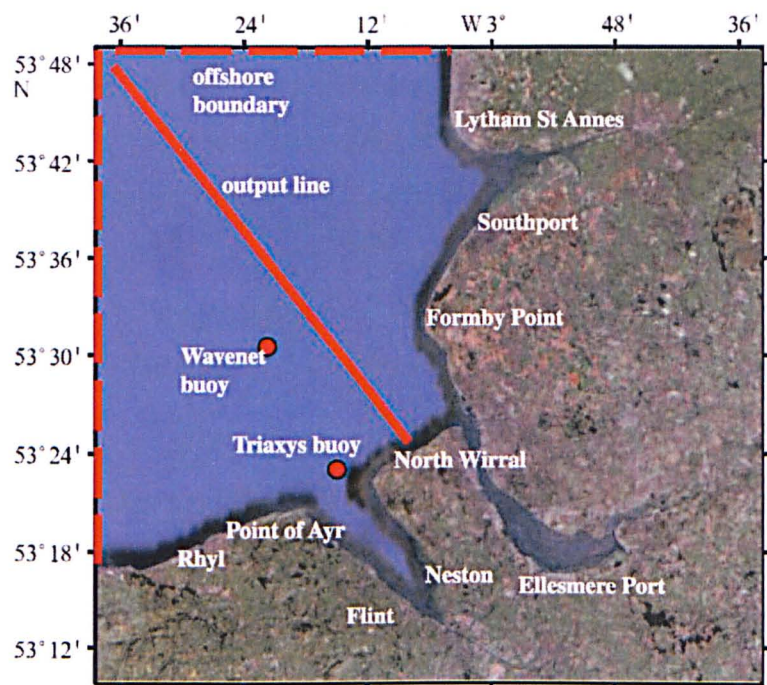
Figure 2.33: The location of the WaveNet and Triaxys wave buoys. From Wolf (2008*b*).

Wolf et al. (2011) analysed directional wave measurements for the WaveNet and Triaxys wave buoys. Figure 2.34 shows WaveNet wave data from 2003 to 2009 and Triaxys wave data for 2006 plotted as compass roses.
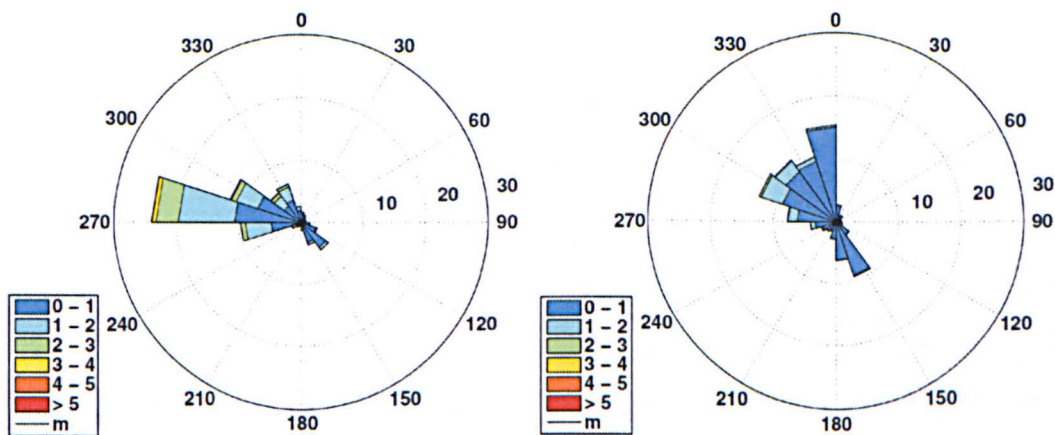
Figure 2.34: Wave rose plots, showing wave 'from' direction for the WaveNet buoy 2003-2009 (left) and the Triaxys buoy 2006 (right). From Wolf et al. (2011).

Waves recorded by the WaveNet buoy can be seen to be predominantly from the west to north west (Figure 2.34), the Triaxys wave data shows a similar trend but with a greater influence of northerly waves. There is also a wave component in the Triaxys data from the south east, this is due to the north west - south east alignment of the Dee Estuary which funnels the wind with associated wind generated waves (Wolf et al., 2011). Using the method of Hurdle and Stive (1989), Wolf et al. (2011)

stated that, if waves are generated in the Irish Sea, a maximum depth of 200m and fetch of 200km with a wind speed of $30ms^{-1}$ would give a maximum wave height of 12m and a peak period of 14s. However, the water depth is much shallower than this over much of the eastern Irish Sea, typically around 40m and even shallower in Liverpool Bay, which will limit the wave height due to shoaling and dissipation.

2.8.4 Morphology of the Dee

The Dee Estuary contains a variety of highly diverse and complex morphological features. As mentioned previously, the main channel bifurcates into two main deep water channels in the mouth of the estuary. The bed of the estuary consists of a mixture of sediments containing a range of non-cohesive and cohesive sediments (Bolanos and Souza, 2010). The underlying solid geology is mainly overlain by 20-30m of deposited sediments (Olds and Davison, 2009). Rocky outcrops are present in the mouth of the estuary, particularly around Hilbre Island.

Morphological change has been studied in the Dee Estuary between 2003 and 2006 by HR Wallingford (2007) and Moore et al. (2009). A net accretion of sediment in the estuary was observed by Moore et al. (2009) between 2003 and 2006 using high resolution Lidar surveys. Moore et al. (2009) suggested that the Dee may be approaching morphological equilibrium and that the rate of accretion may therefore decrease in the future.

2.8.5 Users of the Dee

The Dee estuary is a remarkable site of nature conservation significance and as such it is classified as a Site of Special Scientific Interest (SSSI) under the Wildlife and Countryside Act 1985, a Ramsar site and a Special Protection Area (SPA). The Dee is a nationally and an internationally important wetland habitat which supports large numbers of migratory waterfoul. The Dee is protected by the EU Birds Directive of 1979, implemented through the Wildlife and Countryside Act. The Royal Society for the Protection of Birds (RSPB) has large reserves either side of the estuary. With important RSPB reserves located here, birdwatching is a significant recreational activity occurring in the Dee.

The Dee Estuary has further recreational value from significant water sports activities, especially sailing and windsurfing. It is also a popular destination for ramblers as it is possible to walk from West Kirby across the sand flats to Hilbre Island as the tide recedes. The old lifeboat station and old telegraph station are of historical interest for visitors of Hilbre Island.

There is also significant commercial use of the Dee, despite historical sedimentation and navigational difficulties. Located on the River Dee is a major Airbus factory, manufacturing and assembling wings for the 'superjumbo' A380. The fully assembled wings are transported by sea, via the Dee Estuary, as they are too large to be transported by road. The wings are transported by barge from the factory to Mostyn Docks, located on the western shore of the estuary. From Mostyn the wings are transferred to larger sea going vessels for transportation to France where the assembly of the complete aircraft occurs. Therefore, the transport of sediment and migration of navigation channels in the mouth of the Dee Estuary is of great importance to large commercial enterprises using the estuary for transportation.

2.8.6 Sustainable coastal management

Coastal zones directly support a growing part of the world population, with up to 50% of the world's population living within 60km of the shoreline (Small and Nicholls, 2003). The highest densities of urbanisation are found in sedimentary coastal plains, which have been shaped by land-sea interaction (Dronkers, 2005). The movement of sediment in the sea will therefore have a significant impact on the large population living and working in and around the coastal environment. Engineering strategies can help to slow coastal evolution locally and temporally, however it is extremely hard to stop the large scale evolution. It would be foolish not to consider the mobility of the seabed when studying the future issues associated with the coastal zone, especially when considering projected sea level rise and increased storminess due to climate change. A change in the offshore bathymetry can significantly impact the coastline via wave and tidal action. A good example of this is the loss of the village of Hallsands on the south coast of Devon, U.K., over a 25 year period from 1890, caused by the removal of shingle from the nearshore zone (Davies and Thorne, 2008). The recent introduction of large scale container vessels and super tankers to shallow coastal waters reinforces the need to monitor the stability of navigation channels to reduce the risk of major maritime incidents.

Chapter 3

Field work

Data was collected in the Dee Estuary to determine the flow regime and morphology at West Kirby Sands, in the mouth of the estuary. Current speed and water depth data were collected from two separate two week deployments on 24.01.11-06.02.11 and 03.03.11-17.03.11 so that spring and neap tides were observed. Morphology data were collected from four DGPS surveys on 28.01.11, 31.01.11, 08.02.11 and 11.02.11 which covered changing conditions from calm with little/no waves to increased wind with greater wave activity.

3.1 ADCP deployment

ADCP (Acoustic Doppler Current Profiler) data were collected for the intertidal zone of West Kirby Sands to obtain current speed and water depth information. The mooring was located in the mouth of the estuary in an area of intertidal sand flats (Figure 3.1). The ADCP instrument used was a 12KHz model, and it was deployed during spring tides for the two survey periods covering 24.01.11-06.02.11 (deployment 1) and 03.03.11-17.03.11 (deployment 2). The unit was secured in a bed frame close the sea bed (Figure 3.2) and placed at the spring tide low water line to ensure maximum data recorded by the instrument over the survey periods.
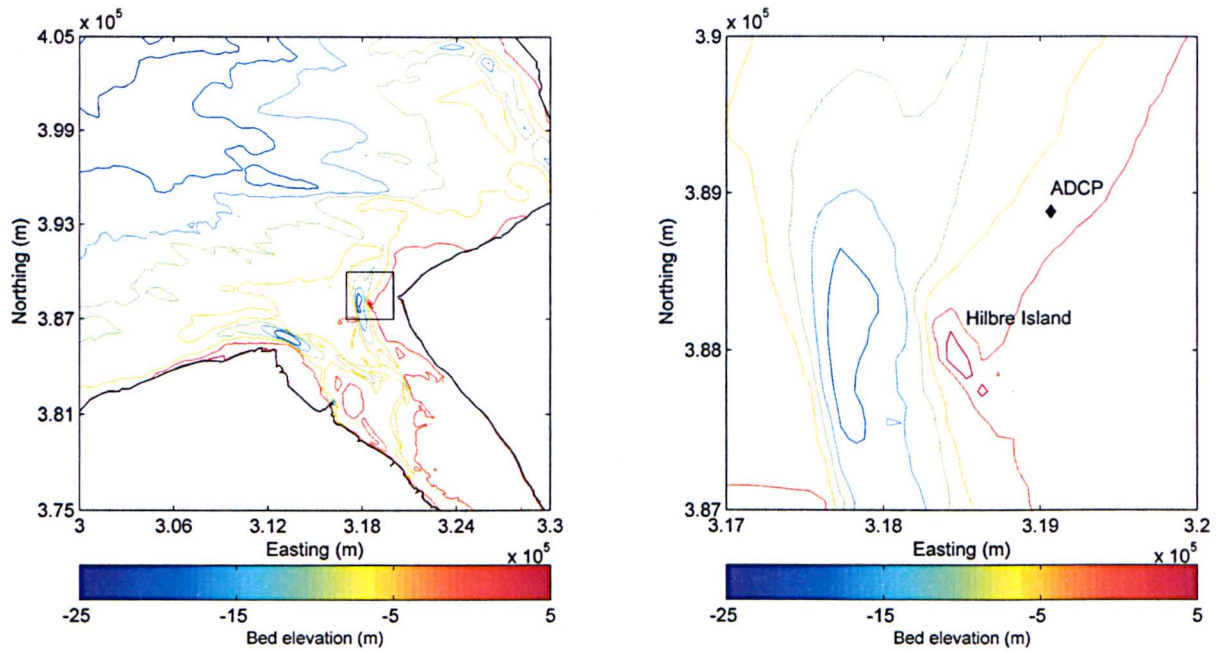
Figure 3.1: The location of the ADCP deployment during the field work campaign on West Kirby Sands. The box outlined (left image) indicates the position of the sub-plot (right image) in relation to the Dee Estuary as a whole.
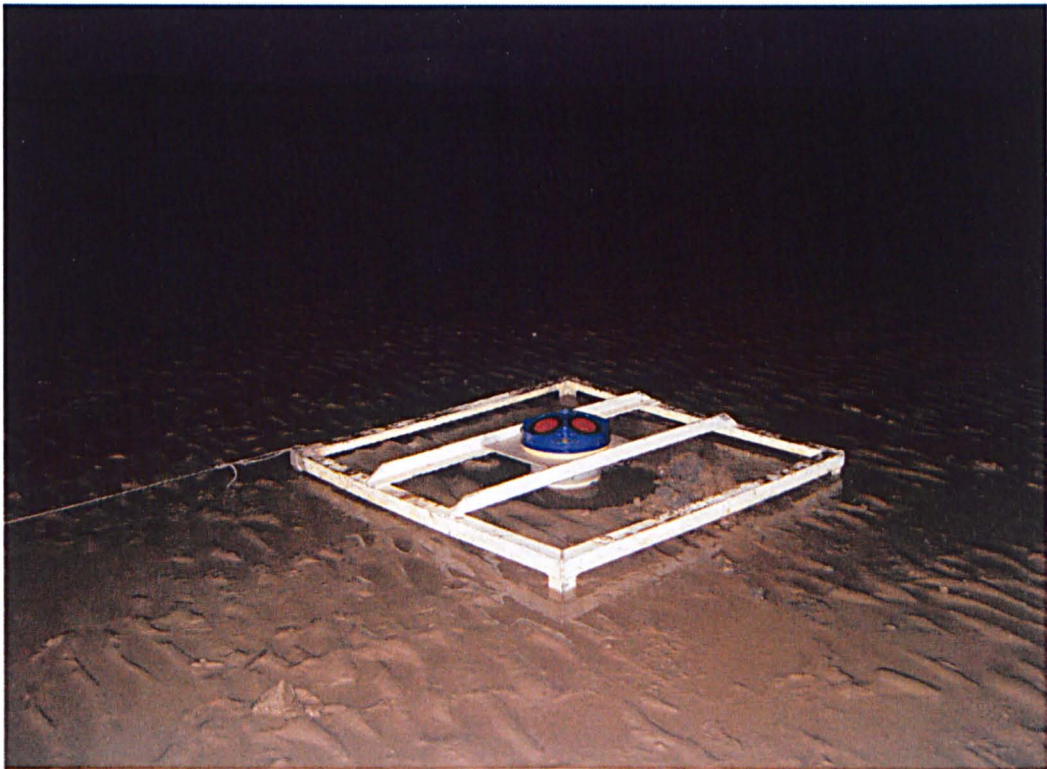
Figure 3.2: ADCP mounted in deployment frame and set in position on the sea bed at West Kirby Sands.

The ADCP was deployed on an intertidal beach slope which approaches the dune field at West Kirby

Sands, seen in the historic aerial photographs in Figure 1.3. Herein times of high water will be referred to as HW and low water as LW. The HW water depths ranged between 7m on spring tide and 4m on neap tide for the first deployment, and 5m on spring tide and 2.5m on neap tide for the second deployment. An ADCP typically comprises three or four transducers inclined at an angle of 20-30° to the vertical. Each transducer transmits a sound pulse, referred to as a 'ping', which is scattered by particles in the water column. A fraction of the scattered signal is reflected back in the direction of the transducer and the Doppler shift of the received signal frequency is used to calculate the along beam component of the water column velocity. This relies on the scattering particles moving, on average, at the same velocity as the water, which is usually the case (RDI, 1996). Velocity profiles are observed over a number of cells, or bins, of constant size, set by the user, increasing in range from the instrument.

For deployment 1 the ADCP was set to record with 5cm bins and ping every second to record data at a high resolution to a maximum water depth of 3.5m. This small bin size allows the LW spring tide to contain a maximal number of bins above the blanking distance of the ADCP, but does not cover the entire water column at HW spring. A 10cm bin depth was used for deployment 2, with the ADCP still set to ping every second, which recorded data for the entire water depth. The ADCP was deployed so that a spring-neap tidal cycle was recorded for deployments 1 and 2, allowing the tidal flow dynamics in the mouth of the estuary to be assessed by measuring the current speed and water depth of these deployment periods. The graphs presented in this section are relative to decimal days, i.e. January 1st 00:00 = day 0.

3.1.1 ADCP deployment 1
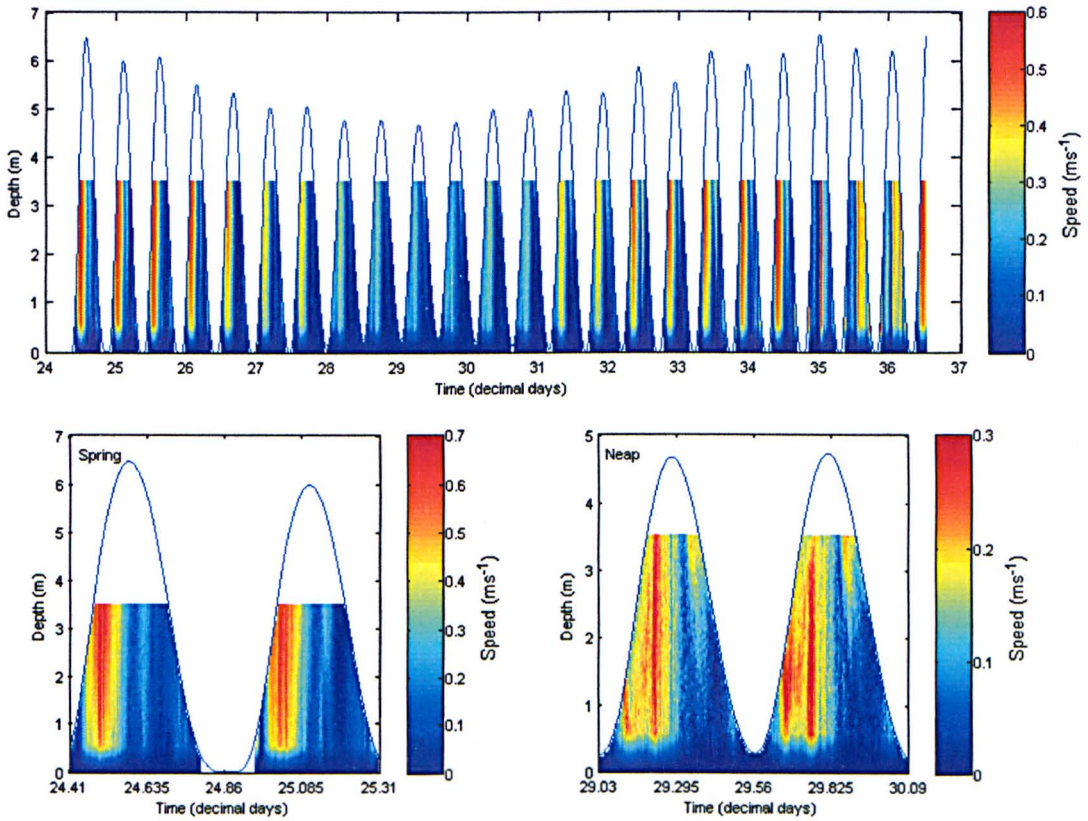
Figure 3.3: Water depths and velocity magnitudes for the complete ADCP deployment 1 at West Kirby Sands. Sub-figures show the water depth and velocity magnitude during spring and neap tides.

The results of the first ADCP survey showed that the smallest neap tide of the spring-neap cycle had depths ranging from 4.81m at HW to 0.17m at LW giving a tidal range of 4.64m (Figure 3.3). The velocity data shows a strong flood asymmetry at both spring and neap tides, with lower velocities attained at neap tides when compared with springs. There is a slight temporal asymmetry in the depth curve, where the period between HW to LW (ebb tide) was 6 hours 44 minutes while LW to HW (flood tide) took 5 hours 52 minutes. Spring tides for the first deployment had HW depths of 6.61m, while at LW water depth was lower than the measurable range for the instrument (Figure 3.3). A similar temporal asymmetry in the depth curve is seen for spring tides, with HW to LW (ebb tide) taking 6 hours 43 minutes and LW to HW (flood tide) taking 6 hours 23 minutes.
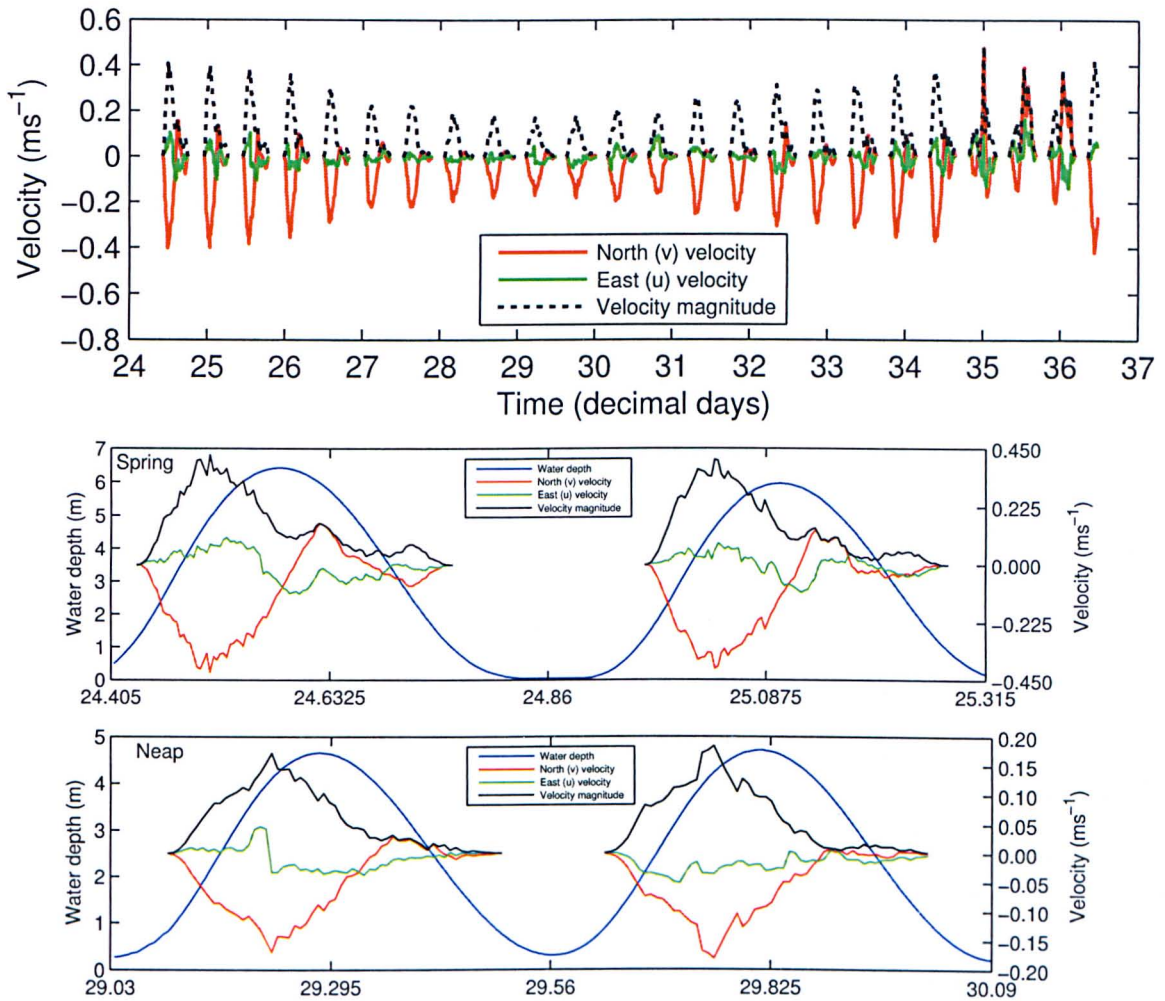
Figure 3.4: Depth averaged velocities for ADCP deployment 1 at West Kirby Sands. Sub-figures show the water depth and depth averaged velocities during spring and neap tides.

Figure 3.4 shows the depth averaged velocities for the x and y components of flow, as well as the velocity magnitude which is calculated as the square root of the sum of the squares for both velocity components. The velocities have been averaged over 10 minute periods to remove the noise in the tidal signal. The north-south flow can be seen to be the dominant component of flow, where southerly directed velocities (flood tide) are given a positive value. There is an abrupt change in the data towards the end of the deployment, from 34.8 to 36.3 decimal days (Figure 3.4), which can be seen to coincide with increased wave activity in Liverpool Bay (Figure 3.5), when tidal elevations are plotted against wave heights from the WaveNet wave buoy located 15km offshore in Liverpool Bay (data were obtained from Cefas).
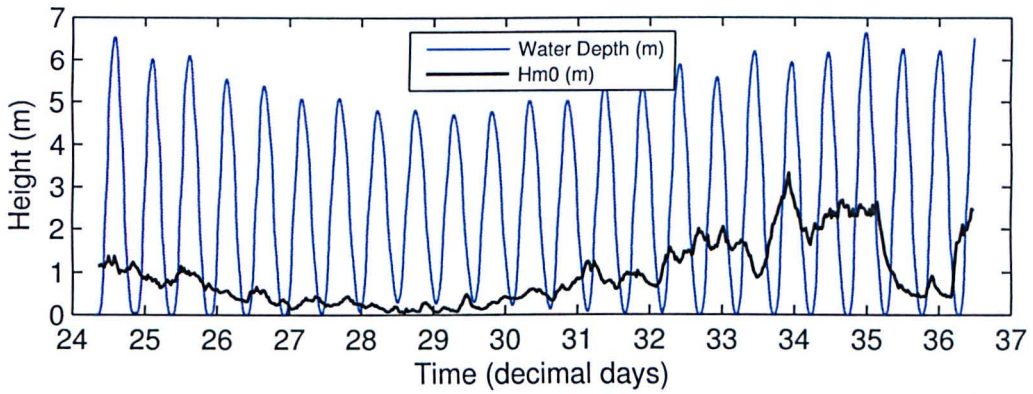
Figure 3.5: Water depths at West Kirby Sands and wave heights from the Liverpool Bay WaveNet wave buoy (from Cefas) for 24.01.11-06.02.11.

The sub-figures in Figure 3.4 show the depth-averaged velocity at sampled spring and neap tidal phases. This shows the peak flood flow to have been $0.18ms^{-1}$ while the peak neap ebb flow was $0.03ms^{-1}$, with the peak spring flood being $0.43ms^{-1}$ and a peak spring ebb of $0.16ms^{-1}$. During the neap tide peak flood flow occurred 1 hour 20 minutes before HW and peak ebb flow 4 hours 29 minutes before LW, while spring tides had peak flood flow occurring 1 hour 44 minutes before HW and peak ebb flow 3 hours 34 minutes before LW. This flood asymmetry in depth-averaged velocities suggests that a net movement of sediment into the estuary via West Kirby Sands may be occurring.
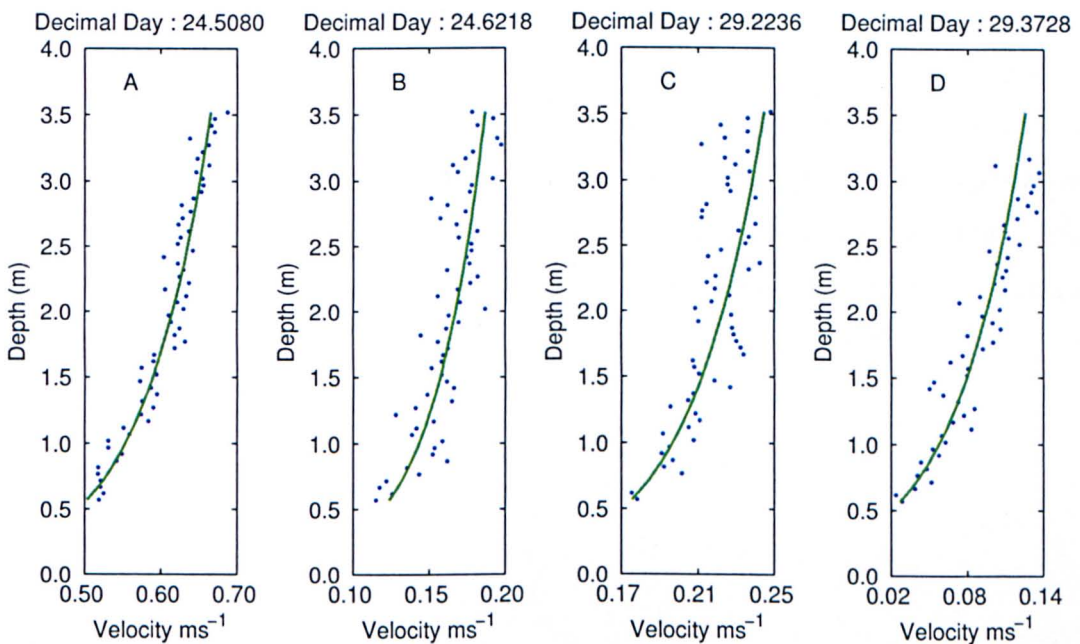
Figure 3.6: Vertical profiles of velocity, averaged over 10 minute intervals, for spring and neap peak flood (A & C) and peak ebb (B & D) tidal phases during the ADCP deployment 1 (24.01.11-06.02.11) at West Kirby Sands.

Figure 3.6 shows vertical profiles of velocity at peak flood and ebb tidal phases for a spring and neap

tide. These vertical velocity profiles start at 0.57m above the bed as this includes the blanking distance of the ADCP before the first data bin. The depth averaged velocities include data down to the bed, as this blanking distance was accounted for by assuming zero velocity at the bed (0m) and fitting a logarithmic curve to the first available data point (0.57m). For this ADCP deployment (deployment 1) the instrument was set to record with a 5cm bin depth, to observe the water column in high resolution. However, this meant that a maximum depth of 3.5m was recorded, which is not the entire water depth in this region. Boundary frictional effects cause lower velocities as seen at the bottom of the water column on both the flood and ebb tide. The current speed increases with height from the bed, to a maximum at or near the surface, with the most rapid increase with height occurring near the bed.

3.1.2   ADCP deployment 2

The second deployment of the ADCP frame, at the same location on West Kirby Sands as deployment 1, covered another spring-neap tidal cycle between 03.03.11-17.03.11. During this deployment spring HW depths of 4.4m and neap HW depths of 2.5m were recorded, while at LW during both spring and neap tides the LW depths were lower than the recordable height for the instrument. Figure 3.7 shows the water depth and velocity magnitude, which is the square root of the sum of the squares of the x and y velocity components, over the deployment period. A similar temporal asymmetry that was seen in the depth curve during deployment 1 was observed during deployment 2. During neap tide the time from LW to HW (flood tide) is 6 hours 1 minute, while LW to HW (ebb tide) took 6 hours 41 minutes. During spring tides the LW to HW (flood tide) lasted for 6 hours and 1 minute and the HW to LW (ebb tide) took 6 hours 13 minutes. The current speeds during spring and neap tides are shown in the sub-figures of Figure 3.7. This shows the strong flood dominance in current velocities during spring tides, while neap tides experience either a weaker flood dominance or possible balance in tidal velocities.
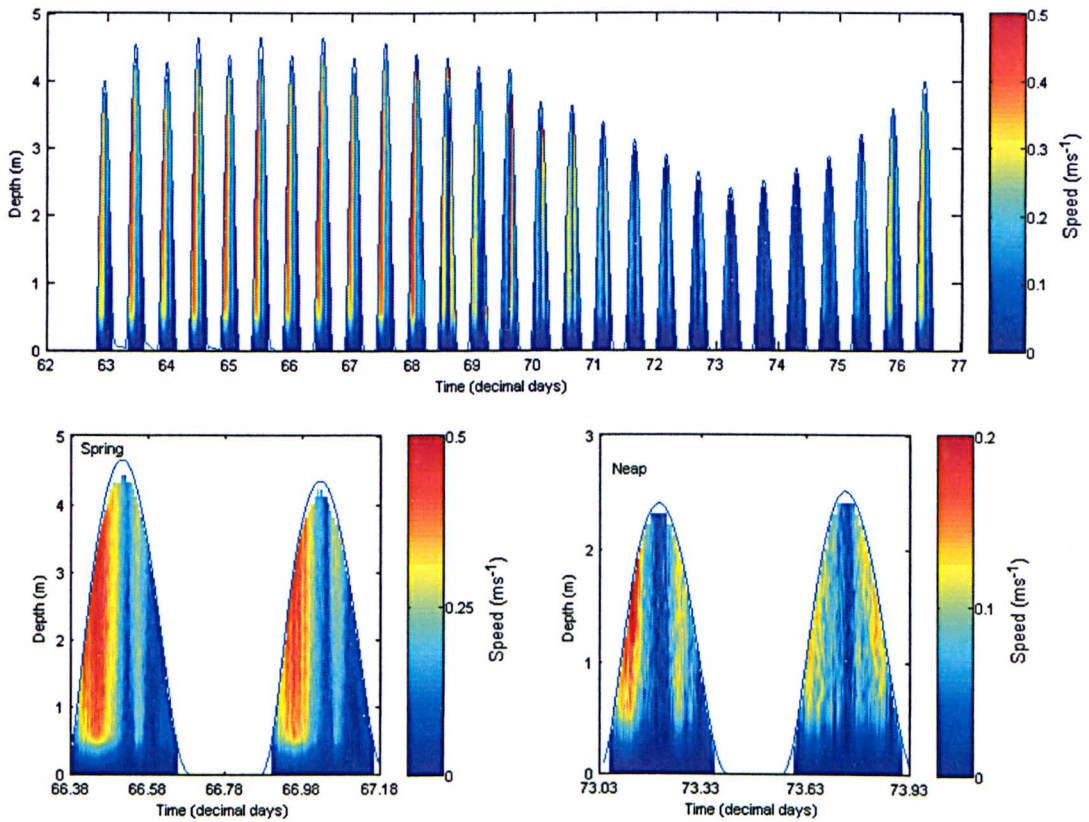
Figure 3.7: Water depths and velocity magnitudes for the complete ADCP deployment 2 at West Kirby Sands. Sub-figures show the water depth and velocity magnitude during spring and neap tides.

Figure 3.8 shows the depth-averaged velocities, averaged over 10 minute intervals, over the deployment period. This shows the strong dominance of the southerly flow component which represents flow into the estuary (flood tide) at West Kirby Sands. The sub-figures show the flood dominance in velocity magnitudes during spring tides, whereas the velocity magnitude is approximately equal during neap tides. Peak flood flow on neap tides, of 0.04ms^{-1}, was 1 hour 54 minutes before HW while the peak ebb flow, of 0.03ms^{-1}, was 3 hours 2 minutes before LW. During spring tides the peak flood flow is 0.27ms^{-1} and occurs 1 hour 34 minutes before HW and the peak ebb flow of 0.15ms^{-1} occurs 2 hours 47 minutes before LW.
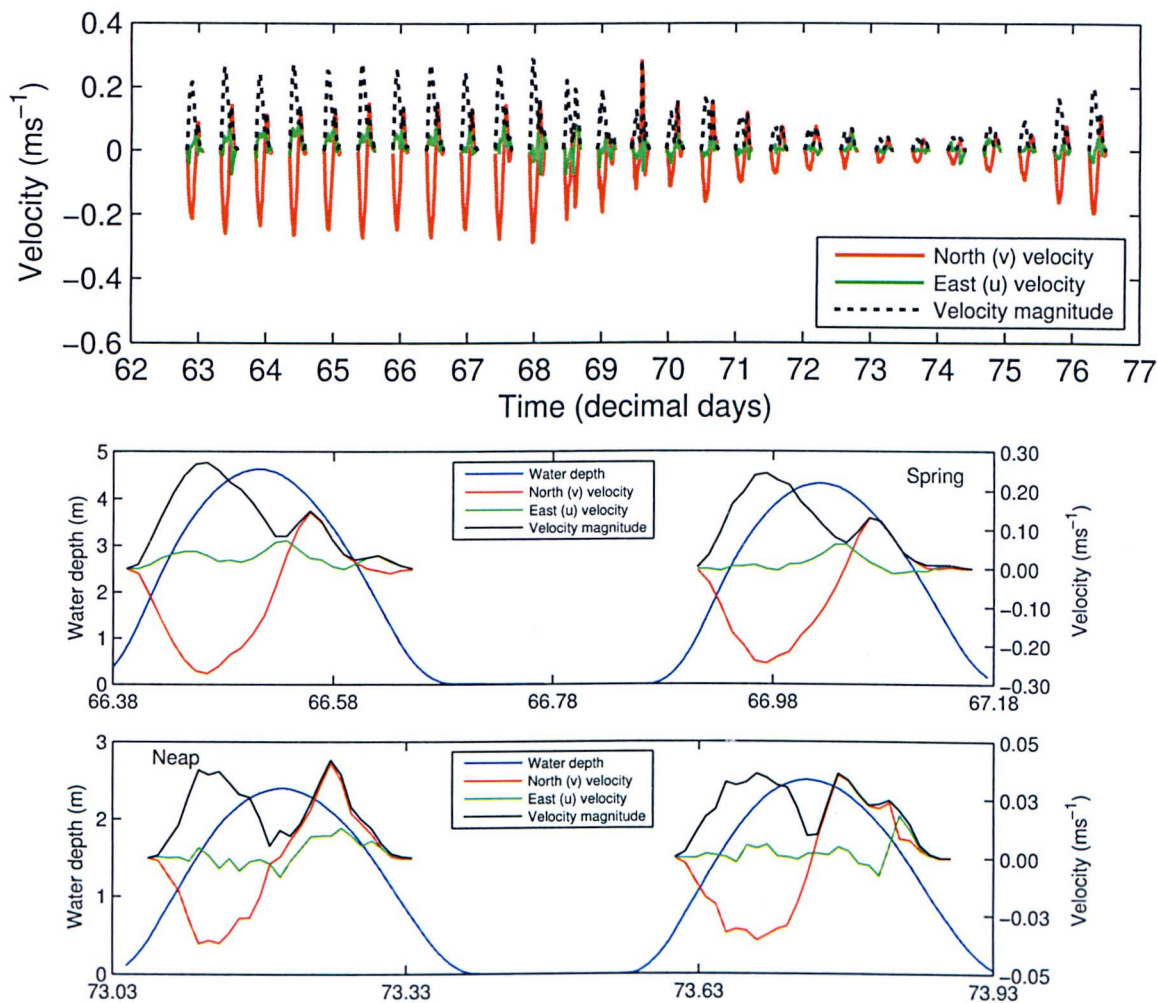
Figure 3.8: Depth averaged velocities for ADCP deployment 2 at West Kirby Sands. Sub-figures show the water depth and depth averaged velocities during spring and neap tides.

Vertical profiles of the velocity (Figure 3.6) show the 0.57m blanking distance of the instrument, as with deployment 1. The data for deployment 2 were collected with a 10cm bin depth so that the entire water column was measured. The velocity profiles were extracted from the data at times of peak flood and ebb for spring and neap tides. The shape of the velocity profiles are similar to those from deployment 1, with lowest velocities occurring at the bed due to boundary frictional effects and maximum velocities occurring at or near the surface.
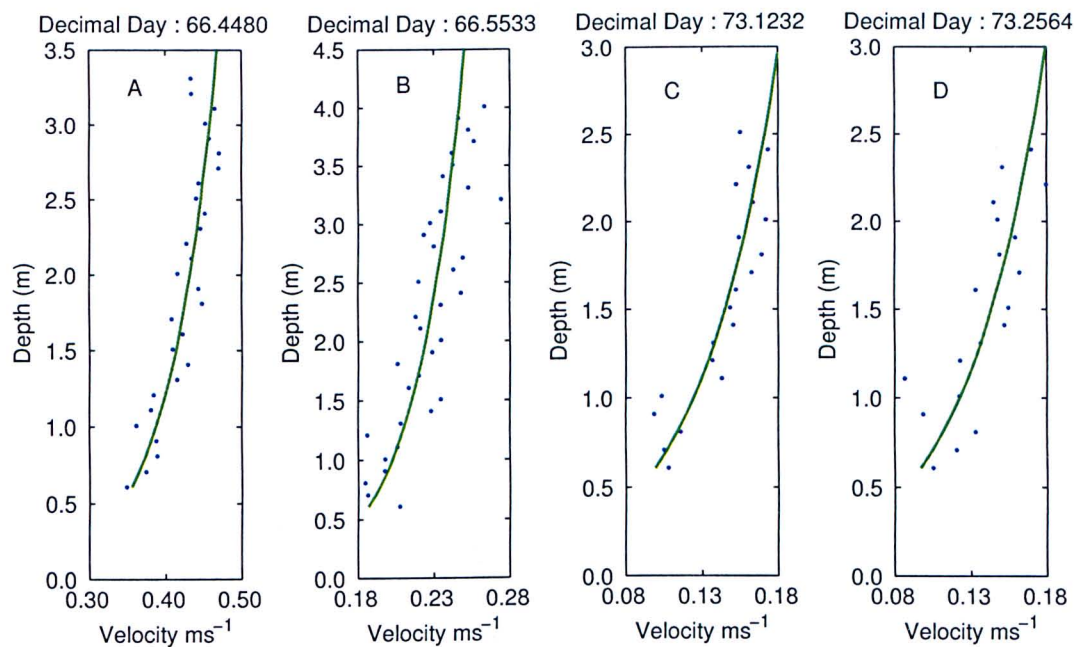
Figure 3.9: Vertical profiles of velocity, averaged over 10 minute intervals, for spring and neap peak flood (A & C) and peak ebb (B & D) tidal phases during the ADCP deployment 2 (03.01.11-17.03.11) at West Kirby Sands.

3.2 Intertidal DGPS survey

Figure 3.10: The DGPS base station set up on West Kirby Sands for the intertidal beach survey.

The intertidal area of West Kirby Sands was surveyed on 4 separate occasions over a period of 2 weeks (28.01.11, 31.01.11, 08.02.11, 11.02.11) using a differential Global Positioning System (DGPS) to determine the bathymetry. The instrument used was the Leica 1200 RTK GPS system which accurately determines the elevations and positioning of survey points. DGPS instruments theoretically have a centimetric precision in the x and y co-ordinates and in elevation z (van Rijn et al., 2000). Observations of the scattering of the co-ordinates of the control points obtained during each survey can also serve as an indication of the precision which is actually achieved in practice. The system consists of a base station (Figure 3.10), the location of which is precisely known, and a portable rover GPS system which uses a pole mounted receiver to reference its position to that of the base station. For best results when collecting data the rover pole system should be kept vertical with the lower end tip in almost constant contact with the bed. This ensures that the elevation data is as accurate as possible and can be reliably used for contouring the topographical features at West Kirby Sands. The positioning and elevation data collected were subject to post processing for further use and manipulation. The data downloaded from the base and rover systems were referenced to a control location of known height; for these surveys Holyhead, Anglesey was used. This gave projected grid coordinates (Easting and Northing) and elevation data referenced to Ordinance Datum Newlyn (ODN). The survey area covered the intertidal beach slope with low profile sand dunes located between Hilbre Island and West Kirby mainland (Figure 3.11). A large area of sand flats is exposed at low tide, and so surveys were conducted at these times for maximum data collection. The measurements were recorded in a continuous collection mode where survey points are logged every second whilst the author walked over a predefined grid of the survey area.
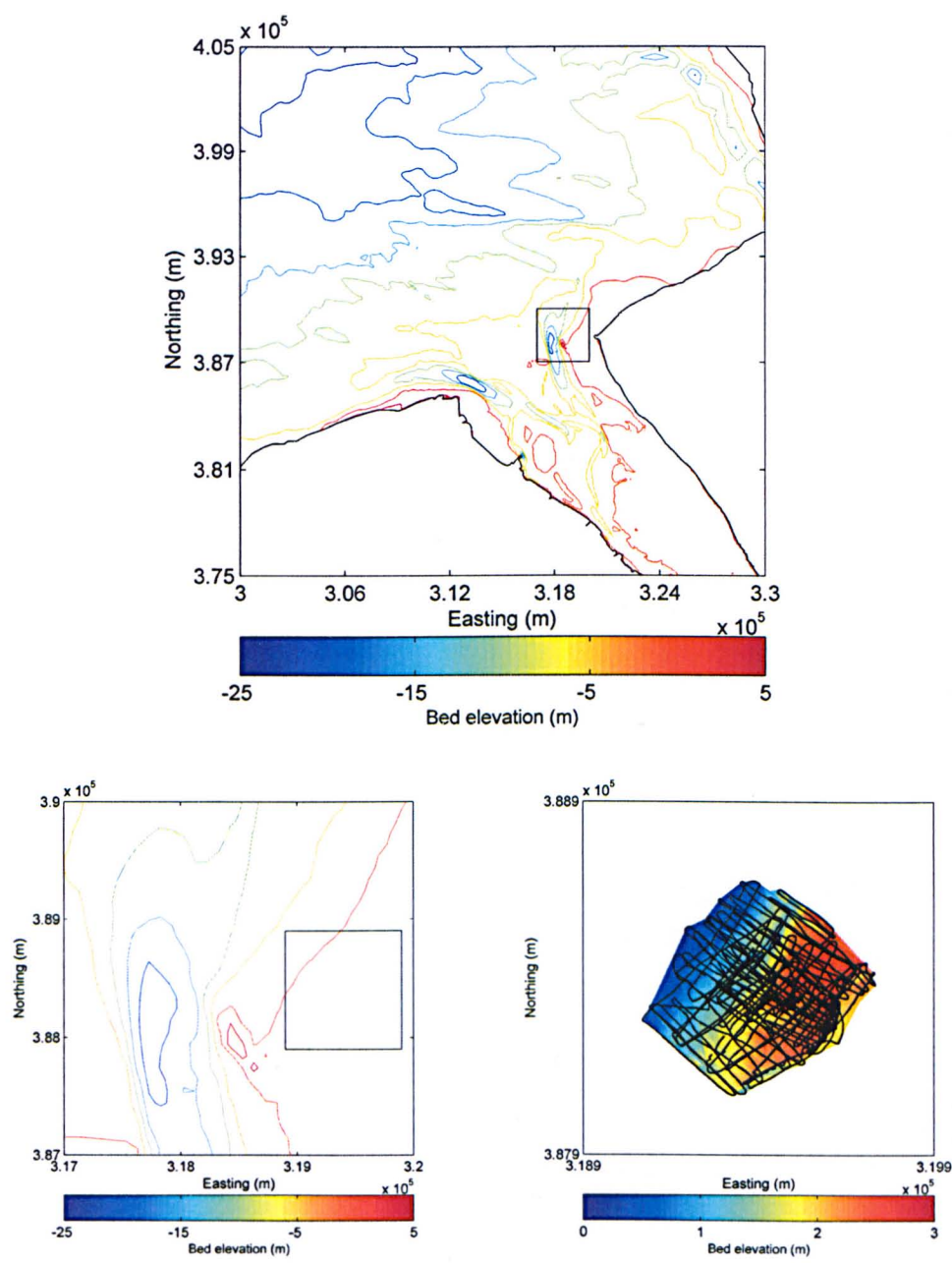
Figure 3.11: The location of the DGPS field survey campaign on West Kirby Sands in the mouth of the Dee Estuary. All collected survey data points along with the interpolated bathymetry are shown.

The survey grid over which the DGPS data points were collected was chosen to cover an area of large scale bed forms visible at low tide on West Kirby Sands. The track walked was oriented so that the grid lines were approximately perpendicular to the bed form crests, with a 2-3m spacing between track lines. Track lines parallel to the bed form crests were also included to increase the amount of elevation data available for interpolation. The data were interrogated using Matlab to produce interpolated topographic maps using the measured data points. The interpolated bathymetry and the measured data points for all of the surveys conducted on West Kirby Sands are shown in Figure 8.1. Beach profiles

were extracted from this interpolated bathymetry data to identify large scale bed forms on West Kirby Sands, which are analysed later in this study. These large scale bed forms were observed by the author during the survey period to be low profile features with bed form crests orientated in a south west to north east direction. The orientation of these bed forms is perpendicular to the orientation of flow, which moves into and out of the estuary mouth, over this intertidal area. This suggests that if these large scale bed forms are migrating they will move into the estuary interior via West Kirby Sands, a notion which is supported by the flood dominance in the current speed observed in the ADCP data (Figures 3.3 & 3.7).

The first DGPS survey conducted on 28.01.11 consisted of a total of 5380 data points. The minimum error in elevation for this survey, determined in the post processing process as the scattering of the observed data, was 0.0013m and the maximum error was 0.0205m. The second survey conducted on 31.01.11 consisted of 4617 data points. After downloading the data and referencing it to the Holyhead, Anglesey control station, the minimum error was 0.0009m and the maximum error was 0.0086m. The third survey, on 08.02.11, was conducted after a period of strong wind and large wave action in the area. It was observed that the topography of the intertidal sand flats at West Kirby Sands had changed since the previous survey on 31.01.11, with small scale ripples superimposed on dunes (Figure 3.12). This gives a first indication that wave activity could have a significant impact on the bed forms, and any associated sediment transport, at West Kirby Sands.

Figure 3.12: Smaller dunes with small scale ripples super-imposed observed on West Kirby Sands after a period of increased wave activity. The ripples are of the order of 10cm long.

The third survey consisted of 6796 data points with a maximum error of 0.0609m and minimum error of 0.0013m. The forth and final survey at West Kirby Sands covered a smaller area than previous surveys due to problems with the instrument's power supply. A total of 4905 data points were collected with a maximum error of 0.0724m and minimum error of 0.0008m.

3.3 Further observations

The morphology of West Kirby Sands was observed to have changed at the time of the third DGPS survey (08.02.11) after a period of increased wave activity. During calm conditions ripples were superimposed on larger sand dunes, however after the influence of waves these bed forms were modified. Without knowledge of the water depth it is not possible to classify these bed forms, however they could be defined as either mega-ripples or possibly hummocks. This follows a period of 8 days with a maximum offshore wave height of 3m. Areas of unconsolidated sand were observed around the crests of the sand dunes, with washed out ripples also present. This could be caused by sheet flow conditions experienced over the sand flats on West Kirby Sands as the water leaves the region during the ebbing tide.

Calm conditions, with low wind speeds and small wave heights, were observed during the first and second surveys on 28.01.11 and 31.01.11. During the survey of 28.01.11 it was noted that there were small symmetrical ripples, with approximately 5-10cm wavelengths, in the troughs of the sand dunes (Figure 3.13). These ripples could be seen to be washed out on the crests of these dunes (Figure 3.13 right panel, marked 'X'), which normally signifies a high energy environment. Areas of unconsolidated sand were observed on the crests of the dunes where washed out ripples were also observed, suggesting recent movement at the crest of the dune under high current conditions (washed out ripples) followed by the deposition of sediment (unconsolidated sand). These washed out bed forms could be generated by water run off during the final phase of the ebb tide.
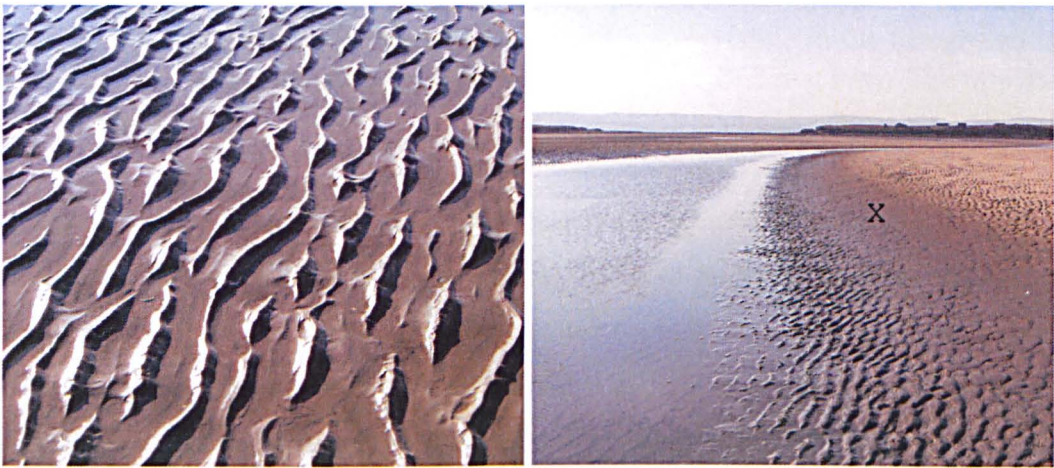
Figure 3.13: Symmetrical ripples (left panel) with 'washed out' ripples with unconsolidated sand at dune crest (approximate height of 1m marked 'X') observed during the 28.01.11 DGPS survey. The ripples are of the order of 10cm long.

Similar ripples in dune troughs were observed on 31.01.11 (Figure 3.14 right panel), as well as areas of washed out ripples with unconsolidated sand (Figure 3.14 left panel).

Figure 3.14: 'Washed out' ripples with areas of unconsolidated sand (left panel), possibly generated by water run off in the final phase of the ebb tide. Ripples also visible in the troughs and stoss (sea ward) slopes of dunes (right panel) observed during the 31.01.11 DGPS survey. The ripples are of the order of 10cm long.

The large scale bed forms present on West Kirby Sands can be seen in Figures 3.13 and 3.14 (right panels), where the image shows the dune lee slope. In these pictures the open sea boundary is to the right and the sand flats are to the left. This shows these dune features to be asymmetric with the steeper 'lee' slope orientated landward. Asymmetry of large scale bed forms has been shown to be a key indicator of tidal asymmetry, and therefore the residual flow direction with associated bed load transport when in equilibrium with the currents which formed the bed form (Stride, 1963; Van Landeghem et al., 2012). Asymmetrical forms generally retain a consistent facing direction over a tidal cycle, because the subordinate current does not transport enough sediment to reverse the profile.

Upon returning to West Kirby Sands to conduct another DGPS survey on 08.02.11 it was clear that the morphology of the area had changed substantially. Smaller dune features were now present with superimposed small scale ripples where previously only small scale ripples were observed (Figure 3.15 (left panel)). These features could be seen to be washed out towards the crest and lee slopes of dunes (Figure 3.15 (right panel)).
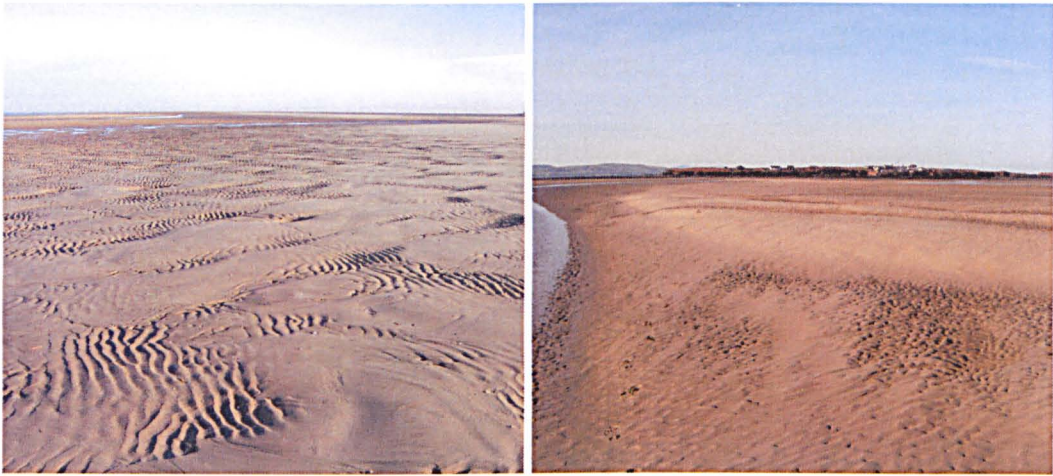
Figure 3.15: Smaller dunes with super-imposed 'washed out' ripples (left panel). These features were observed to be super-imposed onto the sand dunes on West Kirby Sands and displayed signs of 'washing out' around the dune crests (right panel) observed during the 08.02.11 DGPS survey. The ripples are of the order of 10cm long.

3.4   Lidar data

Bathymetry data covering the Dee Estuary was available from Lidar airborne surveys conducted by the Environment Agency in 2003 and 2006. The 2003 and 2006 surveys have a horizontal resolution of 2m and 1m, respectively, with a vertical accuracy between ±5cm to ±15cm (Moore, 2009). The whole of the estuary interior is covered by the 2003 survey, however data covering the mouth of the estuary was available to the author for 2006. The aerial surveys were conducted at low water so that the maximum area of the estuary could be recorded. The deep water channels, which retain water at the lowest stages of the tide, were surveyed separately using boat-based multibeam swath bathymetry, however, these deep water data were only available to the author for the 2003 survey. All Lidar depths presented here are relative to Ordnance Datum Newlyn (ODN).

Figure 3.16 shows the bathymetry of the Dee Estuary from the 2003 Lidar survey. The two main deep water channels, Hilbre Channel and Welsh Channel, are visible at the mouth of the estuary, as well as the creeks and channels of the saltmarsh system of the eastern shore. The estuary can be seen to be a relatively shallow system, with only the deep channels recorded as being less than -20m ODN, while the majority of the estuary has an elevation above -6m ODN.
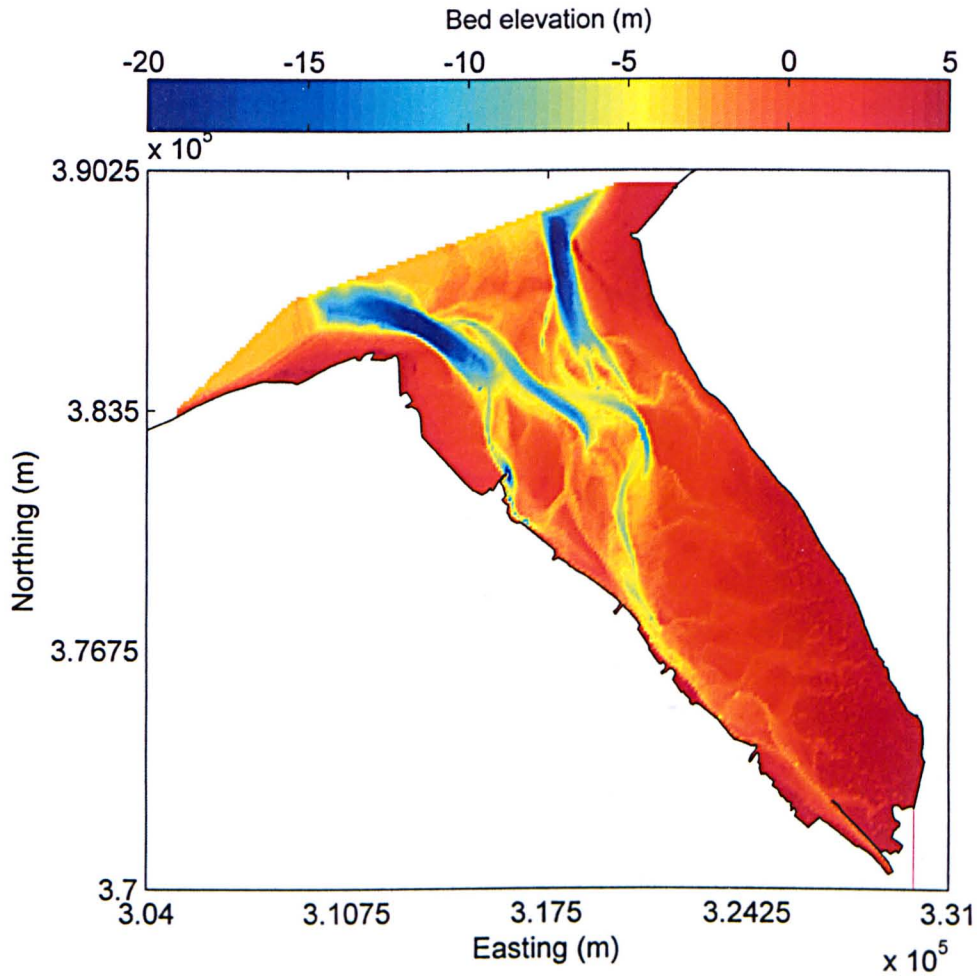
Figure 3.16: Bathymetric data of the Dee Estuary from the 2003 airborne Lidar survey combined with swath bathymetry data.

Figure 3.17 shows the bathymetry obtained during the 2006 Lidar survey. The data which were available to the author covered the mouth of the estuary and did not include the deep water bathymetry for the two main navigation channels. The 2006 survey data does include the intertidal sand flats at West Kirby Sands and West Hoyle Bank. It is possible to determine the large scale bed forms on West Kirby Sands which were surveyed during the 2011 DGPS field campaign, detailed previously.
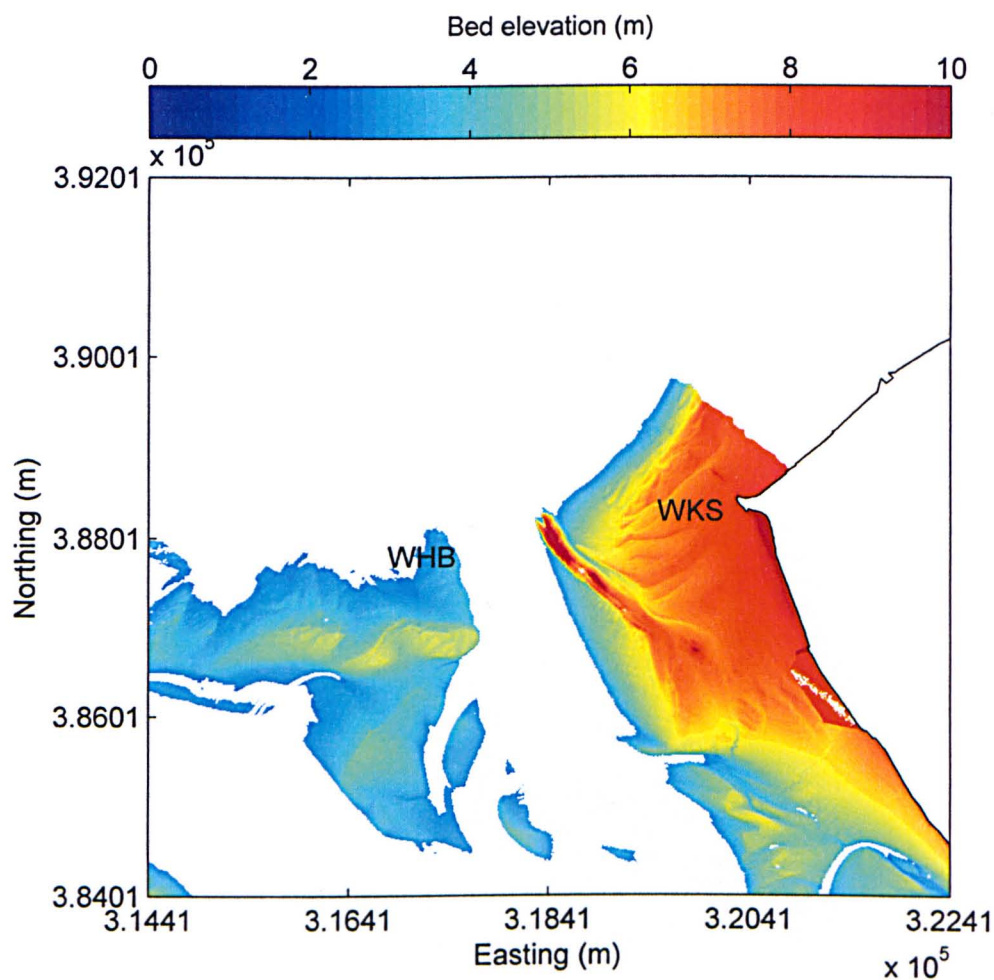
Figure 3.17: Bathymetric data of the Dee Estuary from the 2006 airborne Lidar survey, covering the mouth of the Dee Estuary, including regions of large scale bed forms, namely West Kirby Sands (WKS) and West Hoyle Bank (WHB).

3.5   Sediment

A sediment grain size survey was conducted as part of a research project into bed load transport at West Kirby Sands by McCann (2007) (Figure 3.18). 30 samples of approximately 400g dry weight were taken from the surface in order to represent the sediment which travels as bed load.

Figure 3.18: Sediment sampling route overlain on an aerial photograph of West Kirby Sands. From McCann (2007).

The sediment samples were analysed for median grain size (D_{50}). The distribution of the results showed that the sediment became progressively finer towards the shores of West Kirby (Figure 3.19).
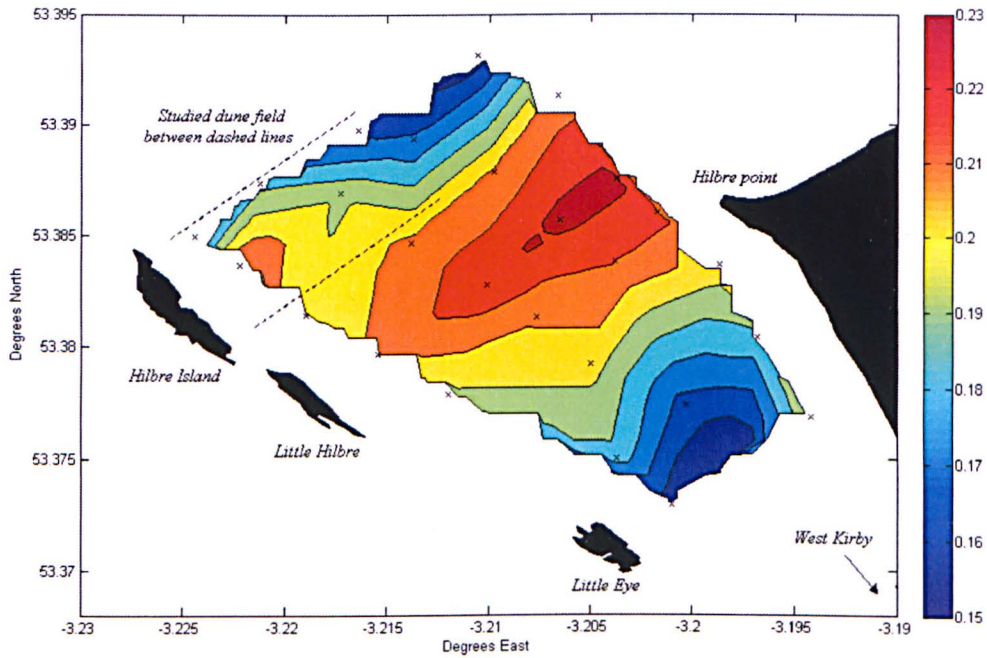
Figure 3.19: Median grain size (mm) contoured map with the location of sample positions (crosses) and land masses (filled black shapes). From McCann (2007).

McCann (2007) also noted the presence of many common lugworm (Arenicola marina) faecal mounds between the island of Little Eye and the head of the Wirral. As lugworms are burrowing creatures which can use a particular burrow for long periods (Wells, 1966), it was hypothesised that towards West Kirby, tidal currents and wave energy are depleted by the sand flats resulting in very little sediment transport. The presence of black sediment within these faecal mounds suggests that the sediment from 10-20cm depth (the burrowing range of the lugworm) is from an anoxic environment, which is maintained in a low transport environment as sediment turnover is reduced.

3.6 Summary

These data have allowed a valuable first look at the flow dynamics and morphology at the mouth of the estuary. It has shown that tidal asymmetry is flood dominant at West Kirby Sands, which should result in a net transport of sediment in the direction of the flooding tide which is into the estuary. This then suggests that these intertidal sand flats could act as a sediment pathway for sediment transport into the Dee Estuary. These data have also allowed an initial indication at the scale of the sand dunes present on this intertidal area. It is the migration of these bed forms which is analysed later to determine the major sediment pathways and their contribution to the overall sediment budget of the estuary.

Chapter 4

Modelling the Dee Estuary

4.1   Introduction

The processes associated with coastal evolution tend to be three-dimensional, however, important aspects of coastal behaviour can be well understood and predicted using modelling concepts based on fewer dimensions (De Vriend et al., 1993).

The TELEMAC computer software system (Version 5.9) was used to model the action of tides and waves in the Dee Estuary and surrounding coastal area (Figure 4.1). The modelling system was applied to simulate tides, waves, wave induced currents and the resulting sediment transport in the estuary system through tidal cycles. TELEMAC is well suited to modelling the coastal domain and hydrodynamics of the Dee Estuary due to the finite element grid allowing for graded resolution. This allows a high model resolution to be applied to near shore processes and a coarser resolution in the deeper water areas, optimising model accuracy and computation time.
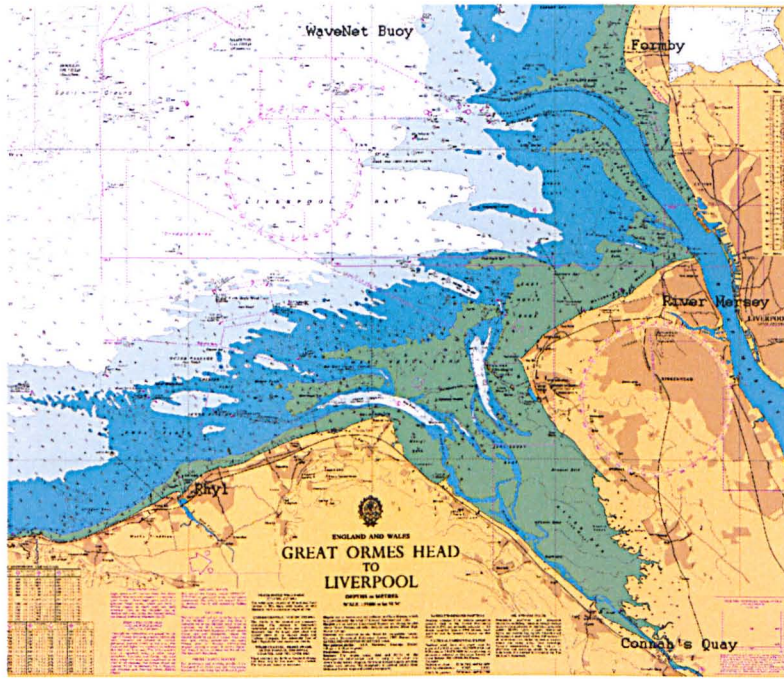
Figure 4.1: The Dee Estuary and surrounding coastline.

Large waves combined with strong currents associated with spring tides are thought to be the driving force behind large scale bed form migration. Specific events can be hindcast for comparison with bed form migration data. Historic wave data from the WaveNet wave buoy is input into the TOMAWAC wave model so that the time varying boundary conditions will more accurately simulate the wave field in the model domain. The 'wetting and drying' feature included in TELEMAC is an essential component when modelling shallow water estuaries such as the Dee which contains extensive tidal sand flats and where the mean volumetric increase from mean low water to mean high water is over 80% (Moore et al., 2009). Previous studies in the Dyfi Estuary, West Wales applied the TELEMAC modelling system to investigate net sediment transport in a shallow sandy macro-tidal estuary (Robins and Davies, 2010; Brown and Davies, 2010).

The model grid extends from Connah's Quay at the head of the estuary to 15km offshore, including the mouth of the River Mersey and coastline from Bootle to just north of Formby and along the Welsh coast west of Rhyl. This computational domain allows the coastal processes influencing the Dee Estuary to be modelled, including data from the WaveNet buoy on the model boundary to simulate waves in the region and incorporating the input from the River Dee at Connah's Quay (Figure 4.1). In order to simulate the interaction of waves, currents and sediment transport in the Dee Estuary all of the modules within TELEMAC must be executed in a precise order. This is represented by the time loop of modules in Figure 4.2
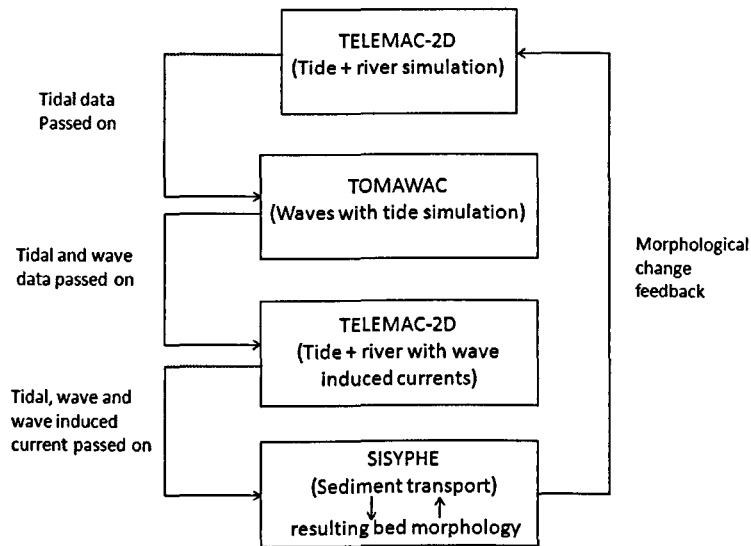
Figure 4.2: Simulating morphological change by looping the individual modules of TELEMAC.

So that the results of each of the modules link together correctly the output period (30 minutes) and duration of model run (a specified number of tidal cycles) must be strictly adhered to. TELEMAC-2D, with model spin-up, generates the initial currents with tide and river input. TOMAWAC is then used to simulate the waves over time varying tidal and wave conditions. The wave induced currents are then simulated with TELEMAC-2D by re-computing the tide with the wave result input also. To predict the resulting sediment transport, SISYPHE is run in a coupled mode with TELEMAC-2D. This predicts the sediment transport due to the wave-current conditions and also updates any change in morphology at every time step so that topographic change feeds back on the hydrodynamics. The input files required to model this area of coast are as follows:

Geometry file (geo)

This file represents the bathymetry for the model domain and contains all of the information for the finite element mesh, such as the number of nodes and their coordinates.

Steering file (cas)

The steering file acts to control the model simulation by allowing the user to assign values to keywords and initiate key functions. An example of a steering file is given in Appendix II. The syntax used within the steering file is defined in the dictionary (dico) file. The main functions performed here are to specify the names of the geometry, boundary conditions, fortran and formatted data files,

as well as allowing the continuation of model runs by including the details of a previous computation.

Boundary conditions file (conlim)

Each of the boundary points for the model domain is represented by successive lines of this file, dictating the conditions set at the limit of the domain. Examples of each of the conlim files used for the three modules of TELEMAC are given in Appendix III. The conlim file is generated with the pre-processing software BlueKenue, giving two main boundary types; solid (e.g. coastline) and liquid (e.g. open sea or river). The conditions on the solid boundary are static, whereas the liquid boundary conditions change in time, allowing the user to vary the free surface or flow rate at the seaward limit of the domain.

Fortran file

This file contains the subroutines which are allocated by the user to each model computation. The name of the fortran file is specified in the steering file so that subroutines specifically developed for that computation can be compiled and linked to when running the simulation.

Formatted data files

Files can be specified to provide data for the Fortran subroutine files (e.g. wave height, wave period and wave direction).

4.2 Generating the model grid

4.2.1 Bathymetry

The first step towards creating the model mesh is to determine the area to be included in the model domain. The coastline boundary was assigned by hand, following the natural limit of the estuary at approximately the 5m contour line and taking into account any man made coastal protection or structures. This limit was chosen so that large amounts of unnecessary landward points are avoided, which would increase computation time. The mouth of the River Dee is included at the eastern edge of the grid so that river flow input can be implemented in the model. It was not seen as necessary to include a greater amount of the river network as this should not have an overriding influence on

the processes occurring at the mouth of the estuary and will only act to increase node points and therefore computation time. The boundary then extends 15km offshore into Liverpool Bay so that the WaveNet wave buoy is situated on the northern grid boundary. The decision to extend the grid this far into Liverpool Bay was made so that measured wave data can be input at the model boundary to accurately represent the wave climate of this area.
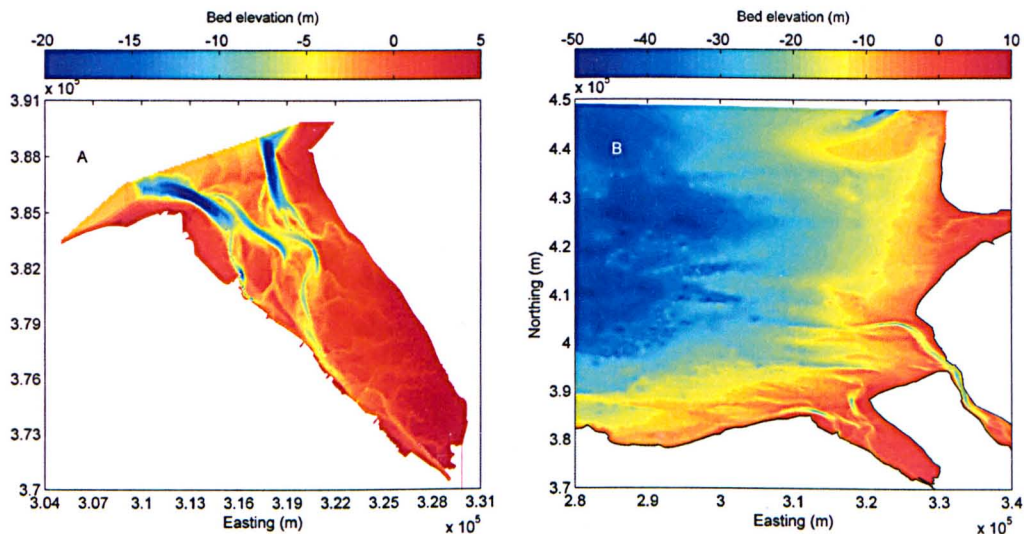
Figure 4.3: Bathymetry data for the Dee Estuary and Liverpool Bay from the 2003 Lidar survey (A) and the POLCOMS Liverpool Bay model (B).

Bed elevation data for the interior of the estuary was obtained from a 2003 Lidar survey which included aerial survey data and bathymetry data for areas below the low water line (Figure 4.3 A). Bathymetry data for the model domain which extends offshore into Liverpool Bay was obtained from the POLCOMS model grid bathymetry, courtesy of the National Oceanography Centre, Liverpool (Figure 4.3 B). POLCOMS (Proudman Oceanographic Laboratory Coastal-Ocean Modelling System) is a three dimensional finite difference hydrodynamic model, which can include the effects of wind and density driven flow (Holt and James, 2001).
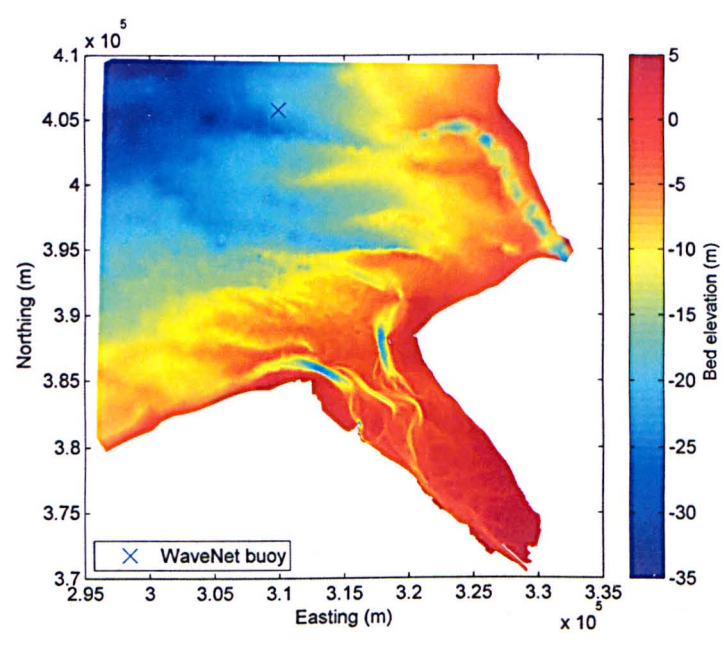
Figure 4.4: Bathymetry for the Dee Estuary model domain, as a combination of Lidar and POLCOMS bathymetry data, covering the inner Dee Estuary and extending out into Liverpool Bay. Bathymetry resolution is 20m in the estuary interior (Lidar) and 160m for the outer model domain (POLCOMS). Bed elevations are in m relative to ODN.

The Lidar data has a resolution of 10m while the POLCOMS data has a courser resolution of 160m. These two bathymetry data sets were combined to create the entire model domain (Figure 4.4). This combination of bathymetry works well with the TELEMAC finite element grid, where higher resolution is imposed in the mouth of the estuary to account for important shallow water processes, while deeper water areas have a coarser resolution to optimise computation time. The Mersey Estuary is neglected from the model grid, which extends to the estuaries mouth at the domains eastern limit. This decision was made so that the model domain does not contain a very large number of grid points which increases computational demand and simulation run time. The hydrodynamic influence of the estuary is addressed in the following section regarding river boundary conditions.

4.2.2 Grid generation

The programme BlueKenue was used to create the model grid of the coastal area of interest to be used with each module within TELEMAC. BlueKenue is a pre- and post-processing platform developed by the Canadian National Research Council. BlueKenue version 3.2.31 allows the user to produce a mesh of very high resolution using large bathymetry data files, as well as the boundary conditions file (conlim) required by TELEMAC. This is something which was previously a challenging task using the

TELEMAC pre-processing module MATISSE, especially when large bathymetry files were involved. The mesh generated is an unstructured flexible mesh of triangles, allowing the resolution to change throughout the domain and be locally refined. The resolution of the mesh is greatest in the mouth of the estuary where it is the aim of this research to resolve the nearshore processes accurately. This mesh format is preferable for modelling coastal environments due to its ability to resolve complex shapes, such as coast lines, something that the simpler finite difference approach struggles with. This does, however, increase the complexity of the model grid and therefore increase computational demand when running the TELEMAC modules.
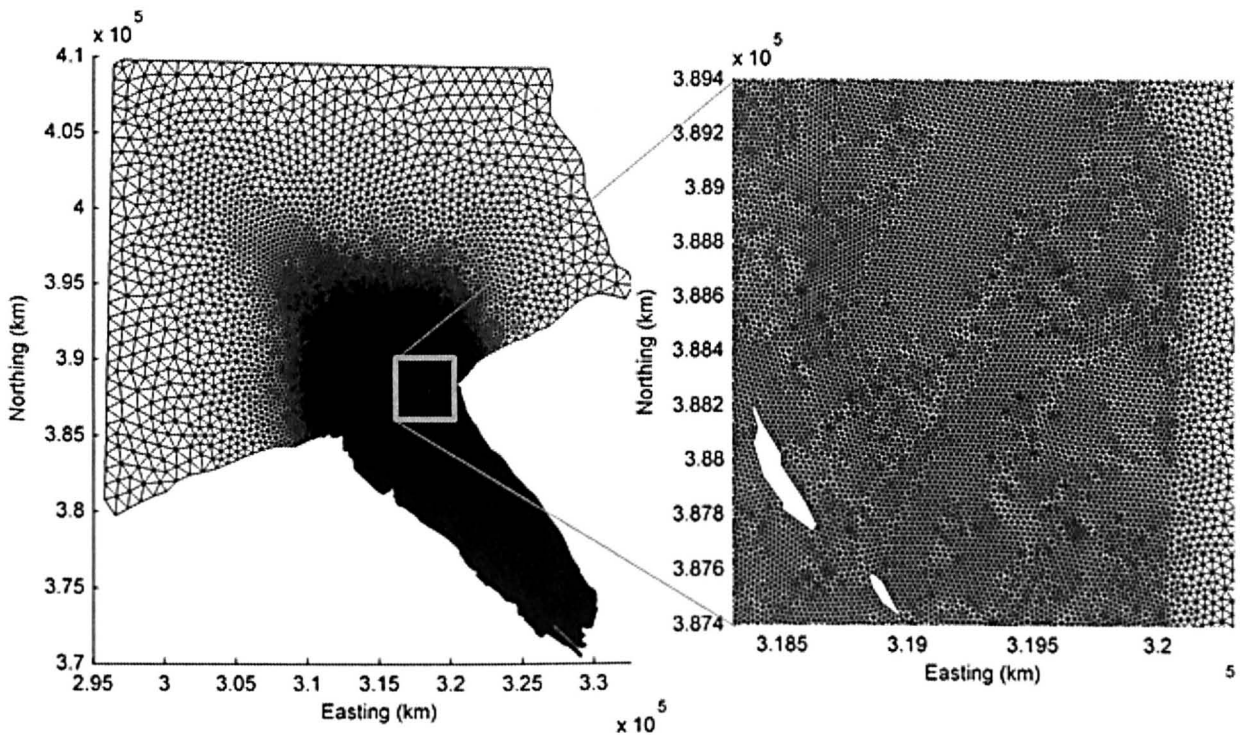
Figure 4.5: The final mesh for the Dee Estuary. The mesh resolution increases from 300m at the outer boundary to 10m in the estuary mouth, an example of which is shown in the inset on the right.

The offshore resolution was set to 300m to keep the total number of grid nodes to a practicable amount. The resolution in the mouth of the estuary increases to 10m which merges into 100m for the inner estuary. This higher resolution focuses on the surf zone and area of bed forms in the mouth of the estuary, where these bed forms are thought to be migrating into the estuary. The final mesh (Figure 4.5) comprises 119824 nodes, the majority of which are around the mouth of the estuary. The domain mesh was then linearly interpolated onto the complete domain bathymetry (Figure 4.4) using BlueKenue to create the geometry ('geo') file used within TELEMAC. Finally the boundary conditions ('conlim') file was also generated with the Boundary Conditions Editor, within BlueKenue. The Boundary Conditions Editor is a new feature for BlueKenue version 3.2.31 and allows the user

to create a conlim file using the finite element mesh that has just been created. The user is able to select boundary points of the domain and specify these as 'open', allowing waves and currents to move through them. All boundary points are set to 'closed' by default in the Boundary Conditions Editor, representing an impermeable wall; the user then allocates which boundary points are 'open' by selecting a boundary and tracer code. The three main conditions in the conlim file to be allocated using a numerical descriptor are: closed condition (value 2) which represents a closed wall with no flux through the boundary, free variable (value 4) sets a free boundary flux or depth, and prescribed variable (value 5) which prescribes a value of free surface, fluid flux or tracer at the boundary. An example conlim file can be found in Appendix III.

4.3   Tidal simulations

4.3.1   Tidal boundary conditions

The tidal forcing on the offshore liquid boundary of the model domain is implemented by the user for TELEMAC-2D to predict the tidal influence. TELEMAC-2D uses the subroutine BORD.f to simulate the variation of the free surface due to the tide. At each liquid boundary node with prescribed free surface the model calculates free surface elevation from the tidal amplitude, frequency and phase of the tidal constituents specified in the subroutine BORD. Any number of tidal constituents can be added to BORD by the user to simulate the tidal elevation for an idealised situation or for a specified time interval. For all of the TELEMAC-2D simulations herein eight tidal constituents were assigned at the offshore liquid boundary ($Q_1, O_1, P_1, K_1, M_2, S_2, K_2, M_4$). These constituents were obtained from the POLCOMS Irish Sea tidal model (courtesy of National Oceanography Centre, Liverpool), with a grid resolution of 1.8km, by linearly interpolating the amplitudes and phases onto the offshore liquid boundary points (Figures 4.6 & 4.7). These were then programmed into the subroutine BORD so that the free surface elevation at each offshore liquid boundary point could be simulated at each model time step.
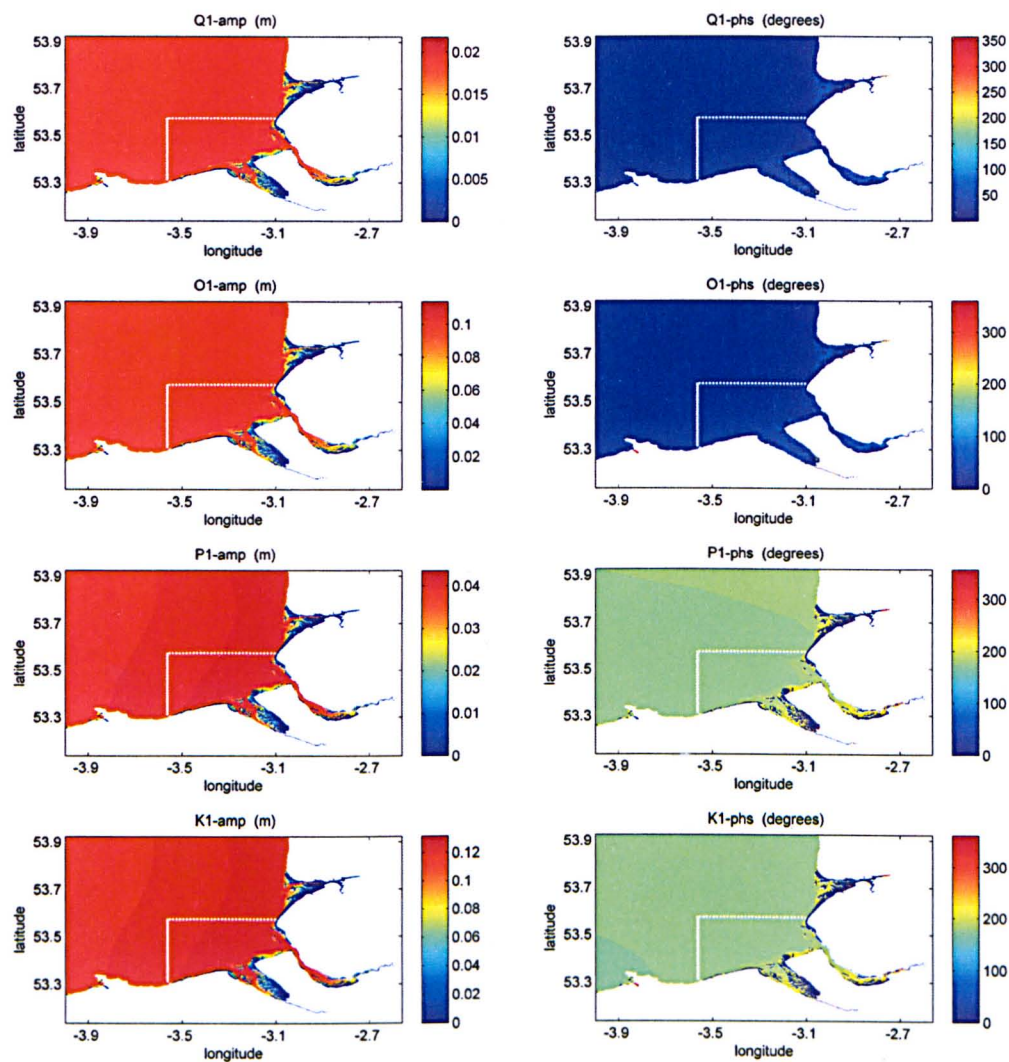
Figure 4.6: Tidal constituents from the POLCOMS Irish Sea model used for liquid boundary conditions by interpolating the amplitude and phase onto the Dee Estuary model open liquid boundary (white line).
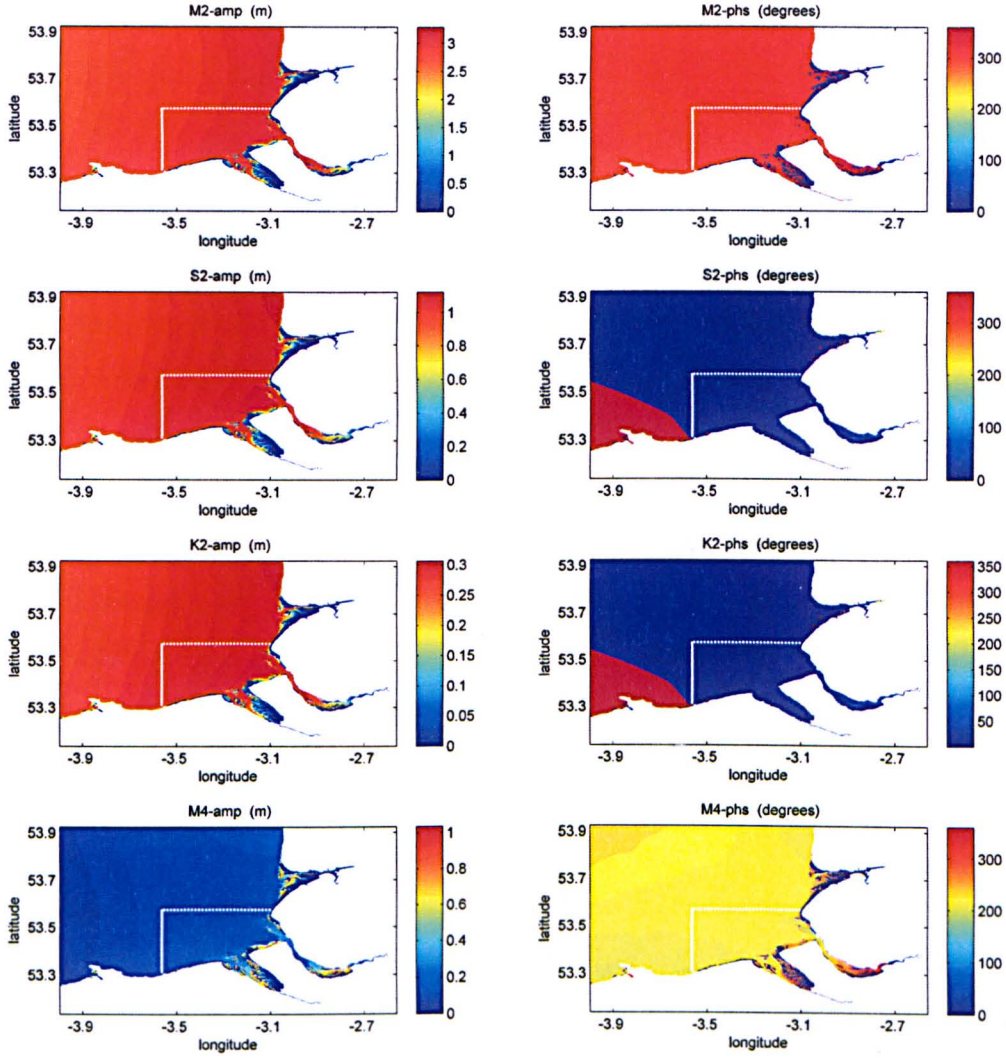
Figure 4.7: Tidal constituents from the POLCOMS Irish Sea model used for liquid boundary conditions by interpolating the amplitude and phase onto the Dee Estuary model open liquid boundary (white line).

The subroutine BORD calculates the free surface elevation z_s at each time step for every liquid boundary point with a prescribed free surface (conlim file value 5) using the formula

$$z_s = A_0 + A_1 \cos(\sigma_1 t + G_1) + A_2 \cos(\sigma_2 t + G_2) + ... A_n \cos(\sigma_n t + G_n) \quad (4.1)$$

where for each of the tidal constituents n, A is the tidal amplitude, σ is the tidal frequency, t is time and G is the tidal phase. Specific tidal elevations at a particular time are simulated by a summation of any number n of tidal constituents, denoted by the subscripts. Tidal constituents can vary in space, where BORD iterates along the liquid boundary to represent the surface elevation at each liquid boundary point. Using tidal amplitudes and phases to force each liquid boundary node was considered the most accurate method to simulate the tide. As an alternative, a single current and elevation time series,

obtained from POLCOMS, could be applied to the entire liquid boundary, however this would lose the spatial variation around the offshore domain.

4.3.2 River boundary conditions

The River Dee is the only major river to flow into the Dee Estuary, however its discharge is relatively small. A mean river input of $31 m^3 s^{-1}$ (Moore et al., 2009) was assigned to the open river boundary. These data were obtained from the UK National River Flow Archive from a gauging station run by the Environment Agency on the River Dee at Manley Hall. The tidal prism is defined as the volume of water that enters an estuary with each tidal cycle (the volume difference between high water and low water), excluding any influence from freshwater inflow. The Dee Estuary has an average tidal prism of $4 \times 10^8 m^3$, making the river discharge equate to 0.35% of the tidal prism over the tidal cycle (Moore et al., 2009). Therefore the inclusion of a river input is an obvious consideration when modelling the Dee Estuary, however correctly simulating the tidal input is of greater importance.

4.3.3 Tidal simulation results

A spring-neap tidal cycle was simulated with TELEMAC-2D for a two week time period with a time step of 10 seconds using eight tidal constituents $(Q_1, O_1, P_1, K_1, M_2, S_2, K_2, M_4)$. The simulation was initially run for 24 hours and input into the spring-neap simulation to remove any spin up errors. An option for parallel processing is available for TELEMAC-2D version 5.9 allowing for significantly increased computational speed. This option is activated with the keyword 'PARALLEL PROCES-SORS' in the steering ('cas') file, with the number of processor cores used specified. The Fortran, geo, conlim and formatted input files (previous results/ spin up files) are then split by the multiple processor implementation (MPI) subroutine into segments according to the number of processors assigned. The maximum number of processors used for the Dee Estuary model is 2 due to model instabilities resulting from the use of a greater number of processors. This is thought to be caused by the way that the model grid is split by the MPI subroutine into sections with a relatively equal number of nodes. The complexity and orientation of the Dee Estuary domain means that the maximum number of processors used is 2, which has the effect of halving the run time for single processor simulations. 'Parallel processors' are only applied to TELEMAC-2D simulations as further model instabilities were experienced with the use of waves (TOMAWAC) with currents (TELEMAC-2D) and sediment transport (SISYPHE).
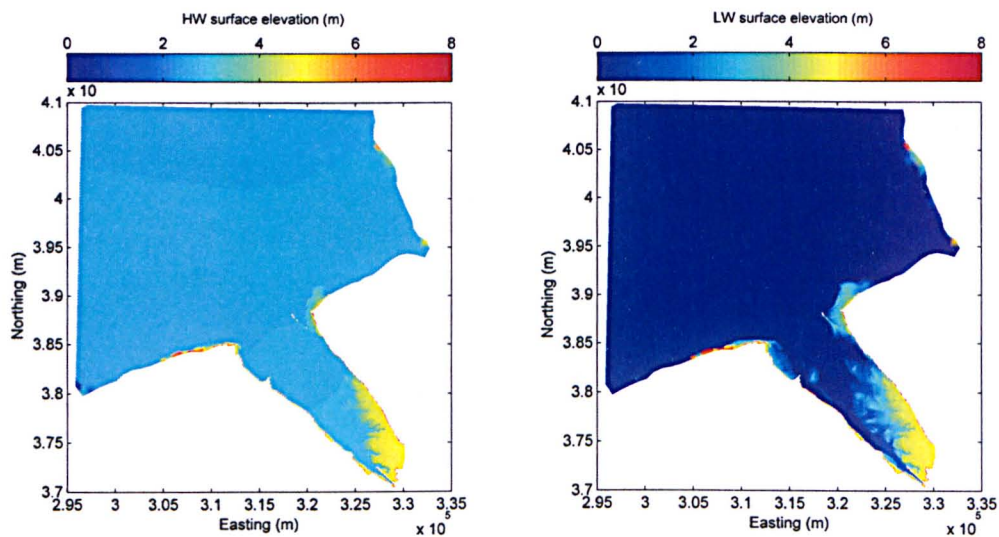
Figure 4.8: Free surface elevation over the model domain at high and low water

The principal factor governing the movement of water and initiation of currents is the difference in water level offshore compared with the inner estuary (Figure 4.8). Figure 4.9 shows depth-averaged velocity vectors overlain onto scalar velocity plots for peak flood and peak ebb tidal flow. The velocity vectors are plotted on a regular grid, due to their generation using Matlab, and with an 800m spacing so not to obscure each other and the underlying data.
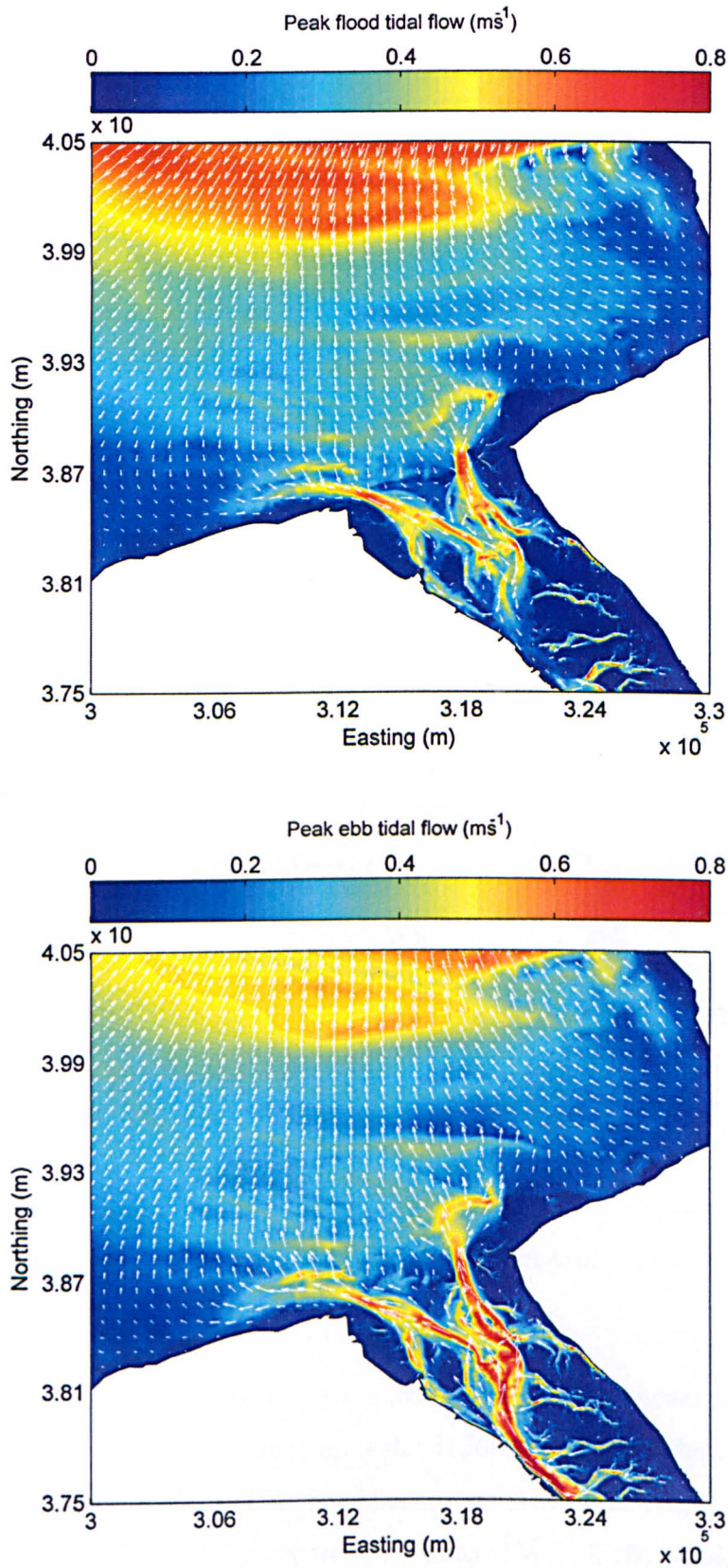
Figure 4.9: Depth-averaged velocity vectors overlain onto scalar velocity during peak flood and peak ebb tidal flow during a two week spring-neap TELEMAC-2D simulation.

The model simulated tidal currents to flow in a south (flood) to north (ebb) direction in the offshore domain (Figure 4.9). The flow direction moves in and out of the estuary mouth, in a north-south direction, making the v velocity the dominant component of flow. A faster movement of water can be seen offshore than inshore caused by the increased friction due to the inshore shallow water environment. However, faster flow can also be observed in the mouth of the estuary where the flow is restricted to the deeper water of the Hilbre and Welsh Channels during LW (Figure 4.9). The wetting and drying of sandbanks is an integrated feature within TELEMAC-2D and is essential when modelling shallow, tidal environments. This is particularly useful when examining the flow in an area of interest containing large scale bed forms, such as West Kirby Sands, as this intertidal sand flat is exposed and submerged with each tide.
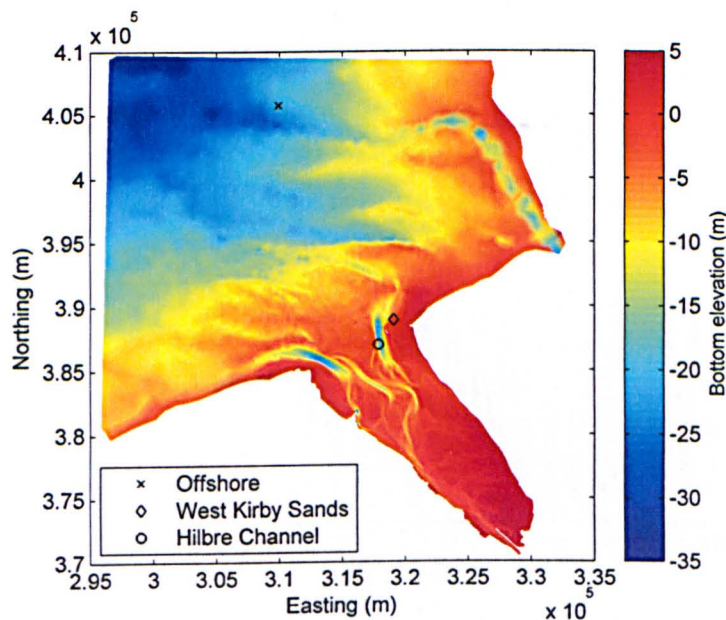
Figure 4.10: Bathymetric chart based on the Dee Estuary model grid showing the location of three regions for TELEMAC-2D tidal analysis.

The two week spring-neap model simulations were examined at three chosen points: offshore, the estuary mouth at West Kirby Sands and the deep water Hilbre Channel in the mouth of the estuary (Figure 4.10). The tidal range is similar throughout the estuary. However, larger velocities are seen at the offshore and Hilbre Channel points compared with values at West Kirby Sands (Figure 4.11). This corresponds with a difference in water depth, with the offshore and Hilbre Channel points being in deeper water than West Kirby Sands. The maximum velocities offshore and at Hilbre Channel were very similar at $1.0ms^{-1}$, while West Kirby Sands was $0.3ms^{-1}$. The v-velocity (north) component is

dominant over the u-velocity (east) component for all three points examined, indicating flow in and out of the estuary. The peak flood exceeds the peak ebb for the offshore and West Kirby Sands points, showing flood dominance, however ebb dominance is seen in the Hilbre Channel (Figure 4.12).
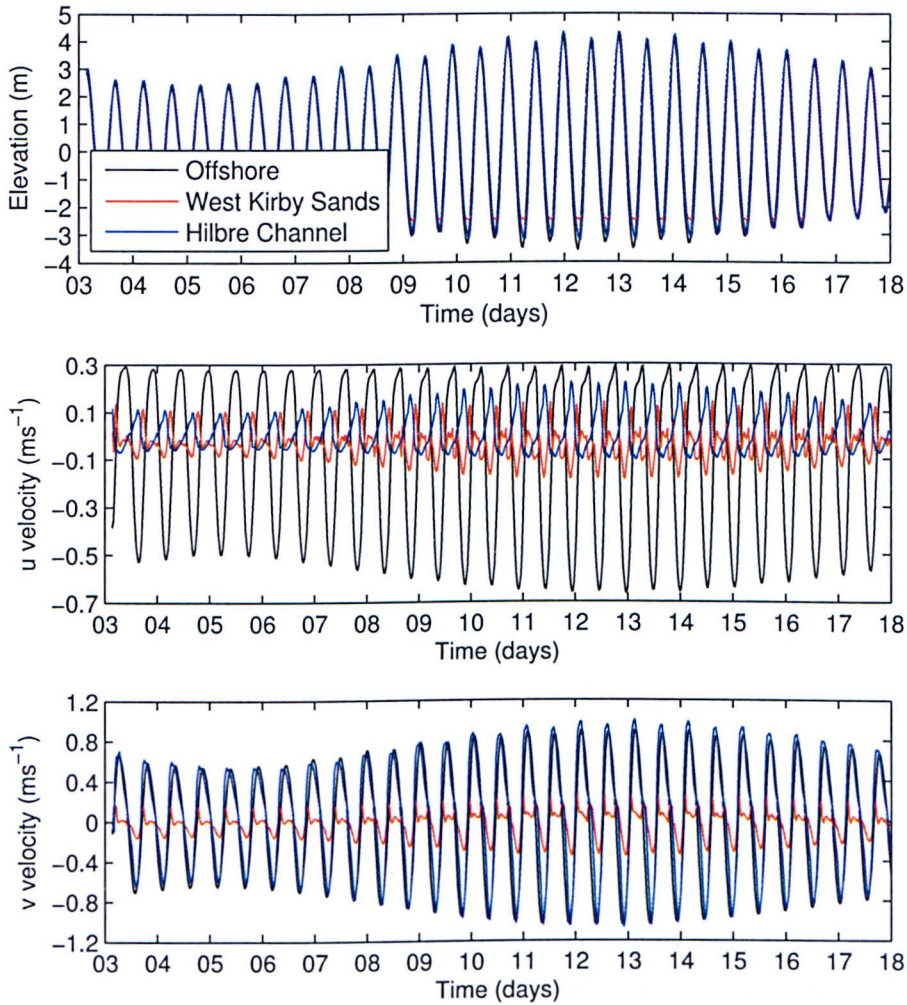
Figure 4.11: Spring-neap TELEMAC-2D tidal simulation showing free surface elevation, and u and v velocity components for 3 points in the model domain. Positive velocity values represent east (u velocity) and north (v velocity).

Figure 4.11 shows that there is contrasting ebb and flood behaviour throughout the estuary domain. An examination of a 12 hour tidal cycle during this 2 week simulation (Figure 4.12) shows that there also exists a variation in tidal asymmetry within the model domain. Offshore velocity can be seen to be flood dominant, whereas in the estuary mouth flood dominance occurs at West Kirby Sands while Hilbre Channel is ebb dominant. This could have significant impacts on sediment transport, as it suggests that there is a net movement of sediment from the offshore location to the estuary mouth. Higher flood velocities will result in increased shear at the sea bed during the flood compared with the ebb. Once the threshold bed shear stress for the initiation of sediment motion has been exceeded,

any further increase will result in greater sediment transport. The sediment transport is therefore a function of the shear stress at a given time and the duration of the flow in which the threshold shear stress has been exceeded. Net sediment transport will then move sediment into the estuary interior via West Kirby Sands, while sediment will be transported out of the estuary in the Hilbre Channel. This flood asymmetry in sediment transport at West Kirby Sands will certainly be an important factor influencing the migration of large scale bed forms in this region.
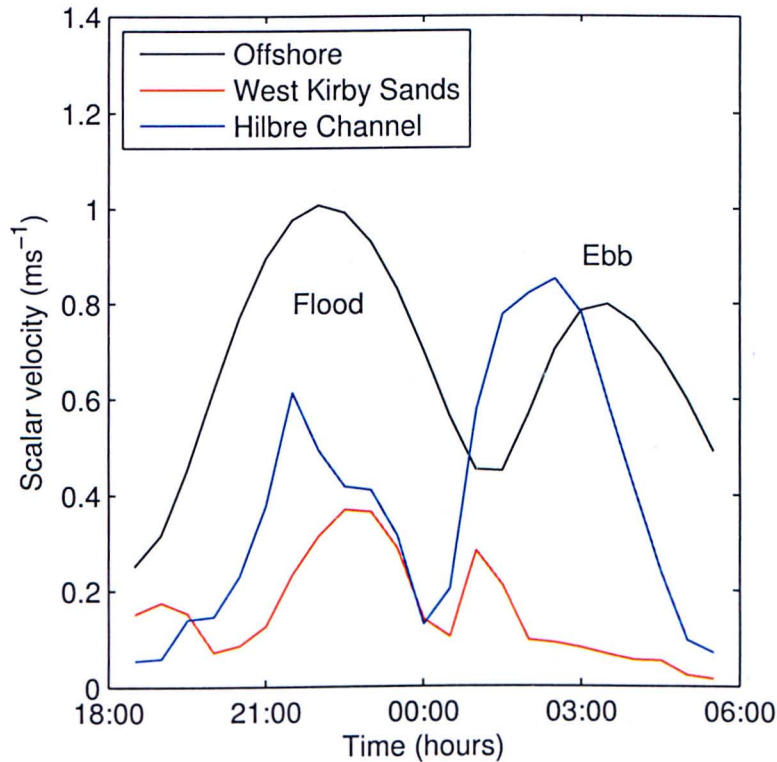
Figure 4.12: The tidal contrast for 3 points examined in the model domain over a 12 hour tidal cycle from the previous 2 week TELEMAC-2D spring-neap simulation.

4.3.4 Validation of the TELEMAC-2D tidal simulation

The components of flow and water depth output by the model for a 2 week simulation, with a 10 second time step and using eight tidal constituents ($Q_1, O_1, P_1, K_1, M_2, S_2, K_2, M_4$), are compared with ADCP data collected in the mouth of the estuary. ADCP data used for tidal model comparison covers two time periods; a STABLE (Sediment Transport and Boundary Layer Equipment) benthic tripod platform deployment in the Hilbre Channel (Figure 4.10) between 14.02.08-11.03.08 as part of the FORMOST (Field observations and modelling of the sediment triad) NERC project (supplied courtesy of National Oceanography Centre, Liverpool), and a second deployment between 03.03.11-17.03.11 (Section 3.1.2) of an ADCP at West Kirby Sands.

4.3.5 Tidal validation at Hilbre Channel

The tidal results file was examined for the Hilbre Channel location where the STABLE deployment was located. The STABLE deployment contained a 600 MHz ADCP in an upward looking orientation, and a 0.5m bin size. The velocities have been averaged every minute over the two week period. The comparisons between measured and modelled data show a good correlation for water depth, as well as both u and v components of flow (Figure 4.13).
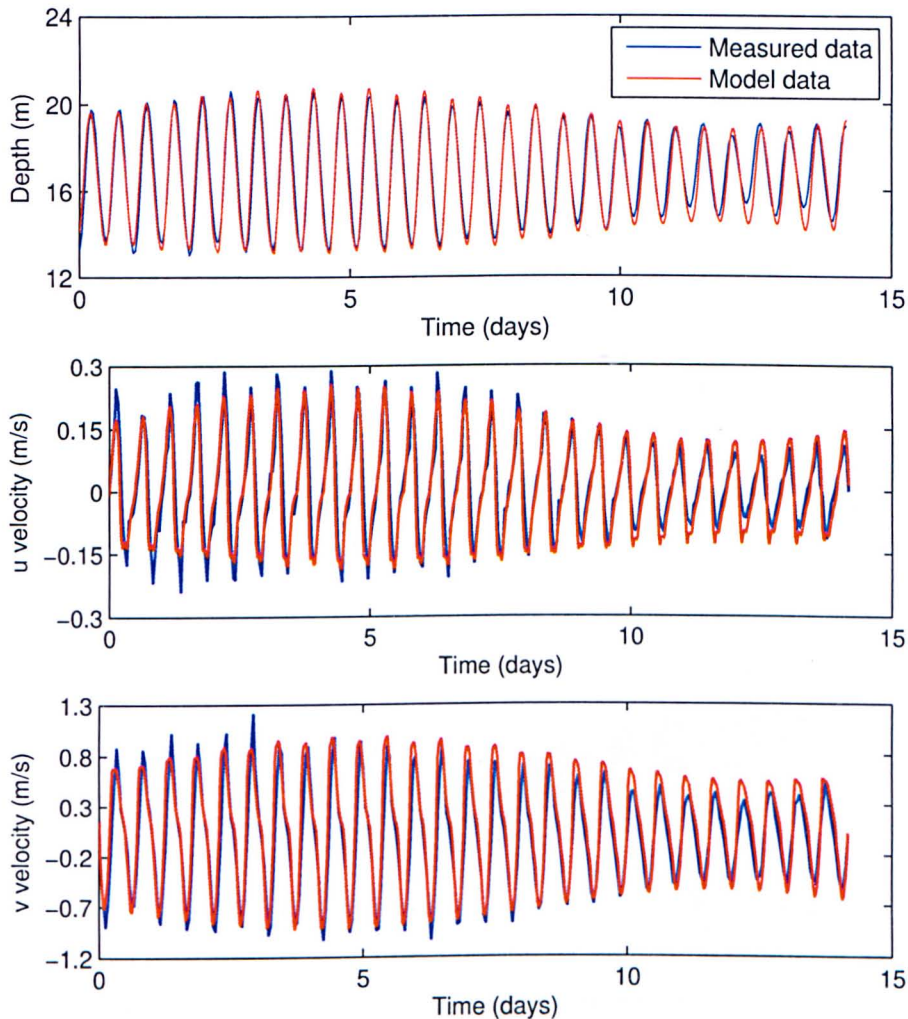
Figure 4.13: Water depth and flow velocity validation at Hilbre Channel in the mouth of the Dee Estuary for TELEMAC-2D tidal simulation.

A 24 hour time period is isolated from the 2 week simulation to show a clearer comparison between measured and modelled water depths and flow speed (Figure 4.14). This covers the period 14-28.02.08, for which velocity magnitude is calculated as a square root of the sum of the square of each component of flow (*u* and *v*).
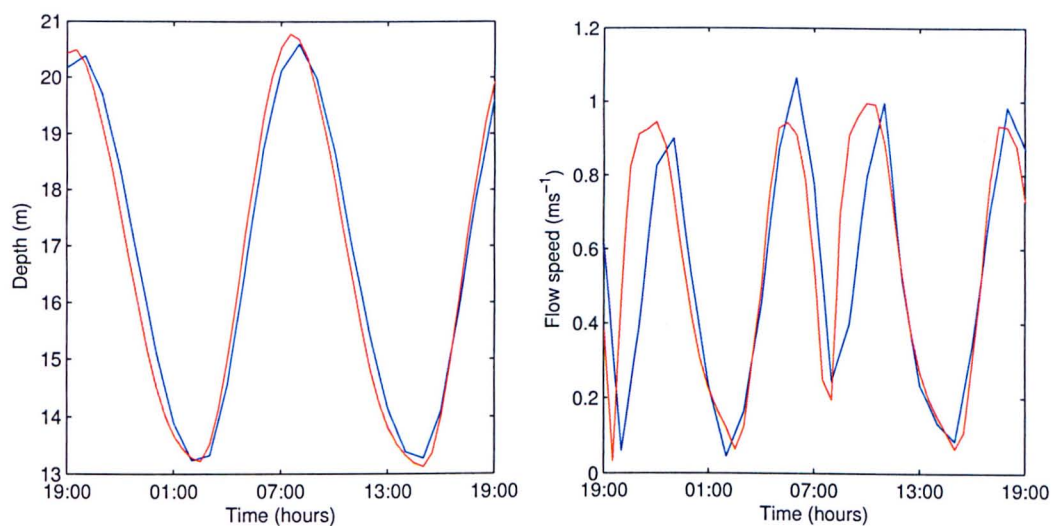
Figure 4.14: Water depth and flow speed validation at Hilbre Channel in the mouth of the Dee Estuary over a 24 hour period of the TELEMAC-2D tidal simulation. The blue line represents measured data while the red line represent modelled data.

The R-squared value (the normalised measure of the linear relationship between prediction and data) of the velocity data shows a good linear relationship between measured and modelled velocity (Figure 4.15). The modelled v (north) component of velocity shows a better correlation to the measured data than the u (east) velocity component. This is an acceptable result as the v velocity is the dominant component of flow for movement in and out of the estuary mouth.
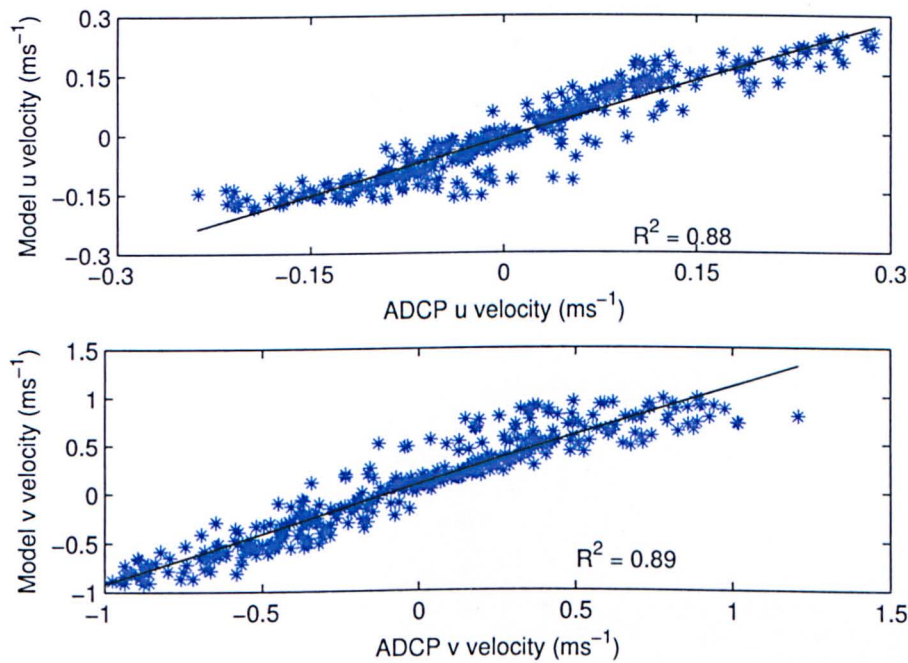
Figure 4.15: A comparison of measured and modelled velocity in the Dee Estuary showing a positive correlation.

4.3.6   Tidal validation at West Kirby Sands

The ADCP deployment at West Kirby Sands, between 03.03.11-17.03.11, was configured with a bin size of 10cm and set to record in a continuous mode to obtain high resolution data over this shallow water intertidal region. Data are averaged over 10 minute intervals to reduce the effect of noise. Figure 4.16 shows a comparison of measured water depths and velocities with tidal simulation results at West Kirby Sands. A reasonable correlation can be seen between water depths, with modelled data slightly under predicting measured values, possibly due to local atmospheric pressure effects. A comparison of velocity data shows that the u (east) velocity component is not well represented by the modelled data, however the v (north) component of velocity is well represented by the simulation. While this does not offer a correlation as good as that seen previously in the Hilbre Channel data, the good representation of the v velocity data is an acceptable result as this is the dominant component of flow in and out of the estuary.
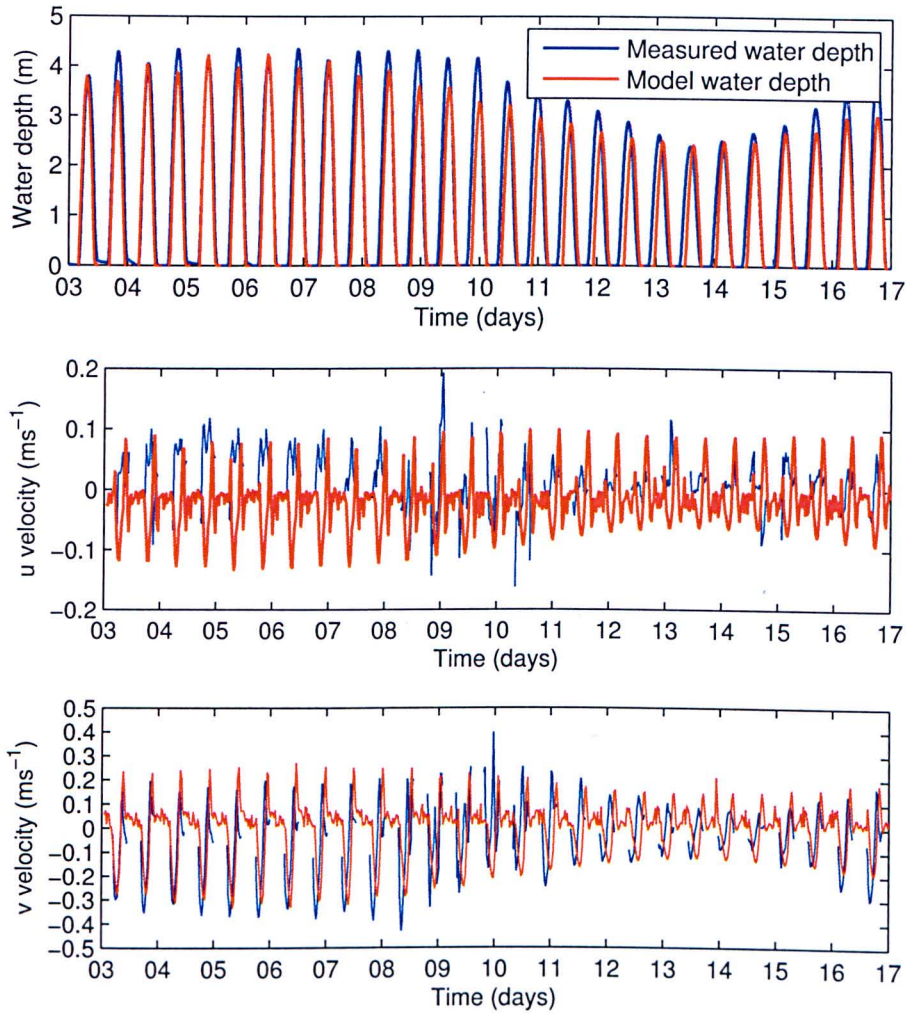
Figure 4.16: Water depth and flow velocity validation at West Kirby Sands for TELEMAC-2D tidal simulation. Measured data collected during an ADCP deployment at the inter-tidal sand flats of West Kirby Sands between 03.03.11-17.03.11.

Figure 4.17 shows a comparison of water depth and flow speed, calculated as a sum of the squares of the u and v velocity components, between 05.03.11-06.03.11. This shows the flood asymmetry at West Kirby Sands well represented by the model simulation. This is a crucial factor when modelling the hydro- and morpho-dynamics of shallow water areas in the mouth of the Dee Estuary due to the effect this asymmetry may have on net sediment transport.
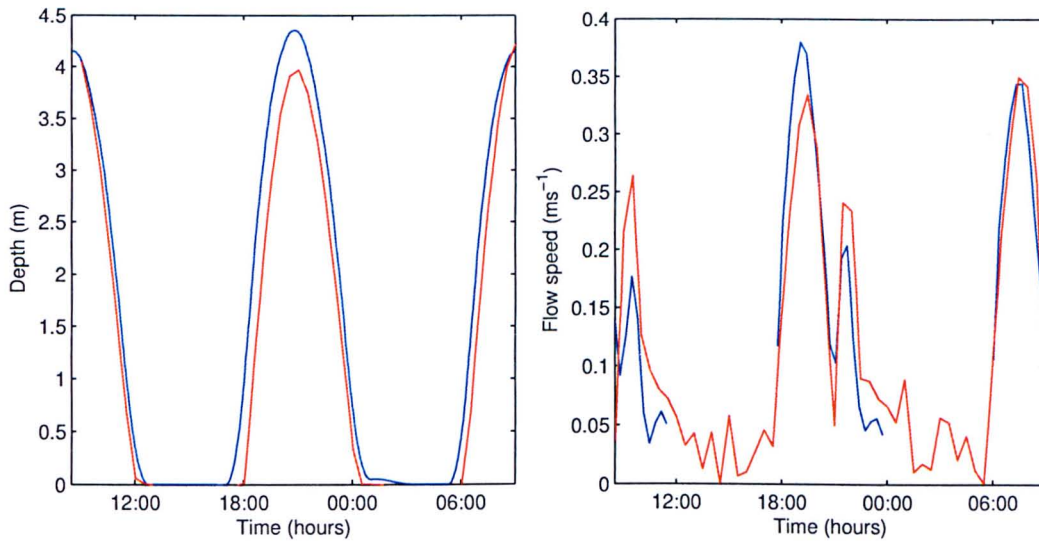
Figure 4.17: Water depth and flow speed validation for a TELEMAC-2D tidal simulation at West Kirby Sands over a 24 hour period between 05.03.11-06.03.11. The measured data was collected during an ADCP deployment at this region of inter-tidal sand flats. The blue line represents measured data while the red line represent modelled data.

4.4 Wave model

4.4.1 Simulating the wave field with TOMAWAC

Liverpool Bay is considered to be a fetch limited environment for waves, as swell does not easily propagate from the North Atlantic into this part of the Irish Sea. The maximum fetch for Liverpool Bay is from the west of the Irish Sea, corresponding to a distance of approximately 200km (Sly, 1966; Pye and Neal, 1994). However, to understand the importance that waves have in transporting sediment, it was seen as important to include waves in the model simulations. For this the third generation wave model TOMAWAC was used, which is designed to model wave propagation in the coastal zone by solving a simplified evolution equation of the directional spectrum of wave action (Hervouet et al., 1994). TOMAWAC also predicts the radiation stresses, which can then be used within TELEMAC-2D to generate wave-induced currents, which are an important consideration especially in the surf zone. The wave field was simulated over the domain whilst including the effect of the tide. It is important to account for the effect of the tide for waves at the estuary mouth as the current direction and strength, as well as water depth will determine the extent that waves can penetrate into the estuary.

The steering file (cas) was set up so that the wave field is simulated across the domain with varying tidal elevations and varying wave input data. The wave data is input as initial conditions including

the significant wave height (m), peak frequency (Hz) and the main direction of propagation (degrees). Waves are not generated within the domain due to the effect of wind, instead a wave field is imposed at the domain liquid open boundary. TOMAWAC has the capacity to simulate wind generated waves within the domain, however this was omitted from the model sequence applied here due to the increased computational demands this would inflict on an already computationally intensive simulation. To impose in TOMAWAC non-stationary boundary conditions that vary in time but are uniform around the boundary the key word 'formatted file1' must be specified in the cas file. This allows a formatted file, in this case a .txt file, to be read in containing the relevant wave information at each time step. The subroutine LIMWAC is modified in order to manage the read operations of the formatted file within the Fortran programme. At each time step LIMWAC will read the spectral parameters from the file and use them as argument variables in the call to subroutine SPEINI. To create the formatted file containing the time depending boundary conditions, data from the Liverpool Bay WaveNet Waverider buoy (http://www.cefas.co.uk/wavenet) were used. The position of this buoy is 53°3'.00N 003°21'.19W (Figure 4.18) which is at the northern extent of the model domain.
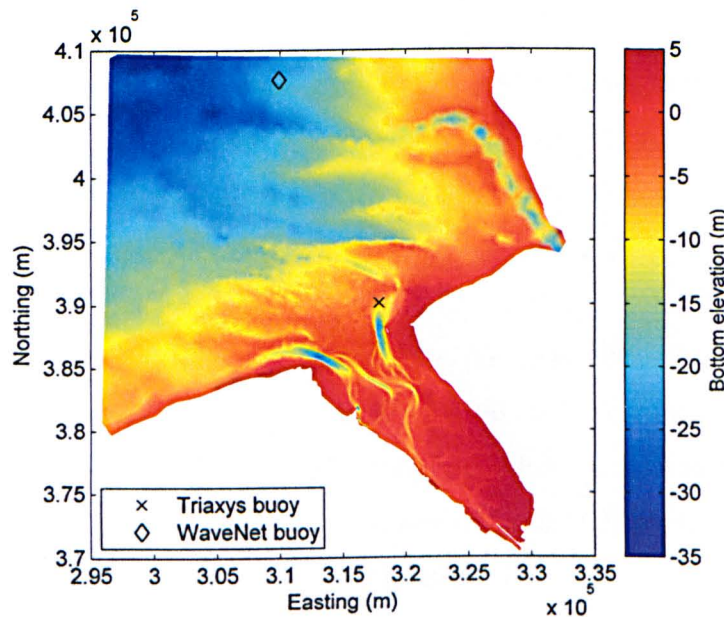
Figure 4.18: WaveNet and Triaxys wave buoy locations in the model domain.

The direction specified in TOMAWAC represents the direction in which the waves are travelling, an unconventional method, so that south = 0°, west = 90°, north = 180° and east = 270°. The direction recorded by the WaveNet buoy is in the direction travelling from so this is converted to direction travelling to for use within TOMWAC. The period is also converted to frequency using $f = 1/\text{period}$.

The data from the WaveNet buoy is recorded at a 30 minute time step, this is then interpolated using Matlab to the 1 minute time step which was set in TOMAWAC. The decision was made to interpolate outside of TOMAWAC to reduce the computation time of the wave model runs, as TOMAWAC is the most computationally demanding part of the modelling process. The number of wave propagation frequencies was set to 20 and the number of wave propagation directions set as 24. The number of directions makes it possible to specify over how many propagation directions the directional spectrum of wave action is discretised. The minimum frequency was set to 0.05Hz and the frequential ratio to 1.12. The frequential ratio (r) is used with number of frequencies (NF) to compute the discretised frequencies using

$$f = f_0 r^{(k-1)}, \text{ where } k = 1, NF \qquad (4.2)$$

The results file for the wave field has a spin up time of 2 hours, with the waves then generated with the changing water elevations set by the input tidal information. To account for the input tidal information the key word 'Tide refreshing period' is included in the TOMAWAC cas file. The tide refreshing period multiplied by the model time step should equal the output period of the TELEMAC-2D result file so the tide is updated every 30 minutes. To generate the wave field in the presence of a tide TOMAWAC interpolates the tidal elevation and current data between two successive data points in the TELEMAC-2D results file. Therefore it is necessary to include an extra time step in the tidal simulation so that the results file contains enough data for interpolation, whether it is a single tidal cycle or an entire spring-neap simulation.

Local wind over the domain was not included. While this may add some accuracy to the simulation it was deemed too computationally demanding for this model set up. It is more important to include the effect of the tide and time-varying boundary conditions, such as the changing tidal elevations, which will then alter the wave breaker positions in the mouth of the estuary. The swell wave component (low height, long period waves) is not included in the WaveNet data which is input at the model boundary. Instead these data accurately represent the locally (Irish Sea) wind generated waves, which have a shorter period. This is seen as an acceptable approach to modelling the wave climate in Liverpool Bay because, as previously stated, this is a fetch limited region where swell waves rarely propagate from the North Atlantic. Malvarez et al. (2004) showed that a combination of waves and tides has a major impact on sediment transport pathways and the morphology of sand tidal flats. This highlights the importance of including a tidally varying water depth while updating the wave parameters, as this will force the sediment transport more accurately, especially in the mouth of the estuary

which is particularly pertinent when modelling the morphological change in the Dee Estuary.

The open liquid boundary in the TOMAWAC conlim file was set to 522, where the first number of this code prescribes the wave field. A setting of 222 was applied to the coastline which represents an impermeable boundary where no wave values are prescribed.

4.4.2   Validation of the wave simulation

Waves are simulated under the influence of spring and neap tides over 24 hour tidal cycles, with a time step of 60 seconds and a time varying wave height imposed at the liquid open boundary. Two tidal simulations are run using eight tidal constituents ($Q_1, O_1, P_1, K_1, M_2, S_2, K_2, M_4$), 12.5 hour spin-up simulations to remove errors, and with the simulation start time set to correspond with the time of spring and neap tidal conditions. Figure 4.19 shows wave height in the model domain at times of high and low water for spring and neap tidal conditions.
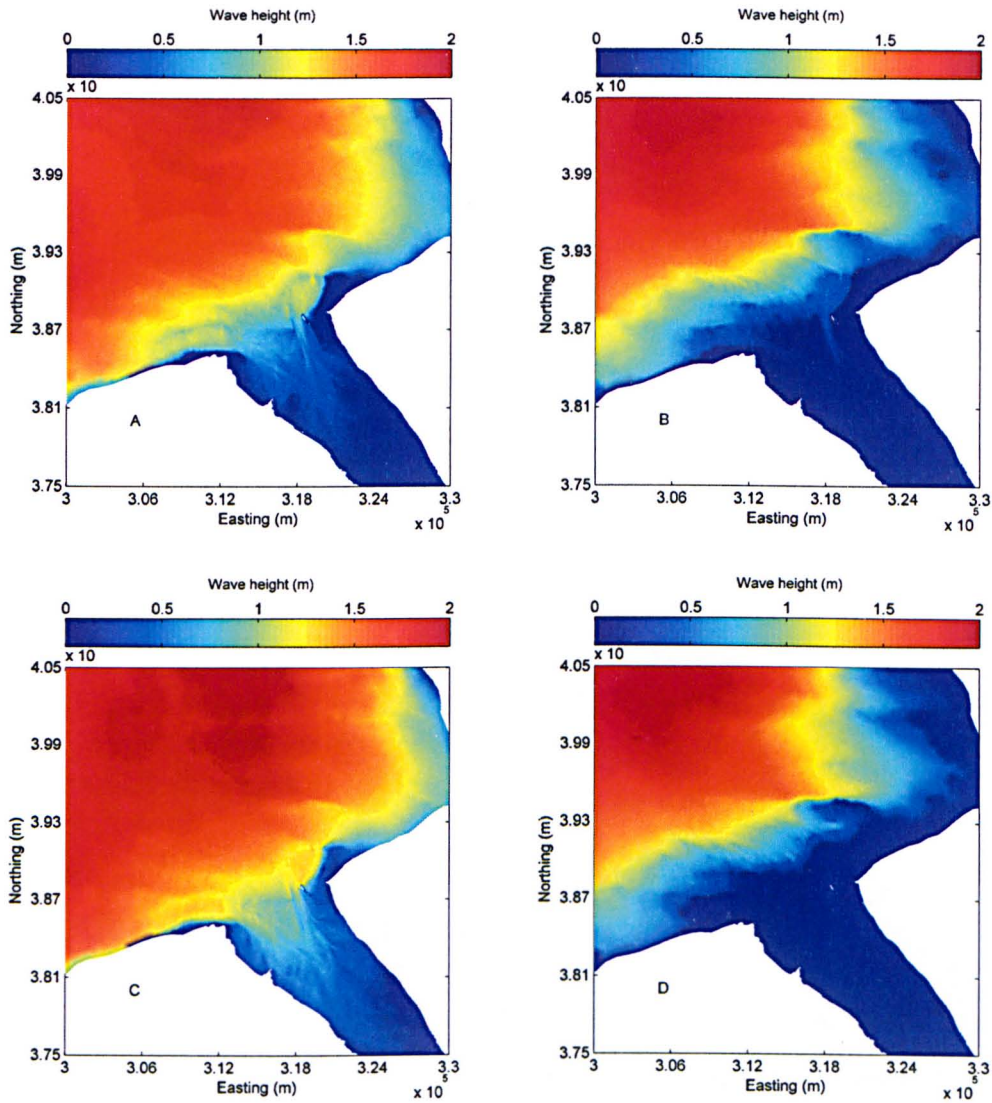
Figure 4.19: Wave heights in the model domain during different tidal stages; A) HW neap B) LW neap C) HW spring D) LW spring.

Waves can be seen to propagate further into the estuary at HW. Waves of zero predicted height are noticeable within the estuary at LW, caused by the drying out of tidal flats in the mouth of the estuary stopping waves from propagating into the estuary interior. Waves have greatest impact on the intertidal dune fields at West Kirby Sands and West Hoyle Bank at HW with little or no wave action occurring at LW. The increased water levels experienced during spring tides act to enhance the wave action. The tidal modulation of wave heights is examined at West Kirby Sands. The wave simulation shows a drop in wave heights at low water similar to the wave height data from the Triaxys buoy (Figure 4.20).
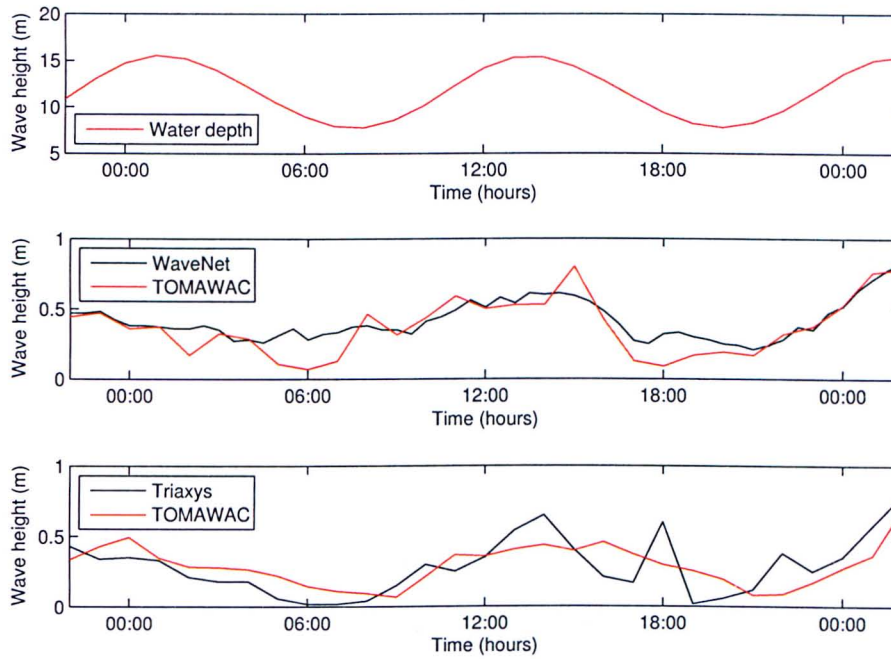
Figure 4.20: A comparison between modelled (TOMAWAC) and measured wave heights from the model boundary (WaveNet) and estuary mouth (Triaxys) between 09-10.10.06, showing the tidal modulation of wave heights in the Dee Estuary.

4.5 The action of wave induced currents

Tidal range has an important influence on the nearshore zone, as the variation in the breaker position due to a change in the tidal elevation will alter the position of wave attack. This is especially true where beach gradients are low (Janmaluddin, 1976), making this relevant for the mouth of the Dee Estuary. To generate wave induced currents whilst also simulating a tide, changes needed to be made to the steering (cas) file so that a wave results file could be read in. The version of TELEMAC (V5P9) used here does not allow TELEMAC-2D to update the wave field through the tidal cycle. The files used for this simulation are modifications of those used in the tide and river case. In this simulation the tide and river simulation is run with wave induced currents included. Doing this allows a more accurate wave breaker position to be simulated as it will vary with the tidal elevation. For this to be implemented the Fortran code was modified to read in successive wave outputs from the previous wave results file whilst the current field was simulated with changing tidal elevations.
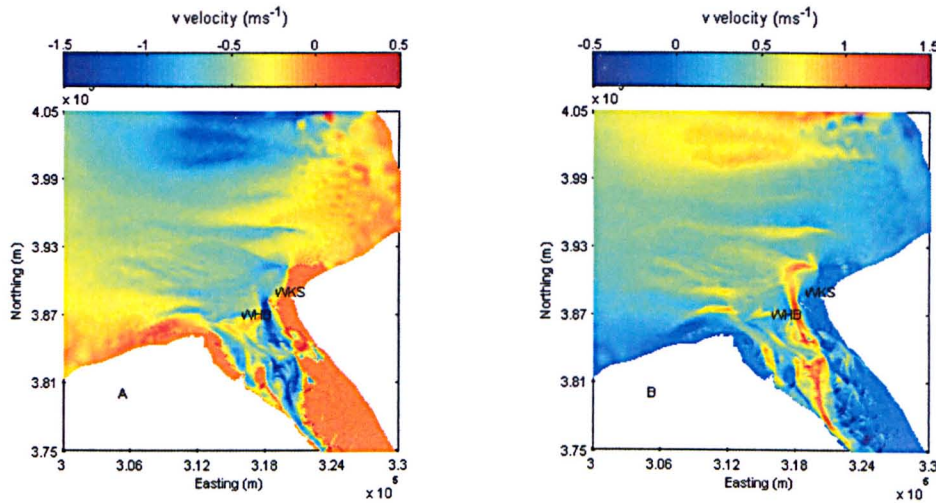
Figure 4.21: Wave induced currents simulated over the Dee Estuary model domain at peak flood (A) and ebb (B).

The forces generated, F_x and F_y, by the radiation stresses, S_{xx} and S_{yy}, due to the waves are passed on from TOMAWAC to TELEMAC-2D to simulate the wave induced currents. The steering (cas) file was adjusted to spin up the current field produced by previously simulated wave cases, with the inclusion of a tide. To account for the varying water level on the wave field, the code was modified to read successive wave outputs from the previous TOMAWAC results file while the current field is being simulated. This updates the time varying wave field with a 30 minute time step, taking 1 hour for the wave induced currents to spin up. The model simulates the highest velocities to be in the deep channels. However areas of high velocity can also be seen around West Kirby Sands and West Hoyle Bank (WKS and WHB Figure 4.21). It is these areas which are being investigated for the migration of large scale bed forms which may be forced by these high current velocities.

Chapter 5

Modelling sediment transport and morphology

Within the TELEMAC Modelling System the morphological module SISYPHE is applied to simulate the sediment transport and morphological change. This continues from the currents and waves which were previously simulated and is run simultaneously with TELEMAC-2D in a coupled mode. For SISYPHE to calculate sediment transport magnitudes and directions in a coupled mode the velocity and depth data are passed internally from TELEMAC-2D. The 'coupling period' is specified in the TELEMAC-2D cas file so that SISYPHE is activated at every multiple of the coupling period and the timestep. Here the coupling period is set to equal 1, therefore SISPHYE is called at every timestep of TELEMAC-2D (10 seconds). The resultant convergence or divergence of sediment flux causes accretion or erosion of bed levels. This resulting bed evolution is passed back to TELEMAC-2D to be used in the next flow computation, so that the bed evolves through a dynamic feedback process between the bed morphology and hydrodynamics. A variety of sand transport equations are programmed into SISYPHE to calculate the bed load or total load, which can be calculated as the sum of bed load and suspended load transport rates, using the hydrodynamic and sediment parameter inputs. Examples of the steering (cas) files for the coupled TELEMAC-2D and SISYPHE run are given in Appendix II. The local sediment transport considerations are discussed herein, detailing the choice of sediment transport formula used, with a description of the effect of including waves in the simulation.

5.1 Sediment transport in the case of superimposed currents and waves
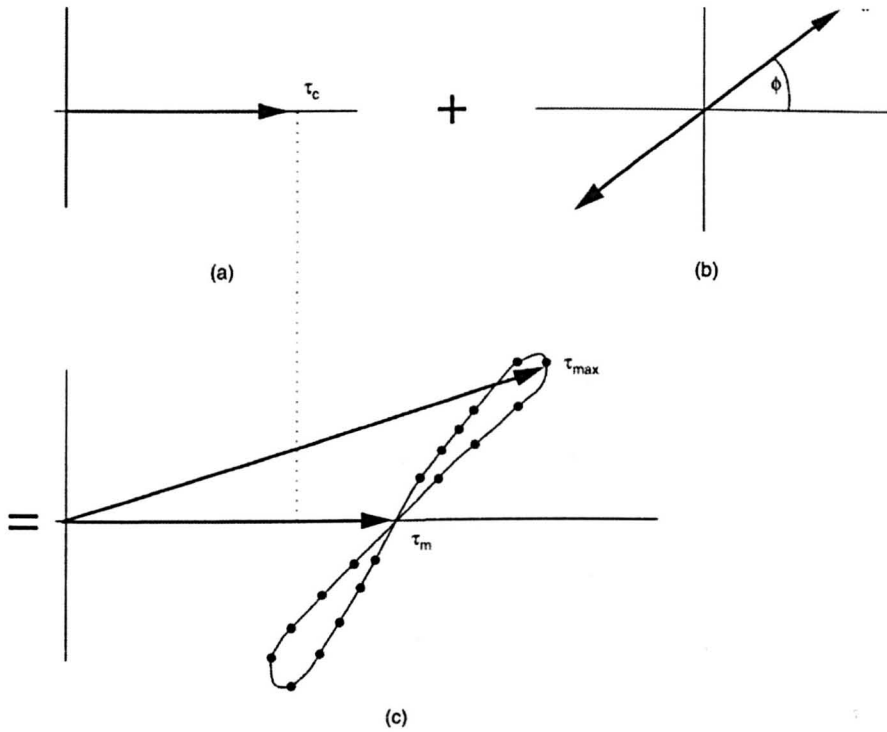
Figure 5.1: The non-linear interaction (c) between shear stresses due to currents (a) and waves (b). The steady current and the oscillatory wave stress components are enhanced beyond the values produced by a simple linear addition of the mean (current) and oscillatory (wave) stresses. The bed shear stress varies through the wave cycle in the manner shown by the dotted line (c).

Wave-current sand transport models are important in the coastal zone. The oscillatory flow under surface waves provides an additional frictional force to the bed and also acts as a stirring mechanism, lifting sediment off the bed so that it can be transported more readily by the underlying current. Bed shear stresses beneath the combined action of waves and currents are enhanced beyond the values corresponding to a linear addition of wave and current alone shear stresses (Figure 5.1). This is caused by turbulence generated in the wave and current boundary layers (Soulsby et al., 1993) which then adds in a non-linear fashion. The boundary layer structure is altered by the superposition of waves onto a mean current, whether it is induced by the waves themselves or by tidal forcing, enhancing the shear stress at the bottom, therefore increasing sediment transport rates. As detailed in Sections 2.2.1 and 2.2.2 the current alone and wave alone components of bed shear stress are proportional to the square of the velocity, therefore wave generated turbulence will affect the current and current generated turbulence also affects the waves, with a resulting enhancement (Grant and Madsen, 1979; Soulsby and Clarke, 2005). SISYPHE has the option of assigning the Bijker (1992), the Bailard

(1981), the Dibajnia and Wantanabe (1992) or the Soulsby-van Rijn formula to predict total load transport (bed load + suspended load).

5.2 Bijker's sand transport model

Bijker's (1992) formula was chosen for this study, which is an extension of a steady flow formula to account for the effect on sediment transport of wave enhanced shear stresses. The Bijker formula is widely used, especially for conditions of combined currents and waves (Villaret, 2001). Although Bijker's model is long established, it is still widely applied by practising engineers (Davies and Villaret, 2002) due to its ready implementation and that its predictions are broadly similar to those of more recent, more complicated, practical models (van Rijn et al., 2001). Davies and Villaret (2000b) compared Bijker's model with data from two field sites and showed that, despite some scatter, the model makes reasonably accurate estimates of total transport rates. Davies et al. (2005) applied Bijker's model in TELEMAC simulations for combined currents and waves with locally predicted bed roughness showing the importance of local variations in bed roughness on morphological modelling. A similar approach is applied to the Dee Estuary and is discusses herein. Bijker's model initially predicts the bed load transport in steady flow as the product of 'stirring' and 'transporting' terms. The instantaneous bed load transport rate q_b is expressed as

$$q_b = b\theta_c^{0.5}\exp\left(-0.27\frac{1}{\mu\theta_{cw}}\right) \tag{5.1}$$

where θ_c and θ_{cw} are the non-dimensional current alone and combined current and wave shear stresses respectively. The parameter b is an exponentially derived coefficient (5). The ripple correction factor μ, relates to the skin friction, and is calculated in the same way as the Meyer-Peter formula

$$\mu = \left[\frac{C_h}{C_{hp}}\right]^{\frac{3}{2}} \tag{5.2}$$

where C_{hp} is the skin friction Chezy coefficient and C_h is the Chezy coefficient corresponding to the total friction

$$C_{hp} = 18\log_{10}\left(\frac{12h}{k_{sp}}\right) \tag{5.3}$$

$$C_h = \sqrt{\frac{2g}{C_D}} \tag{5.4}$$

with g representing the acceleration due to gravity, h the depth, k_{sp} the skin friction roughness ($3D_{50}$)

and C_D the quadratic current friction coefficient

$$C_D = \left[\frac{\kappa}{\log(\frac{12h}{k_s}) - 1}\right]^2 \tag{5.5}$$

where $\kappa = 0.4$ (von Karman's constant) and k_s is the Nikuradse total bed roughness coefficient. The Bijker formula is recommend for conditions that include the combined action of waves and currents for its reliability, simplicity and flexibility (Villaret, 2001; Guillou and Chapalain, 2011). The model was developed from classical transport concepts to be used in wave-current conditions and is not just a curve fitting to measurements. The basic concept is that waves stir up sediment which is transported by the current. The total load sediment transport formula is estimated based on calculating the bed load and the suspended load separately. The development is made on the scalar variables, as Bijker's formula is an extension of a steady flow formula to account for the effect of the wave enhanced shear stress. The breaking wave coefficient b in Equation 5.1 is here set equal to 2 rather than the conventional setting of $b = 5$ (Dibajnia and Watanabe, 1992; Guillou and Chapalain, 2011). A b value of 5 is set as default in TELEMAC and must be changed manually by the user with the key words 'B value for the Bijker formula =' in the SISYPHE steering (cas) file. Villaret, C. and Davies (2004) use b = 2 for regions where the wave height was less than half the water depth and b = 5 when this criteria was not met.

The suspended load component of transport is calculated from a depth integration of the product of the depth averaged concentration and velocity, from a reference level corresponding to the thickness of the bed layer to the water surface. Assuming a Rouse concentration profile and a logarithmic velocity profile the suspended load q_s can be written

$$q_s = q_b I \tag{5.6}$$

where I is the Einstein integral expressed as

$$I = 1.83x0.216\frac{B^{A-1}}{(1-B)^A}\int_B^1 \left(\frac{1-z}{z}\right)^A \ln\left(\frac{33z}{B}\right) dz$$

$$\text{and } A = \frac{w_s}{\kappa u_{*cw}}, B = \frac{k_s}{h} \tag{5.7}$$

where

$$u_{*cw} = \sqrt{\frac{\tau_{cw}}{\rho}} \qquad (5.8)$$

k_s is the bed roughness length, ρ is water density, w_s is the settling velocity, z is the height above the bed, h is the water depth and τ_{cw} is the wave current bed shear stress. To apply the Bijker formula the following words need to be included in the steering (cas) file:

'Effect of waves' = YES

'Bed-load transport formula' = 4 (Bijker's model)

The model can be implemented for a tide alone case by setting 'Effect of waves = NO', this will set the wave stress to zero and use the current stress as the total stress for the simulation. The shear stress due to wave-current interaction is calculated at every timestep as

$$\tau_{cw} = \tau_c + \frac{1}{2}\tau_w \qquad (5.9)$$

with

$$\tau_c = \frac{1}{2}\rho C_D \bar{u}^2 \qquad (5.10)$$

and

$$\tau_w = \frac{1}{2}\rho f_w u_0^2 \qquad (5.11)$$

being the shear stress due to current alone (τ_c) and the shear stress due to waves (τ_w), where ρ is the water density, $\bar{u}$ is the depth average mean flow, C_D is the quadratic current friction coefficient, u_0 is the wave orbital velocity and f_w is the friction factor for waves. The wave friction factor f_w is calculated from the Swart formula using the relative roughness

$$f_w = \begin{cases} \exp(-0.6 + 5.2(A_0/k_s))^{-0.18}, & A_0/k_s > 1.57 \\ 0.3, & A_0/k_s \leq 1.57 \end{cases} \qquad (5.12)$$

where $A_0 = u_0\omega$ and k_s is the bed roughness. When the effect of waves are included in the SISYPHE steering file the wave height H_s, wave period T_p and angle of attack θ_w are passed from TOMAWAC to SISYPHE. The wave orbital velocity u_0 is calculated in SISYPHE according to linear wave theory

$$u_0 = \frac{H_s \omega}{2 \sinh(kh)} \qquad (5.13)$$

where the angular frequency $\omega = 2\pi/T_p$, $k = 2\pi/L_w$ the wave number k is calculated from the wave dispersion relation (Equation 5.14), L_w is the wave length and h the water depth

$$\omega^2 = gk \tanh(kh) \qquad (5.14)$$

The solid discharge simulated with the effect of waves, in this case using the Bijker formula, is oriented in the mean current direction, with a slight modification by bed slope effects. The effect of the bed slope on the transport can be implemented in the SISYPHE steering file with the key word 'Slope effect = YES'. This applies a correction factor, based on the method of Koch and Flokstra (1981), to the magnitude and direction of the transport before the bed evolution is calculated. This reduces the transport rate in an up-slope direction and increases it in a down-slope direction. The transport rate is multiplied by a correction factor so that

$$q_b = q_b \left(1 - \beta_s \frac{\partial Z_b}{\partial i} \right) \qquad (5.15)$$

where i is the coordinate in the direction of the current and β_s is the slope coefficient, set to 1.3 to account for slope effects using the keyword 'BETA' in the SISYPHE steering file. The transport direction is modified by

$$\tan \alpha = \tan \alpha_\tau - T \frac{\partial Z_b}{\partial j} \qquad (5.16)$$

where α and α_τ are the direction of transport and the direction of shear stress in the direction of flow respectively and j is the coordinate along axis perpendicular to the flow. Sediment transport was restricted at low water on the intertidal sand flats by implementing the 'wetting and drying' over the tidal flats. Zero transport is imposed by the model if the depth is less than or equal to the minimum depth set by the user. This allows the sand flats and banks to undergo wetting and drying through the tidal cycle and stops transport occurring on dry land. To apply this method the key word 'Tidal flats' is set to 'YES' in the TELEMAC-2D steering file.

5.3 Bed roughness prediction

It is important to represent bed roughness as it is a highly sensitive parameter for sediment transport applications (van Rijn, 2007a) due to the effect it will have on flow velocities and transport rates. Bed forms, such as sand dunes, will exert a frictional force between the bed and the flow. The frictional force generated by the pattern of pressure around the bed form due to flow separation over the crest, known as form drag, is often the dominant resistive force between the bed and flow in coastal tidal environments (Soulsby, 1997). The effect of bed roughness on morphodynamics is illustrated by Villaret et al. (2011) for the Dee Estuary and the Gironde Estuary. The contribution to Villaret et al. (2011) by the author of this research uses a simplified Dee Estuary model grid, with a resolution scaling from 400m at the model boundary to 100m at the estuary mouth. Currents, waves, wave generated currents and sediment transport are simulated in two TELEMAC simulations where a comparison between a constant bed roughness of 0.01m and predicted bed roughness as a function of the flow and sediment parameters are made. The conclusions of Villaret et al. (2011) showed that the use of a constant bed roughness reduces the transport rates and bed evolution in the Dee Estuary, in comparison to the bed roughness predictor approach. Davies and Villaret (2003b) showed that for an example involving waves incident on a beach the use of variable k_s can affect the results markedly.

The hydraulic roughness of the bed directly influences the flow velocity from a given pressure gradient associated with the bed form driving the flow. This is then represented through the roughness length z_0 in the logarithmic velocity profile. The roughness will also impact on the bed shear stress τ_0, through the drag coefficient C_D. This can either positively or negatively amplify the bed shear stress as τ_0 is proportional to the drag coefficient multiplied by the square of the velocity

$$\tau_0 = \frac{1}{2}\rho C_D \bar{u}^2 \tag{5.17}$$

This in turn will alter the sediment transport as τ_0 is present in the sediment transport formula in the form of the Shields parameter θ raised to a power greater than one.

For the purpose of modelling it is necessary to include the entire spectrum of bed form dimensions, from small scale ripples, mega-ripples, through to dunes. The method of van Rijn (2007a), to simulate a time dependent bed roughness, is coded into the SISYPHE subroutine RIDE for TELEMAC V5P9. The total bed roughness k_s is calculated from the predicted roughness for ripples $(k_{s,r})$, mega-ripples

$(k_{s,m})$ and dunes $(k_{s,d})$ and then combined in a quadratic summation.

The rippled bed roughness length $k_{s,r}$ is approximately equal to the ripple height η (van Rijn and Havinga, 1995). For ripples in a transitional environment $(50 < \psi \leq 250)$ the calculation that is programmed into the RIDE subroutine is

$$k_{s,r} = f_s D_{50}\{85 - 65\tanh[0.015(\psi - 150)]\} \tag{5.18}$$

The contribution of mega-ripples to bed roughness $k_{s,m}$ is estimated from empirical knowledge rather than via the bed form dimensions. They differ from ripples in that the bed roughness length is approximately equal to 0.5η (van Rijn, 1993). It is worthy of note that van Rijn (2007a) predicts k_s and not bed form dimensions explicitly. $k_{s,m}$ is programmed into RIDE, related to h and ψ as

$$k_{s,m} = 0.00002 f_s h[1 - \exp(-0.05\psi)](550 - \psi) \tag{5.19}$$

The greatest contribution to the total hydraulic roughness of the bed is from dunes. Flow separation and an associated increase in turbulence downstream of the dune crest has a significant influence on the flow. $k_{s,d}$ is included in RIDE as

$$k_{s,d} = 0.00008 f_s h[1 - \exp(-0.02\psi)](600 - \psi) \tag{5.20}$$

where f_s is a granular scaling to reduce k_s at large grain sizes, for $D_{50} \leq 0.25 D_{gravel}$ (where $D_{gravel} = 2mm$) $f_s = 1$ which is set in this case. D_{50} is the median grain diameter and ψ is the mobility parameter as defined at the outset, in Equation 2.22.

The total roughness k_s is then obtained by a quadratic summation of all three roughness contributions detailed above

$$k_s = \sqrt{(k_{s,r}^2 + k_{s,m}^2 + k_{s,d}^2)} \tag{5.21}$$

A coupled TELEMAC-2D and SISYPHE simulation is run for 24 hours with a time step of 10 seconds using eight tidal constituents $(Q_1, O_1, P_1, K_1, M_2, S_2, K_2, M_4)$. The TELEMAC-2D module is spun up for 24 hours to remove any start up instabilities, then run for a further 24 hours in coupled mode with

SISYPHE and with k_s feedback activated. The total roughness is calculated in the subroutine RIDE at every timestep and for every grid node that satisfies the condition $\theta' \geq \theta_{cr}$. For this procedure k_s values at every node are written to an external file so that roughness elements are only updated if the θ' condition is met. This external file is then read in to TELEMAC-2D at the next time step using the subroutine CHESTR which applies the k_s values in the file to every node (Figure 5.2). This allows TELEMAC-2D to calculate the depth averaged flow based on the total roughness. This method is applied for use within TELEMAC V5P9 which is used and developed by this research, later versions of TELEMAC, from V6P1 onwards, incorporate this procedure without the need for external files input during the coupled solution. It is worthy of note that the method applied is a quasi-steady approach which does not include history effects, which may cause unreliable results around times of slack water. Further improvement of this bed roughness predictor to include an adaptation time scale would account for these non-stationary effects, and is an interesting topic for further research.
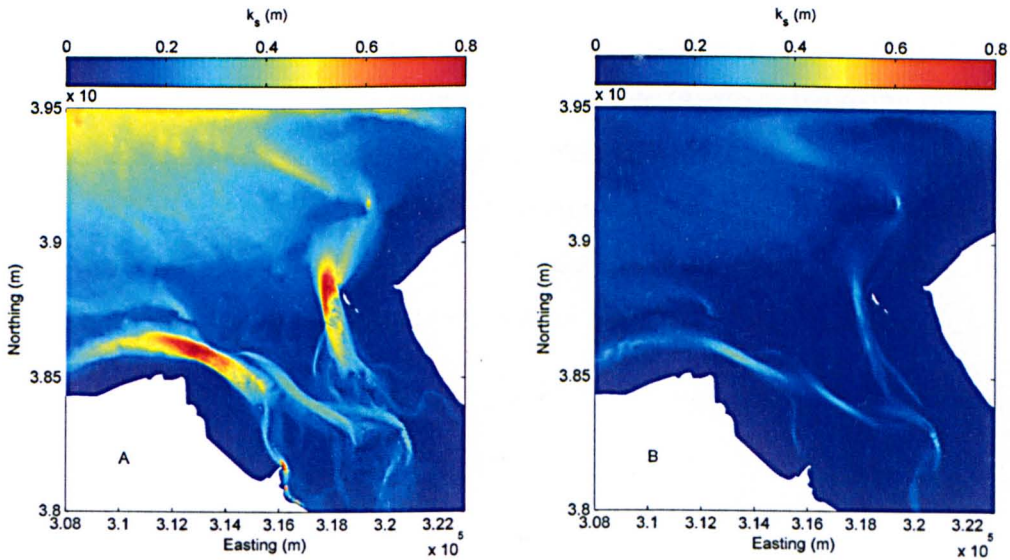
Figure 5.2: Bed roughness k_s (m) from the TELEMAC-2D simulation at times of A) peak flood tide and B) low tide. Note that the locations of maximum bed roughness can be found in the deep water channels of Hilbre Channel and the Welsh Channel.

The greatest k_s values are predicted at the time of peak flood tide in the Hilbre Channel and the Welsh Channel in the mouth of the estuary. These locations are consistent with the greatest tidal velocities in the deep water channels. The shallower regions on West Kirby Sands and West Hoyle Bank have lower peak flood k_s values as these regions have lower tidal velocities compared with the deep water channels. Predicted k_s values are much smaller throughout the estuary at low tide, when water depth and tidal velocities are at their lowest. The mean roughness in the mouth of the estuary is approximately 60% smaller at low tide compared with peak flood, highlighting the significant tidal

variation.

5.4 The effect of waves on sediment transport

A short model simulation of 24 hours was run using the Dee Estuary model domain to test the effect that waves have when included in the simulation. The first part of the modelling sequence was to run TELEMAC-2D to generate a 24 hour tidal cycle with the eight tidal constituents used previously. TOMAWAC was then run using wave data for a 24 hour period from the WaveNet buoy located on the northern boundary of the model domain while the previous TELEMAC-2D tidal results file was input so that waves were generated while taking into account the state of the tide. TELEMAC-2D was then run again, including the effect of the wave generated currents by inputting the wave results file generated previously. This latter TELEMAC-2D simulation was run in a coupled mode with SISYPHE, using the Bijker formula with the 'Effect of waves' set equal to 'YES', so that sediment transport was calculated under the influence of waves, tides and wave generated currents. As a comparison a TELEMAC simulation sequence was run without the influence of waves but using the same tidal inputs so that an identical 24 hour tidal cycle was generated. As there were no wave generated currents being simulated, this TELEMAC-2D simulation was run coupled with SISYPHE, using the Bijker formula with the 'Effect of waves' set equal to 'NO.' Both of these model sequences, including the effect of waves and with no waves, were run with bed roughness feedback initiated.
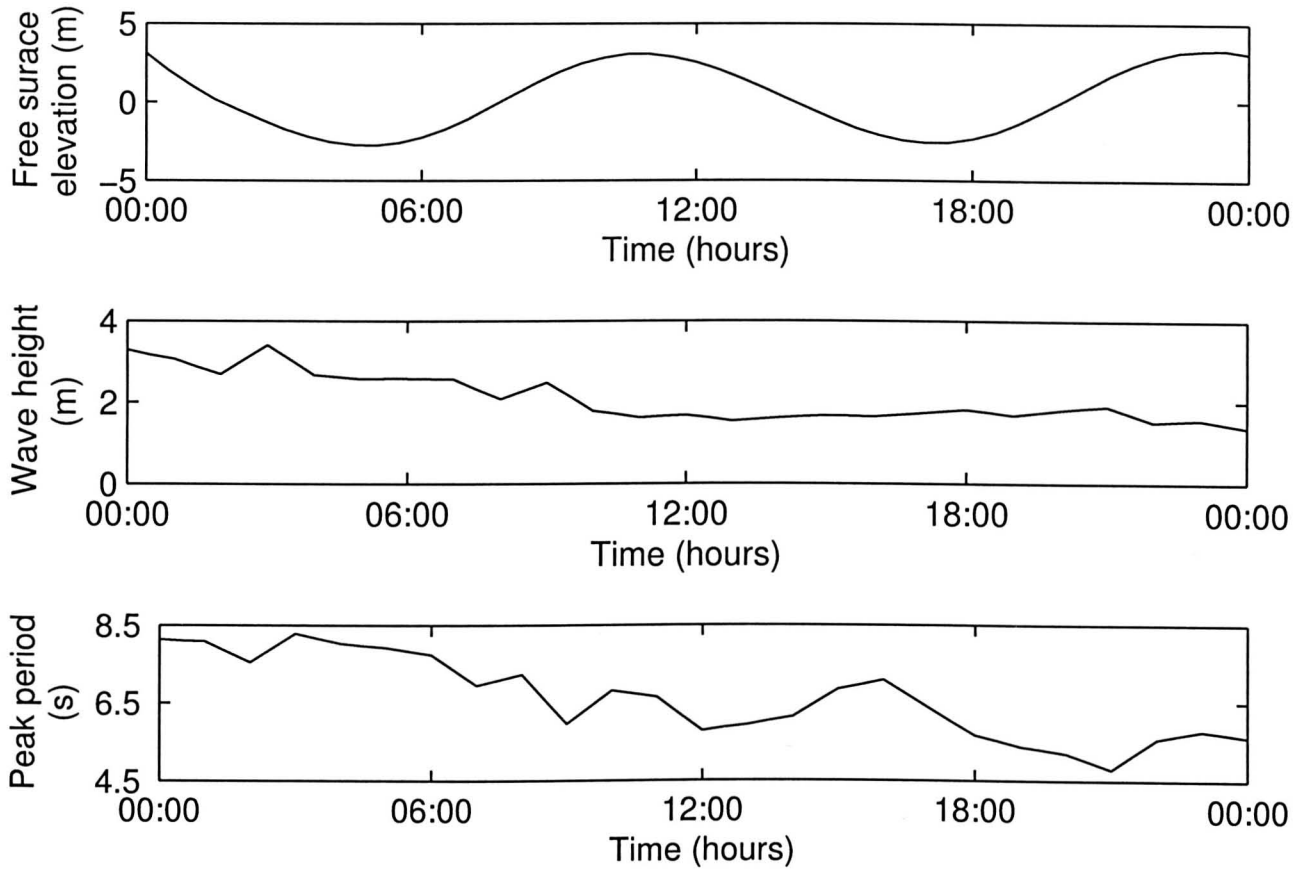
Figure 5.3: Free surface elevation (top panel) for the 24 hour tidal simulation used for the model test run to determine the hydrodynamic and morphological effects of including waves with TELEMAC-2D - SISYPHE coupled simulations. Wave height (middle panel) and wave period (bottom panel) at the model boundary show the time varying wave boundary conditions obtained from WaveNet wave buoy data.

The free surface elevation, wave heights and wave period at the model boundary for the 24 hour simulation period can be seen in Figure 5.3. The extent of wave influence in the mouth of the estuary can be seen at low tide when current velocities are weak (Figure 5.4 A) and at mid tide when current velocities are strongest (Figure 5.4 B).
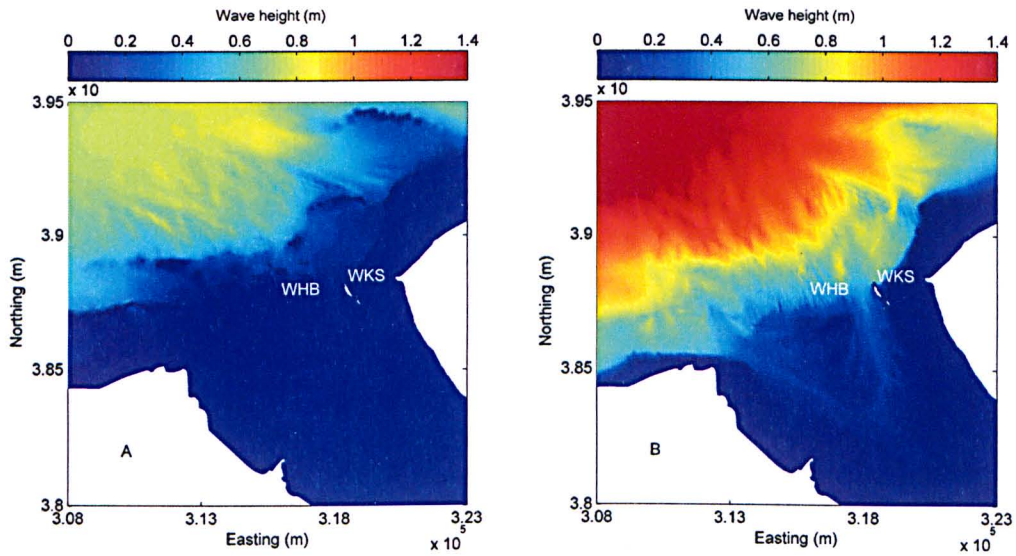
Figure 5.4: Wave heights in the mouth of the Dee Estuary at A) low tide and B) peak flood tide. This corresponds with approximately 05:00 and 09:00 in Figure 5.3, respectively. The position of the dune fields at West Kirby Sands (WKS) and West Hoyle Bank (WHB) are marked for reference.

Figure 5.4 does not show the entire model domain, but a cropped area around the mouth of the estuary. It is clear to see the tidal modulation of wave heights in the mouth of the estuary, where the movement of large scale bed forms into the estuary was being studied. This highlights the importance of simulating the waves with a tidal input using the TELEMAC modelling system. Mean water depth over the sand banks in the mouth of the estuary, not including the deep water channels, is approximately 4m at low tide and 9m at peak flood tide. This corresponds with wave heights at the estuary mouth of 0.2m at low tide and 0.8m at peak flood tide. This 300% increase in wave height, caused by the tidal modulation of the waves, has significant influence on sediment transport at the mouth of the estuary, especially over the dune fields of West Kirby Sands and West Hoyle Bank. Greater wave heights at the time of peak flood tide will cause greater radiation stresses on the sea bed which will act to 'stir' up the sediment which will be transported by the residual current into the estuary. This may have significant impact on the migration of large scale bed forms in the mouth of the Dee Estuary and will be investigated in further detail.
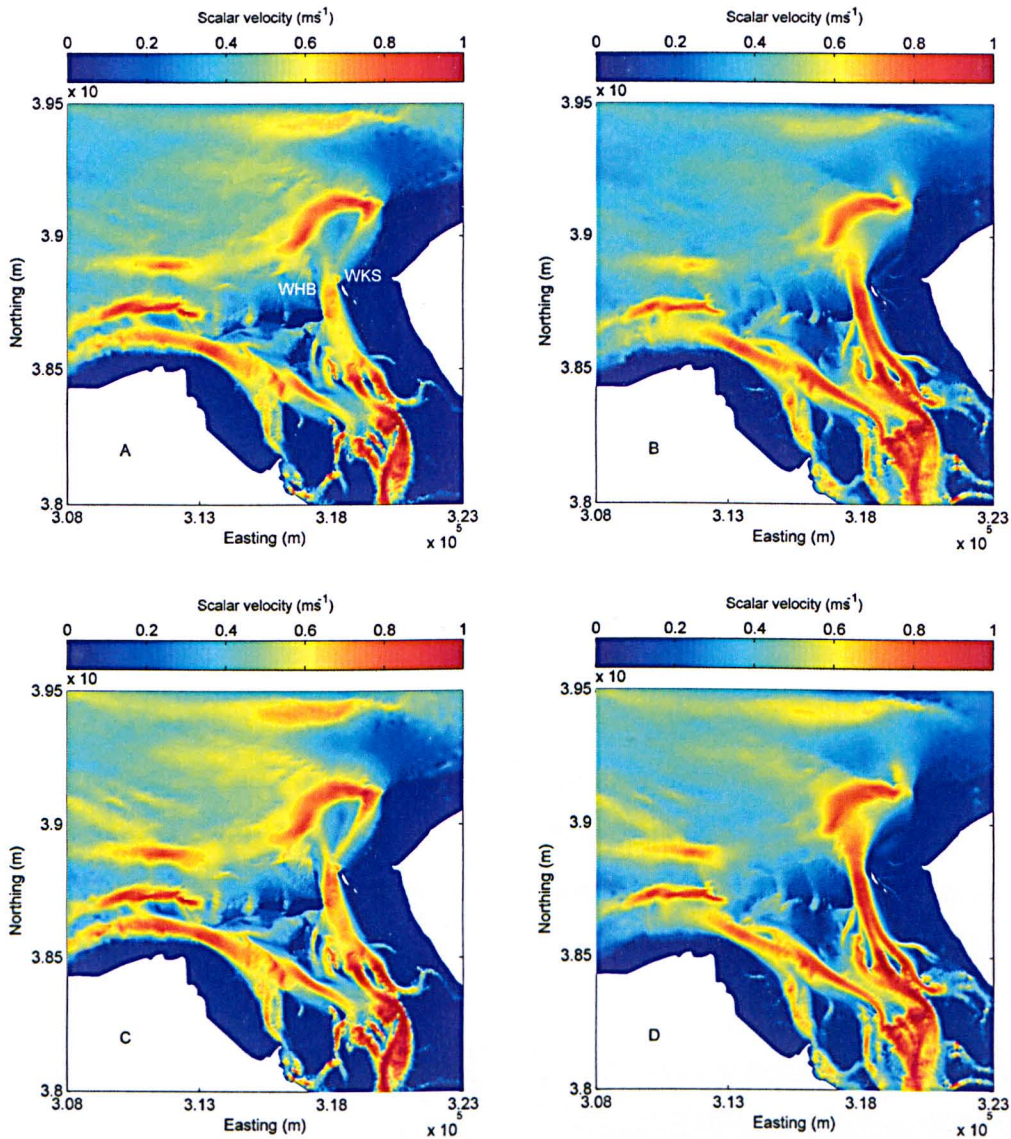
Figure 5.5: Scalar velocity in the mouth of the estuary on the flooding tide with waves (A), ebbing tide with waves (B), flooding tide with no waves (C) and ebbing tide with no waves (D). The timings of peak peak flood and ebb correspond with times 09:00 and 13:00 respectively in Figure 5.3.

The scalar velocities at peak flood and ebb tides for simulations including waves and without can be seen in Figure 5.5, where the upper panels signify no waves and the lower panels represent waves included in the simulation. The velocity magnitudes with and without waves in Figure 5.5 appear to be relatively similar, however the simulations with waves included do show slightly higher velocities, this is particularly evident in the region just north of West Kirby Sands. Figure 5.6 shows the difference in velocity calculated by subtracting the velocity with no waves from the velocity with waves included, so that positive differences represent an increase in velocity magnitude due to the presence of waves. The difference between velocities with waves and those without at peak flood and peak ebb (Figure 5.6) shows an increase in velocity at the estuary mouth. The difference in the magnitude of

velocity for peak flood shows an area of increase to the north of West Kirby Sands (WKS Figure 5.5) and to the south of West Hoyle Bank (WHB Figure 5.5). A greater increase in velocity can be seen to the north of West Kirby Sands and at West Hoyle Bank for peak ebb tide. The increases in velocity at West Kirby Sands and West Hoyle Bank with the presence of waves is caused by the wave induced currents which are simulated when the wave heights are input into the TELEMAC-2D simulation. The greatest increase in velocity is seen in the mouth of the estuary as this is the region of breaking waves, induced by the shoaling bathymetry over the shallower regions of West Kirby Sands and West Hoyle Bank. Note how there is no increase in the deep water of Hilbre Channel, as water depths are too great for waves to break here, there are however increases in velocity on the banks of this channel, where the bathymetry shoals and waves break.

Figure 5.7 A shows the scalar velocity over the 24 hour simulation period at West Kirby Sands, labelled as WKS in Figure 5.5, showing an increase in velocity from approximately 0.20 to 0.26 ms^{-1} at peak flood while peak ebb velocities increase from 0.21 to 0.24 ms^{-1}. Figure 5.7 B shows these two TELEMAC simulations for West Hoyle Bank where peak flood velocities increase from 0.40 to $0.55ms^{-1}$ while peak ebb velocities decrease from 0.58 to $0.50ms^{-1}$. The radiation stress generated by the waves at West Kirby Sands and West Hoyle Bank will enhance the wave generated currents over the tidal currents.
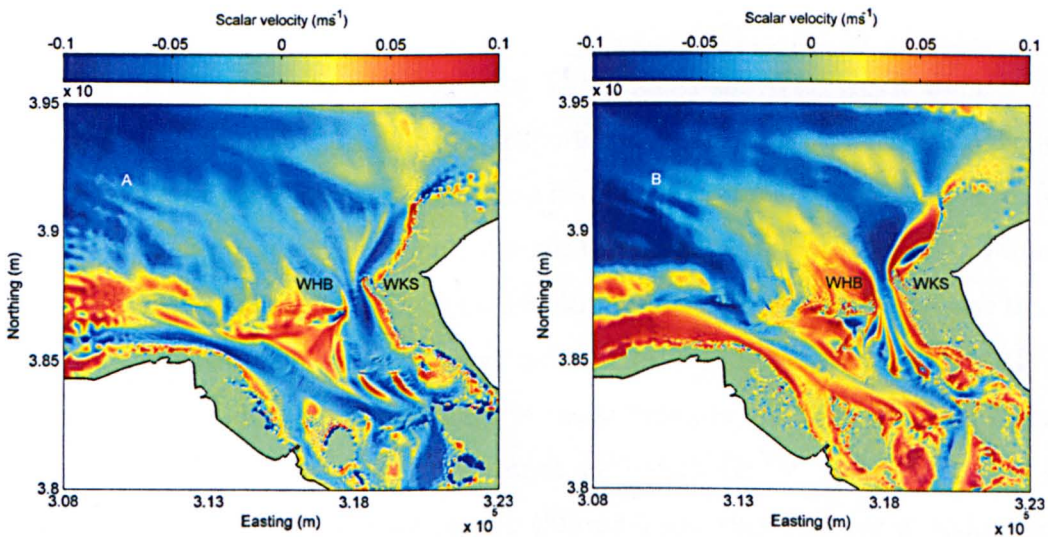
Figure 5.6: The difference in scalar velocity when comparing a TELEMAC simulation that includes waves with on which does not. Two comparisons are made, at peak flood (A) and peak ebb (B).
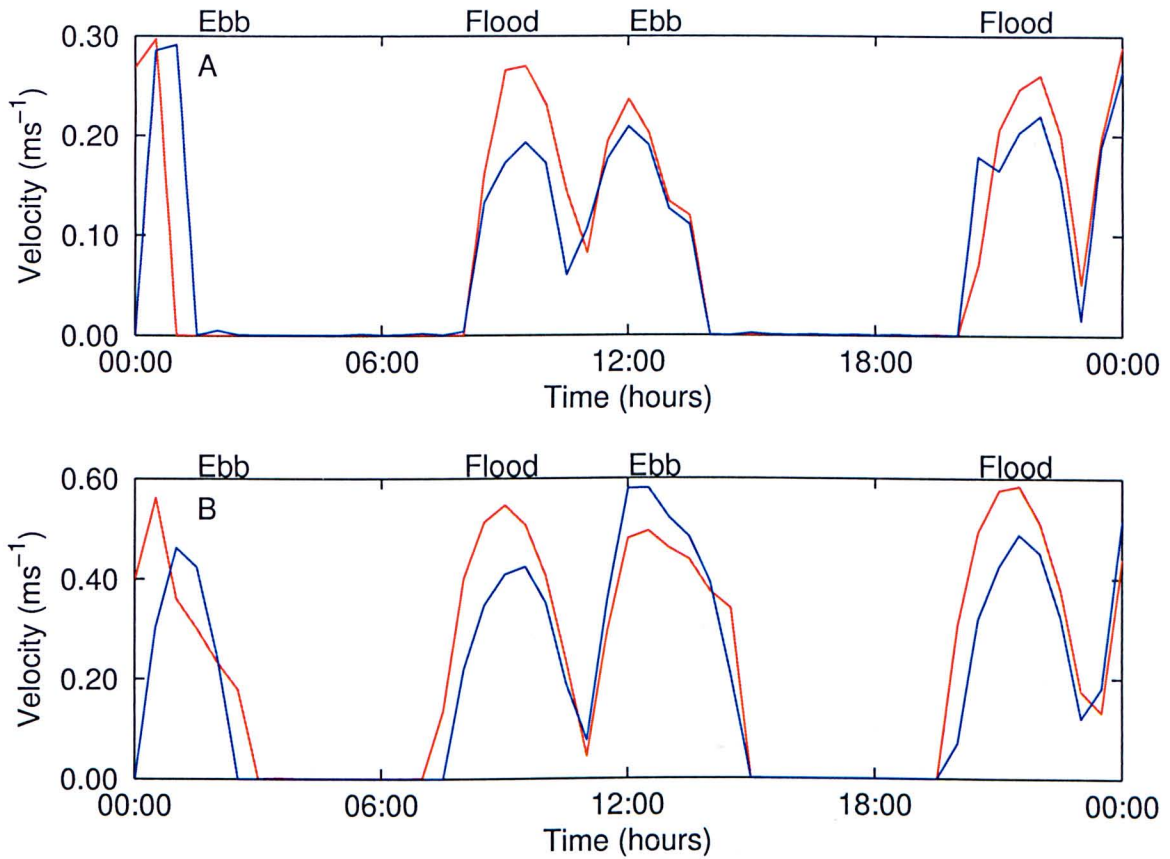
Figure 5.7: Scalar velocities at West Kirby Sands (A) and West Hoyle Bank (B) from a 24 hour TELEMAC simulation where waves are included (red line) and a simulation without waves (blue line).

The effect of waves on the scalar velocities at West Kirby Sands and West Hoyle Bank is transferred to the resulting sediment transport. Total load transported over the 24 hour simulation using Bijker's formula with and without the influence of waves can be seen in Figure 5.8. The simulation which did not include waves is strongly flood dominant, whereas this asymmetry becomes less pronounced but still flood dominant with the inclusion of waves. Including waves does greatly increase the sediment transport, with transport being an order of magnitude larger with waves than without (Figure 5.8). The large transport magnitudes at the beginning of the simulation are a result of the large offshore wave heights in excess of 3m at the start of the input wave data file for the model boundary, which then progressively drop throughout the simulation (Figure 5.4). This increase in sediment transport due to waves can be seen in the evolution of the bed which has occurred after the 24 hour simulation (Figure 5.9), where lighter regions correspond to positive bed evolution caused by greater sediment accumulation than erosion over the simulation period. Figure 5.9 A shows a marked increase in bed evolution in the mouth of the estuary due to the increased amount of sediment transport caused by wave action, compared with the relatively small amount of evolution which occurs without waves

(Figure 5.9 B).
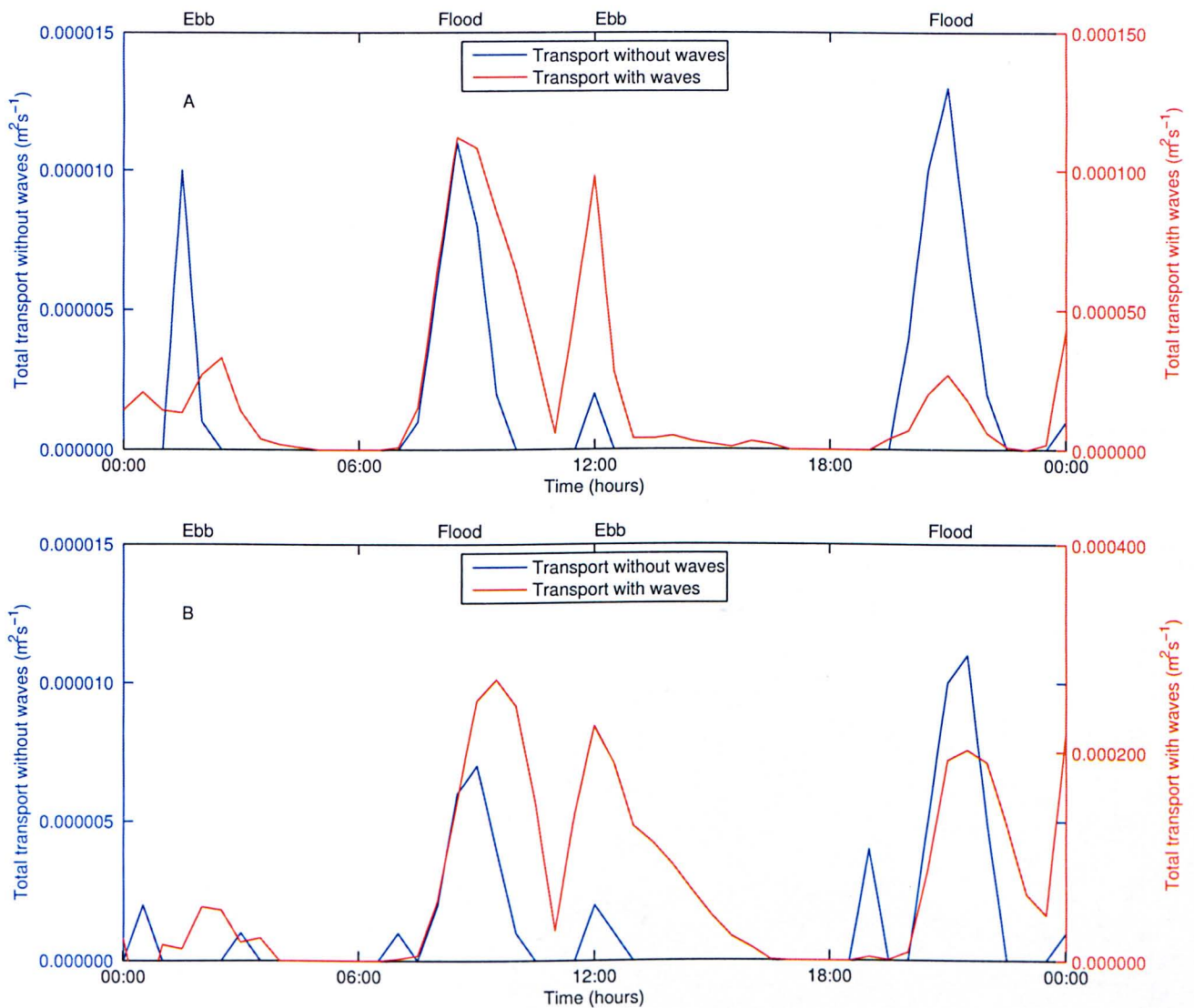
Figure 5.8: Total load transport at A.) West Kirby Sands and B.) West Hoyle Bank calculated using the Bijker formula under two scenarios that did and did not include waves. The y-axis scale shows transport with waves to be an order of magnitude larger than transport without waves.

Figure 5.9 shows significant bed evolution occurring in the mouth of the estuary, with greater magnitudes for simulations including waves. Figure 5.10 shows the same bed evolution simulations, with and without waves, plotted to show the dune fields at West Kirby Sands and West Hoyle Bank, Hilbre Island can be seen in the center of the plots. Focusing on these regions shows that bed evolution is greatly increased at the dune fields of West Kirby Sands and West Hoyle Bank in the presence of waves.
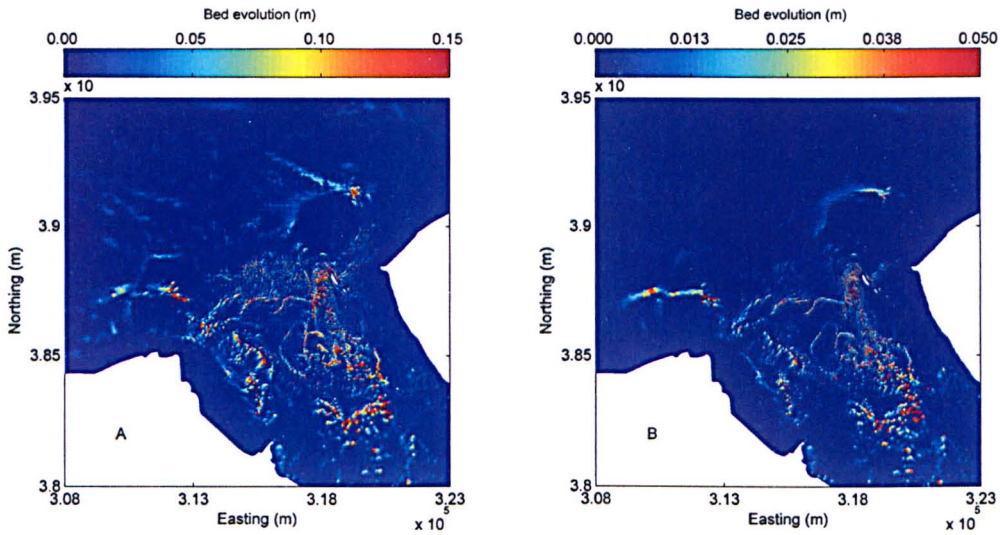
Figure 5.9: Evolution in the mouth of the estuary after a simulation of 24 hours using two model scenarios; including waves (A) and not including waves (B).
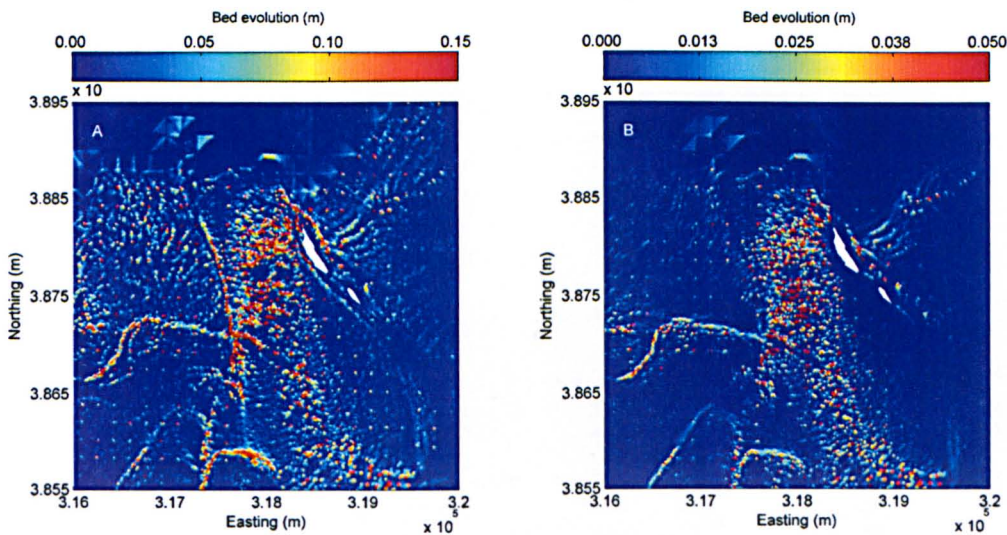
Figure 5.10: Evolution at the dune fields of West Kirby Sands and West Hoyle Bank in the mouth of the Dee Estuary after a simulation of 24 hours using two model scenarios; including waves (A) and not including waves (B). The position of Hilbre Island can be seen in the center of the plots.

A general comparison between simulated wave induced currents with tidal currents and ADCP currents measured at West Kirby Sands shows a similar flood asymmetry. Higher flood velocities result in increased shear at the sea bed during the flood compared to the ebb. Ultimately this creates net sediment transport over a tidal cycle, with flood dominated currents resulting in net sediment transport into the estuary. Sediment is being conserved through the simulation so that sea bed accumulation must be balanced by bed erosion. The pattern of bed evolution seen over the dunes at West Kirby

Sands and West Hoyle Bank (Figure 5.10) suggests that these are active regions for sediment transport, acting as pathways for the movement of sediment into the estuary, for which the evolution of the large scale bed forms likely makes a significant contribution. The increase in bed evolution over the dune fields in the mouth of the estuary due to the action of waves (Figure 5.11) is a result of the increased sediment transport in these areas (Figure 5.8). While this difference in evolution is a significant result, the more interesting outcome with regards to the migration of large scale bed forms in the mouth of the Dee Estuary is the increase in sediment transport which occurs at West Kirby Sands and West Hoyle Bank when waves are included in the simulation. Figure 5.8 shows flood enhanced sediment transport at both dune field sites with the presence of waves. This is caused by the non linear wave-current enhancement of bed shear stress outlined in Section 2.2.3 and included into Bijker's transport formula in the form of Equation 5.9. This highlights the importance of including waves in the TELEMAC simulations as the increase in velocities and sediment transport in the mouth of the estuary occur in similar locations to where bed form migration is being investigated, namely West Kirby Sands and West Hoyle Bank.
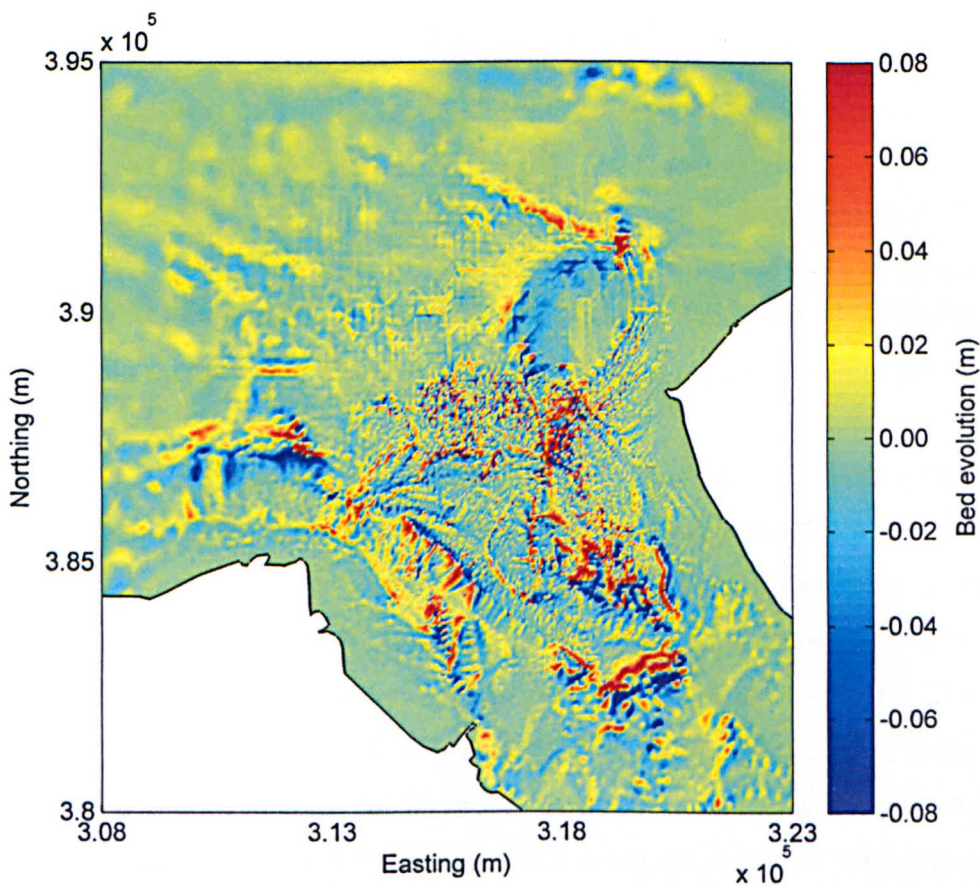
Figure 5.11: The difference in evolution between a 24 hour TELEMAC simulation that includes waves and one with no waves. Yellow to read areas correspond to deposition while blue areas represent erosion

Chapter 6

X-band radar methods

6.1   Hilbre Island X-band marine radar system

Figure 6.1: X-band marine radar installation on Hilbre Island in the mouth of the Dee Estuary

As part of the Liverpool Bay, Coastal Observatory project (National Oceanography Centre, Liverpool) a standard Kelvin Hughes Nucleus 3 5000 series X-band marine radar was installed on Hilbre Island in the mouth of the Dee Estuary in 2005 (Figure 6.1). This X-band radar system was set up to contribute towards integrating (near) real-time measurements with coupled models into a coastal prediction system. The system has a 2.4m antenna which is installed on top of a 30m tower and is operated by the National Oceanography Centre (NOC), Liverpool. The radar overlooks a topographically complex area consisting of intertidal sandbanks and deep subtidal channels, including the dune fields at West Kirby Sands and West Hoyle Bank. The radial range of the radar was set to 4km allowing coverage over the mouth of the Dee Estuary, including the intertidal sand flats at West Kirby Sands and West Hoyle Bank. The radar was used to monitor bathymetric change in the mouth of the Dee Estuary, with the aim of quantifying the migration of large scale bed forms.
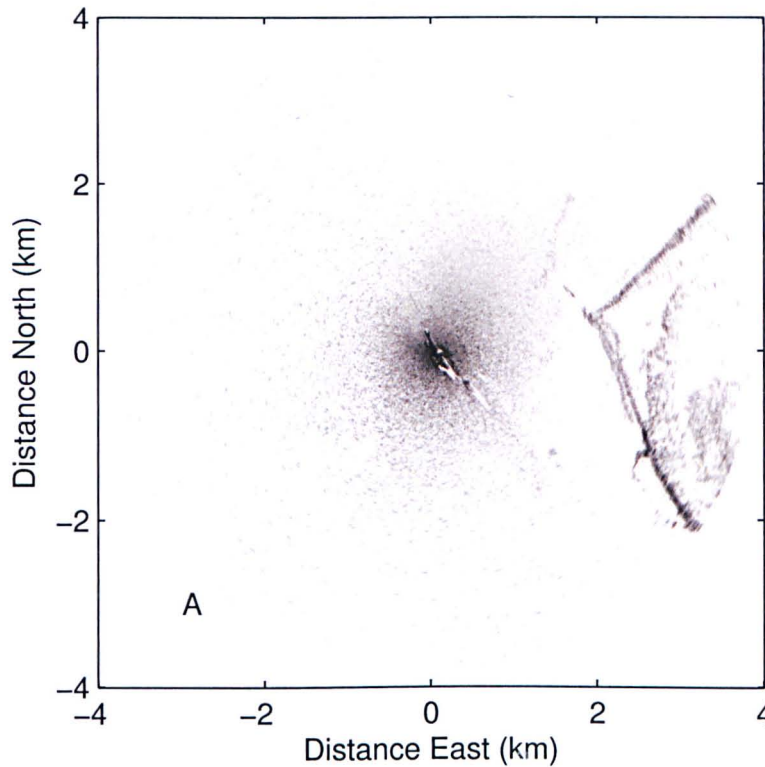
Figure 6.2: Example of a single radar image from the Hilbre Island X-band radar system with a 4km range and a ground resolution of 10m.

The radar antenna rotates every 2.4 seconds recording an image on each rotation. From this a sequence of 256 radar images, each covering approximately 10 minutes, are recorded on an hourly basis. The raw data output by the standard radar equipment (Figure 6.2) is recorded using a Wamos II logger (Hessner et al., 2008) and stored on a conventional PC for further processing. Radar data (courtesy of National Oceanography Centre, Liverpool) was available in two formats; jpg files with a ground resolution of 10m covering the period 01.01.06-31.08.08, and mat files covering 01.01.06-31.01.07 which can be post-processed to maximum ground resolution of 2m. Figure 6.2 shows raw data radar images over the 4km range, clear surface wave patterns can be seen in these images with darker areas corresponding to high radar return, generally referred to as 'sea clutter.'

Radar images are processed in a mean radar return method which averages out the 'sea clutter' signal, highlighting areas of persistently breaking waves. The movement of these wave breaker patterns is tracked using a 2D cross correlation motion tracking algorithm to sequential pairs of monthly mean radar images. Beach profiles are generated using a waterline method which uses tide gauge data and the position of the water's edge visible in the radar data. These methods, which will be discussed herein, allow the morphology in the mouth of the estuary to be continuously remotely monitored.

6.1.1 The physics of radar imaging of the sea surface

The beam pattern generated by the radar antenna is approximately 22° in the vertical, designed so that it is wide enough to account for the pitch and roll of ships on which they are intended to be installed, and 0.8° in the horizontal, which gives a very good angular resolution. Unlike the radial resolution, the resolution perpendicular to the radar beam decreases with range. This means that short waves travelling perpendicular to the radar beam will not be resolved at longer ranges.

In situations where the radar installation is significantly above the mean water level, then a correction for the slant range to the target compared to the horizontal distance might be necessary. However, with increasing range the slant range tends towards the horizontal range making any correction less significant. The greatest slant range correction in a worst case scenario for recorded radar backscatter at a range of 100m is of the order of 1m in range. All Hilbre Island radar data was pre-processed with any correction factors included by the National Oceanography Centre, Liverpool so that the radar data were supplied in two dimensional plan view of the area in view of the radar range.

X-band marine radar works in the radio wave frequency range of 8-12.5GHz, with wavelengths of 2.5-3.75cm, thus operating in the microwave band of the electromagnetic spectrum. It is an active imaging system which relies on emitted electromagnetic waves being scattered by a target. The power of the returned signal is given by the equation

$$P_r = \frac{P_t G_t A_r \beta_r S_r^4}{(4\pi)^2 R^4} \tag{6.1}$$

where P_t is the transmitter power, G_t is the transmitter gain, A_r is the effective radar aperture, β_r is the radar cross section (or scatter coefficient) of the target, S_r is a pattern propagation factor and R is the distance between transmitter and target, assuming that the transmitter is located in the same place. This is true for the Hilbre Island X-band radar system. The radar backscatter is therefore proportional to the inverse fourth power of distance, meaning that the weakest scatter signal will be from objects at the outer limits of the radar's range. It is possible to represent the scattering efficiency of a target by isolating the radar cross section β_r from the radar power equation

$$\beta_r = \frac{(4\pi)^3 R^4 P_r}{P_t G_t A_r^2} \tag{6.2}$$

The radar cross section can be defined as the measure of the ratio of power density in the signal scattered towards the receiver to the power density of the radar wave incident upon the target (Skolnik,

1970). The unit of radar cross section is area, therefore it is usually determined by the target's material, shape and orientation to the radar beam. While a large metallic block would have a large cross sectional area, and a foam sphere would have a much smaller cross section, large cross sections are also generated by groups of much smaller objects such as water droplets in clouds or fog. Similarly the spray generated by breaking waves will produce a large radar cross section which will stand out clearly on radar images as a high level of backscatter return. Two main scattering mechanisms providing a backscatter signal are from steep, breaking waves and also small wind induced 'sea clutter.'

Polarised radar scatterometers designed to allow separate measurements of horizontally and vertically polarised transmitted and received radar energy have provided valuable understanding of the mechanisms responsible for the backscatter signal detected by marine radar systems (Keller et al., 1990; McLaughlin et al., 1995). Two main mechanisms appear to be responsible for providing the backscatter signal in response to the transmitted radar pulses. The first is Bragg resonant scattering (Guinard et al., 1971). This occurs when the wavelength of small capillary waves on the surface of the water have a wavelength component along the axis of the radar beam which satisfies the Bragg condition

$$\lambda_w \cos \theta_R = \frac{\lambda_R}{2} \qquad (6.3)$$

where λ_w is the component of the capillary wavelength along the radar beam, λ_R is the wavelength of the incident radar energy and θ_R is the grazing angle between the incident radar beam and the sea surface. Lee (1977) found that capillary waves are mostly found on the crests of gravity waves with much greater wavelengths. Figure 6.3 shows the Bragg scattering effect of capillary waves on emitted radar energy.
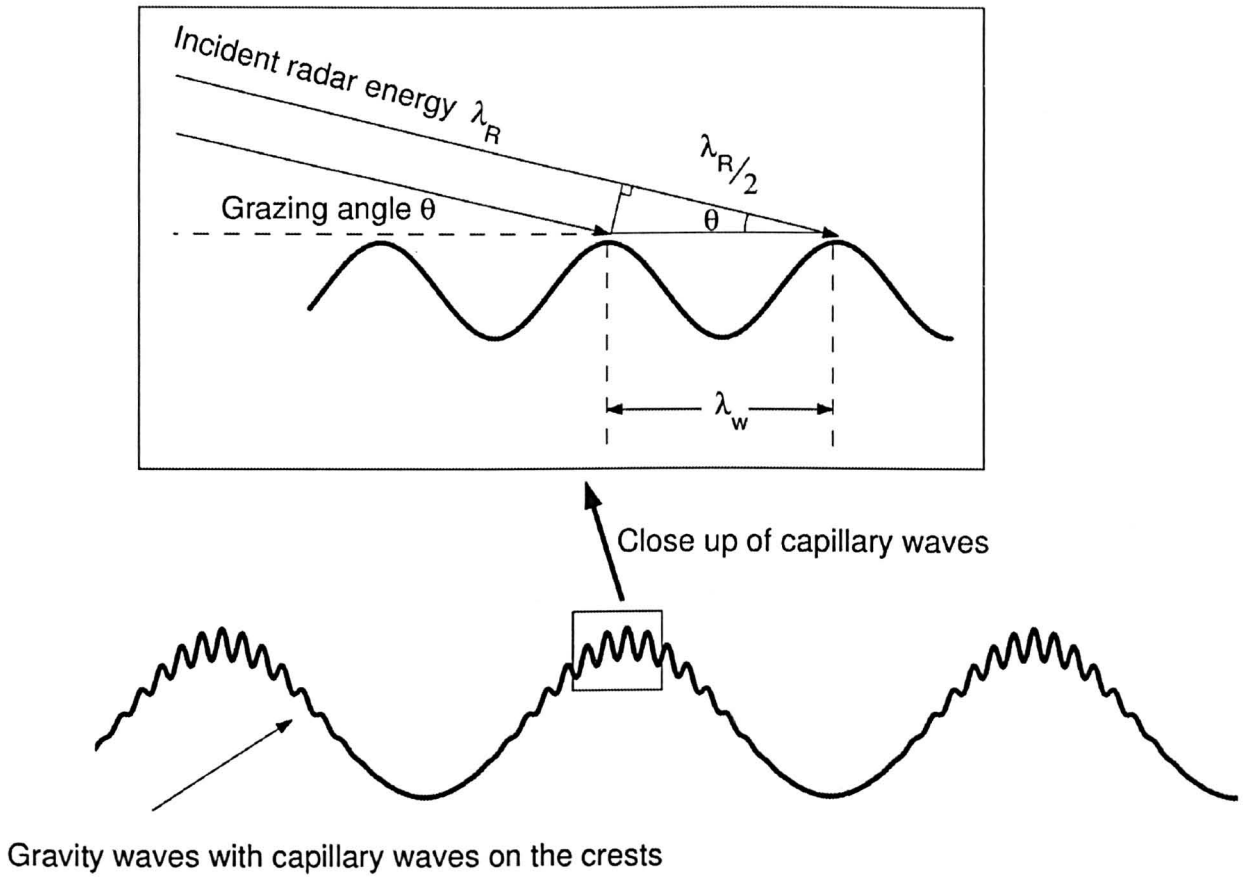
Figure 6.3: The Bragg scattering of radar energy by capillary waves on the crests of gravity waves. From Bell (2005).

For ground based radars, the grazing angle θ is normally less than $10°$ at close range and then tends to zero for longer ranges. X-band radar typically operates with a 3cm wavelength (λ_R). Bragg scattering water waves, also known as capillary waves, will have wavelengths λ_w of the order of 1.5cm. A capillary wavelength of 1.5cm, with crests perpendicular to the radar beam, produces perfect Bragg resonant scattering conditions. Therefore a sea state which is completely smooth and undisturbed by local winds, and so has no capillary waves, will give no radar return signal. Nieto Borge and Reichert (2005) stated that a minimum wind speed of 3ms^{-1} is required to generate capillary waves required for Bragg scattering and therefore produce a radar image.

The second contributor to the radar backscatter signal is sea spikes, associated with steep and breaking waves (Kalmykov and Pustovoytenko, 1976; Jessup et al., 1990; Lee et al., 1995). For horizontally polarised radars (the most commonly used) the signal generated by these sea spikes is significantly greater than the backscatter signal from Bragg scattering of capillary waves. This strong backscat-

ter signal is thought to be the result of a combination of effects including specular and non-specular reflections (Jessup et al., 1990; Ericson et al., 1999). These sea spike radar returns, from breaking waves, produce a much clearer signal in the radar image than normal backscatter levels, creating a useful opportunity to remotely sense nearshore, large scale bed forms, on which the waves are breaking (Ruessink et al., 2002).

6.2   Processing radar raw data images

The raw radar images obtained every 2.4 seconds are manipulated to obtain information on features within the radar's range. The two main methods are; mean intensity images, which consist of the mean intensity for each pixel in the image over a 30 or 60 minute period (Figure 6.4 A), or a maximum intensity image, which consists of the maximum intensity for each pixel over a 10 minute period (Figure 6.4 B).
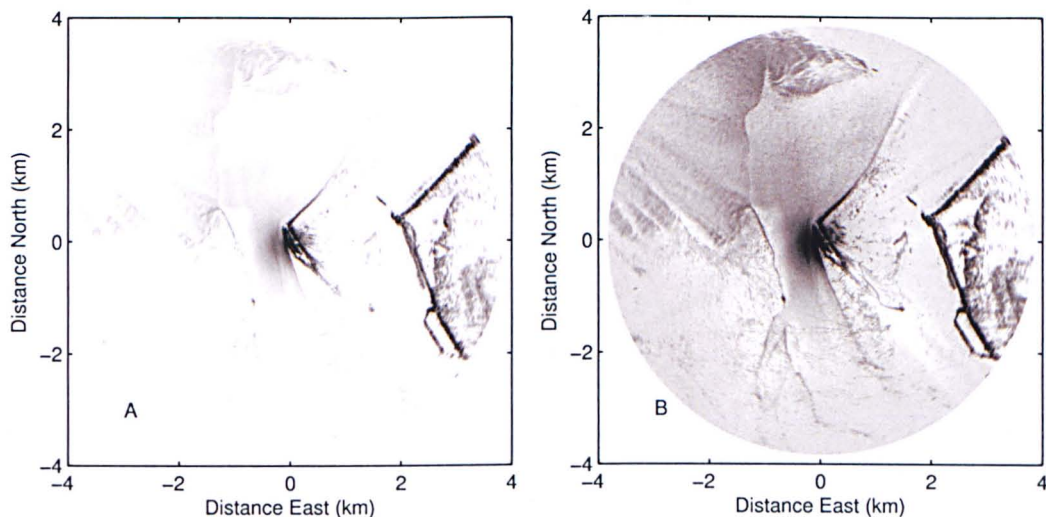
Figure 6.4: Examples of two types of radar images; A) mean intensity image and B) maximum intensity image over the same time period, with a 4km radar range. Hilbre Island is located at the centre of each image and the Wirral coastline is the black boundary to the east of the images. The water's edge can be seen in both images as the long strip of high intensity radar return from breaking waves. Dark lines in the max intensity image are the flight paths of birds and walkers tracks on the sand flats.

The Wirral coastline can be seen as the dark edge of high backscatter return in the east of the radar images. Moving towards Hilbre Island at the center of the image is West Kirby Sands, with West Hoyle Bank located beyond Hilbre Island. It is possible to see dark trails in the maximum intensity image, which are areas of increased radar reflectance, caused by the flight of birds through the radar domain or the tracks of walkers on the sand flats at West Kirby Sands. In the mean intensity image it

is the prolonged reflectors which are clearest, such as areas of breaking waves or stationary objects. The sea clutter signal which is prominent in the snap shot images (Figure 6.2) is averaged out of the mean intensity image (Figure 6.4 A). This is due to a point within the sea clutter oscillating between a range of values, which when averaged over time returns a value close to zero (Hoekstra et al., 2004). The water's edge is visible in the mean and max images as the stripe of high intensity backscatter return running from the centre to the north east of the image. This is due to the presence of breaking waves at the transition between the sea and land. Therefore, the position of the water's edge will be recorded in the radar data, a phenomenon which is explored as one of the methods to determine intertidal morphology.

6.3 Precipitation effects

Unfortunately X-band radar is affected by precipitation, so that periods of persistent rainfall will increase the background backscatter received by the radar. This effect can be enough to completely obscure the signal during heavy rainfall. Figure 6.5 shows hourly mean intensity images from January 2007 where a rain storm can be seen to pass through the radar domain.
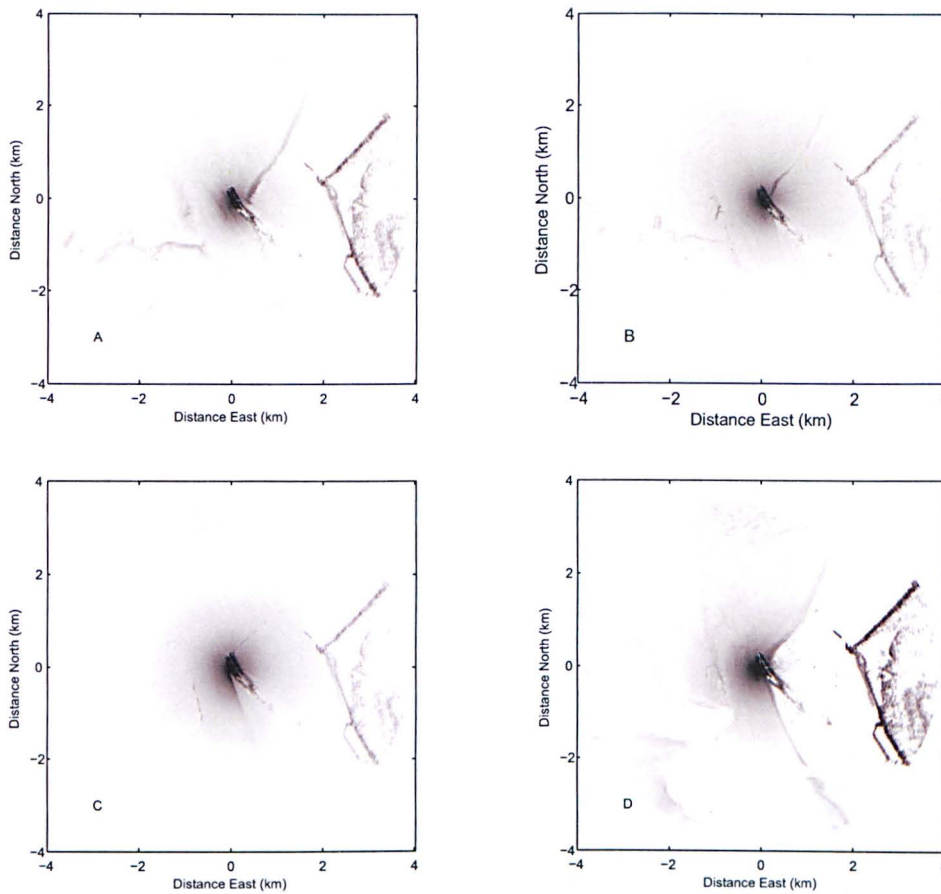
Figure 6.5: The effect of rainfall on the quality of the radar output. The detrimental rainfall effect is most evident in image C, making the water's edge in the centre of the image harder to determine.

It is possible to determine the water's edge in the centre of the radar image as well as the high radar return of the Wirral coastline to the east of the radar images (Figure 6.5 A). The onset of rainfall obscures the backscatter signal from the water's edge and significantly reduces the coastline backscatter signal (Figure 6.5 B), before almost completely obscuring the water's edge backscatter signal (Figure 6.5 C). As this precipitation moves out of the radar domain the backscatter intensity throughout the radar images become clearer (Figure 6.5 D).

6.4 Types of radar data

All data from the Hilbre Island X-band marine radar system were supplied by the National Oceanography Centre, Liverpool. Originally data were supplied in jpg format covering the period 17.08.05 to 31.08.08. These data were recorded as mean and max images at a time step of 30 minutes from 17.08.05 to 07.04.06, with the remaining data being recorded at a 1 hour time step. The jpg images were recorded at a resolution of 10m. Due to the limitations of the recorded resolution and errors

associated with the jpg file format, such as compression artefacts causing image distortion, X-band radar images were also supplied in uncompressed mat format. These mat data files cover the period 06.03.06 to 01.02.07, with a 30 minute time step up to 07.04.06 and a time step of 1 hour for the remaining data files up to 01.02.07. The use of mat files allows the resolution to be set manually by the user through post processing in Matlab and removes any loss in image quality due to compression.
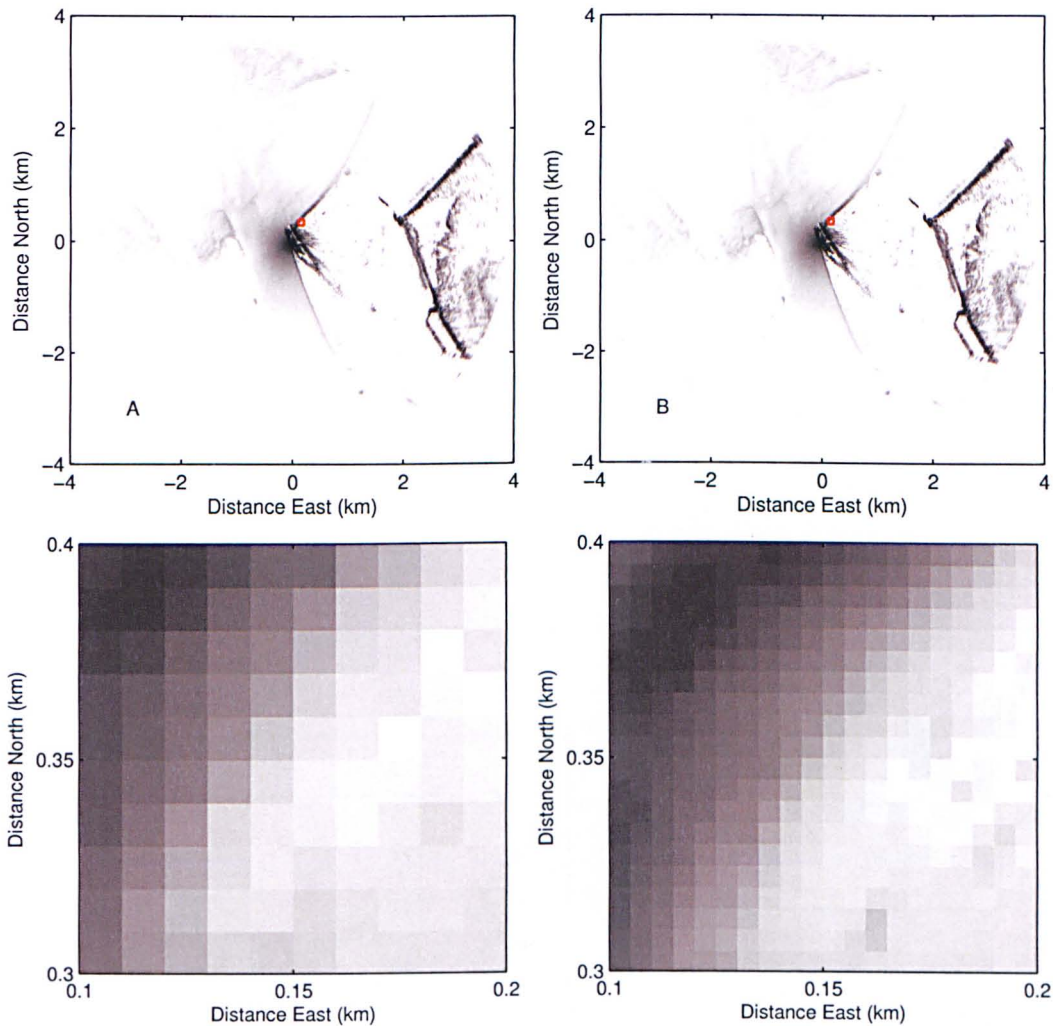
Figure 6.6: Hourly mean intensity X-band radar image showing examples of A) jpg data and B) mat data files. A 100m^2 area window focuses on the water's edge to show the improvement in image quality with increased resolution.

Figure 6.6 shows hourly mean radar images for jpg and mat radar data with 10m and 5m resolution, respectively. Looking at the entire radar domain there does not appear to be a difference in radar images between data types, however a region focusing on the water's edge shows an increase in image quality with increased resolution. The X-band radar has a wide beam angle and so the length of the sector traced out by the beam width increases with range. This causes the resolution perpendicular to the radar beam to decrease with range, however this is not a significant effect. The mat radar data

is post-processed to a specified resolution using Matlab to edit the 'gridsquare' (i.e. pixel) size. Increasing the grid resolution increases computational demand and it was found that computer memory was the limiting factor when increasing the resolution of mat radar data. This resulted in a maximum resolution of 5m for when creating monthly mean mat radar data images and 2m for weekly mean mat radar images.

6.5 Mean radar return

The process of creating a mean intensity radar image removes the signal from the sea clutter, described previously as the Bragg scattering effect of capillary waves, and leaves areas of persistently breaking waves which occur at the shoreline or over steep topography, such as the crests of large submerged sand dunes. Monthly mean images were created by averaging the hourly mean intensity radar images over the period of that month. The monthly averaging process (Figure 6.7) creates a mean greyscale intensity value for each pixel $P_{(x,y)}$ in the monthly mean image using hourly mean images covering the specified time period.
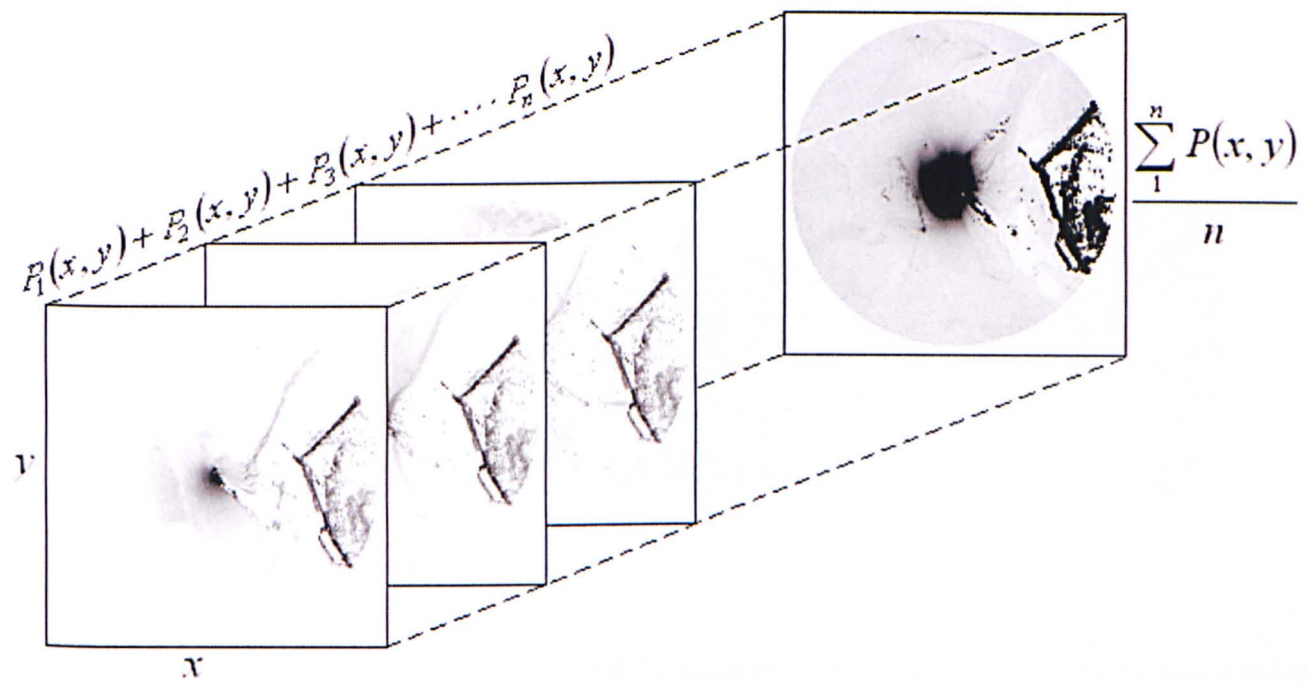
Figure 6.7: Schematic diagram detailing the process of creating a monthly mean X-band radar image. From McCann (2007).

The darkest areas on the monthly mean images represent persistent high intensity return over the averaging period, such as land masses (Figure 6.8). The signal detected by the water's edge (Figure 6.6) is lost when averaged over the period of a month as the position will regularly change with

the tide. However, areas of persistently breaking waves remain in the monthly mean images. The waves are breaking over submerged bathymetry, which will add to a mean signal if the position of the bathymetry remains fairly constant over the averaging period. Therefore, this breaking wave backscatter signal offers the opportunity to remotely sense the location of large scale bed forms in the mouth of the Dee Estuary using X-band radar data and potentially track their migration through time.
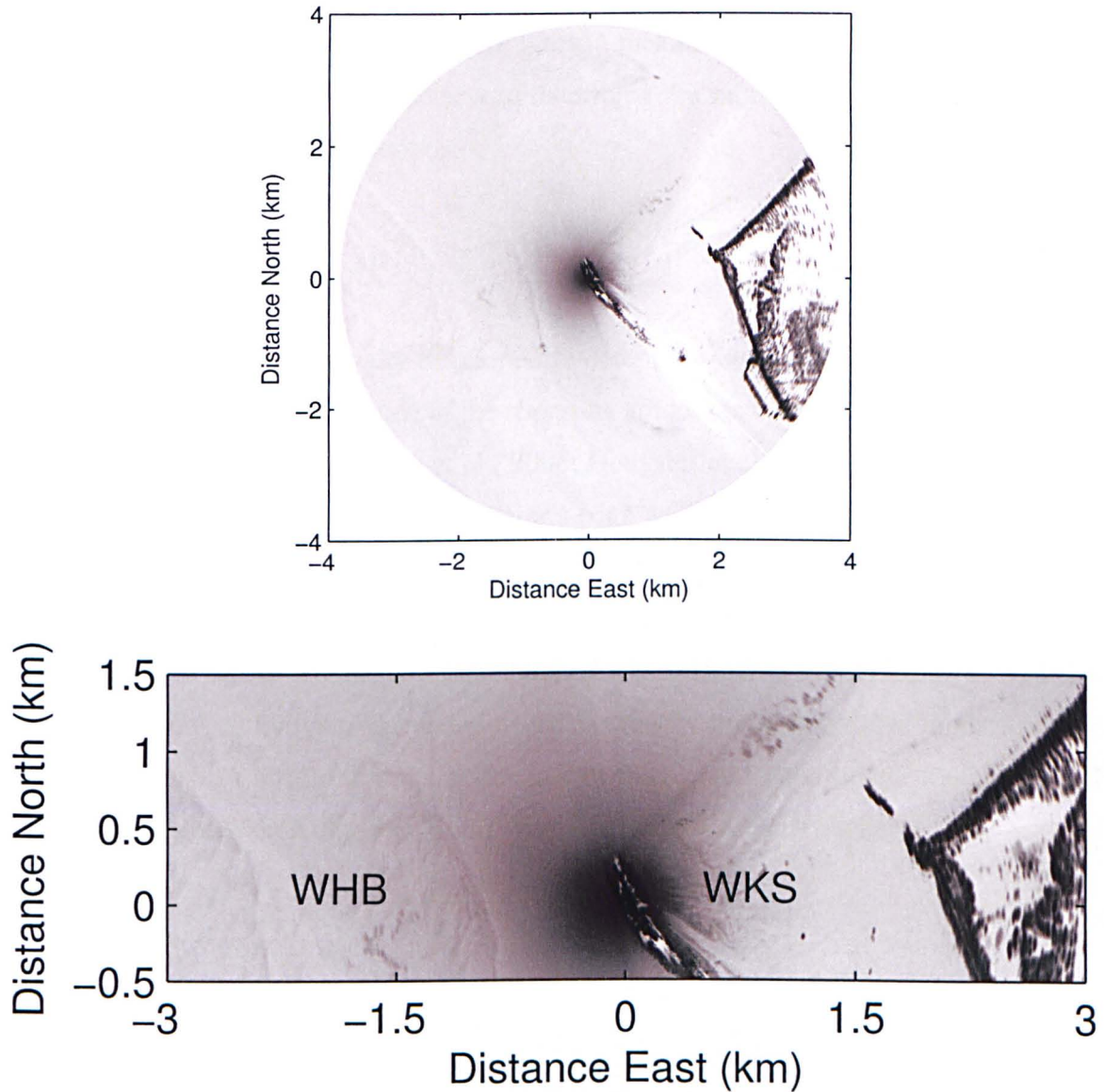
Figure 6.8: Monthly mean intensity X-band radar image for October 2006. The subplot shows mean intensity backscatter return from breaking waves over West Kirby Sands (WKS) and West Hoyle Bank (WHB).

The subplot in Figure 6.8 shows wave breaker patterns over the intertidal sand flats at West Kirby Sands (WKS) and West Hoyle Bank (WHB) in the mouth of the Dee Estuary. The pixel intensity values in this subplot image are the square root of the pixel intensity values for the monthly mean

image covering the entire radar domain, so that the breaking wave signal is clearer for the reader. The wave breaker patterns are most clearly visibly by eye over West Kirby Sands (WKS), where variations in backscatter intensity can be seen between Hilbre Island and the Wirral Peninsula. The dark area at the center of the image, around the Hilbre Island chain, is caused by high return from objects close to the radar antenna (Equation 6.1). Monthly mean images were generated for all months of available radar data, covering the period of August 2005 to August 2008 for the jpg file format and March 2006 to January 2007 for the mat data, while weekly mean radar images were created for October 2006 using mat and jpg files, with the view to determine the migration of the breaking wave radar backscatter signal over these time periods.

6.6 Waterline method

The Waterline Method was originally developed to determine intertidal bathymetry using waterline contours from aerial photographs taken of the shoreline at recorded times so that tidal height data can be used to calculate the elevation (Ryu et al., 2008; Heygster et al., 2010; Mason et al., 2010). The radar backscatter signal associated with the water's edge was used by Takewaka (2005) to determine beach profile morphology (Section 2.6.4). The waterline method can be applied to the hourly mean X-band radar data, utilising the backscatter signal associated with the water's edge (Figure 6.6). In this study a variation on the original waterline method was applied so that an image of a vertical slice through the intertidal bathymetry is created using the hourly mean radar data in combination with local tidal elevations. A profile through an area of interest in the radar image was selected (Figure 6.9), the dune fields at West Kirby Sands and West Hoyle Bank are chosen here.
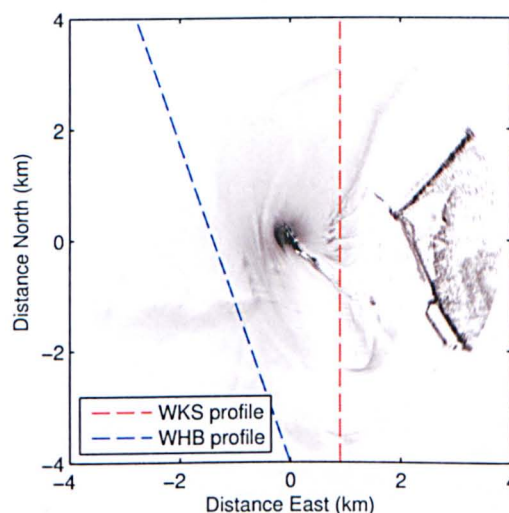
Figure 6.9: Location of waterline profiles for West Kirby Sands (WKS) and West Hoyle Bank (WHB).

Tidal elevation data was obtained from the Hilbre Island tide gauge, located on the northernmost tip of Hilbre Island, for the time period covered by the radar data (17.08.05-31.08.08). Greyscale intensity values are then extracted from the hourly mean radar images along the waterline profile and stored with tidal elevations corresponding to the time of the radar image. The profiles were then binned at 10cm intervals by sorting using their corresponding tidal height, placing them into 10cm partitions, and then averaging all the profiles in each bin. This creates a scaled array of greyscale intensity values where the rows correspond to bed elevation above chart datum and columns represent the ground distance from the radar antenna (Figures 6.10).
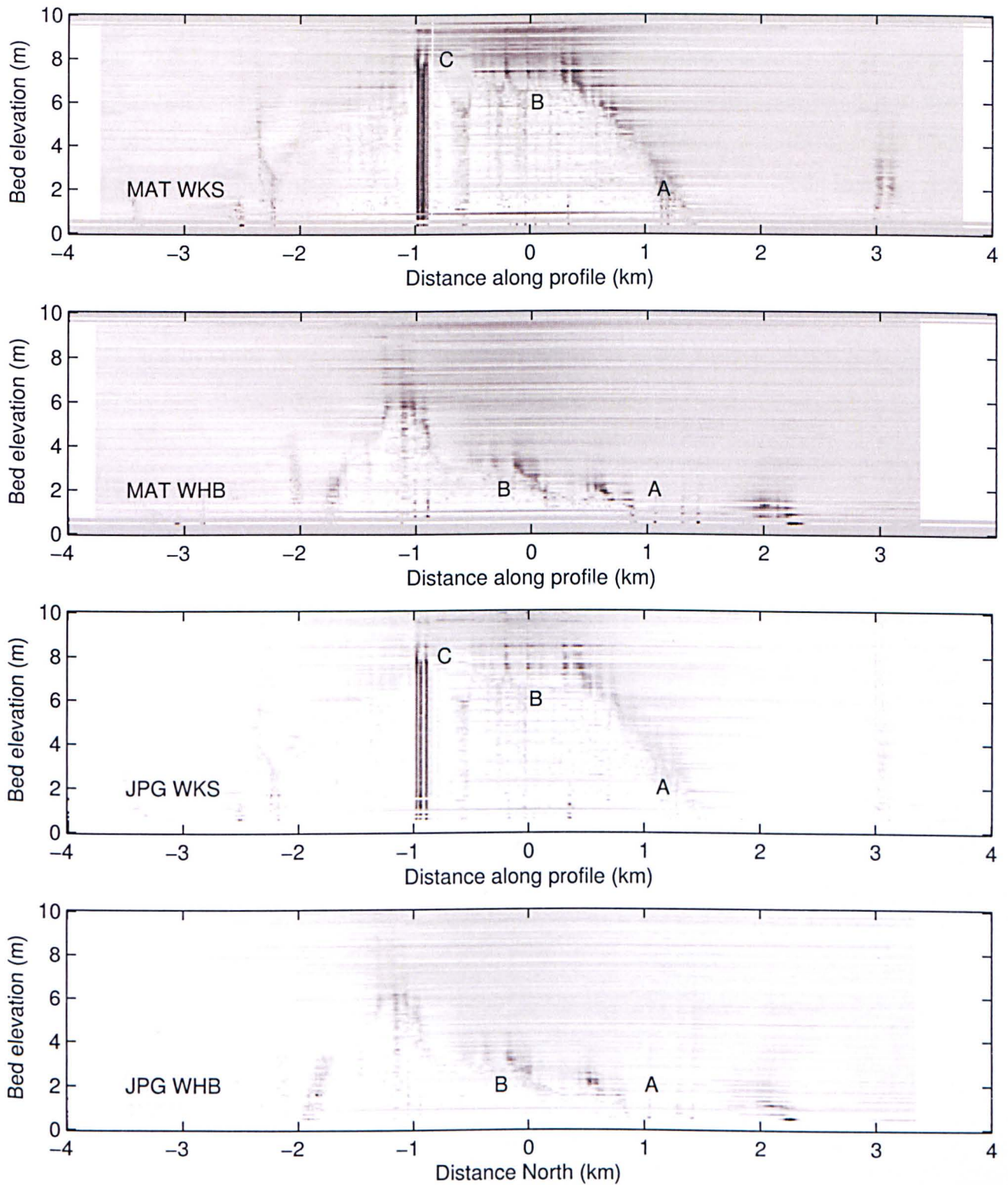
Figure 6.10: Waterline images for West Kirby Sands (WKS) and West Hoyle Bank (WHB) created using mat and jpg file formats from October 2006.

The resulting waterline images show a topographic slice through the areas of interest (West Kirby Sands (WKS) and West Hoyle Bank (WHB)) created using the mat and jpg file format (Figure 6.10). The beach profile images created using the mat radar data are more clearly defined than those created

with the jpg data. This could be a result of the increased horizontal resolution from 10km for the jpg radar data to 5km for the mat data and also the loss of inherent errors related to jpg artefacts which the mat radar data does not contain. A difference in pixel intensity values can be seen to mark the location of the beach profile at West Kirby Sands and West Hoyle Bank, with the open sea boundary located at 4km along the profile. The beginning of the shoreline, at the low tide limit, is visible at point A in Figure 6.10, with the beach slope leading to undulating regions containing large scale bed forms at point B. Figure 6.11 shows the large scale bed forms visible in the waterline beach profiles at West Kirby Sands and West Hoyle Bank. Unfortunately precise geometries of these bed forms can not be extracted from the waterline data, however, estimates made by eye of bed form height and wavelength are approximately 0.5-1.0m and 100m, respectively.
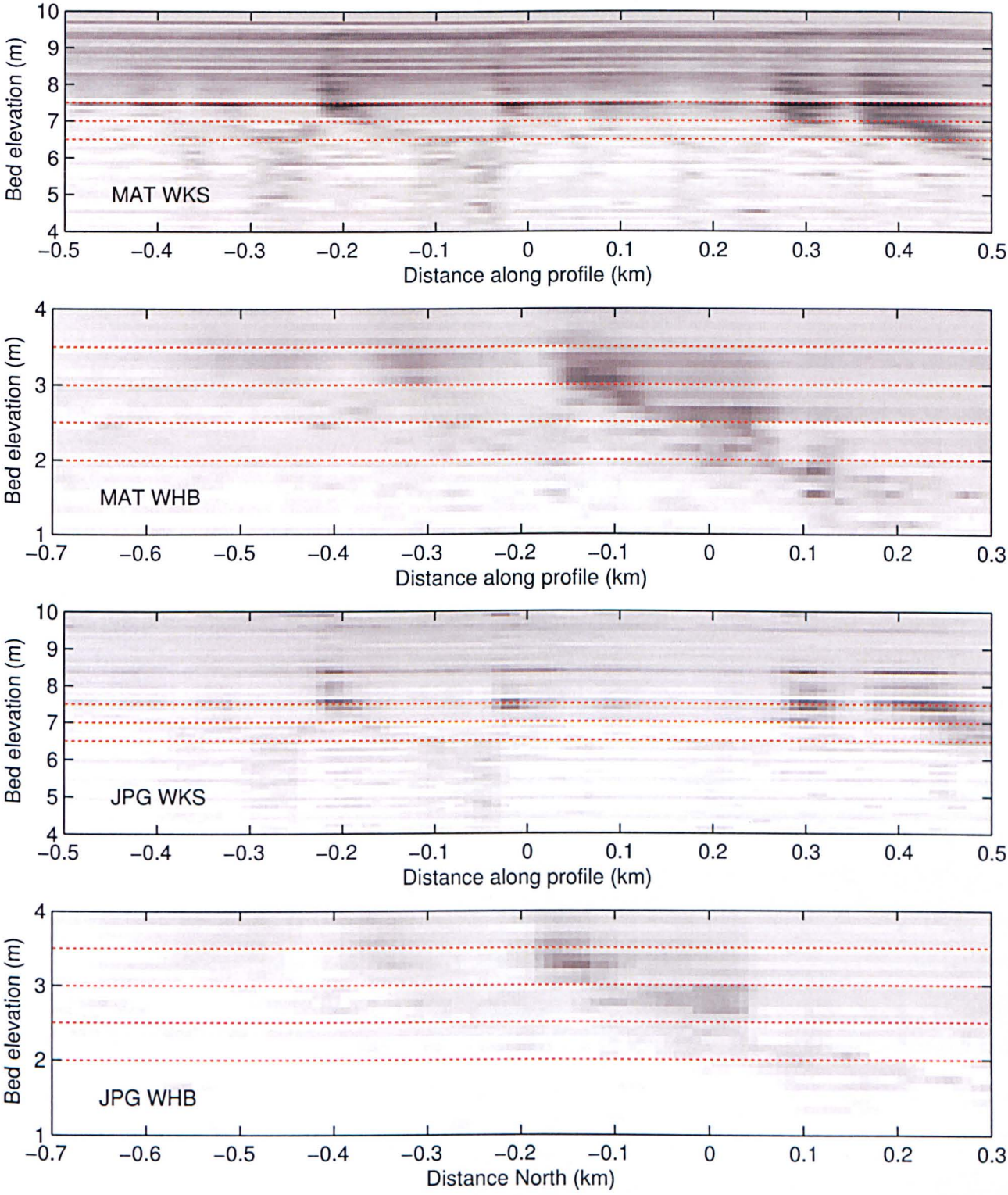
Figure 6.11: Waterline images for the dune fields at West Kirby Sands (WKS) and West Hoyle Bank (WHB) created using mat and jpg file formats from October 2006. Grid lines are spaced at 0.5m intervals. Estimates of bed form height and wavelength are approximately 0.5-1m and 100m, respectively.

The position of the water's edge is visible in the X-band radar images due to presence of persistently breaking waves in this region. The averaging process removes the radar backscatter signal from the

sea clutter, meaning there is little backscatter from the land and sea surface, whereas the land-sea boundary will produce greater levels of backscatter due to waves breaking here. Waves will most likely break seaward of the water's edge, as the bathymetry shoals, however this offset should be of similar magnitude to the horizontal resolution (10m for jpg and 5m for mat). Any feature which is stationary over the waterline period (in this case a month) will appear as a vertical bar through the image. This can be seen at point C (Figure 6.10 WKS) which represents Little Eye, the smallest island in the Hilbre Island chain. Waterline images were generated at West Kirby Sands and West Hoyle bank for all months of available data in mat and jpg format.

6.7   Tidal data for the waterline method

It is important to have consistent and reliable tidal elevation data to create clear waterline images. This method can suffer from the effect of atmospheric surge, where changes in tidal elevation are caused by atmospheric pressure variations and wind stresses, if the tidal data is generated from a model or the tide gauge is not in close proximity to the study area. Tide data for this study was obtained from the tide gauge on Hilbre Island which is located on the northern tip of Hilbre Island. The close proximity of the tide gauge to the waterline profile locations at West Kirby Sands and West Hoyle Bank should mean that the tidal data includes any surge effects, which will be present uniformly across the study area. This eliminates the need to run a tide-surge model for the study area. Mason et al. (1995, 1998) stated that the use of a tide-surge model is the most significant source of error when determining waterline elevations. The Hilbre Island tidal data was limited by periods of inactivity caused by silting effects when it is thought fine sediment blocked the intake pipe of the gauge. These erroneous points were manually deleted from the tidal data leaving an incomplete data set (Figure 6.12). Tidal data from the nearby Gladstone Dock, Liverpool tide gauge were used to fill the gaps in the Hilbre Island tidal record. Figure 6.13 shows a good correlation when the residuals at Hilbre Island and Gladstone Dock are plotted against each other.
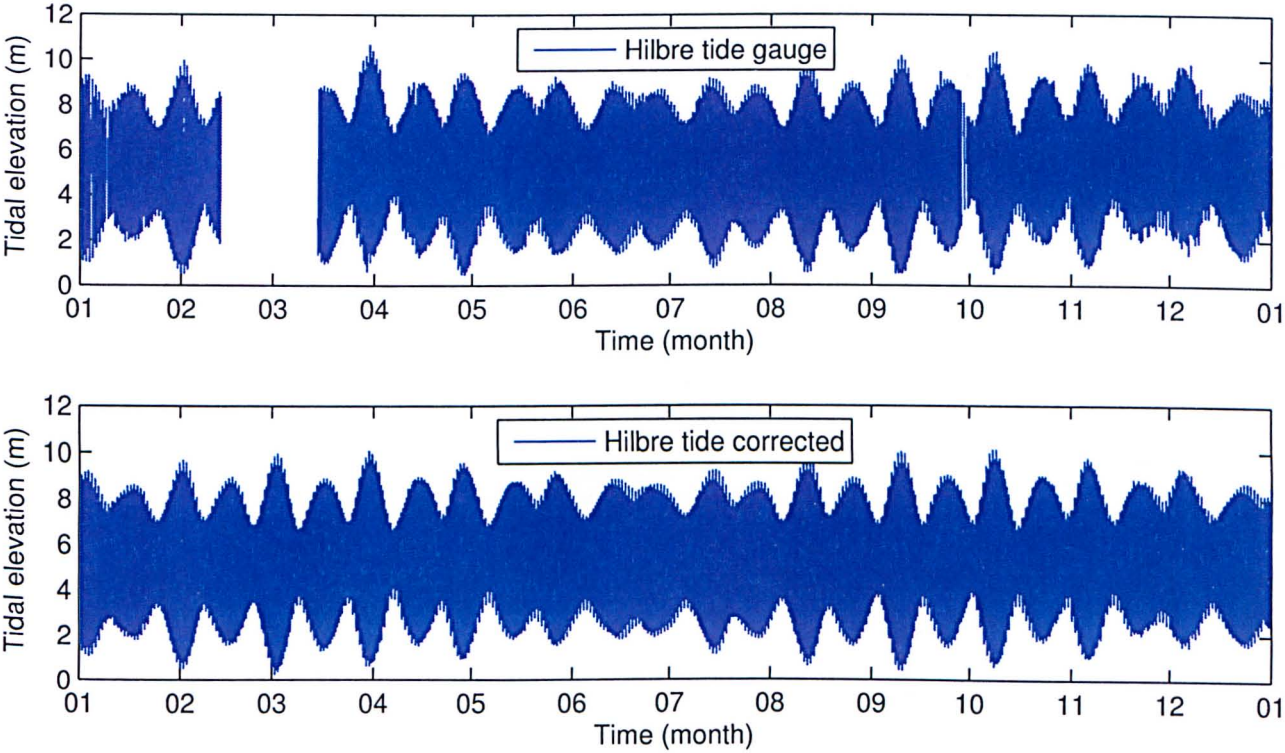
Figure 6.12: Tidal elevation data for 2006 from the Hilbre Island tide gauge, showing periods where erroneous data were removed to be corrected with Liverpool surge and Poltips tidal prediction data.

The difference between tidal observations and predictions from the Poltips tidal model were used to obtain the surge at Liverpool. Then assuming that the atmospheric surge at Liverpool is the same as Hilbre, the surges were added to Poltips tidal predictions for Hilbre Island and used to fill any gaps in the Hilbre Island tide gauge data (Figure 6.12). Tidal data for Hilbre Island and Gladstone Dock, Liverpool as well as Poltips tidal predictions at Liverpool and Hilbre Island were supplied by the National Oceanography Centre, Liverpool for 2006, 2007 and 2008. Tidal corrections were applied by the author to all tidal data used with X-band radar monthly mean images to create waterline beach profile images.
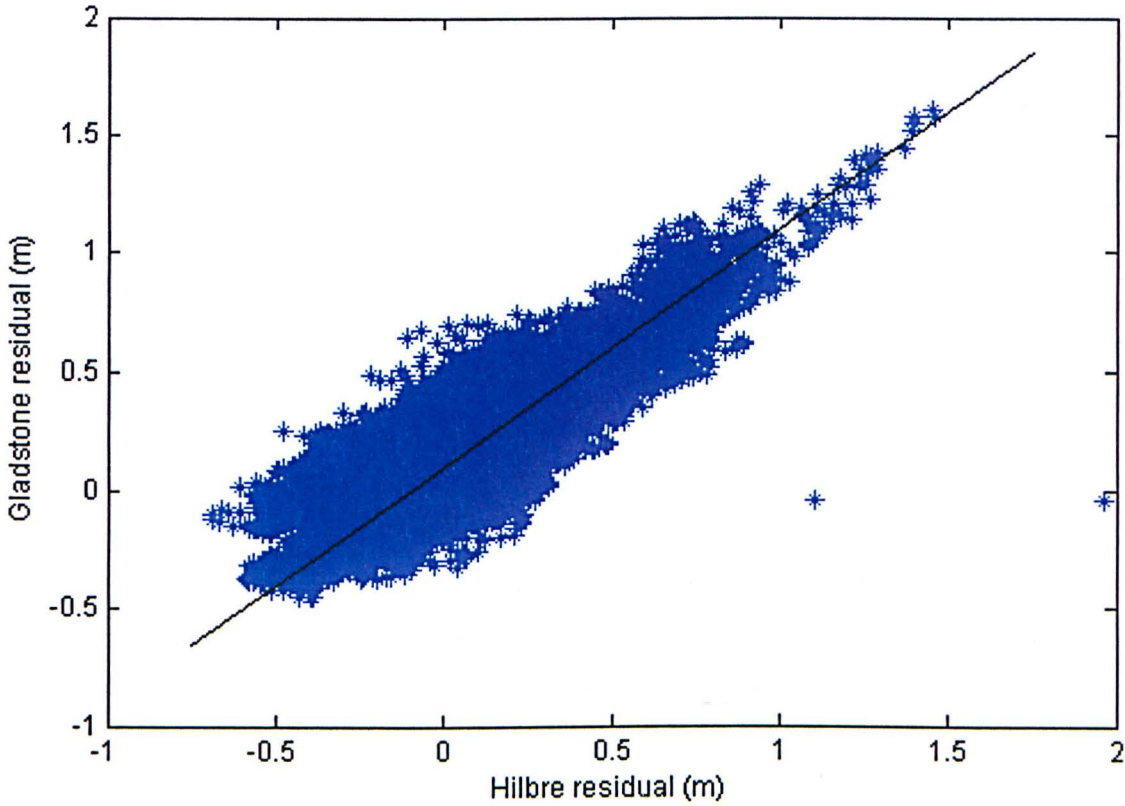
Figure 6.13: A comparison between the residuals at Hilbre Island and Gladstone Dock.

6.8 Motion Tracking

There is a high level of similarity between successive monthly mean radar images due to the relatively slow change in the breaker patterns over the dunes covered by the radar. Therefore it is possible to apply a 2D cross correlation motion tracking algorithm to sequential pairs of monthly mean radar images based on the method of Bell (2005), and previously implemented by McCann (2007), to determine the migration of wave breaker patterns at a sub-pixel accuracy. As an initial step, a subsection of the radar image is chosen for motion tracking analysis, Figure 6.14 shows an area of interest at West Kirby Sands 60x60 pixels, corresponding to a $0.36km^2$ area. On inspection the pattern of wave breaker backscatter intensity can be seen to move in a south east direction between images. The size of the image sub-section is chosen so that it contains at least one wave breaker pattern wavelength, defined as the distance between two peaks in breaking wave radar backscatter intensity.
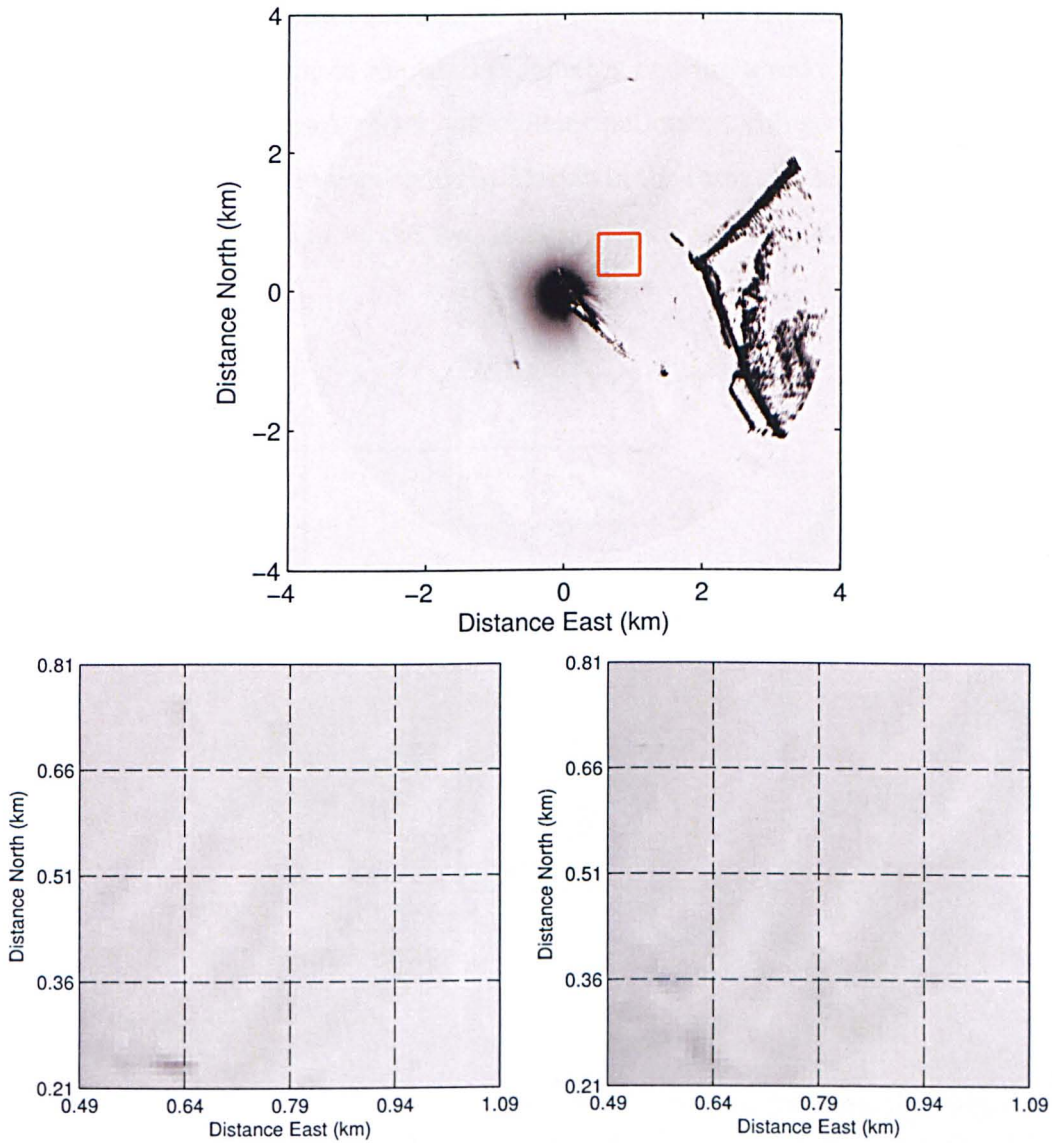
Figure 6.14: Image sub-sections of breaking wave radar backscatter return at West Kirby Sands (location shown by red outline on total radar range) from monthly mean jpg images for October 2006 (left) and November 2006 (right).

The image sub-section can be compared with a corresponding area from the second image to determine the migration of wave breaker patterns over the time between the two images. In the example in Figure 6.14 monthly mean radar images are compared between October and November 2006. The algorithm used to compare image sub-sections is a linear cross correlation (Press et al., 1992), which standardises the results of the image comparison between the two sets of data X and Y compromising n points. The correlation coefficient r is output between -1 and 1, where 1 indicates a perfect match and zero indicating no match

$$r = \frac{\sum_n (X_n - \bar{X}_n)(Y_n - \bar{Y}_n)}{\sqrt{\sum_n (x_n - \bar{x}_n)^2}\sqrt{\sum_n (Y_n - \bar{Y}_n)^2}} \qquad (6.4)$$

This method of spatial domain cross correlation was chosen over Matlab's inbuilt frequency domain 2-D cross correlation. This is due to the Matlab function causing a reduction in the number of data points used to calculate r with each offset, which does not occur with spatial cross correlation. The spatial cross correlation algorithm was coded in Matlab in the form of a search routine which creates a cropped template from the latter of the two images, which is then passed over the earlier search image (Figure 6.15).
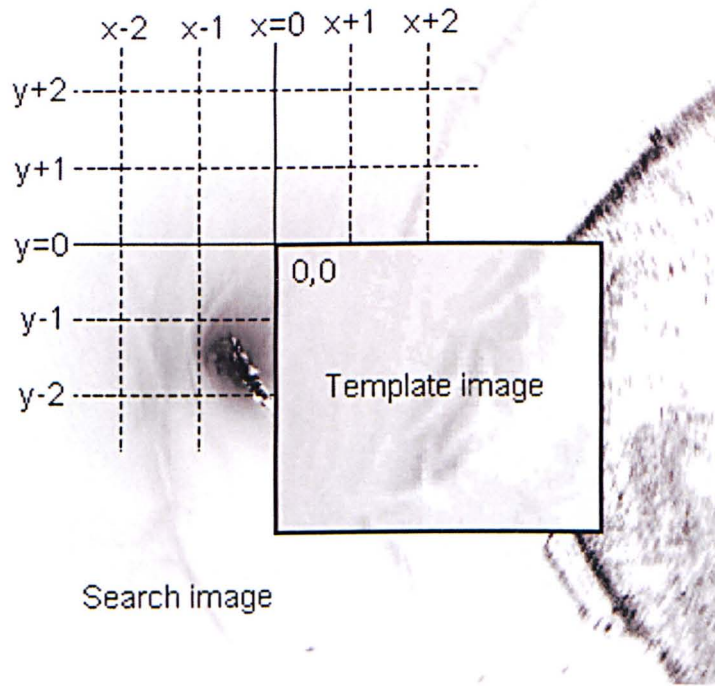
Figure 6.15: Schematic diagram of the search routine for the motion tracking algorithm programmed into Matlab. The search grid is on a pixel scale but is displayed larger than the actual image pixel distance in the schematic diagram for clarity. From McCann (2007).

The search routine was limited to 8 pixels in all directions from a pre-determined origin, due to the similarity between the breaker patterns in successive monthly mean images compared to the size of the images. A correlation coefficient r is generated by the search routine at each offset, where the offset of the maximum calculated r in relation to the origin shows the distance and direction of migration of the template from the search image. A correlation matrix is generated from each correlation coefficient calculated at every displacement of the template over the search image. Polynomial curves are fitted vertically through the correlation matrix for each horizontal displacement, assuming a smoothly varying data set. The point of maximum r is estimated by taking the derivative of the polynomial curves. Figure 6.16 shows a correlation matrix from the motion tracking algorithm, for the example shown previously, the white crosses represent the polynomial fits for maximum r at each horizontal offset. The motion vector is defined as a line passing through the zero offset position with a gradient

that is the reciprocal of a line fitted through the points of maximum r in the correlation matrix, and is perpendicular to the fitted line. The length and direction of this vector, shown as the black arrow in Figure 6.16, represents the migration distance and direction of the wave breaker patterns between the two radar images.
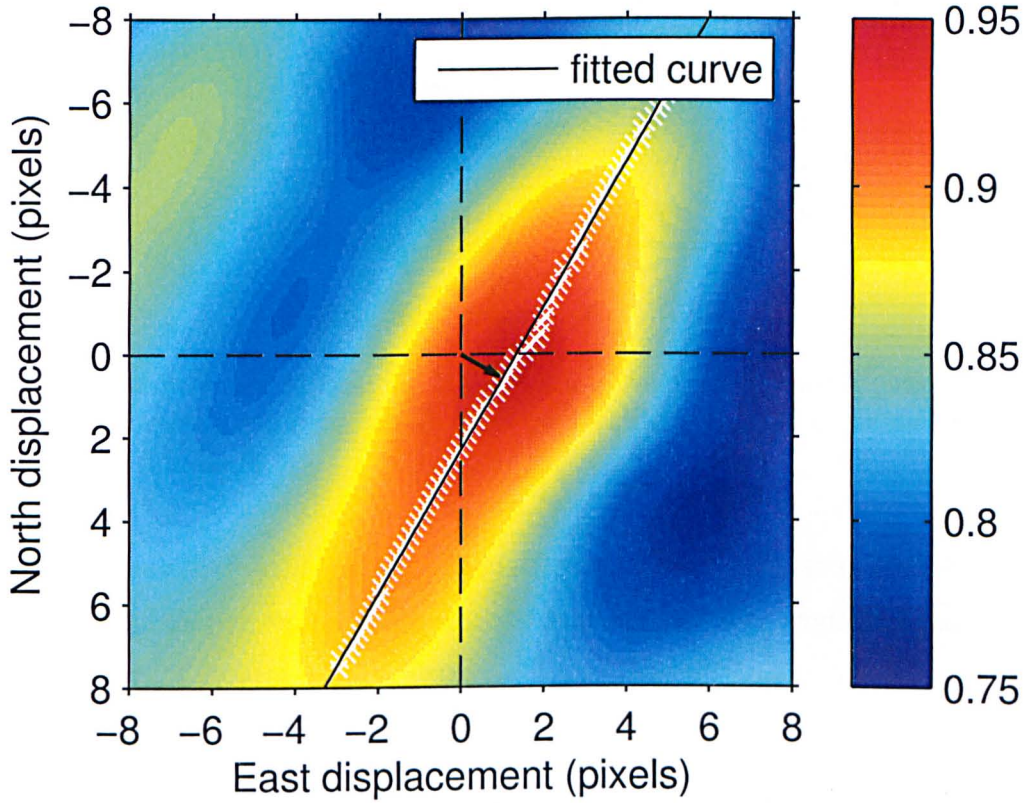
Figure 6.16: Matrix of correlation coefficients from the motion tacking algorithm applied to a search area at West Kirby Sands between monthly mean radar images from October and November 2006. The motion vector represents the displacement of the breaker pattern between radar images. The polynomial fit for maximum r at each offset are shown as white crosses. The colour scale corresponds to the correlation coefficient.

To find the angle δ in degrees between the motion vector m and the vertical the following equation was used

$$\frac{1}{\alpha} = \tan \delta \qquad (6.5)$$

where α is the gradient of the fitted line. The distance between the zero offset and the position of maximum r at this offset ϑ can then be used to calculate the length of the motion vector m (in pixels)

$$m = \vartheta \sin \delta \qquad (6.6)$$
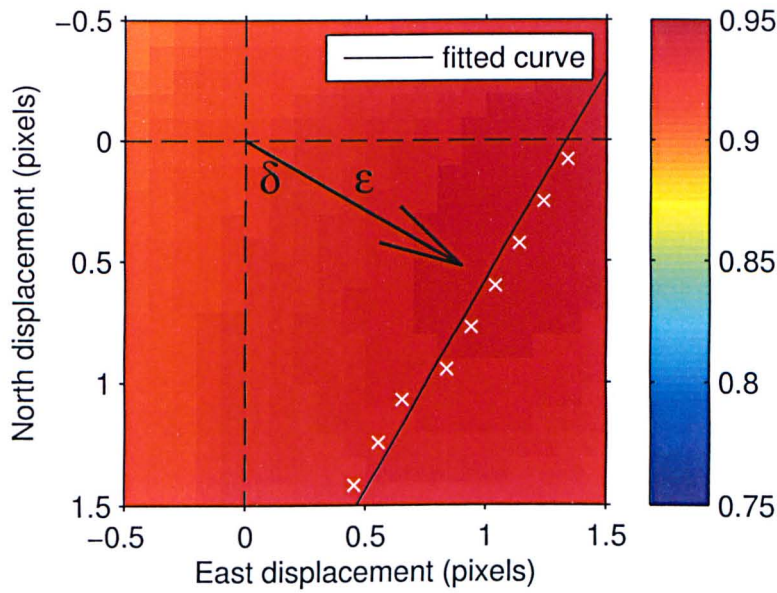
Figure 6.17: The motion vector originating at the point of zero offset, showing the distance between zero offset and peak correlation ε and angle from the vertical δ used to calculate vector length and direction in degrees from north.

Figure 6.17 shows a sub-section of the correlation matrix in Figure 6.16, showing the position of zero offset, from which the motion vector originates, as well as the vector angle from the vertical δ and distance from zero offset to maximum r at this offset ε. The bearing of the migration direction in degrees from north is then

$$|180° - \delta| \qquad (6.7)$$

This assumes that a distinct linear ridge of high correlation is present in the correlation matrix and that the breaker patterns are regular wavelike features. The size of the template image was chosen to cover the dune field so that the crest length of the breaker patterns does not cause problems when fitting a linear regression through the correlation matrix peaks. The breaker patterns visible in the radar images are well suited to produce a linear ridge in the correlation matrix as they are long crested, wave like features which are relatively similar along their crest line. However, an assumption is made that any change in shape of the individual breaker patterns will be too small over the period of one month to cause an effect on the cross correlation algorithm. This motion tracking algorithm is applied to all available monthly mean and selected weekly mean radar data for both mat and jpg file formats to determine the migration of wave breaker patterns, and therefore the underlying morphology, at West Kirby Sands and West Hoyle Bank.

Chapter 7

X-band radar results

In this chapter the application of marine X-band radar images is described in order to determine the direction and magnitude of migration of large scale bed forms in the mouth of the Dee Estuary. Historic aerial photographs of the Dee Estuary (Figure 1.3) show the presence of large scale bed forms on the intertidal sand flats in the mouth of the estuary. Imaging the location of persistently breaking waves by averaging instantaneous radar images over time, removing the signal of surface capillary waves (Bragg scattering), is shown in Figure 6.7. The method of determining 'sea spikes' in radar backscatter is applied to remotely sense the large scale bed forms on which these waves are breaking. This should allow the location of these wave breaker signals to be tracked over time, allowing an estimation of bed form migration to be made.

7.1 Monthly mean radar return images
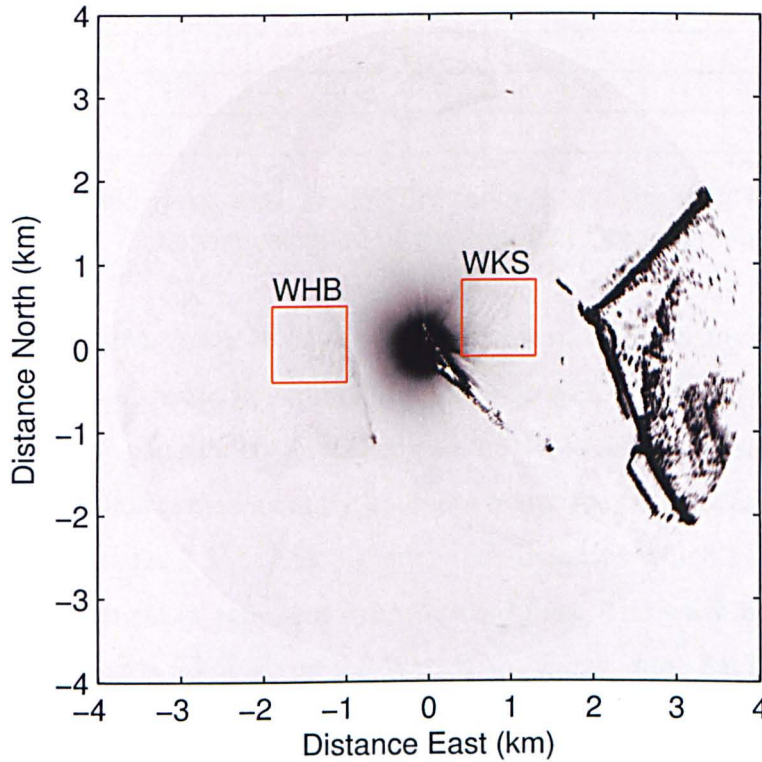
Figure 7.1: Monthly mean radar return image showing areas of interest; dune fields at West Kirby Sands (WKS) and West Hoyle Bank (WHB). The origin of the coordinates is located at the X-band radar installation on Hilbre Island.

X-band radar data supplied by Dr. Paul Bell (NOC, Liverpool) were available in jpg and mat formats. Initially jpg radar data were used to remotely sense the morphology in the mouth of the Dee Estuary before applying the methods to mat radar data to improve the resolution of the data. Approximately 22390 hourly mean jpg files were supplied for this study, which are referenced to a 10m square pixel size and each of which was created from 10 minutes of radar data collected by the Wamos II data logger. Hourly mean X-band radar data in mat format comprised of 7917 files which were each created from 10 minutes of radar data processed to a 5m square pixel size. All images were used to create monthly composite images for further analysis. Table 7.1 shows the availability of X-band radar data to create monthly mean images.

Monthly mean images centered over the West Kirby Sands dune field (Figure 7.1) can be seen in Figure 7.2 for all available jpg data for 2006 to 2008. Figure 7.3 shows the West Hoyle Bank dune field (Figure 7.1) for the 2006 to 2008 radar jpg data. Figures 7.4 and 7.5 show the West Kirby Sands

Radar data	Jan	Feb	Mar	Apr	May	Jun	Jul	Aug	Sep	Oct	Nov	Dec
2006 JPG	✓	✓	✓	✓	✓	✓	✓	✓	✓	✓	✓	✓
2006 MAT	-	-	✓	✓	✓	✓	✓	✓	✓	✓	✓	✓
2007 JPG	✓	✓	✓	✓	✓	✓	✓	✓	✓	✓	✓	✓
2007 MAT	✓	-	-	-	-	-	-	-	-	-	-	-
2008 JPG	✓	✓	✓	✓	✓	✓	✓	✓	-	-	-	-
2008 MAT	-	-	-	-	-	-	-	-	-	-	-	-

Table 7.1: Periods of X-band radar data availability for mat and jpg data formats used to create monthly mean radar images. Data were supplied by the National Oceanography Centre, Liverpool.

and West Hoyle Bank dune fields, respectively, for all available radar mat data covering March 2006 to January 2007. The dark areas visible in the monthly mean images represent areas of increased radar backscatter, with the regular patterns corresponding to the position of persistently breaking waves. Stationary dark spots, particularly evident at the southern boundary of the West Hoyle Bank monthly mean dune field images (Figures 7.3 & 7.5), signifies rock outcrops which are periodically covered and uncovered by the movement of sediment over the sand flats. The wave breaker patterns can be seen to be very regular in shape, more so on the West Kirby Sands dune field, but still evident over the West Hoyle Bank dune field. This represents the positions of multiple dune crests in both dune fields which can be seen to migrate by eye over monthly time scales. It is the movement of these radar backscatter patterns that is interrogated in this chapter to determine the direction and magnitude of large scale bed form movement in the mouth of the Dee Estuary. The pattern of time averaged radar intensity, shown here to represent the location of large scale bed forms at West Kirby Sands and West Hoyle Bank, is predominantly due to the surface roughness generated by breaking waves.
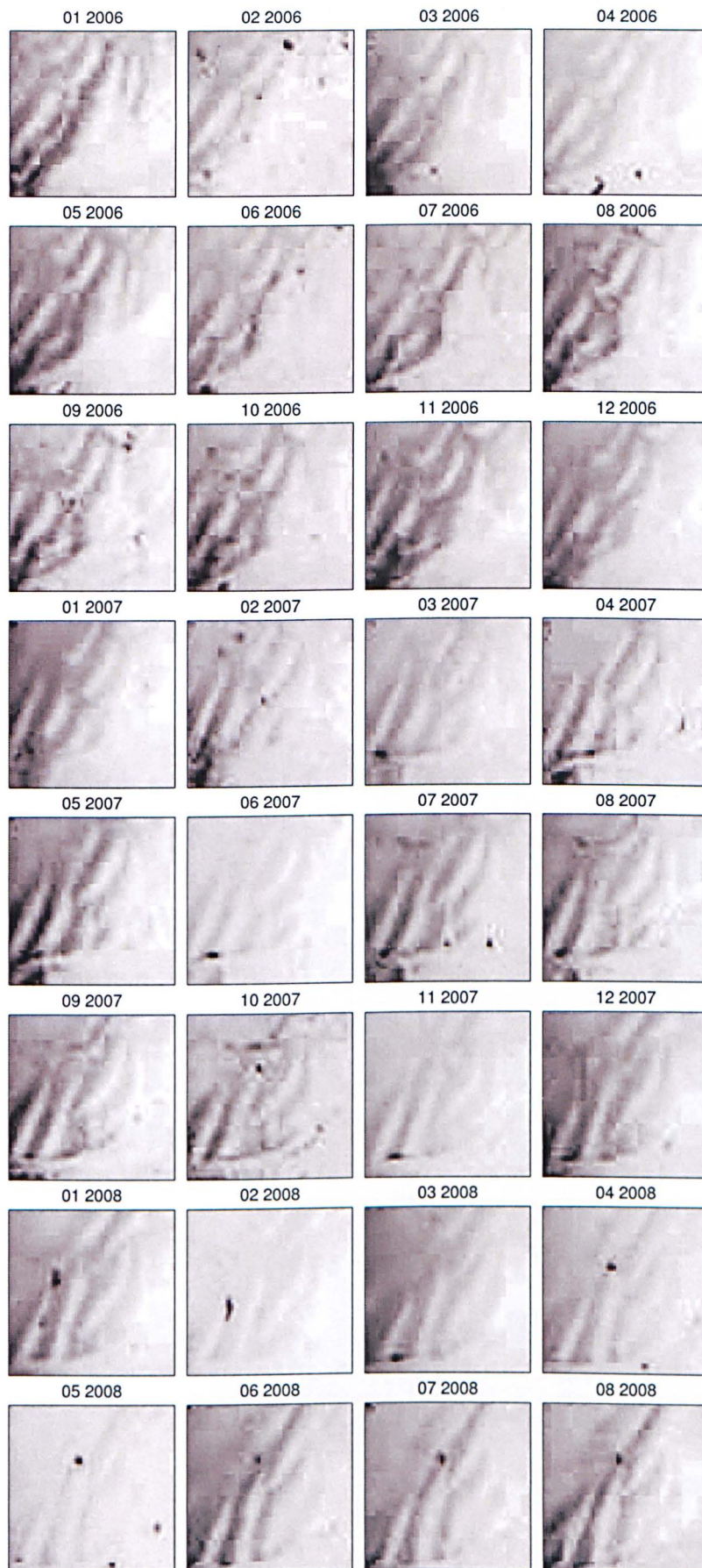
Figure 7.2: Monthly mean backscatter radar images focused on the dune field of West Kirby Sands for all available jpg data from 2006 to 2008. The direction of the current is in a north south direction, while waves approach the Dee Estuary from the north west.
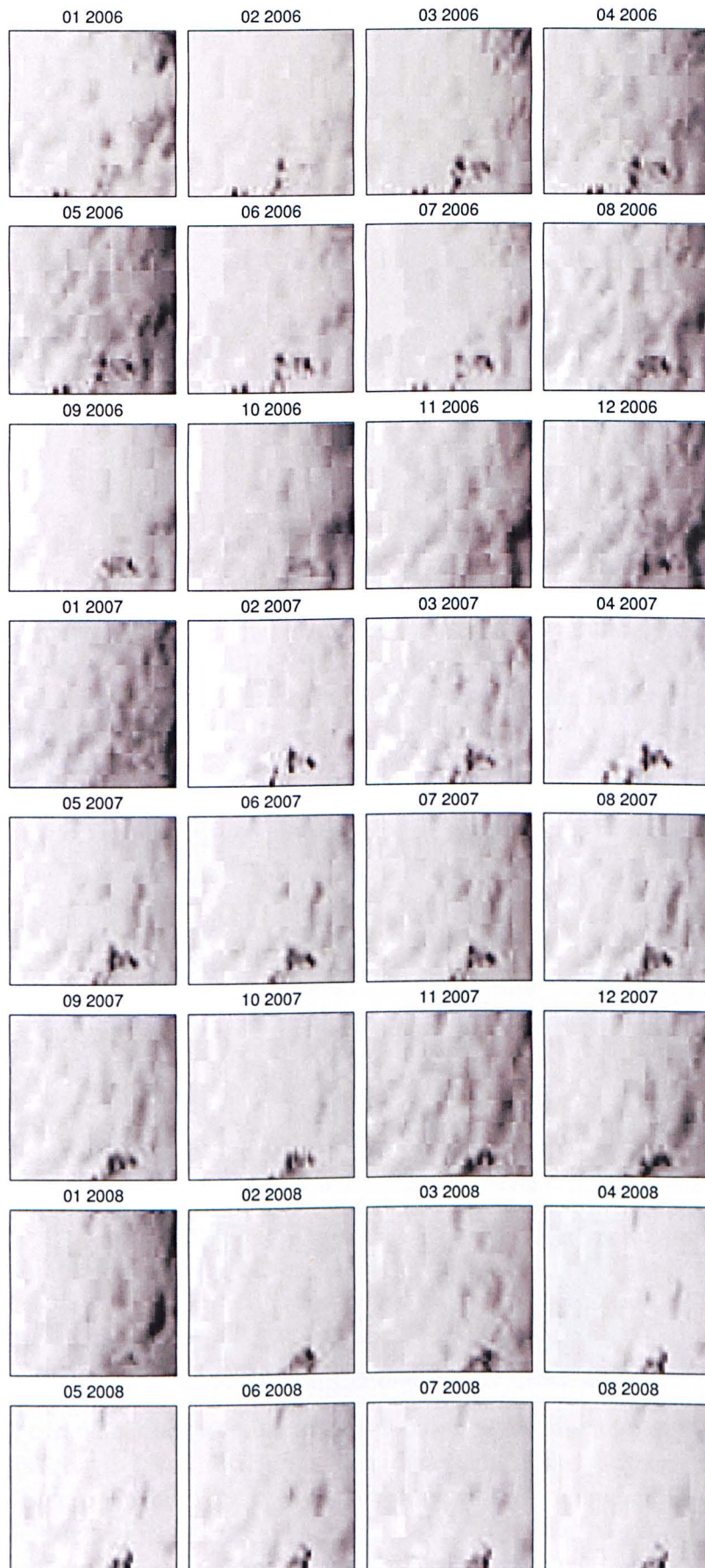
Figure 7.3: Process is the same as for Figure 7.2 but generated over West Hoyle Bank. Persistent dark spots at the southern boundary of the dune field represent rock outcrops which are periodically covered and uncovered, giving an indication of sediment transport in this region.

158
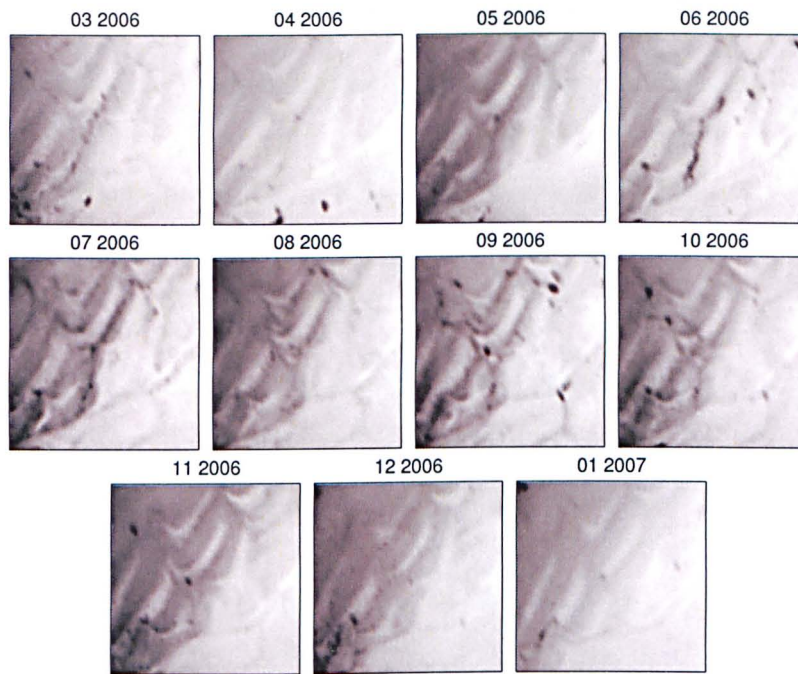
Figure 7.4: Monthly mean backscatter radar images focused on the dune field of West Kirby Sands for all available mat data from 2006 to 2007. The direction of the current is in a north south direction, while waves approach the Dee Estuary from the north west. Wave breaker crests appear oriented normal to the direction of wave approach.
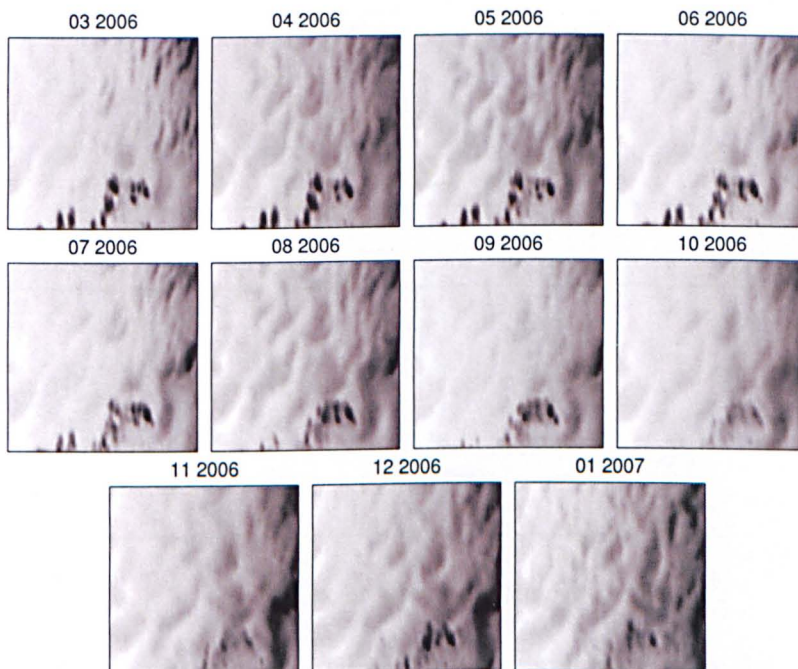
Figure 7.5: Monthly mean backscatter radar images focused on the dune field of West Hoyle Bank for all available mat data from 2006 to 2007. Persistent dark spots at the southern boundary of the dune field represent rock outcrops which are periodically covered and uncovered, giving an indication of sediment transport in this region.

Ruessink et al. (2002) assumed that the breaking wave radar backscatter signal varies as the energy of

the surface roller E_r, modelling the cross shore evolution of E_r using two coupled differential equations describing the time-averaged (covering multiple wave periods) wave and roller energy balances. For waves, incident on an alongshore uniform beach, which have a narrow frequency and direction band, the wave energy balance according to Battjes and Janssen (1978)

$$\frac{d}{dx}\left(\frac{1}{8}\rho g H_{rms}^2 C_g \cos\bar{\theta}\right) = -D_{br} \tag{7.1}$$

where x is the cross-shore coordinate, H_{rms} is the root mean square wave height, ρ is the water density, g is gravity, C_g is the group velocity, $\bar{\theta}$ is the mean wave angle and D_{br} is the breaking wave dissipation. Strive and De Vriend (1994) stated the energy balance for rollers to be

$$\frac{d}{dx}(2E_r c \cos\bar{\theta}) = -\frac{2gE_r \sin\beta_w}{c} + D_{br} \tag{7.2}$$

where c is the phase speed and β_w is the wave-front slope, usually set to 0.1 or less (Walstra et al., 1996). Snell's law is used to calculate $\bar{\theta}$ from offshore measurements and linear wave theory is applied to determine c_g and c.
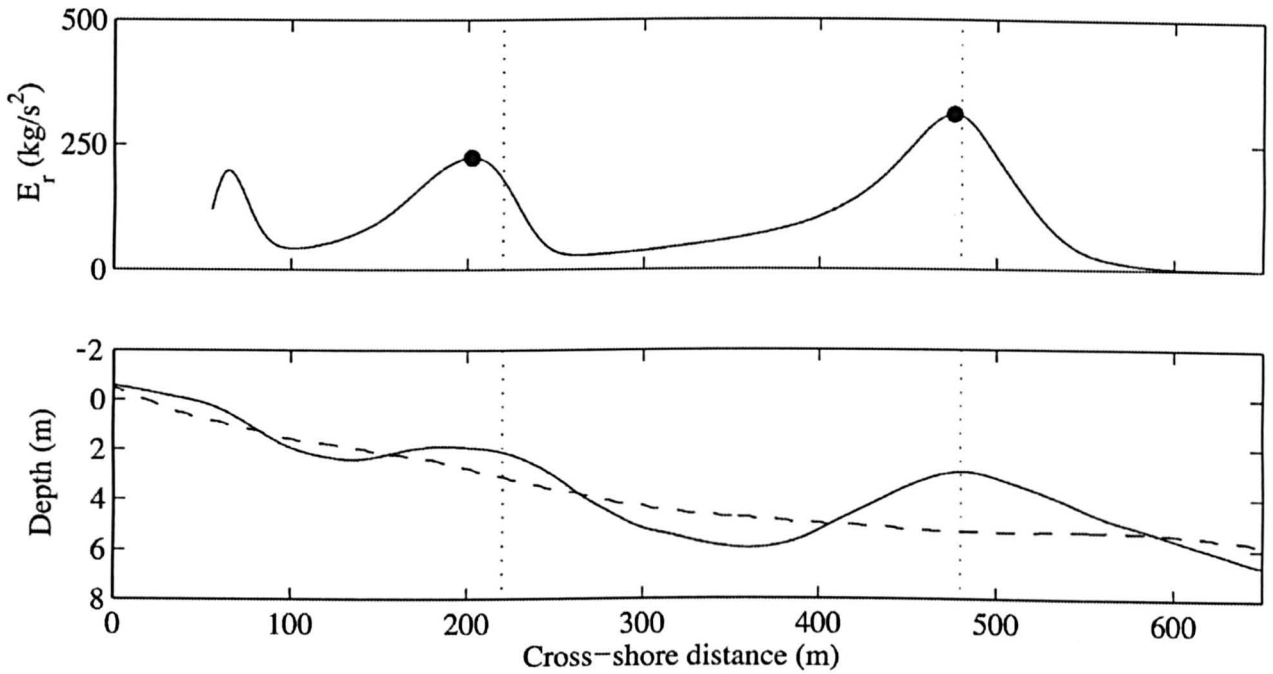
Figure 7.6: Roller energy E_r over a depth profile. The black dot markers in the upper panel show the locations of maximum roller energy. The vertical lines in both panels represents the bed form crest locations. The smoothed featureless dashed profile line is the decadal mean profile. From Ruessink et al. (2002).

Ruessink et al. (2002) assumed the location of maximum E_r to be coherent with the location of maximum radar return. Figure 7.6 shows this maxima to be displaced shoreward of the bed form

crest, with a difference between δE_r the bathymetry crest and peak in E_r being 18m for the inner crest and 4m at the outer. Van Enckevort and Ruessink (2001) found δE_r to depend on the root mean square wave height H_{rms}, water depth z and the morphology, with an increase in z causing E_r peaks to shift in an onshore direction while an increase in H_{rms} shifts peaks in E_r offshore. A smaller peak in E_r is also visible in Figure 7.6 towards the shoreline, at approximately 75m along the profile, a feature that is used in this research to determine beach profiles using a variation on the 'waterline method' and is discussed further later in this chapter.

7.2 Tidal influence on radar backscatter

Tidal variation must be affecting the location of the wave breaker backscatter signal over West Kirby Sands and West Hoyle Bank. For example, it was found that the radar backscatter signal from the breaker patterns deteriorated depending on the state of the tide. Figure 7.7 shows how at times of spring tide high water (11:00 08/10/2006 MWL=9.79m) wave breaker patterns are less visible than at times of lower tidal height (09:00 08/10/2006 MWL=6.92m).
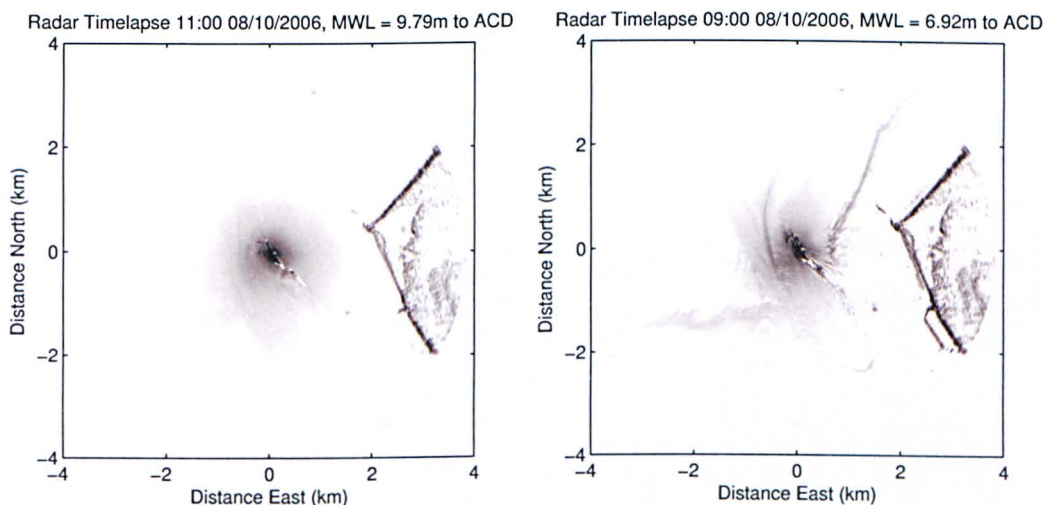
Figure 7.7: Hourly mean radar images showing how wave breaker signals are less visible at times of spring tide high water (left panel), whereas wave breaker patterns can be seen at West Kirby Sands and West Hoyle Bank during times of lower tidal height (right panel).

To investigate the tidal effect on wave breaker patterns, monthly mean radar images were created from hourly mean radar images limited to specific tidal heights. This was achieved by finding the times of appropriate tidal heights over the specific averaging time period from the Hilbre Island tide gauge data. These time stamps were then used to select corresponding hourly mean radar images to generate the monthly mean image. Pre-analysis of these tide selected monthly mean images revealed

that limiting the data to times where water levels were less than or equal to 8m increased image quality over West Kirby Sands, whereas West Hoyle Bank image quality was increased between tidal heights of 2 to 4m. This is likely due to the greater water depth at West Hoyle Bank which has a mean depth of 5.86m, whereas West Kirby Sands has a mean water depth of 4.72m. Therefore waves will break more consistently over large scale bed forms at West Kirby Sands at higher water levels, while West Hoyle Bank will experience a similar process at lower water levels. Figure 7.8 shows monthly mean radar images at West Kirby Sands and West Hoyle Bank for November 2006 created with all available radar data and also with radar data limited to less than or equal to 8m at West Kirby Sands and between 2 to 4m at West Hoyle Bank.
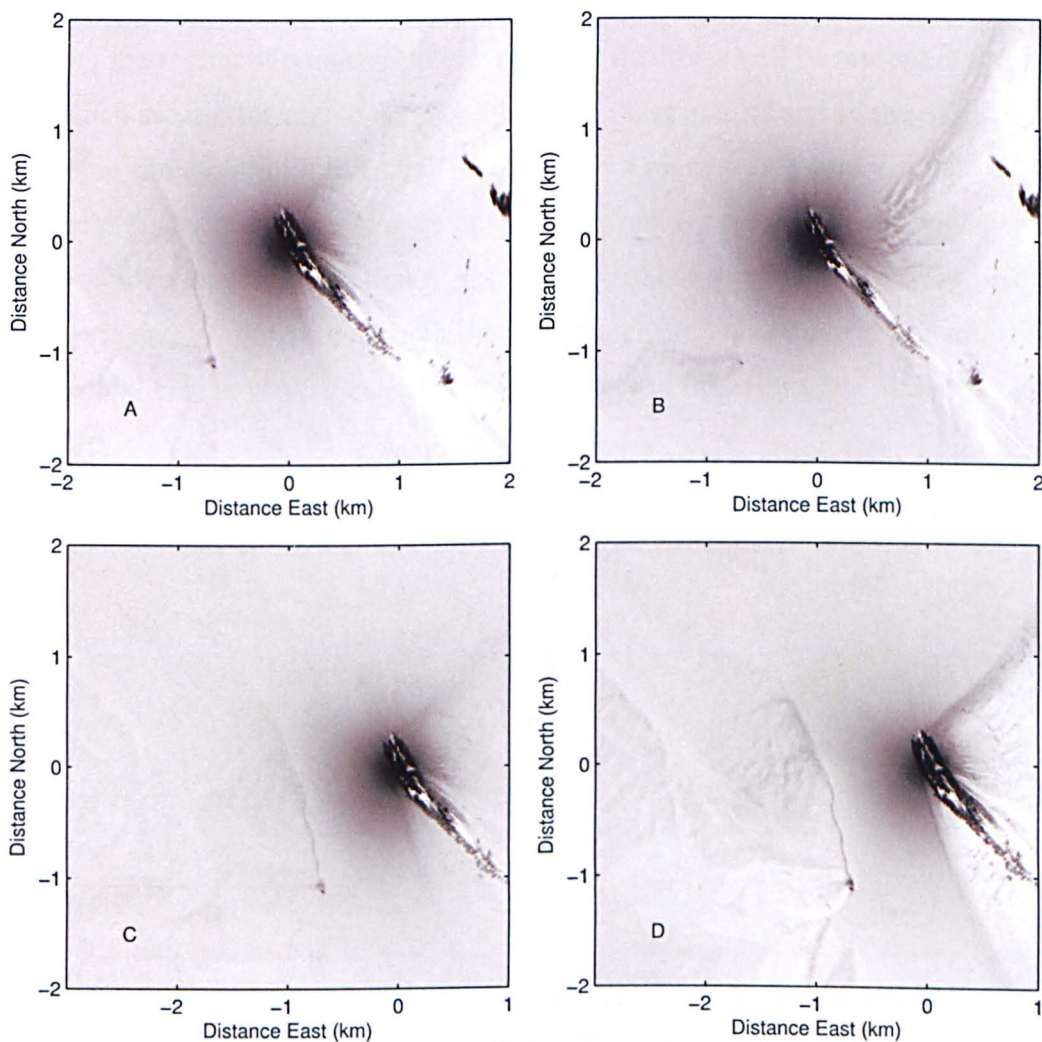
Figure 7.8: A comparison of monthly mean radar images for November 2006 created with all available radar data at West Kirby Sands (A) and West Hoyle Bank (C) with November 2006 monthly mean images created from radar data at selected tidal heights for identical locations (B & D).

While Figure 7.8 shows an increase in definition of wave breaker patterns for the November 2006 tide selected monthly mean image, similar effects were not reproduced for all monthly mean radar

images. Figure 7.9 shows April 2006 monthly mean images created with all available radar data and tide limited radar data. The wave breaker signal at West Kirby Sands for the tide limited monthly mean image (Figure 7.9 B) can be seen to be significantly different to the wave breaker signal from the monthly mean image using all available radar data (Figure 7.9 A). The disparity of the wave breaker signal in this tide limited monthly mean image to other tide limited wave breaker signals was seen as inappropriate for future correlation analysis between monthly mean radar images. Therefore all monthly mean radar images were created with all available radar data. There will be a discrepancy in the location of the wave breaker patterns, which are used as a proxy for the location of large scale bed forms, caused by the tidal variation. If the position of the bed form were to remain constant then a tidal bias would show erroneous movement due to the changing depth over the bed form and therefore moving the region of persistent breaking. This tidal bias will be present in the hourly mean radar images which are used to create the monthly mean radar images and so the position of the wave breaker patterns in the monthly mean images represents a mean tidal position. This tidal bias is an inherent weakness in any remote sensing technique that detects breaking waves, whether it is a radar or video based technique, as the location of the wave breaking over the underlying bed form varies with the tidal cycle and is a function of both the wave height and water depth. Ruessink et al. (2002) suggest that the tidal bias in wave breaker location is likely to fall within the measuring resolution of the X-band radar.
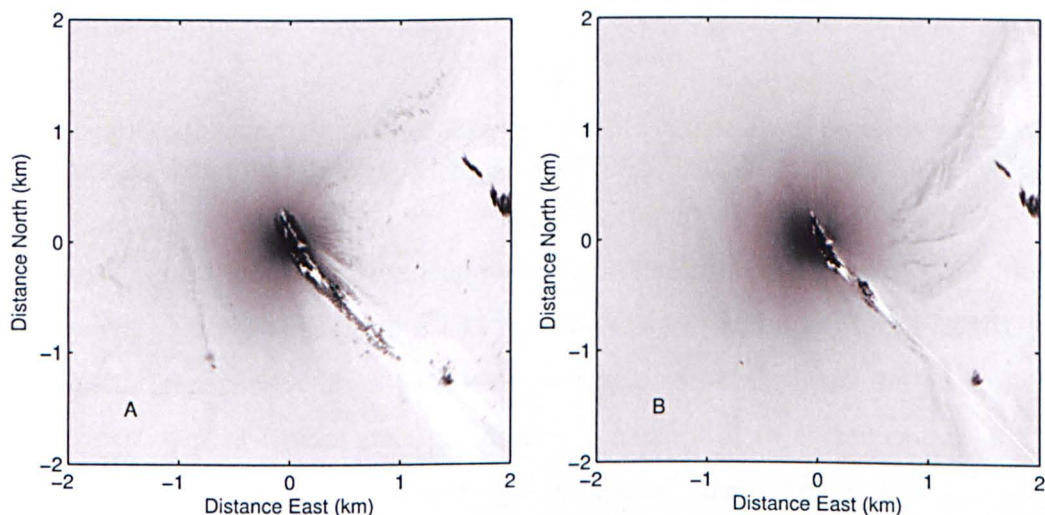
Figure 7.9: Monthly mean radar images for April 2006 created using all available radar data (A) and radar data limited to times where water level at Hilbre Island tide gauge (located at the centre of the image) is less than or equal to 8m (B). The wave breaker pattern shown in the tide limited monthly mean image (B) was seen to be inappropriate for analysis between other monthly mean images.

7.3 Radar backscatter intensity profiles

In order to analyse the wave breaker patterns at West Kirby Sands and West Hoyle Bank in greater detail profiles of radar backscatter intensity at these locations were extracted (Figure 7.10). Profile lines were selected to give the clearest distinction between peaks and troughs in the radar backscatter. This allowed a comparison of radar backscatter and the underlying bathymetry to be made and should also show any shift in intensity peaks over the time period covered by the monthly mean radar images.
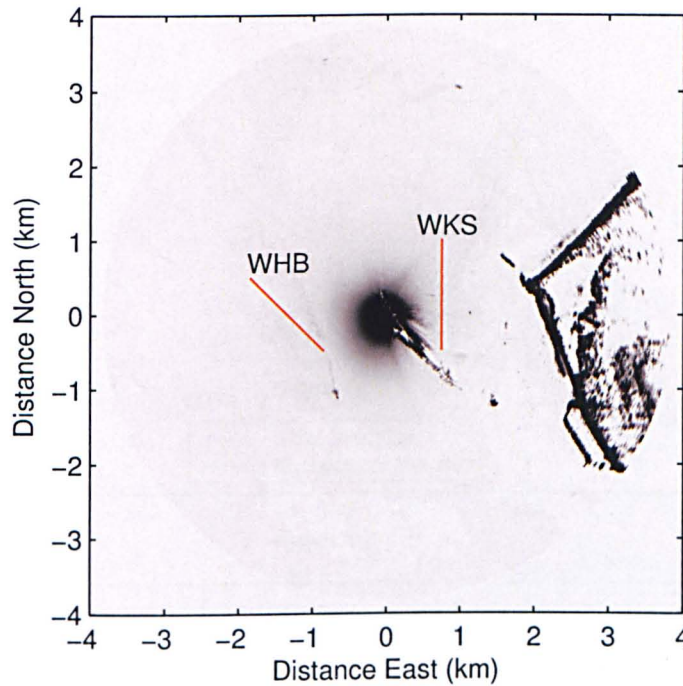
Figure 7.10: Location of radar backscatter intensity profiles taken from monthly mean radar images for jpg and mat radar data through West Kirby Sands (WKS) and West Hoyle Bank (WHB).

Figure 7.11 shows a profile of monthly mean radar backscatter intensity for all available jpg data in October 2006 at West Kirby Sands (Figure 7.11 A) and West Hoyle Bank (Figure 7.11 B) plotted with the same profiles through the October 2006 Lidar survey data. This shows the peaks in backscatter return, which are shown as darker areas in Figures 7.2 and 7.3, to correspond to the location of underlying bed forms. Monthly mean radar images processed from jpg radar data have pixel intensity values which scale from 0 to 255. In these monthly mean jpg radar images values of 0 correspond to dark areas which represent high radar return while the lighter areas, representing less radar return, scale towards 255. Therefore the radar backscatter intensity plot was inverted in the y-axis so that peaks in the radar backscatter return could be correlated with dune crests in the Lidar profile. Figure 7.11 A shows a pronounced dune field over West Kirby Sands with the peaks in radar backscatter occurring just seaward of the dune crest. The profile through West Hoyle Bank (Figure 7.11 B) shows

a shoaling bathymetry with a less pronounced dune field, however two radar backscatter peaks can be seen to occur close to the crests of two dune features. Radar backscatter peaks are offset sea ward of the underlying bed form crests, an occurrence associated with larger wave heights (Ruessink et al., 2002). The time period of these radar backscatter profiles (October 2006) is characterised by periods of increased wave activity, with the Triaxys wave buoy in the mouth of the estuary recording a monthly mean wave height of 0.6m and maximum wave height of 2.7m.
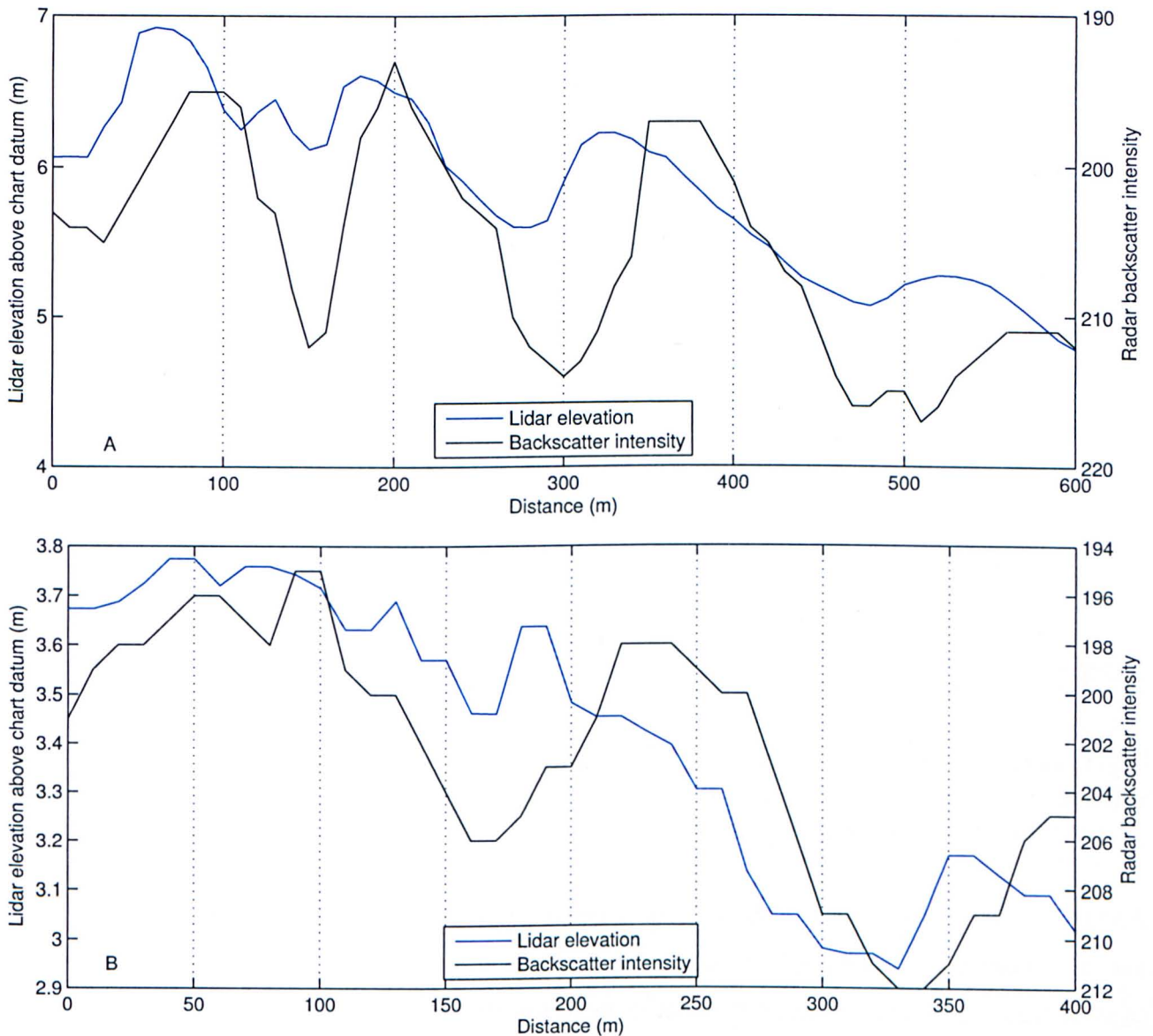
Figure 7.11: Monthly mean backscatter profiles for October 2006 at A) West Kirby Sands and B) West Hoyle Bank from all available jpg data overlain on the same profile taken from Lidar data. The open sea, to the north, is to the right of the Figure and the sand flats, to the south, are to the left.
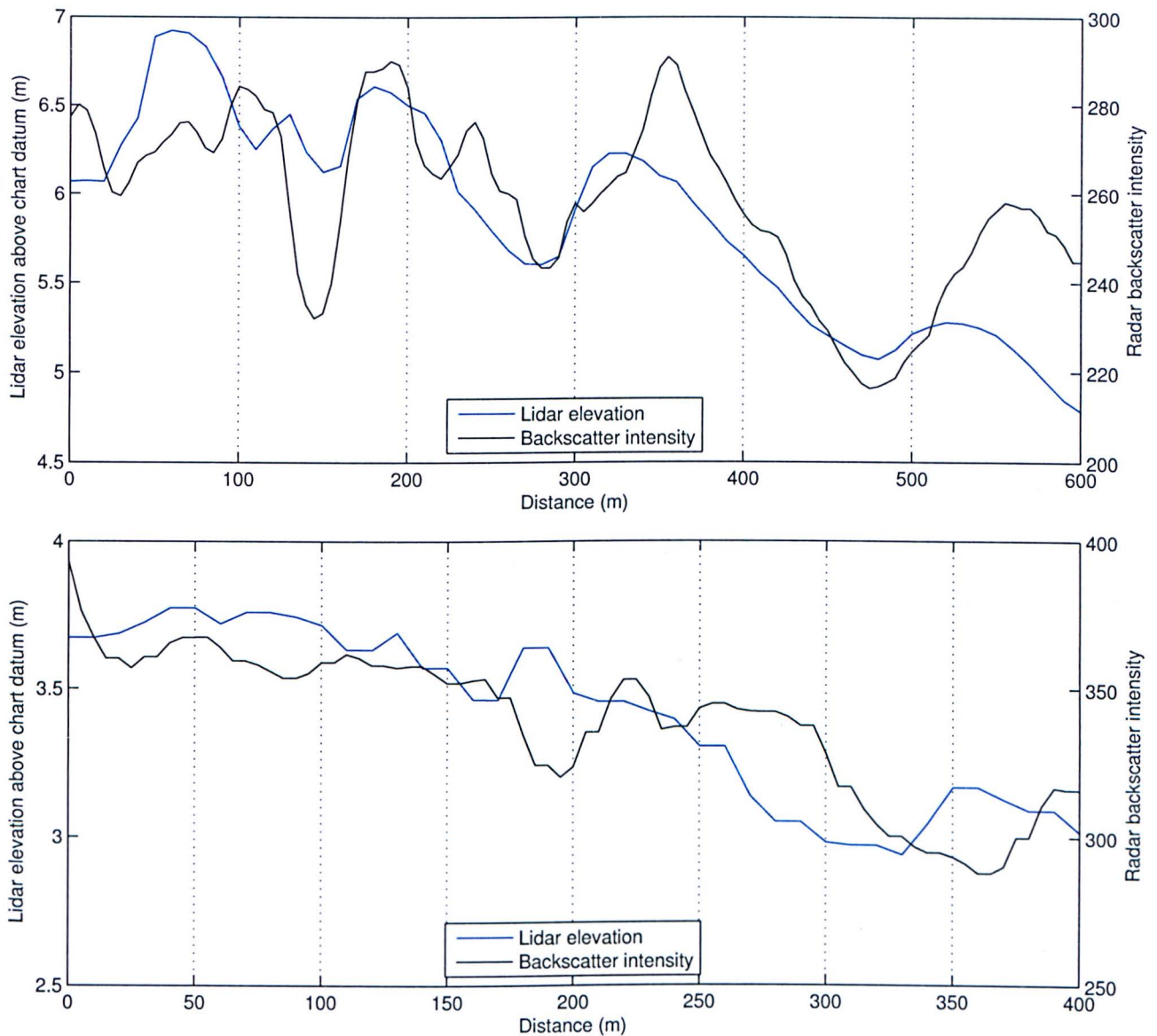
Figure 7.12: Monthly mean backscatter profiles for October 2006 at A) West Kirby Sands and B) West Hoyle Bank from all available mat data overlain on the same profile taken from Lidar data. The open sea, to the north, is to the right of the Figure and the sand flats, to the south, are to the left.

Figure 7.12 shows radar backscatter profiles extracted through West Kirby Sands and West Hoyle Bank for all available mat radar data with the Lidar survey data profiles overlain. The radar mat files, not originating from jpg images, have a different range of intensity values where 0 represents no radar return with values scaling to 1445 for maximum radar return. This means that the backscatter intensity profiles from the radar mat data are not inverted in the y-axis, as with the jpg profiles. Figure 7.12 A shows that peaks in the backscatter intensity profile correspond to a point just seaward of the dune crests in the Lidar profile, similar to what is shown by the jpg backscatter intensity profile. Figure 7.12 also shows the peaks in the radar backscatter intensity to occur just seaward of the dune crests on West Hoyle Bank, which are related to similar backscatter peak locations seen in the jpg radar data

(Figure 7.11).

Quarterly radar backscatter profiles were created for all available jpg and mat data at West Kirby Sands and West Hoyle Bank (Figures 7.13 - 7.20). The right of the plot is the seaward end of the profile and the left of the plot is towards the sand flats. These profiles show clear peaks in backscatter intensity which should represent the approximate location of dune crests according to the previous comparison of backscatter intensity and Lidar survey profiles (Figures 7.11 & 7.12). It is possible to see that the peaks in the backscatter intensity are migrating along the profiles from left to right, indicating that there is an onshore migration of sand dunes on the intertidal beaches of West Kirby Sands and West Hoyle Bank. There appears to be a seasonal variation in the migration of the backscatter intensity peaks, with less movement occurring in the summer but greater shifts in the position of peaks in the winter months. For the jpg quarterly profiles, the months of April - June and July - September show less migration than January - March and October - December. Whereas, in the mat quarterly profiles the months of March - May and June - August show less migration than September - November and December - January. The migration in the peaks of backscatter intensity indicate that the wave breaker patterns visible in the monthly mean radar images are moving into the estuary. However, the migration rates calculated along the backscatter profiles might not represent the true resultant migration rate if the profile orientation does not match the propagation direction. To determine the magnitude and direction of the wave breaker pattern migration, and therefore the migration of the underlying dune fields, a 2-D spatial cross correlation algorithm was applied to all available monthly mean radar images. This is discussed further in the following section.
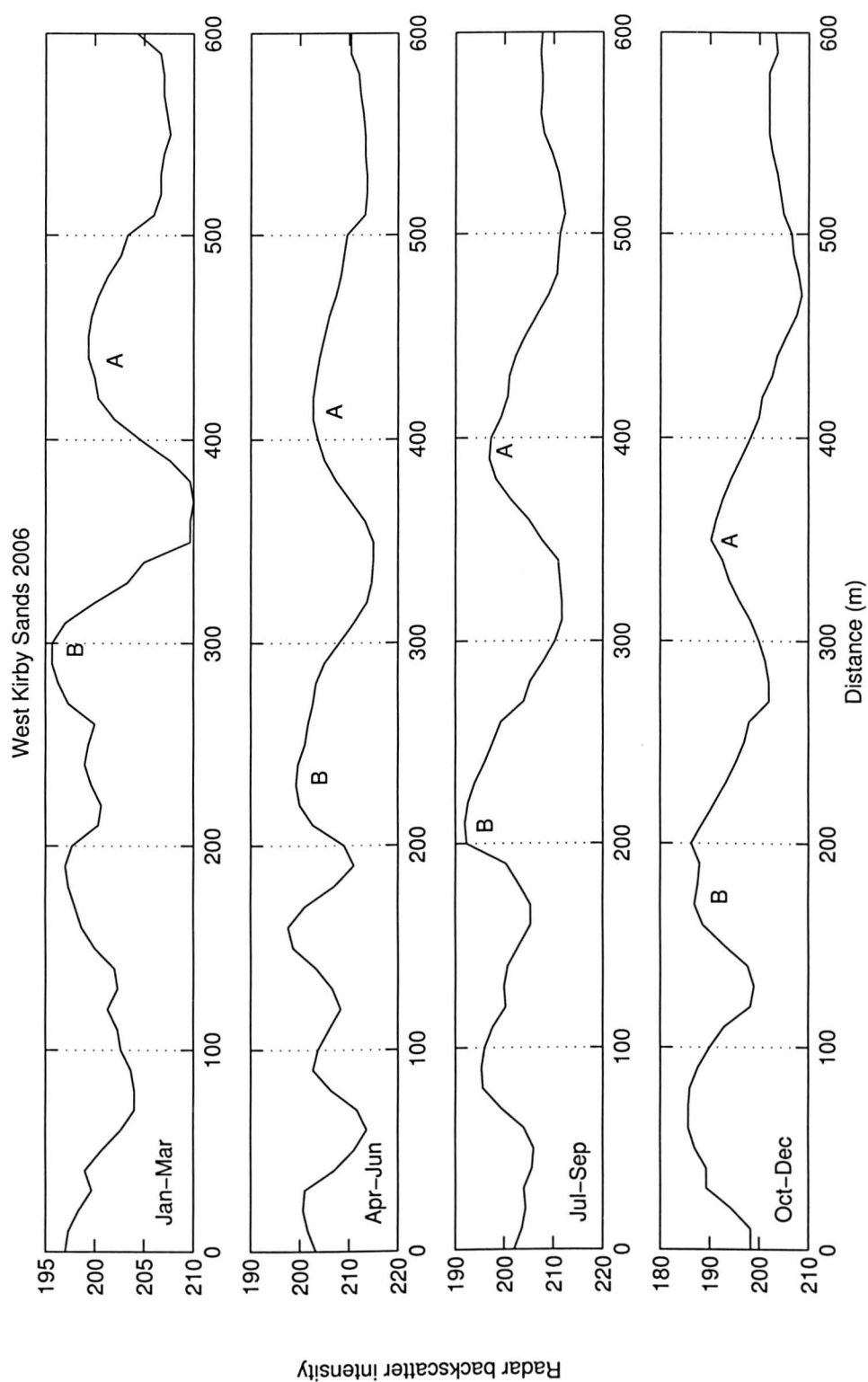
Figure 7.13: Radar backscatter intensity profiles taken through West Kirby Sands for all available jpg data for 2006.The open sea is to the right of the Figure and the sand flats to the left. The y-axis is inverted for clarity.
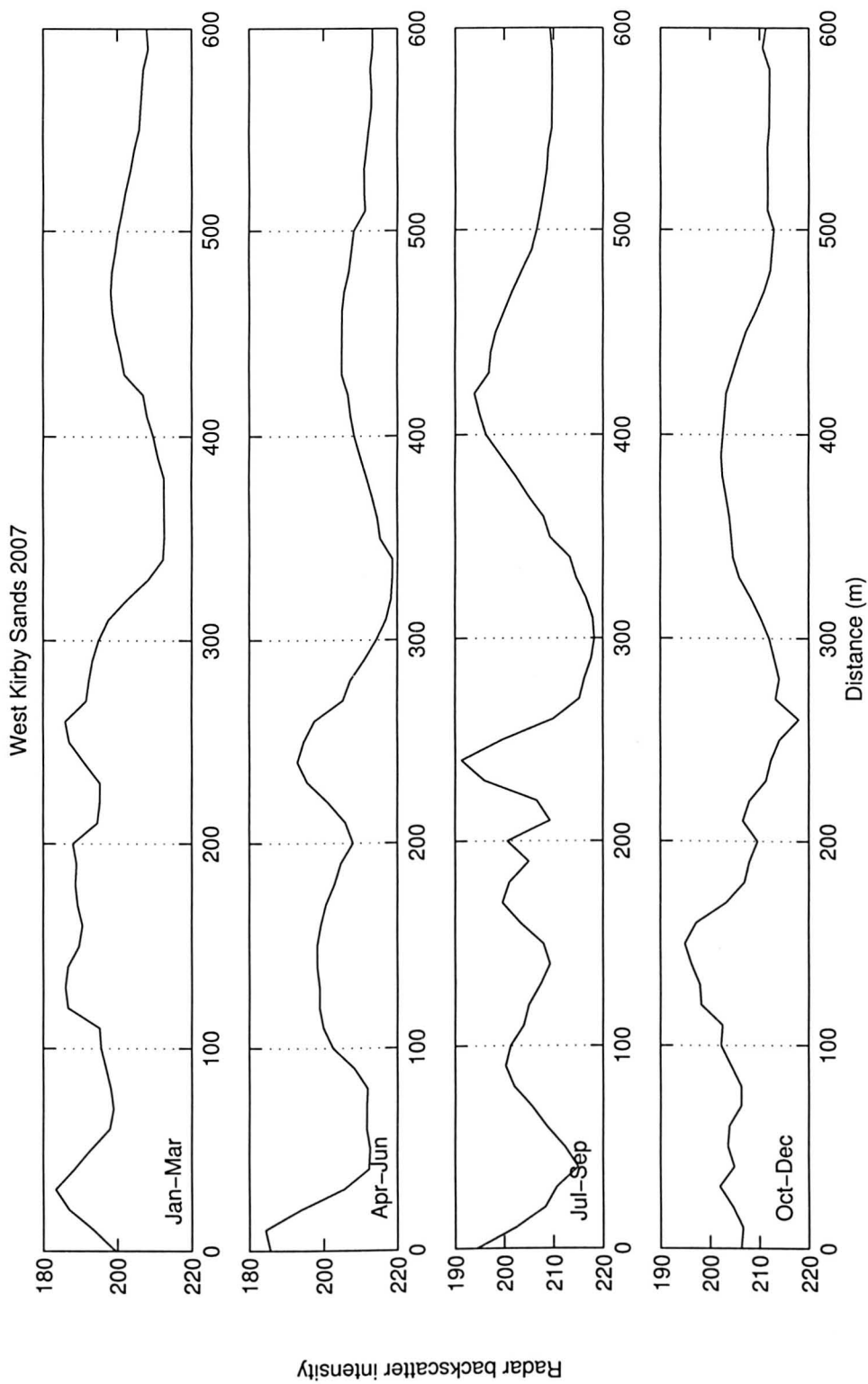
Figure 7.14: Radar backscatter intensity profiles taken through West Kirby Sands for all available jpg data for 2007.The open sea is to the right of the Figure and the sand flats to the left. The y-axis is inverted for clarity.
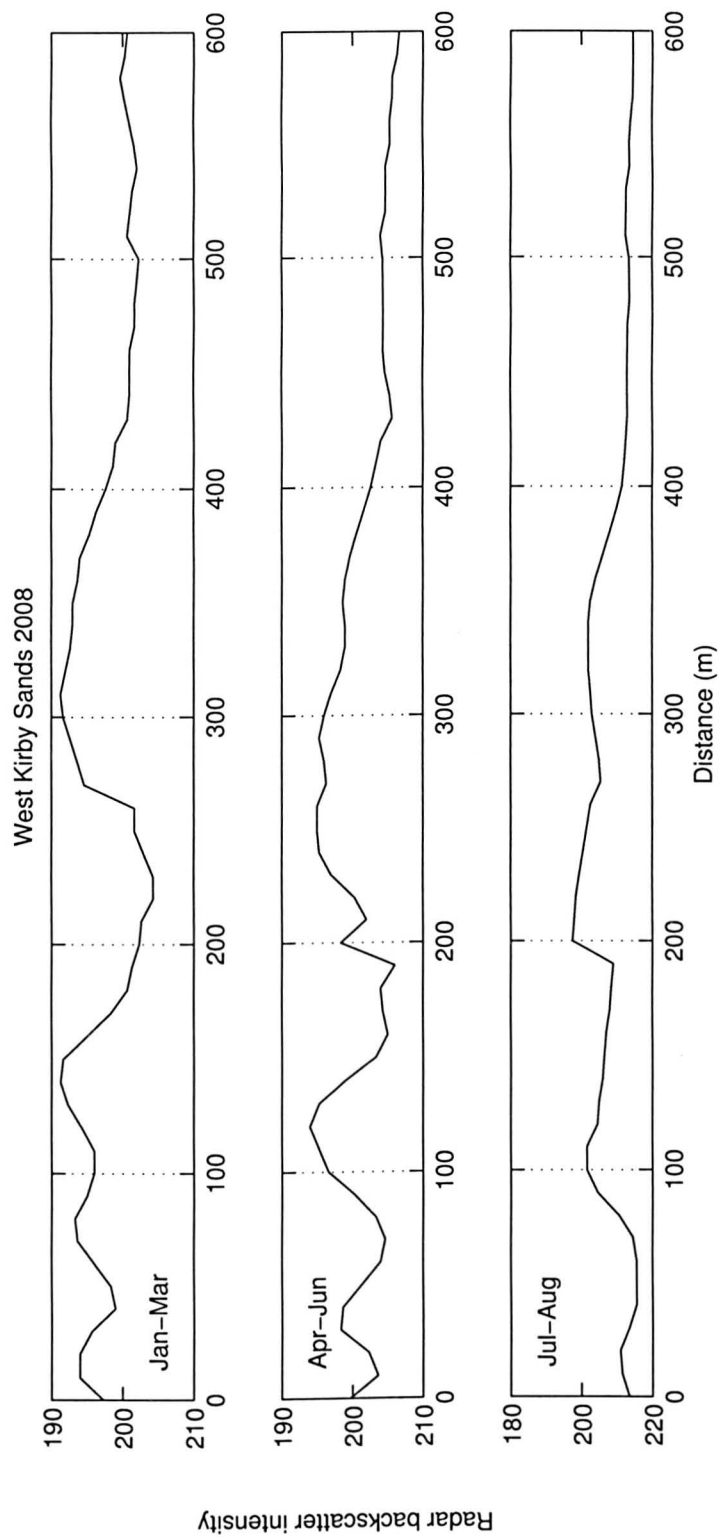
Figure 7.15: Radar backscatter intensity profiles taken through West Kirby Sands for all available jpg data for 2008.The open sea is to the right of the Figure and the sand flats to the left. The y-axis is inverted for clarity.
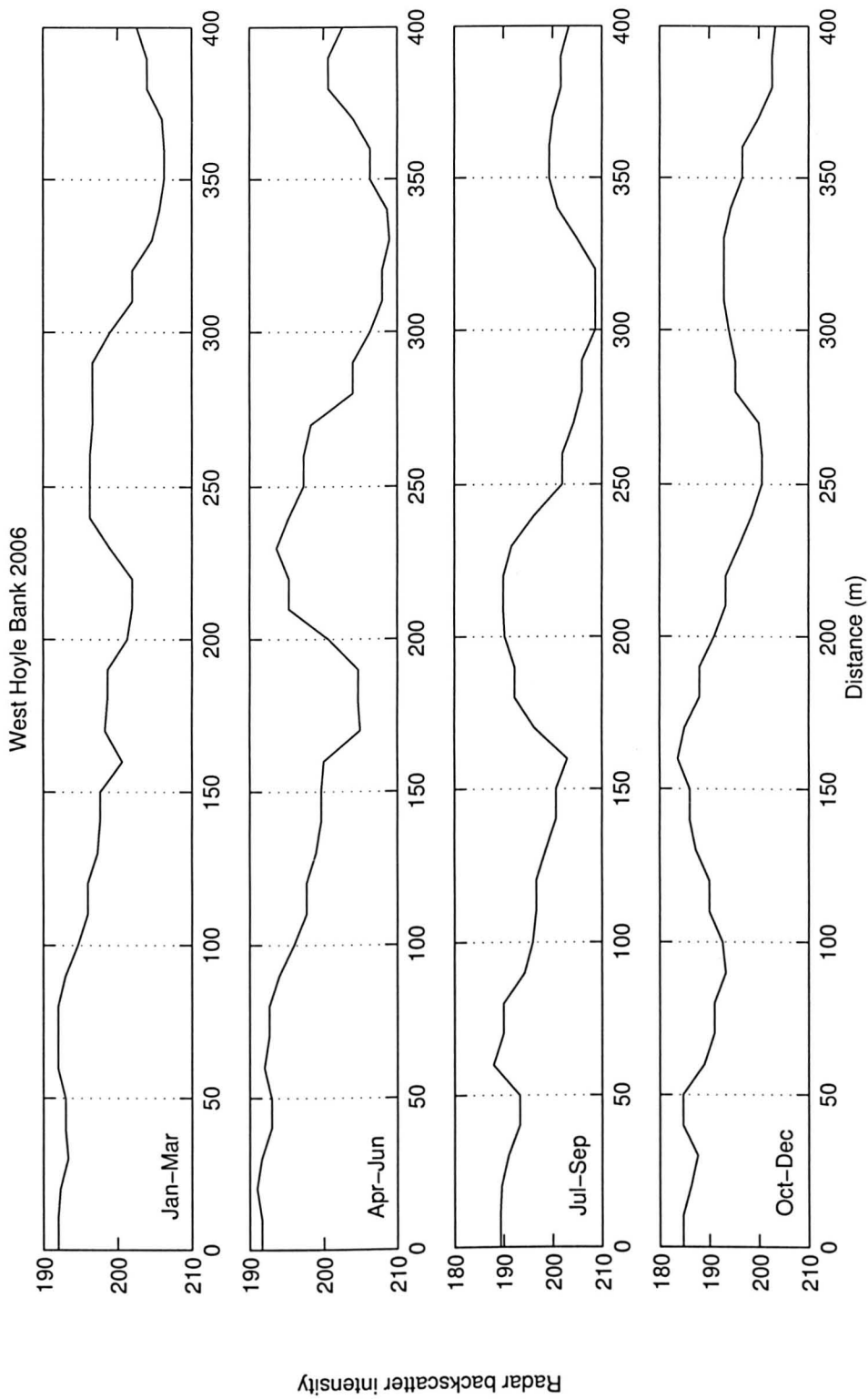
Figure 7.16: Radar backscatter intensity profiles taken through West Hoyle Bank for all available jpg data for 2006.The open sea is to the right of the Figure and the sand flats to the left. The *y*-axis is inverted for clarity.
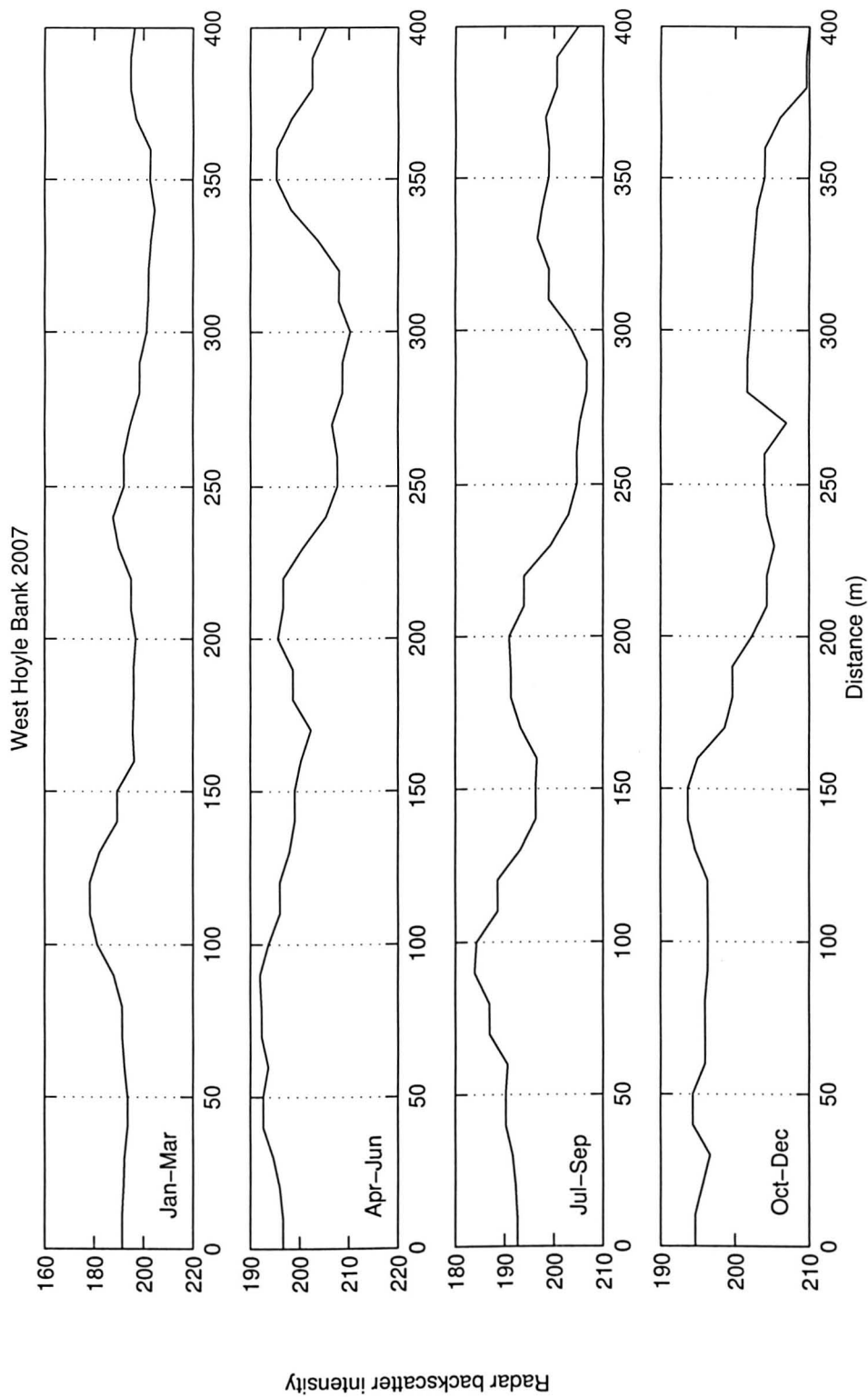
Figure 7.17: Radar backscatter intensity profiles taken through West Hoyle Bank for all available jpg data for 2007.The open sea is to the right of the Figure and the sand flats to the left. The y-axis is inverted for clarity.
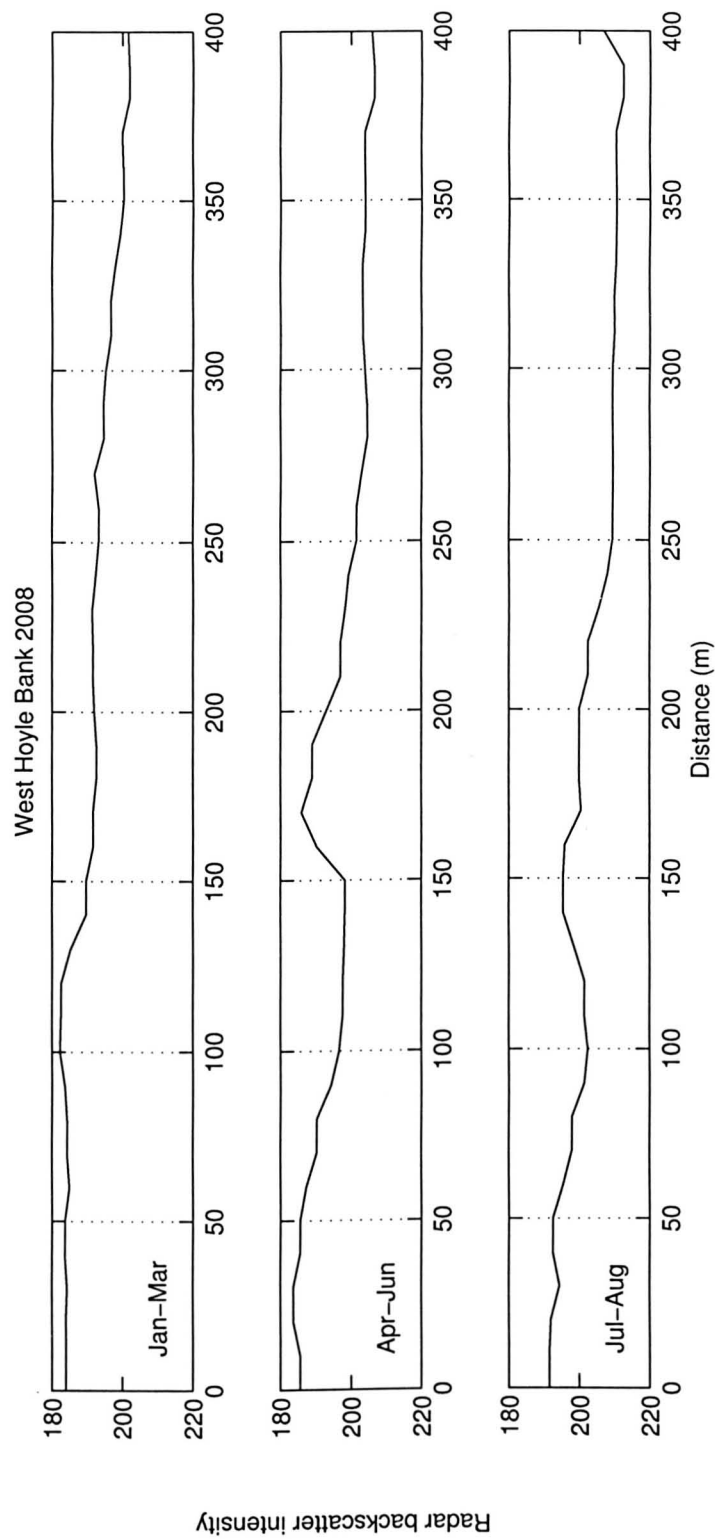
Figure 7.18: Radar backscatter intensity profiles taken through West Hoyle Bank for all available jpg data for 2008.The open sea is to the right of the Figure and the sand flats to the left. The *y*-axis is inverted for clarity.
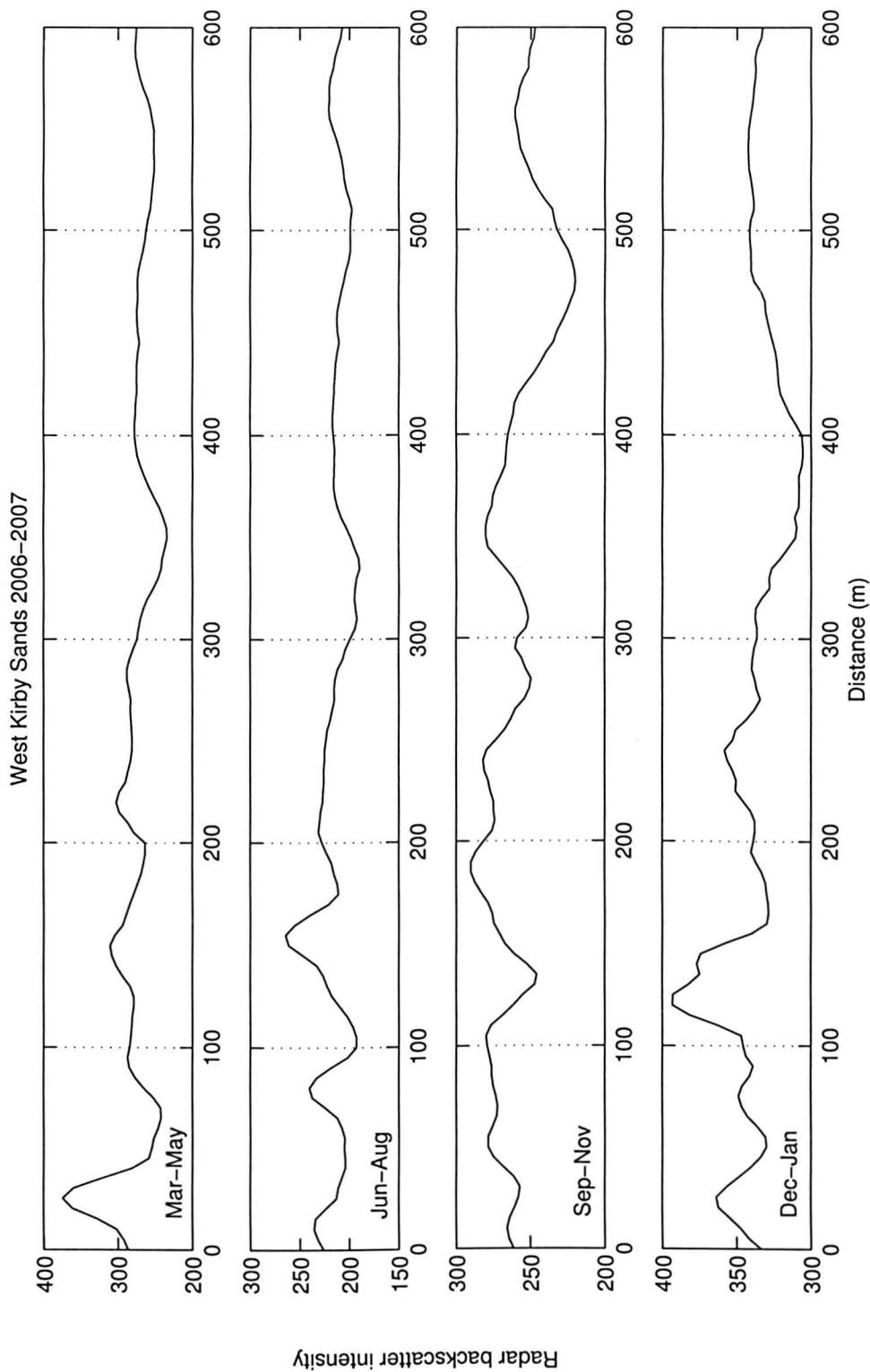
Figure 7.19: Radar backscatter intensity profiles taken through West Kirby Sands for all available mat data.The open sea is to the right of the Figure and the sand flats to the left.
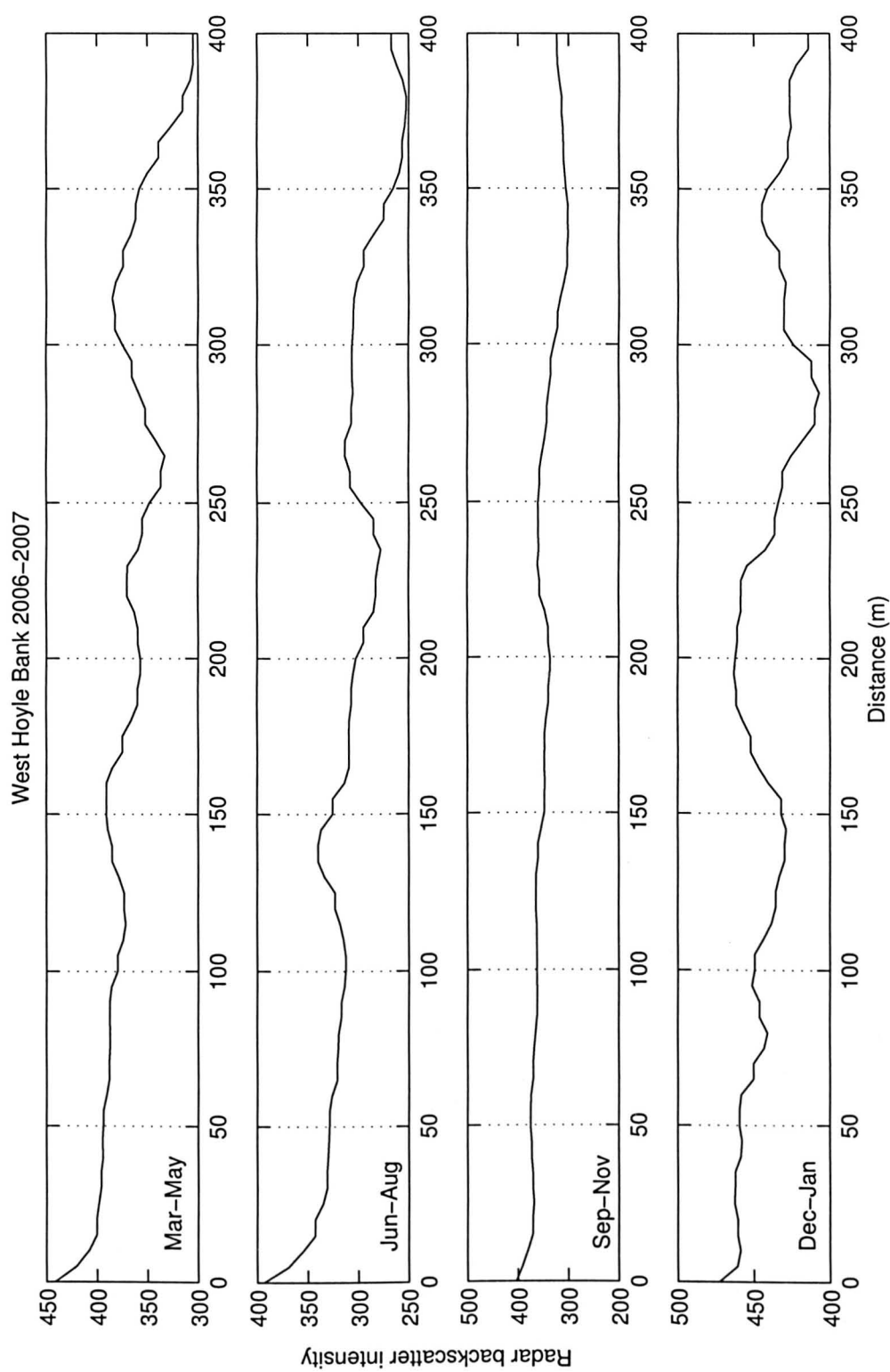
Figure 7.20: Radar backscatter intensity profiles taken through West Hoyle Bank for all available mat data. The open sea is to the right of the Figure and the sand flats to the left.

7.4   Migration of wave breaker patterns

A 2-D spatial cross correlation algorithm was applied to successive monthly mean radar images throughout 2006, 2007 and all available 2008 data for jpg radar data and for all available 2006 and 2007 mat radar data. The wave breaker patterns over West Kirby Sands and West Hoyle Bank (Figures 7.2 - 7.5) can be seen to migrate by eye over the time period covered by the monthly mean radar images (Figures 7.13 - 7.20). Pre-analysis of successive monthly mean radar images by eye shows that maximum migration of wave breaker patterns occurred on the scale of approximately one to two pixels a month, where one pixel corresponds to 10m for the jpg radar data and 5m for the mat radar data. Applying the 2-D cross correlation motion tracking algorithm, detailed in Section 6.8, allows the magnitude and direction of wave breaker pattern migration to be determined down to sub pixel accuracy. The migration rates from the 2-D spatial cross correlation algorithm for all available jpg and mat data at West Kirby Sands and West Hoyle Bank (Figure 7.21) shows a similar seasonal signal to the migration as seen in the quarterly radar backscatter intensity profiles (Figure 7.13 - 7.20), with winter months experiencing increased migration compared with summer months.
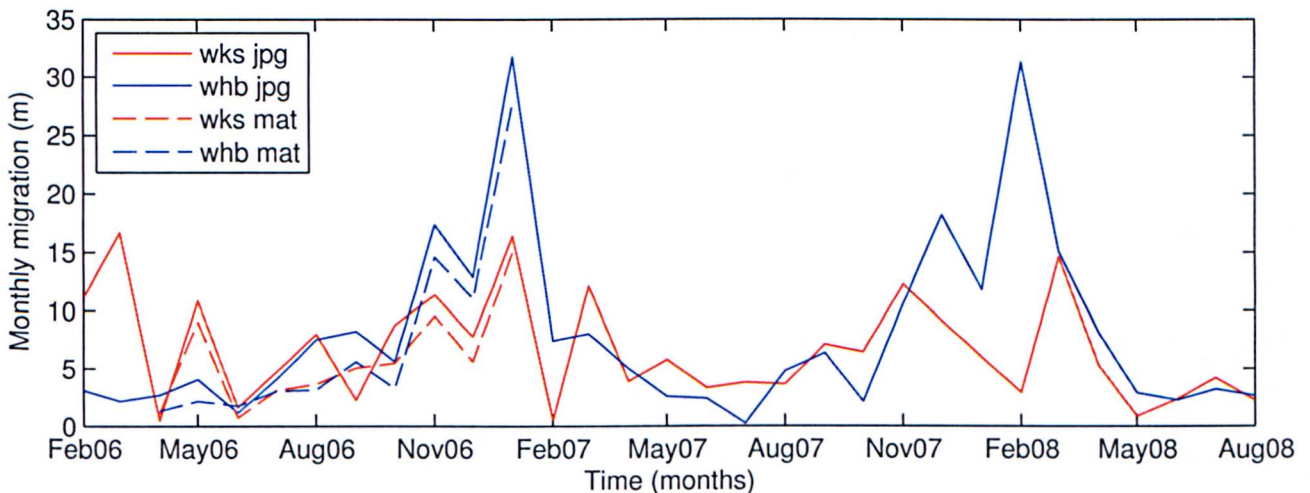
Figure 7.21: Time series of monthly migrations from the cross correlation motion tracking algorithm at West Kirby Sands and West Hoyle Bank for jpg and mat data formats.

The migration determined from the 2-D motion tracking algorithm represents a migration of similar backscatter intensity features seen in the radar backscatter intensity profiles (Figures 7.13 - 7.20) but over a larger spatial domain and at a higher temporal resolution, of monthly time intervals rather than quarterly time periods. The migration rates from the jpg and mat data correspond reasonably well, with the jpg migrations being slightly greater than mat migrations at West Kirby Sands and West Hoyle Bank. West Kirby Sands experiences large migration values at the beginning of 2006 which is not seen in the migration at West Hoyle Bank. However, for the remainder of the data period migration remains fairly similar during the summer months at West Kirby Sands and West Hoyle Bank. During the winter months, at times of much greater migration, West Hoyle Bank can be seen to experience much larger migrations than West Kirby Sands. This pattern can be seen to occur in both jpg and mat data for the winter of 2006/2007 and with the jpg data again during the winter of 2007/2008. Wave height, wave period and wave direction (Figure 7.22) data were obtained from the Liverpool Bay WaveNet Buoy, and averaged over weekly time periods, as well as tidal heights from the Hilbre Island tide gauge, covering the same time period as the radar data, to determine any possible forcing factors behind the variation in migration rates seen in Figure 7.21.

There are two significant peaks in migration, shown in both the jpg and mat radar data and at both locations, during October 2006 to February 2007. Another peak in migration occurs at West Kirby Sands and West Hoyle Bank approximately a year later, from October 2007 to March 2008, however these dates are only covered by the jpg radar data. This variation in migration rates appears to be similar to the change in wave heights and wave period (Figure 7.22) seen in the Liverpool Bay WaveNet buoy data, while no obvious correlation can be seen with the wave direction or Hilbre Island tide gauge heights. This appears to indicate that an increase in migration rates is a direct response to the local sea state, with larger more powerful waves causing more migration of features. Migration rates can also be seen to vary between West Kirby Sands and West Hoyle Bank, with West Hoyle Bank experiencing significantly larger migration rates.
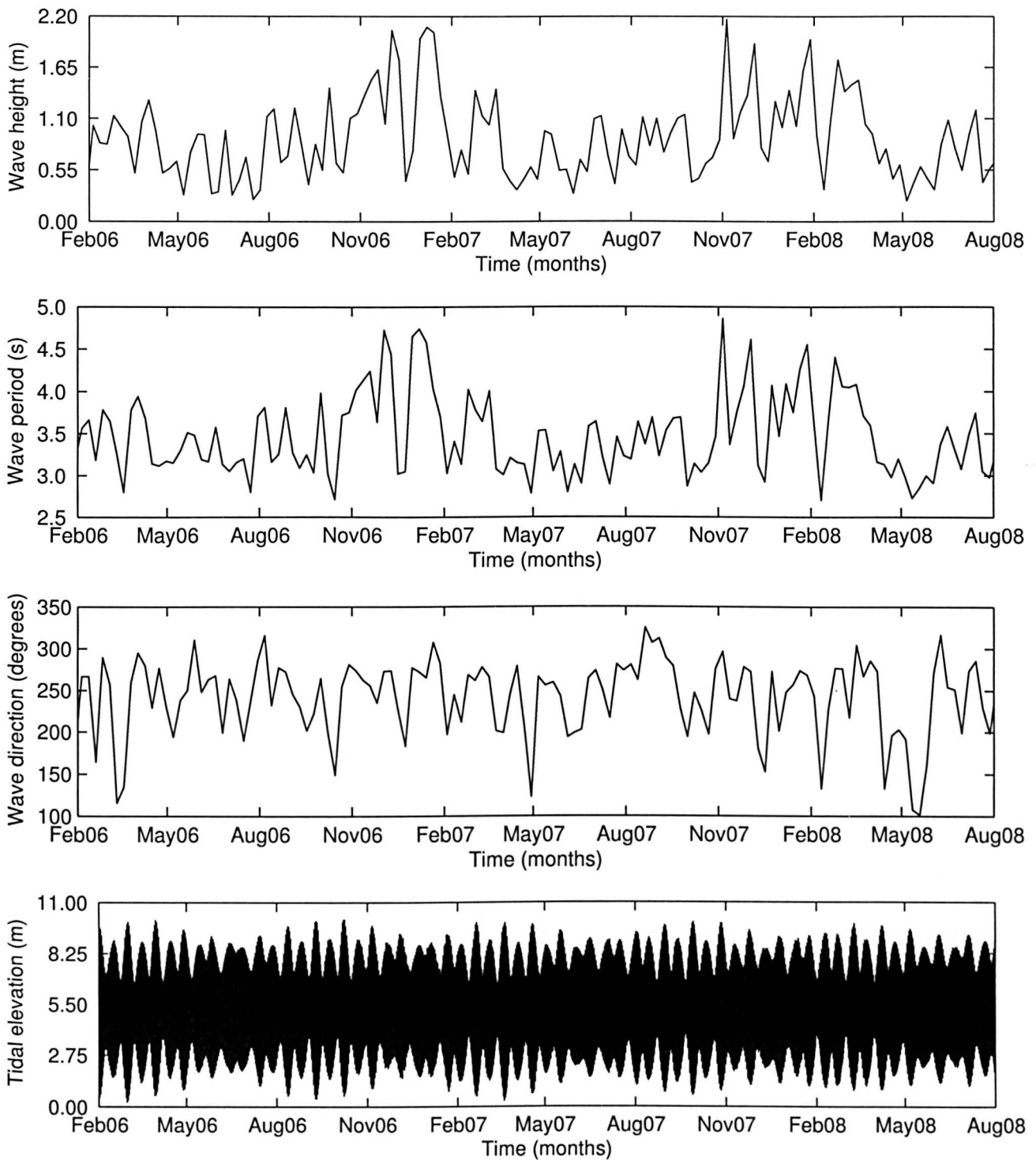
Figure 7.22: Time series of wave data from the Liverpool Bay WaveNet buoy and tidal elevations from the Hilbre Island tide gauge covering the motion tracking analysis period of January 2006 to August 2008.

Migration rates peak during January of the winter of 2007 with jpg radar data showing a monthly migration of 16m occurring at West Kirby Sands and 32m at West Hoyle Bank, while the mat radar data gave monthly migrations of 15m and 27m at West Kirby Sands and West Hoyle Bank respec-

tively. This increase of almost 50% could be caused by the increased exposure to wave heights in the center of the estuary, as the dominant wave direction is from 270 to 330 degrees (Figure 7.22), which is from a north west direction. Model simulations using TELEMAC also show wave heights to be larger around West Hoyle Bank with corresponding strong depth averaged velocities (Figure 5.5).

Monthly migration rates are plotted against monthly averaged significant wave heights to show the influence of larger wave heights causing increased migration rates of wave breaker patterns at both West Kirby Sands and West Hoyle Bank (Figure 7.23). The R^2 values for each migration plot are shown in (Figure 7.23). This shows a significant positive relationship between migration rate and wave height. The migration rates calculated from the mat data show larger R^2 values than those calculated from the jpg data. Monthly mean wave heights are created from a months worth of significant wave height data from the WaveNet buoy recorded every 30 minutes, monthly mean wave heights are plotted with standard error bars. A significant number of the migrations are less than one pixel per month, 10m for the jpg radar data and 5m for the mat radar data, something that can only be determined using a statistically powerful analysis technique such as 2-D cross correlation. The migration rates are calculated by this means to an accuracy of $1/10^{th}$ of a pixel, which equates to 1m for the jpg radar data and 0.5m for the mat radar data. Therefore a standard error of 2m per month was applied to the monthly migration rates derived from the jpg radar data, while the mat data being processed to a higher resolution has a standard error of 1m per month. A pixel analysed by the 2-D cross correlation algorithm for the jpg and mat radar data covers an area of $100m^2$ and $25m^2$ respectively. The cross correlation algorithm analyses monthly mean radar images, which are the product of a month's worth of hourly mean radar images, and so each pixel will also contain information from a month's worth of data, which can be in excess of 800 values. This introduces an adverse effect from radar image noise due to the large amount of data used in the creation of monthly mean radar images. This noise can be quantified by calculating the migration distance from two identical radar images. Despite the fact that there is no mathematical difference between two identical images, a migration is still calculated by the motion tracking algorithm. However, the error calculated may be largely due to the polynomial curves fitted to the correlation r matrix (Figure 6.16), in particular when calculating the distance ε between the zero offset and the position of peak r at this offset. Significant changes in the calculated length of the migration vector will be caused by small changes in the calculated length of ε. Therefore, the motion tracking algorithm is likely to be most sensitive to ε, as opposed to the gradient α of the line fitted through the polynomial fits for maximum r at each offset.

Tables 7.2 and 7.3 show the monthly migrations for jpg and mat radar data at both West Kirby Sands

and West Hoyle Bank, as well as migration from identical images. All the identical image migrations are below the threshold of $1/10^{th}$ of a pixel for both the jpg and mat data, which have a 10 and 5m pixel size, respectively. Total migration rates are significantly larger for 2007 with West Kirby Sands experiencing a cumulative migration of 83m, whereas 2006 shows total migration rates of 57m for jpg data and 58m for mat data, while 2008 experienced 37m. Total migration at West Hoyle Bank was significantly larger than West Kirby Sands, with greatest migration seen during 2007 at 98m, however considerable migration also occurred during 2008 with 83m, while 2006 experienced 67m total migration using the jpg data and 73m from the mat data. Mean migration rates vary more considerably than the total migration quoted previously. For 2006 the mean jpg monthly migration at West Kirby Sands is $8.33m \pm 1.55m$ and at West Hoyle Bank is $8.37m \pm 2.65m$, whereas mat mean monthly migrations are $5.83m \pm 1.38m$ and $7.34m \pm 2.53m$ at West Kirby Sands and West Hoyle Bank, respectively. Less total migration for 2007 is seen at West Kirby Sands compared with West Hoyle Bank, an aspect which is also shown in the mean migration at West Kirby Sands at $9.12m \pm 1.13m$ while West Hoyle Bank experiences a lower mean migration of $6.15m \pm 1.51m$. The total and mean migration for 2008 is greater at West Hoyle Bank than West Kirby Sands by approximately 50% with mean migration at $9.66m \pm 3.53$ compared with $4.80m \pm 1.52m$.

The 2-D cross correlation migration rates can be validated against the migration of backscatter intensity peaks from the quarterly radar intensity profiles (Figures 7.13 - 7.20). Table 7.4 shows total yearly migration at West Kirby Sands and West Hoyle Bank calculated using the 2-D cross correlation of wave breaker patterns and the migration of peaks in radar backscatter intensity from the intensity profiles at West Kirby Sands and West Hoyle Bank (Figure 7.13-7.20). In general the total yearly migrations calculated from the radar backscatter intensity profiles, which assumes that a dune does not migrate further than one wavelength between consecutive profiles, are in good agreement with migration from the 2-D cross correlation method. This assumption can be seen to be satisfied by the migration rate results in Table 7.4, where only the largest yearly total migration rates are less than or equal to the approximate wavelength of the radar backscatter intensity wave forms. There is, however, a large increase in the error associated with calculating migration rates by eye with the backscatter profiles compared with the 2-D cross correlation method, highlighting the importance of using the cross correlation motion tracking technique for monitoring the migration of large scale bed forms in the mouth of a dynamic estuary, such as the Dee.
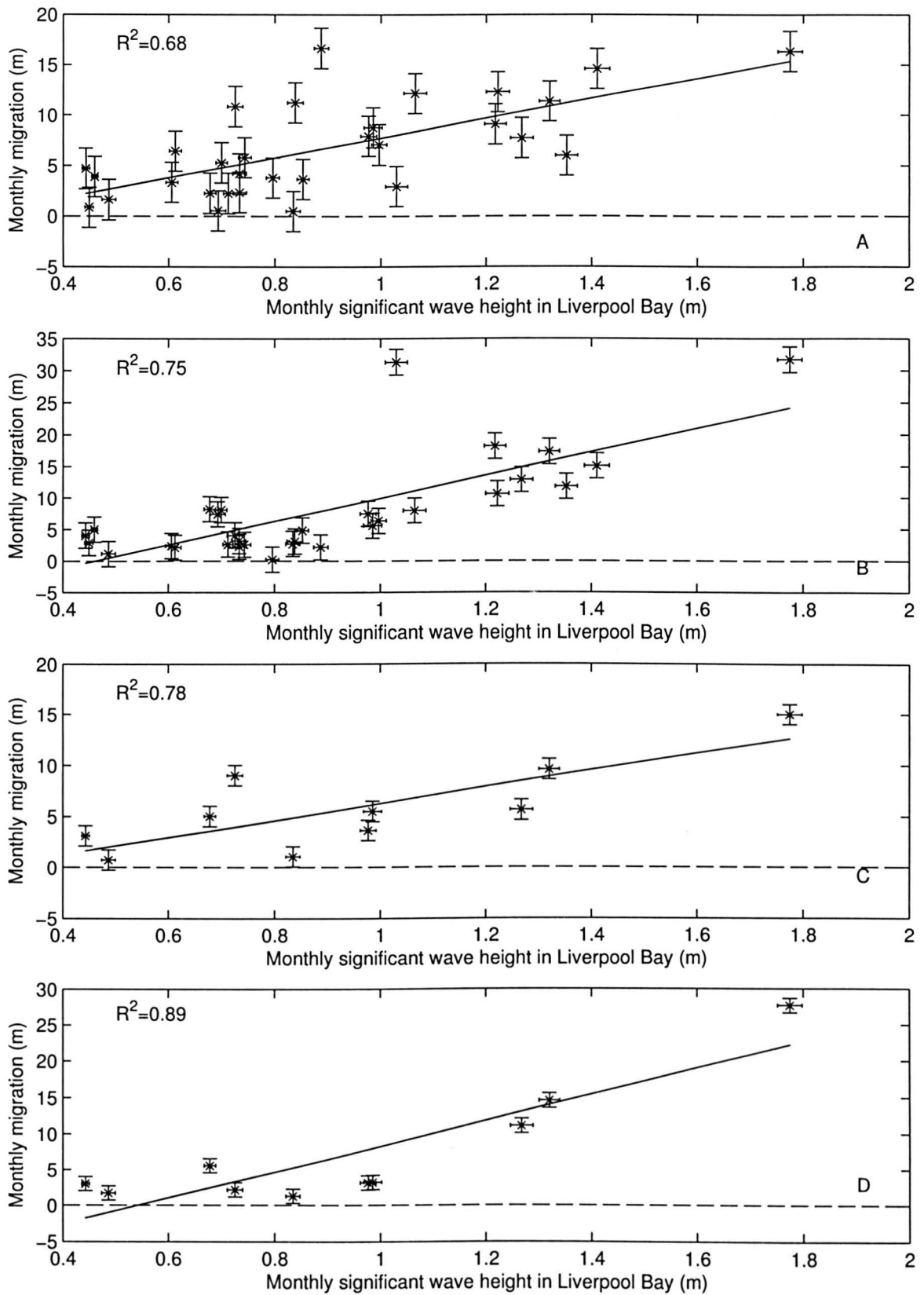
Figure 7.23: Monthly breaker pattern migration for A) jpg data at West Kirby Sands B) jpg data at West Hoyle Bank C) mat data at West Kirby Sands D) mat data at West Hoyle Bank using all available data plotted against the monthly average significant wave height in Liverpool Bay.
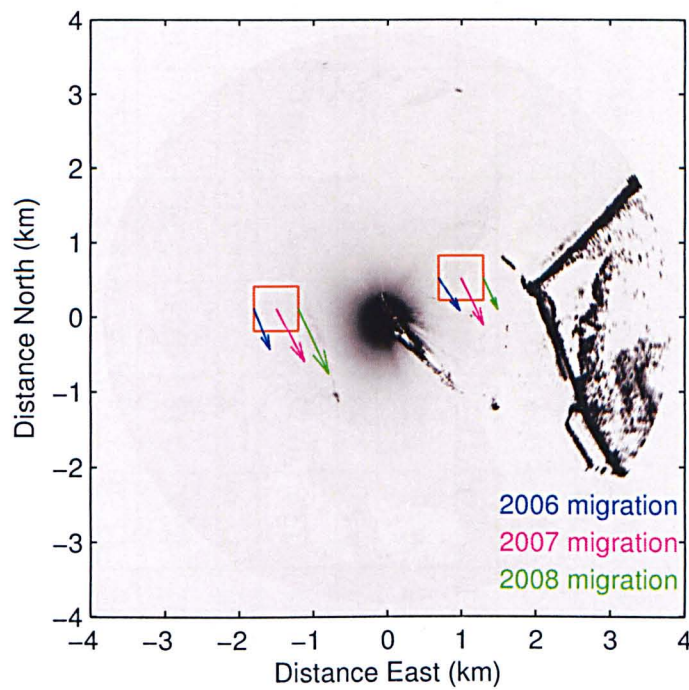
Figure 7.24: Yearly average migration vectors from the 2-D cross correlation analysis at West Kirby Sands and West Hoyle Bank

The 2-D cross correlation algorithm calculates the migration between monthly mean radar images from a quadratic summation of the x and y migration components, which is then multiplied by the image resolution. Therefore, it is possible to use the x and y components to plot a migration direction vector. Figure 7.24 shows yearly average migration vectors calculated from the average x and y migration components for each year. This shows a net migration into the mouth of the estuary for all of the radar data analysed, indicating that large scale bed forms are migrating into the Dee Estuary contributing to the positive sediment input to the estuary.

Month 2006	Feb	Mar	Apr	May	Jun	Jul	Aug	Sep	Oct	Nov	Dec	Jan 07	Mean	Total	StErr
JPG migration at WKS (m)	11.24	16.66	0.47	10.86	1.61	4.70	7.93	2.26	8.76	11.39	7.74	16.36	8.33	99.98	1.55
Migration from identical jpg images at WKS (m)	0.38	0.38	0.38	0.37	0.13	0.49	0.04	0.11	0.32	0.18	0.18	0.04	0.25	3.02	0.04
JPG migration at WHB (m)	3.07	2.17	2.70	4.04	1.13	4.06	7.47	8.21	5.59	17.34	12.89	31.75	8.37	100.42	2.65
Migration from identical jpg images at WHB (M)	0.47	0.02	0.41	0.38	0.47	0.05	0.04	0.14	0.35	0.19	0.25	0.15	0.24	2.93	0.05
MAT migration at WKS (m)			1.06	9.02	0.73	3.11	5.03	3.63	5.47	9.57	5.62	15.03	5.83	58.26	1.38
Migration from identical mat images (m)			0.38	0.43	0.37	0.33	0.24	0.49	0.25	0.43	0.23	0.35	0.35	3.49	0.03
MAT migration at WHB (m)			1.28	2.16	1.71	3.01	3.14	5.57	3.23	14.56	11.08	27.68	7.34	73.43	2.53
Migration from identical mat images at WHB (m)			0.13	0.04	0.12	0.16	0.27	0.10	0.18	0.14	0.18	0.10	0.14	1.43	0.02

Table 7.2: Monthly breaker pattern migration rates for 2006 calculated using the motion tracking algorithm at West Kirby Sands (WKS) and West Hoyle Bank (WHB).

Month 2007	Jan	Feb	Mar	Apr	May	Jun	Jul	Aug	Sep	Oct	Nov	Dec	Mean	Total	StErr
JPG migration at WKS (m)		0.52	12.17	3.89	5.79	3.33	3.77	3.63	7.06	6.43	12.31	9.12	6.18	68.03	1.13
Migration from identical jpg images at WKS (m)		0.23	0.18	0.17	0.04	0.07	0.20	0.16	0.16	0.27	0.09	0.04	0.15	1.60	0.02
JPG migration at WHB (m)		7.39	7.99	4.99	2.58	2.38	0.20	4.81	6.35	2.11	10.65	18.19	6.15	67.64	1.51
Migration from identical jpg images at WHB (m)		0.11	0.45	0.01	0.38	0.23	0.42	0.31	0.37	0.28	0.41	0.38	0.31	3.36	0.04
Month 2008	Jan	Feb	Mar	Apr	May	Jun	Jul	Aug	Sep	Oct	Nov	Dec	Mean	Total	StErr
JPG migration at WKS (m)	5.99	2.93	14.62	5.27	0.86	2.35	4.17	2.24					4.80	43.22	1.52
Migration from identical jpg images at WKS(m)	0.09	0.04	0.05	0.30	0.04	0.32	0.11	0.17					0.14	1.25	0.04
JPG migration at WHB (m)	11.84	31.32	15.07	8.07	2.90	2.27	3.17	2.62					9.66	86.92	3.53
Migration from identical jpg images at WHB (m)	0.44	0.28	0.85	0.14	0.10	0.46	0.03	0.30					0.32	2.92	0.09

Table 7.3: Monthly breaker pattern migration for 2007 to 2008 calculated using the motion tracking algorithm at West Kirby Sands (WKS) and West Hoyle Bank (WHB).

Method	Total migration (m) 2006	Standard error ± (m) 2006	Total migration (m) 2007	Standard error ± (m) 2007	Total migration (m) 2008	Standard error ± (m) 2008
2-D Cross correlation WKS jpg	99.98	1.55	68.03	1.13	43.22	1.52
Intensity profile WKS jpg	90.00	5.77	80.00	6.66	50.00	5.00
2-D Cross correlation WKS mat	58.26	1.38				
Intensity profile WKS mat	75.00	2.88				
2-D Cross correlation WHB jpg	100.42	2.53	67.64	1.51	86.92	3.53
Intensity profile WHB jpg	100.00	8.82	90.00	5.77	90.00	7.21
2-D Cross correlation WHB mat	73.43	2.65				
Intensity profile WHB mat	85.00	5.77				

Table 7.4: A comparison between total yearly 2-D cross correlation migrations and total yearly migration from the radar backscatter intensity profiles.

7.5   Bed load transport inferred from dune migration

It is possible to use the migration distances produced by the 2-D cross correlation algorithm to calculate the bed load sediment flux per unit length along the bed form crest resulting from dune migration

$$q_{b,dunes} = (1 - \varepsilon)A_d \left(\frac{L_d}{\lambda_d} \right) \tag{7.3}$$

where ε is porosity, A_d is dune cross sectional area (defined as the area between successive trough points), L_d is dune migration distance per month and λ_d is dune wave length. These bed form parameters can be obtained from the October 2006 Lidar survey, where it is possible to determine individual dunes. This method was chosen over the dune migration method described in Section 2.4.4 as bed form dimensions could be determined from the Lidar data, therefore removing the need to use a bed form coefficient. However, porosity ε is included to account for the pores between the sand grains which are part of the bed form. This Lidar survey of the Dee Estuary was carried out by the Environment Agency and has a horizontal resolution of 1m with vertical accuracy between ±5cm to ±15cm. A profile can be extracted perpendicular to the dune crest using the 'interp2' function in Matlab and the profile is set to the 'true' length using Pythagoras' theorem. An assumption is made that the dune shape and size does not vary significantly in time, however this may not be the case. Figure 7.25 shows a profile extracted through West Kirby Sands from the Lidar data with the dune field highlighted, from which individual dunes are isolated to extract dune geometries.
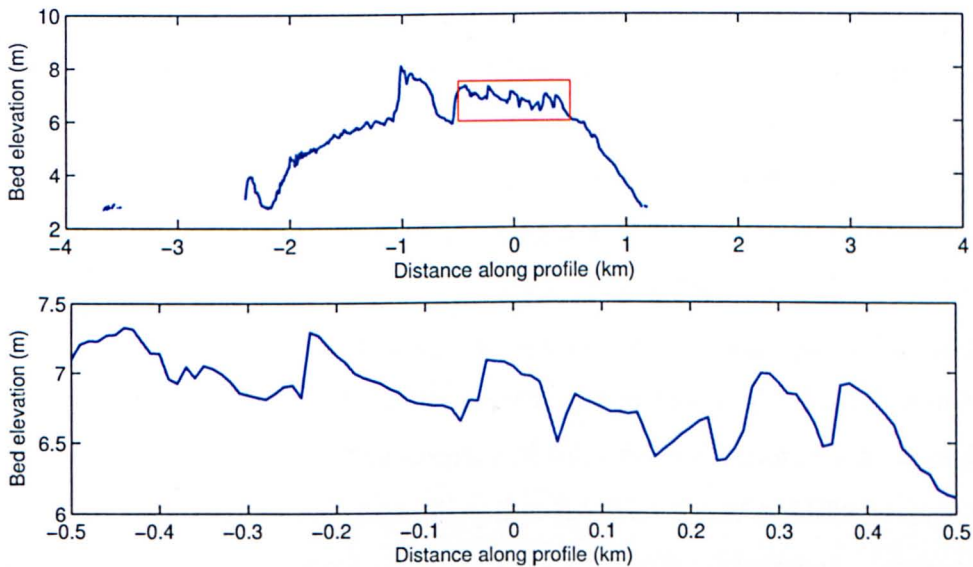
Figure 7.25: West Kirby Sands profile extracted from Lidar data, showing individual dunes for which geometries are calculated.

The gradient of the beach slope is removed to obtain the absolute values for dune trough to trough wavelength and height calculated as the distance from dune crest to the position normal to a line passing from trough to trough, rather than referenced to chart datum. Figure 7.26 shows the Lidar elevation across a typical dune on West Kirby Sands with a cross sectional area of $25m^2$.
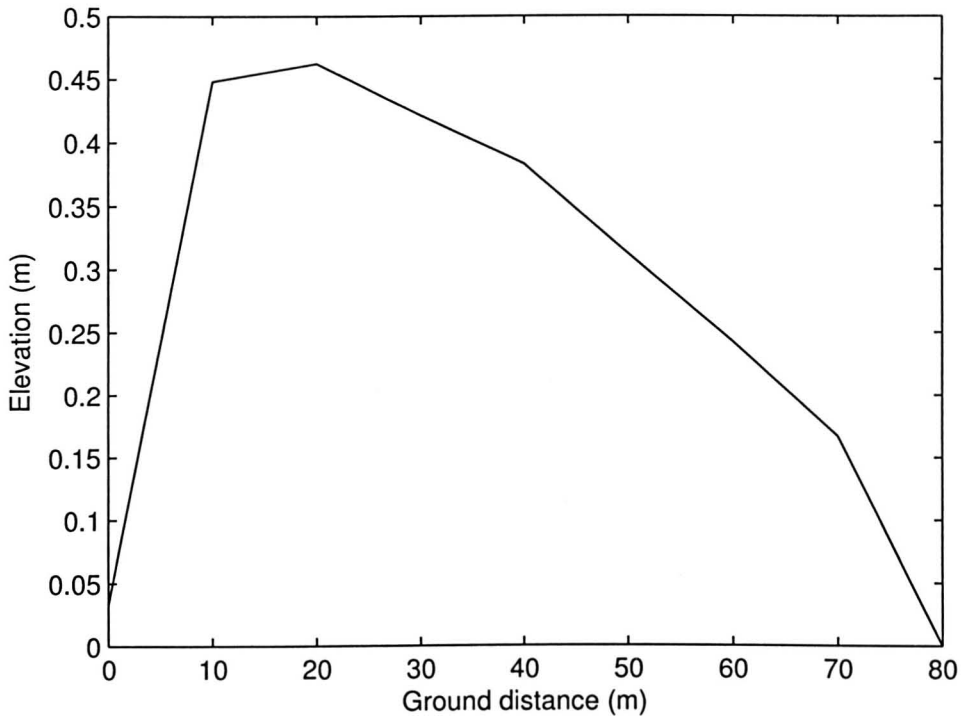
Figure 7.26: Cross sectional profile through a single dune on the West Kirby Sands dune field taken from the Lidar survey. The open sea boundary is to the right of the plot and the sand flats are to the left.

A total of eight dunes were identified on West Kirby Sands (Figure 7.25 lower panel) giving an average cross sectional area of $31.5m^2$, with a standard error of $\pm 3.8m^2$, and a mean wavelength measured between dune troughs of $110m \pm 3.4m$. A similar process was repeated over West Hoyle Bank dune field with a total of six dunes used to calculate bed form dimensions. Figure 7.27 shows a typical dune on West Hoyle Bank with a cross sectional area of $26m^2$. The dune field at West Hoyle Bank has an average cross sectional area of $18.5m^2 \pm 4.1m^2$ and wavelength of $98.3m \pm 3.6m$. Table 7.5 shows the transport rate calculated with bed form dimensions and dune migrations determined using the motion tracking algorithm. The number of tides for each monthly time period is used to calculate the transport rate in $m^2 tide^{-1}$, assuming that the tidal period at Hilbre Island was the same as the principal lunar tide (12.42 hours), giving 1.93 tides per day. The yearly average transport rate associated with dune migration is greater at West Kirby Sands during 2006 and 2007, but slightly larger at West Hoyle Bank during 2008. This is due to the dunes identified at West Hoyle Bank

having a 41% smaller cross sectional area than those on West Kirby Sands. So despite the migrations from the 2-D cross correlation being of similar magnitudes or greater throughout 2006 and 2007, the transport rate associated with dunes is actually significantly greater at West Kirby Sands. However this does not account for the migration of larger bed forms such as sand bars which could be seen to be present and migrating at West Hoyle Bank.
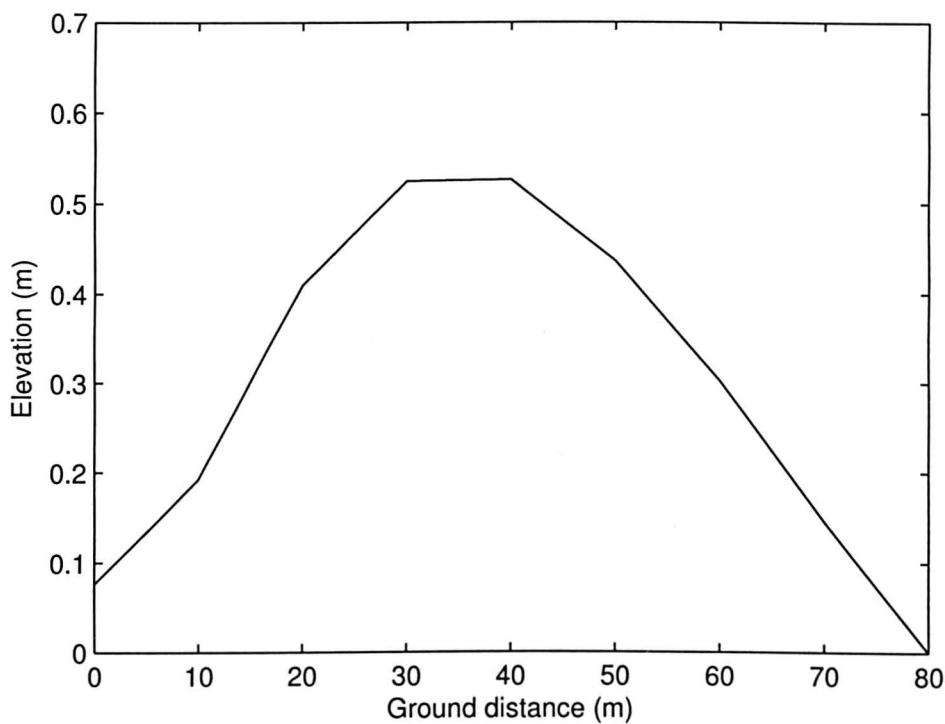
Figure 7.27: Cross sectional profile through a single dune on the West Hoyle Bank dune field taken from the Lidar survey. The open sea boundary is to the right of the plot and the sand flats are to the left.

Dune migration (m^{2}tide^{-1})	Jan	Feb	Mar	Apr	May	Jun	Jul	Aug	Sep	Oct	Nov	Dec	Mean	Total	St Err
2006 WKS jpg transport		0.035	0.047	0.001	0.031	0.005	0.014	0.025	0.007	0.025	0.034	0.022	0.022	0.246	0.0001
2006 WKS mat transport				0.003	0.026	0.002	0.009	0.014	0.011	0.016	0.028	0.016	0.014	0.125	0.0001
2006 WHB jpg transport		0.007	0.004	0.005	0.008	0.002	0.008	0.014	0.016	0.011	0.034	0.025	0.012	0.133	0.0009
2006 WHB mat transport				0.002	0.004	0.004	0.006	0.006	0.011	0.006	0.028	0.021	0.010	0.088	0.0010
2007 WKS jpg transport	0.047	0.002	0.035	0.011	0.017	0.010	0.011	0.010	0.021	0.019	0.037	0.026	0.020	0.245	0.0011
2007 WKS mat transport	0.043														
2007 WHB jpg transport	0.067	0.016	0.015	0.010	0.005	0.005	0.004	0.009	0.013	0.004	0.021	0.034	0.017	0.199	0.0015
2007 WHB mat transport	0.052														
2008 WKS jpg transport	0.017	0.009	0.042	0.016	0.002	0.007	0.013	0.007					0.014	0.113	0.0016
2008 WHB jpg transport	0.022	0.063	0.028	0.016	0.005	0.004	0.006	0.005					0.019	0.149	0.0025

Table 7.5: Inferred transport rates (m^{2}tide^{-1}) from the 2-D cross correlation migration rates using the dune dimension parameters extracted from the Lidar data.

7.6 Waterline beach profiles

The 'waterline method' was introduced in Section 6.6 as the use of hourly mean radar images with tidal data from the Hilbre Island tide gauge to create beach profile images for intertidal regions covered by the range of the radar. Grey scale intensity values are extracted from an hourly mean radar image along a profile taken through an area of interest. This profile of radar backscatter intensity values are then stored along with the tidal elevation corresponding to the time the image was created by the radar. The initial aim of this method was to identify bed forms and extract bed form dimensions, however low image resolution over the identified dune fields meant that the application of this technique shifted towards analysing the general form of beach profiles between monthly images.

7.6.1 West Kirby Sands waterline beach profiles

Figure 7.28 shows a waterline beach profile through West Kirby Sands created using all available jpg data for October 2006 with an identical profile taken from the Lidar survey data overlain (the red line). This Lidar profile extends the entire length of the radar range, which at the time of October 2006 was 4km. The open sea boundary is towards 4km along the profile in Figure 7.28 and the sand flats are towards -4km. West Kirby Sands beach slope starts at approximately 1.5km north, and this then progresses into the dune field moving south-ward along the profile. The vertical stripe at approximately -1km north along the West Kirby Sands profile is an object which is stationary for the entire month, in this case it is Hilbre Island. The elevation of the Lidar profile corresponds well with an increase in radar backscatter intensity over the waterline beach profile, represented by the transition from lighter to darker values at the water's edge.

Figure 7.28: Waterline beach profile at West Kirby Sands created with all available hourly mean jpg (A) and mat (B) radar data for October 2006 with a similar profile extracted from the Lidar data overlain (red line).

An identical profile through West Kirby Sands was extracted from the mat radar data for October 2006 with the Lidar elevation profile overlain in red (Figure 7.28). This also shows the dune field between approximately 0.5km north to 0.5km south along the West Kirby Sands profile, with the beach slope extending to 1.5km towards the open sea boundary. Hilbre Island is visible as the vertical dark stripe at -1km north on the West Kirby Sands profile.

Figure 7.29: Vertical profiles of backscatter intensity taken from the October 2006 jpg waterline beach profile at six separate locations along the West Kirby Sands dune field. There is a distinct increase in backscatter intensity at the approximate elevation of the seabed (dashed line).

Figure 7.29 shows six vertical profiles extracted from the October 2006 jpg waterline beach profile over the dune field at West Kirby Sands, with the mean Lidar elevation of the six points overlain as the dashed black line. This shows a clear increase in the radar backscatter at the approximate level of the sea bed, indicating that the waterline method is recreating the level of the beach profile to a reasonable degree of accuracy. An identical set of profiles are extracted from the October 2006 mat waterline image showing similar peaks in backscatter intensity at the approximate elevation of the sea bed (Figure 7.30). This peak in radar backscatter intensity is associated with the shoreline peak in wave energy seen in Figure 7.6. Ruessink et al. (2002) corresponded this peak in radar backscatter to the swash zone on the beach. It is this swash zone signal of high radar return which defines the intertidal bathymetry seen in waterline beach profile images (Figure 7.28). This plot also highlights the difference in radar return between the two data sets, as both Figures 7.29 and 7.30 show the peak in radar backscatter associated with the approximate bed elevation. However the individual pixel values for the jpg radar data scale from 0 to 255 with lower radar backscatter intensity produced by a higher radar return, whereas mat radar data pixel values range from 0 to 1445 with higher radar backscatter intensity signifying a greater radar return.

Figure 7.30: Vertical profiles of backscatter intensity taken from the October 2006 mat waterline beach profile at six separate locations along the West Kirby Sands dune field. There is a distinct increase in backscatter intensity at the approximate elevation of the seabed (dashed line).

Unfortunately the waterline beach profile does not create a very strong contrast defining the level of the sea bed, despite Figures 7.29 and 7.30 showing peaks in radar backscatter intensity at the approximate elevation of the sea bed. An attempt was made to use the maximum intensity hourly mean images (Figure 7.31) to create a stronger contrast to show the waterline derived bed level. The maximum intensity images contain radar return signals from moving objects within the radar range, such as bird flight paths or walker tracks, whereas the mean intensity images contain radar return signals from prolonged reflectors, such as areas of persistently breaking waves. However, it was found that using the maximum intensity images increases the noise in the waterline beach profile images as theses images contain radar backscatter due to moving targets on the sand flats and noise due to rain clutter.
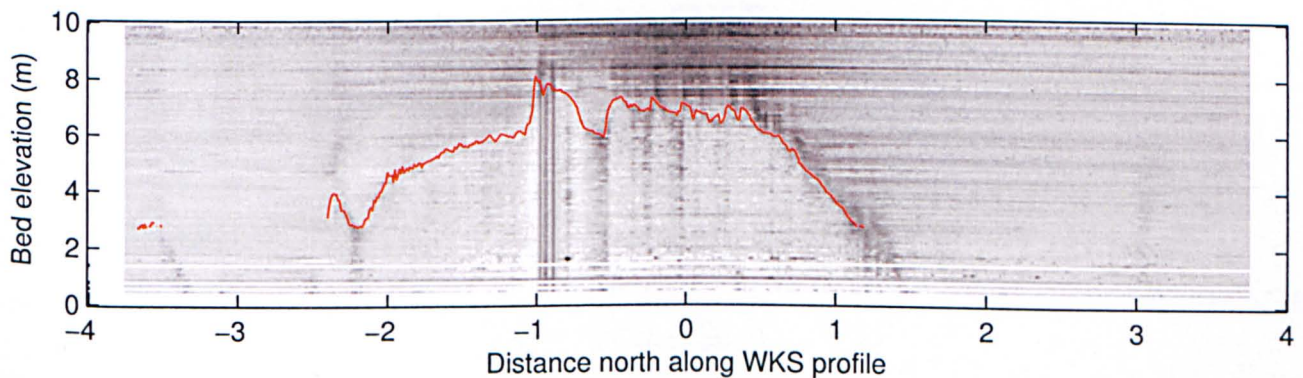
Figure 7.31: Waterline beach profile at West Kirby Sands created with all available max jpg data for October 2006 with a similar profile extracted from the Lidar data overlain

The waterline method was applied to all available monthly mean radar images for jpg and mat radar data along profiles through West Kirby Sands and West Hoyle Bank. This covers the time period of January 2006 to August 2008 for the jpg data and March 2006 to January 2007 for the mat data. To increase the image clarity of the dunes the waterline beach profiles have been cropped to include just the intertidal dune fields at West Kirby Sands and West Hoyle Bank. Figures 7.32 to 7.35 show waterline beach profiles through West Kirby Sands created using all available jpg radar data. Figure 7.36 shows waterline beach profiles extracted from mat radar data along an identical profile through West Kirby Sands. The dark vertical stripes at approximately 1 to 1.2km north along the West Kirby Sands profile are objects which are stationary for the entire month, in this case most likely a small rock outcrop, which is progressively covered and uncovered through out 2006 to 2008. This is an interesting process which is imaged effectively using this waterline method, suggesting times of sediment erosion and deposition when this area of rock is covered and uncovered. The open sea boundary is to the right of these plots, with the waterline method creating a reasonably clear image of the progression of West Kirby Sands beach slope to the undulating dune field. Unfortunately there is still a large amount of noise present in the beach profile images, making it hard to distinguish a clear bed level and bed form dimensions. The waterline beach profile images created with the jpg radar data have a horizontal and vertical resolution of 10m and 1m respectively, while the waterline images created using the mat radar data have a horizontal resolution of 5m and 1m vertical resolution.
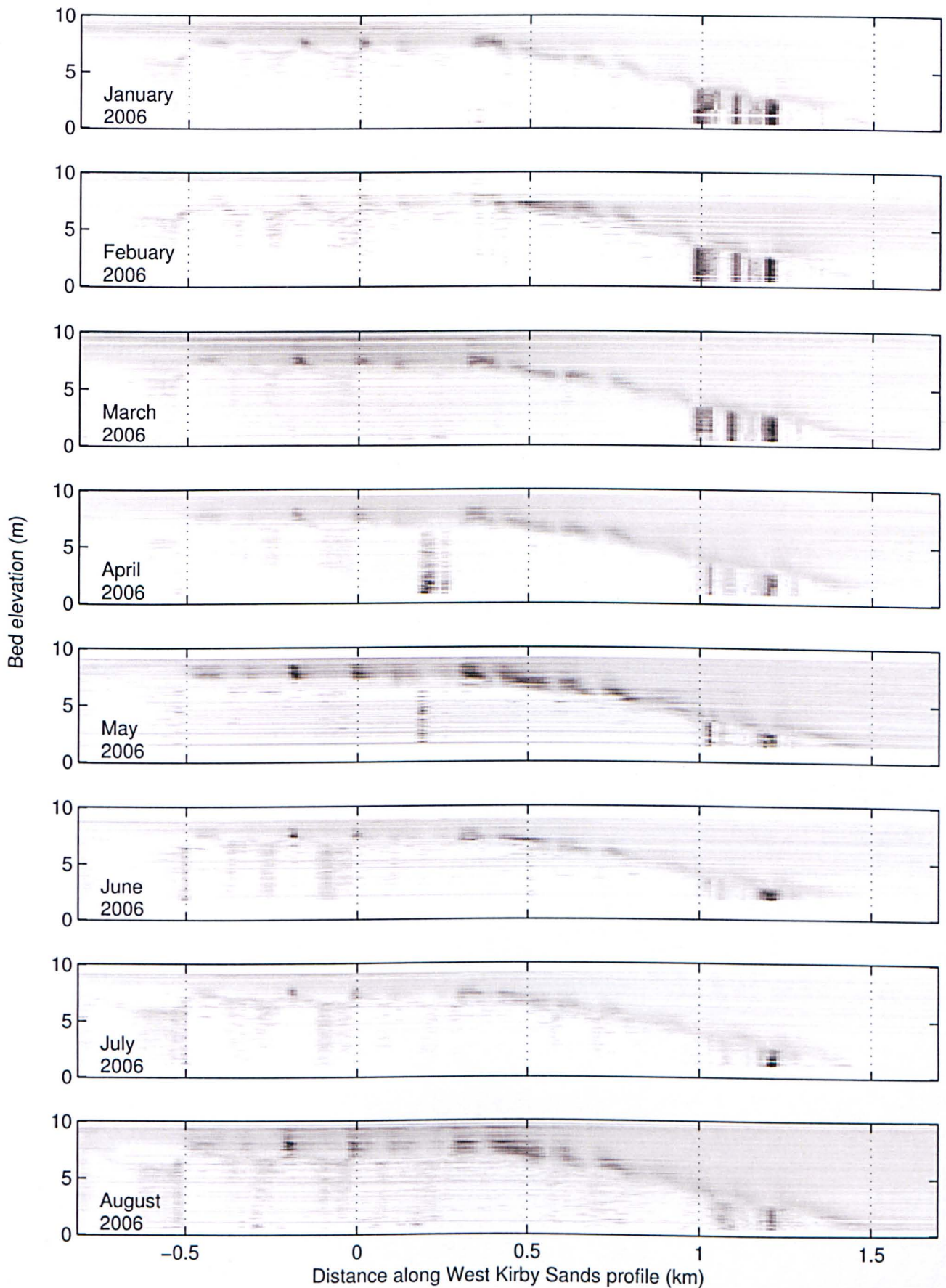
Figure 7.32: Waterline beach profiles through West Kirby Sands for all available jpg data from January to August 2006.
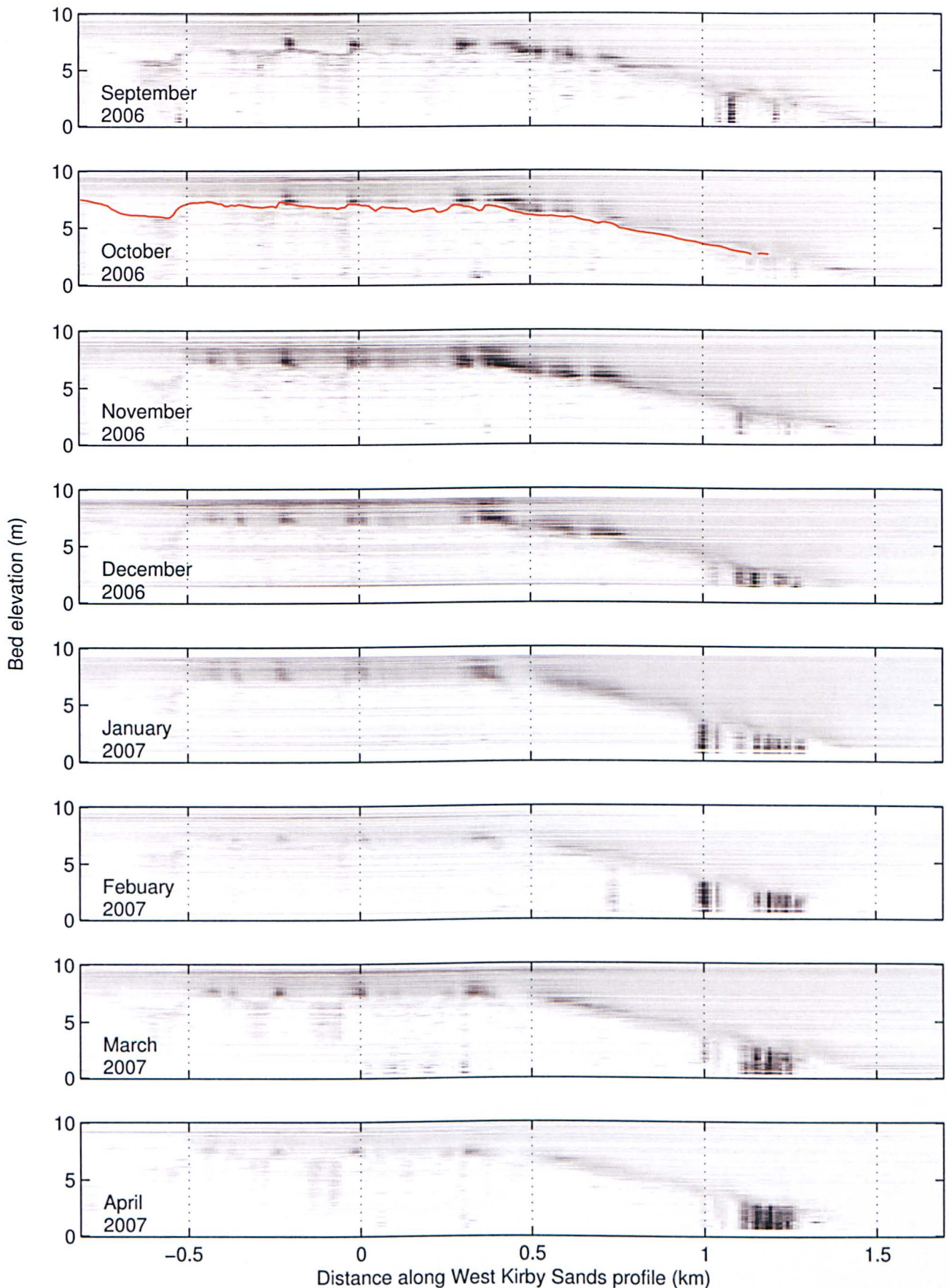
Figure 7.33: Waterline beach profiles through West Kirby Sands for all available jpg data from September 2006 to April 2007. The red line overlain onto the October 2006 waterline image is the Lidar elevation taken along an identical profile.
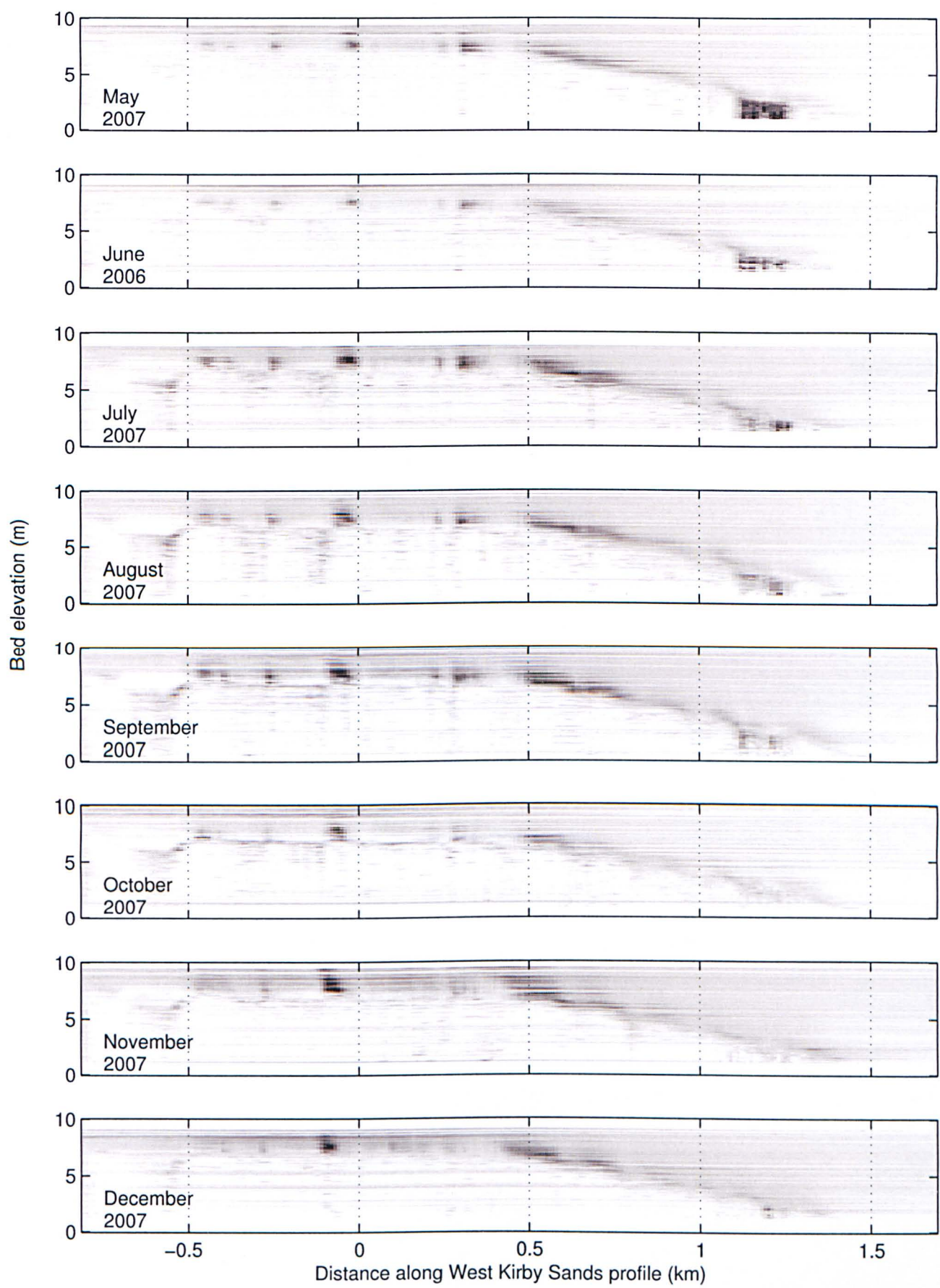
Figure 7.34: Waterline beach profiles through West Kirby Sands for all available jpg data from May 2007 to December 2007.
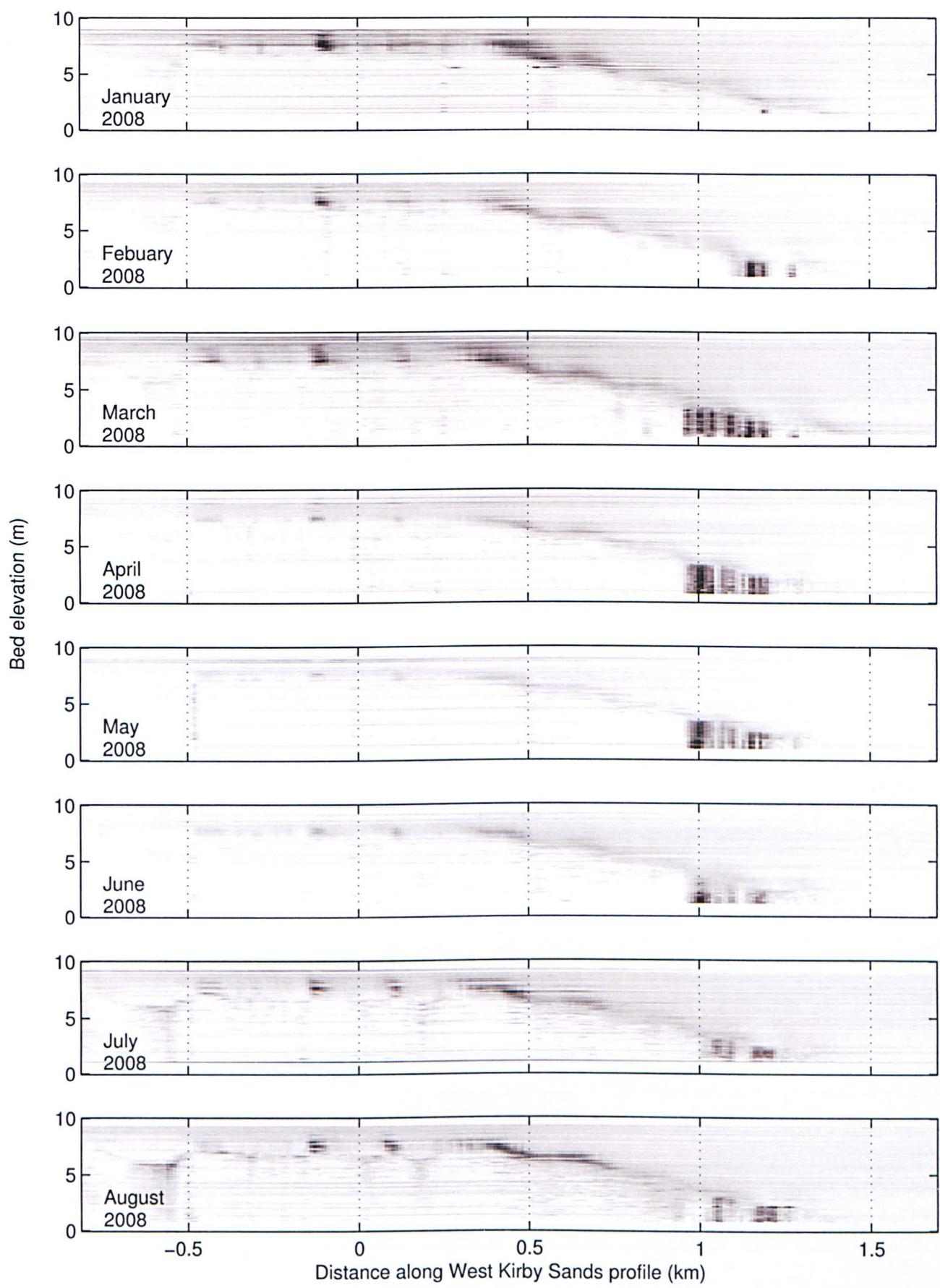
Figure 7.35: Waterline beach profiles through West Kirby Sands for all available jpg data from January 2008 to August 2008.
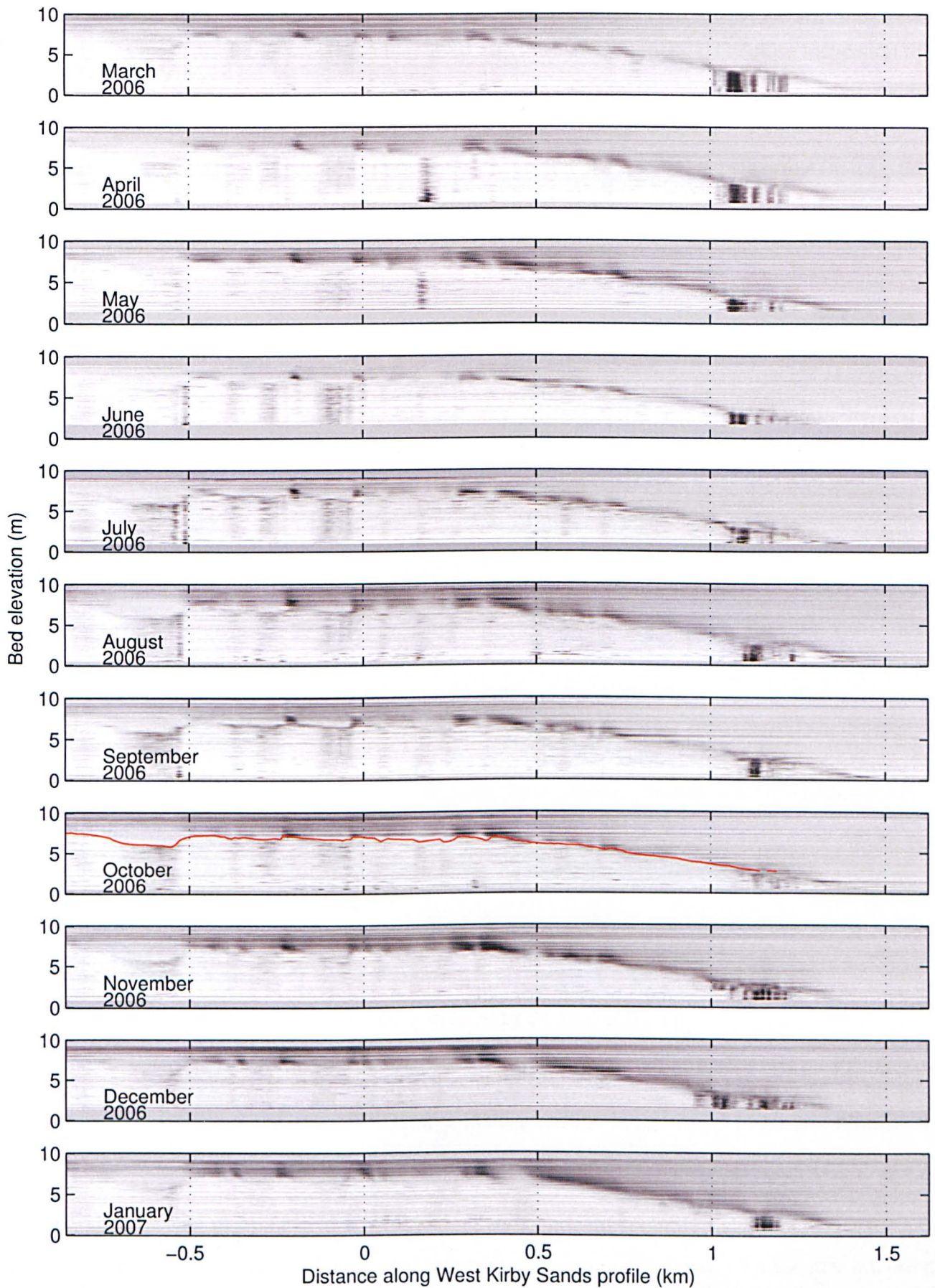
Figure 7.36: Waterline beach profiles through West Kirby Sands for all available mat data from March 2006 to January 2007. The red line overlain onto the October 2006 waterline image is the Lidar elevation taken along an identical profile.

The darker areas visible above dune crests are the wave breaker patterns which have been tracked using the 2-D cross correlation algorithm discussed previously (Section 7.4). On close inspection the position of the wave breaker patterns can be seen to migrate into the estuary, from right to left, on the West Kirby Sands profile (Figures 7.32 to 7.36). This is most noticeable in the mat radar data (Figure 7.36) which creates a clearer definition at the water's edge than the jpg derived waterline images, due to the increased resolution of the data better defining features such as the water's edge in the mat radar hourly mean images (Section 2.4).
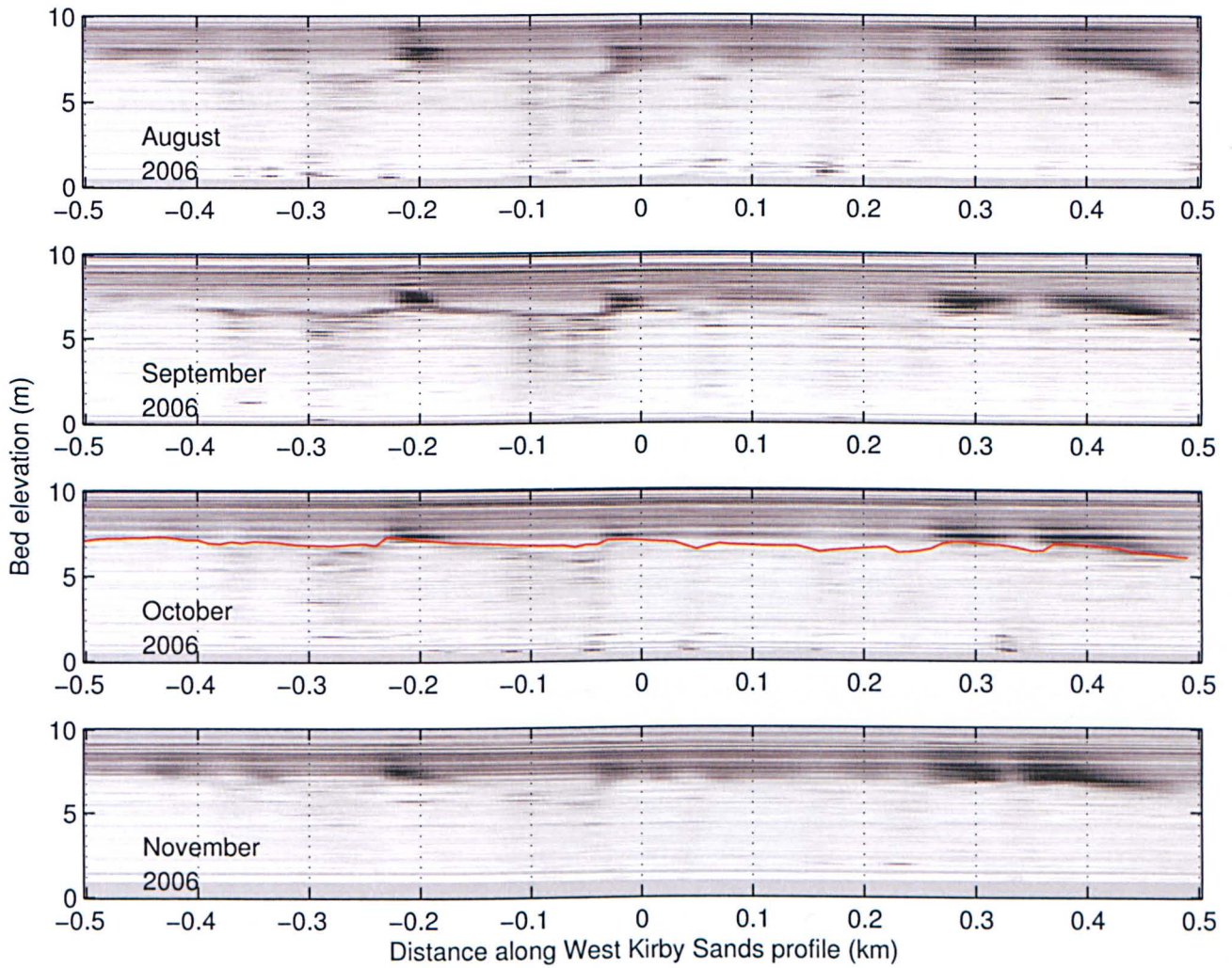
Figure 7.37: Waterline beach profiles through West Kirby Sands for all available mat data from August 2006 to November 2006, focusing on the dune field to show the migration of wave breaker patterns. The red line overlain onto the October 2006 waterline image is the Lidar elevation taken along an identical profile.

Figure 7.37 focuses on the dune field at West Kirby Sands, showing monthly waterline images for August to November 2006 created using the mat radar data. Peaks in wave breaker backscatter intensity, which are taken as a proxy for the location of large scale bed forms, are most visible at approximately

0km and 0.2km along the profile. Between the period of August to November 2006 these peaks in wave breaker backscatter intensity appear to migrate from the right to the left of the Figure (in an onshore direction). However, no quantitative bed form migration results could be extracted from the waterline images due to the prevalence of noise above the dune field. The intensity of the wave breaker patterns can be seen to change between waterline profile images, with winter months showing a higher return due to breaking waves (Figure 7.33 November 2006), while summer months have a weaker wave breaker pattern above dune crests (Figure 7.32 July 2006). This correlates well with annual wave energy with winter months experiencing larger wave heights due to winter storm events.

7.6.2 West Hoyle Bank waterline beach profiles

Figure 7.38 shows waterline beach profiles taken through West Hoyle Bank using jpg and mat radar data for October 2006. Overlain on these plots is the Lidar elevation along an identical profile. Unfortunately the length of the Lidar profile does not cover the full extent of the West Hoyle Bank waterline beach profile due to limits in the Lidar data survey range. This location was chosen for waterline analysis to examine the morphology in an area which has greater wave exposure than West Kirby Sands. The open sea boundary is towards 4km along the profile of the plot while the sand flats are located towards -4km. The topography of West Hoyle Bank can be seen to progress from a shallow beach slope at just over 2km north along the West Hoyle Bank profile to an undulating beach profile with to what appears to be a large sand bar feature at approximately -1km north. The vertical stripes of high radar return visible at approximately -1km are persistent radar reflectors, presumably rocky outcrops which are visible in the West Hoyle Bank monthly mean images (Figures 7.3 & 7.5).
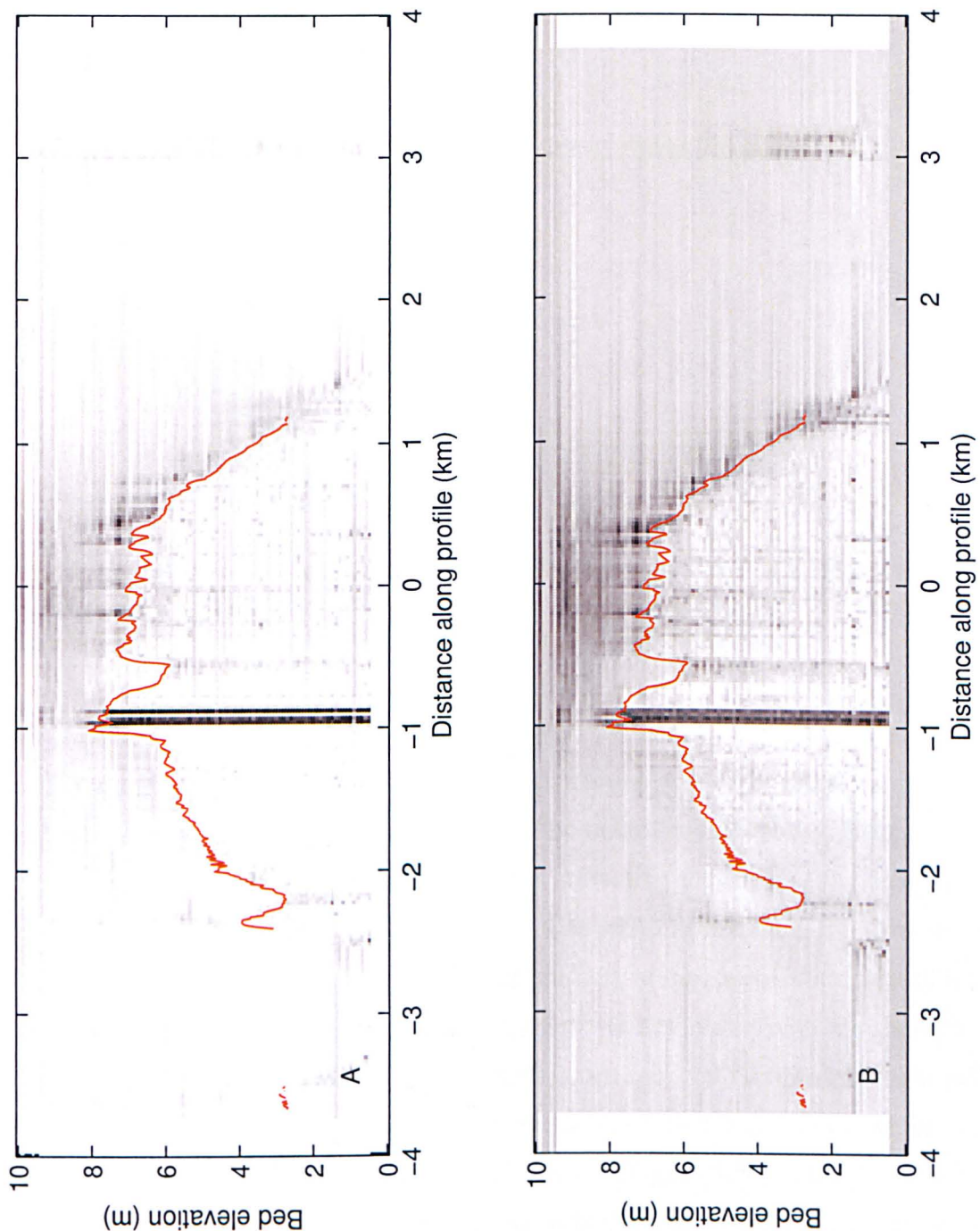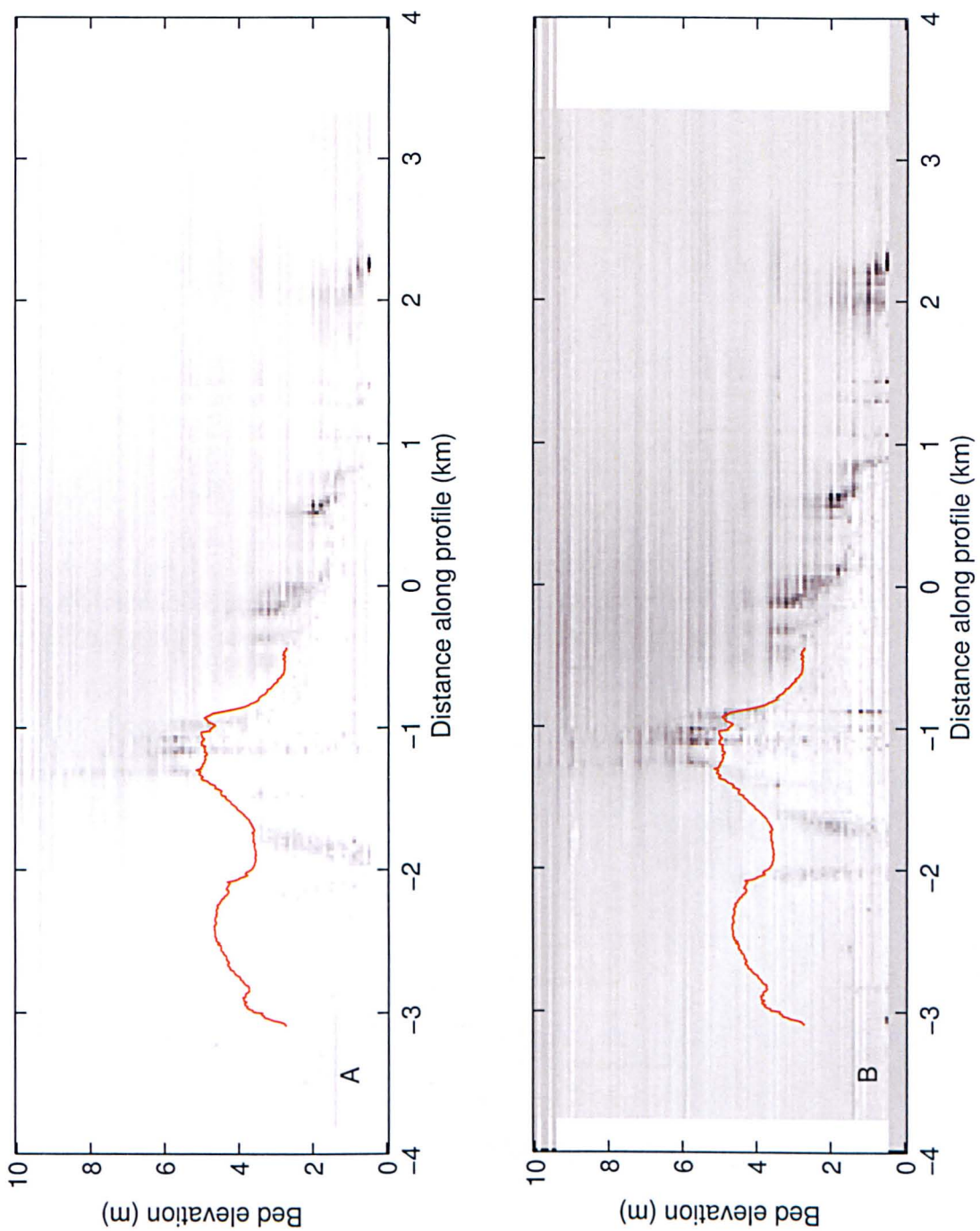
Figure 7.38: Waterline beach profile at West Hoyle Bank created with all available hourly mean jpg (A) and mat (B) radar data for October 2006 with a similar profile extracted from the Lidar data overlain (red line).
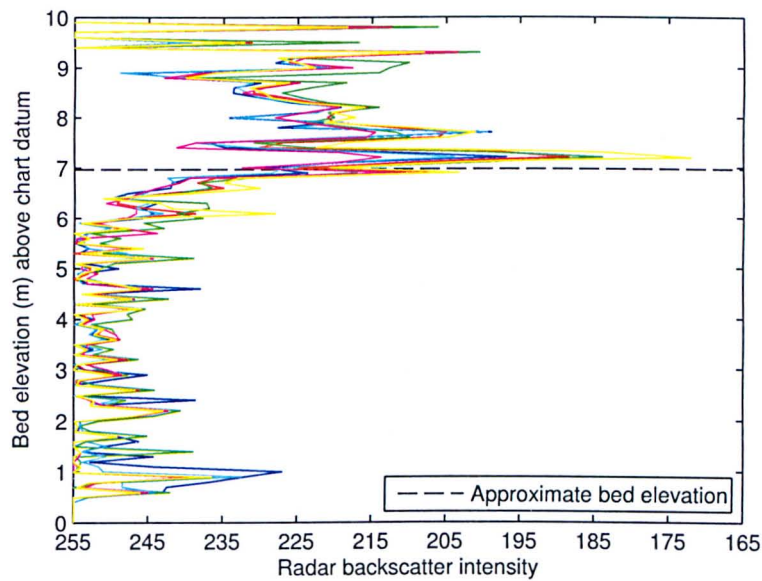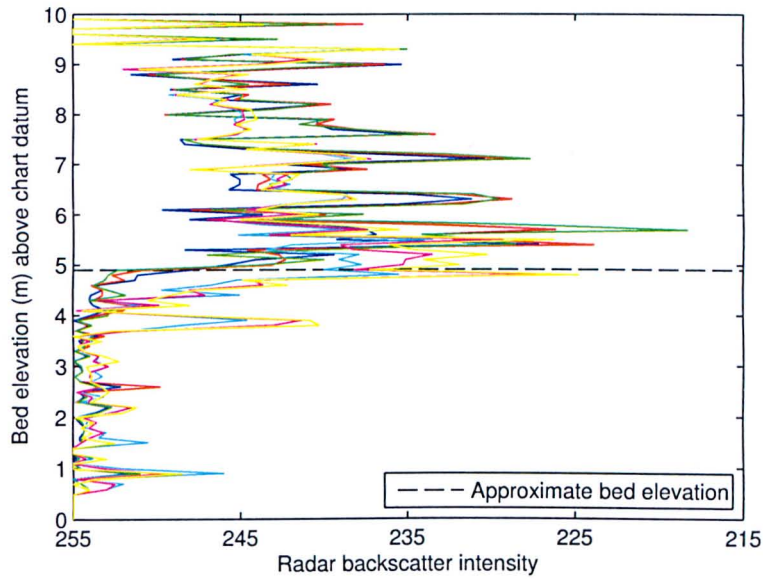
Figure 7.39: Vertical profiles of backscatter intensity taken from the October 2006 jpg waterline beach profile at six separate locations along the West Hoyle Bank dune field. There is a distinct increase in backscatter intensity at the approximate elevation of the seabed (dashed line).

Vertical profiles were extracted at six locations on West Hoyle Bank for the jpg and mat October 2006 waterline images with the mean Lidar elevation from these six profiles overlain as the dashed black line (Figures 7.39 and 7.40). These Figures show a clear peak in the radar backscatter intensity at the approximate bed elevation level.
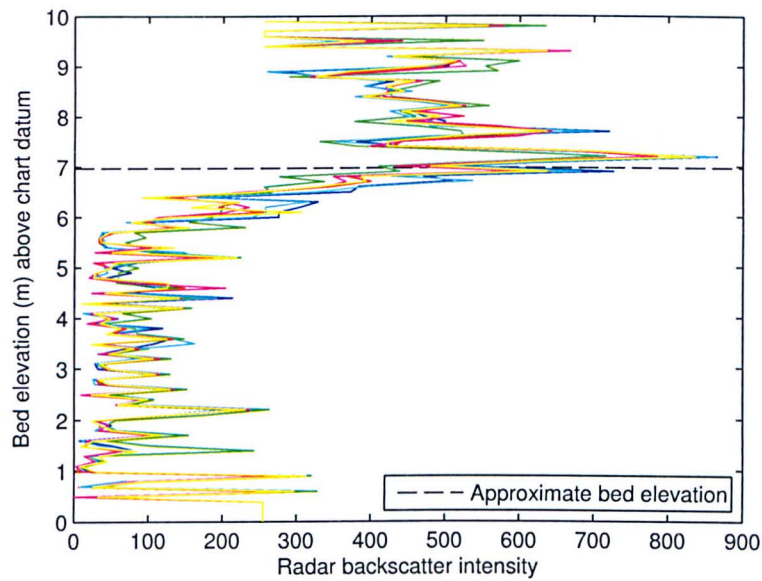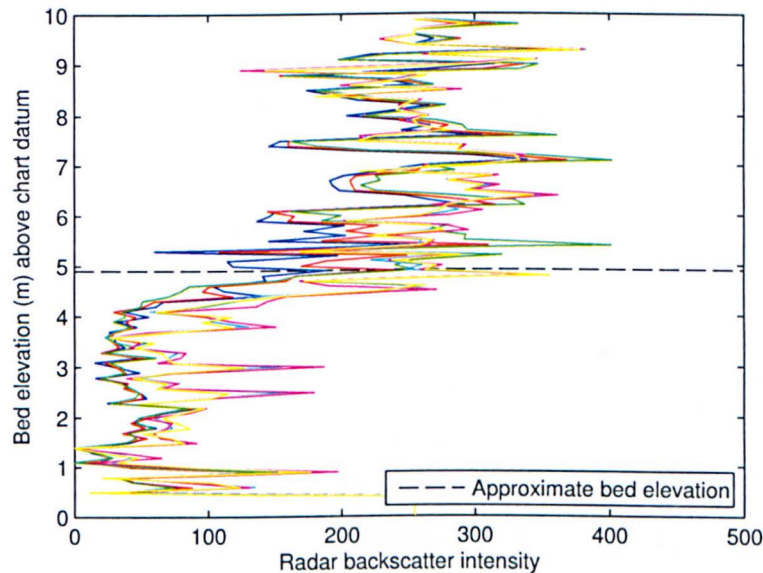

Figure 7.40: Vertical profiles of backscatter intensity taken from the October 2006 mat waterline beach profile at six separate locations along the West Hoyle Bank dune field. There is a distinct increase in backscatter intensity at the approximate elevation of the seabed (dashed line).

Figures 7.41 to 7.44 show waterline beach profiles at West Hoyle Bank using all available jpg radar

data covering the period of January 2006 to August 2008. These images have been cropped to focus on the beach slope at bed forms at West Hoyle Bank. The waterline beach profile at West Hoyle Bank shows the beach slope progressing from the open sea boundary to the right of the plot, with a less defined dune field compared with West Kirby Sands. However, there is a large sand bar at approximately 1km south along the West Hoyle Bank profile with a wavelength of approximately 0.5km. This large sand bar feature is well defined in the waterline images and appears to be relatively stable throughout the waterline beach profile images, however the effect of image noise makes it hard to accurately define the bed elevation at this location. The wave breaker patterns tracked with the 2-D cross correlation algorithm are visible as darker areas along the West Hoyle Bank profile. These also vary seasonally with winter months having a stronger radar return from breaking waves while summer months appear lighter with less radar backscatter return.
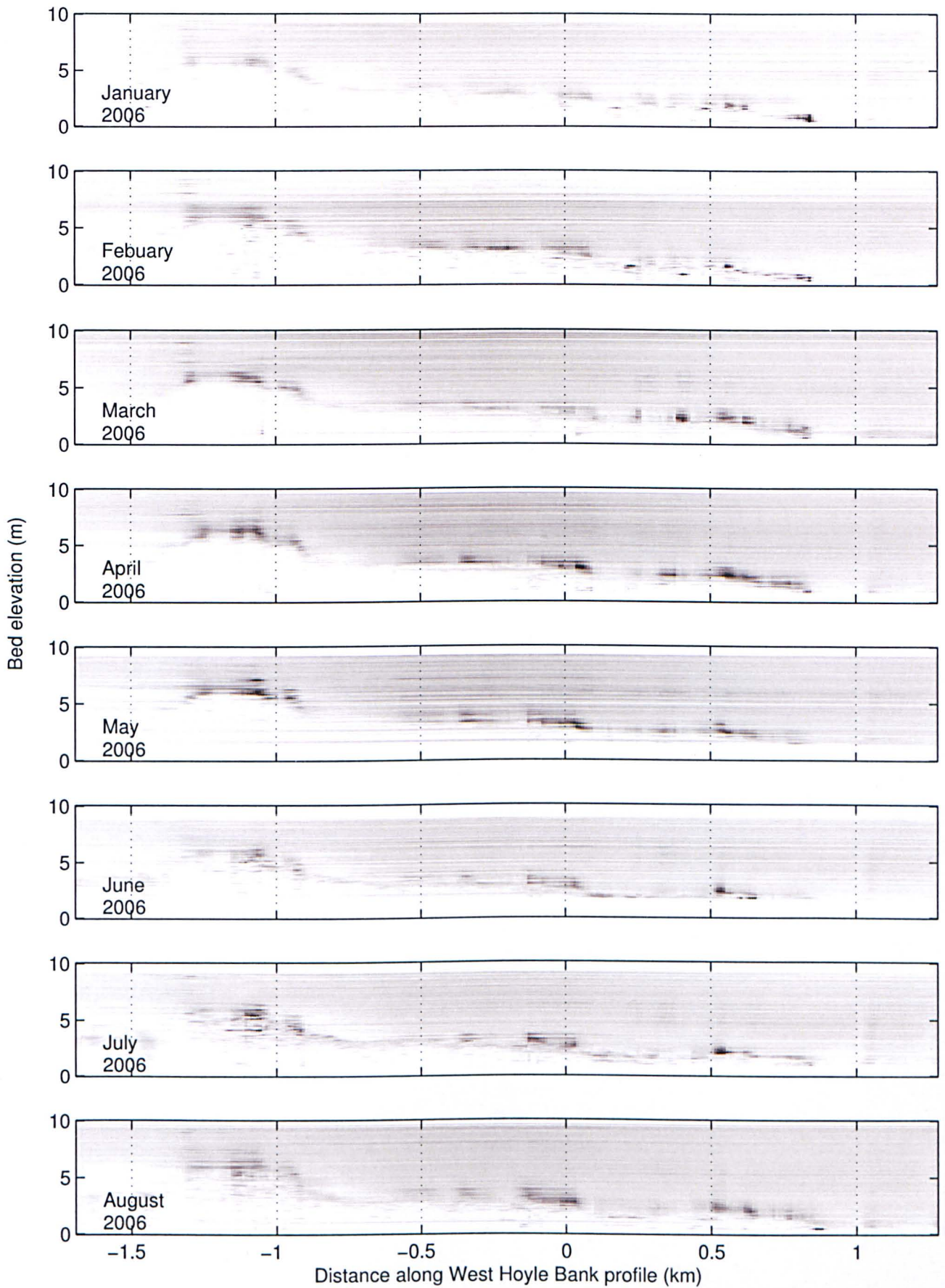
Figure 7.41: Waterline beach profiles through West Hoyle Bank for all available jpg data from January 2006 to August 2006.
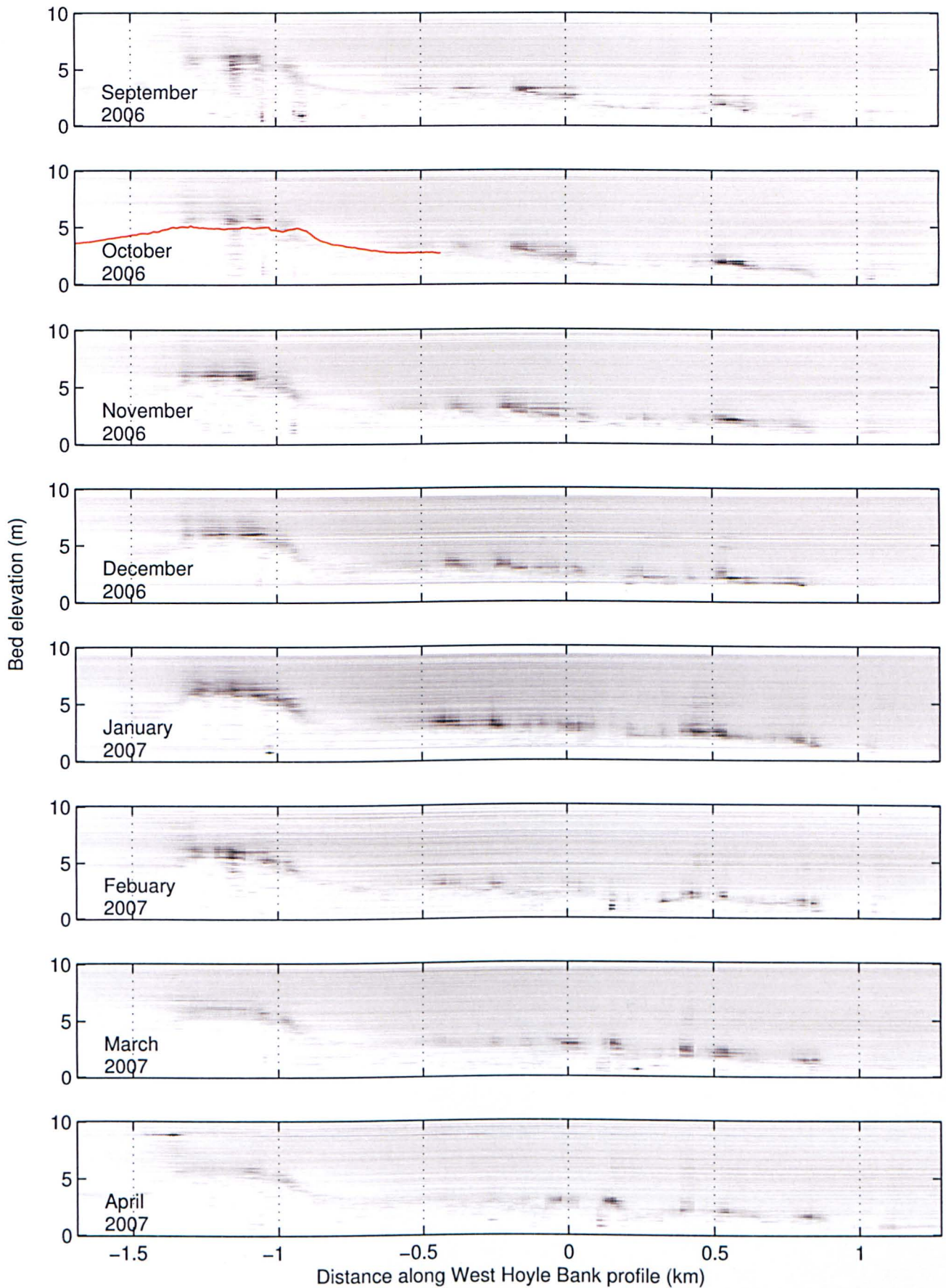
Figure 7.42: Waterline beach profiles through West Hoyle Bank for all available jpg data from September 2006 to April 2007. The red line overlain onto the October 2006 waterline image is the Lidar elevation taken along an identical profile.
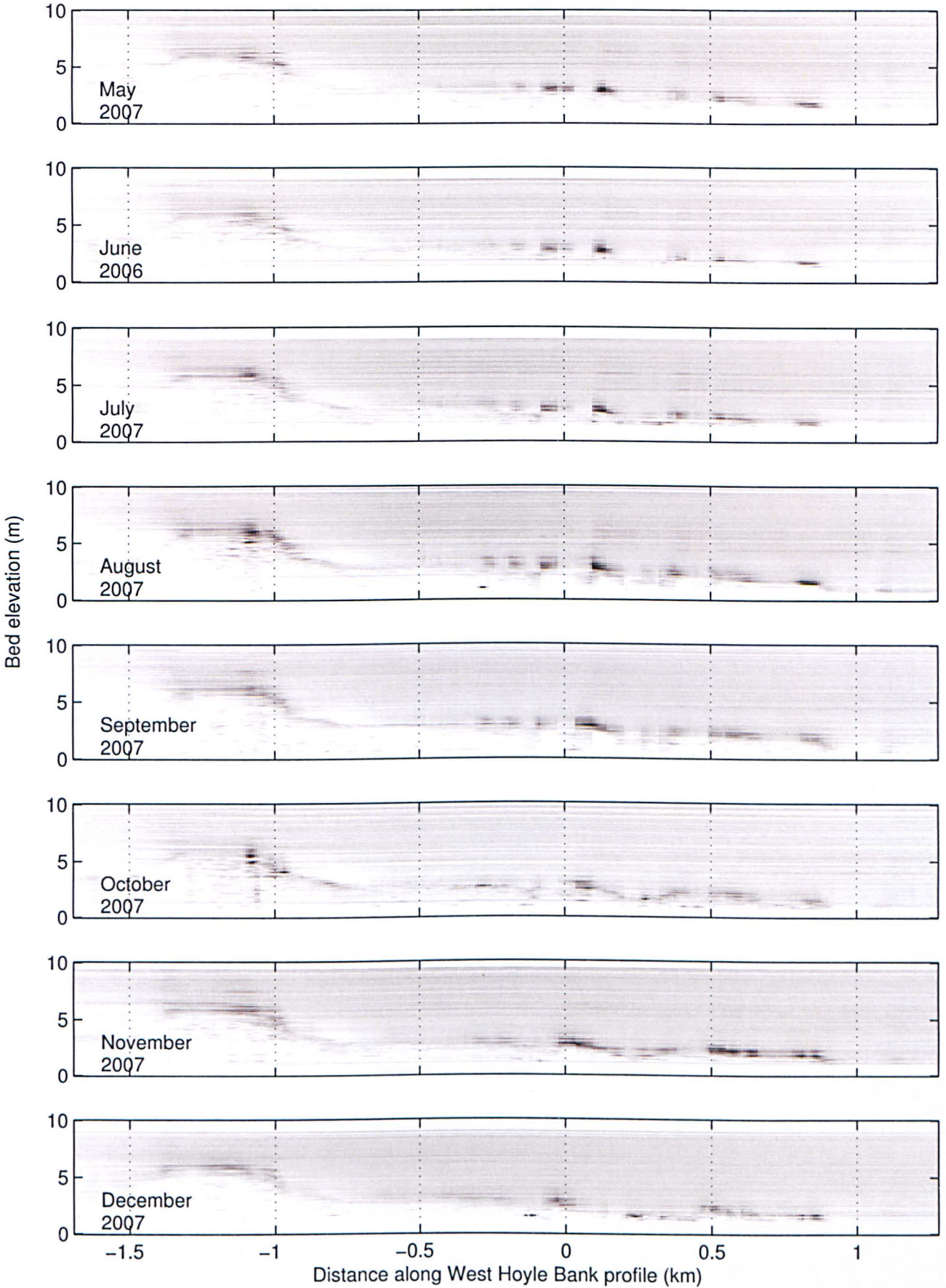
Figure 7.43: Waterline beach profiles through West Hoyle Bank for all available jpg data from May 2007 to December 2007.
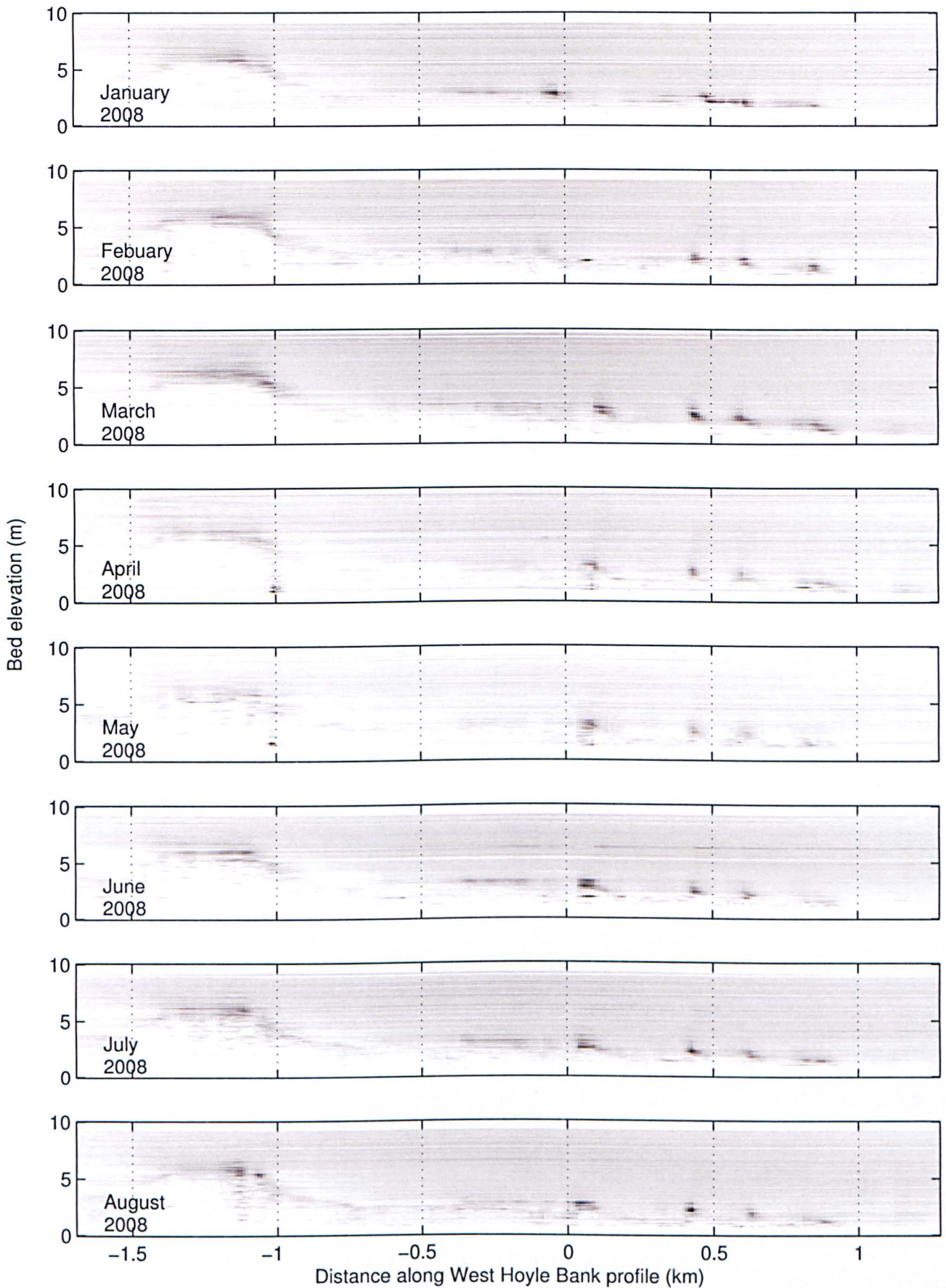
Figure 7.44: Waterline beach profiles through West Hoyle Bank for all available jpg data from January 2008 to August 2008.
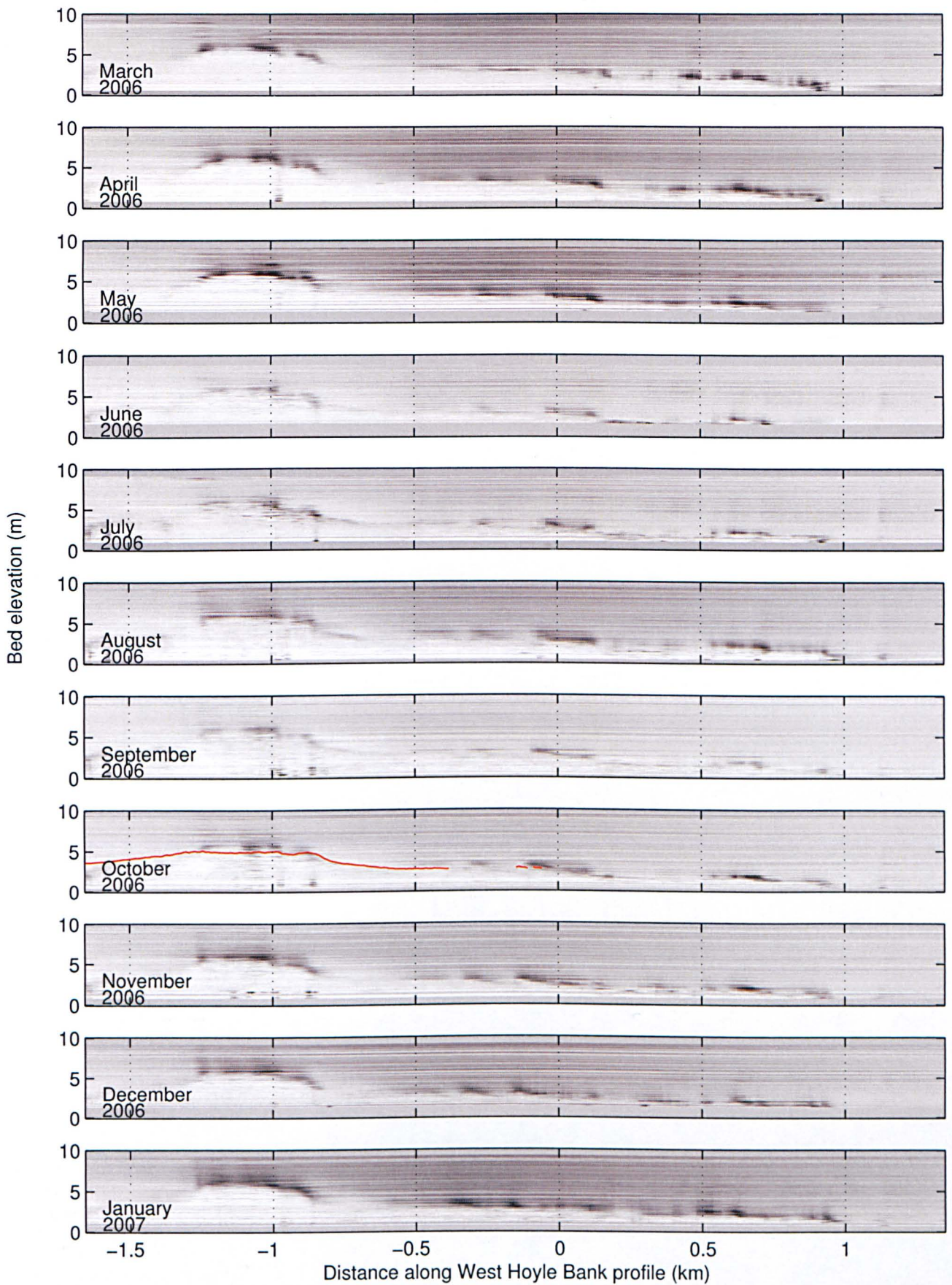
Figure 7.45: Waterline beach profiles through West Hoyle Bank for all available mat data from March 2006 to January 2007. The red line overlain onto the October 2006 waterline image is the Lidar elevation taken along an identical profile.

Figure 7.45 shows monthly waterline images for March 2006 to January 2007 created using the mat radar data. While the West Hoyle Bank waterline images contain less bed forms than the West Kirby Sands waterline images (Figure 7.37), a large bed form is visible at approximately 0.3km along the profile, which can be seen to migrate towards the left of the Figure (onshore) over the time period of August to November 2006 (Figure 7.46).
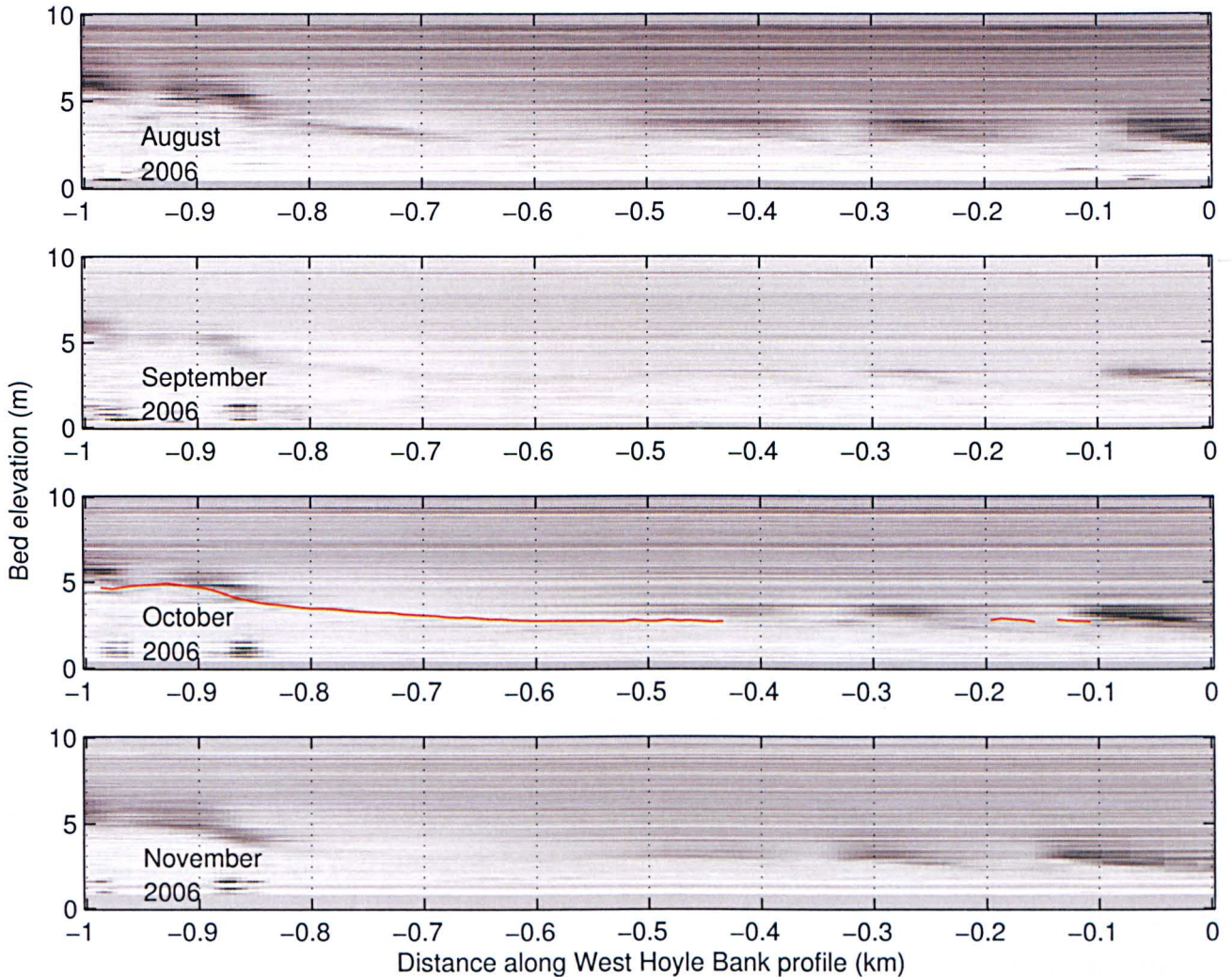
Figure 7.46: Waterline beach profiles through West Hoyle Bank for all available mat data from August 2006 to November 2006, focusing on the dune field to show the migration of wave breaker patterns. The red line overlain onto the October 2006 waterline image is the Lidar elevation taken along an identical profile.

7.7   Waterline image edge detection

Defining the sea bed in waterline beach profile images would allow individual bed forms to be identified so that their movement could be quantified between monthly waterline images. Various attempts

were made to apply edge detection algorithms to the waterline beach profile images using Matlab's 'edge' function, where the 'canny' method was applied, with limited success (Figure 7.47).This did not detect the bed elevation boundary seen in the waterline images from the peak in radar backscatter intensity at West Kirby Sands (Figures 7.29 & 7.30) and West Hoyle Bank (Figures 7.39 & 7.40). Instead the 'canny' algorithm appears to detect the change in pixel intensity between radar data at each elevation, shown by the horizontal lines in Figure 7.47. Therefore an alternative edge detection algorithm was developed to detect this peak in radar backscatter intensity so that a quantitative assessment could be made of morphological change using the waterline beach profile images at West Kirby Sands and West Hoyle Bank.
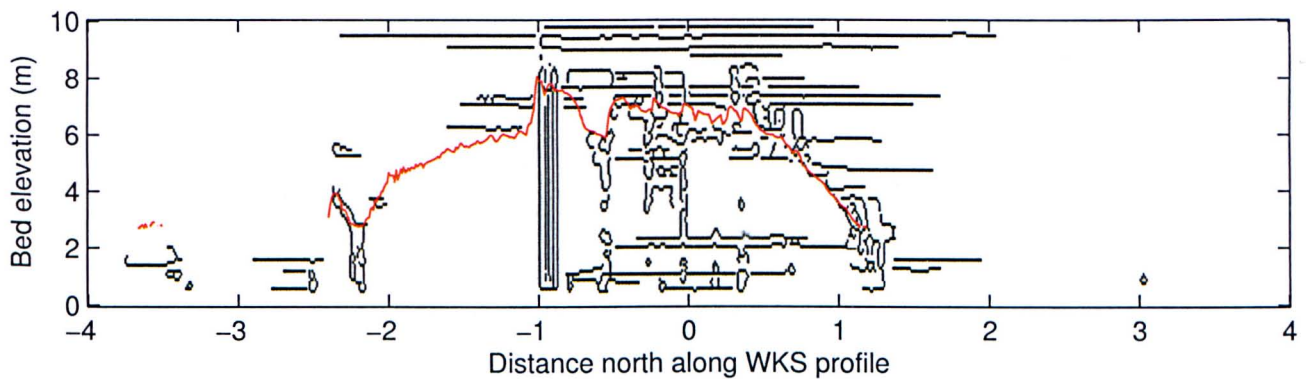
Figure 7.47: Matlab's canny edge detection applied to West Kirby Sands October 2006 waterline image. The red line represents the Lidar elevation extracted along the West Kirby Sands profile. This method of edge detection does not produce any useful results, leading to the development of an edge detection algorithm specifically design for the waterline images.

The waterline image edge detection algorithm was designed to detect the large change in radar backscatter intensity at the bed elevation level. Figure 7.48 shows a vertical profile of radar backscatter intensity extracted from the October 2006 jpg waterline image. The water surface can be identified as the spike in radar intensity to approximately 192. The radar backscatter intensity is smoothed so that a turning points algorithm can be applied to identify peaks and troughs in the backscatter intensity. The greatest difference between trough and peak backscatter values is found so that the increase in radar backscatter intensity at the bed elevation can be identified. A percentile value of the location along this increase in backscatter intensity is extracted which corresponds with the actual bed elevation from the October 2006 Lidar survey. The position of this percentile value along the original vertical profile of radar backscatter intensity is then identified as the edge detection backscatter intensity level to be used for determining the bed elevation along the waterline beach profile. Figure 7.48 shows the position of the detected edge (green square) to correspond with the Lidar elevation and backscatter intensity for an identical position along the October 2006 West Kirby Sands waterline

image profile.
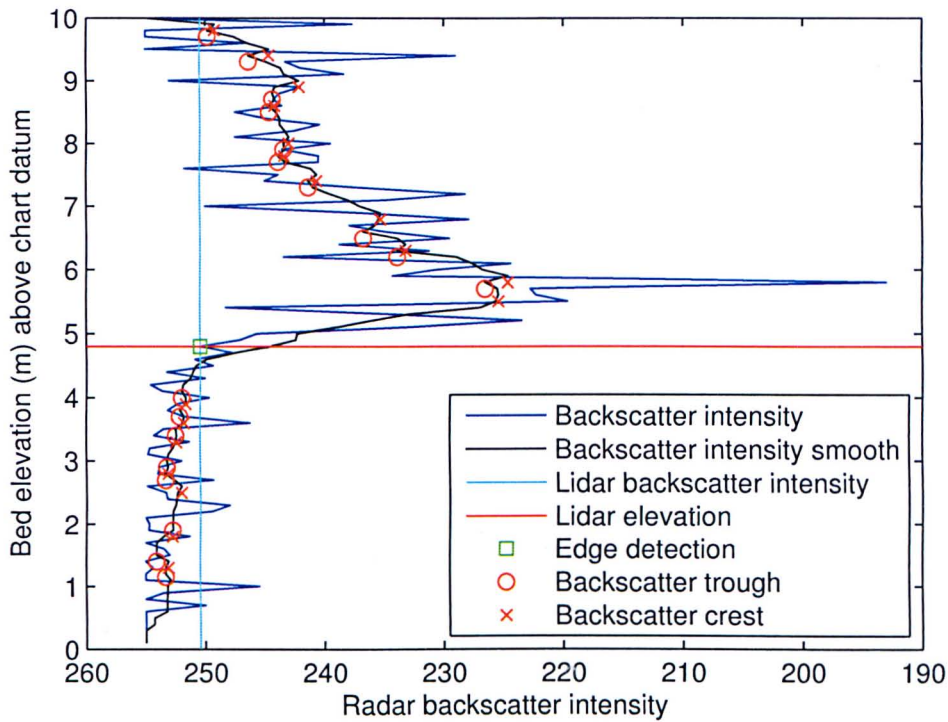
Figure 7.48: Radar backscatter intensity extracted along the West Kirby Sands waterline beach profile. The position of the edge detection (green square) on the radar backscatter intensity can be seen to correspond with the Lidar elevation and Lidar backscatter intensity.

This edge detection algorithm is then applied to the beach slope and dune field for the October 2006 West Kirby Sands waterline image, so that a profile is extracted at each iteration along the profile and the position of the bed is determined using a percentile value between the greatest difference in backscatter intensity. The level of the bed derived from the October 2006 waterline image can be seen to be in close agreement with the Lidar elevation initial beach slope before the dune field, at 0.5 to 0.9km north along the West Kirby Sands beach profile (Figure 7.49). However, image derived bed level does not accurately represent the dunes along the West Kirby Sands profile. This is due to the variation in radar backscatter intensity along the waterline profile caused by waves breaking over the undulating topography creating a variation in radar backscatter return. It is this variation in return, or wave breaker patterns, which are tracked using the 2-D cross correlation algorithm. Further complications are created by the seasonal variation in radar backscatter intensity, as this causes the threshold percentile value used to determine the backscatter intensity of the bed elevation to change from month to month. This problem could potentially be overcome with further ground survey data to validate the radar data. Unfortunately only historic radar data are available as the radar installation at Hilbre Island is no longer in use. For these reasons this waterline edge detection algorithm was

not applied to the entire radar data set. The 'waterline method' which has been applied here shows potential to be used as a tool for detecting beach profiles on a broad scale, however the low resolution produced from using hourly mean radar images is probably limiting its success. The application of this method to mean radar images created from 10-20 minutes worth of data with tidal elevation data for corresponding times could increase the definition of the 'waterline' signal.
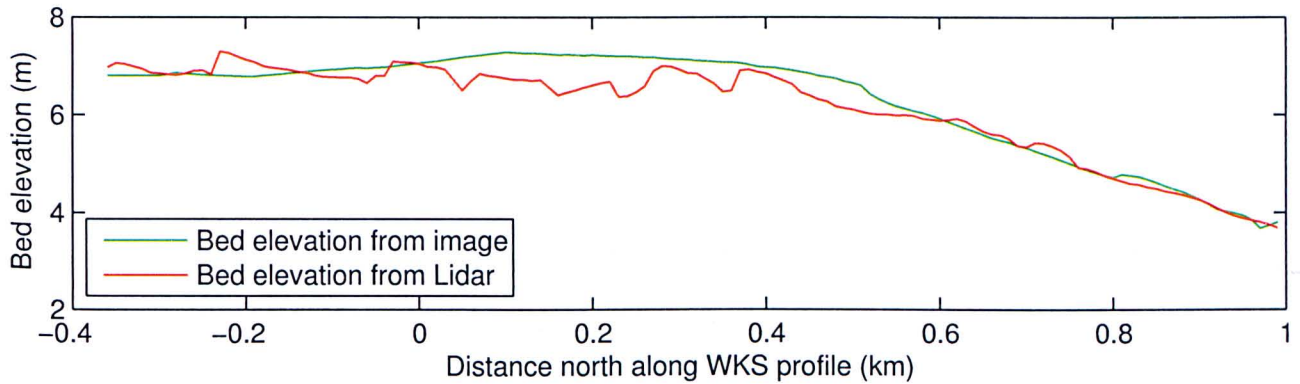
Figure 7.49: Waterline edge detection algorithm applied to the October 2006 jpg waterline image. The Lidar elevation is overlain (red line) for comparison with the image derived bed elevation (green line). Unfortunately the prevalence of noise over the dune field make it hard to determine the elevation of bed forms.

7.8 Summary

The monthly mean radar images created using all available jpg and mat data show the presence of wave breaker patterns over West Kirby Sands and West Hoyle Bank (Figures 7.2 - 7.5). There is a noticeable increase in image quality in the mat over the jpg radar images when comparing the West Kirby Sands and West Hoyle Bank image crops. This is partly due to the increased resolution of 5m in the mat radar data compared with 10m in the jpg data. However, there is also an image quality enhancement due to the loss of compression artifacts which are present in the jpg data but not in the mat data and are caused by the loss of data during compression for storage, resulting in the loss of edge clarity (Section 6.4). The position of these breaker patterns can be seen to change over the monthly period for both the jpg and mat data.

Quarterly profiles of radar backscatter intensity taken through West Kirby Sands and West Hoyle Bank (Figure 7.10) show the wave breaker patterns seen in the monthly mean images as peaks in radar backscatter intensity. These peaks can be seen to correspond with the underlying dune fields at West Kirby Sands (Figure 7.11 A & 7.12 A) and West Hoyle Bank (Figure 7.11 B & 7.12 B). The

position of these crests can be seen to migrate onshore (Figures 7.13 - 7.20), moving from the right to the left in these plots, giving a firm indication that large scale bed forms are migrating into the estuary.

A 2-D cross correlation algorithm has been applied to the monthly mean radar images to track the movement of the breaker patterns and therefore quantify the migration of the underlying dune field. The migration at both West Kirby Sands and West Hoyle Bank increased in the winter months with significant peaks in migration occurring from October 2006 to February 2007 and from October 2007 to March 2008. West Hoyle Bank experienced significantly larger migrations, up to 50% greater than West Kirby Sands, during these periods of enhanced activity (Figure 7.21) which occurred at times of increased wave height (Figure 7.22). Figure 4.19 shows the area of West Hoyle Bank to have a greater exposure to waves than West Kirby Sands, which could explain the increased migration. The correlation of increased migration with greater wave heights can be seen when migrations are plotted against wave heights (Figure 7.23) at both West Kirby Sands and West Hoyle Bank and for both the jpg and mat radar data. Figure 7.23 also highlights the significance of using a 2-D cross correlation technique with the radar data as a significant amount of the migrations calculated are less than the distance of one pixel and so would not be noticed if a non statistical method was used. Figure 7.24 shows yearly average migration vectors for West Kirby Sands and West Hoyle Bank. This shows that there is a net onshore migration calculated by the 2-D cross correlation algorithm which is generally of larger magnitude at West Hoyle Bank than at West Kirby Sands. A good comparison can be made between the migration from the 2-D cross correlation algorithm and migrations observed in the backscatter intensity profiles, with the cross correlation method having much lower standard errors (Table 7.4). Migration values have also been used with bed form dimensions to calculate the sediment flux per unit length associated with dune migration (Table 7.5). Yearly average dune migration rates were greater at West Kirby Sands in 2006 and 2007, but greater at West Hoyle Bank in 2008.

The waterline beach profiles generated using jpg and mat radar data have focused on vertical slices through the topography at West Kirby Sands and West Hoyle Bank. Peaks in backscatter intensity can be seen along the waterline profiles as darker areas above the approximate bed elevation. These correspond to the wave breaker patterns tracked with the 2-D cross correlation algorithm which are shown to occur immediately prior to the dune crests (Figures 7.11 & 7.12). Analysis of the waterline images shows the undulating topography of the dune fields on West Kirby Sands (Figures 7.32 - 7.36) and West Hoyle Bank (Figures 7.41 - 7.45) with peaks in radar backscatter above these large scale bed forms. The approximate Lidar elevation of the bed can be seen to correspond well with a peak in the radar backscatter when sampling multiple dune points along West Kirby Sands and West Hoyle Bank

for both the jpg and mat radar data (Figures 7.29, 7.30, 7.39 & 7.40). Unfortunately the waterline images suffer from a large amount of image noise inherent in the X-band radar data. An attempt was made to use the maximum return radar images (Figure 7.31), however the radar backscatter return from moving objects and rain events make these images impractical for application of the waterline method. The variation in radar backscatter return, which changes with the underlying topography along the waterline profile, and the addition of image noise, make defining the bed elevation using edge detection unfeasible. Attempts at using Matlab's 'edge' function were unsuccessful (Figure 7.47), whilst using a threshold value of radar backscatter intensity to determine the bed elevation (Figure 7.48) only produced a reasonable correlation with Lidar data on West Kirby Sands beach slope (Figure 7.49). This method was not applied to the entire radar data set due to its inability to determine the bed elevation over the dune field.

Chapter 8

West Kirby Sands: bed forms and morphology

8.1 DGPS survey of West Kirby Sands

A field work campaign was undertaken at West Kirby Sands to get a better understanding of the processes effecting sediment transport and bed form migration on the intertidal sand flats in the mouth of the Dee Estuary. Topographic surveys were conducted over the dune field at West Kirby Sands which is accessible at low tide from the north west tip of the Wirral peninsula (Figure 8.1).
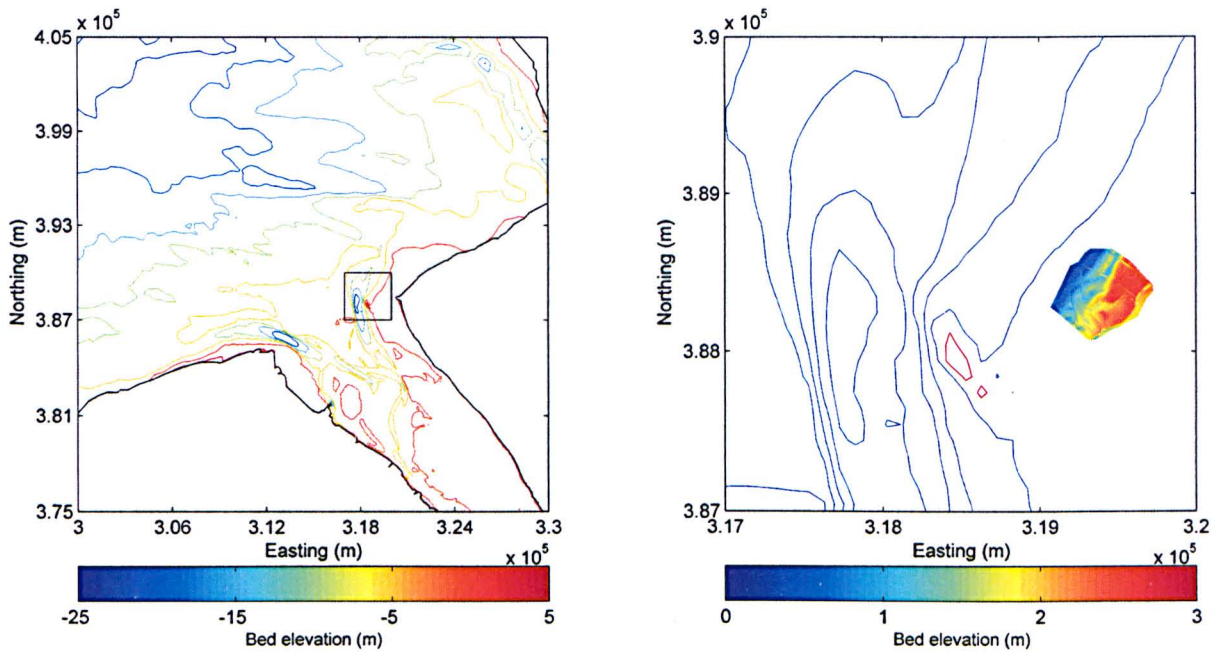
Figure 8.1: The location of the total area surveyed during the field work campaign on West Kirby Sands. The box outlined (left image) indicates the position of the sub-plot (right image) in relation to the Dee Estuary as a whole.

Over the course of two weeks bed elevation surveys were conducted at West Kirby Sands using a Leica 1200 RTK GPS system on four separate occasions; 28.01.11, 31.01.11, 08.02.11 and 11.02.11 using the method outlined in Section 3.2. The data from these surveys are interpolated over a grid with Matlab using the maximum distance surveyed in the x (east) and y (north) directions for the grid size for all surveys, so that the data are plotted over an identical set of coordinates for ease of comparison (Figure 8.2).
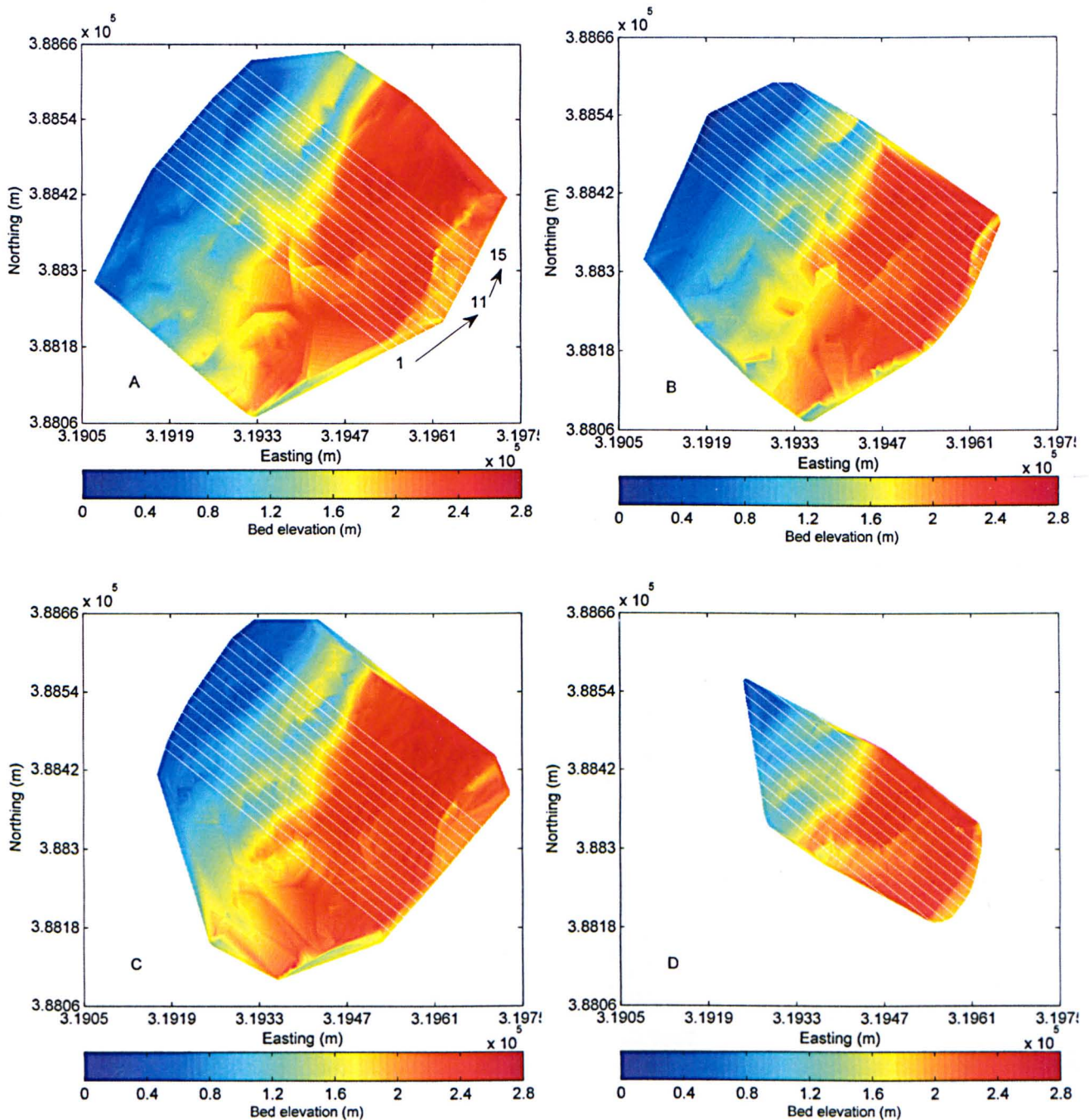
Figure 8.2: Interpolated bathymetry for all of the DGPS surveys of West Kirby Sands covering a two week period; A.) 28.01.11 B.) 31.01.11 C.) 08.02.11 D.) 11.02.11. Overlain as white dashed lines are profiles 1 to 15 (shown on A) which are used to extract bathymetric data for further analysis

Figure 8.2 shows the survey areas for 28.01.11 to 08.02.11 to be relatively similar, covering an area of West Kirby Sands which has an undulating topography superimposed on the general trend of the mean sloping bathymetry. The final survey, conducted on the 11.02.11, covers a smaller total survey area. This is due to the problems with the instrument occurring during the survey, resulting in the survey having to be terminated early with less data collected. The open sea boundary in all of the plots is

218

to the north west while the sand flats are to the south east. At each elevation data point recorded by the DGPS system an error value is also recorded. Figure 8.3 shows the error values for each survey. While there is some variation for the 08.02.11 and 11.02.11 surveys, the mean error values are all less than or equal to 0.0050m.
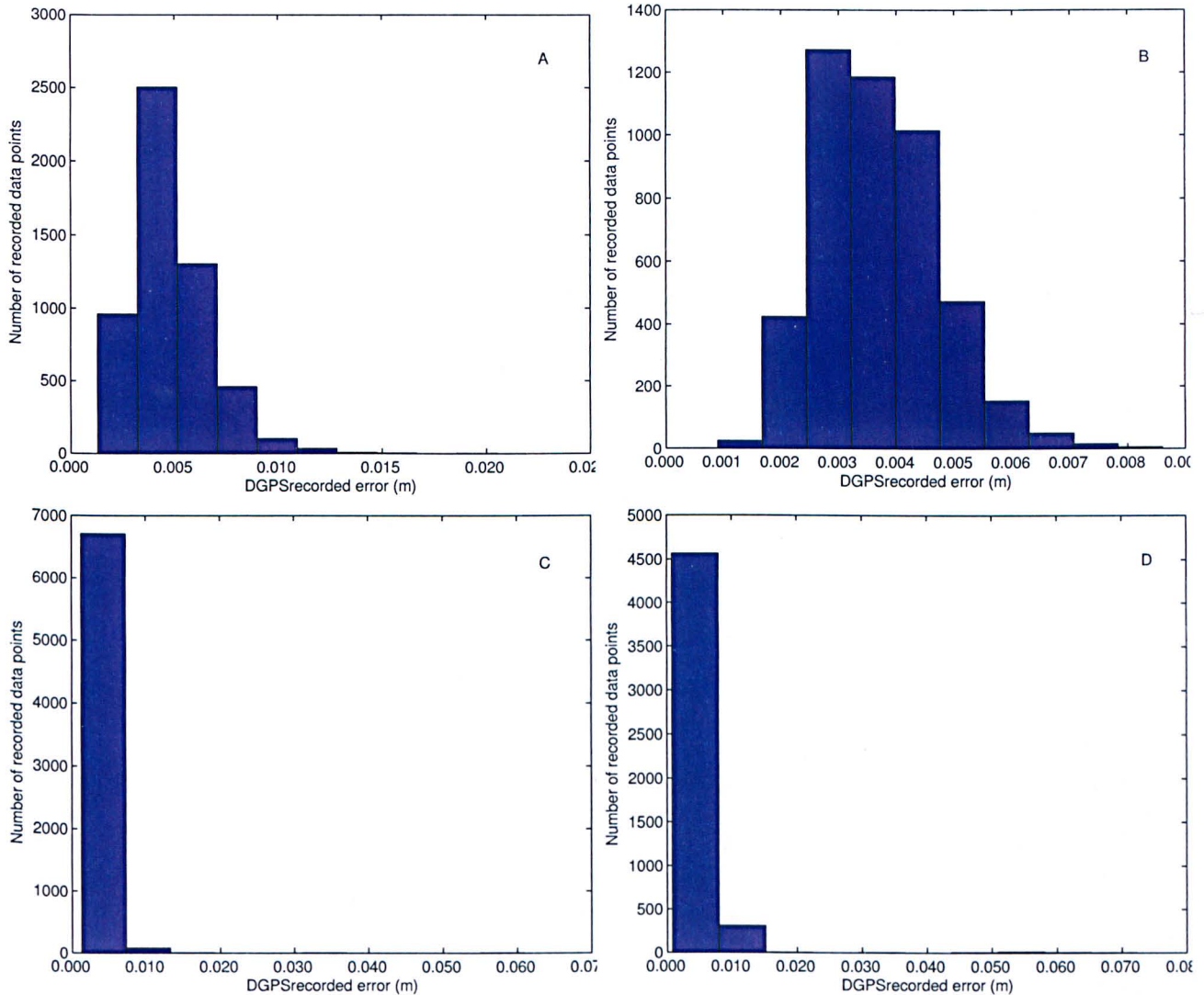
Figure 8.3: Recorded error values for all of the DGPS surveys of West Kirby Sands covering a two week period; A.) 28.01.11 B.) 31.01.11 C.) 08.02.11 D.) 11.02.11.

Two bed forms are immediately obvious from the survey data. The first is a small dune feature to the north of plots A to C; the bathymetry can be seen to decrease through a dune trough before increasing in elevation over a much larger sand dune towards the south east. Overlain as white lines in Figure 8.2 are eleven profile lines common to each survey area (Figure 8.2 A) which were used to examine the dunes surveyed on West Kirby Sands in cross section. A further four profile lines continuing north east were applied to the survey data excluding the final survey of 11.02.01 due to lack of data available. There is a 2.5m spacing between successive profile lines which were chosen

to run approximately perpendicular through the dune crests. This profile spacing and orientation was chosen so that change in bed form size and location could be determined over the total survey area, without being too computationally demanding. The length of the profiles are determined by simple geometry and then the elevation data extracted at an equal spacing of 10cm and interpolated onto the profile length using Matlab. A similar process has been repeated to extract the coordinates along each profile to determine a common x-axis for profiles 1-15. This allows a direct comparison between individual profiles on each of the survey dates. The extracted elevation data along the profile length varies between survey dates, but covers approximately 40 to 50m for surveys A to C (28.01.11 to 08.02.11). Profile lengths are shorter for the 11.02.11 survey due to the smaller area surveyed on this date. Figures 8.4 to 8.6 show the beach slope of West Kirby Sands, for three selected profiles, with the open sea boundary to the right of the plot and the sand flats to the left. The remaining profiles can be found in Appendix IV. These profiles display an undulating topography with the presence of large scale bed forms along their length. These bed forms are later identified and dimensions determined for bed form classification.
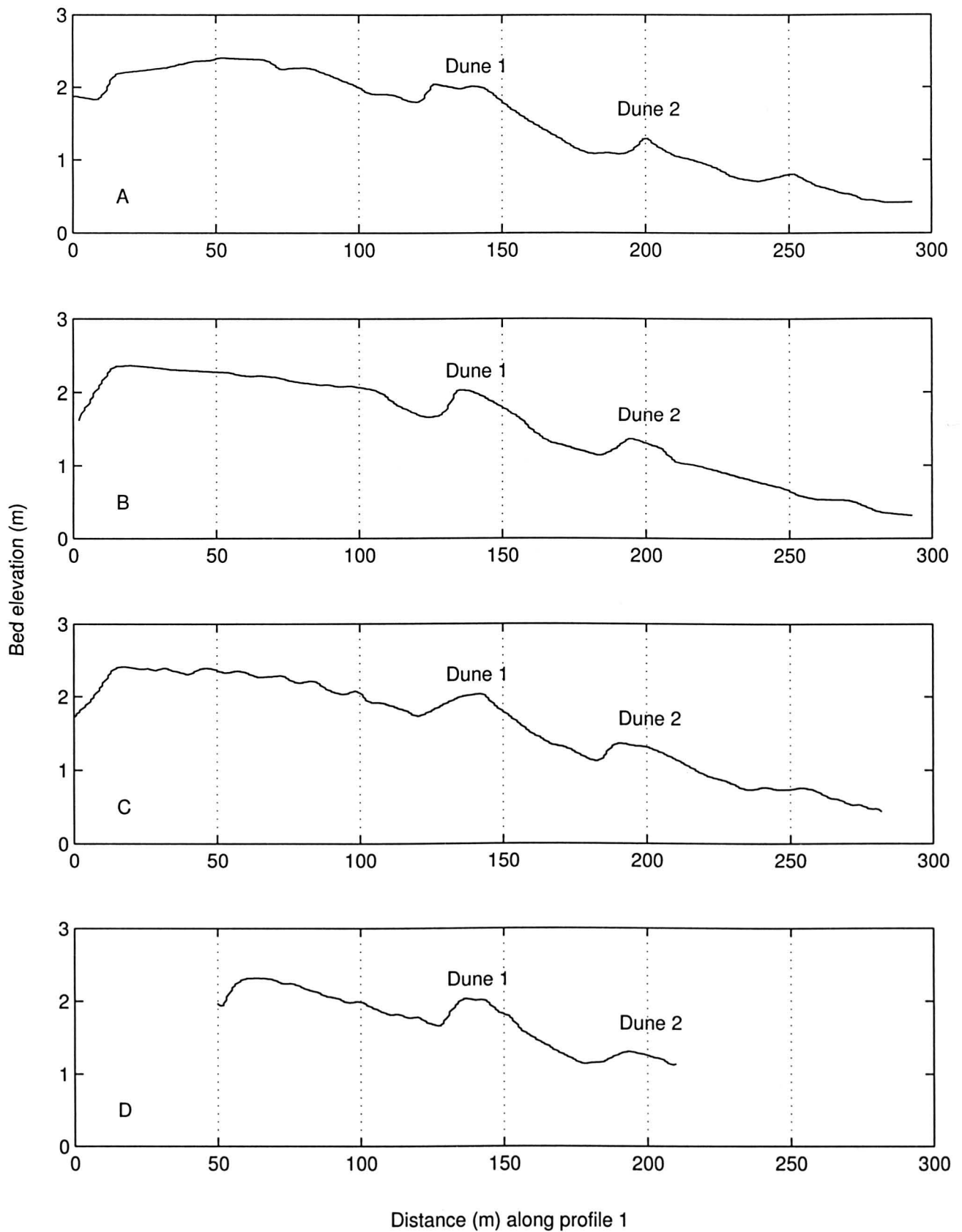
Figure 8.4: Bed elevation profile along profile 1 for all West Kirby Sands survey data A) 28.01.11 B) 31.01.11 C) 08.02.11 D) 11.02.11.

Distance (m) along profile 5
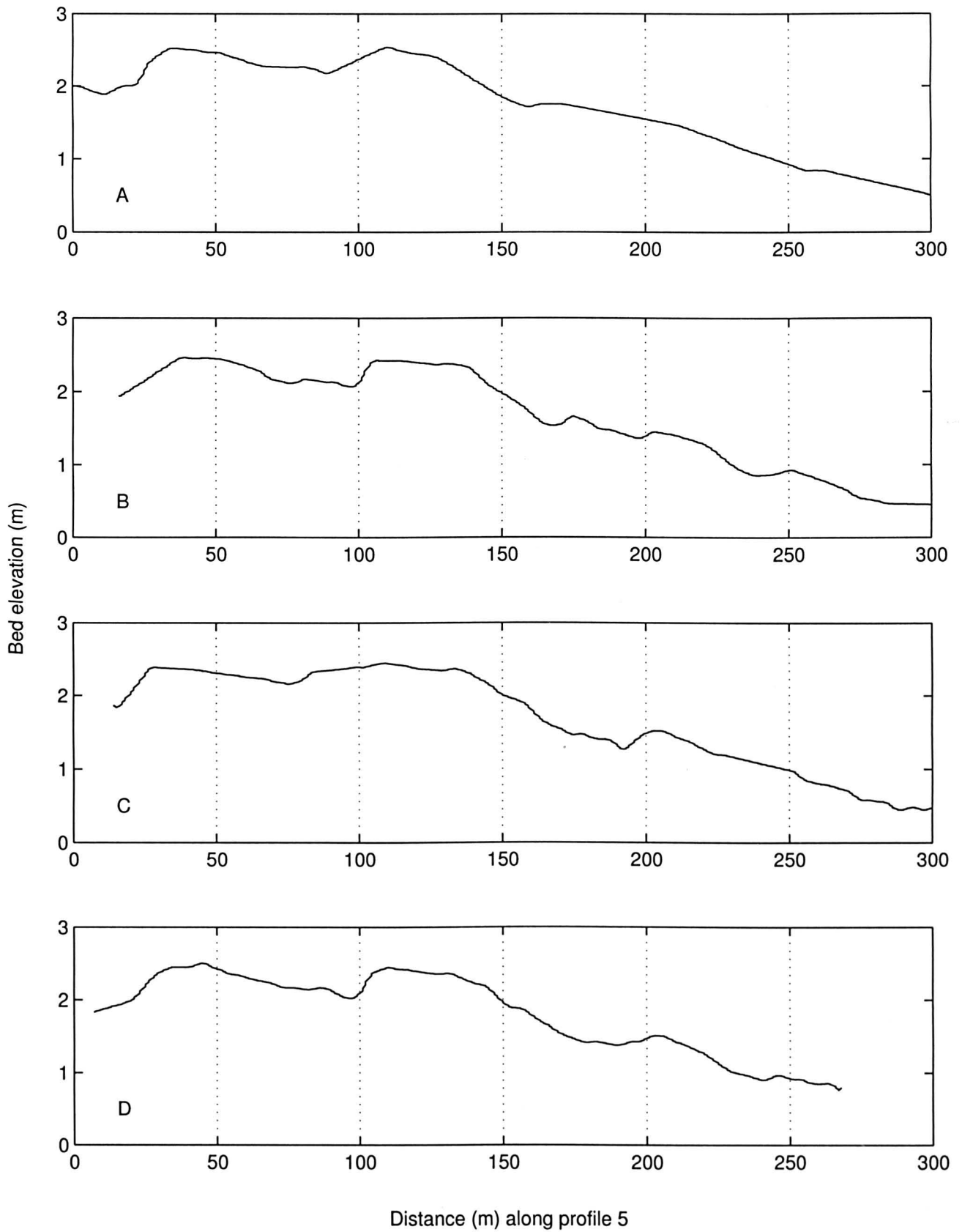
Figure 8.5: Bed elevation profile along profile 5 for all West Kirby Sands survey data A) 28.01.11 B) 31.01.11 C) 08.02.11 D) 11.02.11.
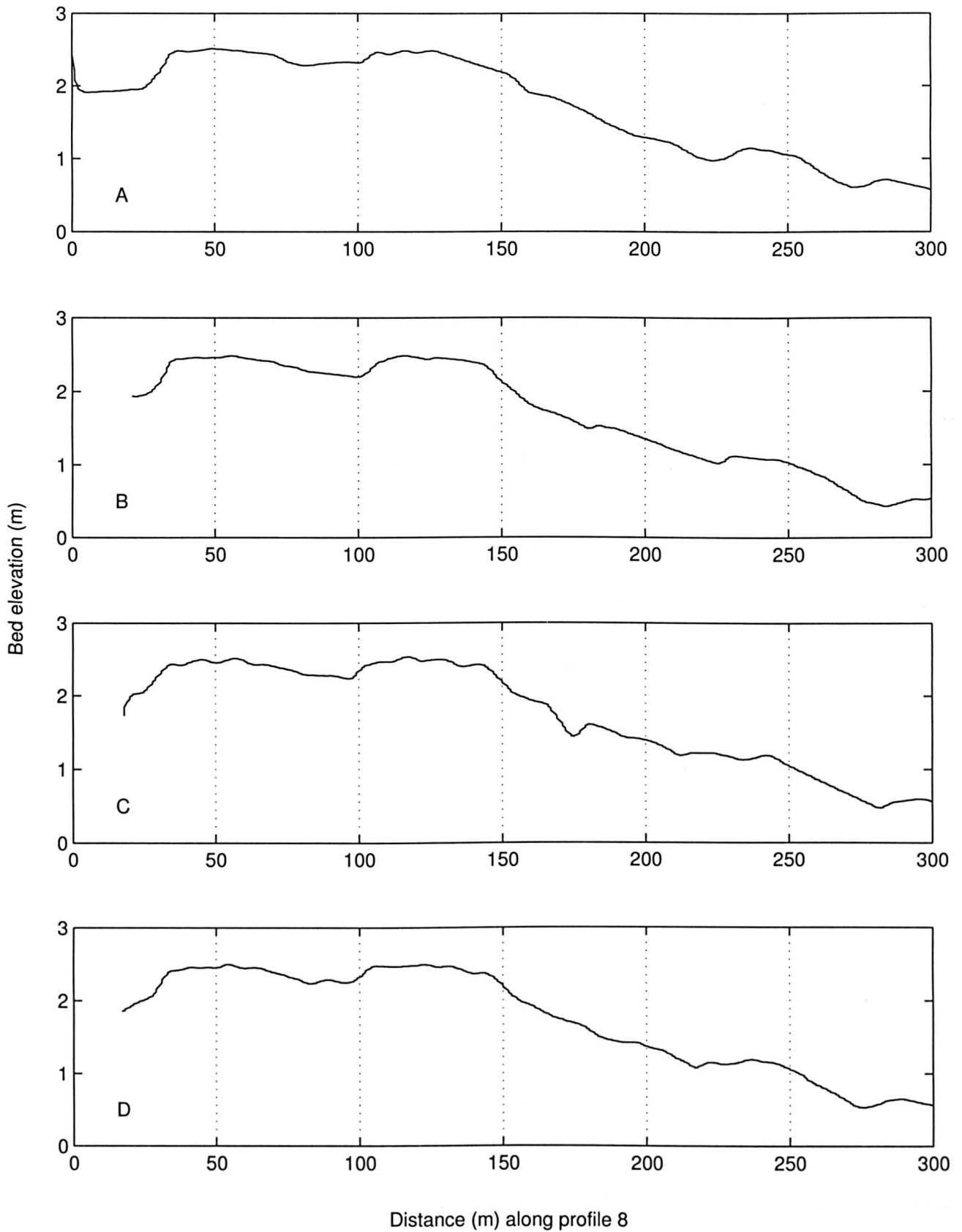
Figure 8.6: Bed elevation profile along profile 8 for all West Kirby Sands survey data A) 28.01.11 B) 31.01.11 C) 08.02.11 D) 11.02.11.

8.2 Identifying bed forms from survey data

A total of sixty six profile lines were extracted from the survey data. A turning points algorithm was then applied to these profiles to identify the coordinates of bed form crests and troughs. Figure 8.7 shows an example of a profile taken through the West Kirby Sands survey data with positions of bed form crests and troughs identified using the turning points algorithm.

8.2.1 Turning point algorithm
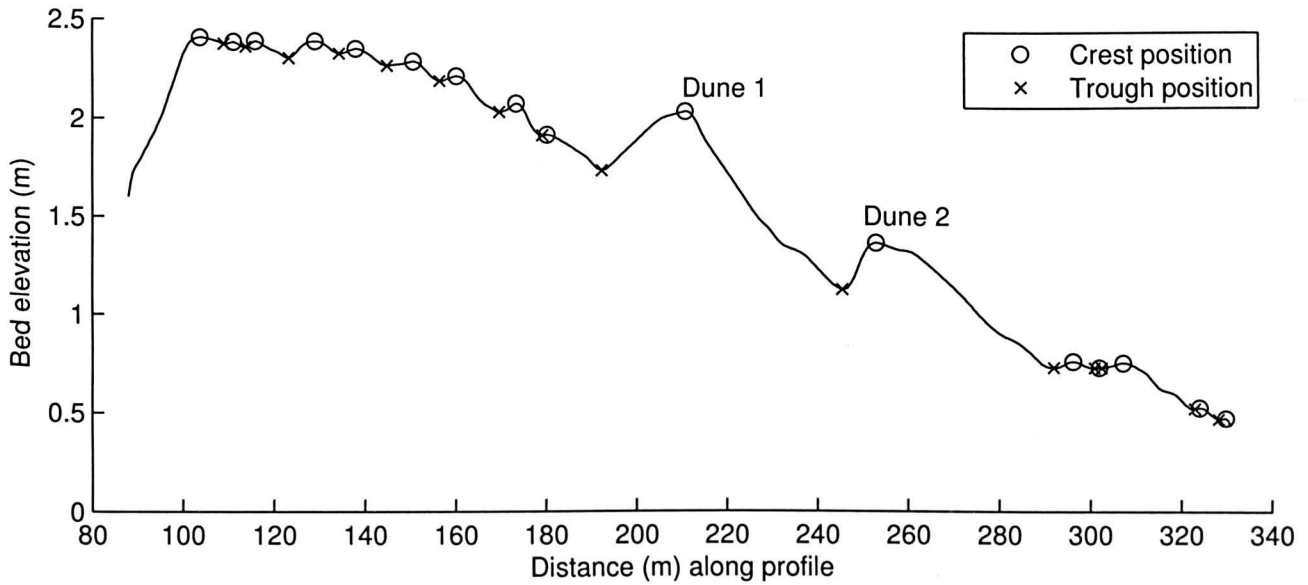
Figure 8.7: Profile 1 extracted from 08.02.11 West Kirby Sands DGPS survey data. The profile was chosen to run perpendicular to bed form crests. A turning points algorithm has been applied to this profile to identify bed form crests (circles) and troughs (crosses).

The turning points algorithm identifies the positions of bed form crests and troughs by calculating the gradient along the profile $(Z_b(i=1), Z_b(i=2), ..., Z_b(n))$ so that the forward and backwards profile gradients $(\triangle\vec{Z}_b$ and $\triangle\overleftarrow{Z}_b)$ are calculated as

$$\triangle\vec{Z}_b = \frac{Z_b(i+1) - Z_b(i)}{x(i+1) - x(i)} \qquad \triangle\overleftarrow{Z}_b = \frac{Z_b(i-1) - Z_b(i)}{x(i-1) - x(i)} \tag{8.1}$$

Crest positions are identified when $\triangle\vec{Z}_b < 0$ and $\triangle\overleftarrow{Z}_b > 0$ while trough positions correspond to $\triangle\vec{Z}_b > 0$ and $\triangle\overleftarrow{Z}_b < 0$ (Figure 8.7). It is possible to determine the bed form length λ and height η from the position of two troughs and an intervening crest. The distance between two trough points is calculated to be λ, assuming that the bed forms are long crested and two dimensional in plan form.

To account for the effect of bed slope, causing the true ground distance to be greater than the distance between the two trough x coordinates, the bed form length was calculated by a line connecting both trough points. A perpendicular line to that between the two trough points and connecting to the intervening crest point has been used to determine the bed form height η (Figure 8.8).
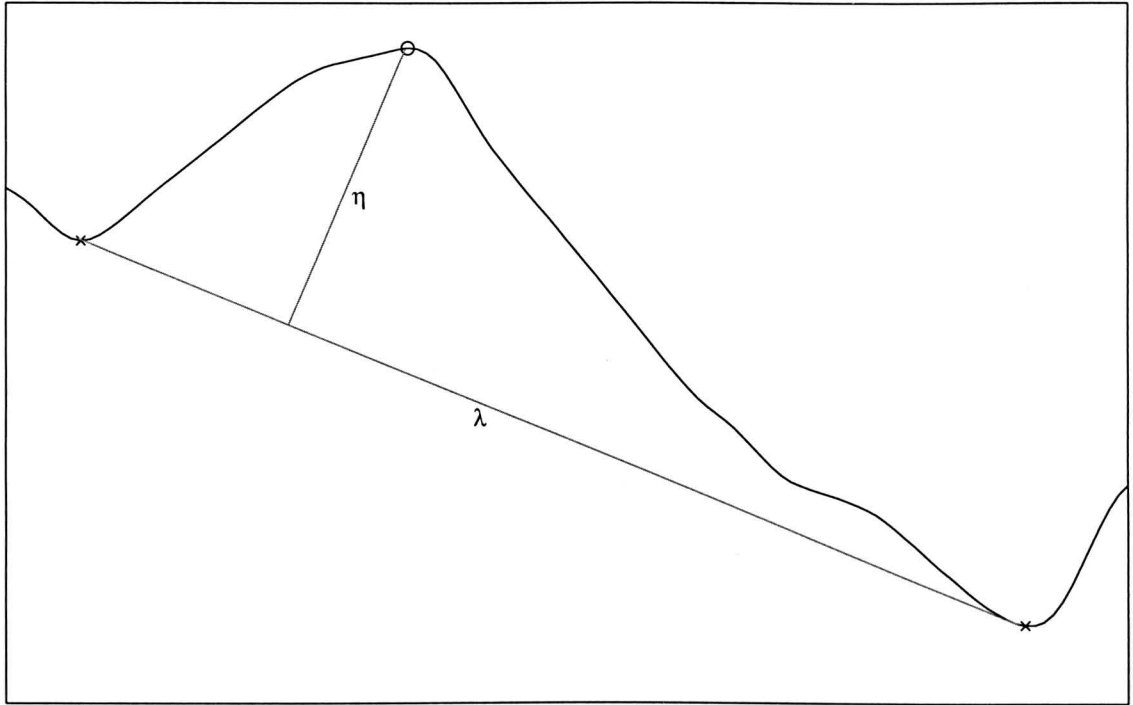
Figure 8.8: Example of a bed form on the sloping bed at West Kirby Sands. Bed form length λ is calculated from a line connecting two trough points and height η is taken from a line perpendicular to this from the crest point.

In Figures 8.4 to 8.6 the open sea boundary is to the right of the plots while the sand flats are to the left. Two large sand dunes are visible from these beach profiles, labelled as Dune 1 and Dune 2 in Figure 8.4 A. Not all of the profiles show both of these bed forms clearly, due to slight lateral change in bed form dimensions and loss of data when interpolating over the 2D mesh (Figure 8.2). A total of thirty two bed form dimensions were calculated for Dune 1 while twenty measurements were made for Dune 2, across the 15 profiles. This gives an average dune length λ_d 53.49m ±3.36m for dune 1 and 41.14m ±4.76m for Dune 2 and average dune heights η_d of 0.60m ±0.04m for dune 1 and 0.67m ±0.02m for Dune 2. The mean cross sectional areas for Dunes 1 and 2, calculated between each trough point identified from the turning points algorithm, are 56.72 ±2.23m^2 and 120.29 ±9.32m^2. These two dunes identified on West Kirby Sands from the DGPS survey data are low profile bed forms, with similar dune heights but with long wavelengths for which, the pre-averaged individual

estimates, are greater for Dune 2 than for Dune 1. This greater mean dune length means that the mean dune cross sectional area for Dune 2 is 52% larger than Dune 1 (Table 8.1). Calculating the cross sectional area for Dunes 1 and 2 should show any change in dune size (area) between surveys, which would suggest the movement of sediment through this region with times of erosion (loss of area) and deposition (increase in area). A comparison of the difference in mean area for each of the surveys (Table 8.2) shows that there is an initial loss in dune area for Dunes 1 and 2 between 28.01.11 and 31.01.11. This is then followed by a significant increase in dune area between 31.01.11 and 08.02.11 before decreasing again from 08.02.11 to 11.02.11.

Dune area (m^2)	A	B	C	D
Dune 1	56.52	54.85	59.66	50.76
Dune 2	119.36	114.71	139.92	107.37

Table 8.1: Mean dune area (m^2) calculated for dunes 1 and 2 identified from the DGPS survey data between survey dates 28.01.11 (A), 31.01.11(B), 08.02.11 (C) and 11.02.11 (D).

Dune area (m^2)	A-B	B-C	C-D
Dune 1	-1.67	4.81	-8.90
Dune 2	-4.65	25.21	-32.56

Table 8.2: Difference in mean dune area (m^2) for dunes 1 and 2 between survey dates 28.01.11-31.01.11 (A-B), 31.01.11-08.02.11 (B-C), 08.02.11-11.02.11 (C-D) and 28.01.11-11.02.11 (A-D).

8.2.2 Bed form classification

In tidal estuaries the frequently observed larger bed forms are asymmetric mega-ripples and sand dunes (van Rijn, 2007b). van Rijn (2007b) relates the length scale of dunes to the water depth h so that dune wavelength λ_d is in the range of 3-15 h. A water depth of 2.5m is extracted at the DGPS survey site (Figure 8.1) from TELEMAC tidal simulations (Figure 4.11), at the time of peak scalar velocity. This gives an expected dune wavelength in the range of 7.5-37.5m, with the mean wavelength values observed in the survey data being in agreement with the top end of this range, affirming the notion that the large scale bed forms present on West Kirby Sands are sand dunes.

Figures 8.4 to 8.6 show these bed forms to be distinctly asymmetrical in shape with short and steep downstream (lee) slope compared with the longer and shallower upstream (stoss) slope. One way to

assess the asymmetry of bed forms is the 'modified symmetry index' (MSI=[(stoss side length/ lee side length)-1]; Allen, 1968). Large tidal dunes have been found to have an MSI of around 4 (Mosher and Thomson, 2000). The mean MSI values for Dunes 1 and 2 from this survey are 5.18 ±0.31 and 4.57 ±0.51, indicating that they are strongly asymmetric as an MSI of 0 would represent perfect symmetry. The crest position for both dunes surveyed can be seen to be offset in the landward direction, to the left of Figures 8.4 to 8.6. This orientation of asymmetry has been well documented to represent the direction of bed form migration, with bed forms migrating in the direction of the shortest (lee) slope (Van Den Berg, 1987; Nielsen, 1992; Hoekstra et al., 2004). Therefore the orientation of the large scale bed forms seen in the DGPS survey profiles at West Kirby Sands suggest that they are migrating in an onshore direction.

Survey data from 08.02.11 and 11.02.11 show evidence of smaller bed forms landwards of Dune 1. Figure 8.7 shows the crest and trough positions of these smaller bed forms identified using the turning points algorithm, from which bed form dimensions can be determined. These bed features are much smaller bed forms than the two dunes previously examined, with an average length λ_r of 1.13m ±0.08m, average height η of 0.06m ±0.006m and an average area of 25.23m^2 ±1.82m. The smaller size of these bed forms suggests that they are ripples, albeit fairly large ripples with wavelengths λ_r of nearly 2m, and so may be classed as megaripples. The average MSI value for all ripples measured from the profiles comes to 0.46 ±0.19, indicating that they are only slightly asymmetric. This suggests these large ripple features, which are predominantly visible in the 08.02.11 survey data, are the product of wave action where the more symmetric form is caused by the oscillatory wave motion. van Rijn (2007b) stated that megaripples have a height 0.03-0.1 times the water depth h and a length scale of the order of the water depth. A water depth of 2.5m, at the time of peak current velocity, used previously for dune classification is the same order of magnitude as the bed form wavelength and gives a predicted megaripple height of 0.075-0.25m. This suggests that these bed forms, which are larger than ripples but smaller than dunes, can be classed as mega-ripples.

8.2.3 Bed form migration from DGPS data

The strongly asymmetric shape of the dunes shown by their high MSI values, which are skewed in a landward direction indicates that these bed forms are migrating onto the sand flats. It is possible to track the migration of bed form crests between survey dates along the length of the profiles. The

migration distance of dune crests between surveys is used to calculate the mean migration rates per tide for Dunes 1 and 2 (Table 8.3) by taking into account the number of tides between successive surveys. Assuming that the tidal period at Hilbre Island is the same as the principal lunar tide (12.42 hours), then there are 1.93 tides per day.

V_{mig} (m tide^{-1})	A-B	B-C	C-D	A-D	Std Err
Dune 1	-0.008	0.026	-0.011	0.009	0.003
Dune 2	-0.022	0.046	-0.012	0.090	0.012

Table 8.3: Mean dune migration rates V_{mig} per tide (m tide^{-1}) calculated from dune crest migration for dunes 1 and 2 between survey dates 28.01.11-31.01.11 (A-B), 31.01.11-08.02.11 (B-C), 08.02.11-11.02.11 (C-D) and 28.01.11-11.02.11 (A-D). The position of dune crests are located using the turning points algorithm.

The crest migration per tide for Dunes 1 and 2 is significantly greater between surveys B and C (31.01.11 and 08.02.11), than between surveys A and B (28.01.11-31.01.11) and C and D (08.02.11-11.02.11). The direction of bed form migration is onshore between surveys B and C (31.01.11 and 08.02.11), denoted by positive crest migration values, while negative crest migration between surveys A and B (28.01.11-31.01.11) and C and D (08.02.11-11.02.11) represents offshore migration. The rates calculated from the migration of the dune crests are larger for Dune 2 compared with Dune 1, with the net migration (A and D) of Dune 2 between the first and last survey being an order of magnitude larger than Dune 1.

Bed form crest migration distance can be used to provide a method of estimating the bed load transport rate (Soulsby, 1997) using knowledge of the bed form dimensions and bed form migration velocity. The volumetric sediment transport associated with the celerity of bed forms (q_c) per unit width and time, including the voids between individual grains, is the product of dune cross sectional area (A_d) and dune celerity (V_{mig}) divided by the dune length (λ_d). The transport rate per unit crest length of an assumed triangular bed form of height η can be calculated by (Van Den Berg, 1987)

$$q_c = \frac{V_{mig}}{\lambda_d} A_d = \frac{V_{mig}}{\lambda_d} 0.5 \lambda_d \eta = 0.5 \eta V_{mig} \tag{8.2}$$

When Equation 8.2 is expressed in terms of dry weight of the sediment being transported it becomes

$$q_c = 0.5 \rho_s (1 - \varepsilon) \eta V_{mig} \tag{8.3}$$

where ρ_s is the sediment density and ε is the porosity. This does, however, assume that the bed form shape does not change from a triangular shape. Inaccuracies also arise from the area below the wake behind dunes which experiences negligible net bed-load transport (Engel and Lam Lau, 1981). Therefore only the part of the dune cross sectional area above the point of flow re-attachment should be included when calculating the bed load transport (Van Den Berg, 1987). The use of the numerical coefficient 0.5 implies that the bed form under consideration is triangular in form when viewed in cross section, parallel to the downstream direction of migration. Subsequent studies (Kostaschuk et al., 1989; Villard and Church, 2003; Gaeuman and Jacobson, 2007) have shown that the use of a shape coefficient β accounts for the deviation of bed form shape from an idealised triangle. The migration of dunes could also be effected by suspension of bed material at the dune front and settling of suspended grains in the wake behind the dune. Taking this into consideration and including the shape coefficient β, the bed load transport per unit width q_b is calculated by

$$q_b = \rho_s(1 - \varepsilon)\beta \eta V_{mig} \qquad (8.4)$$

Van Den Berg (1987) reviews appropriate β values from several previous authors, finding that a β value of 0.6 provides the best agreement. Masselink et al. (2009) use a factor a_m to account for the dune shape and porosity when converting dune migration rates to volumetric transport rate in the shallow mixed tide and wave dominated Avon Estuary, so that

$$q_b = a_m \eta V_{mig} \qquad (8.5)$$

A range of values for a_m (0.2-0.37) have been quoted in the literature (Van Den Berg, 1987; Hoekstra et al., 2004), here a value of 0.32 will be used (Soulsby, 1997). The mean dune heights η obtained from the turning points algorithm previously are used to obtain the volumetric transport in m^2 tide^{-1} (Table 8.4).

q_b (m^2 tide^{-1})	A-B	B-C	C-D	A-D	Std Err
Dune 1	0.0015	0.0050	0.0002	0.0017	0.0042
Dune 2	0.0047	0.0099	0.0026	0.0024	0.0022

Table 8.4: Volumetric bed load transport rate (m^2 tide^{-1}) calculated from the dune migration rates for dunes 1 and 2 between survey dates 28.01.11-31.01.11 (A-B), 31.01.11-08.02.11 (B-C), 08.02.11-11.02.11 (C-D) and 28.01.11-11.02.11 (A-D).

This method of estimating bed load requires the determination of bed form crest and trough position, in this case using a turning points algorithm, which was shown to define primary peaks and troughs with reasonable confidence. However, this relies on the need to identify and correlate individual dunes for the local analysis. Bed load computations were not attempted in cases where there was uncertain dune morphology between paired profiles.

Table 8.4 shows that greater volumetric bed load transport rates are seen for Dune 2 than for Dune 1. Both dunes display greatest bed load transport rates per tide between 31.01.11 and 08.02.11. This increase is likely to be caused by a change in the local sea state and is explored further in the following sections.

Equation 8.5 relies on the assumption that all mobile sediment moves over the bed form, up the stoss face, down the lee face before coming to rest in the bed form trough. In essence, it assumes that the individual sediment grains are linked to a particular bed form. However, not all sediment will come to rest in the bed form trough, instead it may continue to move along the bed or be carried into suspension. For these reasons bed load transport rates calculated from the migration of bed forms in this way may underestimate the true magnitude of bed load transport by up to a factor of two (Soulsby et al., 1993). Using a_m in Equation 8.5 to calculate the bed load transport assumes that the migrating bed forms maintain a constant shape between successive surveys. An analysis of the bed form area from profiles 1-11 and for surveys A-D shows that dune area increased during the 08.02.11 survey for both dunes 1 and 2. This increase in dune area corresponds with the increase in volumetric bed load transport observed between 31.01.11 and 08.02.11 (Table 8.4).

As a first step to better understanding the erosion and deposition occurring between paired profiles, where a sequence of bed forms can not be reliably identified across profiles, the difference in bed elevation must be considered along the entire profile length. At each point along the paired profiles, the bed elevation from the later survey ($z_{x,t2}$) is subtracted from the elevation of the earlier survey ($z_{x,t1}$) to produce δz_x. Erosion is recorded where δz_x is positive, while deposition occurs where δz_x is negative. Figure 8.9 shows a profile pair from survey A (28.01.11 t1) and survey B (31.01.11 t2). The red shaded areas represent regions where erosion has taken place and the blue shaded regions represent deposition. This poses the question of how these changes in bed level can be interpreted as a sediment transport rate representative of the profile as a whole.
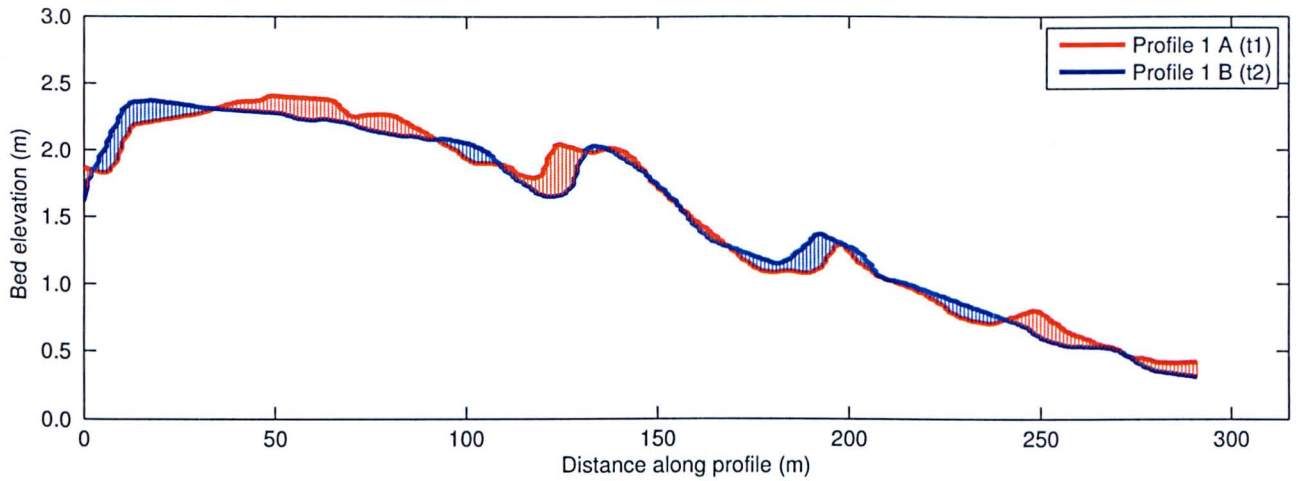
Figure 8.9: Paired bathymetric profiles displaying regions of erosion (red shading) and deposition (blue shading) determined from the difference in bed elevation δz between $z_{x,t2}$ and $z_{x,t1}$.

8.2.4 Exner equation

Changes in bathymetry due to flow induced sediment transport processes can be described using the sediment conservation equation (Equation 8.6). This allows a calculation of sediment transport to be made which does not rely on the shape of the bed form migrating, but describes the conservation of mass between sediment in the bed and sediment that is being transported. It states that bed elevation increases, with bed accumulation, proportional to the amount of sediment that falls out of transport, and conversely decreases, with bed erosion, proportional to the amount of sediment that is entrained by the flow. However, this does only consider the along profile bed load transport, and as such may suffer from the same under estimation as the volumetric bed load transport calculated earlier. The standard form of the Exner equation for bed sediment continuity (Fredsoe and Deigaard, 1992) in one dimension can be written in the form

$$\frac{\partial Z_b}{\partial t} = -\left(\frac{1}{1-\varepsilon}\right)\frac{\partial q_b}{\partial x} \tag{8.6}$$

where ε is the bed porosity, Z_b denotes the bed elevation, t the time, x the distance and q_b the volume transport rate of bed material load per unit width. If $\frac{\partial z}{\partial t}$ is positive then accretion occurs, while if $\frac{\partial z}{\partial t}$ is negative then erosion occurs. This equation can be written alternatively

$$(1-\varepsilon)\frac{\partial Z_b}{\partial t} + \frac{\partial q_b}{\partial x} = 0 \tag{8.7}$$

and then integrated to obtain the volumetric bed load transport q_b along the profile $(x(i = 1), x(i = 2), ..., x(n))$ such that

$$q_{b_x} = -(1 - \varepsilon) \int_{x_1}^{x} \frac{\partial z}{\partial t} \partial x \tag{8.8}$$

This method implements an approach in which the local volumetric bed load flux per unit bed width at any point along the profile is related to the upstream volume of eroded material. Figure 8.10 shows a schematic diagram to explain how the change in bed level relates to the bed continuity equation (Equation 8.8) integrated along the bed profile. Suppose in discretised form, the bed elevation changes as shown in Figure 8.10, over a period t with no sediment input/output at either end of the profile.
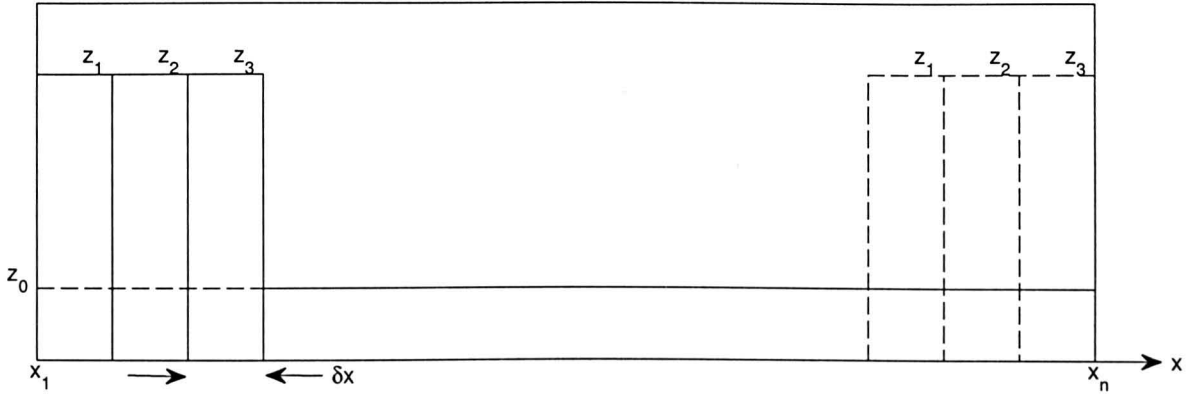
Figure 8.10: An idealised diagram showing change in bed elevation z over time t along a bed profile in the direction x. The three 'columns' of sediment depicted by the solid rectangular lines migrate to the right and are found in the positions shown by the dashed rectangular lines at time t. It should be noted that there is no through flow of sediment in this idealised example.

Integrating from the left of Figure 8.10 $(x = x_1)$ then

$$q_{x_2} = -(1 - \varepsilon) \left(\frac{z_0 - z_1}{t} \right) \delta x \quad (> 0) \tag{8.9}$$

$$q_{x_3} = -(1 - \varepsilon) \left\{ \frac{z_0 - z_1}{t} + \frac{z_0 - z_2}{t} \right\} \delta x \tag{8.10}$$

$$q_{x_4} = -(1 - \varepsilon) \left\{ \frac{z_0 - z_1}{t} + \frac{z_0 - z_2}{t} + \frac{z_0 - z_3}{t} \right\} \delta x \tag{8.11}$$

The positive amount of transport found at x_4 remains constant along the central section of Figure 8.10

where no change in bed elevation occurs. Then, towards the right end of this idealised profile the local transport decreases as follows

$$q_{x_{n-2}} = -(1-\varepsilon)\left\{\frac{z_0 - z_1}{t} + \frac{z_0 - z_2}{t} + \frac{z_0 - z_3}{t} + \frac{z_1 - z_0}{t}\right\}$$

(8.12)

$$q_{x_{n-1}} = -(1-\varepsilon)\left\{\frac{z_0 - z_2}{t} + \frac{z_0 - z_3}{t} + \frac{z_2 - z_0}{t}\right\}$$

(8.13)

$$q_{x_n} = -(1-\varepsilon)\left\{\frac{z_0 - z_3}{t} + \frac{z_3 - z_0}{t}\right\} = 0$$

(8.14)

In this initial simplified example, the zero on the right of Equation 8.14 arises because all of the sediment transport is within the range $[x_1, x_n]$, therefore there is no ambiguity at the end points of the idealised example. For illustrative purposes Equation 8.8 has initially been applied to an idealised bed form, which is symmetrical and triangular in shape with a 12m wavelength and 1.1m height, migrating along a profile (Figure 8.11). This idealised bed form migrates from its initial position as 'Dune 1' to its final position as 'Dune 6' in Figure 8.11. The volumetric bed load transport rate calculated per tide using Equation 8.8 can be seen to increase as the bed form migrates greater distances, until it reaches a maximum value and plateaus where the bed form has migrated a distance greater than one wavelength (Figure 8.12). As with the previous example (Figure 8.10) the transport remains constant where there is no change in bed elevation, in this case, when the idealised bed form migrates one full wavelength. As the bed form migrates along the profile (from left to right Figure 8.11) the bed level will increase, resulting in an increase in bed load transport (Figure 8.12). A greater amount of sediment is entering than exiting this point x_n along the idealised profile causing a net deposition of bed load. Again in this example there is no ambiguity at the end points of the profile where no transport occurs, as seen in Figure 8.12.
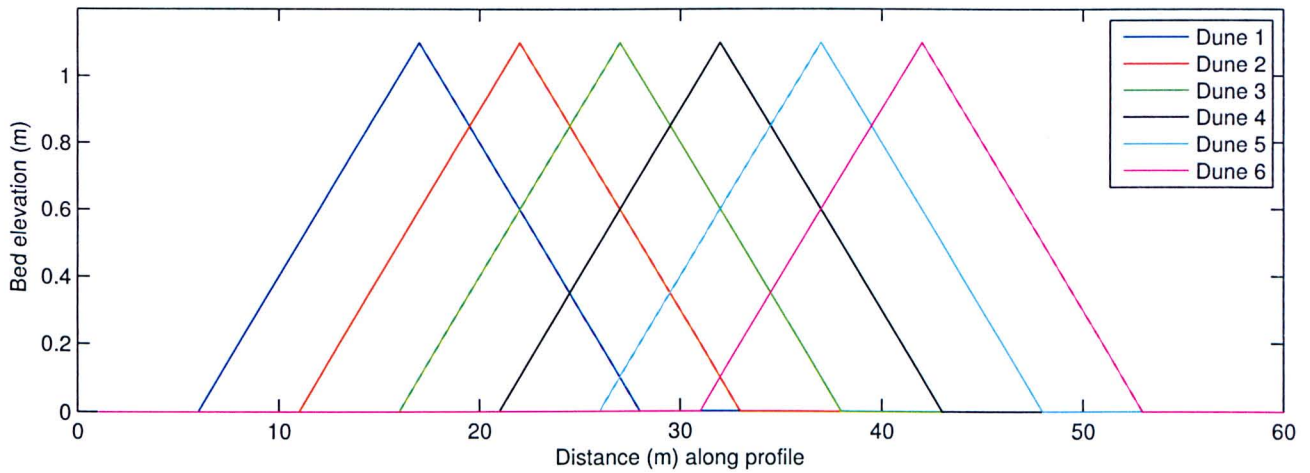
Figure 8.11: An idealised symmetrical triangular bed form migrating from the left to the right of the figure (Dune 1 - Dune 6) over a 24 hour period.
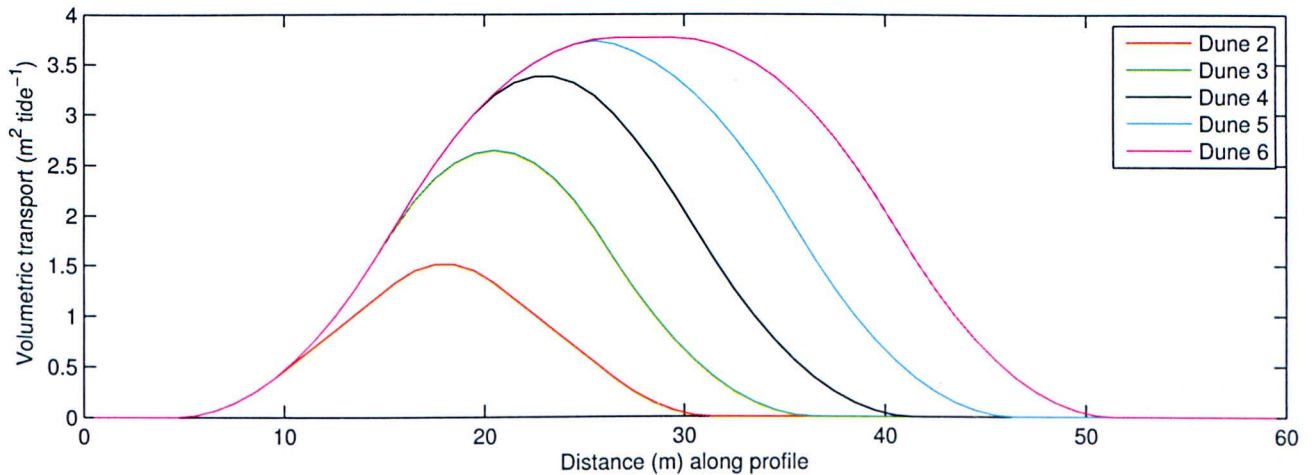
Figure 8.12: Volumetric transport implied by successive movements of the triangular bed form in Figure 8.11 and calculated by applying the bed continuity equation (Equation 8.8) to the migration of the (idealised symmetrical) triangular bed form.

The bed load transport calculated using the mass conservation technique (Equation 8.8) can be validated by calculating the volume moved when the idealised bed form migrates one complete wavelength. In this example the bed form wavelength λ and height η are 22m and 1.1m, calculating the area of the triangular bed form ($0.5\lambda\eta$) and applying a 1m profile width, gives a bed form volume v_i of 12.1m^3. Manually calculating this bed form volume migrating one wavelength over the period of one day the volumetric sediment transport per tide is simply given by

$$q_b = 0.5\eta \left(\frac{v_i}{t}\right) \tag{8.15}$$

234

where η is the bed form height and t, the number of tides in one day, is 1.93. This gives an ide-
alised bed form volumetric transport rate calculated manually (Equation 8.15) of 3.76m^{2}tide^{-1}. This
is equal to the transport calculated using Equation 8.8 for this idealised bed form migrating one wave-
length.

Figure 8.13 shows another idealised example, this time using a sine wave to represent a symmet-
rical dune field migrating along its axis from Dune 1 to Dune 6. The volumetric transport calculated
using the bed continuity equation (Equation 8.15) can be seen to oscillate along the profile length as
the sine wave migrates distances less than one wavelength. Peaks in the transport rate can be seen to
occur at the mid point between the original bed form crest position and its subsequent position. As
with the idealised triangular example (Figure 8.11) the transport rate tends towards a plateaux at a
maximum as the migration of Dune 6 approaches one bed form wavelength.
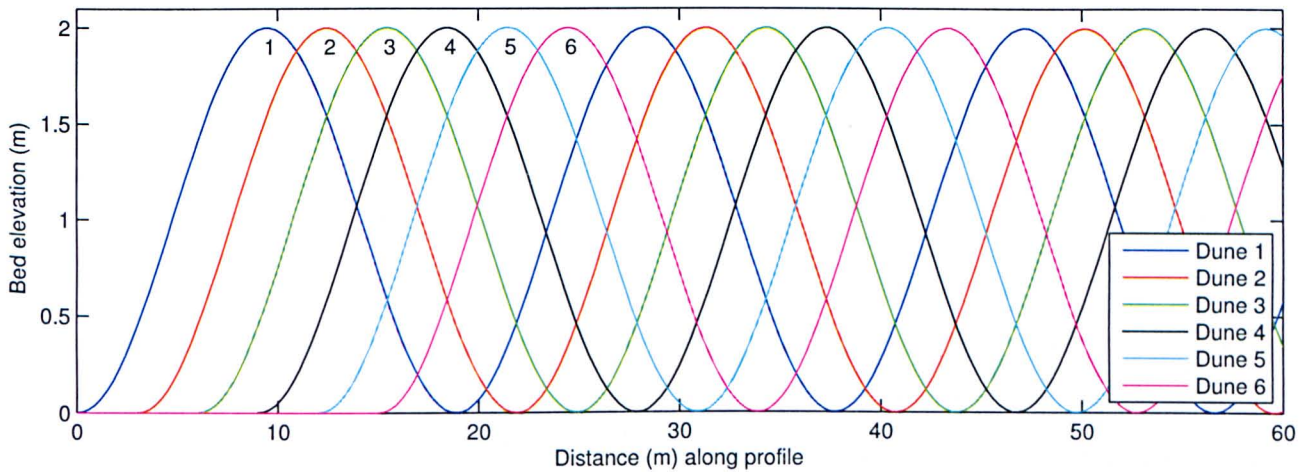
Figure 8.13: An idealised sinusoidal bed form migrating from the left to the right of the figure (Dune
1 - Dune 6) over a 24 hour period.
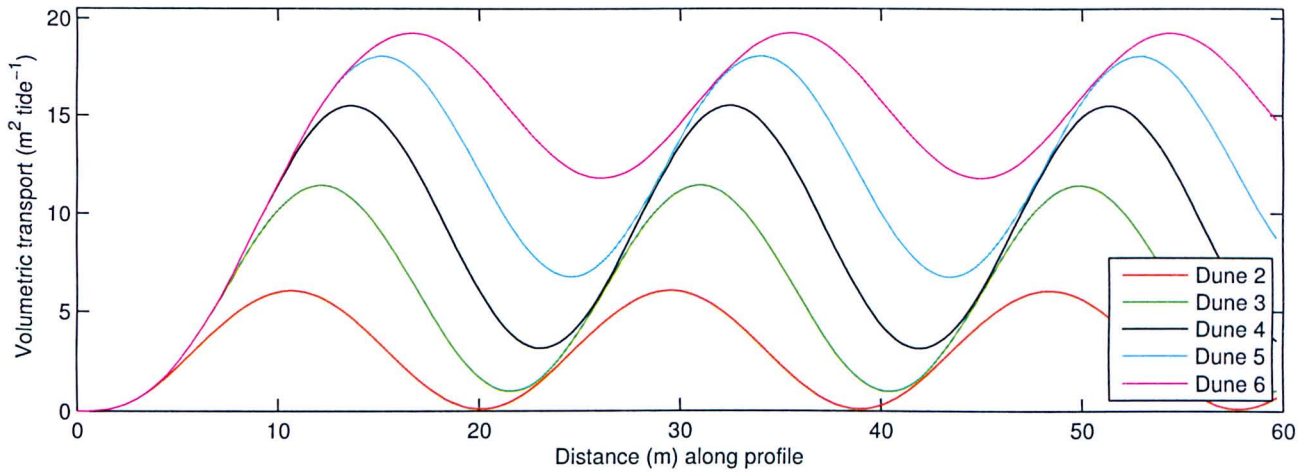
Figure 8.14: Volumetric transport implied by successive movements of the sinusoidal bed forms in Figure 8.13 and calculated by applying the bed continuity equation (Equation 8.8) to the migration of the idealised sinusoidal bed forms.

There are no bed forms to the left of Dune 1 in Figure 8.13, which is the reason why the transport is zero at $x = 0$ in Figure 8.14. This idealised example has been designed to avoid any ambiguity at $x = 0$. Using the Matlab function 'trapz' to calculate the area of one idealised sine wave bed form and assuming a 1m bed form width, the idealised sine wave bed form volume is 62.83m^3. Applying Equation 8.15 to manually calculate the transport rate over one wavelength for one day gives 19.53m^2 tide^{-1}, which is in agreement with that calculated using the bed continuity equation (Equation 8.8). Equation 8.8 has next been applied to profiles 1-15 from West Kirby Sands to determine the bed load transport per tide between surveys. This provides a more inclusive calculation of bed load transport than using the migration speed of bed forms as it is determined using the change in bed level over the entire profile. The volumetric bed load transport has been calculated by applying the Exner equation from the right, seaward, end of the profile to the left, landward end. The assumption was made that the dominant direction of sediment transport was in the landward direction due to the asymmetry of bed forms observed which were skewed in the landward direction, indicating their dominant direction of migration. The mass conservation equation has been integrated along the bed profile where each step represents approximately 0.5m. The profiles have been forced to be of equal length, using the coordinates along which each profile has been extracted, so that profile pairs are limited by the minimum profile extent from a central position. This is so that any disparity in profile length does not affect the sediment transport calculated from a comparison of two bed level heights between profile pairs. Ultimately this should show whether there was a net gain or loss of sediment at West Kirby Sands during the survey period and whether it was affected by locally changing hydrodynamic conditions. Unfortunately, the quantity of sediment transport at the open boundaries for each of the profiles is

an unknown. In an attempt to minimize this effect the ends of the profiles have been forced to have equal elevations for a distance of 1m, resulting in zero transport at the profile open boundaries. While this open boundary unknown may seem to represent a severe limitation of this method, the signal produced by the exner equation along the profile is a direct response to the change in bed elevation. Therefore, it was deemed a suitable method to apply to the DGPS survey profiles for determining the relative change in bed level and sediment transported between survey dates. The ambiguity in the method is that there may be a constant transport through the domain which this method does not detect.
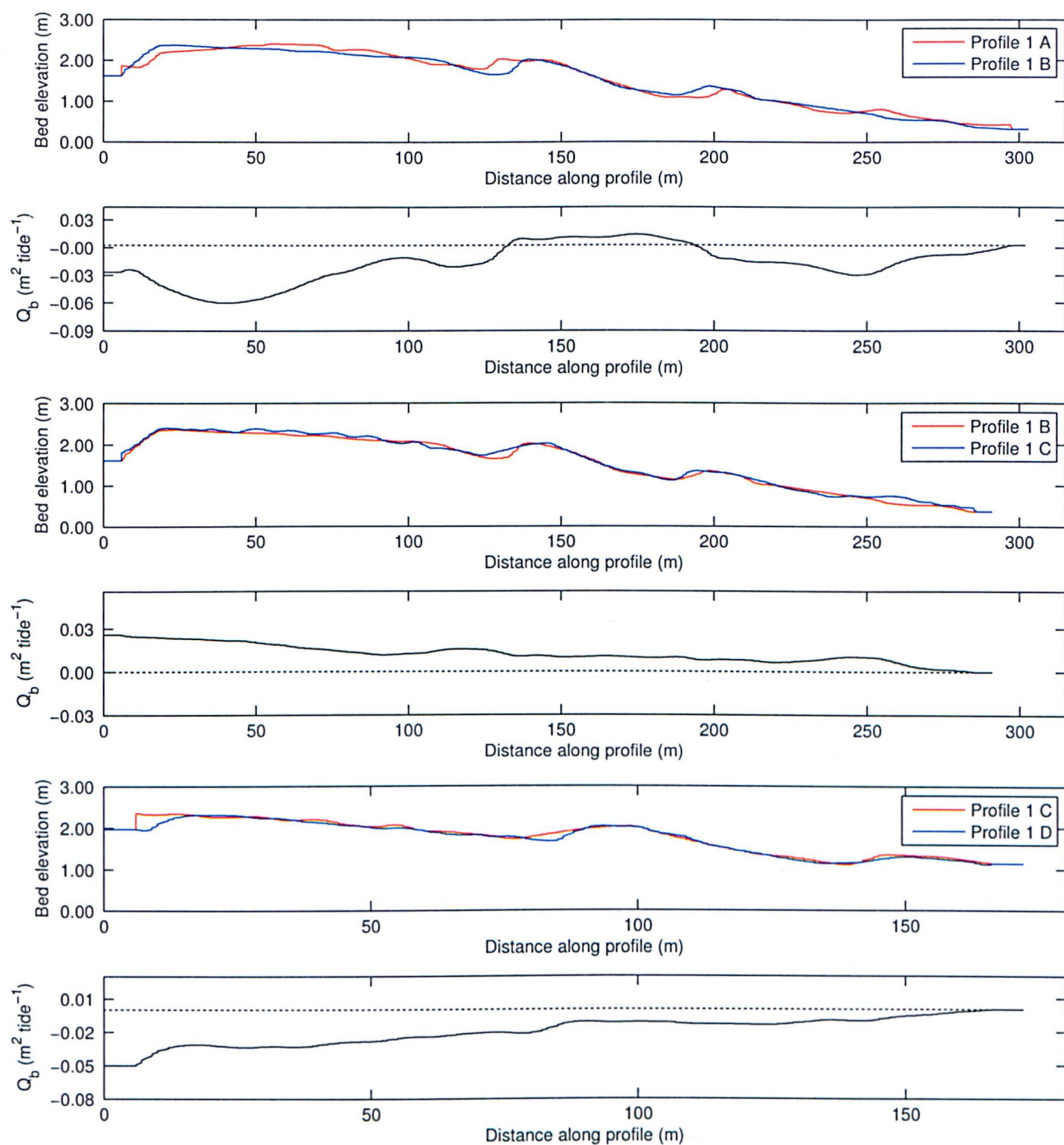
Figure 8.15: Bed elevation for paired profiles (profile 1) for A) 28.01.11, B) 31.01.11, C) 08.02.11 and D) 11.02.11 survey data. The respective profiles pairs have elevations set to the minimum value at both ends and profile lengths are equal as explained in the text. The volumetric transport rate (m^2 $tide^{-1}$) is calculated by integrating the bed continuity equation (Equation 8.8) from the right of the Figure (open sea boundary) to the left (sand flats).
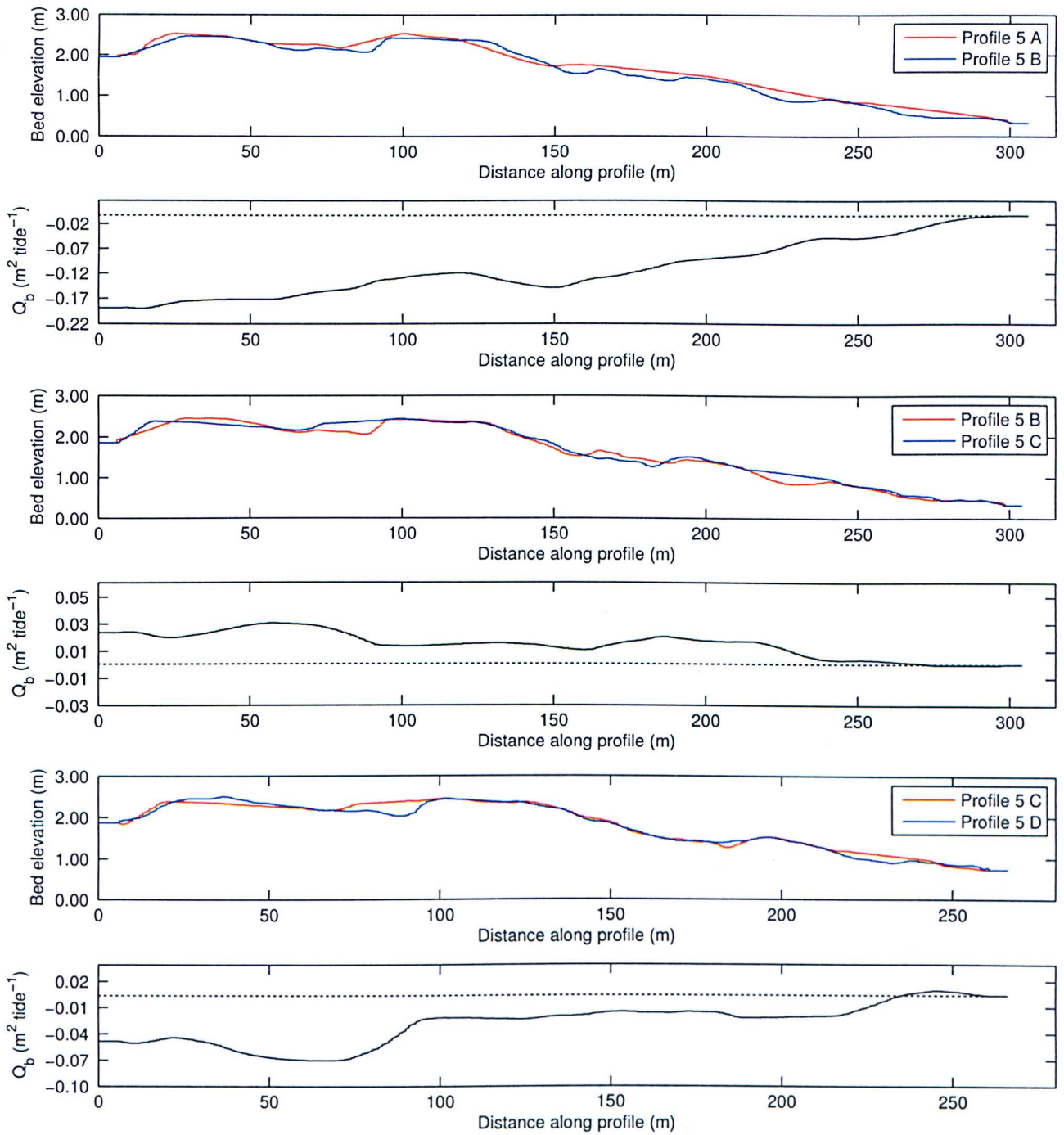
Figure 8.16: Bed elevation for paired profiles (profile 5) for A) 28.01.11, B) 31.01.11, C) 08.02.11 and D) 11.02.11 survey data. The respective profiles pairs have elevations set to the minimum value at both ends and profile lengths are equal as explained in the text. The volumetric transport rate (m^2 $tide^{-1}$) is calculated by integrating the bed continuity equation (Equation 8.8) from the right of the Figure (open sea boundary) to the left (sand flats).
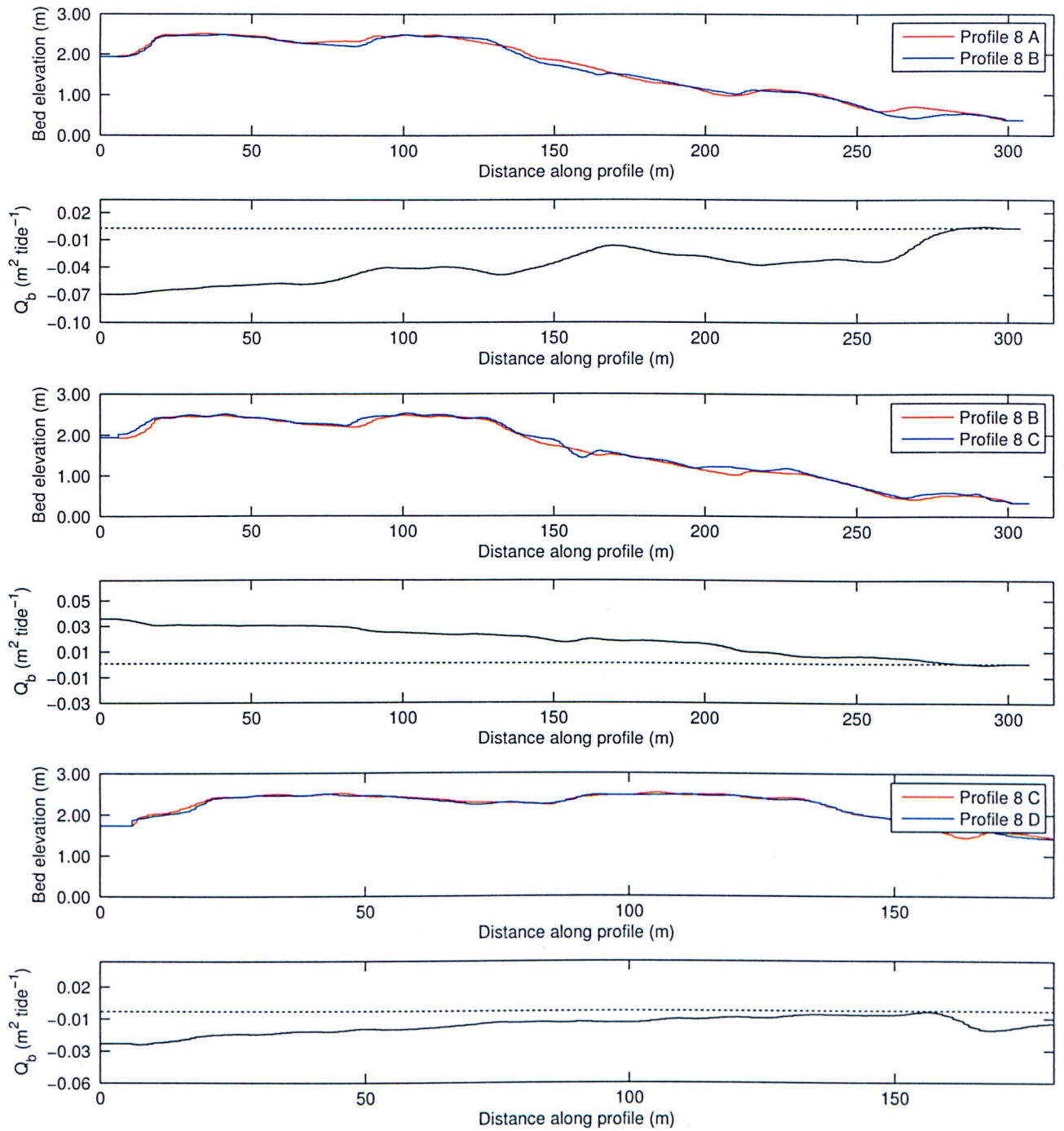
Figure 8.17: Bed elevation for paired profiles (profile 8) for A) 28.01.11, B) 31.01.11, C) 08.02.11 and D) 11.02.11 survey data. The respective profiles pairs have elevations set to the minimum value at both ends and profile lengths are equal as explained in the text. The volumetric transport rate (m^2 $tide^{-1}$) is calculated by integrating the bed continuity equation (Equation 8.8) from the right of the Figure (open sea boundary) to the left (sand flats).

Figures 8.15 - 8.17 show the volumetric transport per tide calculated using the bed continuity equation for three profiles (1,5,8) covering all survey dates (28.01.11 - 11.02.11). Paired profiles for the remaining 12 profiles (2-4,6,7,9-15) extracted from the West Kirby Sands survey data covering all survey dates can be found in Appendix IV. Equation 8.8 is integrated along the profile length from right (seaward) to left (landward) in Figures 8.15 - 8.17. The open sea boundary is to the right of the Figures, while the sand flats are to the left, with the dominant direction of sediment transport occurring in a (positive) landward direction as detailed previously. The bed elevation at the horizontal limits of each profile can be seen to be set to the minimum elevation and profile lengths set equal so that a direct comparison between profiles can be made. Figure 8.15 profile pair 1A and 1B is a good example of how a change in bed elevation, due to migrating bed forms, can effect the transport rate. At approximately 200m along the profile pair of 1A and 1B of Figure 8.15 there is a dune feature, referred to as 'Dune 1' previously. This bed form can be seen to migrate in a landward direction, from right to to left, between Profile 1 A and Profile 1 B (profile 1 for surveys 28.01.11 - 31.01.11). This movement of bed volume on to the sand flats can be seen to correspond with an increase in the volumetric transport. Alternatively, at approximately 130m along the profile pair of 1A and 1B for Figure 8.15 another dune feature, referred to as 'Dune 2', can be seen to migrate in a seaward direction. This loss of bed volume can be seen to correspond with a decrease in the volumetric transport. All of the transport calculations start at 0 and remain constant for the first 5m due to the bed elevation of both profiles being forced to be equal. In Figures 8.15 - 8.17 the dashed line represents zero transport so that any deviations towards positive or negative transport can be easily identified. Positive transport represents bed accumulation while negative transport represents bed erosion. A clear trend can be seen in transport rates between survey dates, with 28.01.11 - 31.01.11 and 08.02.11 - 11.02.11 experiencing an overall negative (seaward) transport, while positive (landward) transport occurs between 31.01.11 - 08.02.11. Figure 8.18 shows mean transport rates from profiles 1-15 for all survey dates. This shows there is some variation between positive and negative transport between profiles, however the results follow the same trend shown in Figures 8.15 - 8.17 where positive transport occurs between 31.01.11 - 08.02.11 whereas negative transport occurs between 28.01.11 - 31.01.11 and 08.02.11 - 11.02.11. Taking the mean transport from all profiles for each survey period removes the variation and shows (Table 8.5) the negative, positive to negative shift in transport observed in Figures 8.15 - 8.17. The sediment transport over the dune field at West Kirby Sands is being forced by the local hydrodynamic conditions. The shift in transport direction from seaward, to landward and back to seaward could be the result of changing hydrodynamic forcing, with a switch from a tidally dominated regime to a tide and wave influenced system. It was noted that local wind and wave conditions increased during the middle of the survey period, with calm conditions experienced at the

start and end of the period covering 28.01.11-11.02.11. The local wave, wind and tidal conditions are investigated further in this chapter to determine any correlation between the influence of waves and sediment transport at West Kirby Sands.
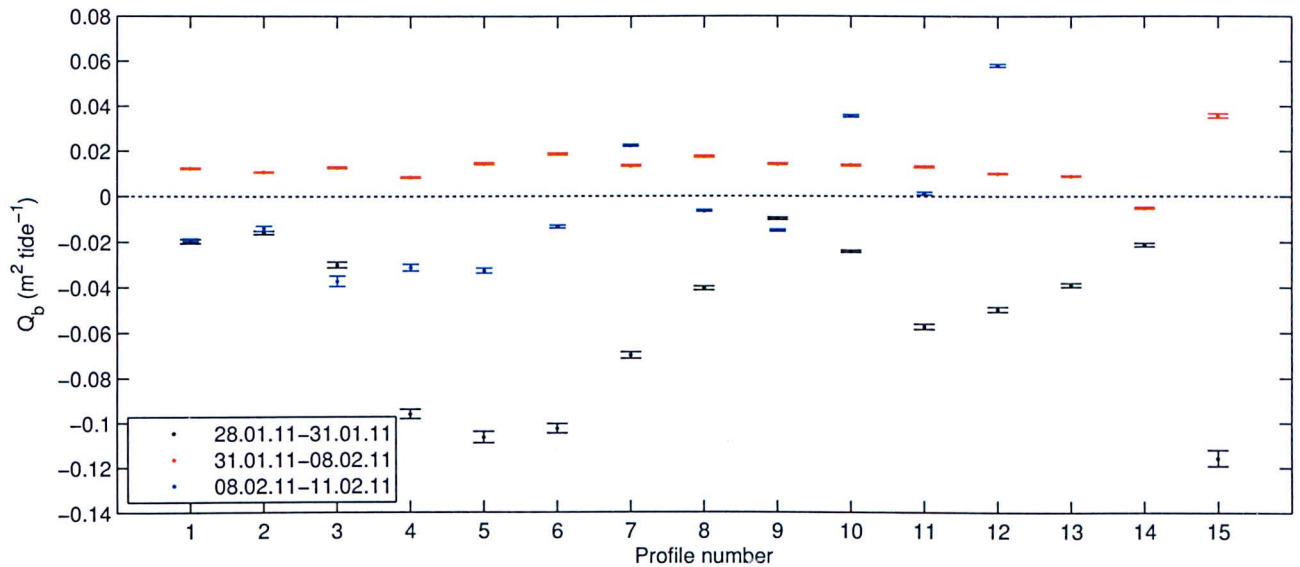
Figure 8.18: Mean profile volumetric transport (m^3 tide^{-1}) for profiles 1-15 extracted from all paired survey data (28.01.11-31.01.11, 31.01.11-08.02.11, 08.02.11-11.02.11). Positive values represent landward transport while negative values represent seaward transport. The main period landward migration can be seen to occur between 31.01.11-08.02.11.

q_b (m^2 tide^{-1})	A-B	Err	B-C	Err	C-D	Err
Mean transport	-0.053	±0.0014	0.013	±0.0003	-0.004	±0.0008

Table 8.5: Mean volumetric transport rate (m^2 tide^{-1}) calculated from the bed continuity equation for profiles 1-15 between survey dates 28.01.11-31.01.11 (A-B), 31.01.11-08.02.11 (B-C), 08.02.11-11.02.11 (C-D).

Since the analysis of West Kirby Sands survey data described hitherto has been limited to transport along the chosen profile lines, a 2-D cross correlation algorithm has been applied to the survey data to determine whether there was any significant lateral migration of bed features over the sand flats between survey dates. The cross correlation algorithm used was similar to that described in Section 6.8 to determine the migration of wave breaker patterns from the X-band radar data. This technique resolves the direction and rate of migration of topographic features from two bathymetry surveys recorded at different moments in time. The survey data was input on identical grids limited in the x and y direction to the minimal value between the two surveys. This was to ensure that the input survey data had similar coordinates so that an accurate comparison by cross correlation could be made.

A search window was defined over the first survey data which covered bathymetry points from both surveys. Some pre-analysis was required of the migration vectors and the bathymetry data so that suitable values for the search window size and search parameter could be determined. The correlation of points between the search window and the second survey data set was then calculated. The displacement of the window that resulted in the largest correlation has been considered to be the displacement of the bathymetric features. The size of the search window was set to the maximum extent which contains data points from both surveys, therefore the area was limited by data availability. Ideally, the size of the search window should be large enough to contain enough distinct features for the correlation analysis to unambiguously identify the location with the best correlation. In this case the search window contained two large bed forms, previously identified as dunes.
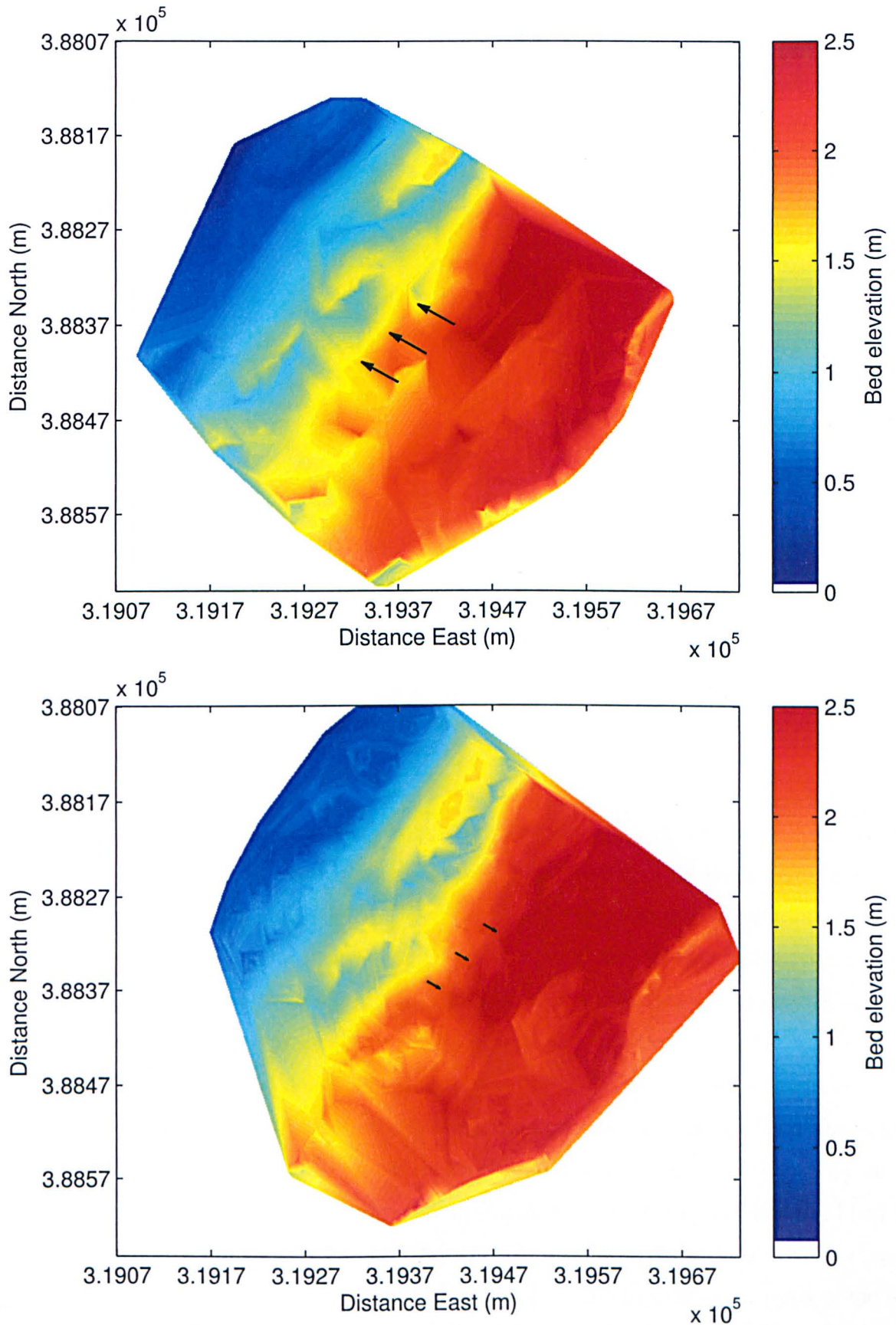
Figure 8.19: Migration vectors from 2D cross correlation analysis of 28.01.11 - 31.01.11 and 31.01.11 - 08.02.11 DGPS survey data. Three corresponding migration vectors are plotted along the dune crest for clarity, calculated from the x and y components of migration.
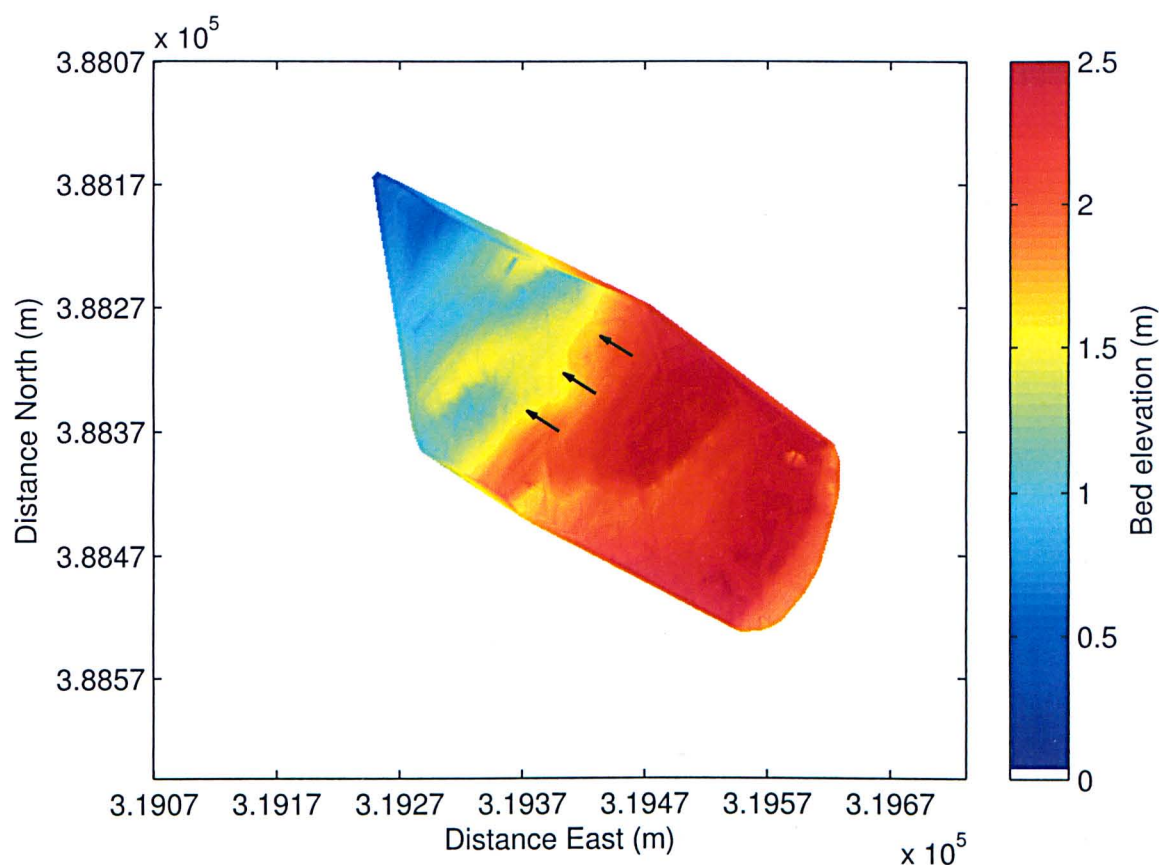
Figure 8.20: Migration vectors from 2D cross correlation analysis of 08.02.11 - 11.02.11 DGPS survey data. Three corresponding migration vectors are plotted along the dune crest for clarity, calculated from the *x* and *y* components of migration.

The direction and magnitude of migration from the cross correlation of survey data can be seen in Figures 8.19 - 8.20. Migration vectors are plotted on each Figure, using the *x* and *y* components of migration, and are along the crest of Dune 2 to represent migration over the whole domain. The direction of the migration vector can be seen to follow the orientation of bed profiles in a north west to south east direction. This affirms the notion that there was no significant lateral migration of bed features and that the dominant pathway for sediment transport was normal to the bed form crests. The size of the migration vectors does not directly represent the magnitude of migration, however all vectors are scaled equally and so their relative size represents difference in magnitude. The migration velocity was calculated by dividing the migration given by the cross correlation analysis by the number of tides between individual surveys. This was then used with the average height of all bed forms identified from the survey data together with Equation 8.5 to produce the volumetric transport q_b (Figure 8.21). The sediment transport calculated from the 2D cross correlation analysis of the survey data is in good agreement with the transport calculated using the 1D bed continuity method (Equation 8.8). The pattern of migration between survey dates is represented by both methods; the greatest off-

shore transport was experienced between 28.01.11-31.01.11, followed by onshore transport between 31.01.11-08.02.11, before returning to offshore transport between 08.02.11 and 11.02.11. However, it should be noted that for both methods there is still an underlying ambiguity of a possible background net transport that remains unknown. Further work at West Kirby Sands, including the deployment of sediment traps, in conjunction with further modelling work would help to determine the magnitude of this ambiguity.
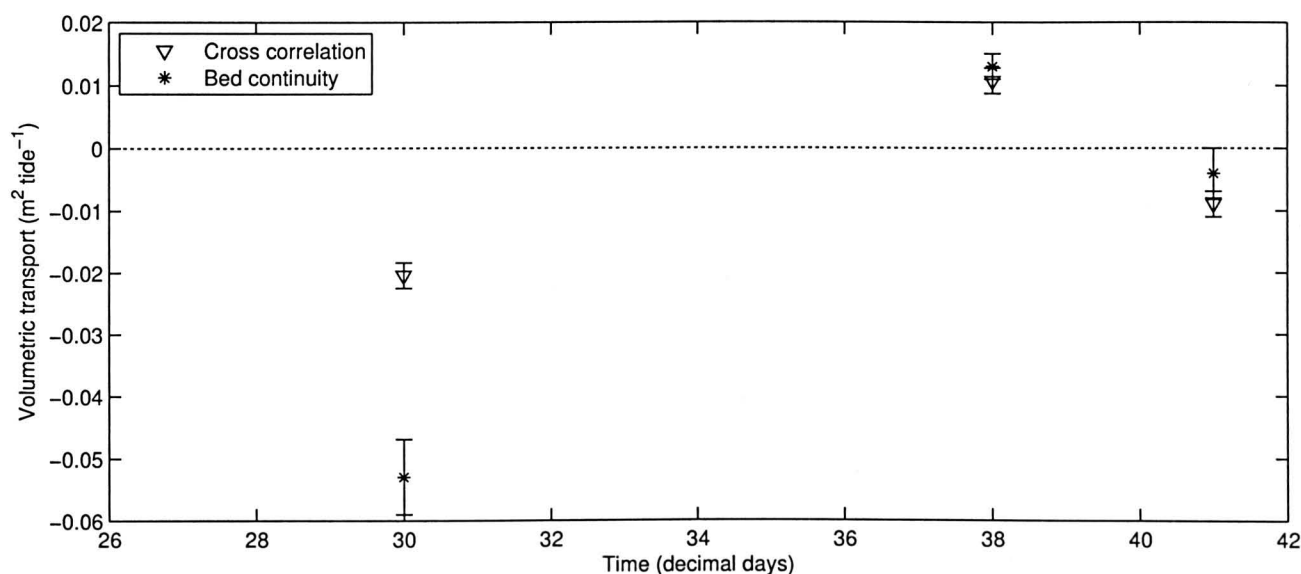
Figure 8.21: Mean volumetric transport calculated using the 1D bed continuity equation and the 2D cross correlation method. The zero transport line is marked for reference, as negative transport represents bed erosion (offshore transport) while positive transport represents bed accumulation (onshore transport).

8.3 Current and wave conditions during survey period

8.3.1 Wave and tidal data

Figure 8.22 shows the tidal elevations at Hilbre Island for the DGPS survey period with all of the four survey dates indicated by the vertical red lines. The first two survey dates (28.01.11 and 31.01.11) coincided with a period of neap tides, while spring tides occurred between surveys two and three (31.01.11 and 08.02.11), before returning to neap tides between surveys 3 and 4 (08.02.11 and 11.02.11). Mean tidal height between the 28.01.11 and 31.01.11 was 5.26 ± 0.09m, increasing to 5.46 ± 0.08m during 31.01.11 to 08.02.11, then falling to 5.33 ± 0.11m for 08.02.11 to 11.02.11. Figure 8.22 shows that West Kirby Sands experiences large tides, with a spring tidal range of approximately 8m observed during the survey period. This means that the area of sand dunes which

have been surveyed will be inundated with water at times of high water and will be exposed at low water. This will have the effect of tidally modulating the wave heights at West Kirby Sands, with waves potentially breaking over the dune field at high water while little to no wave action will occur at low water. Therefore, it is expected that there will be a tidal asymmetry in sediment transport rates experienced at this site with greater transport occurring when water levels are deepest.
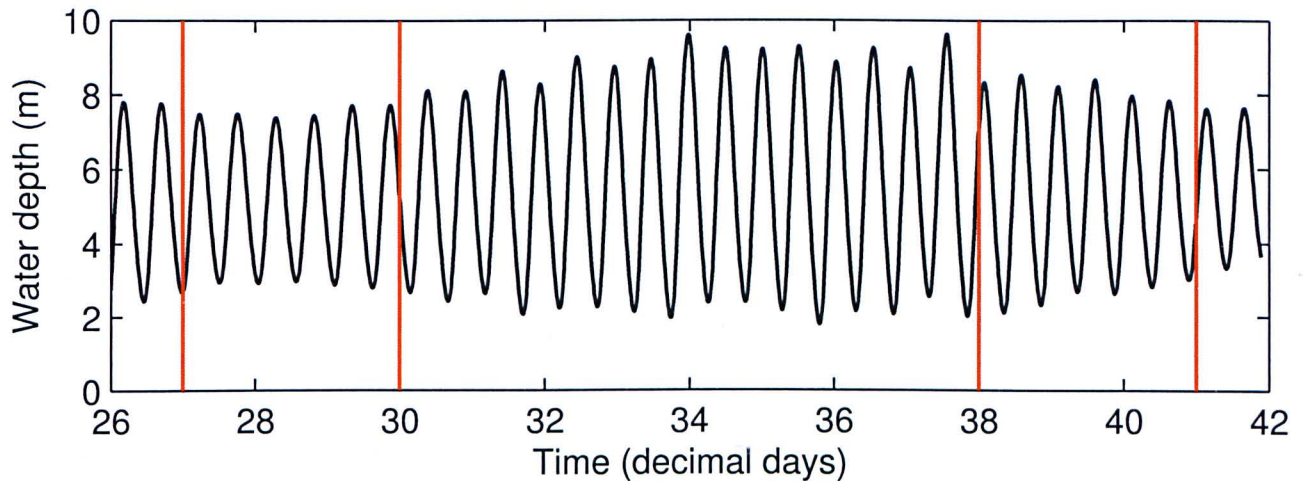
Figure 8.22: Tidal elevations from the Hilbre tide gauge covering the two week survey period. The red lines mark the position of each DGPS survey.
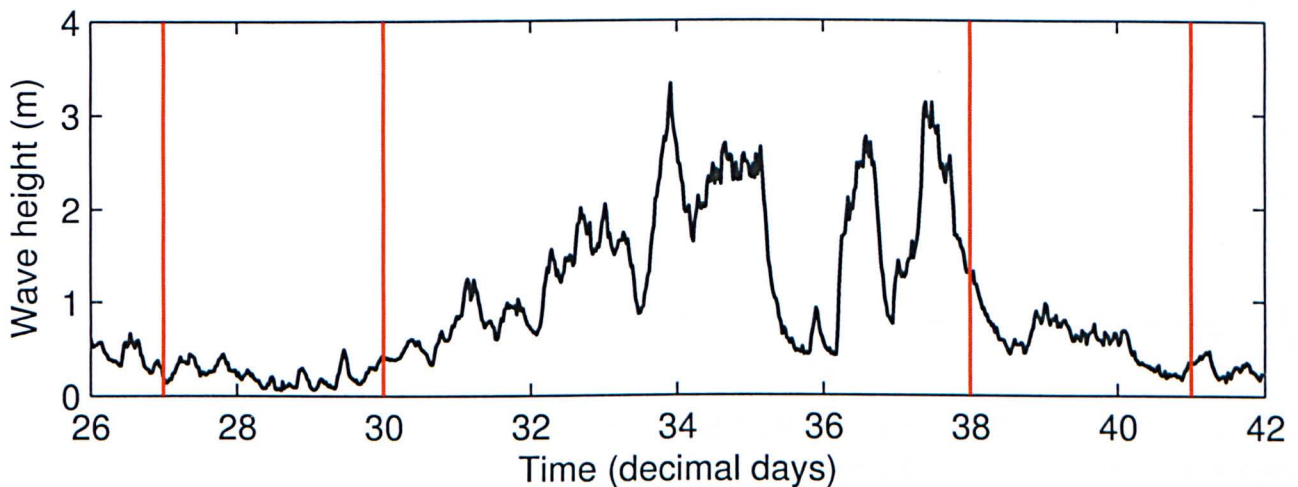
Figure 8.23: Significant wave height for Liverpool Bay from the WaveNet buoy covering the two week DGPS survey period. The red lines mark the position of each DGPS survey.

Wave conditions for the survey period, obtained from the Liverpool Bay WaveNet Buoy, are shown in Figure 8.23. This wave buoy is located in Liverpool Bay and as such does not represent the actual wave height at West Kirby Sands. It does however provide a good indication of the general sea state during the survey period. As in Figure 8.22 the time of each DGPS survey is shown on the x

axis. There is a clear increase in wave heights between the second and third surveys (31.01.11 and 08.02.11). Mean wave height for 28.01.11 to 31.01.11 was 0.22 ± 0.009m, increasing to 1.45 ± 0.039m for 31.01.11 to 08.02.11, before falling to 0.59 ± 0.021m between 08.02.11 to 11.02.11. It is also interesting to note the maximum wave height experienced during each of these surveys periods, as the action of short intense wave events has the potential to cause significant bed form migration. Maximum wave height between 28.01.11 to 31.01.11 was 0.49 ± 0.009m, increasing to 3.33 ± 0.039m for 31.01.11 to 08.02.11, before falling to 1.33 ± 0.021m during 08.02.11 to 11.02.11. Figure 8.24 shows a comparison of mean wave heights for Liverpool Bay and average bed load transport per tide calculated by applying the bed continuity equation to all DGPS profile data. A comparison between the mean survey 1D transport rate, calculated as the mean transport of all profiles, and the 2D cross correlation transport rate (Figure 8.25) shows good agreement for each survey period, with smaller mean wave heights experiencing greater mean offshore (negative) transport and larger mean wave heights resulting in onshore (positive) mean transport.
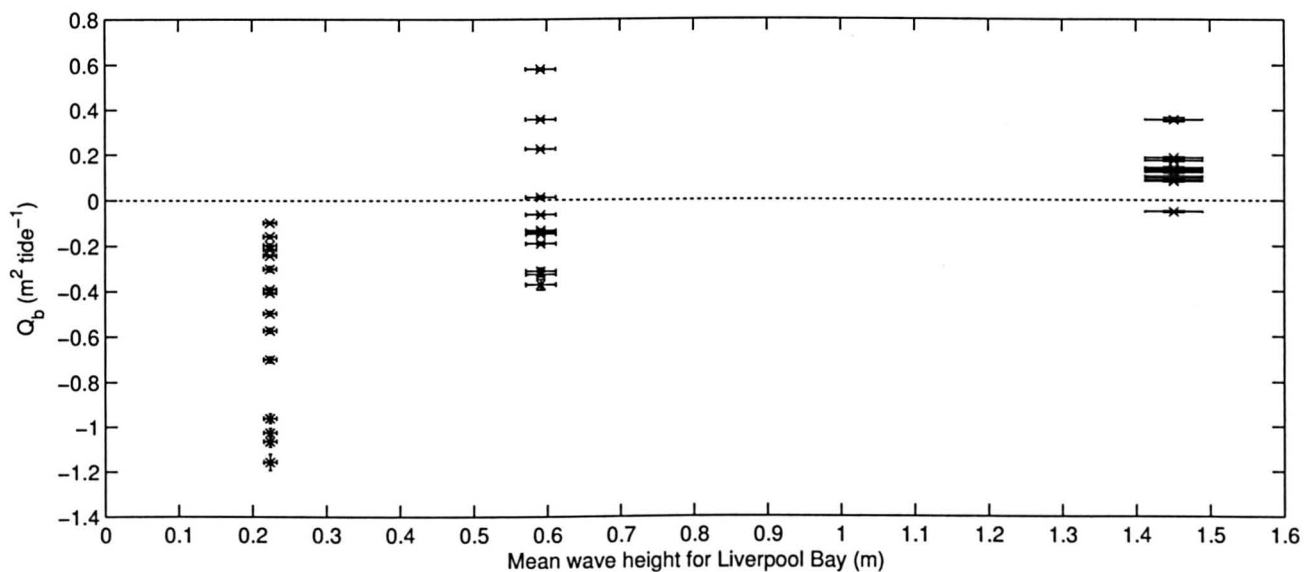
Figure 8.24: Mean profile volumetric transport (q_b) calculated from the 1D bed continuity equation for profiles 1-15 on all paired survey data plotted against mean wave height for Liverpool Bay using data from the WaveNet buoy. The zero transport line is plotted for reference.
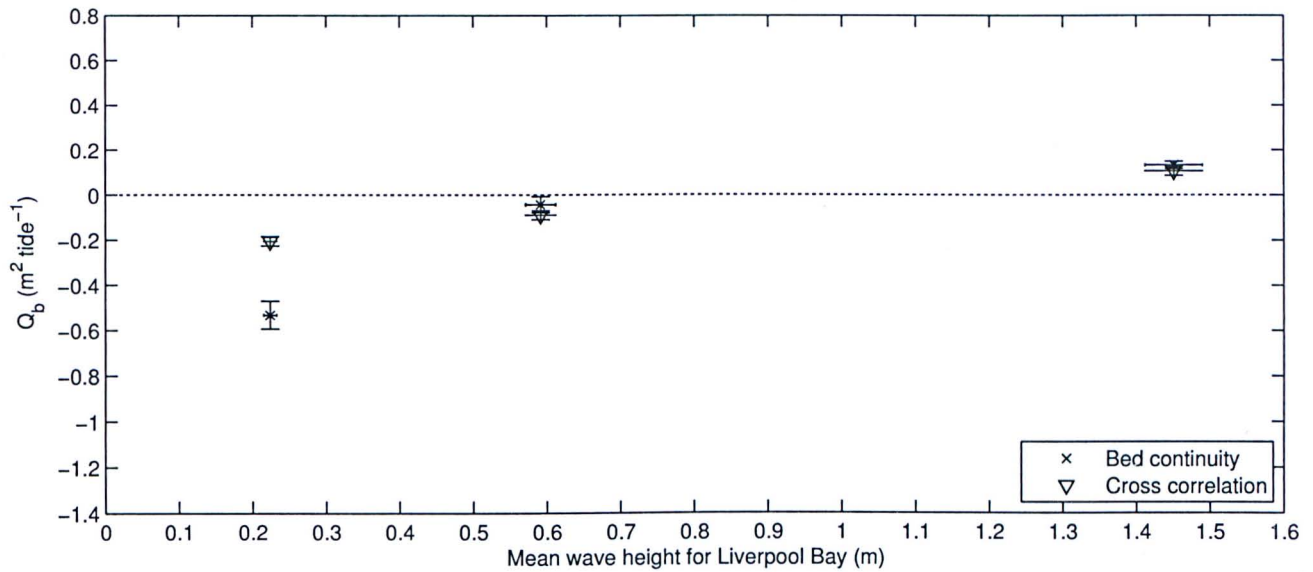
Figure 8.25: Mean volumetric transport (q_b) calculated from the 1D bed continuity equation using all available profiles and from the 2D cross correlation method plotted against mean wave height for Liverpool Bay using data from the WaveNet buoy. The zero transport line is plotted for reference.

8.3.2 West Kirby Sands ADCP deployment

An ADCP was deployed on the intertidal sand flats at West Kirby Sands between 24.01.11 and 06.02.11. The battery life of the instrument means that the deployment was limited to 14 days. Data were collected over this deployment period showing water depth and depth-averaged velocity (Figures 8.26 & 8.27) which cover the first and second DGPS surveys but the record terminates two days before the third survey. The details of this ADCP deployment are given in Section 3.1.1.
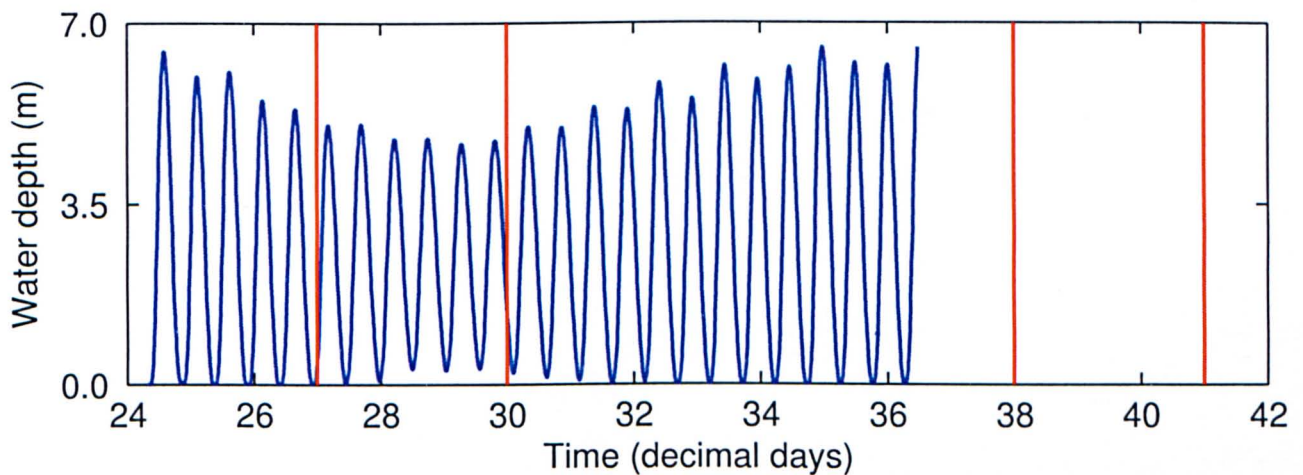
Figure 8.26: Water depth at West Kirby Sands from the ADCP frame deployed between 24.01.11 and 06.02.11. The vertical red lines mark the time of each DGPS survey.

249
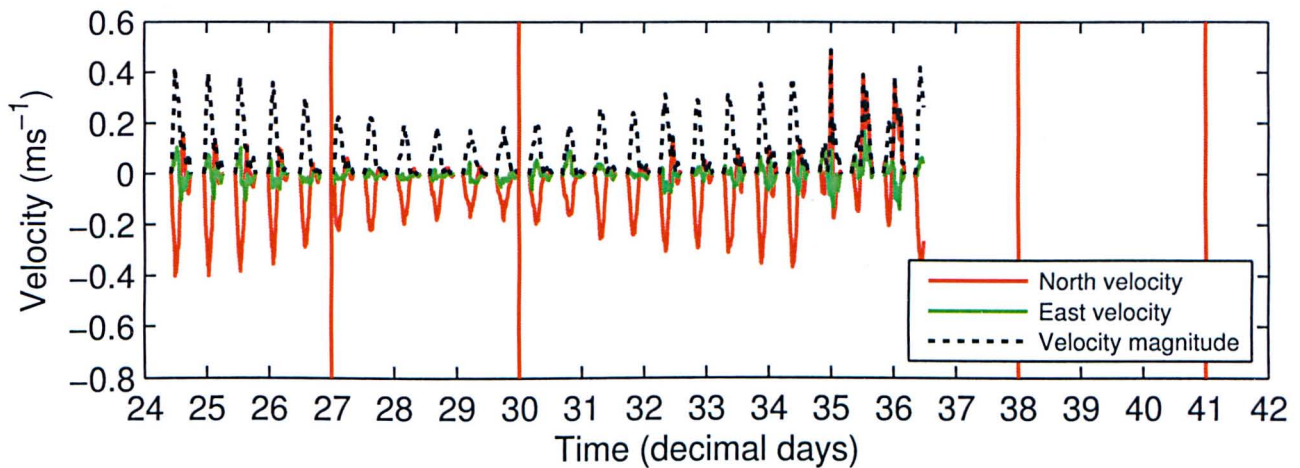
Figure 8.27: Depth-averaged velocity components and velocity magnitude at West Kirby Sands calculated from the ADCP deployed between 24.01.11 and 06.02.11. The vertical red lines mark the time of each DGPS survey.

The deployment period covered a two week tidal cycle, changing from springs to neaps before returning to spring tides (Figure 8.26). The depth averaged velocities follow this change in tidal elevation and display an asymmetrical form, which is flood dominant, with greater southerly velocities (Figure 8.27). A change in the southerly dominant velocity occurs at day 35, becoming an apparent northerly dominant velocity. This change can be seen to occur at the same time as a drop in the local wave height (Figure 8.23). Figure 8.28 shows the local wind conditions over the survey period from the Hilbre Island meteorological station operated by the National Oceanography Centre, Liverpool. Mean wind speeds are calculated for 10 minute time intervals with the maximum wind speed during this time interval also recorded. The wind direction is recorded in degrees from north, so that a direction of 0° represents wind coming from the north.
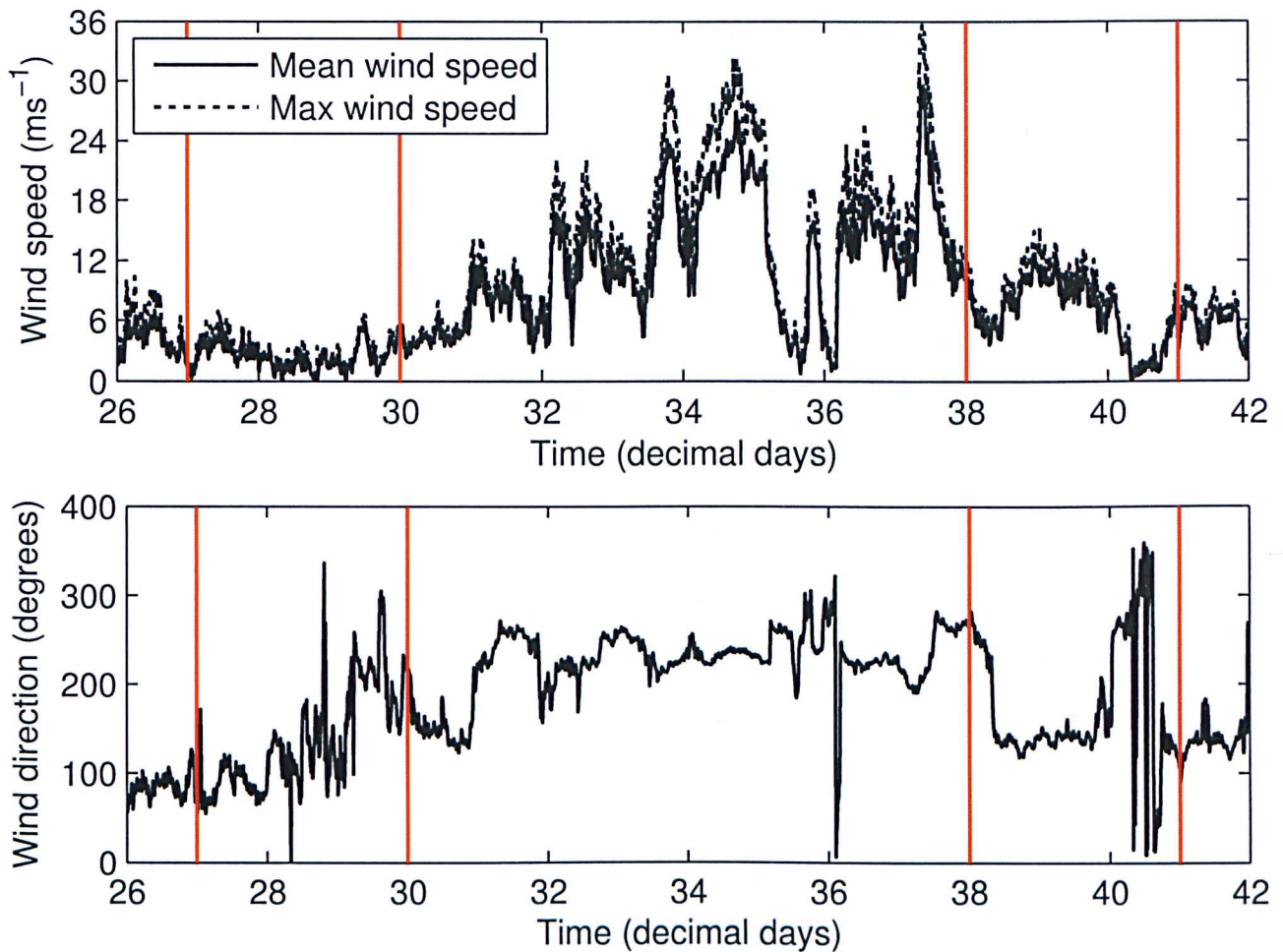
Figure 8.28: Wind speed and direction data from Hilbre Island weather station covering the two week survey period. The vertical red lines mark the time of each DGPS survey.

The wind conditions for this period (Figure 8.28) show wind directions to range between 190-320° (south west to north west), with a brief drop to 6° (north) during day 36. Figure 8.28 shows that wind speeds dropped with the wave height at this time, suggesting that it was not locally wind generated currents causing the directional change. These results are surprising as this corresponds with the only time of onshore sediment transport during the survey period. While this might seem counter-intuitive this may have been caused by increased levels of suspended material, not accounted for by the previous methods which estimate bed load transport from bed elevation changes, but associated with times of increased transport creating anomalous results recorded by the ADCP. Thorne et al. (1993) and Lee and Hanes (1995) state that the acoustic backscatter measured by the ADCP transducer can be strongly influenced by the attenuation caused by suspended matter along the sound path. Figure 8.29 shows the change in ADCP velocity measurements occurring from a peak in the north velocity component at approximately day 35.
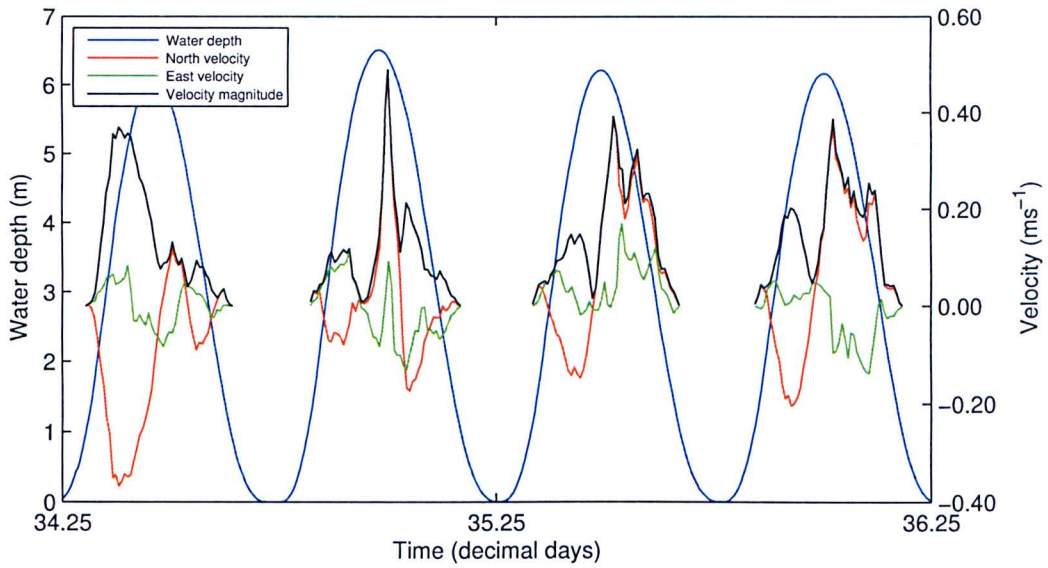
Figure 8.29: The change in ADCP velocity measurements recorded at the end of the instrument deployment period on West Kirby Sands.

8.3.3 Predicted bed load transport at West Kirby Sands

The velocity measurements shown in Figure 8.27 were used to predict the bed load transport rates due to the action of tidal currents by using the following procedure, as outlined by Soulsby (1997). The skin friction bed shear velocity u_* which is produced by and acts upon the sediment particles is calculated from the velocity data assuming a logarithmic velocity profile as detailed in Section 2.1. The bed shear stress τ_0 is used to obtain the Shields parameter θ_{sf} (skin friction). Masselink et al. (2009) compared volumetric transport rates derived from sand dune dimensions and migration rates with predicted bed load transport rates using the equation of Meyer-Peter and Muller (1948). Masselink et al. (2009) investigated the migration of dunes on an intertidal shoal near the mouth of the shallow tide/wave dominated Avon Estuary on the English Channel coast of south west Britain. The Meyer-Peter and Muller (1948) equation was chosen due to its widespread use, simplicity and validation in similar environments. McCann (2007) also applied the Meyer-Peter and Muller (1948) equation as well as the Soulsby (1997) equation when investigating the migration of large scale bed forms in the mouth of the Dee Estuary. A comparison is made here between the predicted bed load transport rates using the equations of Meyer-Peter and Muller (1948) and Soulsby (1997) based on the velocity magnitude from the ADCP measurements, and volumetric transport rates derived from the 1D bed continuity equation and 2D cross correlation motion tracking algorithm. The Meyer-Peter and Muller (1948) equation, subject to a modification in the value of θ_{cr} used for the threshold of motion, calculates the dimensionless bed load transport rate Φ_b as

$$\Phi_b = 8(\theta_{sf} - \theta_{cr})^{1.5} \tag{8.16}$$

and the equation of Soulsby (1997) can be written

$$\Phi_b = 12\theta^{0.5}(\theta_{sf} - \theta_{cr}) \tag{8.17}$$

where θ_{cr} is the critical Shields parameter calculated from an algebraic expression given by Soulsby and Whitehouse (1997) which fits the Shields curve for threshold of motion of sediments

$$\theta_{cr} = \frac{0.30}{1 + 1.2D_*} + 0.055[1 - \exp(-0.020D_*)] \tag{8.18}$$

where D_* is the dimensionless grain size given by

$$D_* = \left[\frac{g(s-1)}{v^2} \right]^{1/3} d \tag{8.19}$$

where v is the kinematic viscosity of water and d is the grain size. The dimensionless transport rate Φ_b is then converted to a volumetric bed load transport rate per unit width ($m^2 s^{-1}$) as follows

$$q_b = [g(s-1)d^3]^{0.5}\Phi_b \tag{8.20}$$

The current profile is assumed to be logarithmic with height above the bed in order to calculate the bed shear stress due to a current alone. The shear velocity u_* is obtained from the gradient of the logarithmic velocity profile given by

$$U = \frac{u_*}{\kappa} \ln\left(\frac{z}{z_0} \right) \tag{8.21}$$

where κ is Von Karman's constant (equal to 0.4) and z is the height above the bed to which U pertains. The approach taken here was to assume that $U = 0$ at the value of the skin friction roughness length z_0, neglecting the effect of form drag caused by topography, where for a hydrodynamically rough bed the roughness length according to Kamphuis is given as

$$z_0 = \frac{D_{50}}{12} \tag{8.22}$$

The depth averaged flow speed $\bar{u}$ is calculated by integrating the logarithmic profile over the flow depth, from z_0 to h, so that

$$\bar{u} = \frac{1}{h - z_0} \int_{z_0}^{h} \frac{u_*}{\kappa} \ln \left(\frac{z}{z_0} \right) dz \tag{8.23}$$

which leads to

$$\bar{u} = \frac{1}{h - z_0} \frac{u_*}{\kappa} \left[z \ln \left(\frac{z}{z_0} \right) - (z - z_0) \right]_{z_0}^{h} \tag{8.24}$$

Therefore, $\bar{u}$ is calculated by evaluating between z_0 and h as

$$\bar{u} = \left(\frac{u_*}{\kappa(h - z_0)} \right) \left(h \ln \left(\frac{h}{z_0} \right) - (h - z_0) \right) \tag{8.25}$$

which can be rearranged to determine u_* from

$$u_* = \frac{\bar{u} \kappa (h - z_0)}{\left[h \ln \left({}^h/_{z_0} \right) - (h - z_0) \right]} \tag{8.26}$$

The current alone bed shear stress can then be calculated from the shear velocity relationship

$$\tau_c = \rho u_*^2 \tag{8.27}$$

which has been used here to determine the current-only Shields parameter θ_{sf} for use within the bed load formula detailed previously (Equations 8.16 & 8.17). Figure 8.30 shows the calculated Shields parameter θ_{sf} derived from the current measurements over the deployment period of the ADCP, with the critical Shields parameter θ_{cr} overlain (0.009), calculated with a D_* value of 4.425 from a D_{50} of 220 μm.
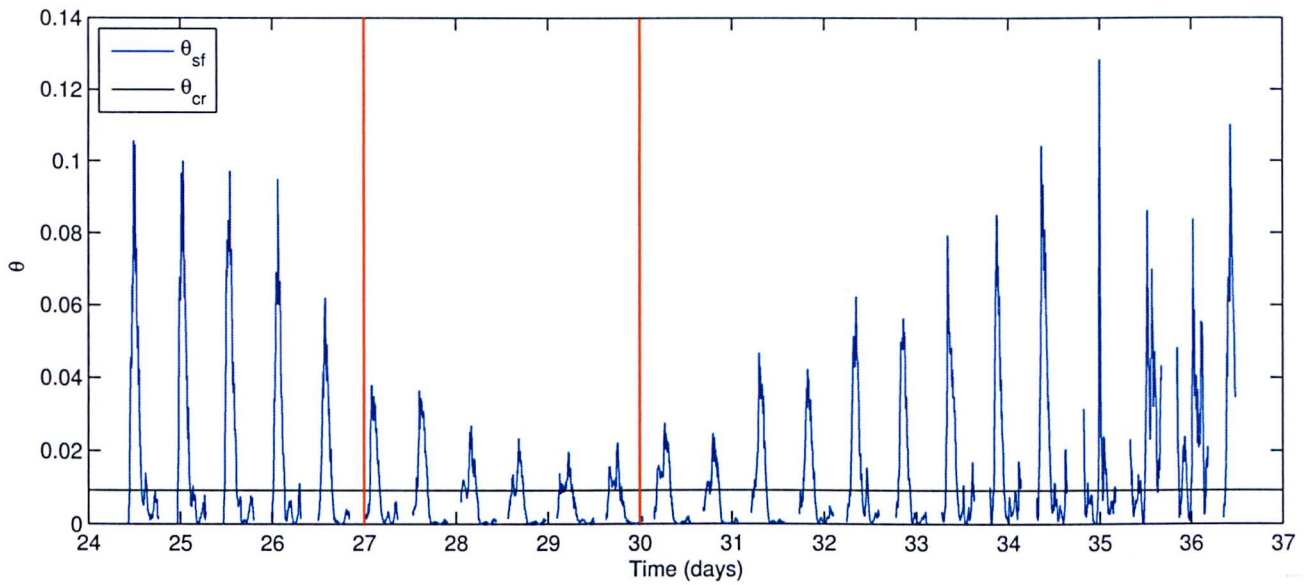
Figure 8.30: Magnitude of Shields parameter (θ_{sf}) and the critical value of Shields (θ_{cr}) parameter at the threshold of sediment motion calculated from the ADCP velocity magnitude between 24.01.11 and 06.02.11. The vertical red lines mark the times of DGPS survey 1 (28.01.11) and survey 2 (31.01.11).

The ADCP was deployed at the spring tide low water mark to record the fastest current speeds. Figure 8.30 shows that θ_{sf} exceeds θ_{cr} over the entire deployment. Greater θ_{sf} values are attained during spring tides, when velocity magnitudes are greatest. The vertical red lines on Figure 8.30 mark the times of the 1st and 2nd DGPS surveys which are covered by the ADCP deployment period. This period is shown to be the time of least predicted bed load transport due to the action of currents alone. Figure 8.31 shows the predicted current-only bed load transport using the Meyer-Peter and Muller (1948) and Soulsby (1997) formulae over the ADCP deployment period. The sign of the transport is preserved from the north-south velocity component, so that positive transport values represent times of flood tide and negative values represent ebb tide conditions. The predicted bed load transport due to currents alone shows that flood dominant transport is predicted to occur for the majority of the ADCP record using both the Meyer-Peter and Muller (1948) and Soulsby (1997) formulae. However, there is a switch to ebb dominance during the change in recorded current conditions mentioned previously during day 35 and 36.
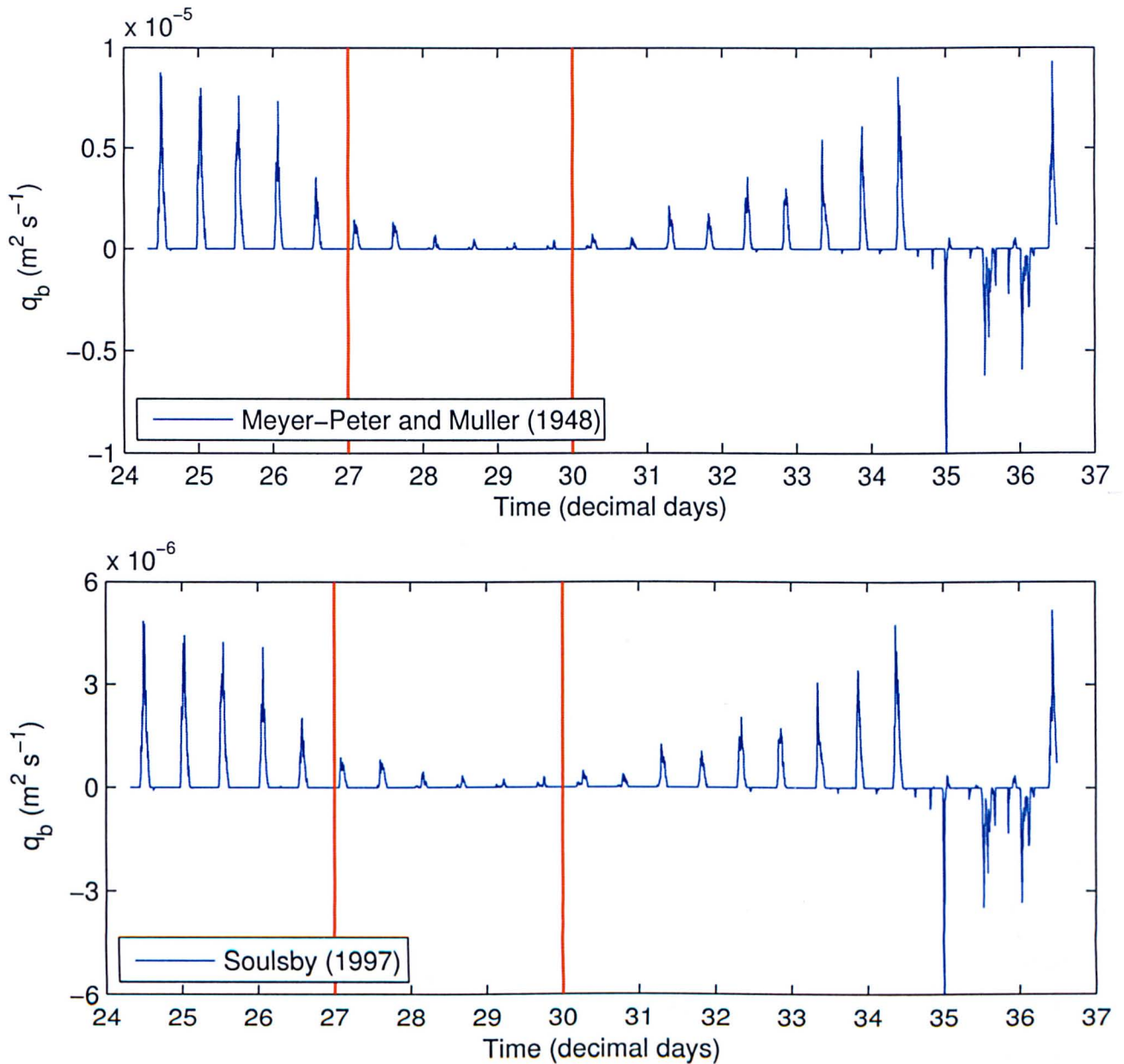
Figure 8.31: Magnitude of bed load transport for current-only conditions using the formulae of Meyer-Peter and Muller (1948) and Soulsby (1997) based on the velocity magnitude calculated from the ADCP deployment at West Kirby Sands between 24.01.11 and 06.02.11. The vertical red lines mark the times of DGPS survey A (28.01.11) and survey B (31.01.11).

A comparison between the predicted bed load transport and the bed load transport derived from the 1D bed continuity and 2D cross correlation analysis of the DGPS survey data between 28.01.11-31.01.11 shows a reasonable agreement in transport magnitudes. The net transport between surveys A and B predicted using the Meyer-Peter and Muller (1948) formula was 5.56×10^{-7} m^{2}s^{-1} the Soulsby (1997) formula calculated 3.24×10^{-7} m^{2}s^{-1}. These values slightly under-predict the transport derived from the 1D bed continuity equation which was 1.06×10^{-6} m^{2}s^{-1} but are of a similar order of magnitude to the 2D cross correlation derived transport of 4.2×10^{-7} m^{2}s^{-1}. However, the formulae of Meyer-Peter

256

and Muller (1948) and Soulsby (1997) predict onshore (positive) net transport of sediment, caused by the strong flood dominance observed in the ADCP velocity measurements, while the transport derived from the DGPS survey data shows a net offshore (negative) transport. This disparity in the direction of transport could be caused by wave action between the times of surveys A and B or by suspended load transport which is not included in these sediment transport models. Figure 8.23 shows low wave heights of less than 0.5m in Liverpool Bay between surveys A and B, suggesting that the action of small waves on the intertidal sand flats at West Kirby Sands may cause the offshore migration of the large scale bed forms. Unfortunately no wave data were available at the mouth of the estuary during the DGPS survey period to allow the wave-current Shields parameter to be calculated. Future work concerning the 1D bed continuity equation applied to bed elevation profiles should concern the local wave influence on sediment transport as well as the profile open boundary ambiguity, so that regular survey data of intertidal sand flats can be used to make a reliable estimate of the transport rate.

The predicted bed load transport presented above relies on one grain size D_{50} (0.22mm) representing the whole dune field at West Kirby Sands. This introduces an error into the calculated value of θ_{ctr} (Equation 8.18) which relies on D_{50} as well as an assumed value for v (Equation 8.19). This will then also effect predicted transport rates. Here v was assumed to equal $1.36 \times 10^{-6} \text{m}^2\text{s}^{-1}$, which applies to seawater, with a density of 1027kgm^{-3} at 35psu and 10°C. As stated previously θ_{cr} is calculated using D_* which is proportional to D_{50} and $v^{2/3}$. The skin friction roughness length applied here (Equation 8.22) is also proportional to D_{50}. While it is important to consider the skin friction component of z_0, due to the forces acting on sediment grains, when calculating bed load transport, suspended load transport may also make a significant contribution to the migration of bed forms at West Kirby Sands. The form drag, associated with the pressure variation around dunes and ripples in the flow, is an important consideration when modelling suspended load transport due to the effect it has on the total roughness length. An important consideration with the above bed load transport calculation is the assumption of a logarithmic velocity profile when calculating u_*. The bed load transport formulae are proportional to u_*^3 ($\Phi \propto \theta_{sf}^{2/3}$), therefore a 10% error in u_* will cause a 33% error in q_b.

8.4 Summary

Four topographic surveys were conducted of the West Kirby Sands dune field on 28.01.11, 31.01.11, 08.02.11 and 11.02.11 (Figure 8.2) using a Leica 1200 RTK GPS system. Fifteen longitudinal profiles of bed topography were extracted approximately perpendicular to bed form crests to analyse bed form dimensions and identify any change in bed form position over the survey period. A turning

points algorithm was applied to these profiles to identify the position of dune troughs and crests. It was then possible to determine the bed form height from the position of bed form troughs and crest, as well as the bed form area, index of symmetry and bed form migration rate. Mean dune length λ_d for Dune 1 is smaller than for Dune 2, at 13.49 ± 3.36m and 18.90 ± 4.76m respectively. However, mean dune height η_d for Dune 1 and 2 was of similar magnitude, at 0.60 ± 0.04m and 0.67 ± 0.02m. Dune area for Dune 2 was consistently larger than Dune 1 for all surveys, with a mean dune area of 120.29 ± 9.32m^2 compared with 56.72 ± 2.23m^2. Dune area for Dunes 1 and 2 was seen to increase dramatically between surveys B and C (Table 8.1 & 8.2). These dunes were distinctly asymmetrical in shape, with MSI values of 5.18 and 4.57, typical of large tidal dunes. The crest positions of Dunes 1 and 2 were offset in a landward direction, suggesting that the main direction of bed load transport is on to West Kirby Sands from the open sea boundary. By tracking the migration of dune crests using paired profiles between survey dates and considering the number of tides between each survey it is possible to assess the migration velocity (m tide^{-1}) of each dune (Table 8.3). An increase in crest migration velocity can be seen between surveys B-C (Table 8.3), occurring over the same time period (31.01.11 - 08.02.11) an increase in dune area is observed. The dune crest migration can then be used with dune height and a factor to account for bed form shape and porosity (a_m) to determine the volumetric transport rate using Equation 8.5. However, this only considers the bed load sediment transport associated with dune migration and not suspend load transport.

A method was developed which does not rely on identifying and correlating individual bed forms, but uses the change in bed elevation instead. Figure 8.9 shows the difference in bed elevation between two paired profiles and how sediment transport calculated from dune migration can underestimate the transport occurring along the entire profile. This led to an application of the 1D Exner equation which states that bed elevation increases, with bed accumulation, proportionally to the amount of sediment which falls out of transport and conversely decreases with bed erosion, proportionally to the amount of sediment that is entrained by the flow. Integrating the bed continuity equation, in the form of Equation 8.8, along paired profiles calculates sediment transport along the entire profile length (Figures 8.15 - 8.17). A positive transport gradient represents bed accumulation whereas negative transport gradient represents bed erosion. The results show a clear change from negative transport gradient (erosion) between 28.01.11 - 31.01.11, to positive transport gradient (accumulation) from 31.01.11 - 08.02.11, before returning to negative transport (erosion) for 08.02.11 - 11.02.11. This switch from erosion to accumulation can be seen to correspond with the increase in dune area (Table 8.1 & 8.2) and increase in dune crest migration (Table 8.3) between 31.01.11 - 08.02.11. This suggests that there is a change in the hydrodynamic conditions which results in onshore migration of large scale bed

forms at West Kirby Sands.

A 2D cross correlation algorithm was applied to the survey data to determine if there is significant two dimensional bed form migration. Migration vectors plotted on interpolated survey bathymetry show the direction of movement to have been perpendicular to dune crests and approximately aligned with the survey profiles (Figures 8.19 - 8.20). The direction of these migration vectors indicates that West Kirby Sands is a pathway for sediment to move in and out of the estuary, which the migration of large scale bed forms likely plays an important role. The migration vectors in Figures 8.19 - 8.20 show a switch from offshore to onshore migration between 31.01.11-08.02.11, which corresponds to the switch from negative (erosion) to positive (accumulation) seen in the 1D bed continuity results (Figures 8.15 - 8.17). The migration velocity (m tide^{-1}) from the cross correlation analysis has been used to calculate the volumetric transport using Equation 8.5. These results are in good agreement with the volumetric transport calculated using the bed continuity equation (Figure 8.21). Tidal (Figure 8.22) and wave (Figure 8.23) data were obtained from the Hilbre tide gauge and the Liverpool Bay WaveNet buoy covering the two week survey period. This shows a significant increase in wave height coinciding with spring tides between 31.01.11 and 08.02.11, which is the period of sediment accumulation shown in the 1D bed continuity analysis and onshore migration of bed forms shown in the 2D cross correlation analysis. A direct correlation can be seen between an increase in mean wave height and transport of sediment in an onshore direction (Figure 8.24).

While both the 1D and 2D analysis of the DGPS survey data provide useful information for the evolution of intertidal sand flats, and how local sediment transport responds to changing hydrodynamic conditions, an ambiguity remains in the form of a possible background constant level of sediment transport through the domain. Velocity measurements from an ADCP deployment between 24.01.11 and 06.02.11 show flood dominant tidal asymmetry at West Kirby Sands (Figure 8.27). The formulae of Meyer-Peter and Muller (1948) and Soulsby (1997) are applied to predict the current only bed load transport from the current magnitude during the period covered by DGPS surveys A and B. While the Meyer-Peter and Muller (1948) and Soulsby (1997) transport magnitudes are of a similar order of magnitude to the 1D and 2D DGPS derived transport rates, the direction is not coherent, with the DGPS data showing offshore net transport while the bed load formulae show onshore net transport. These formulae of Meyer-Peter and Muller (1948) and Soulsby (1997) do not include the effect of waves, which are an important consideration as the oscillatory flow under surface waves not only increases the bed shear stress but also acts as a stirring mechanism so that the sediment is more readily transported by the underlying steady current. It is also important to note that these transport formu-

lae do not include the suspended load component of transport which could prove to be an important component of the total load transport occurring at West Kirby Sands. Therefore it is hard to make a direct comparison between the sediment transport calculated from the ADCP measurements and the sediment transport derived from the DGPS data, due to the fact that they are in opposing directions. Further field measurements of current velocities and local wave conditions would allow for a more accurate sediment transport calculation and would help to validate the transport calculated from the DGPS data.

Chapter 9

A synthesis of sediment transport observations and modelling in the Dee Estuary

Modelling sediment transport in the Dee Estuary (Figure 5.8) shows flood tidal asymmetry with associated asymmetric total load transport simulated using the Bijker sediment transport equation. Observations of large scale bed form migration in the mouth of the estuary using X-band radar data (Figure 7.23) shows the movement of sand dunes at West Kirby Sands and West Hoyle Bank into the estuary interior on monthly time scales. This chapter aims to show large scale bed form migration at West Kirby Sands and West Hoyle Bank over shorter timescales, so that the influence of tides and waves on bed form migration can be identified. A comparison of transport rates will also be made between observations and modelling results to determine the contribution that observed transport rates inferred from the migration of large scale bed forms makes to total load transport simulated using the validated Dee Estuary TELEMAC model.

9.1   Bed form migration

The migration of wave breaker patterns analysed with the cross correlation method in Section 7.3 shows a period of increased migration from September 2006 to January 2007 (Figure 9.1). As outlined in Section 7.3 the migration of these wave breaker patterns represents the migration of the underlying large scale bed forms, namely sand dunes. Figure 9.1 shows a distinct increase in migration from October to November, followed by a decrease in migration between November and December before increasing again from December to January. These migration results were shown to correlate

261

positively with offshore wave height (Section 7.3). The increase in migration during October 2006 was chosen to test the effectiveness of the X-band radar dune tracking method at isolating specific migration events. Storm warning data from the Environment Agency for the Dee Estuary identifies three consecutive days where storm warnings were issued, between 06.10.06 - 08.10.06 (personal communication, 2010). During these dates Gladstone Dock, Liverpool recorded sea level to be at least 5.0m above ordinance datum and wind speed to be force 8 or above. The month of October 2006 was chosen over the month of January 2007, despite having lower migration distances, as Lidar bathymetry data for the mouth of the Dee Estuary was obtained on 08.10.06. Therefore, bed form dimensions from these data were considered to be most accurate for use in calculating sediment transport due to bed form migration during October 2006.
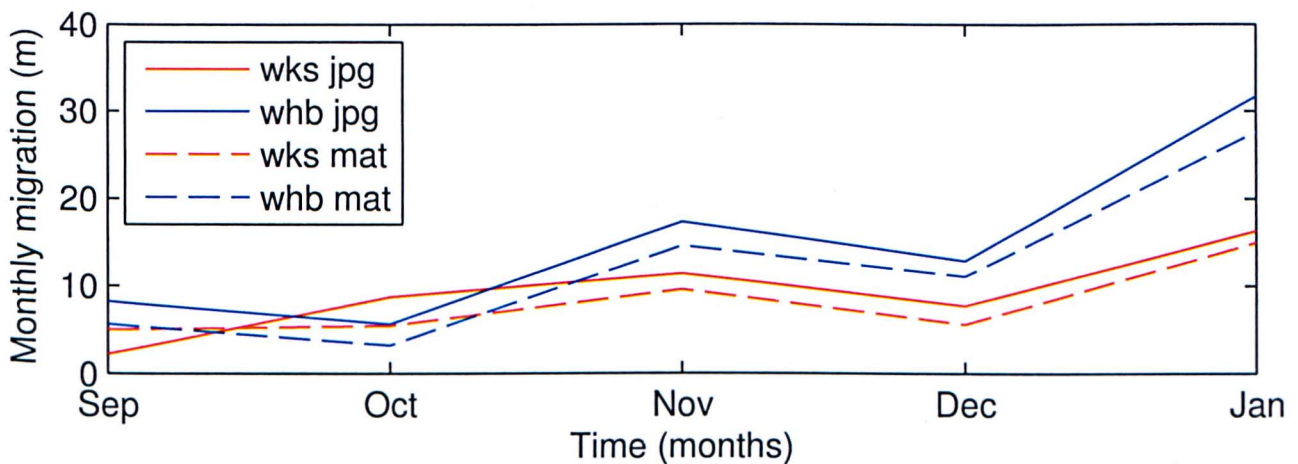
Figure 9.1: Time series, for September 2006 to January 2007, of monthly onshore migrations from the cross correlation motion tracking algorithm at West Kirby Sands and West Hoyle Bank for jpg and mat data formats. This figure is a subsection of the monthly migration of wave breaker patterns from 2006 - 2008 presented in Section 7.3.

9.2   October 2006 storm conditions

Figure 9.2 shows tidal height predictions from the POLTIPS model (courtesy of the National Oceanographic Centre, Liverpool) and actual tidal height data from the Hilbre Island tide gauge for October 2006. This shows how the storm period identified by the Environment Agency, between 06 to 08 October 2006 occurs during a time of spring tides, with a maximum high water level of 10.29m. The mean tidal surge for this time, calculated as the actual tidal height from the Hilbre tide gauge minus the predicted tidal height from the POLTIPS model, was 0.4m. This increase in the recorded tidal height from the predicted height was caused by low atmospheric pressure associated with an

anticyclonic storm.
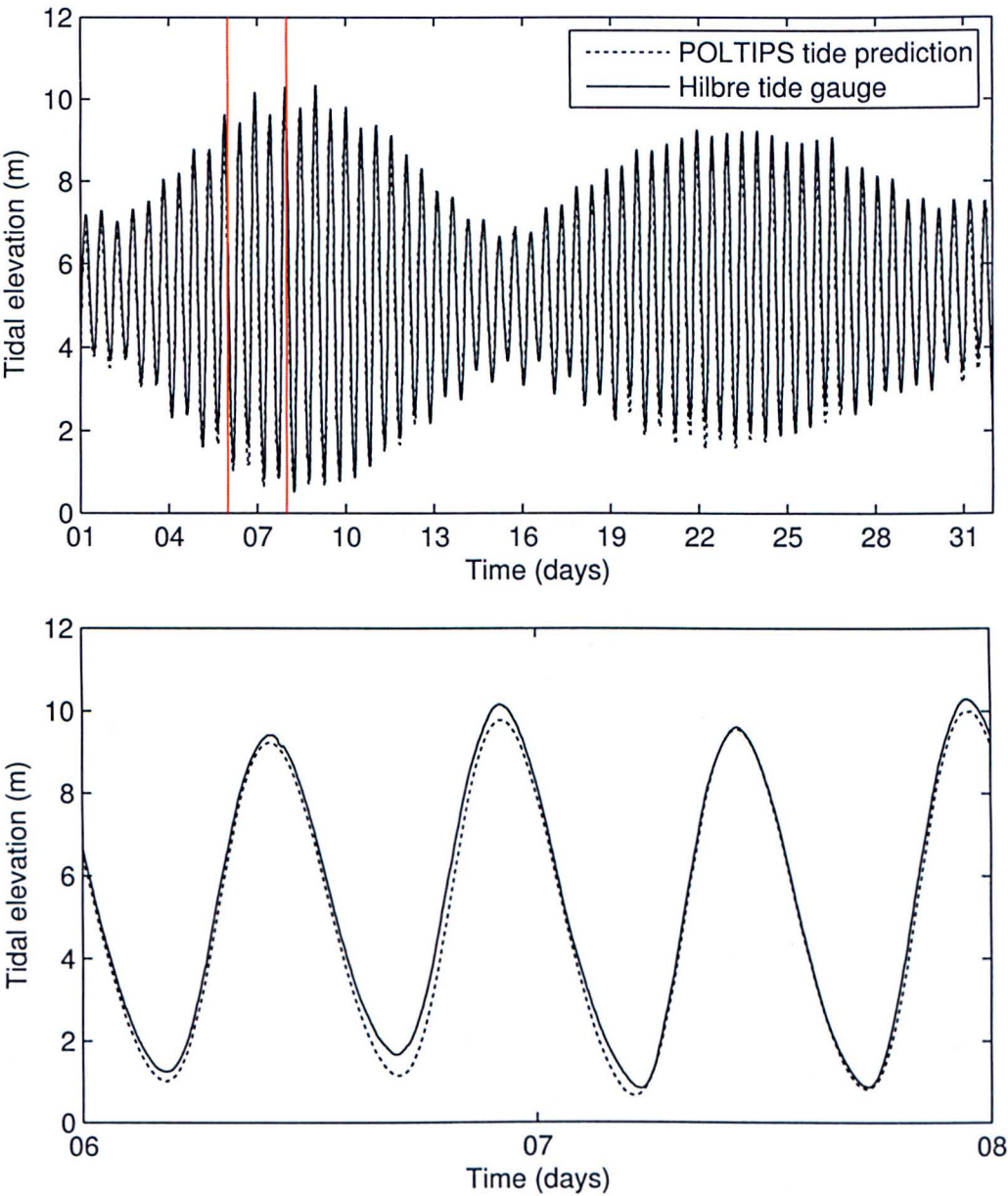
Figure 9.2: Tidal elevation data from the POLTIPS tidal prediction model and the Hilbre Island tide gauge for October 2006. The red lines mark the start and finish of the storm on 06-08 October 2006 recorded by the Environment Agency, which is shown in the sub-plot.

Figure 9.3 shows wave heights for October 2006 recorded at the WaveNet buoy located in Liverpool Bay and the Triaxys buoy, located in the mouth of the estuary, in the Hilbre Channel (Section 4.4.2). Wave heights dramatically increased between 06 and 08 October 2006 (Figure 9.3) to the maximum wave heights recorded in October 2006, of 3.4m at the WaveNet buoy and 2.7m at the Triaxys buoy. There were two other large wave events recorded by the WaveNet buoy on 27.10.06 and 31.10.06, where wave heights reached 3.2 and 3.4m respectively. Despite these wave heights being the same

as, or similar to, the 3.4m wave height recorded at the WaveNet buoy on 07.06.10, the Triaxys wave heights for 27.10.06 and 31.10.06 were 2.1 and 2.2m. These smaller wave heights at the estuary mouth, during large offshore waves, can be seen to occur at the time of smaller tides. In contrast, large offshore wave heights, recorded at the WaveNet buoy, occurring at a time of large spring tides, correlate positively with the large nearshore wave heights measured in the estuary mouth at the Triaxys buoy. This tidal modulation of wave heights in the mouth of the estuary can also be seen to influence wave heights on a semi diurnal time scale, with Triaxys wave heights increasing at high tide and decreasing at low tide (Figure 9.3). Wolf et al. (2007) investigated wave-current interaction in the Irish Sea and notes how the tidal modulation seen in the wave heights at the Triaxys buoy are in phase with the water depth, stating how this is almost entirely due to the reduction in fetch at lower water depths.
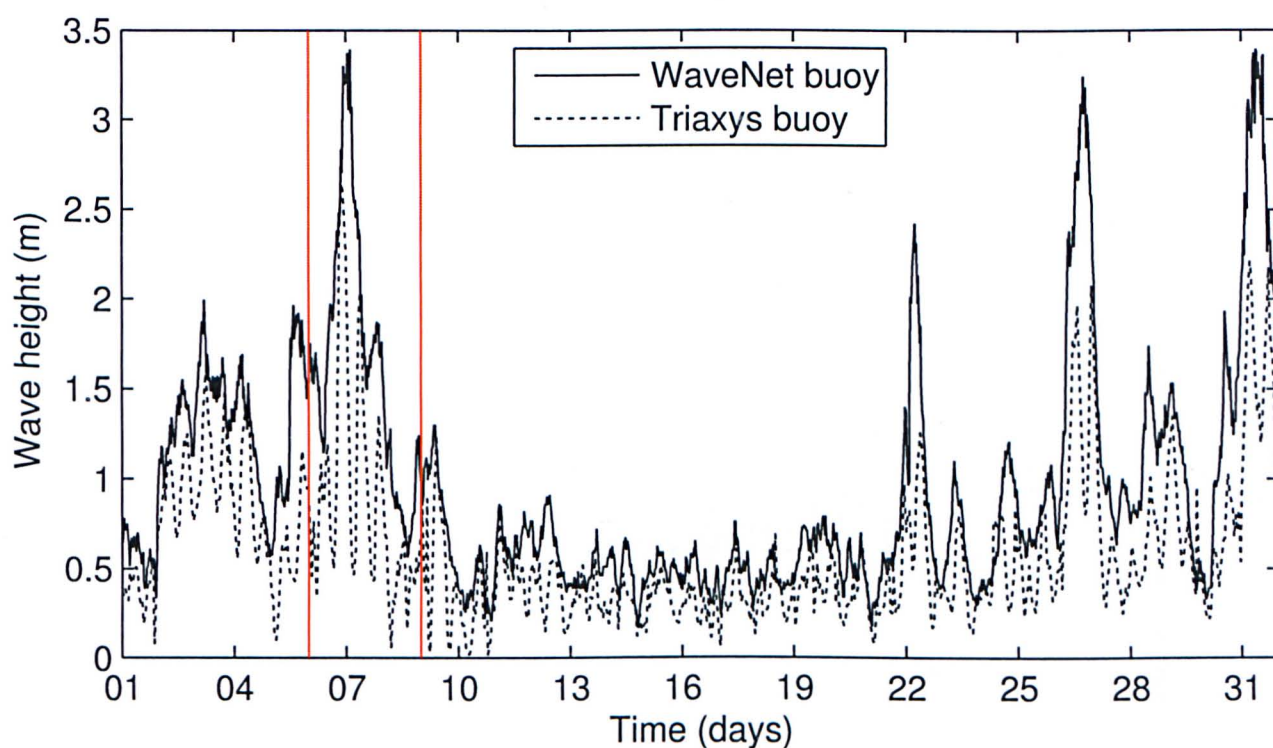
Figure 9.3: Wave height data from the WaveNet (offshore) and Triaxys (nearshore, Hilbre Channel) wave buoys for October 2006. The red lines mark the start and finish of the storm on 06-08 October 2006 recorded by the Environment Agency.

Guillou and Chapalain (2012) showed that the influence of including a tidal input when simulating waves with TOMAWAC increases wave heights by approximately 30% at high tide and decreases wave heights by approximately 10% at low tide in the mouth of an estuary. These variations are consistent with the numerical estimates of Wang et al. (2006) who found a tide-induced increase in wave heights of 10-20% in the Peal River estuary, China. The increase in wave heights also

corresponds to an increase in the local wind speed (Figure 9.4). This is to be expected in the Dee Estuary as it is situated in the fetch limited Liverpool Bay, Irish Sea, and so any waves will be locally wind generated.
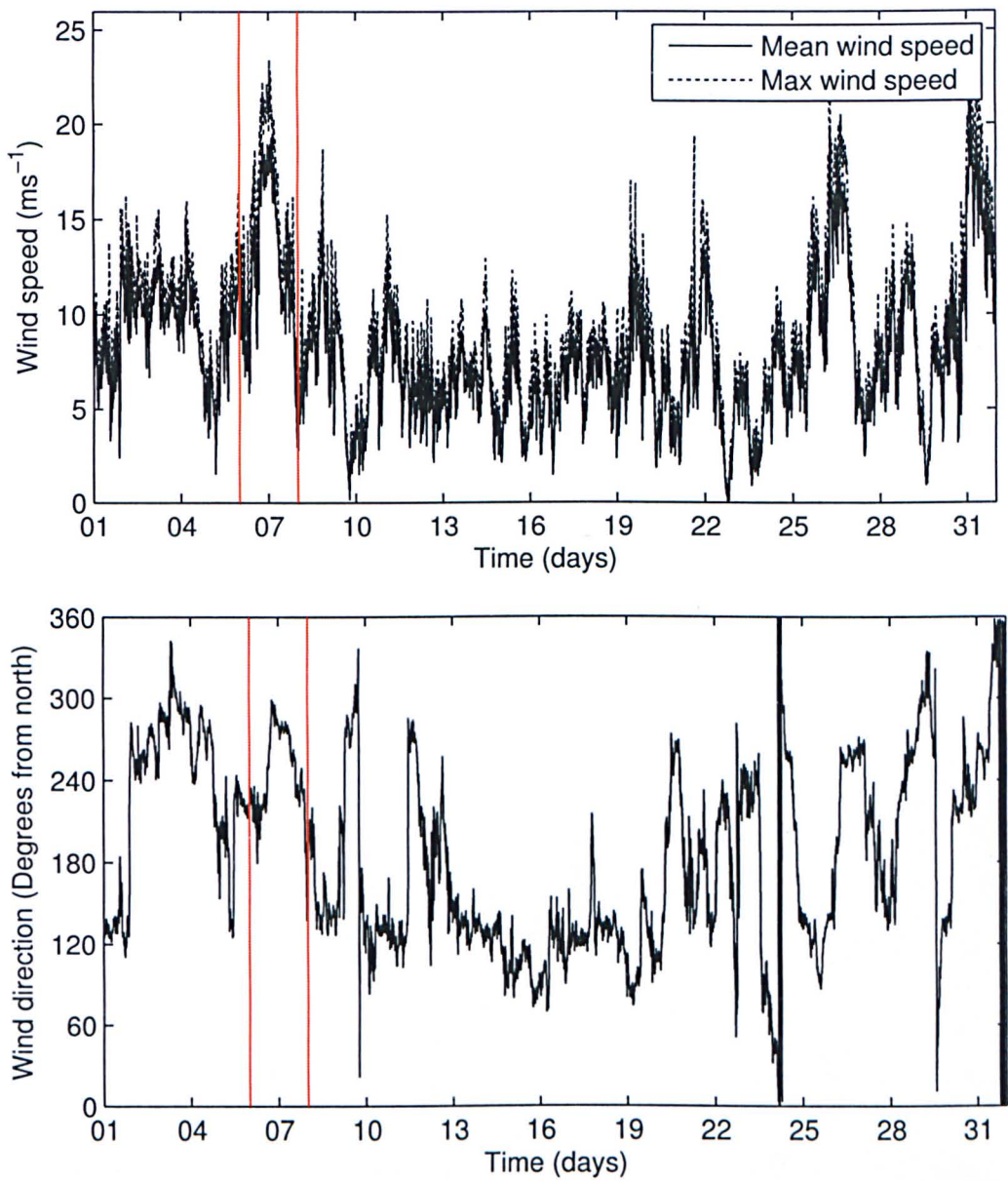
Figure 9.4: Wind speed and direction from the Hilbre Island weather station for October 2006. The red lines mark the start and finish of the storm on 06-08 October 2006 recorded by the Environment Agency.

9.3 October 2006 X-band radar data

To determine if significant migration of large scale bed forms could be detected using the X-band radar image data during the storm event of 06-08.10.06, weekly mean radar images were created

265

for further analysis. A total of five weekly mean radar images were created using the hourly mean intensity jpg and mat radar data, with the same averaging method as used to create the monthly mean images (Section 6.2). The mat mean intensity images were processed to a resolution of 2m for this storm analysis, whereas the jpg mean intensity images have a 10m resolution. The dates included in each weekly mean image time period are; 29.09-05.10 (week 1), 06.10-12.10 (week 2), 13.10-19.10 (week 3), 20.10-26.10 (week 4), 26.10-02.11 (week 5). This was so that each weekly mean image consists of seven days worth of hourly mean intensity radar data and so that the storm event is contained within one weekly mean image. As with the monthly mean radar images (Section 7.1), the dune fields on West Kirby Sands and West Hoyle Bank were chosen as areas of interest for the October 2006 weekly mean radar images. Figure 9.5 shows the weekly mean radar images for West Kirby Sands and West Hoyle Bank created using the jpg and mat radar data. Herein migration of wave breaker patterns is taken as a proxy for the migration of large scale bed forms.
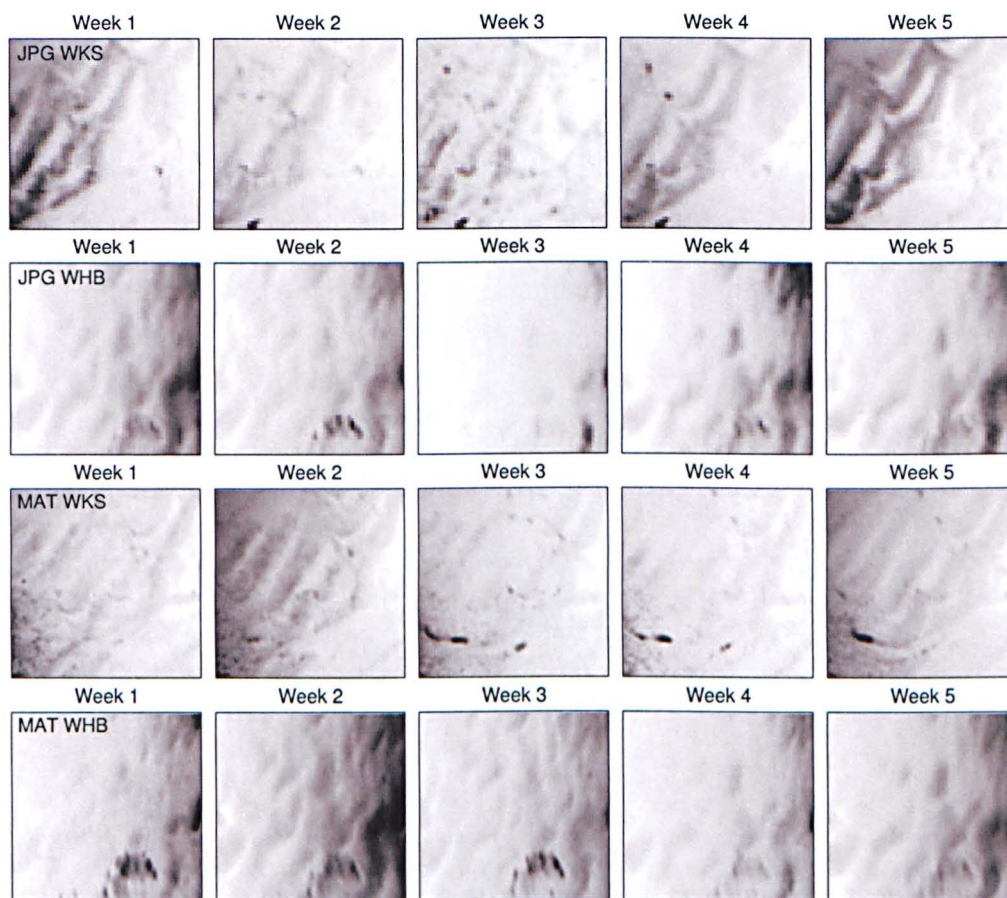
Figure 9.5: Weekly mean backscatter radar images focused on the dune fields at West Kirby Sands and West Hoyle Bank for October 2006, created using seven days worth of jpg and mat radar data for each mean image; Week 1 (29.09-05.10), Week 2 (06.10-12.10), Week 3 (13.10-19.10), Week 4 (20.10-26.10), Week 5 (26.10-02.11).

The breaking wave signal is clearly defined in all weekly mean images for West Kirby Sands and

West Hoyle Bank (Figure 9.5). The clear regular pattern observed in the monthly mean radar images (Section 7.1) can also be seen over the shorter time scale used to create the weekly mean radar images. The darker areas visible in the weekly mean radar images correspond to increased radar backscatter, as a result of persistently breaking waves over an underlying dune field. As detailed in Section 7.2 the areas of persistently breaking waves detected by the radar would have occurred primarily at high tide, with observations at other tidal stages being less weighted in the averaging process. It is hard to distinguish the migration of wave breaker patterns by eye between these weekly mean images. However the application of the 2D cross correlation algorithm to these data is considered in the following section in order to attempt to detect any movement of features on a pixel to sub-pixel scale.

9.4   Motion tracking of weekly mean radar images

Cross correlation analysis of weekly mean radar images shows the migration of wave breaker patterns between weekly images, showing how short wave events such as the storm on 06-08.10.06 can affect the magnitude and direction of the migration of large scale bed forms in the mouth of the Dee Estuary. The x and y components of migration are used to plot migration vectors, positioned in the center of the cross correlation search windows, for West Kirby Sands (Figures 9.6 & 9.8) and West Hoyle Bank (Figures 9.7 & 9.9) using both the jpg and mat radar data.
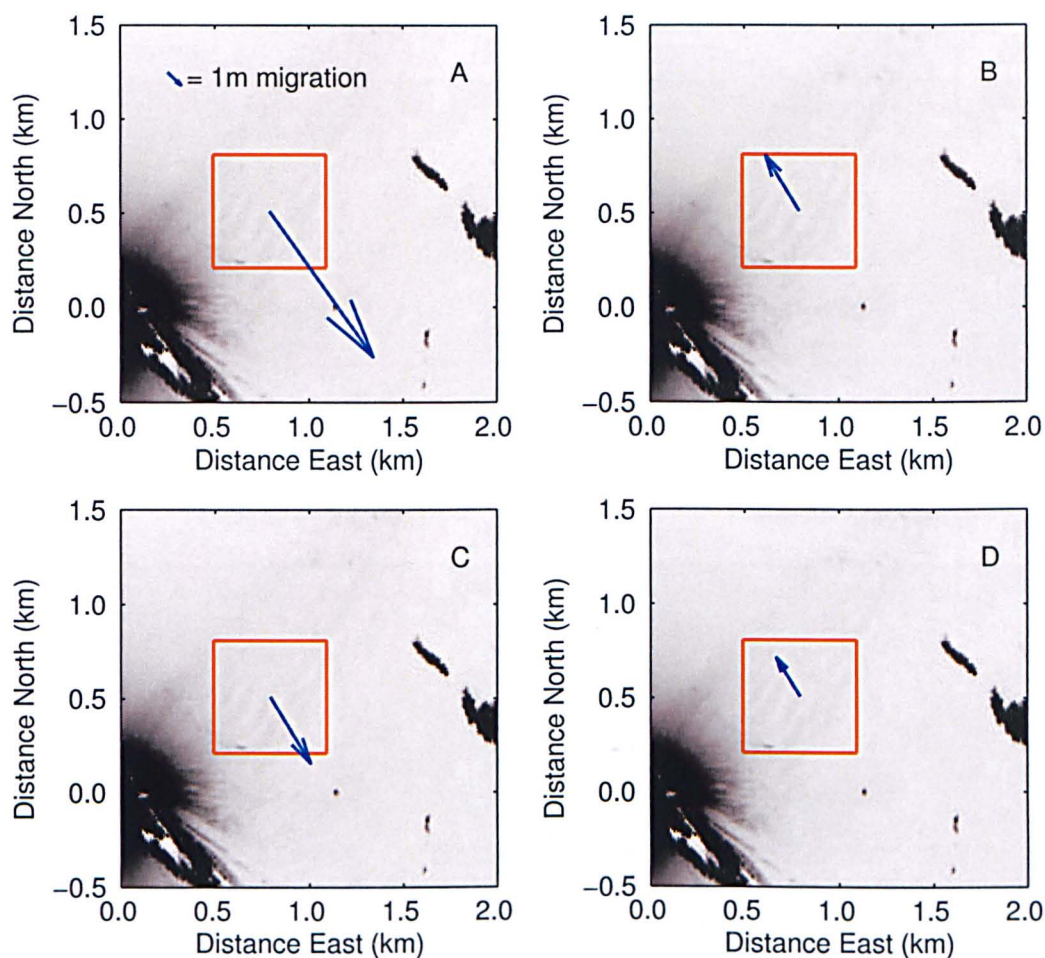
Figure 9.6: Migration vectors of wave breaker patterns at West Kirby Sands from cross correlation analysis of weekly mean jpg radar images for A) week 1 -2, B) week 2-3, C) week 3-4 and D) week 4-5.
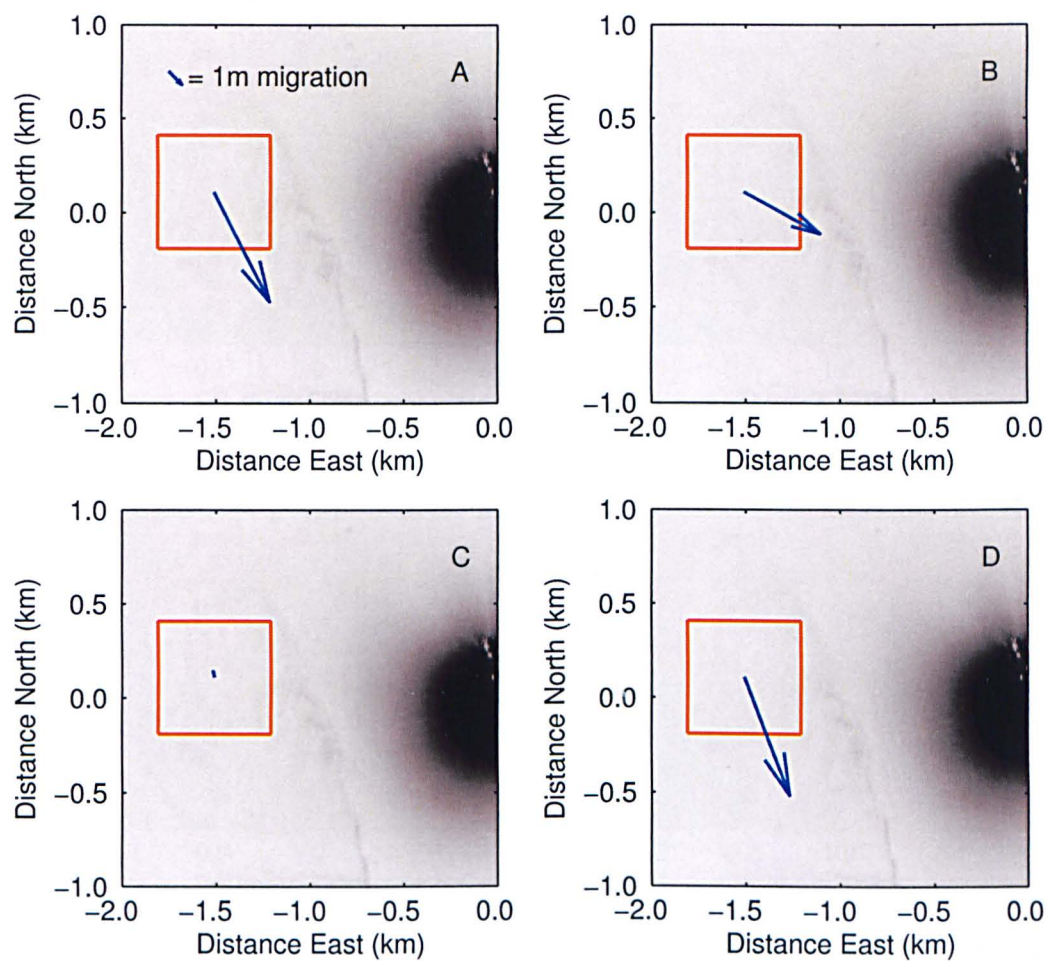
Figure 9.7: Migration vectors of wave breaker patterns at West Hoyle Bank from cross correlation analysis of weekly mean jpg radar images for A) week 1 -2, B) week 2-3, C) week 3-4 and D) week 4-5.
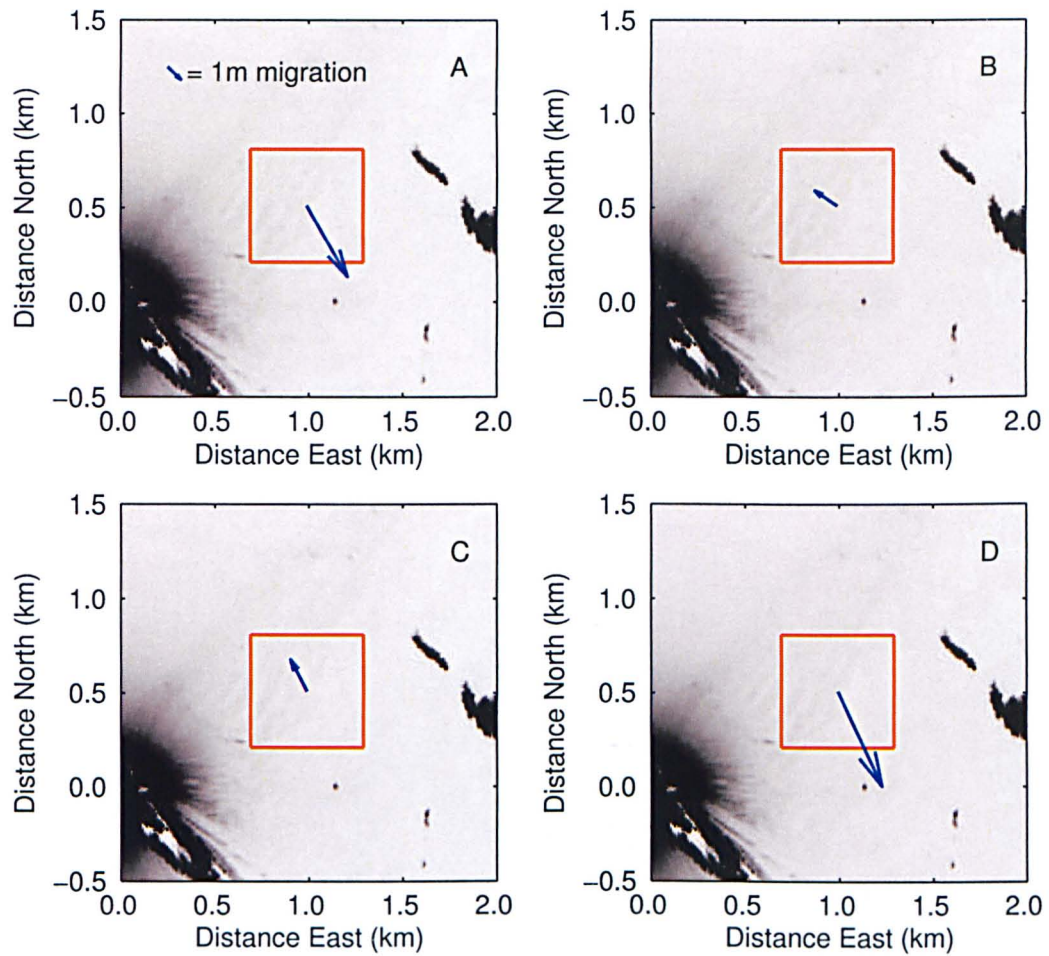
Figure 9.8: Migration vectors of wave breaker patterns at West Kirby Sands from cross correlation analysis of weekly mean mat radar images for A) week 1 -2, B) week 2-3, C) week 3-4 and D) week 4-5.
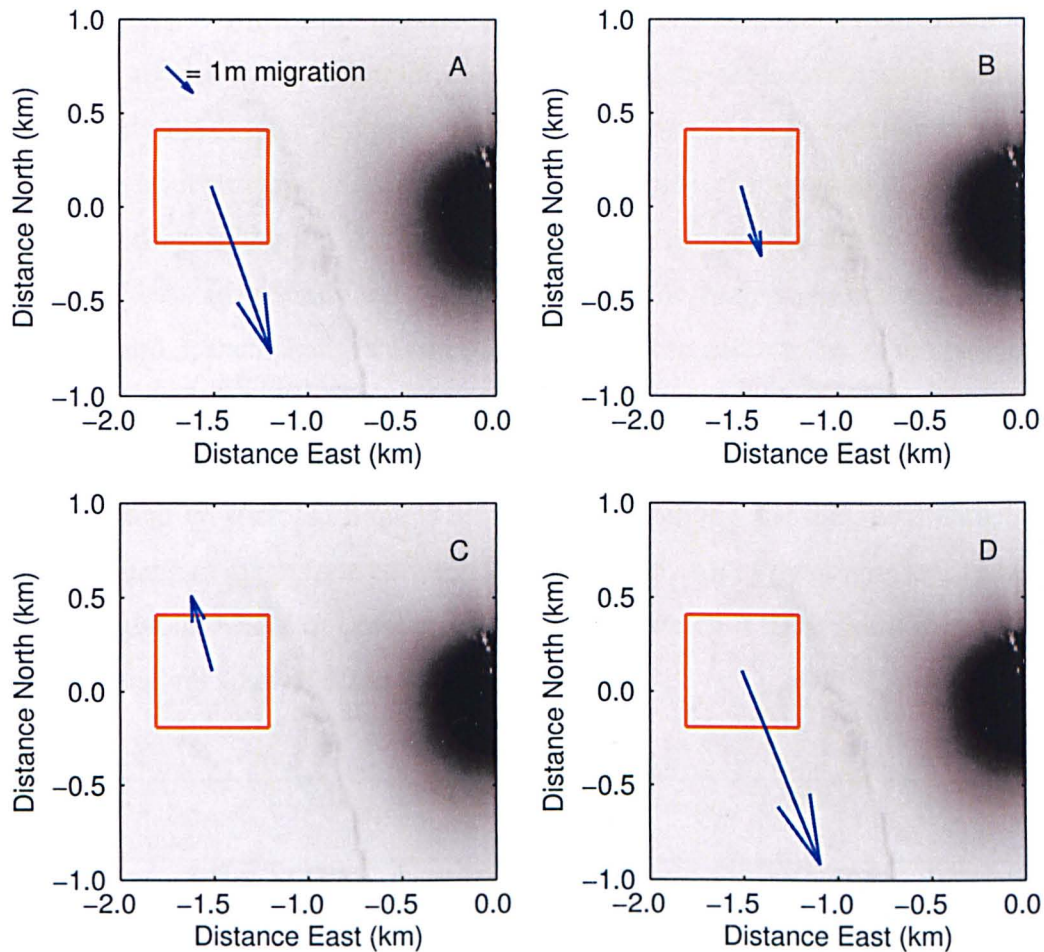
Figure 9.9: Migration vectors of wave breaker patterns at West Hoyle Bank from cross correlation analysis of weekly mean mat radar images for A) week 1 -2, B) week 2-3, C) week 3-4 and D) week 4-5.

The migration vectors show that there is a significant change in the direction and magnitude of migration between weekly mean radar images (Figures 9.6 - 9.9). Table 9.1 shows the magnitude of cross correlation migration (m) for West Kirby Sands and West Hoyle Bank using the jpg and mat radar data along with the migration from identical images (zmig). The identical image migration accounts for the adverse effect of image noise originating from using large quantities of radar data to create weekly mean radar images. This image noise effect is detailed in Section 7.4, stating how the images are mathematically identical, yet the motion tracking algorithm will detect a migration due to the polynomial curves fitted to the correlation matrix. A pixel analysed with the cross correlation algorithm for the jpg and mat radar data covers an area of $100m^2$ and $4m^2$ respectively. Weekly radar images contain, on average, 193 values for each pixel, which introduces a significant amount of image noise. This noise is quantified by calculating the migration distance between two identical images (Table 9.1). The cross correlation analysis calculates migration to an accuracy of $1/10^{th}$ of

a pixel, which equates to 1m for the jpg data and 0.2m for the mat data. Therefore a standard error of 2m per week is applied to the migration calculated using the cross correlation method for jpg and 0.4m for mat weekly mean radar images. Migration values are to set to negative numbers where migration vectors are orientated in a northerly direction to represent migration offshore, while positive values represent onshore migration. Large magnitude onshore migration can be seen to occur between weeks 1 and 2 at West Kirby Sands and West Hoyle Bank for the jpg and mat radar data. Migration, between weeks 2 and 3, then changes to an offshore direction and smaller magnitude at West Kirby Sands but remains onshore at West Hoyle Bank, at a smaller magnitude but significantly greater than the offshore migration seen at West Kirby Sands during this interval. From week 3 to 4 migration at West Kirby Sands and West Hoyle Bank is offshore from both jpg and mat radar data, before turning onshore and increasing in magnitude between weeks 4 and 5. All of the migrations between identical images are below the threshold of cross correlation error, which is $1/10^{th}$ of a pixel, for the jpg and mat radar data with pixel sizes of 10 and 2m respectively.

Migration (m week^{-1})	A	zmig ($\pm$)	B	zmig ($\pm$)	C	zmig ($\pm$)	D	zmig ($\pm$)
WKS JPG	7.89	0.17	-1.05	0.31	-2.71	0.28	2.79	0.19
WKS MAT	3.33	0.13	-0.33	0.21	-1.10	0.35	4.45	0.22
WHB JPG	6.49	0.28	4.63	0.39	-0.34	0.28	6.68	0.49
WHB MAT	4.68	0.01	1.92	0.05	-2.07	0.06	5.52	0.06

Table 9.1: Weekly breaker pattern migration rates for October 2006 calculated using the motion tracking algorithm at West Kirby Sands (WKS) and West Hoyle Bank (WHB). Identical image migration (zmig) represents image noise contained within each weekly mean radar image. A) week 1 -2, B) week 2-3, C) week 3-4 and D) week 4-5.

The net migration, calculated as the sum of all weekly migration distances, for West Kirby Sands is 6.92m for the jpg radar data and 6.35 for the mat data, while West Hoyle Bank has a higher net weekly migration of 17.46m for the jpg radar data and 10.05m for the mat data. These net migration values compare favourably with the October 2006 monthly migration distances based on the motion tracking algorithm (Section 7.4) at West Kirby Sands which are 8.76m and 5.47m for the jpg and mat data respectively. However, the net weekly migration distance for West Hoyle Bank is significantly larger than the monthly migration distances for October 2006 which are 5.59m and 3.23m for the jpg and mat radar data. This suggests that significant short term migration was occurring at West Hoyle Bank which is not detected by the motion tracking algorithm over the longer time scales of the monthly mean radar images. Figure 9.10 shows a time series of the weekly mean radar image migration, the zero migration line is marked (dashed line) for reference showing the change in migration direction

from onshore, to offshore before returning to onshore during October 2006. The migration values are plotted at the last day of each weekly period, as the migration being calculated is the product of the local wave and current conditions during each weekly time interval. The general migration trend follows that seen in the cross correlation analysis of the monthly mean radar images (Figure 9.1) with greater migration occurring at West Hoyle Bank.
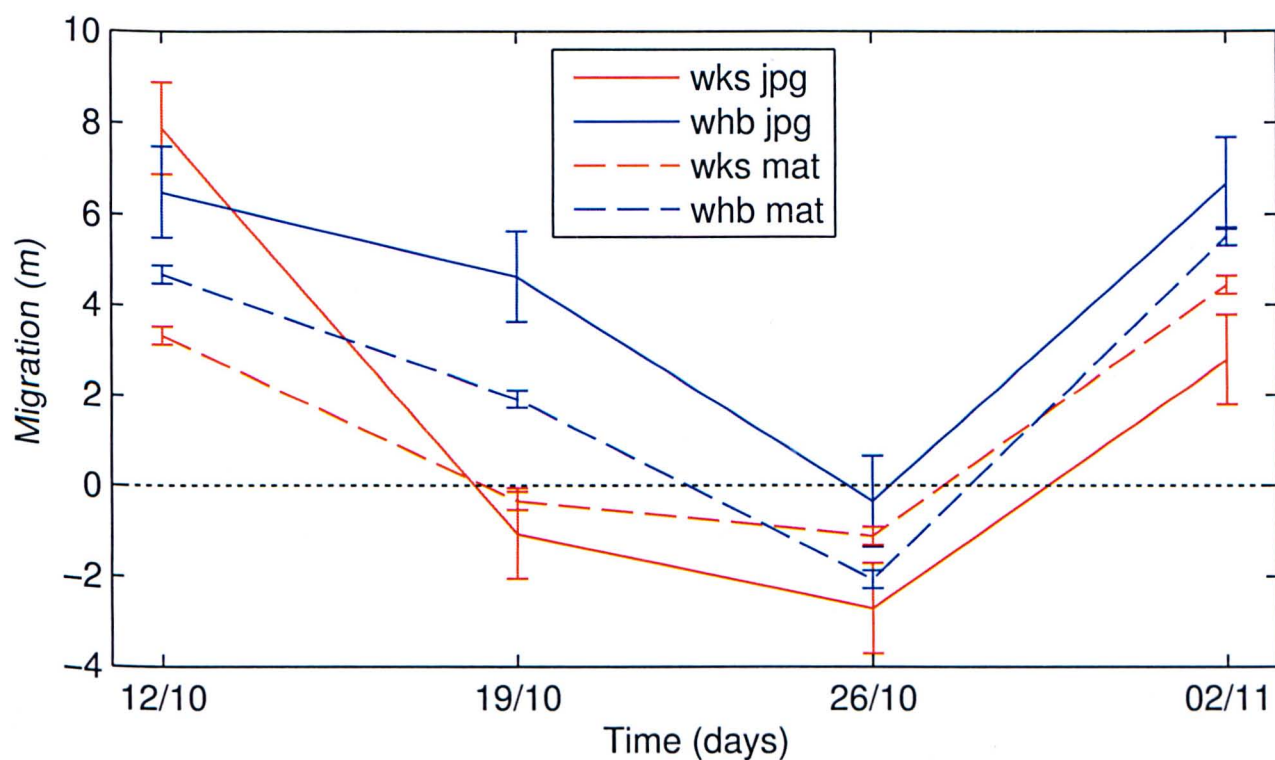
Figure 9.10: Time series of weekly wave breaker pattern migration from the cross correlation motion tracking algorithm at West Kirby Sands and West Hoyle Bank for jpg and mat data formats.

The wave conditions from the Wavenet and Triaxys buoys can be seen in Figure 9.11, showing significant wave height for weeks 1-5 of the weekly mean radar images. The start of each weekly mean radar image is marked with the blue dashed lines and the beginning and end of the 06-08.10.06 storm event are marked with solid red lines. The start of the storm period (06.10.06) coincides with the start of week 2 and as such the red marker appears over written by the blue dashed marker in Figure 9.11. An increase in wave height to the maximum values recorded, by the WaveNet and Triaxys buoys, over the weekly cross correlation analysis period occurs at the beginning of week 2, which coincides with the 06-08.10.06 storm event. Mean wave height at the WaveNet buoy increases from 0.96 to 1.15m from week 1 to week 2. Week 3 is characterised by small wave heights, with a mean wave height of 0.47m, before increasing to 0.74m during week 4. Another significant increase in wave height occurs during week 5, with a mean value of 1.39m. The mean wave height from the WaveNet buoy

for week 5 is 17% larger than for week 2, which contains the storm event identified earlier. However, the maximum wave height experienced in the mouth of the estuary, recorded by the Triaxys buoy, is 2.65m for week 2 and 2.21m for week 5.
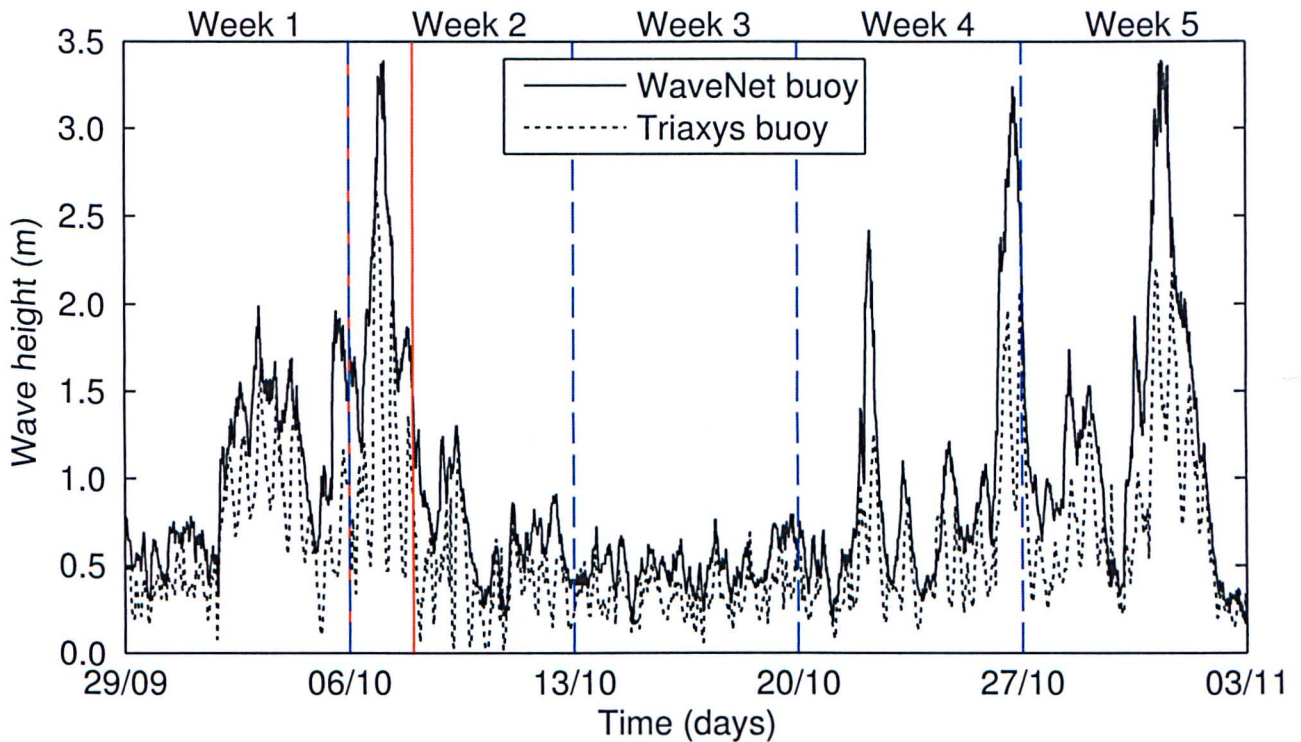
Figure 9.11: Wave height data presented in figure 9.3, here supplemented by weekly mean intervals shown by the blue dashed lines. The red lines mark the October storm period.

Weekly migration of the wave breaker patterns are plotted against weekly average wave heights for Liverpool Bay, WaveNet buoy (Figure 9.12) and the mouth of the Dee Estuary, Triaxys buoy (Figure 9.13). All of the migration values calculated are less than 10m, which is less than one pixel of the jpg radar data. Therefore the cross correlation analysis method is better suited to identifying the direction and magnitude of sub pixel change on shorter, weekly time scales using the jpg radar data. Figures 9.12 and 9.13 show a generally increasing trend in migration with larger wave heights, with the greatest migration occuring between weeks 1-2 and 4-5, when mean recorded wave heights were greater than 1m at the WaveNet buoy and 0.5m at the Triaxys buoy. While greater migration of wave breaker patterns can be seen to occur with larger wave heights in Figures 9.12 and 9.13, the correlation is not as strong as the migration calculated from the monthly mean radar images using the 2D cross correlation motion tracking algorithm. This could be due to other factors occurring on relatively short time scales which are influencing the relationship between migration and wave height. These could include variations in wave direction, spring-neap tidal variation and bed form hysteresis effects.
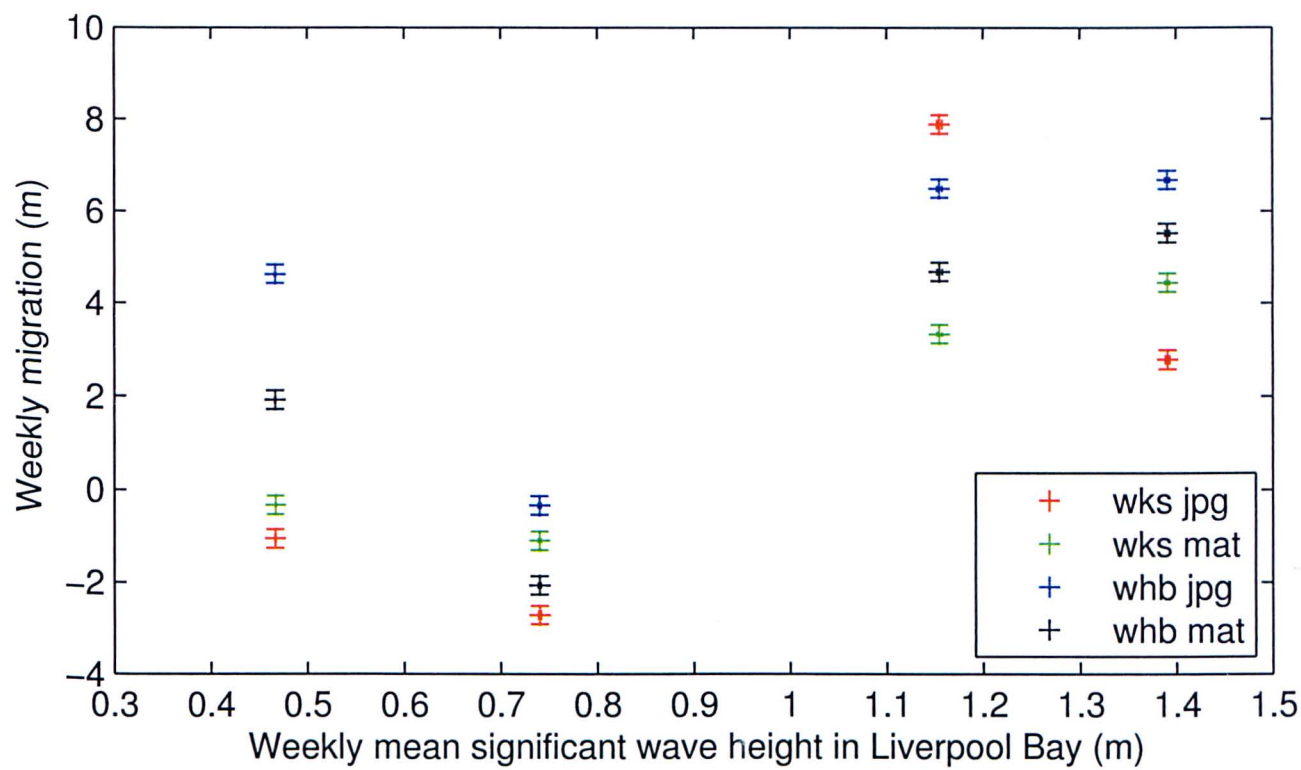
Figure 9.12: Weekly wave breaker pattern migration from the cross correlation motion tracking algorithm at West Kirby Sands and West Hoyle Bank for jpg and mat data formats plotted against weekly mean wave heights for Liverpool Bay from the WaveNet buoy.
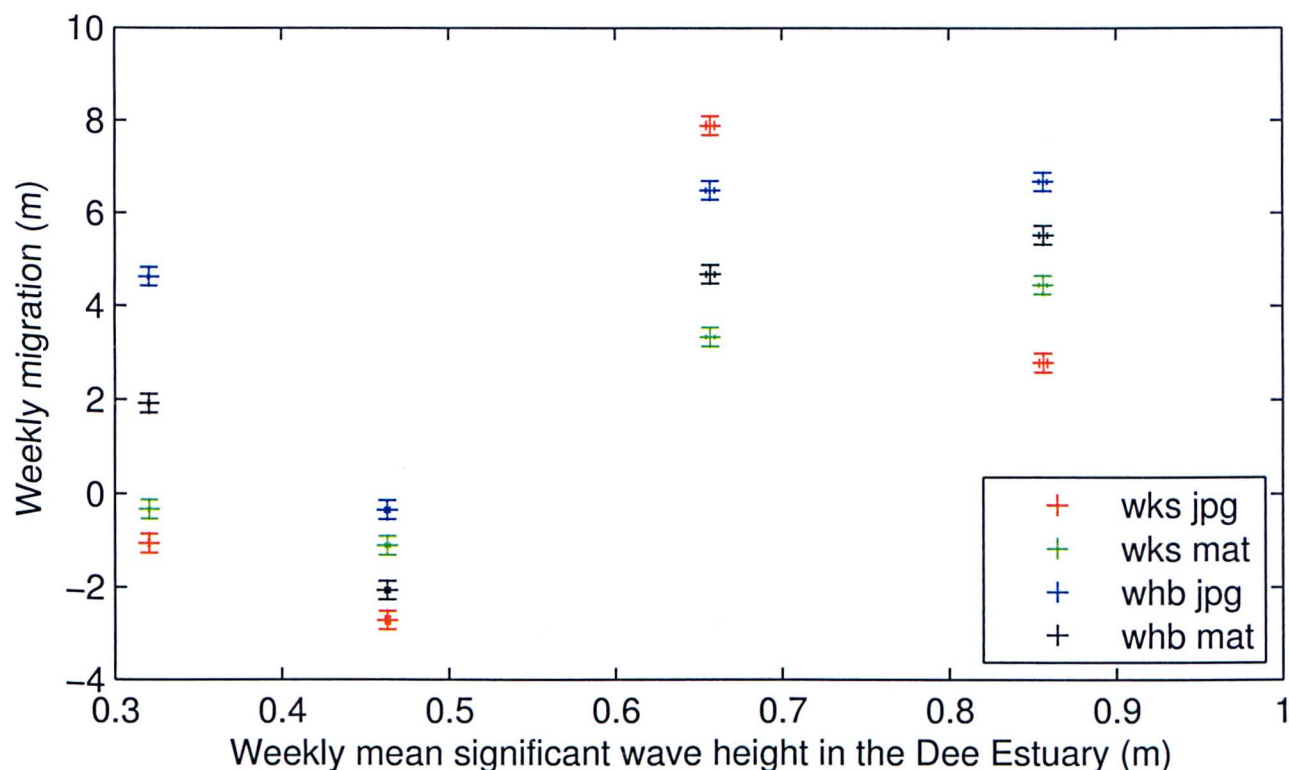
Figure 9.13: Weekly wave breaker pattern migration from the cross correlation motion tracking algorithm at West Kirby Sands and West Hoyle Bank for jpg and mat data formats plotted against weekly mean wave heights for the mouth of the Dee Estuary from the Triaxys buoy.

9.4.1 Bed load transport inferred from weekly dune migration

Using the same method that was applied to monthly migration distances (Equation 7.3), but applying it here to weekly migration distances, the weekly bed load sediment flux per unit length along the bed form crest can be calculated using the bed form cross sectional area and wavelength while also accounting for porosity (Table 9.2). Large scale bed forms were previously extracted from the October 2006 Lidar data, as outlined in Section 7.4, and bed form dimensions calculated. The dune field at West Kirby Sands was found to have a mean cross sectional area of $31.5 \pm 3.8 m^2$ and mean wavelength of $110 \pm 3.4 m$. The mean dune cross sectional area at West Hoyle Bank was $18.5 \pm 4.1 m^2$ and mean wavelength was $98.3 \pm 3.6 m$.

Bed load flux (m² tide⁻¹)	A	B	C	D
WKS JPG	0.100	-0.013	-0.035	0.037
WKS MAT	0.042	-0.004	-0.014	0.056
WHB JPG	0.054	0.038	-0.002	0.056
WHB MAT	0.039	0.016	-0.017	0.046

Table 9.2: Weekly bed load flux calculated from dune migration distances for October 2006 calculated using the motion tracking algorithm at West Kirby Sands (WKS) and West Hoyle Bank (WHB) with jpg and mat radar data at A) week 1 -2, B) week 2-3, C) week 3-4 and D) week 4-5.

9.5 Simulating the October storm in TELEMAC

The TELEMAC modelling system was set up to simulate the wave and current conditions during the 6th-8th October 2006 storm event for the Dee Estuary and surrounding coastline using the Dee model grid outlined in Chapter 4. The model was run in a chained mode (Section 4.1) so that tidal currents, waves, wave generated currents and the resulting sediment transport were simulated. This model chaining process requires three separate model runs; initially the tide alone is generated with TELEMAC-2D, followed by a wave simulation using TOMAWAC including the previous tidal elevations to create the wave generated currents, and then finally TELEMAC-2D and SISYPHE are run in coupled mode with the wave simulation input. In addition the simulation involved bed roughness feedback between TELEMAC-2D and SISYPHE which affect both the flow and sediment dynamics. This simulated the hydrodynamic conditions, including tides and waves, and the resulting sediment transport over the simulation period of 6th-13th October 2006. This simulation period was chosen so that it coincided with the period covered by the week 2 radar mean image and contained the October storm event.

9.5.1 Tidal boundary conditions

A tidally varying free surface elevation was imposed at the offshore liquid open boundary of the model domain using eight tidal constituents (Q_1, O_1, P_1, K_1, M_2, S_2, K_2, M_4) obtained from the POLCOMS Irish Sea tidal model (Section 4.3.1). The amplitudes and phases of each of the tidal constituents were linearly interpolated onto the 62 model liquid open boundary points and programmed into the BORD subroutine to calculate the free surface elevation at each boundary node at each time step. The start date was set to 6th October 2006 and the number of 10-second time steps was 69480, giving a simulation duration of 8 days plus one hour for the use in the subsequent wave simulation. Free surface elevations are compared in Figure 9.14 for the open liquid boundary and the two areas of

interest for sand dune migration in the mouth of the Dee Estuary, namely West Kirby Sands and West Hoyle Bank.
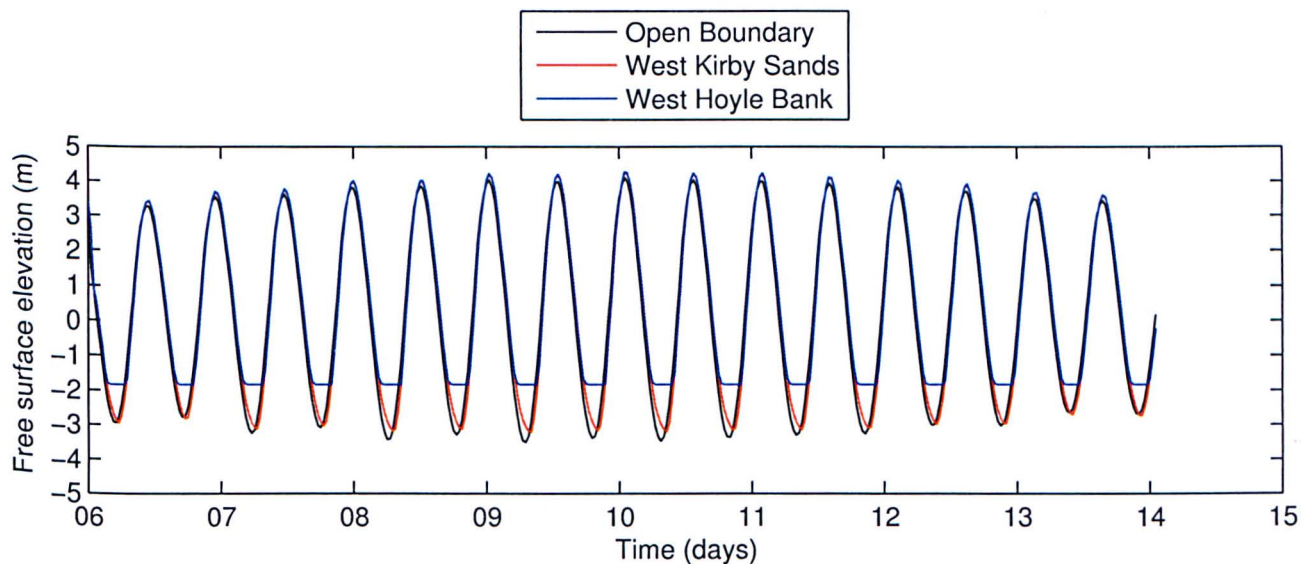
Figure 9.14: Free surface elevations from simulated tidal elevations for 6th-13th October 2006 at three locations within the model domain: Offshore open liquid boundary, West Kirby Sands and West Hoyle Bank. The lowest free surface elevation value for West Hoyle Bank is -1.8m due to its location on a large sand bank which dries out at low tide.

A comparison between tidal elevations from the Hilbre tide gauge and tidal simulation data from a similar location shows good agreement between measured and simulated elevations (Figure 9.15). The simulation slightly under predicts tidal elevations at the beginning of the model run, most noticeably around the time of the storm event, between days 06 to 08. This could be a result of low atmospheric pressure associated with the storm event increasing the local sea level, something which the model does not account for.
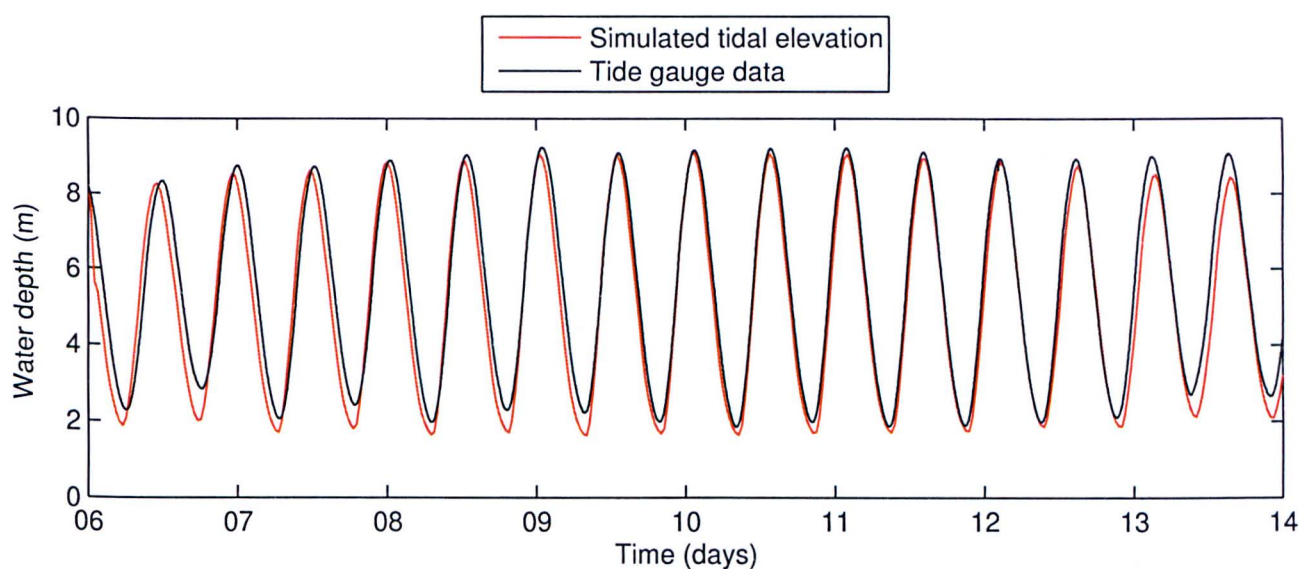
Figure 9.15: Validation of TELEMAC-2D tidal simulation with Hilbre tide gauge data between 6th-13th October 2006.

9.5.2 Wave conditions at the model boundary and estuary mouth

To simulate the wave conditions between 6th - 13th October 2006 the TELEMAC wave module TOMAWAC was run with a tidal elevation input from the previous TELEMAC-2D simulation (Figure 9.15). This enabled the simulation to include the time varying effects of water depth and currents on the wave height. TOMAWAC not only simulates the wave field over the domain using the boundary forcings but also predicts the radiation stresses, which can then be used by TELEMAC-2D to simulate the resulting wave generated currents. Malvarez et al. (2004) stated that the combination of waves and tide has a major influence on the sediment transport pathways and morphology of sand flats. Guillou and Chapalain (2012) also showed the importance of the tide in the semidiurnal wave height modulation in the outer Seine Estuary using the TOMAWAC wave module. Previous analysis of wave height data from the Triaxys buoy in the mouth of the Dee Estuary showed significant tidal modulation of wave heights (Figure 9.3), therefore simulating the wave height with a tidal input is an important step in the modelling process. This is especially true when sediment transport over the sand banks in the mouth of the estuary is being examined as the time varying water depth, currents and wave heights will have a significant impact on critical bed shear stress at these locations.
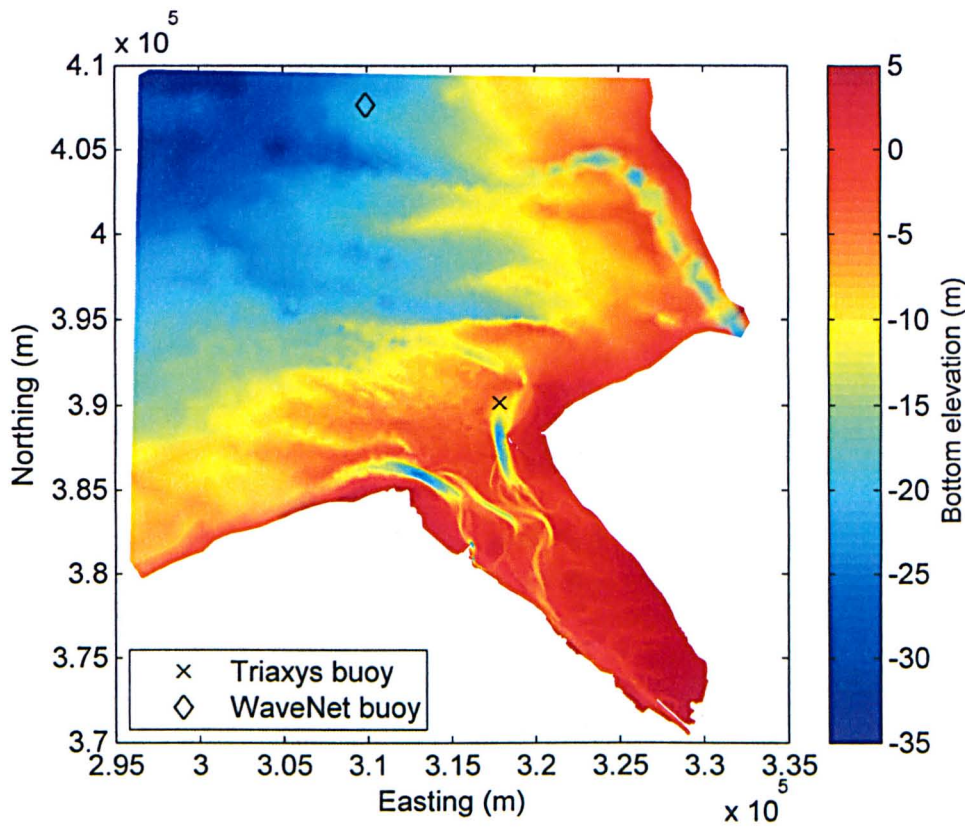
Figure 9.16: Location of the WaveNet and Triaxys wave buoys on the Dee Estuary model grid. Wave data extracted from these locations for the simulated wave field are compared with measured data from the wave buoys for validation of the TOMAWAC simulation.

Waves were simulated with non-stationary boundary conditions which varied in time but were uniform around the liquid open boundary (Section 4.4.1). Data, including wave height, frequency and direction, from the WaveNet buoy were imposed as boundary conditions so that a realistic simulation of the wave conditions during this time period was made. Wave height data from the WaveNet and Triaxys buoys are compared with wave simulation data from similar locations shown in Figure 9.16. The TOMAWAC simulated wave heights at the model boundary are in very close agreement with the WaveNet wave heights (Figure 9.17), which is to be expected as the WaveNet wave data provided the time varying boundary conditions at the liquid open boundary. A large increase in wave height can be seen during the October storm event (6th - 8th October 2006), wave heights remain low, generally less than 1m, for the remainder of the simulation.
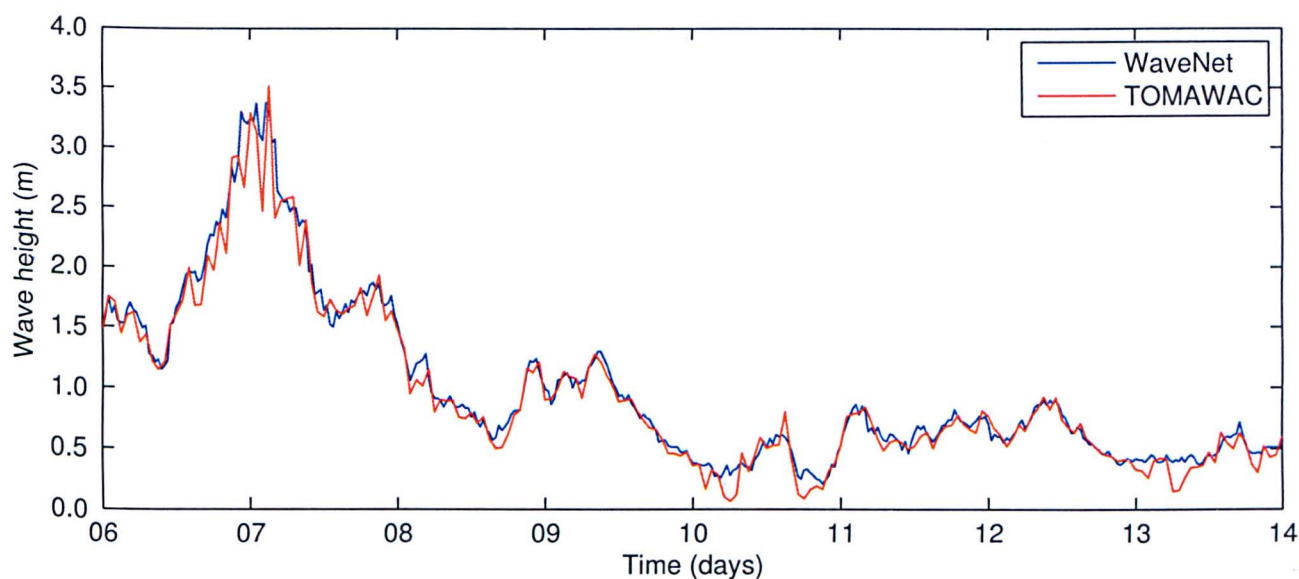
Figure 9.17: Wave heights from the WaveNet buoy at the model boundary and TOMAWAC wave simulation extracted from the same location as the wave buoy for 6th - 13th October 2006.

The simulated wave heights at the estuary mouth tend to underpredict the measured wave data from the Triaxys buoy (Figure 9.18) during the storm event. However, the remainder of the simulation where wave heights are less extreme is well correlated with the wave buoy data. Tidal modulation of the wave heights in the estuary mouth is visible in the measured data over the simulation time period, especially during the large wave heights experienced here between 6th - 8th October 2006. Smaller wave heights are experienced at low water as water depths are lower during this time and so larger waves will break on the sand banks further offshore of the wave buoy location. This tidal modulation is simulated by the model, due to the inclusion of the tidal input file whilst simulating the wave field. However the maximum wave heights are underpredicted by approximately 20% during the storm event.
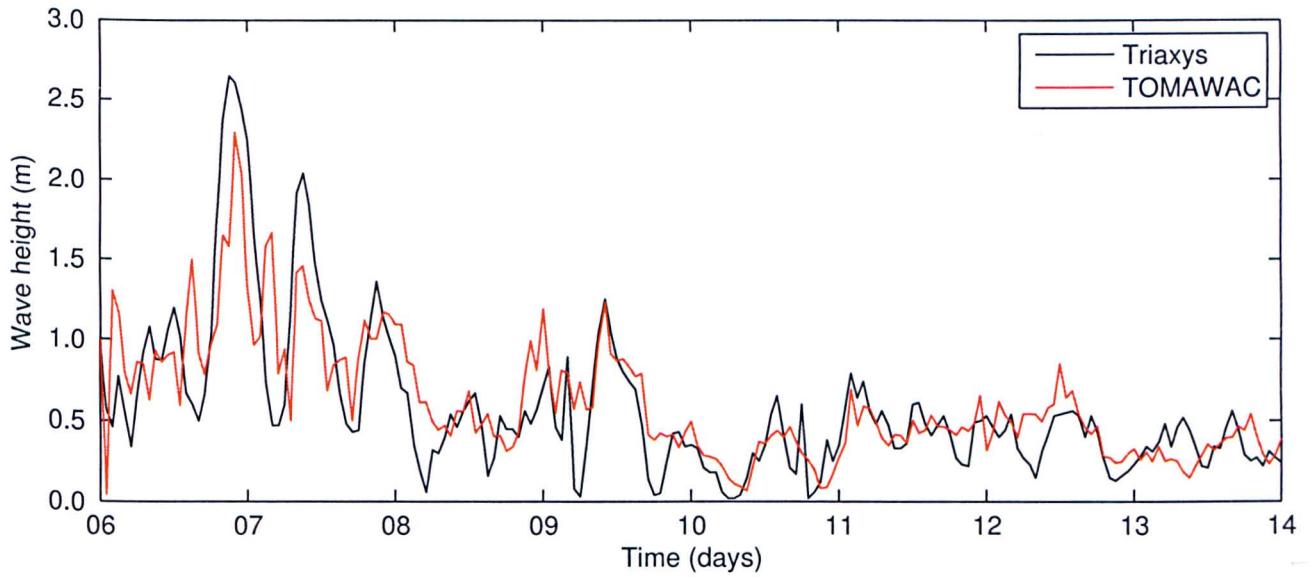
Figure 9.18: Wave heights from the Triaxys buoy at the estuary mouth and TOMAWAC wave simulation extracted from the same location as the wave buoy for 6th - 13th October 2006.

9.5.3 TOMAWAC wave model performance assessment

Differences between simulated wave results and field measurements are usually attributed to model error, assuming that the measured data are accurate. Here, statistical methods are employed to compare the numerical wave simulation results with field measurements from the WaveNet and Triaxys wave buoys over the eight day simulation period at hourly intervals. Brière et al. (2007) compared numerical results from TOMAWAC with field measurements in the Adour River mouth and the surrounding beaches of Anglet, France, using model performance statistics to assess the accuracy of predictions. To evaluate scalar quantities, such as wave height (H_s) and period (T_p), a root mean square error RMSE and scatter index SI can be used to quantify the performance of ocean wave models (Ris et al., 1999). The scatter index is defined as the RMSE normalised by the average observed value

$$RMSE = \sqrt{\frac{1}{N} \sum_N (X_n - Y_n)^2} \tag{9.1}$$

$$SI = \frac{RMSE}{\bar{X}} \tag{9.2}$$

where X_n are the observed values, Y_n are the simulated values, N is the number of observations and $\bar{X}$ is the mean observed value. The bias is then defined as

$$bias = \frac{1}{N} \sum_N (X_n - Y_n) \qquad (9.3)$$

For comparison of directional wave data the angular bias can be used (Bowers et al., 2000)

$$bias_a = \begin{cases} \tan^{-1} \frac{S}{C}, \text{for} S > 0, C > 0; \\ \tan^{-1} \frac{S}{C} + \pi, \text{for} C < 0; \text{and,} \\ \tan^{-1} \frac{S}{C} + 2\pi, \text{for} S < 0, C > 0; \end{cases} \qquad (9.4)$$

where S and C are computed from the directional difference $\Delta\theta = |\theta_x - \theta_y|$ using

$$S = \sum_N \sin(\Delta\theta_n) \qquad (9.5)$$

$$C = \sum_N \cos(\Delta\theta_n) \qquad (9.6)$$

and the circular correlation (Tracy, 2002)

$$cor = \frac{\sum_N \sin(\theta_x - \bar{\theta}_x) \sum_N \sin(\theta_y - \bar{\theta}_y)}{\sqrt{\sum_N [\sin(\theta_x - \bar{\theta}_x)]^2 \sum_N [\sin(\theta_y - \bar{\theta}_y)]^2}} \qquad (9.7)$$

Simulated wave data have been extracted from the locations of the WaveNet and Tiraxys buoys within the model grid (Figure 9.16) in order to study the offshore and nearshore wave fields. Table 9.3 shows these simulation results analysed using the aforementioned statistical methods to quantify the hindcast skill in reproducing the physical wave attributes; significant wave height (H_s), peak period (T_p) and wave direction (*Dir*).

Location	RMSE	SI	Bias	Bias$_a$	Cor
WaveNet Hs (m)	0.12	0.11	0.04		
WaveNet Tp (s)	0.57	0.12	-0.06		
WaveNet Dir (°)				1.26	0.82
Triaxys Hs (m)	0.28	0.50	-0.05		
Triaxys Tp (s)	1.85	0.49	-0.28		
Triaxys Dir (°)				2.39	0.57

Table 9.3: Error metrics for wave height (H_s), peak period (T_p) and wave direction (θ) to compare the simulated TOMAWAC wave results with wave measurement data from the WaveNet and Triaxys wave buoys

This initial assessment of wave simulation using TOMAWAC shows that the SI error for H_s is 11%

at the model boundary (WaveNet buoy) and 50% at the mouth of the estuary (Triaxys buoy). The simulation of peak period (T_p) follows a similar trend, with a lower SI error of 12% at the WaveNet buoy but 49% at the Triaxys buoy. The bias values for wave height (H_s) show that the simulation over-predicts by 0.04m at the WaveNet buoy but underpredicts by 0.05m at the Triaxys buoy. The peak wave period (T_p) shows an underprediction by 0.06s at the WaveNet buoy but a much greater underprediction of 0.28s at the Triaxys buoy. The simulated wave direction (θ) shows a similar trend to the simulated wave height and peak period, with better correlation between model and measured data at the model boundary compared with the mouth of the estuary. The circular correlation (cor) is a normalised value, with results which range from 0 (uncorrelated) to 1 (perfect correlation). Table 9.3 shows the accuracy of θ at the WaveNet location to be 0.82 and 0.57 at the Triaxys location. The well correlated error metrics at the WaveNet buoy location adds confidence to the application of time varying boundary conditions when simulating waves in the Dee Estuary. The reduction in the correlation values between simulated and measured wave data in the mouth of the estuary could be due to the simulation method implemented, which does not include wind generated waves within the model domain and applies the time varying boundary conditions uniformly around the open boundary, whereas in reality there may be significant spatial variation.

The error metrics (Table 9.3) have been reduced to a smaller set of performance indicators for overall skill assessment. The first step in this process is to normalise all of the error metrics to produce performance scores. For the non directional, scalar wave properties these include RMSE performance

$$\widehat{RMSE} = \left(1 - \frac{RMSE}{X_{RMS}}\right) \tag{9.8}$$

where the root mean square of the observed values is given by

$$X_{RMS} = \sqrt{\frac{1}{N}\sum_N (X_n)^2} \tag{9.9}$$

bias performance

$$\widehat{bias} = \left(1 - \frac{|bias|}{X_{RMS}}\right), \tag{9.10}$$

scatter index performance

$$\widehat{SI} = (1 - SI) \tag{9.11}$$

while for the directional wave data, angular bias performance is calculated using

$$\widehat{bias_a} = \left(1 - \frac{|bias_a|}{180}\right) \tag{9.12}$$

and the circular correlation performance, which is already normalised

$$\widehat{cor} = cor \tag{9.13}$$

The non-dimensional performance indicators range from 1 (perfect correlation) to 0 (uncorrelated) and are averaged across the eight day simulation period. Therefore, for each wave component, the performance at each wave buoy location is given by

$$P_s = \frac{\widehat{RMSE} + \widehat{bias} + \widehat{SI}}{3} \quad \text{(non-directional metrics)} \tag{9.14}$$

$$P_s = \frac{\widehat{bias_a} + \widehat{cor}}{2} \quad \text{(directional metrics)} \tag{9.15}$$

Location	P_s for H_s	P_s for T_p	P_s for θ
WaveNet	0.91	0.92	0.91
Triaxys	0.72	0.70	0.78

Table 9.4: Normalised nondimensional performance scores calculated using equations 9.8 to 9.13 for significant wave height (H_s), peak period (T_p) and wave direction (θ) using wave measurements from the WaveNet and Triaxys buoys with data extracted from similar locations in the model grid for the October 2006 simulation.

The initial error analysis shows a set of error metrics that quantify hindcast skill in reproducing physical attributes in the wave model, such as wave height, wave period and wave direction. The performance scoring method was introduced to reduce the number of error metrics in Table 9.3 into a normalised set of performance indicators which can be easily compared for overall skill assessment. By normalising and combining the error metrics a clearer overall assessment of the wave model performance at the model boundary (WaveNet) and the mouth of the estuary (Triaxys) can be made. Performance scores for significant wave height (H_s), peak period (T_p) and wave direction (θ) are shown in Table 9.4 at the two sample locations, WaveNet and Triaxys, within the model domain (Figure 9.16). This shows that the wave model performance at the domain boundary is very good for all wave parameters H_s T_p and θ with performance estimates at just over 90%. At the estuary mouth (Triaxys wave buoy) all wave parameters H_s T_p and θ are again simulated with good confidence but show lower performance values at approximately 70%. The lower performance values seen at the

Triaxys location could be caused by the not applying spatially as well as temporally varying bound-
ary conditions and could also be effected by the model bathymetry not being sufficiently accurate.
However, this being said, performance values of 70% at the estuary mouth were seen as sufficiently
accurate.

9.5.4 Simulated depth average velocity including wave influence

As the final stage in the TELEMAC modelling process, for the October 2006 simulation, TELEMAC-
2D and SISYPHE were run in a coupled mode (Section 5.4). The bed roughness was predicted
as outlined in Section 5.3 and was updated with the evolving morphology, which was output from
SISYPHE and fed back into TLEMAC-2D at every time step. This resulted in currents over the
model domain which include the influence of tides and waves. While no measurement data is available
for validation of this October 2006 simulation, previous validation of TELEMAC-2D data using this
model grid with a similar model chaining process showed good agreement (Section 4.3.4). Figure 9.19
shows the absolute depth averaged velocity, with the u and v scalar velocity components, simulated
with the influence of tides and waves at West Kirby Sands and West Hoyle Bank.
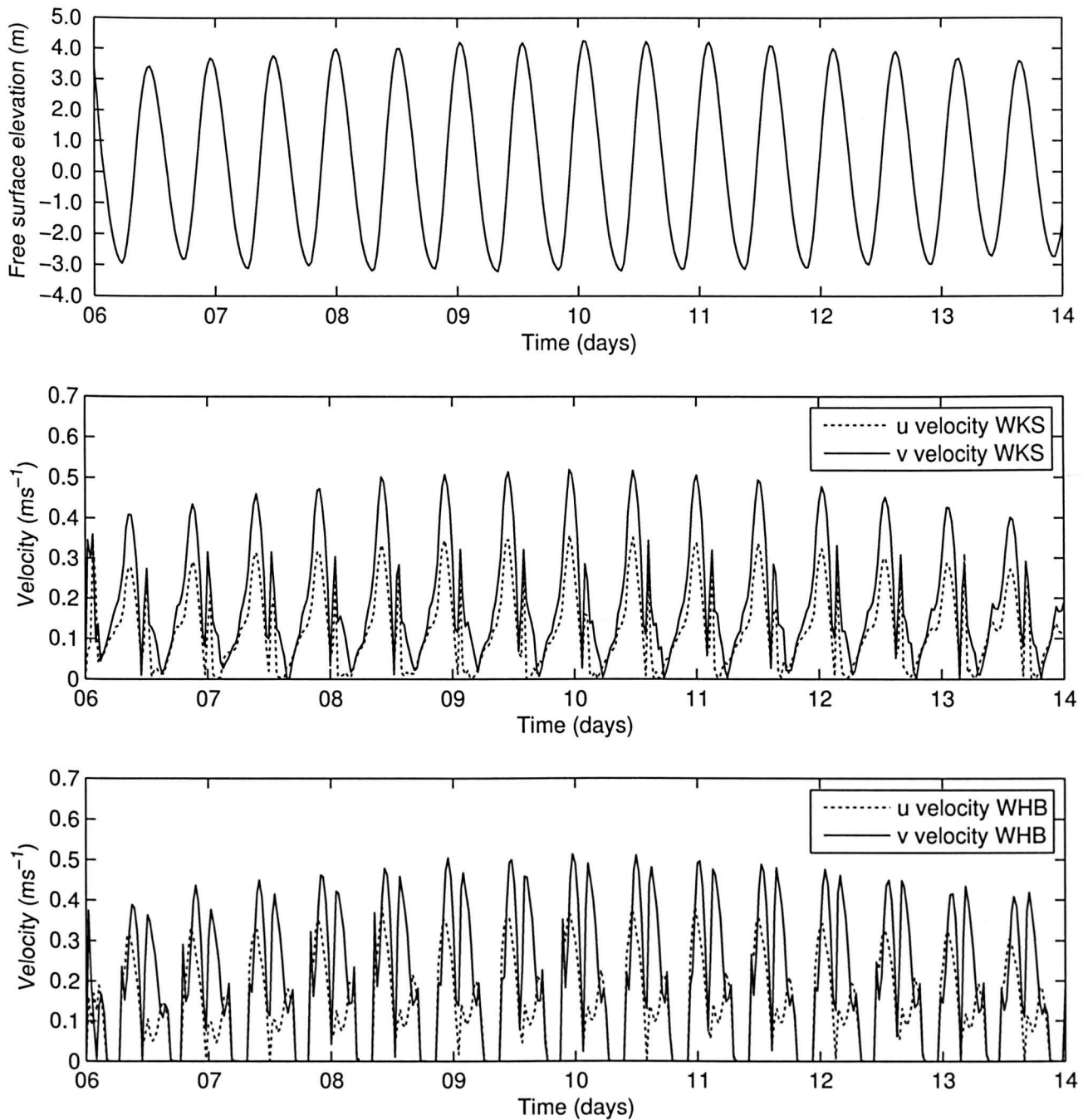
Figure 9.19: Velocity simulated using the previous wave results file so that the influence of tides and waves were represented. The free surface elevation at the model boundary (top) is for reference to show the tidal asymmetry in the u and v velocity components at West Kirby Sands (middle (WKS)) and West Hoyle Bank (bottom (WHB)).

Current speed simulation results show a dominance of the v velocity component at West Kirby Sands and West Hoyle Bank. This component of velocity relates to the flow along a north-south direction, which is the flow in and out of the Dee Estuary. This north-south dominance of flow is to be expected at the estuary mouth and is in agreement with previous field measurements at West Kirby Sands and the Hilbre Channel (Section 4.3.4). The velocity simulation can be seen to be asymmetric with

flood dominance. A stronger asymmetry is experienced at West Kirby Sands than West Hoyle Bank, where the v component of velocity is only slightly flood dominated. The flood velocities are of a similar magnitude at West Kirby Sands and West Hoyle Bank, with maximum flood speeds of approximately 0.5ms^{-1} experienced during the simulation. In contrast, the maximum ebb speed over the simulation period at West Hoyle Bank is 0.48ms^{-1} and approximately 0.35ms^{-1} at West Kirby Sands. The predicted bed roughness evolves throughout the simulation with the changing hydrodynamic conditions and so varies with changing tidal elevations. The bed shear stress and bed roughness are shown in Figure 9.20 at West Kirby Sands and West Hoyle Bank. The predicted bed roughness (k_s) shows a tidally oscillating signal with greatest depth and velocity producing the greatest roughness values.
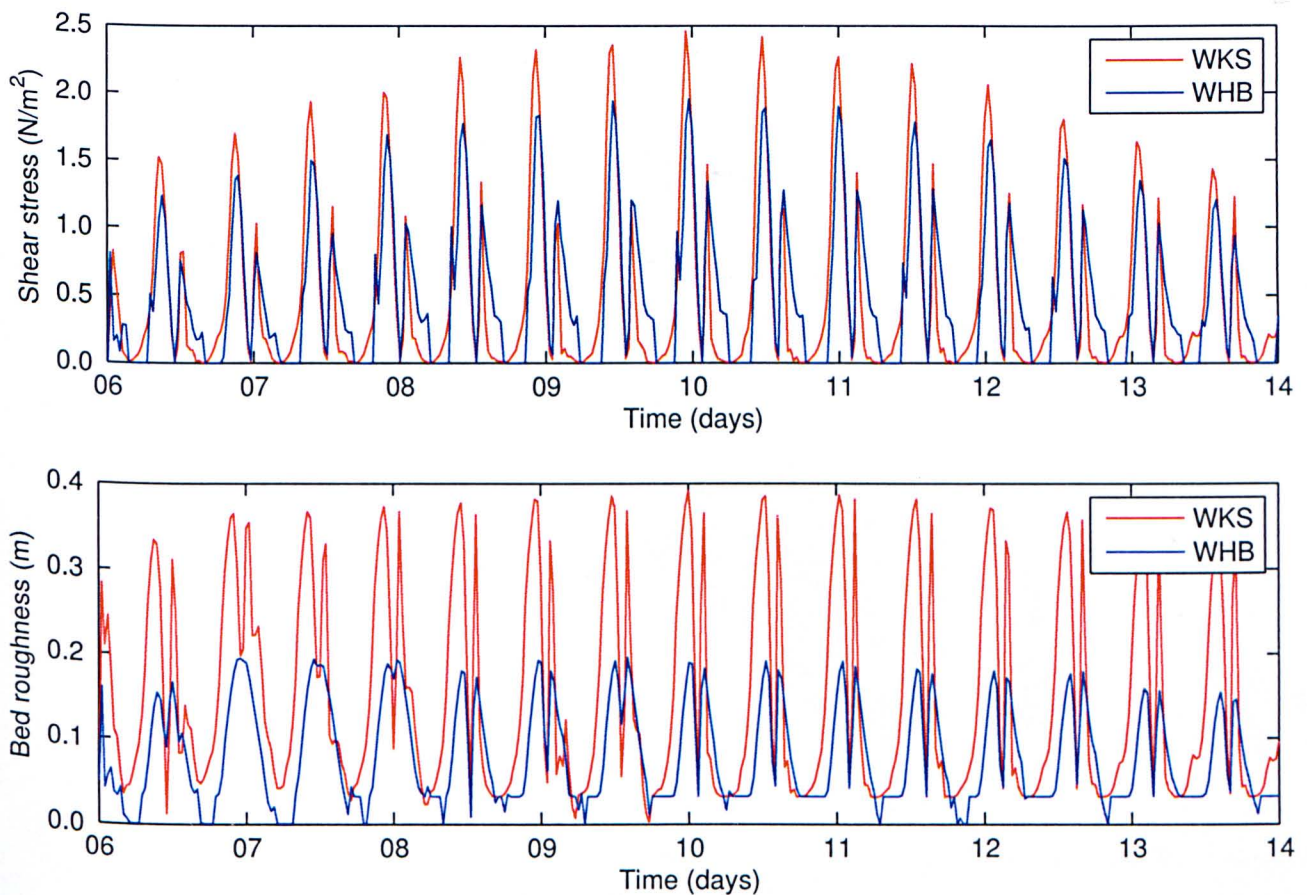
Figure 9.20: Bottom friction and bed roughness at West Kirby Sands (WKS) and West Hoyle Bank from the October 2006 with bed roughness feedback initiated.

The predicted bed roughness is a function of the water depth and velocity and so will vary in time, with the changing hydrodynamic conditions (tides and waves) and spatially throughout the model domain. The mean roughness from the October 2006 simulation can be seen in Figure 9.21 which shows the spatial variation in predicted roughness values.

The k_s feedback approach produces a dynamic roughness environment which responds to changes in water depth and currents, with ripples and dunes evolving and devolving with the local state of the mobility parameter ψ (Equation 2.22), which is a product of the depth averaged flow velocity. The roughness values for mega-ripples and dunes are related to the flow depth h and the mobility parameter ψ (Equations 5.19 & 5.20). The largest k_s values can be seen to occur at the model domain open sea boundary and in the two deep water channels in the mouth of the estuary. Here the depth and flow velocities are relatively high, producing the greatest roughness lengths in the model domain. The intertidal sand flats at West Kirby Sands and West Hoyle Bank have significantly smaller roughness values than those seen in Hilbre Channel due to smaller water depths and lower velocities.
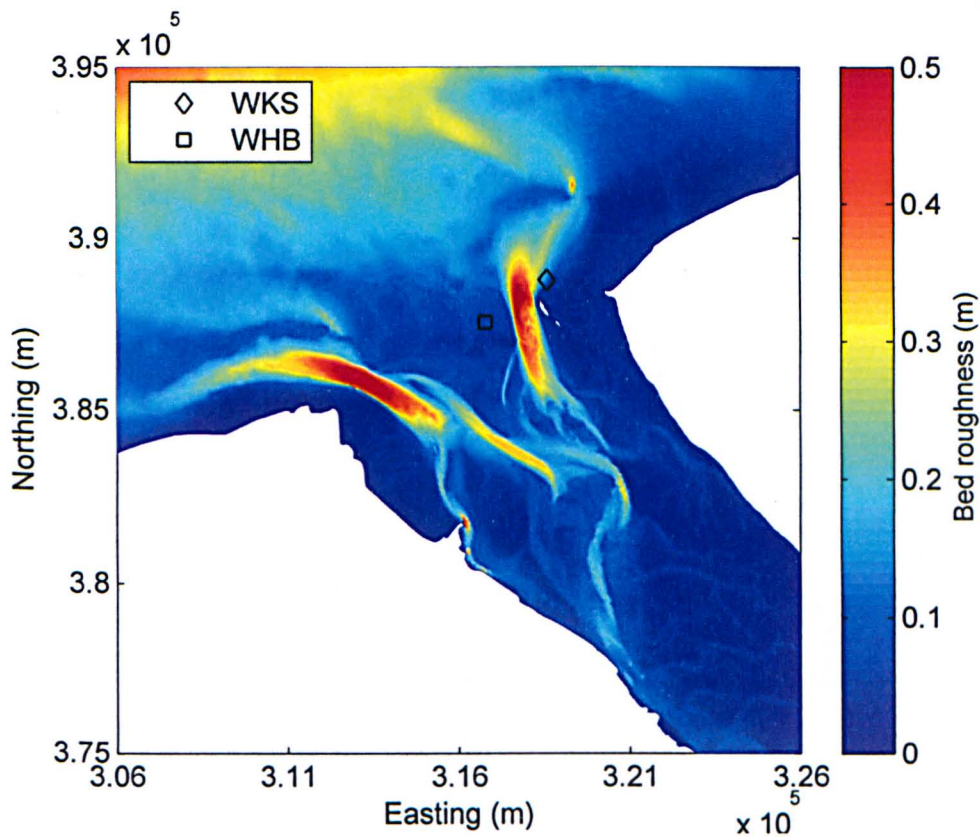
Figure 9.21: Mean predicted bed roughness over the Dee Estuary model domain from the October 2006 coupled TELEMAC-2D - SISYPHE model simulation.

9.5.5 The effect of variable bed roughness on simulated sediment transport

To determine the effect of roughness feedback on sediment transport the Dee Estuary model was set up to simulate tidal elevations, waves and sediment transport for a 12 hour tidal period. Eight tidal constituents (Q_1, O_1, P_1, K_1, M_2, S_2, K_2, M_4) were used to simulate the tidal elevations and wave data from the WaveNet buoy, covering the 12 hour simulation period, were input at the model

boundary. Waves were superimposed on the simulated tidal input and with wave generated currents included (Figure 9.22). These hydraulic conditions were simulated using TELEMAC-2D coupled with SISYPHE with the k_s feedback process initiated and also with k_s feedback disabled, but with a constant 0.01m bed roughness, over the same tidal period and with the same wave conditions for comparison. The sediment transport formula of Bijker (Section 5.2) was implemented to calculate the total sediment flux with the influence of waves included. Time series of simulated data including free surface elevation, wave height, velocity magnitude, magnitude of bed shear stress, bed roughness and total sediment flux were extracted from the two areas of interest for this study, namely the dune fields on West Kirby Sands and West Hoyle Bank labelled in Figure 9.21.

The free surface shows the evolution of the tide from high water to the next high water over the 12 hour period. At low tide West Hoyle Bank can be seen to dry out as the free surface elevation reaches a minimum of -1.98m. Including the k_s feedback into the coupled simulation reduces the velocity on average by 2% at West Kirby Sands and 8% at West Hoyle Bank. There are also periods in Figure 9.22 where the velocity in the k_s feedback simulation is greater than the constant k_s simulation. This could be the result of tidally varying wave heights seen in the mouth of the estuary. The bed roughness feedback process increases the bed friction from 0.01m to 0.04m (Figure 9.23), which results in a mean percentage increase in the shear stress of 240% at West Kirby Sands and 33% at West Hoyle Bank.
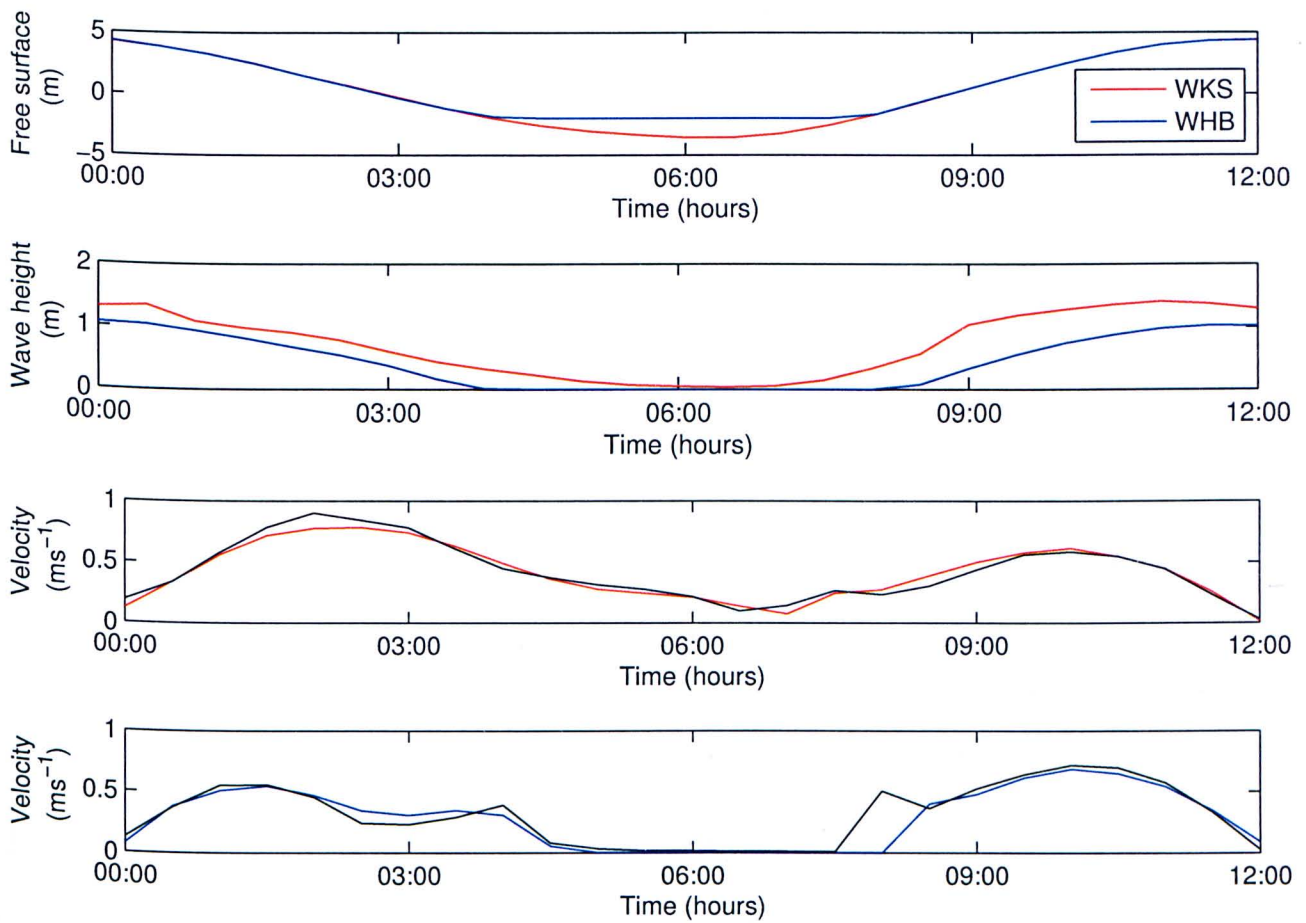
Figure 9.22: Free surface elevation, wave height and simulated current speed for West Kirby Sands (WKS (red)) and West Hoyle Bank (WHB (blue)) over a 12 hour simulation. Results are shown from a simulation which does include the bed roughness feedback (coloured lines), which varies temporally and spatially, when simulating velocity and a simulation which uses a constant bed roughness (black lines) over the entire model domain.

This increase in the magnitude of the shear stress through the inclusion of k_s feedback when simulating sediment transport with TELEMAC-2D and SISYPHE in a coupled mode results in an increase in the total sediment flux of 60 and 70% at West Kirby Sands and West Hoyle Bank. This is a significant difference and particularly important when considering the migration of large scale bed forms in these areas. Therefore the inclusion of the k_s feedback is a significant process in simulating the morphodynamic processes in the mouth of the Dee Estuary. Using a constant k_s throughout the model domain and over the entire simulation period could significantly underestimate the sediment transport occurring.
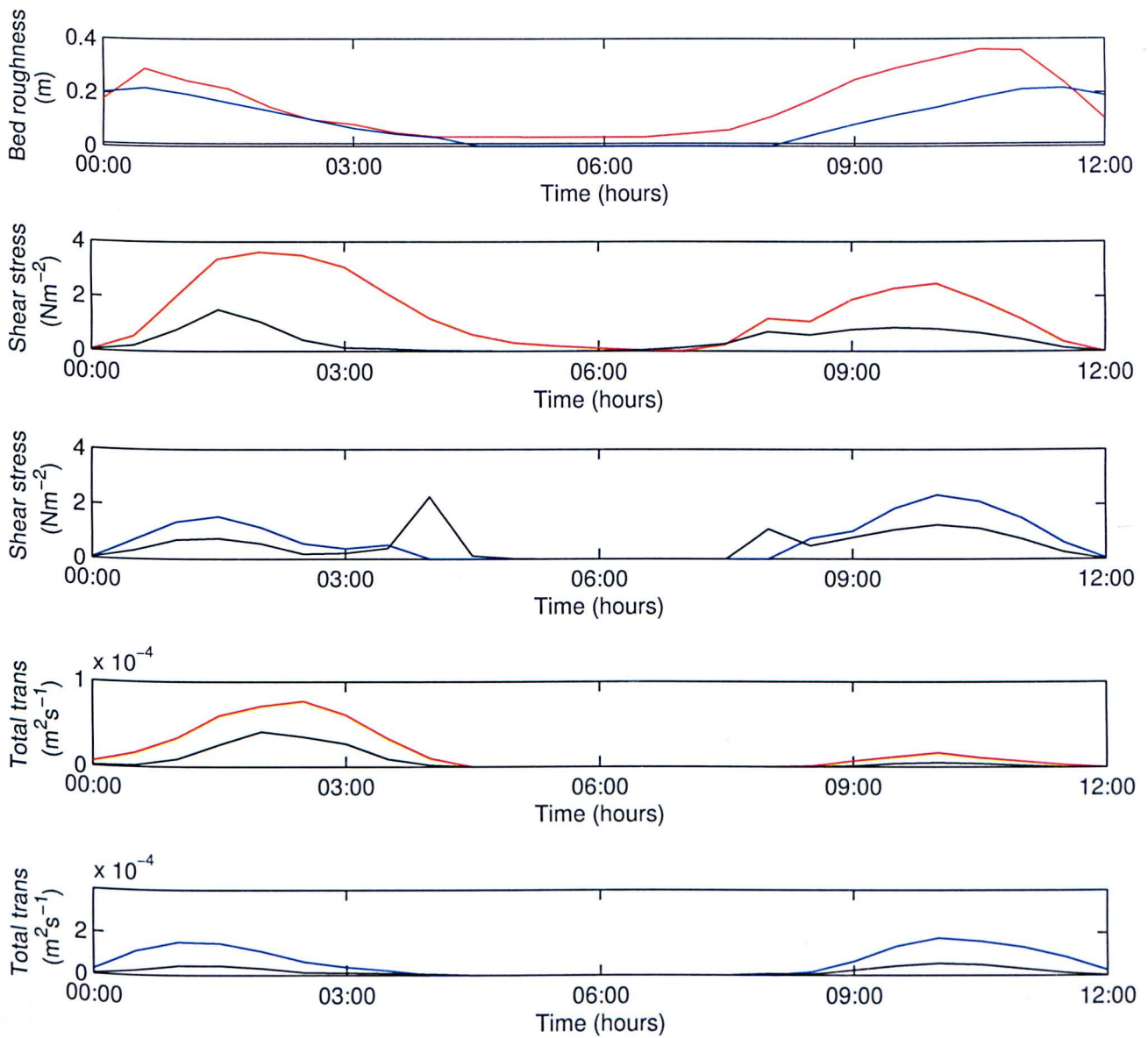
Figure 9.23: Bottom roughness, shear stress and total transport at West Kirby Sands (red line) and West Hoyle Bank (blue line) over the 12 hour simulation for the bed roughness feedback assessment. Results from an otherwise identical simulation with the bed roughness feedback not implemented are plotted for comparison (black lines).

9.5.6 Simulating sediment transport during October 2006 storm event

Sediment transport, forced by tides, waves and wave generated currents, have been simulated over the October 2006 simulation using TELEMAC-2D and SISYPHE run in a coupled mode with bed roughness feedback activated. As with previous SISYPHE simulations in this study the Bijker sediment transport formula was used with the effect of waves included to calculate the total load transport. Figure 9.24 shows the total load sediment transport at West Kirby Sands and West Hoyle Bank. The storm event from 6th-8th October 2006 coincides with the period of greatest transport during the sim-

ulation, which is to be expected as wave heights were largest during this time. Waves have the effect of setting the sediment into motion which is then transported by the current. Waves also impact the current directly, either through the radiation stress generated during the breaking process, or as mass transport in the wave direction of travel near to the sea bed, as a result of boundary layer processes. The maximum rate of transport occurred on 7th October 2006 when West Kirby Sands and West Hoyle Bank attained similar total transport values of 3.9×10^{-4} and 3.1×10^{-4} $m^2 s^{-1}$, respectively. This maximum rate of transport occurred during the time of peak flood tide which corresponds to the sediment transport direction being into the estuary.
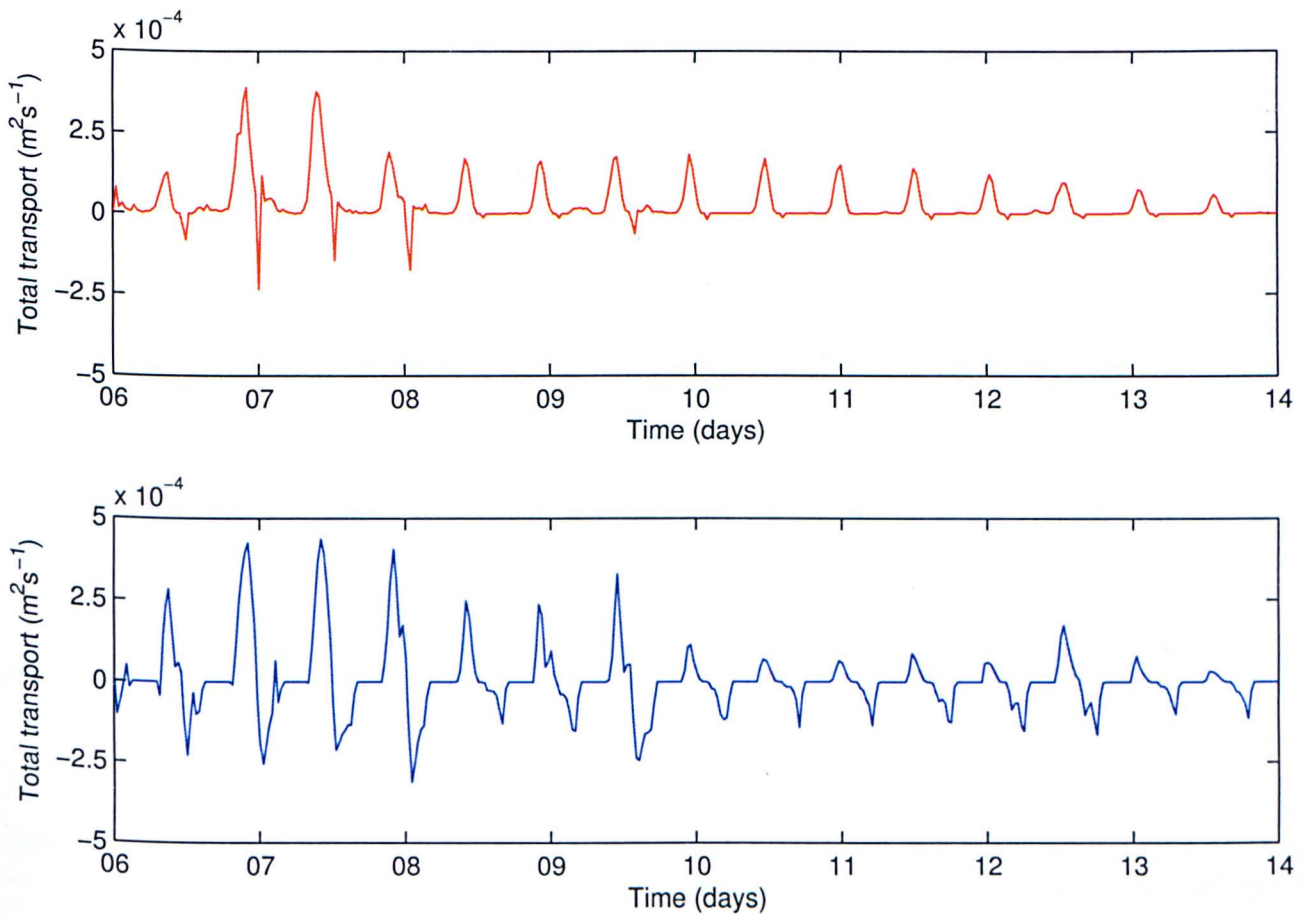
Figure 9.24: Total load sediment transport at West Kirby Sands (red line) and West Hoyle Bank (blue line) during the October 2006 simulation including the effect of waves, wave generated currents and bed roughness feedback.

Figure 9.25 shows simulated wave height, extracted from the position of the Triaxys wave buoy, plotted against sediment transport magnitude at West Kirby Sands and West Hoyle Bank, sampled at hourly intervals from the transport rates shown in Figure 9.24. As expected, greatest transport rates occur at times of largest wave height at West Kirby Sands and West Hoyle Bank. The sign of the transport rate has been preserved in the sampling process, with positive transport indicating an

onshore direction, while negative transport represents offshore transport. Greatest offshore transport can be seen to occur at times of moderate wave heights, between 0.5 to 1.5m. This trend is also seen in the weekly migration of wave breaker patterns in the weekly mean radar images (Figure 9.13). This suggests that onshore sediment transport and the resulting migration of large scale bed forms occurs at times of large wave heights in the estuary mouth, while moderate wave conditions will result in offshore sediment transport and migration of large scale bed forms. The asymmetry of the dunes was not observed to reverse in the field campaign during the periods of offshore transport. Therefore the offshore movement detected in the radar data could be the result of the bed form crest moving in an offshore direction. The asymmetry of the dunes is not reversed due to the magnitude and duration of offshore transport not being great enough to change the orientation of the dunes at West Kirby Sands and West Hoyle Bank to an ebb asymmetry.
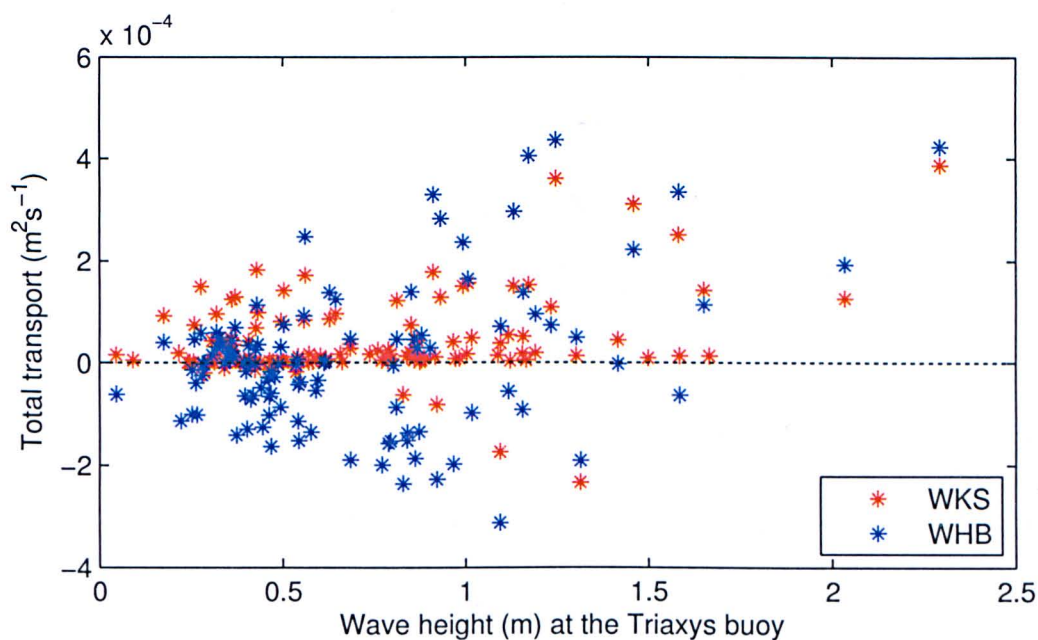
Figure 9.25: Simulated wave heights in the estuary mouth extracted from the location of the Triaxys wave buoy plotted against simulated total load sediment transport at West Kirby Sands and West Hoyle Bank.

The x and y components of the magnitude of total load transport are plotted as sediment transport vectors of the time mean transport rates, averaged over the 8 day simulation period, to show the direction of sediment transport overlain onto the mean transport over the simulation period (Figure 9.26). The migration vectors from the simulated sediment transport are oriented in a similar direction to the migration vectors calculated from the cross correlation motion tracking analysis based on the mean radar images (Figures 9.6-9.9) showing the direction of mean sediment transport to be in to the estuary.
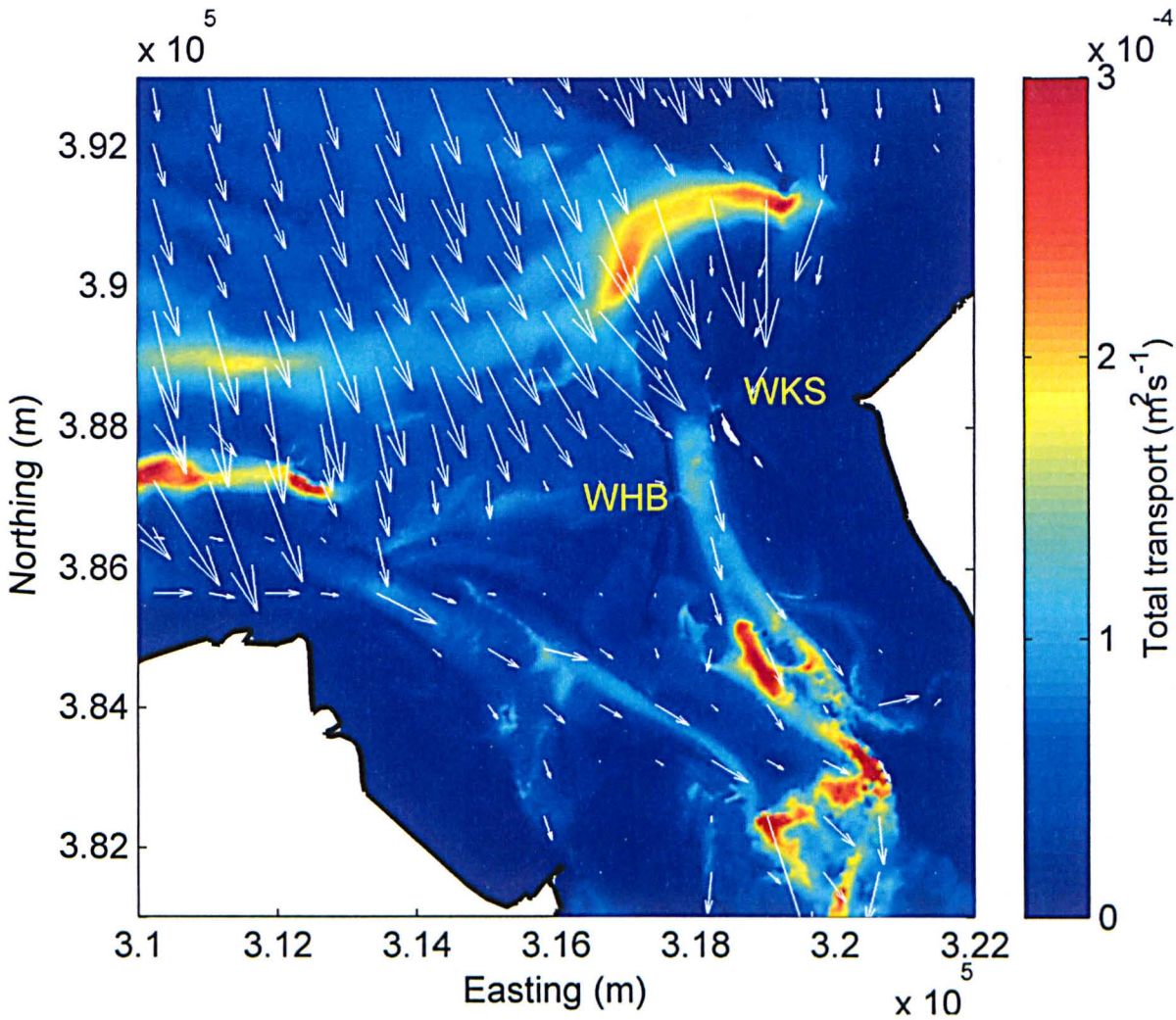
Figure 9.26: Mean simulated total transport with transport vectors overlain. The position of West Kirby Sands (WKS) and West Hoyle Bank (WHB) are marked for reference. Greatest sediment transport can be seen to be occurring at the mouth of the estuary, rather than the estuary interior, and in an onshore direction.

The net simulated transport rates at West Kirby Sands and West Hoyle Bank are determined by taking into account the positive (flood) and negative (ebb) total transport values shown in Figure 9.24. These simulated net transport rates are compared with the transport rates from the cross correlation motion tracking analysis for weeks 1 and 2 of the radar data (Table 9.5).

Transport (m^2s^{-1})	JPG	Err	MAT	Err	TELE	Err
WKS	0.22×10^{-5}	1.7×10^{-6}	0.10×10^{-5}	3.3×10^{-7}	4.01×10^{-5}	1.7×10^{-7}
WHB	0.12×10^{-5}	1.7×10^{-6}	0.09×10^{-5}	3.3×10^{-7}	6.35×10^{-5}	1.9×10^{-7}

Table 9.5: A comparison of simulated net sediment transport rates (TELE) for 6th-13th October 2006 with the radar derived sediment transport from the wave breaker pattern migration distance (JPG & MAT).

The comparison between the simulated net sediment transport and the radar derived sediment transport shows that radar derived transport underpredicts the simulated transport at West Kirby Sands and West Hoyle Bank (Table 9.5). The direction of transport is in agreement between radar derived transport and simulated transport with each method predicting an onshore (positive) movement of sediment. The disparity in the magnitude of sediment transport rates could be due to the fact that the simulation uses the Bijker transport equation which is a total load equation, including the suspended and bed load components of transport, whereas the transport rates derived from the radar data use the migration distance and bed form dimensions of dunes, which does not include the suspended transport. Soulsby (1997) stated that measurements of bed load transport rates using bed form migration may be underestimated by up to a factor of two. Calculating bed load transport from the migration of dunes may underpredict the sediment transport as sediment may not come to rest in the bed form trough, but will either continue to move along the bed or be carried into suspension. The difference between simulated (TELEMAC) and remotely sensed (radar) transport rates could also be related to the accuracy of the radar data as the jpg data have a resolution of 10m whereas the weekly mat radar images were processed to a resolution of 2m. The migration distance of wave breaker patterns between weeks 1 and 2 were 7.89m for West Kirby Sands and 6.49m for West Hoyle Bank using the jpg radar data, but 3.33m and 4.68m for West Kirby Sands and West Hoyle Bank using the mat radar data. These migration distances are sub-pixel in the jpg data while they are over one to two pixels in the mat radar data. While the cross correlation motion tracking algorithm is able to detect sub-pixel change, and calculates migration to an accuracy of $1/10^{th}$ of a pixel, the position and subsequent migration of wave breaker patterns in the mat radar data will be more clearly defined than in the jpg data, which are inherently less accurate due to image artifact errors (Section 6.1.4).
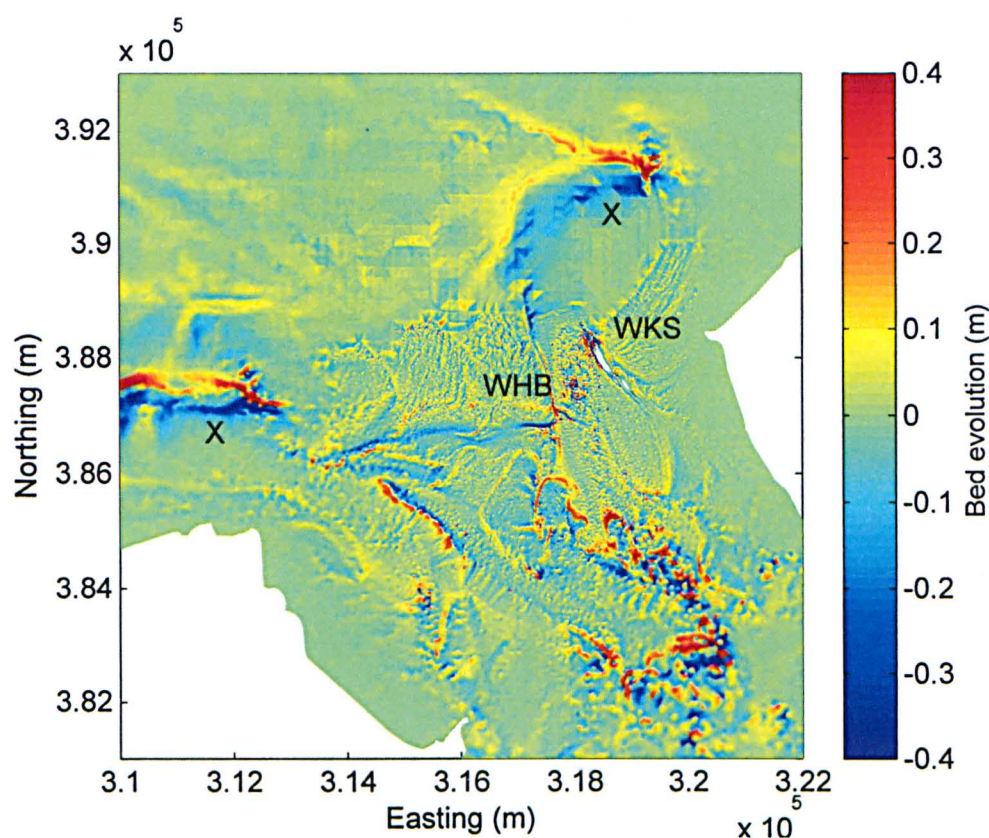
Figure 9.27: Bed evolution at the mouth of the Dee Estuary at the end of the eight day simulation. The position of West Kirby Sands (WKS) and West Hoyle Bank (WHB) are marked for reference as well as the two regions of significant evolution (X) located where the Hilbre (East) and Welsh (West) Channels enter Liverpool Bay.

There is significant spatial variation in bed evolution at the estuary mouth after the seven day simulation period (Figure 9.27). There are two areas of significant deposition and erosion, marked 'X' in Figure 9.27, which are located where the Welsh (west) and Hilbre (east) channels join Liverpool Bay. At these locations erosion (negative evolution) occurs landward of the area of deposition (positive evolution), suggesting that the deep water channels are regions of significant sediment erosion and transport, with sediment apparently moving northwards, while deposition and sediment accumulation occurs on the surrounding shallower sand flats. The bed evolution seen at the deeper water regions marked as 'X' in Figure 9.27 may not be accurately represented by the uniform grain size applied to the model domain, as in reality these regions of greater water depths and greater velocity will have a larger grain size than that of the shallower sand flats such as West Kirby Sands. An area of significant evolution can be seen to the east of West Hoyle Bank (Figure 9.28) which is located on the western bank of the Hilbre Channel. This positive bed evolution represents the migration of the Hilbre Channel in an easterly direction, something which can lead to a navigational hazard. This has been known to occur in the past and is shown in Figure 1.2 as initial evidence for the dynamics of the sea

bed around the mouth of the Dee Estuary and the need for a better understanding of the processes governing its movement. These simulation results show that significant change in the location of Hilbre Channel can occur after a relatively short period (7 day simulation) and with storm conditions, where maximum wave heights are between 2-2.5m, which occur on short time scales (6th-8th October 2006). The sub-plot of West Kirby Sands in Figure 9.28 shows bed evolution to be occurring over the dune field at West Kirby Sands, suggesting that the hydrodynamic conditions simulated over the October storm period have caused a simulated migration of large scale bed forms at West Kirby Sands.
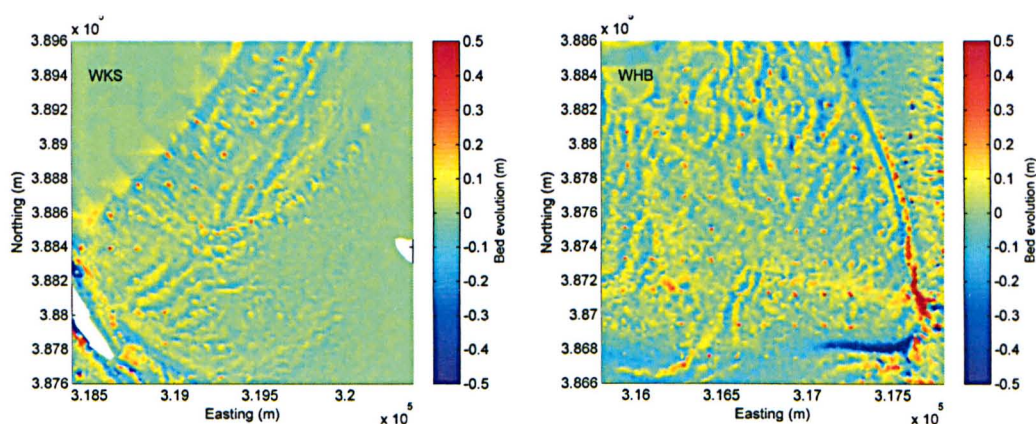
Figure 9.28: Bed evolution at West Kirby Sands (WKS) and West Hoyle Bank (WHB) at the end of the simulation period. Significant evolution over the dune fields previously examined for bed form migration using the X-band radar data can be seen at both locations. Migration of the eastern extent of West Hoyle Bank occurs, suggesting a migration of the Hilbre Channel.

The final bed evolution at West Kirby Sands and West Hoyle bank at the end of the simulation period shows sediment erosion (negative bed evolution) and accumulation (positive bed accumulation) at regions of dune features which are similar in shape and orientation to the sand dunes visualised using the mean radar image method (Figure 9.29). The bed evolution over these regions of bed forms does not represent the generation of bed forms, rather bed accumulation and erosion over existing bed forms which are resolved in the model bathymetry. Evolution of these dune features in the simulation is the result of sediment being transported through these regions, therefore the migration of these large scale bed forms shown using the radar data, and also seen in the simulated bed evolution, will likely play a significant role for sediment to be transported into the estuary interior.
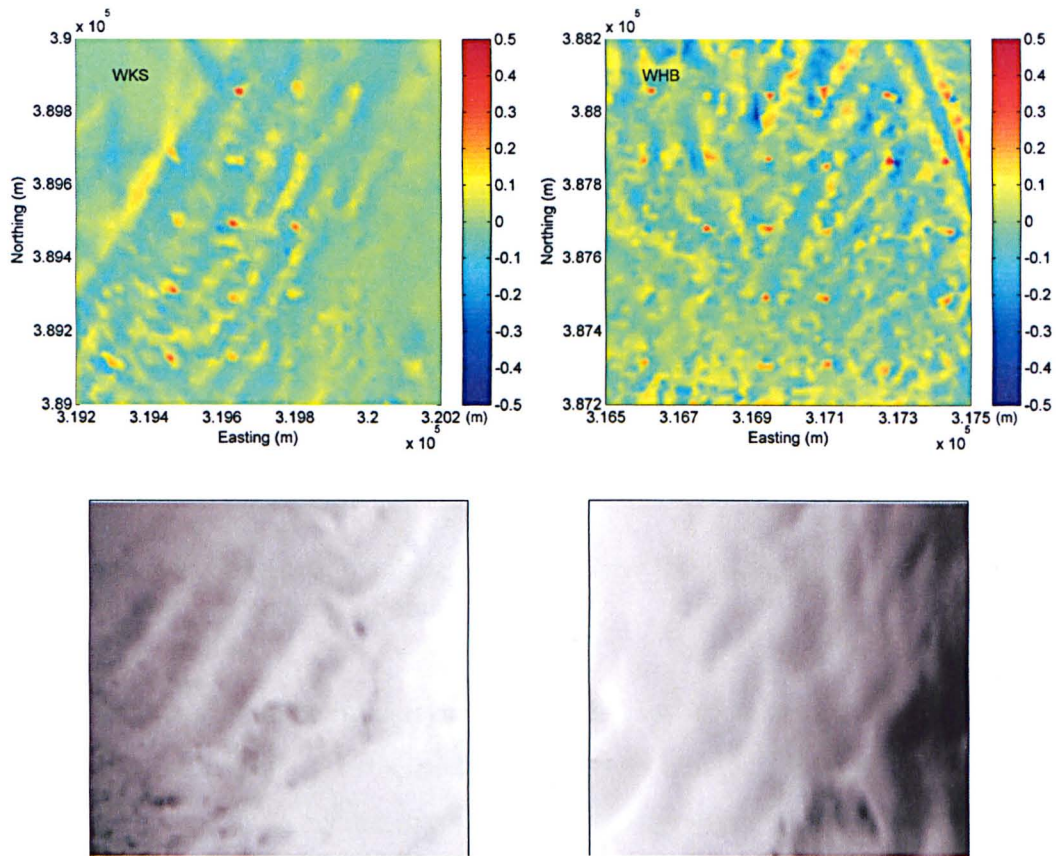
Figure 9.29: Evolution over the dune fields at West Kirby Sands (WKS) and West Hoyle Bank (WHB) displaying similar patterns to the wave breaker signal detected by the X-band radar system over similar locations. The top panels show simulated evolution and the bottom panels display the X-band radar data.

Figure 9.30 shows the location of three profiles extracted from West Kirby Sands and West Hoyle Bank so that the bed evolution over these dune field regions can be analysed. These profiles are chosen to be oriented normal to the crests of evolution patterns which are simulated over the dune fields at West Kirby Sands and West Hoyle Bank (Figure 9.29).
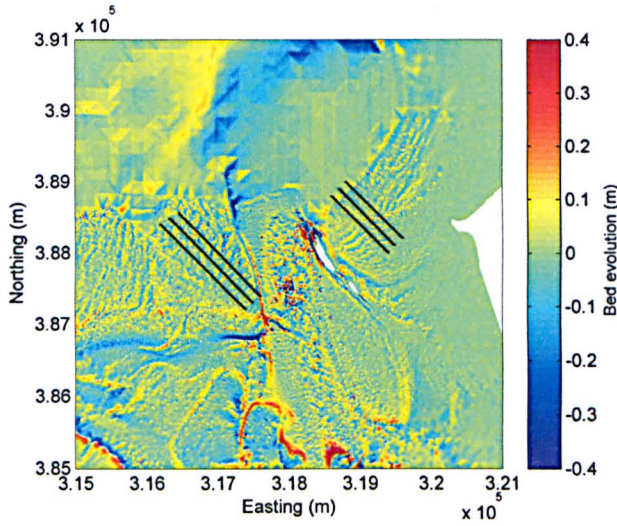
Figure 9.30: Location of three profiles through West Kirby Sands and West Hoyle Bank from which the original bathymetry and bed evolution are extracted.

From these profiles the original bathymetry and the bed evolution at the end of the simulation are extracted. The original bathymetry for the model domain was obtained from a Lidar survey conducted on 8th October 2006 and so is an accurate representation of the bathymetry for the October 2006 simulation (6th-13th October 2006). The original bathymetry and bed evolution data are summed creating a new bathymetry profile at the end of the model simulation. Figure 9.31 shows paired profiles at West Kirby Sands and West Hoyle Bank for the bed elevation from the initial model bathymetry (black line) and the final bed elevation (initial bathymetry + bed evolution) resulting from the model simulation (red line).
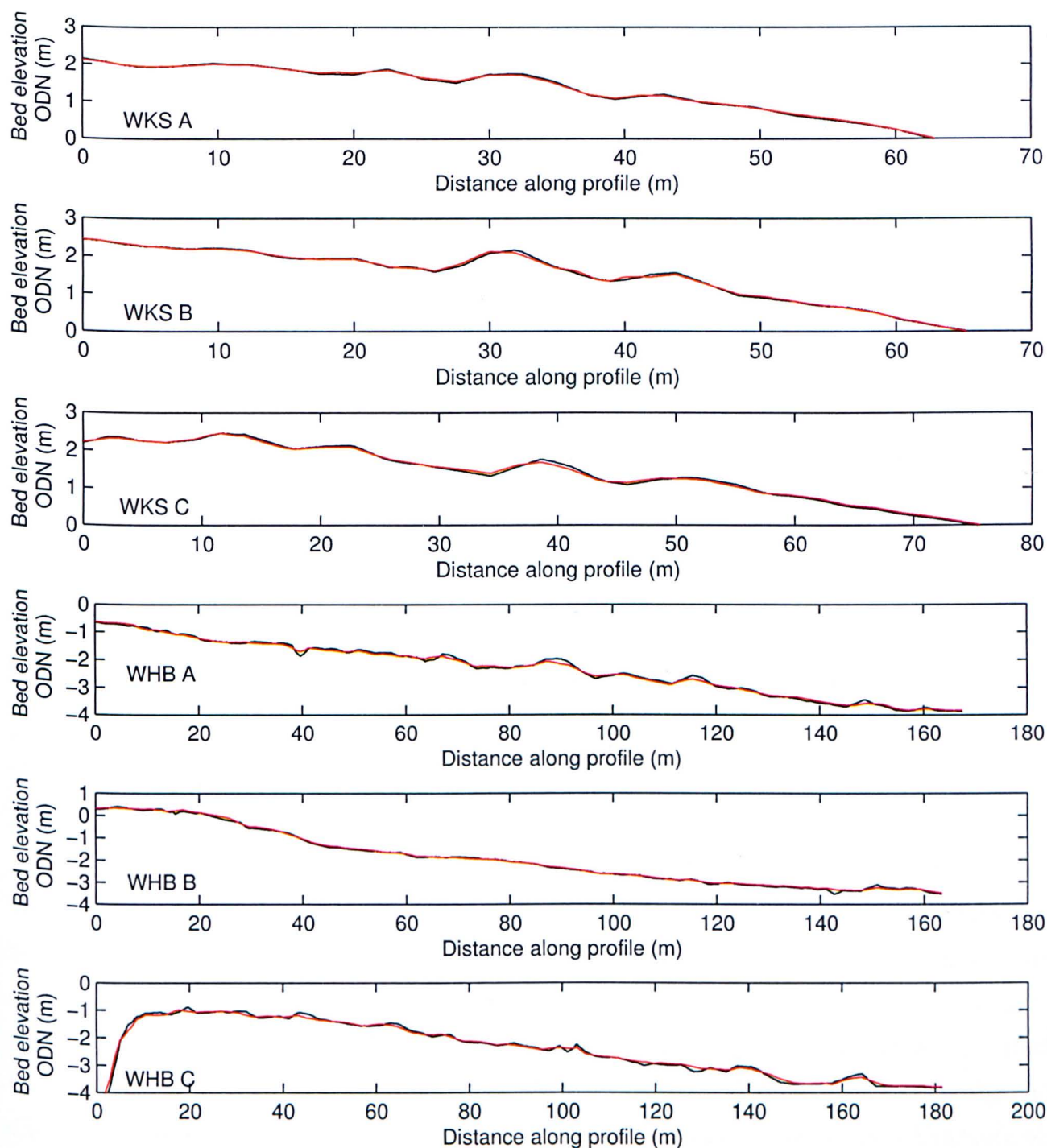
Figure 9.31: Profiles taken through bed evolution over the dune fields at West Kirby Sands (WKS) and West Hoyle Bank (WHB), where the open sea boundary is to the right of the Figure and the estuary interior to the left. The black line represents the bed elevation of the initial model bathymetry and the red line represents the bed elevation at the end of the October 2006 simulation.

Large scale bed forms are visible within the initial bathymetry as these features are resolved within the Lidar data, which has a resolution of 10m, used to create the model bathymetry in the estuary mouth. On close inspection it is evident that evolution along these profiles corresponds to the migration of these large scale bed forms along the profile length, moving in an onshore direction (from right

to left in Figure 9.31). Figure 9.32 shows bed elevation profiles for two individual dunes at West Kirby Sands and West Hoyle Bank at their original position (black line) and their position after the simulation period (red line). A clear onshore migration can be seen to occur during the simulation period which corresponds well with the onshore dune migration observed in the radar data between weeks 1 and 2.
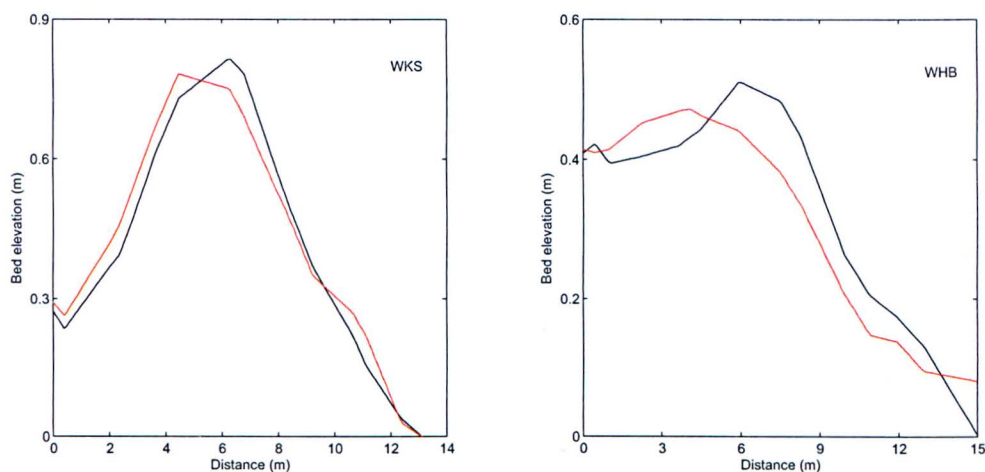
Figure 9.32: Individual dunes identified from the West Kirby Sands (WKS) and West Hoyle Bank (WHB) profiles through simulated bed evolution. The black line indicates the original bed elevation and the red line shows the position of the bed at the end of the October 2006 simulation. The open sea boundary is to the right of the Figures and the estuary interior is to the left. The asymmetry in these large scale bed forms, skewed in an onshore direction, is in agreement with the evolution of the dunes into the estuary.

The turning points algorithm used previously to identify bed forms from the DGPS survey data (Section 8.2.1) was applied to the simulation profile data (Figure 9.31). This determines the crest position of the large scale bed forms so that dune crest migration distances can be calculated for all bed forms sampled by the profiles. Mean crest migration distances for West Kirby Sands and West Hoyle Bank from the simulated evolution in bathymetry are 1.82m and 2.40m. These simulated crest migration distances underestimate the radar migration distances where values of 7.89m and 3.33m were observed at West Kirby Sands for the jpg and mat radar data, while West Hoyle Bank experienced 6.49m and 4.68m using the jpg and mat radar data. However, the direction of migration is consistent between the X-band radar and TELEMAC dune tracking methods, with both data showing onshore migration during this period. It is reasonable to expect the bed form migration distance from the TELEMAC simulation to be smaller than the bed form migration distance observed with the X-band radar data. This is due to the 2D depth averaged numerical model being unable to determine accurate flow patterns, with flow separation, over the bed forms at West Kirby Sands and West Hoyle Bank.

The migration vectors calculated using the cross correlation motion tracking algorithm for weeks 1 and 2 mean radar images are also in good agreement with the net sediment transport simulated over this time period using this TELEMAC model in that they both indicate onshore movement of sediment over the dune fields of West Kirby Sands and West Hoyle Bank. Figure 9.33 shows sediment transport vectors overlain onto week 2 mean radar images for West Kirby Sands and West Hoyle Bank. Also plotted are the cross correlation migration vectors for this time period (red arrow). The TELEMAC sediment transport vectors show how sediment is being transported into the estuary interior via these two regions, with the migration vectors from the radar data confirming the movement of sediment into the estuary through the migration of large scale bed forms.
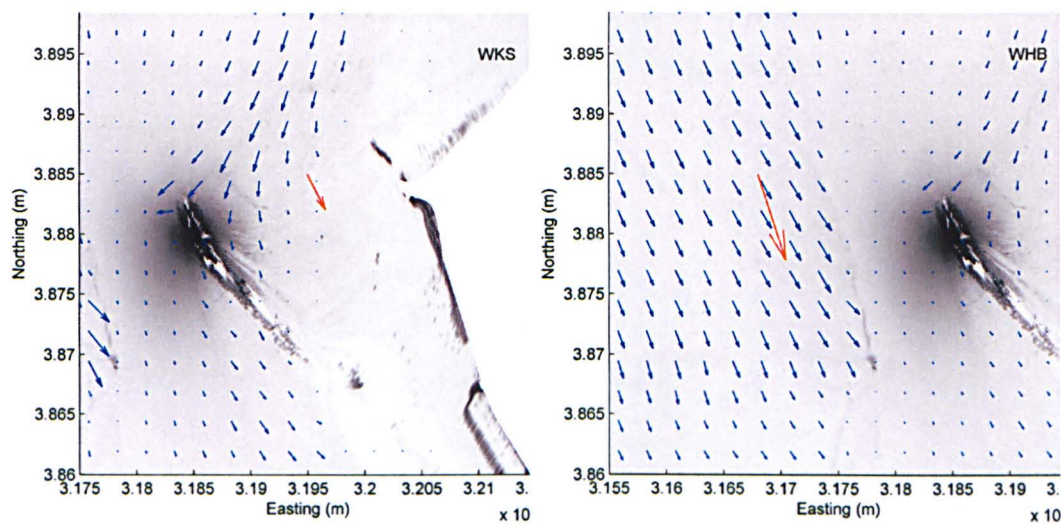
Figure 9.33: Simulated sediment transport vectors overlain onto mean radar images for week 2 of the mat radar data at West Kirby Sands (WKS) and West Hoyle Bank (WHB). The migration vectors from the cross correlation motion tracking analysis of wave breaker patters between weeks 1 and 2 are overlain also and show good correlation with the direction of simulated transport. The radar image is cropped with the model boundary for WKS to show the alignment of model and radar data.

9.6 Sediment continuity along simulated bed profiles

The 1D bed continuity equation detailed in Section 8.2.4, where it is used to determine the sediment transport associated with the change in bed elevation between DGPS survey profile lines, has been applied to the paired profiles, shown in Figure 9.31, extracted from the initial and final model bed elevation at West Kirby Sands and West Hoyle Bank. The bed continuity equation has been applied from the right, seaward, end of the profile to the left, landward end. The positive mean transport values simulated at West Kirby Sands and West Hoyle Bank (Table 9.5) indicate that the dominant direction of sediment transport is in an onshore direction. This simulated onshore transport of sediment is also

seen in the migration of large scale bed forms identified along the profiles of simulated bathymetry at West Kirby Sands and West Hoyle Bank (Figure 9.32). Therefore the bed continuity equation has been integrated along the profile in a landward direction from the offshore limit of the profile. As with the application of this method to the DGPS profiles, the quantity of sediment transport at the profile open boundaries is an unknown. Therefore, in an attempt to minimize this effect the ends of the profiles have been forced to have equal elevations for a distance of 1m, resulting in zero transport at the profile open boundaries. Applying the 1D bed continuity equation to the profiles extracted from the simulated bathymetry allows a comparison to be made between the mean sediment transport calculated from changing bed elevations along the bed profile lengths and the sediment transport simulated using Bijker's total load equation. This should allow an estimate to be made of the profile open boundary ambiguity, where a constant net transport along the profile is not be detected by the 1D bed continuity equation.
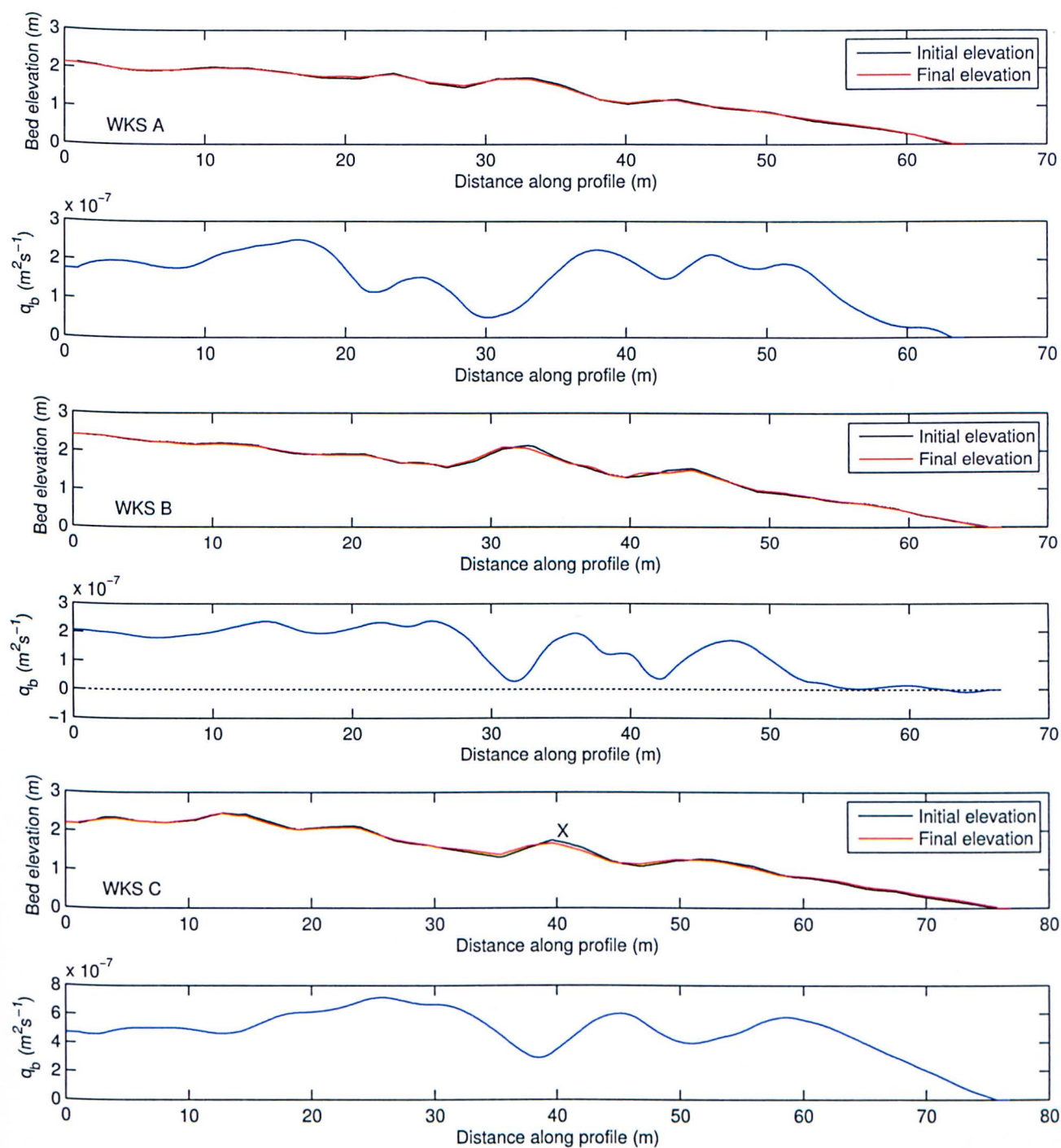
Figure 9.34: Paired bathymetry profiles extracted at West Kirby Sands from the initial model bathymetry (black line) and final model bathymetry (red line) as a result of predicted bed evolution. Volumetric transport rates (blue line) have been calculated using the 1D bed continuity equation, integrated along the paired profiles A-C from the right (seaward) end of the Figure to the left (landward) end.
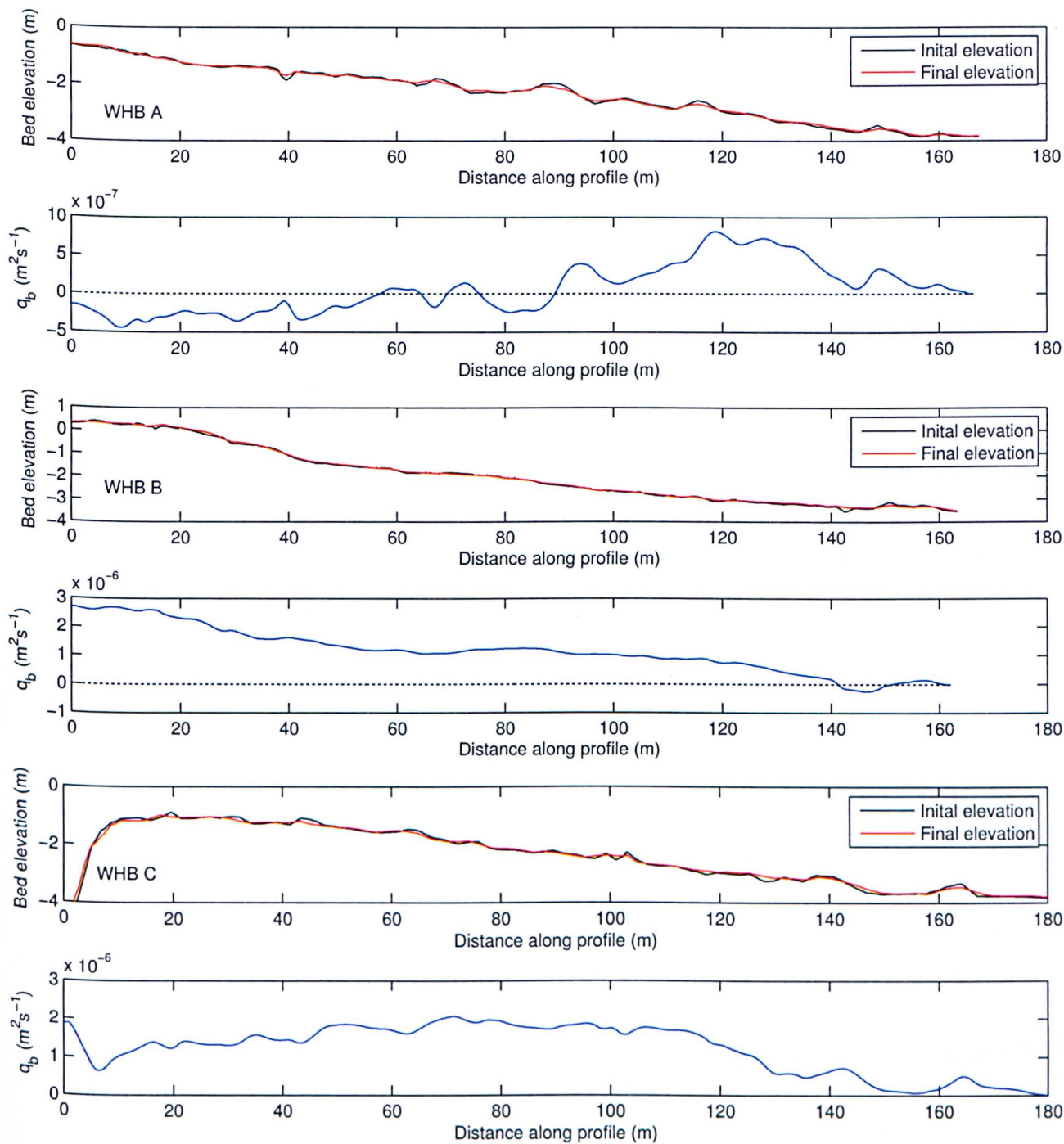
Figure 9.35: Paired bathymetry profiles extracted at West Hoyle Bank from the initial model bathymetry (black line) and final model bathymetry (red line) as a result of predicted bed evolution. Volumetric transport rates (blue line) are calculated using the 1D bed continuity equation, integrated along the paired profiles A-C from the right (seaward) end of the Figure to the left (landward) end.

Figures 9.34 and 9.35 show the volumetric transport rate $q_b(m^2 s^{-1})$ calculated using the bed continuity equation for the three profiles extracted from the model simulation at West Kirby Sands and West Hoyle Bank (Figure 9.30). Each of the profiles extracted from the initial bed elevation at West Kirby Sands and West Hoyle Bank (A-C) are paired with an identical profile which represents the product

of the initial bed elevation and simulated bed evolution. The volumetric transport rate at West Kirby Sands can be seen to be positive (Figure 9.34). This represents a landward transport of sediment due to a landward migration of the topography along the profile length. The effect of bed form migration on the transport rate calculated using the bed continuity method is well represented in profile C Figure 9.34 point 'X', where a large scale bed form can be seen to migrate onshore (left along the profile). Figure 9.36 shows this bed form and the resulting local volumetric transport due to onshore bed form migration. The volumetric transport can be seen to have a negative gradient with a reduction in bed elevation on the stoss (seaward) slope of the bed form, this transport gradient then becomes positive with an increase in bed elevation on the lee (landward) slope as the bed form migrates along the profile.
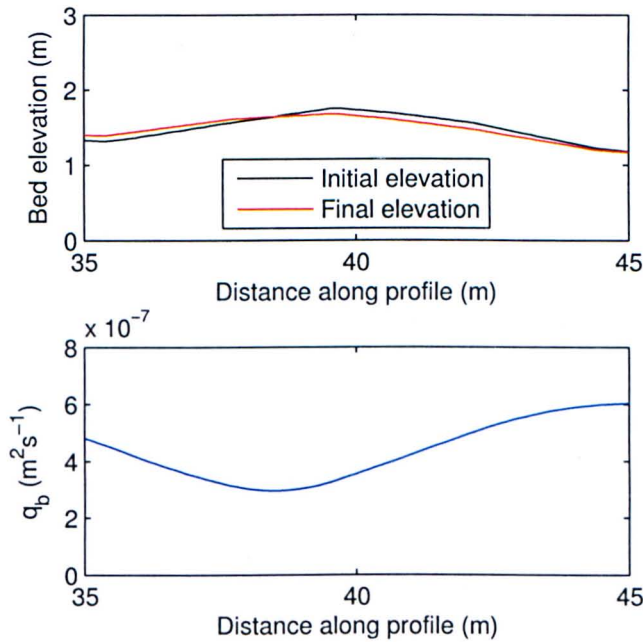
Figure 9.36: Volumetric transport due to the migration of a large scale bed form along profile WKS C (Figure 9.34) calculated using the 1D bed continuity equation.

The volumetric transport rate calculated along the profiles from West Hoyle Bank show an overall positive trend in transport rate, however, negative transport is seen along profile A (Figure 9.35). The western bank of the Hilbre Channel can be seen in the West Hoyle Bank profile C as the steep bed gradient between 0 to 10m along the profile. The bed continuity transport rate shows a large increase at the channel bank, corresponding to the bed evolution highlighted in Figure 9.28, representing a 0.8m migration distance of the channel bank over the October 2006 storm simulation period.

Mean transport rates have been calculated for West Kirby Sands and West Hoyle Bank from the three

Paired profiles. This allows a comparison between the predicted transport rates determined from the bed continuity method and the sediment transport simulated using Bijker's sediment transport equation (Table 9.6) to be made. Sediment transport simulated by the model and inferred from the radar and bed continuity analysis show a net onshore movement of sediment during the storm period of 6th-14th October 2006. However, the bed continuity derived transport can be seen to underestimate the Bijker prediction at both West Kirby Sands and West Hoyle Bank by two orders of magnitude. As detailed previously the 1D bed continuity method for estimating bed load transport does not account for a net through flow of sediment, or the suspended load component of transport. The large difference between the bed continuity and Bijker total load transport rates could indicate that these are significant factors affecting sediment transport at West Kirby Sands and West Hoyle Bank.

Table 9.6 also shows the transport rates derived from the 2D cross correlation analysis of weekly X-band radar jpg and mat images covering the October 2006 simulation period. The 2D correlation analysis tracks the movement of wave breaker patterns, which are used as a proxy for large scale bed forms, over the intertidal dune fields at West Kirby Sands and West Hoyle Bank. This shows the radar derived transport rate to be in better agreement than the bed continuity method. However, the radar derived transport is an order of magnitude smaller than the total load simulated using the Bijker transport formula. This could be due to the fact that the radar method relies on tracking the movement of large scale bed forms, therefore neglecting the role of suspended load transport, which likely acts as a significant contributor to the total sediment transport rate. Suspended sediments have been shown to play an important role in stabilising dune growth (Engelund, 1970), and therefore may play an import role in dune migration. The 2D motion tracking analysis of wave breaker patterns will also suffer from the same open boundary ambiguity as the 1D bed continuity analysis of bed elevation profiles. This is where a background level of sediment transport may be occurring through the motion tracking analysis domain which the method can not account for, but which is represented by the simulated total load transport.

Transport (m^2s^{-1})	WKS	Err	WHB	Err
Bijker	4.01×10^{-5}	1.7×10^{-7}	6.35×10^{-5}	1.9×10^{-7}
1D continuity	2.56×10^{-7}	3.9×10^{-9}	8.11×10^{-7}	1.4×10^{-8}
JPG	0.37×10^{-5}	1.7×10^{-6}	0.20×10^{-5}	1.7×10^{-6}
MAT	0.16×10^{-5}	3.3×10^{-7}	0.15×10^{-5}	3.3×10^{-7}

Table 9.6: A comparison of sediment transport rates at West Kirby Sands and West Hoyle Bank between 6th-14th October 2006 calculated using three methods: bed continuity of paired bathymetry profiles (1D continuity), motion tracking of wave breaker patterns from weekly X-band radar images (JPG & MAT) and simulated within TELEMAC using the Bijker formula (Bijker).

9.7 Summary

This chapter has focused on an intense storm event between 6th-8th October 2006 to determine the effectiveness of the X-band radar data at detecting morphological change over short time scales. Weekly mean radar images were created for the month of October 2006 to which cross correlation motion tracking analysis of wave breaker patterns was applied, by a similar method to that used for monthly mean radar images (Section 7.3), to detect the migration of large scale bed forms at West Kirby Sands and West Hoyle Bank. A total of five weekly mean radar images were generated, each consisting of seven days worth of radar data and separated in time so that the storm event was contained within week 2. Wave breaker patterns were clearly visible in all weekly mean images over West Kirby Sands and West Hoyle Bank using the jpg and mat radar data (Figure 9.5). The cross correlation motion tracking algorithm was applied to all weekly radar images to determine the migration of these wave breaker patterns, which represents the migration of the underlying topography. The migration vectors from this cross correlation analysis showed that there is a change in migration direction between weekly mean images (Figures 9.6-9.9). The time series of wave breaker pattern migration distances (Figure 9.10), where positive migration indicates an onshore direction while negative is offshore, shows that between week 1 and 2 dunes migrated in to the estuary at West Kirby Sands and West Hoyle Bank. This time period includes the storm event (week 2) suggesting that the large wave heights experienced at the mouth of the estuary (Figure 9.3) during the time of the storm cause large scale bed forms to migrate into the estuary interior via West Kirby Sands and West Hoyle Bank. Two periods of significant onshore migration occurred during the weekly mean radar image analysis period; the first between weeks 1 and 2 and the second is between weeks 4 and 5. Wave data from the Triaxys wave buoy showed that this onshore migration corresponds to two periods where wave heights were greater than 2m (Figure 9.11).

To gain a better understanding of the forces responsible for the observed onshore migration of large scale bed forms the hydrodynamic conditions were simulated between 6th-13th October 2006 using TELEMAC. This simulation period was chosen so that the storm event between 6th-8th October 2006 was included and also because the bathymetry used to generate the model grid is from the 8th October 2006 Lidar survey and will therefore represent the bed forms most accurately during this time period. The model was run using a model chaining sequence (Section 4.6) so that the tide, waves, wave generated currents and sediment transport were simulated. The TELEMAC-2D module simulated the tidal elevations at the estuary mouth between 6th-13th October 2006 with good confidence when compared with tidal height data from the Hilbre tide gauge (Figure 9.15). Waves were then simulated with the TOMAWAC module using the previous tidal simulation file as an input so that waves were generated with changing tidal elevations. Wave data from the WaveNet buoy was used as time varying boundary conditions for the wave simulation so that the simulated wave field closely resembles the actual wave conditions over the simulation period. Simulating the wave field with a tidal input was seen as a necessary procedure as previous studies (Guillou and Chapalain, 2012) have shown the importance of the tide in the semidiurnal wave height modulation in estuaries. Wave statistics were used to assess the performance of the wave model (Table 9.3) against measured wave data at the model boundary (WaveNet) and the estuary mouth (Triaxys). These normalised performance indicators show that the wave model simulates wave height and peak period with 90% efficiency at the model boundary and 70% at the estuary mouth (Table 9.4). Wave direction was simulated with less confidence with model performance values of approximately 60% for the model boundary and estuary mouth. The final stage of the model chaining process runs TELEMAC-2D with SISYPHE in coupled mode with the previous wave simulation result file input. This allows for wave generated currents to be simulated by TELEMAC-2D which when coupled with SISYPHE has the updated bed evolution input at every time step. Bed roughness feedback is also initiated at this stage of the modelling process as detailed in Section 5.3, which updates the total roughness calculated at each timestep for every grid node where shear stress is greater than the critical shear stress. The effect of the total bed roughness is calculated as a function of the flow velocity, wave characteristics and sediment grain size by the morphodynamic model (SISYPHE) and then passed to the hydrodynamic model (TELEMAC-2D). This was considered to be an important modelling process and has been validated with an extensive bed form data set by McCann (2011). Sediment transport is simulated using the Bijker transport formula including the effect of waves. The influence of bed roughness feedback on sediment transport is determined by comparing two hydrodynamically identical simulations where bed roughness feedback is initiated and the other which uses a constant bed roughness. The results of these test simulations show that

bed roughness feedback has the effect of increasing the shear stress, which in turn causes increased rates of sediment transport (Figure 9.23).

Simulated sediment transport over the October 2006 simulation period includes the effects of currents, waves, wave generated currents and bed roughness feedback. The results of this eight day simulation are examined at West Kirby Sands and West Hoyle Bank and show greatest sediment transport rates to occur during the storm event of 6th-8th October 2006. Sediment transport vectors for peak transport rates show onshore movement of sediment over the dune fields previously examined for the migration of large scale bed forms using X-band radar data at West Kirby Sands and West Hoyle Bank. A comparison of simulated wave heights in the mouth of the estuary and simulated sediment transport at West Kirby Sands and West Hoyle Bank (Figure 9.25) shows greatest onshore transport of sediment to occur at times of largest wave heights, while greatest offshore transport occurs during moderate wave conditions. Peak onshore transport is greater than peak offshore transport at both West Kirby Sands and West Hoyle Bank, suggesting a net onshore movement of sediment during the October 2006 storm simulation. Bed evolution at the end of the simulation period shows the evolution of large scale bed forms at West Kirby Sands and West Hoyle Bank with a similar shape and orientation to the large scale bed forms seen in the X-band radar mean images (Figure 9.29). Profiles of bathymetric and evolution data extracted from the model domain at West Kirby Sands and West Hoyle Bank show the migration of large scale bed forms into the estuary interior over the simulation period (Figure 9.32). The 1D bed continuity equation (Section 8.2.4) was applied to the paired bathymetry profiles (Figures 9.34 & 9.35). This showed onshore volumetric transport during the October 2006 storm simulation associated with the positive evolution at West Kirby Sands and West Hoyle Bank.

The transport vectors for peak simulated sediment transport also show sediment moving into the estuary interior at West Kirby Sands and West Hoyle Bank which are similarly oriented to the onshore migration of large scale bed forms seen in the X-band radar data between weeks 1 and 2 (Figure 9.33). A comparison of the total simulated sediment transport and transport derived from the 1D bed continuity equation and the cross correlation of radar weekly mean images shows a net movement of sediment into the estuary interior via West Kirby Sands and West Hoyle Bank over the period of 6th-13th October 2006. However, the bed continuity method significantly underpredicts the simulated transport by two orders of magnitude, while the radar derived transport underpredicts the total transport (Bijker) by one order of magnitude (Table 9.6). This highlights the ambiguity associated with the open boundaries of the bed profiles analysed by the 1D bed continuity and 2D cross correlation methods, which does not account for the through flow of sediment along the profile. It also

suggests that suspended load transport may play a significant role in the net sediment transport into the estuary, as the simulated (Bijker) total load transport is made up of bed load and suspended load, whereas the 2D correlation analysis of X-band radar images and 1D continuity analysis of bed profiles will only account for bed load transport. The 1D bed continuity method does capture the direction of sediment transport, with positive volumetric transport occurring at times of simulated net onshore transport, showing that it resolves local change in bathymetry effectively. Future work including the combination of repeat DGPS intertidal survey data with a fully coupled modelling technique, similar to the process applied in this research, would help to understand the ambiguities associated with the 1D bed continuity method. This could potentially be a useful tool for determining the bed load transport determined from repeat bathymetric surveys as applying the bed continuity equation to paired bathymetric profiles eliminates the need to identify individual dunes for more convential dune tracking methods. This is particularly useful in regions where complex bed form morphology makes the definition of individual dunes difficult.

The agreement between the direction of simulated transport and the radar derived transport between 6th-13th October 2006 shows the ability of the X-band radar system at detecting the migration of bed forms over short time scales, making it a useful tool for remotely sensing the impact of storm events on dynamic estuary systems, particularly the migration of large scale bed forms. The advantage of using an X-band radar system over other video monitoring techniques to remotely sense morphological change in estuaries during storm events is that the radar system is not limited by the time of day or moderate levels of fog or rain which adversely effect video images. Haller and Lyzenga (2003) have shown that radar is less sensitive than video monitoring techniques to relict foam not directly associated with breaking waves, which reduces the ability of video imaging to identify the bed form crest location, and require less tuning to distinguish breaking and non breaking waves. This make the radar system particularly useful for monitoring during storm events which can have a duration of over 24 hours and are associated with large wave heights.

Chapter 10

Discussion

The previous chapters have shown the migrations of large scale bed forms in the mouth of the Dee Estuary, observed using X-band radar data over monthly and weekly timescales. Repeat ground surveys at West Kirby Sands have shown the evolution of the dune field on this intertidal sand flat over daily timescales, showing the impact of a wave event on beach profile evolution. Fully coupled simulations of the hydrodynamic forcings behind the observed large scale bed form migration show a good correlation between simulated water depths, currents and wave heights. A hindcast simulation of a significant migration event observed with the X-band radar data during a storm event in October 2006, shows the impact of increased wave heights on sediment transport in the mouth of the estuary during the storm events. The simulated total transport rates at West Kirby Sands and West Hoyle Bank have also allowed an estimate of the contribution to the total transport which has been inferred from the migration of wave breaker patterns using the X-band radar data.

10.1   X-band radar

X-band radar data from the Hilbre Island radar installation has been used to track the migration of large scale bed forms in the mouth of the Dee Estuary. The position of wave breaker patterns in time-averaged radar images has been shown to correlate well with the crest positions of large scale bed forms, with some spatial offset. This relationship is, however, a complex one, with their association being related to the wave height, water depth, current speed and the angle between wave and current directions. The creation of time-averaged radar images should increase the accuracy of the crest position. The position of wave breaker patterns is therefore used as a proxy for the position of large scale bed forms in the mouth of the Dee Estuary, and their migration used to estimate the sediment transport associated with the dune migration.

The ability of the X-band radar system to track the migration of wave breaker patterns, using the cross correlation method of Bell (2005), has been shown to be temporally and spatially accurate when applied to wave breaker patterns over the dune field sites in the mouth of the estuary, namely West Kirby Sands and West Hoyle Bank. The migration rates of wave breaker patterns at West Kirby Sands and West Hoyle Bank were observed to increase during the winter months between October 2006 to February 2007 and October 2007 to March 2008. All monthly mean migration show an onshore direction of transport into the estuary interior via the sand flats at West Kirby Sands and West Hoyle Bank.

The monthly migration of wave breaker patterns at West Kirby Sands and West Hoyle Bank were shown to positively correlate with wave heights in Liverpool Bay, with larger wave heights resulting in greater onshore migration. The greater migration distances observed at West Hoyle Bank during the large winter migration events are thought to be due to a greater wave exposure, resulting in greater wave induced shear stress, at West Hoyle Bank compared with West Kirby Sands. Previous model simulations (Figure 5.7) have shown the increased scalar velocity in the mouth of the estuary when including waves, which in turn effects the sediment transport. This can be seen to effect a greater area of West Hoyle Bank compared with West Kirby Sands, due to the position of West Hoyle Bank in the center of the estuary mouth, which makes it more exposed to the dominant wave direction of 270-330 degrees (north west).

Unfortunately a full validation of the migration of the dunes throughout the radar data set, from DGPS, Lidar or Sonar surveying, was not available due to the Hilbre Island radar station going offline, meaning only historic radar data between 2006 to 2008 were available. Repeat ground truthing of the dune fields at either West Kirby Sands or West Hoyle Bank would enable an assessment of the accuracy of dune migration derived from the radar data. These bathymetry data could be used to model the shift between dune crest and wave breaker pattern as a function of distance up the shore. This would allow the radar to determine the dune wavelengths on a regular basis. This is an important consideration, as this research assumes that dune migration occurs with a constant dune shape, with the dune cross sectional area determined from the October 2006 Lidar survey.

A net onshore migration of sand dunes is observed at West Kirby Sands and West Hoyle Bank from analysis of monthly mean X-band radar images. This onshore dune migration must play a significant role in the large scale accretion observed in the Dee Estuary over the last two decades. Moore et al.

314

(2009) showed predominantly a net accretion between 2003 and 2006 from analysis of Lidar surveys. Hydrodynamic modelling results for the mouth of the estuary (Section 4.3.3) show the shallow water regions, such as West Kirby Sands to have a flood dominant tidal asymmetry, while the deep water areas of Hilbre Channel show an ebb dominant tidal asymmetry. This suggests that the dune fields in the mouth of the estuary, at West Kirby Sands and West Hoyle Bank, act as pathways for sediment to be transported into the estuary, while sediment is exported from the estuary in the deep water channels, such as the Hilbre Channel.

The time-averaged analysis of X-band radar images is similar to that used on video based surveys such as the Argus system (Holman et al., 1993; Holman and Stanley, 2007). Video imaging techniques have been used to map intertidal bathymetry with good results (Plant and Holman, 1997; Aarninkhof et al., 2003), however video systems suffer from limitations which do not affect the X-band radar system. For instance, the Argus system cannot operate at night, and requires good visibility to record accurate data. X-band radar can operate over 24 hours and in poor weather conditions which would adversely affect a video system. It also has the advantage of a much greater range. This makes the X-band radar system ideally suited to monitoring the migration of large scale bed forms over a large area in the mouth of estuaries during large storm events. Unfortunately the X-band radar system is much more susceptible to image noise, caused by objects within the radar range providing a backscatter signal which are not intended to be observed.

The application of the 'waterline method' to the X-band radar data has been shown to create beach profile images at West Kirby Sands and West Hoyle Bank with only limited success. The waterline beach profile images show the gradient of the beach slope and the presence of large scale bed forms on the intertidal sand flats in the mouth of the Dee Estuary. However, quantifying the actual bed elevation from these images proved more complicated than originally anticipated. This was due to complexities in determining the boundary between the land and water in the mean intensity radar images.

An attempt was made to determine the shoreline position from the waterline radar images using the peak in radar intensity observed at the water's edge (Section 7.7), in a similar method to that applied by Takewaka (2005). While this produced a reasonable estimation of the intertidal beach slope at West Kirby Sands the large scale bed forms were not well resolved. Further application of this echo intensity edge detection algorithm to additional monthly mean waterline images was not considered to be accurate to a high level of confidence. This was due to the fact that the only validation of the

waterline edge detection algorithm could be made during October 2006 using the Lidar survey data. Further survey data would help to validate this edge detection algorithm so that it can be applied to monthly mean waterline images with reasonable confidence.

The 'waterline method' is complicated further when applied to the intertidal sandflats of West Kirby Sands and West Hoyle Bank due to the fact that these are not beaches backed by shoreline. This creates significant radar backscatter interference when identifying the water's edge through areas of standing water not normally present on a simplified beach case which is backed by a shoreline. The 'waterline method' has the potential to offer useful information on dune dimensions which could be used with the motion tracking algorithm to increase the accuracy of dune migration measurements. Repeat measurements of dune cross sectional area would eliminate the use of a constant dune area as was applied in this research. The application of this method to a simplified beach case, with more pronounced bed features, could possibly show the 'waterline method' to be a valuable tool for remote surveying of coastal morphology.

10.2 DGPS intertidal survey

Repeat DGPS surveys (A-D: 28.01.11, 31.01.11, 08.02.11, 11.02.11) of the intertidal sand flats at West Kirby Sands have shown morphological change associated with the migration of large scale bed forms over short, daily timescales. The symmetry index of identified dunes shows them to have been distinctly asymmetrical with the steeper lee slope orientated landwards, indicating a net dune migration into the estuary, as seen in the motion tracking of monthly mean X-band radar wave breaker patterns. An increase in dune area was observed to correspond with an increase in dune crest migration in an onshore direction along the survey profiles. This occurred during a period of increased wave activity and suggests that a change in the hydrodynamic conditions with increased wave influence resulted in an onshore net sediment transport at West Kirby Sands. This is consistent with the net onshore migration of large scale bed forms observed in the motion tracking analysis of the monthly mean X-band images.

To determine the bed load transport associated with the change in bed elevation the Exner equation was applied in 1D to paired bathymetry profiles. A positive gradient in the Exner derived transport rate represents bed accumulation and a negative transport gradient signifies bed erosion. This method eliminates the need to identify individual bed forms making it particularly useful in circumstances where bed form morphology makes delineation of individual bed forms difficult. Commonly used

316

methodologies for estimating bed load transport rates using bed form migrations require the identification and correlation of individual bed forms at two or more points in time. The bed volume is then estimated using a bed form shape factor, usually 0.6. Eliminating the need to identify individual bed forms removes the need for the bed form shape factor. The bed continuity method calculates the local sediment flux over the profile length on the basis of local erosion and deposition volumes and the principle of mass continuity. Positive transport derived from the Exner equation was observed to occur during an increase in wave activity. This suggests that large scale bed forms are migrating into the interior of the Dee Estuary via West Kirby Sands as a result of the increased bed shear stress from the wave activity.

Migration rates between DGPS surveys have also been calculated using a 2D cross correlation algorithm, based on the method of Bell (2005) applied to the X-band radar images to determine the migration of wave breaker patterns. Migration vectors calculated with the x and y components of the 2D cross correlation derived migration are orientated approximately normal to the dune crests and along the bathymetry profiles to which the bed continuity equation was applied. The volumetric transport rates derived from the 2D correlation analysis of DGPS survey data are in good agreement with those calculated using the 1D bed continuity equation. A difference in the migration rates determined from the X-band radar data and the DGPS data is observed. This is likely to be the result of different associated errors with each data set, with the X-band radar data having a larger error. Therefore in reality the DGPS derived transport will be more accurate than the transport obtained from the X-band radar data. It is to be expected that the field data (DGPS) is more accurate than the remotely sensed data (X-band radar).

Both the 1D continuity and 2D correlation methods provide useful information on local bathymetric response to changing hydrodynamic conditions. However, an ambiguity remains at the open boundaries where a constant background level of sediment transport through the survey domain could be occurring and not detected by either method. Another source of error is introduced by the interpolation of the survey bathymetry between the measured data points. This could be eliminated by repeat surveys of predefined profile lines to which the Exner analysis can be applied. However, to reduce the effect of interpolation on the 2D cross correlation analysis the distance between measured survey profiles needs to be reduced, ideally to a 1m spacing which should provide adequate accuracy. The DGPS surveys at West Kirby Sands were conducted on foot at times of low water, where time is the limiting factor, as a significant survey area needs to be measured before the intertidal sand dunes are submerged by the incoming tide. An improvement on this method could be achieved with the use

of a motorised vehicle which would allow a significant survey area to be measured at a high spatial resolution.

10.3 Hydrodynamic simulation of observed dune migration event

Large onshore dune migration rates observed in the X-band radar data at West Kirby Sands and West Hoyle Bank were further investigated to determine the influence of waves on the migration of large scale bed forms in the mouth of the Dee Estuary. Dunes were tracked between weekly mean radar images, showing increased onshore migration during a storm event between 6th-8th October 2006. A comparison of migration rates with wave heights in the mouth of the estuary (Triaxys wave buoy) showed onshore migration occurring during times of largest wave heights. This demonstrates the capability of the X-band radar at detecting the migration of large scale bed forms over shorter timescales than has previously been attempted (i.e. monthly). Applying the cross correlation dune tracking method to weekly X-band radar images is an effective technique for remotely sensing morphological change in dynamic, shallow water regions during high energy storm events.

A hindcast simulation, of eight day duration between 6th-13th October 2006, was set up to cover the storm event where onshore dune migrations were observed in the X-band radar data. The effect of tides, waves and wave-induced currents have been included in the simulation process to achieve a high level of accuracy in morphological modelling in the Dee Estuary.

The bed roughness was represented within the simulation by using a set of formulae to predict the hydraulic roughness of the bed (van Rijn, 2007a) implemented in SISYPHE which was then fed back into TELEMAC-2D at regular intervals for use within the flow computation. A test case simulation of 12.5 hours duration in the Dee Estuary (Section 9.5.5) showed that the inclusion of bed roughness feedback increased the total bed shear stress resulting in an enhanced total load transport rate at West Kirby Sands and West Hoyle Bank. While the procedure implemented is appropriate it does assume that the bed roughness, and therefore the bed forms, will evolve in time with the changing hydrodynamic conditions. This assumes that bed forms are in equilibrium with the local flow conditions, having the effect of allowing bed forms to grow and decay at unnaturally high rates. Due to the constantly changing nature of tidal currents it may be possible that bed forms do not reach equilibrium within one tidal cycle. Bed forms will also change from a previous form to a new one depending on the flow conditions at the time. Therefore, bed forms in tidal environments will always be adapting to the changing hydrodynamic conditions. This makes hysteresis effects an import consideration for

future bed roughness feedback methods.

As TELEMAC-2D is a depth-averaged model it cannot simulate particular aspects of estuarine behaviour, such as the fresh water influence on residual estuarine circulation, which may significantly influence sediment transport. To accurately simulate the baroclinic circulation a three dimensional model is needed. Moore (2009) found this to be important in the Dee Estuary, despite it being a well mixed, macrotidal estuary. When the river flow was increased fresh water at the surface flowed seaward, with a compensating landward flow of denser water at the sea bed. Therefore, it is possible that this could contribute to onshore transport of sediment, especially during winter months when the river discharge is greatest. However, West Kirby Sands may be beyond the influence of the River Dee. Another consideration for 3D numerical modelling could be to resolve the flow structure around sand dunes. This would aim to resolve the flow separation at the bed form crest with reattachment occurring in the dune trough. On the upstream side of the dune the shear stress moves sediment particles uphill until they pass the crest, as sediment is deposited on the lee side of the dune a downstream migration of the dune occurs (Fredsoe and Deigaard, 1992). Resolving this process would allow for a more accurate simulation of sand dune migration to be made.

The total load sediment transport formula of Bijker is implemented in SISYPHE which is a widely used standard 'engineering' formula. This transport formula includes the effect of waves. However, the Bijker formula assumes that sediment transport as a result of waves and currents occurs in the mean current direction with a slight modification by bed slope effects. Any deviation to the transport in the wave direction is not accounted for by SISYPHE and may be important in the nearshore environment. The use of a 'research' model to account for the physical processes occurring in a wave cycle could allow for a more accurate representation of wave-current interaction in the morphological simulation.

A net onshore transport of sediment was simulated at West Kirby Sands and West Hoyle Bank during the storm period. The evolution of the sea bed was also simulated over the dune fields at West Kirby Sands and West Hoyle Bank. Significant evolution was predicted along the western bank of Hilbre Channel, representing sediment transport over West Hoyle Bank, into the estuary interior, causing the bank of the Hilbre Channel to migrate east during the October 2006 storm event. This appears to be a realistic outcome as reports of the movement of marker buoys in this region are reported by the 'notice to mariners' (Figure 1.2).

Profiles at West Kirby Sands and West Hoyle Bank extracted from the initial model bathymetry and the final model bathymetry (bathymetry + evolution) showed large scale bed forms migrating into the estuary during the simulation. The 1D bed continuity equation which was used to calculate volumetric transport between paired DGPS profiles at West Kirby Sands was applied to the paired initial and final bathymetry profiles from the model. The volumetric transport rates derived from the bed continuity equation all showed positive magnitudes which represented sediment accumulation in these regions over the simulation period. This corresponds with the positive predicted bed evolution simulated over the dune fields at West Kirby Sands and West Hoyle Bank.

A comparison was made between the transport rates derived from the 1D continuity analysis of model bathymetry profiles, 2D correlation analysis of weekly X-band radar images and the predicted total load transport from the model simulation. The migration vectors from the 2D correlation analysis of wave breaker patterns showed onshore migration of dunes at West Kirby Sands and West Hoyle Bank which corresponded with the mean predicted transport vectors from the model simulation. The 1D continuity derived transport from the bed profiles at West Kirby Sands and West Hoyle Bank also showed positive magnitudes. This represents an increase in bed elevation from the initial bed elevation to the final bed elevation, suggesting the movement of sediment into these dune field regions from outside of the estuary mouth. The magnitude of the transport rates shows that the 1D continuity derived transport is two orders of magnitude smaller than the simulated total load transport, while the 2D correlation derived transport is one order of magnitude smaller than the total load transport.

It is to be expected that the radar dune tracking derived transport rate underpredicts the simulated total load transport as a background level of transport may be occurring through the radar analysis region which cannot be detected by the motion tracking algorithm. The underprediction of the 1D continuity derived transport by two orders of magnitude compared with the simulated total load transport will also be a result of not representing the suspended load transport as well as the transport ambiguity at the profile boundaries. A net transport of sediment through the study area might occur at the same time as little or zero movement of large scale bed forms.

However the question remains as to whether the 2D modelling simulates enough physical processes to accurately predict bed form migration. Dunes will affect the flow above the bed form, with flow separation occurring at the crest and reattachment at the trough, so that flow is reversed in eddies formed on the lee side of the dune. Above this a zone of significant turbulence is formed in which a large production and dissipation of turbulent energy occurs (Fredsoe and Deigaard, 1992). Close to the zone

320

of reattachment sediment is transported, even when the local shear stress is below the critical value (Raudkivi, 1963). These physical processes will not be represented by a 2D depth-averaged hydrodynamic model. The alternative would be to use a 3D hydrodynamic model, such as TELEMAC-3D, which could resolve the effect the bed form has on the surrounding flow. However, these results show that the model is able to represent some of the observed bed form migration. Further DGPS field surveys, ADCP current measurements and wave measurements coupled with model simulations would allow an accurate investigation into the effectiveness of the 1D bed continuity analysis in determining bed load transport from repeat bed survey profiles.

10.4 Future work

The application of the TELEMAC modelling system to the Dee Estuary has allowed for tides, waves and sediment transport to be simulated over a complex coastal region. The TELEMAC model developed here can be used and extended for future investigations of the Dee Estuary and the surrounding area. Further field campaigns to obtain wave, current, bathymetry and sediment data across the mouth of the estuary, including West Hoyle Bank, would improve the model input data and improve the understanding of the hydrodynamic forcings and the migration of large scale bed forms in the mouth of the Dee Estuary.

An extension to the Burbo Bank offshore wind farm in Liverpool Bay has been proposed by DONG Energy. The proposed extension will cover an area of $40km^2$. Therefore, future monitoring of the migration of large scale bed forms in the mouth of the Dee will show if this construction affects the movement of sediment into the estuary. The construction of the wind farm extension may also mean an increase in the use of coastal transport vessels, which furthers the need to monitor and model the hydrodynamics and morphodynamics in the mouth of the Dee Estuary.

The hydrodynamic modelling of the Dee Estuary could be improved further with more efficient methodology to reduce the model computational time. This could involve using the latest version of TELEMAC (V6P1) which includes internal coupling between TELEMAC-2D and TOMAWAC, and may be more efficient than the modifications made to the subroutines by the author to simulate a similar process using TELEMAC V5P9. Further use of parallelisation would also reduce run times and allow more morphological simulations to be made over longer time periods and including a greater range of wave heights.

The bed roughness feedback process implemented in this research and in Villaret et al. (2011), using a similar Dee Estuary model domain, is a key improvement for morphological modelling. However, this method does assume that the bed forms are in equilibrium with the flow at each computational time step. In reality bed forms will experience changes in their geometry at a rate that is determined by the relative strength of the flow. A time-evolving ripple predictor, such as that developed by Soulsby and Whitehouse (2005), could be included with the bed roughness prediction method.

The inclusion of a method to account for wind blown sand within the Dee Estuary using TELEMAC would be an interesting modelling development. Wind blown sediment transport could be a significant factor over the large area exposed at low tide in the mouth of the Dee Estuary, potentially influencing dune migration on the intertidal sand flats at West Kirby Sands and West Hoyle Bank. Further investigation into how significant wind blown transport is in the Dee Estuary would allow a more accurate estimation of net sediment transport over the entire estuary regime. Including the effect of wind generated waves in the modelling process would also improve the realism of the model. This would allow for wind generated waves inside the estuary, which is relatively sheltered from offshore waves by the large sandflats in the mouth of the estuary, namely West Hoyle Bank and West Kirby Sands.

Waves have been simulated with time-varying water depths (by including the tide) and with time-varying wave boundary conditions. This simulates the wave conditions over the model domain with reasonable accuracy, allowing for tidal modulation of wave heights and varying wave conditions throughout the simulation time period. However, the accuracy of the wave simulation could be improved further by implementing spatially, as well as temporally, varying boundary conditions. This can be achieved with a modification of the LIMWAC subroutine, so that at each time step a loop is made over the boundary nodes which impose the appropriate boundary condition for that node.

Unfortunately the X-band radar installation on Hilbre Island is no longer active. However, regular surveys of the dunes at West Kirby Sands and West Hoyle Bank would allow for a verification of dune migration rates to be made, whilst also showing any change in dune cross sectional area over the monthly migration periods. This could also be useful to test the shape factor β used in Equation 2.38 for sediment transport derived from dune tracking methods. Further dune surveys could also allow for an accurate determination of the relationship between the position of dune crests and the location of maximum radar backscatter intensity. This would allow for dune wavelengths to be determined on a regular basis from the radar data, an important consideration as in this study the dunes were assumed

to migrate with constant shape.

Surveying the intertidal dune fields in the mouth of the Dee Estuary using a similar method to that used for the DGPS surveys here, but with a greater spatial resolution, with less spacing between measured survey profiles would give more accurate survey data. This can be used to further test the Exner equation applied in 1D to the paired bathymetry profiles. A motorised vehicle such as a quad bike could be very useful for this purpose. Beach surveys are often conducted using DGPS receivers mounted on small vehicles. The COAST3D project used a DGPS receiver mounted on a small trailer pulled by a 4-wheel vehicle. The trailer can penetrate the bed depending on its resistance characteristics, however the overall accuracy was found to be about 0.05m on flat smooth areas and 0.10m on steep slopes (van Rijn et al., 2000).

The waterline method could be applied to a simpler intertidal location to create beach profile images containing less radar image noise. A beach which is backed by a land mass, so that the water's edge might be clearer defined, and containing large intertidal bed forms could be an interesting location to test this waterline method. This could allow remote measurements of bed form dimensions to be made on a regular basis. A combination of video imaging techniques with X-band radar images might help to reduce the effect of image noise.

Chapter 11

Final Conclusions

This research has used three different methods to identify and understand the migration of large scale bed forms in the mouth of the Dee Estuary. Sand dunes were remotely sensed using X-band radar data, DGPS field surveys of the intertidal dune field at West Kirby Sands were conducted and numerical modelling techniques were employed to simulate the hydrodynamics and morphological change in the mouth of the Dee Estuary. All three methods have shown that large scale bed forms are migrating into the Dee Estuary via the intertidal sand flats at West Kirby Sands and West Hoyle Bank. The importance of waves for large onshore migration events has also been shown through remote sensing, field work and numerical modelling.

Are large scale bed forms migrating into the Dee Estuary?

Regions of persistently breaking waves in the X-band radar images were taken as a proxy for the location of large scale bed forms at West Kirby Sands and West Hoyle Bank. Motion tracking analysis of these wave breaker patterns has shown that large scale bed forms migrated into the Dee Estuary for all monthly mean radar images between 2006-2008. The motion tracking analysis of wave breaker patterns for weekly mean radar images showed onshore and offshore migration. This suggests that while there is some variability in large scale bed form migration in the mouth of the Dee, the net migration is into the estuary interior.

Is the X-band radar installation on Hilbre Island in the mouth of the Dee Estuary an effective tool for remotely sensing the migration of large scale bed forms?

The X-band radar installation located on Hilbre Island in the mouth of the Dee Estuary has been

shown to be an effective remote sensing tool over a range of 4km. The radar data covers the intertidal sand banks in the mouth of the estuary. Time-averaged radar images allowed regions of persistently breaking waves to be located and tracked over monthly and weekly time scales. The ability of the X-band radar to record data over 24 hours and during moderate rain conditions makes this an effective tool for remotely sensing estuaries during energetic storm events. The motion tracking algorithm of Bell (2005) shows good potential to be applied to time-averaged X-band radar images from other shallow water regions where the migration of large scale bed forms are of interest. Transport rates derived from the radar data are an order of magnitude smaller than the simulated total transport. This shows that the dune tracking analysis using X-band radar data is capable of representing a significant component of the sediment transport occurring in the mouth of the Dee Estuary. However, further onshore transport is occurring at the intertidal sandflats which is either not represented by the motion tracking analysis or is not associated with dune migration.

Do the intertidal sand flats in the estuary mouth act as pathways for sediment transport into the estuary?

The onshore migration of large scale bed forms at West Kirby Sands and West Hoyle Bank suggests that these intertidal sand flats in the mouth of the Dee Estuary act as pathways for sediment transport into the estuary. Hydrodynamic modelling of the Dee Estuary showed flood asymmetry in current velocities and sediment transport at the shallow water intertidal sand flats of West Kirby Sands and West Hoyle Bank. The deep water regions in the mouth of the estuary, namely the Hilbre and Welsh Channels, show an ebb asymmetry. This suggests that the intertidal sand flats at West Kirby Sands and West Hoyle Bank are regions where sediment is transported into the estuary, while the deep water channels act as regions for sediment export from the estuary.

Can the hydrodynamics and sediment dynamics of the Dee Estuary be accurately represented using numerical modelling techniques?

Accurate hydrodynamic and morphological simulations are of great importance for coastal management. TELEMAC has been shown to accurately simulate tidal elevations and currents when compared with tide gauge and ADCP data, and wave heights when compared with Triaxys wave buoy data from the mouth of the Dee Estuary. The process of simulating waves is coupled with the simulated tide to include the tidal modulation of wave heights. This is an important consideration for the dune fields at West Kirby Sands and West Hoyle Bank in the mouth of the Dee Estuary. A further comparison

should be made with sediment field data so that the morphological change can be validated. There is a close relationship between the maximum current related bottom shear stress and the maximum bed load transport rates when waves are included in model simulations. Larger depth average currents under the influence of wave generated currents than under the influence of waves and tides alone result in greater sediment transport occurring around the areas of interest in the mouth of the estuary. This adds strength to the conclusion that waves are an important driving force for the migration of large scale bed forms and the transport of sediment into the estuary. The waves have the effect of re-suspending sediment, therefore increasing the amount of sand available to be transported by the mean current.

What are the driving forces behind large scale bed form migration in the mouth of the Dee Estuary? Is the action of waves, tidal currents or a combination of the two important?

A comparison of wave heights from the Liverpool Bay WaveNet wave buoy with dune migration rates derived from the X-band radar data showed a positive correlation, with greater wave heights resulting in greater dune migration. Hydrodynamic modelling of a storm event in October 2006, where large migration rates were inferred from the radar data, showed a similar trend between wave heights and simulated transport. The increased transport rate is due to the higher levels of bed shear as a result of wave action. The influence of waves will likely act to stir up the sediment on the bed, which will then be transported in the mean current direction. Measured and simulated current data at the intertidal sand flats in the mouth of the estuary, such as West Kirby Sands, shows flood tidal asymmetry. This suggests that the magnitude of migration of large scale bed forms in the mouth of the Dee Estuary is a result of wave action while the net transport of the sediment into the estuary is due to the tidal currents.

Can field surveys of intertidal dune fields in the mouth of the Dee Estuary determine the mobility of sediment in these regions?

DGPS surveys of West Kirby Sands have shown the morphological change at these intertidal sandflats over two weeks. The application of the Exner equation in 1D to paired bathymetry profiles aimed to show the sediment transport associated with the change in sea bed elevation between survey dates. The ambiguity at the profile open boundaries, where a net transport of sediment could be occurring through the survey region, will cause the Exner derived transport rates to under predict the actual sediment transport occurring. Positive Exner derived transport gradients show sediment accretion at West Kirby Sands during times of increased wave activity. Cross correlation analysis of the interpo-

lated survey data shows the migration of dunes into the estuary via West Kirby Sands during times of increased wave activity. Further field surveys would allow a greater range of hydrodynamic conditions to be covered and potentially increase the resolution of the interpolated survey data. This would allow further testing of both the 1D Exner and 2D cross correlation analysis techniques which display good potential to show sediment transport inferred from morphological change at complex intertidal regions of mobile bed forms.

References

Aarninkhof, S. G. J., Turner, I. L., Dronkers, D. T., Caljouw, M. and Nipius, L. (2003), 'A video-based technique for mapping intertidal beach bathymetry', *Coastal Engineering* **49**, 275–289.

Allen, J. R. L. (1984), *Sedimentary Structures, Their Character and Physical Basis, Developments in Sedimentology*, Elsevier, Amsterdam.

Ashley, G. M. (1990), 'Classification of large scale subaqueous bedforms: a new look at an old problem', *Journal of Sediment Petrology* **60**, 160–172.

Aubrey, D. G. and Speer, P. E. (1985), 'A study of non-linear tidal propagation in shallow inlet/estuarine systems. Part I: observations', *Estuarine and Coastal Shelf Science* **21**, 185–205.

Bagnold, R. A. (1973), The nature of Saltation and Bedload transport in water, *in* 'Proceedings of the Royal Society, London, England', pp. 473–504.

Battjes, J. A. and Janssen, J. P. F. M. (1978), Energy loss and set-up due to breaking of random waves, *in* 'Proceedings of the 16th International Conference on Coastal Engineering, ASCE, New York', pp. 570–587.

Bell, P. S. (1999), 'Shallow water bathymetry derived from an analysis of X-band marine radar images of waves', *Coastal Engineering* **37**, 513–517.

Bell, P. S. (2001), Determination of bathymetry using marine radar images of waves, *in* 'Waves 2001: 4th International Symposium on Ocean Wave Measurement & Analysis, San Francisco, USA'.

Bell, P. S. (2005), Remote determination of bathymetric changes using ground based radar, PhD thesis, University of Wales, Bangor.

Bell, P. S. (2008), Mapping of bathymetry and tidal currents in the Dee Estuary using marine radar data, *in* 'Physics of Estuaries and Coastal Seas, Liverpool, 25-29 August 2008'.

Bell, P. S., Williams, J. J., Clark, S., Morris, B. D. and Vila-Concejo, A. (2006), Nested Radar Systems for Remote Coastal Observations, *in* 'Proceedings of the 8th International Coastal Symposium, Itajai, SC, Brazil, 14-19 March 2004', pp. 483–487.

Bijker, E. (1992), 'Mechanics of sediment transport by the combination of waves and current.', *Proceedings of the 23rd International conference on Coastal Engineering*. pp. 147–173.

Bijker, E. W. (1967), Some considerations about scales for coastal models with movable bed, Technical report, Delft Hydraulics Laboratory, Pub No. 50.

Bolanos, R. and Souza, A. (2010), 'Measuring hydrodynamics and sediment transport processes in the Dee estuary', *Earth system Science* **3**, 79–107.

Booij, N. (1981), Gravity waves on water with non uniform depth and current, Technical report, Department of Civil Engineering, Delft University of Technology.

Bowers, J. A., Morton, I. D. and Mould, G. I. (2000), 'Directional statistics of the wind and waves', *Applied Ocean Research* **22**(1), 13–30.

Brière, C., Abadie, S., Bretel, P. and Lang, P. (2007), 'Assessment of TELEMAC system performances, a hydrodynamic case study of Anglet, France', *Coastal Engineering* **54**(4), 345–356.

Brown, J. M. and Davies, A. G. (2010), 'Flood / ebb tidal asymmetry in a shallow sandy estuary and the impact on net sand transport', *Geomorphology* **114**, 431–439.

Brown, J. M., Souza, A. J. and Wolf, J. (2009), 'An investigation of recent decadal-scale storm events in the eastern Irish Sea', *Journal of Geophysical Research Oceans* **115**.

Brown, J. M., Souza, A. J. and Wolf, J. (2010), 'An 11 year validation of wave-surge modelling in the Irish Sea, using a nested POLCOMS-WAM modelling system', *Ocean Model* **33**(1-2), 118–128.

Cameron, W. M. and Pritchard, D. W. (1963), Estuaries, *in* 'The Sea', Wiley, New York.

Charlesworth, J. K. (1957), *The Quaternary Era*, Arnold, London.

Christofferson, J. B. and Jonsson, I. G. (1985), 'Bed friction and dissipation in a combined current and wave motion', *Ocean Engineering* **12**, 387–423.

Cloin, B. (1998), Gradation effects on sediment transport in oscillatory sheet flow, Master thesis, Delft University of Technology.

Dalrymple, R. W. and Rhodes, R. N. (1995), Estuarine dunes and bars, *in* G. M. E. Perillo, ed., 'Geomorphology and Sedimentology of Estuaries, Developments in Sedimentology', pp. 359–422.

Davies, A. G. (1992), Modelling the vertical distribution of suspended sediment in combined wave-current flow, *in* D. Prandle, ed., 'Dynamics and Exchanges in Estuaries and the Coastal Zone A.G.U. Coastal and Estuarine Studies', p. 25.

Davies, A. G., Berx, B. E., Brown, J. M. and Villaret, C. (2005), *Morphological modeling of trenches and pits in wave-current flows*, Aqua Publications, The Netherlands.

Davies, A. G., Soulsby, R. L. and King, H. L. (1988), 'A numerical model of the combined wave and current bottom boundary layer.', *Journal of Geophysical Research* **93**(491-508).

Davies, A. G. and Thorne, P. D. (2008), 'Advances in the study of moving sediments and evolving seabeds', *Surveys in Geophysics* **29**(1), 1–36.

Davies, A. G. and Villaret, C. (2000*a*), 'Sand Transport by waves and currents: predictions of research and engineering models.', *Proceedings of the 27th International Conference on Coastal Engineering* (Sydney. ASCE, Reston VA, USA), 2481–2494.

Davies, A. G. and Villaret, C. (2000*b*), 'Sand transport by waves and currents: predictions of research and engineering models', *Proceedings of the Conference American Society of Civil Engineers* **Sydney, Au**.

Davies, A. G. and Villaret, C. (2002), 'Prediction of sand transport rates by waves and currents in the coastal zone', *Continental Shelf Research* **22**(18-19), 2725–2737.

Davies, A. G. and Villaret, C. (2003*a*), Morphodynamical evolution of (laboratory) trenches beneath waves and currents: Benchmarking Test #1, #2 and #3. Morphodynamical evolution of (laboratory) trenches beneath waves and currents: Benchmarking Test #1, #2 and #3, *in* 'Sand Pit abstract', p. 10.

Davies, A. G. and Villaret, C. (2003*b*), 'Sediment transport modelling for coastal morphodynamics', *Proceedings of Coastal Sediments* **Clearwater**, 14.

De Vriend, H. J., Zyserman, J. A., Nieholson, J., Roelvink, J. A., Peehon, P. and Southgate, H. N. (1993), 'Medium term 2DH coastal area modelling', *Special Issue Coastal Engineering* pp. 193–224.

Dibajnia, M. and Watanabe, A. (1992), 'Sheet flow under nonlinear waves and currents', *Proceedings of the International Conference on Coastal Engineering* **23**, 2015–2028.

Dronkers, J. (1986), 'Tidal asymmetry and estuarine morphology', *Netherlands Journal of Sea Research* **20**, 117–131.

Dronkers, J. (1998), Morphodynamics of the Dutch Delta. Morphodynamics of the Dutch Delta, *in* J. Dronkers and M. B. A. M. Scheffers, eds, 'Physics of Estuaries and Coastal Seas', A. A. Balkema, Rotterdam, pp. 297–304.

Dronkers, J. (2005), Dynamics of Coastal Systems, *in* 'Advanced Series onOcean Engineering', World Scientific, p. 519.

Dyer, K. R. (1986), *Coastal and Estuarine sediment dynamics*, Wiley-Interscience, Chichester, New York.

Dyer, K. R. (1997), *Estuaries: a physical introduction*, John Wiley, Chichester, New York.

Engel, P. and Lam Lau, Y. (1980), 'Computation of bedload using bathymetric data', *Journal of the Hydraulics Division* **106**, 369–380.

Engel, P. and Lam Lau, Y. (1981), 'Bed load discharge coefficient', *Journal of the Hydraulics Division* **107**(11), 1445–1454.

Engelund, F. (1970), 'Instability of erodible beds', *Journal of Fluid Mechanics* **42**, 225–244.

Environment Agency (2005), Porty of Mostyn: Application for dredging and disposal consents, Technical report, The Environment Agency.

Ericson, E. A., Lyzenga, D. R. and Walker, D. T. (1999), 'Radar backscatter from stationary breaking waves', *Journal of Geophysical Research* **104**, 29679–29695.

Fahy, F. M., Hansom, J. D. and Comber, D. P. M. (1993), Estuaries Management Plans Coastal Processes and Conservation: Dee Estuary, Technical report, Coastal Research Group, University of Glasgow, Department of Geography and Topographic Science on behalf of English Nature.

Fairbanks, R. G. (1989), 'A 17,000 year glacio-eustatic sea level record: influence of glacial melting rates on the Younger Dryas event and deep ocean circulation', *Nature* **342**, 637–642.

Fredsoe, J. (1984), 'Turbulent boundary layer in wave-current motions', *Journal of Hydraulic Engineering* **110**, 1103–1120.

Fredsoe, J. and Deigaard, R. (1992), *Mechanics of coastal sediment transport. Advanced series on ocean engineering, vol 3.*, World Scientific, Singapore.

Friedrichs, C. T. and Aubrey, D. G. (1988), 'Non-linear tidal distortion in shallow well-mixed estuaries: a synthesis', *Estuarine and Coastal Shelf Science* **27**, 521–545.

Friedrichs, C. T. and Madsen, O. S. (1992), 'Nonlinear diffusion of the tidal signal in frictionally dominated estuaries', *Journal of Geophysical Research* **97**, 5637–5650.

Gaeuman, D. and Jacobson, R. B. (2007), 'Field assessment of alternative bed load transport estimators', *Journal of Hydraulic Engineering* **133**, 1319–1327.

Galland, J. C., Goutal, N. and Hervouet, J. M. (1991), 'TELEMAC: A new numerical model for solving shallow water equations', *Advances in Water Resources* **14**, 138–148.

Grant, W. D. and Madsen, O. S. (1979), 'Combined wave and current interaction with a rough bottom.pdf', *Journal of Geophysical Research* **84**.

Greidanus, H. (1997), 'The use of radar for bathymetry in shallow seas', *The Hydrographic Journal* **83**, 13–18.

Guillou, N. W. and Chapalain, G. (2011), 'Effects of the coupling between TELEMAC-2D and TOMAWAC on SISYPHE modelling in the outer Seine estuary.', *Proceedings of the XVIIIth Telemac & Mascaret User Club* pp. 51–58.

Guillou, N. W. and Chapalain, G. (2012), 'Modeling the Tide-Induced Modulation of Wave Height in the Outer Seine Estuary', *Journal of Coastal Research* **282**(ii), 613–623.

Guinard, N. W., Ransone Jr, J. T. and Daley, J. C. (1971), 'Variation of NRCS of the sea with increasing roughness', *Journal of Geophysical Research* **76**, 1525–1538.

Haller, M. C. and Lyzenga, D. R. (2003), 'Comparison of radar and video observations of shallow water breaking waves', *IEEE Transactions in Geosciences and Remote Sensing* **41**(4), 832–844.

Heathershaw, A. D., Blackley, M. W. L. and Hardcastle, P. J. (1980), 'Wave direction estimates in coastal waters using radar', *Coastal Engineering* **3**, 249–267.

Hedges, T. S. (1976), An empirical modification to linear wave theory, *in* 'Proceedings of the institution of Civil Engineers Part 2 Research and Theory', pp. 575–579.

Henderson, F. M. and Lewis, A. J. (1998), Principles and Applications of Imaging Radar, *in* 'Manual of Remote Sensing', 3rd editio edn, John Wiley and Sons, p. 866.

Hervouet, J. M. (2007), *Hydrodynamics of free surface flows*, Wiley, New York.

Hervouet, J. M. and Bates, P. (2000), 'Special Issue: The TELEMAC Modelling System', *Hydrological Processes* **14**(13), 2207–2364.

Hervouet, J. M., Hubert, J. L., Hanin, J. M., Lepeintre, F. and Peltier, E. (1994), 'The computation of free surface flows with TELEMAC: an example of evolution towards hydroinformatics', *Journal of Hydraulic Research* **32**, 45–64.

Hessner, K. G. and Bell, P. S. (2009), High resolution current and bathymetry determined by nautical X-Band radar in shallow waters, *in* 'Proceedings of IEEE Oceans âĂŹ09 Conference, Bremen, Germany, 11-14th May 2009'.

Hessner, K. G., Nieto-Borge, J. C. and Bell, P. S. (2008), Nautical Radar Measurements in Europe - Applications of WaMoS II as sea state, current and bathymetry sensor, *in* V. Barale and M. Gade, eds, 'Remote Sensing of the European Seas', Springer, Geosciences, Dordrecht, The Netherlands,, pp. 435–446.

Hessner, K. G., Reichert, K., Dittmer, J., Nieto-Borge, J. C. and Gunther, H. (2001), Evaluation of WaMoS II Wave data, *in* 'Proceedings of WAVES 2001, San Francisco, USA.'.

Heygster, G., Dannenberg, J. and Notholt, J. (2010), 'Topographic Mapping of the German Tidal Flats An-
alyzing SAR Images With the Waterline Method', *IEEE Transactions on Geoscience and Remote Sensing*
48(3), 1019–1030.

Hoekstra, P., Bell, P., van Santen, P., Roode, N., Levoy, F. and Whitehouse, R. (2004), 'Bedform migration and
bedload transport on an intertidal shoal', *Continental Shelf Research* 24(11), 1249–1269.

Holland, K. T., Holman, R. A., Lippmann, T. C., Stanley, J. and Plant, N. (1997), 'Practical use of video
imagery in nearshore oceanographic field studies', *Journal of Ocean Engineering* 22, 81–92.

Holman, R. A., Sallenger, A. H., Lippmann, T. C. and Haines, J. W. (1993), 'The application of video image
processing to the study of nearshore processes.', *Oceanography* 6(3), 78–85.

Holman, R. A. and Stanley, J. (2007), 'The history and technical capabilities of Argus', *Coastal Engineering*
54, 477–491.

Holt, J. T. and James, I. D. (2001), 'An s coordinate density evolving model of the northwest European conti-
nental shelf 1 , Model description and density structure against both on and off the shelf , the whole of the
North Sea Project sources', *Journal of Geophysical Research* 106, 15–34.

HR Wallingford (2007), Dee Estuary Modelling. Port of Mostyn EIA 2007 Hydraulic Modelling Studies, Tech-
nical report, HR Wallingford Report EX5514, Release 1.0 April 2007.

Hurdle, D. P. and Stive, R. J. H. (1989), 'Revision of SPM 1984 wave hindcast model to avoid inconsistencies
in engineering applications', *Coastal Engineering* 12, 339–351.

Huynh-Thanh, S. and Temperville, A. (1992), A numerical model of the rough turbulent boundary layer in
combined wave and current interaction, *in* R. L. Soulsby and R. Bettess, eds, 'Sand Transport in Rivers,
Estuaries and the Sea'.

IEEE (1984), IEEE standard letter designations for radar-frequency bands, Technical report, The Institute of
Electrical and Electronic Engineers, New York.

Janmaluddin, J. M. (1976), Interaction between wave tide and wind at the distal end of the sand spit at Ynyslas,
Dyfi., Msc, UCW, Aberystwyth.

Jessup, A. T., Keller, W. C. and Melville, W. K. (1990), 'Measurements of sea spikes in microwave backscatter
at moderate incidence.', *Journal of Geophysical Research* 95, 9679–9688.

Joo-Hyung, R., Won, J.-S. and Kyung Duck, K. (2002), 'Waterline extraction from Landsat TM data in a tidal
flat: A cast study from Gonso Bay, Korea', *Remote Sesning of the Environment* 83, 442–456.

Kalmykov, A. I. and Pustovoytenko, V. V. (1976), 'On polarization features of radio signals scattered from the
sea surface at small grazing angles', *Journal of Geophysical Research* 81, 1960–1964.

Keller, W. C., Jessup, A. T. and Melville, W. K. (1990), 'Measurements of Sea Spikes in Microwave Backscatter
at Moderate Incidence.', *Journal of Geophysical Research* 90(C6), 9679–9688.

Kennedy, J. F. (1963), 'The mechanics of dunes and antidunes in erodible bed channels', *Journal of Fluid
Mechanics* 16, 521–544.

King, C. A. M. (1959), *Beaches and coasts*, Edward Arnold.

Kleinhans, M. G. (2005), Phase diagrams of bed states in steady, unsteady, oscillatory and mixed flows, *in*
'SANDPIT, Sand Transport and Morphology of Offshore Mining Pits', Aqua Publications, The Netherlands.

Koch, F. G. and Flokstra, C. (1981), 'Bed level computations for curved alluvial channels.', *19th Congress of the International Association for Hydraulic Research, New Delhi India* .

Koopmans, B. N. and Wang, Y. (1994), Satellite radar data for topographic mapping of the tidal flats in the Wadden Sea, The Netherlands, *in* 'Proceedings of the 2nd Thematic Conference on Remote Sensing for Marine and Coastal Environments, New Orleans'.

Kostaschuk, R. A., Church, M. A. and Luternauer, J. L. (1989), 'Bed material, bed forms and bed load in a salt-wedge estuary', *Canadian Journal of Earth Sciences* **26**(7), 1440–1452.

Lanzoni, S. and Seminara, G. (2009), 'Long-term evolution and morphodynamic equilibrium of tidal channels', *Geomorphology* **103**, 588–596.

Lee, P. H. Y. (1977), 'Doppler measurements of the effects of gravity waves on windgenerated ripples', *Journal of Fluid Mechanics* **81**, 225–240.

Lee, P. H. Y., Barter, J. D., Beach, K. L., Hindman, C. I., Lake, B. M., Rungaldier, H., Shelton, J. C., Williams, A. B., Yee, R. and Yuen, H. C. (1995), 'X band microwave backscattering from ocean waves', *Journal of Geophysical Research* **100**, 2591–2611.

Lee, T. H. and Hanes, D. M. (1995), 'Direct inversion method to measure the concentration profile of suspended particles using backscattered sound', *Journal of Geophysical Research* **100**(C2), 2649–2657.

Li, M. Z., Wright, L. D. and Amos, C. L. (1996), 'Predicting ripple roughness and sand resuspension under combined flows in a shoreface environment', *Marine Geology* **130**(1-2), 139–161.

Lippmann, T. C. and Holman, R. A. (1989), 'Quantification of sand bar morphology: a video technique based on wave dissipation', *Journal of Geophysical Research* **94**, 995–1011.

Lippmann, T. C. and Kannan, S. (2003), Observations of large scale alongshore variability in nearshore sand bars, *in* 'The 5th International Conference on Coastal Sediments, 18-23 May 2003, Clearwater Beach Florida', pp. 236–237.

Malvarez, G. C., Navas, F. and Jackson, D. W. T. (2004), 'Investigations on the morphodynamics of sandy tidal flats: a modeling application', *Coastal Engineering* **51**, 731–747.

Marker, M. E. (1967), 'The Dee Estuary âĂŞ its progressive silting and salt marsh development', *Transactions of the Institute of British Geographers* **41**, 65–71.

Mason, D. C., Amin, M., Davenport, I. J., Flather, R. A., Robinson, G. J. and Smith, J. A. (1999), 'Measurement of recent intertidal sediment transport in Morecambe Bay using the Waterline Method', *Estuarine, Coastal and Shelf Science* **49**, 427–456.

Mason, D. C., Davenport, I. J., Flather, R. A. and Gurney, C. (1998), 'A digital elevation model of the intertidal areas of the Wash, England, produced by the waterline method', *International Journal of Remote Sensing* **19**(8), 1455–1460.

Mason, D. C., Davenport, I. J., Flather, R. A., McCartney, B. S. and Robinson, G. J. (1995), 'Construction of an intertidal digital elevation model by the waterline method', *Geophysical Research Letters* **22**, 3187–3190.

Mason, D., Scott, T. and Dance, S. (2010), 'Remote sensing of intertidal morphological change in Morecambe Bay, U.K., between 1991 and 2007', *Estuarine, Coastal and Shelf Science* **87**(3), 487–496.

Masselink, G., Cointre, L., Williams, J., Gehrels, R. and Blake, W. (2009), 'Tide-driven dune migration and sediment transport on an intertidal shoal in a shallow estuary in Devon, UK', *Marine Geology* 262(1-4), 82–95.

McCann, D. L. (2007), Dune tracking in the Dee with X-band radar: a new remote sensing technique for quantifying bedload transport, PhD thesis, Bangor University.

McCann, D. L. (2011), Long term morphological modelling of tidal basins, PhD thesis, Bangor University.

McLaughlin, D. J., Allan, N., Twarog, E. M. and Trizna, D. B. (1995), 'High Resolution Polarimetric Radar Scattering Measurements of Low Grazing Angle Sea Clutter', *IEEE Journal of Oceanic Engineering* 20(3), 166–178.

McLean, S. R. (1990), 'The stability of ripples and dunes', *Earth-Science Reviews* 29, 131–144.

McLeish, W., Swift, D. J. P., Long, R. B., Ross, D. and Merrill, G. (1981), 'Ocean surface patterns above sea-floor bedforms as recorded by radar, Southern bight of North Sea', *Marine Geology* 43(M1-M8).

McNinch, J. E. (2007), 'Bar and Swash Imaging Radar (BASIR): A Mobile X-band Radar Designed for Mapping Nearshore Sand Bars and Swash-Defined Shorelines Over Large Distances', *Journal of Coastal Research* 23(1), 59–74.

Meyer-Peter, E. and Muller, R. (1948), Formulas for bedload transport., *in* 'Proceedings 2nd meeting of the International Association for Hydraulic Research, Stockholm', pp. 39–64.

Moore, R. D. (2009), Hydrodynamic and morphometric modelling of a macro-tidal estuary: the Dee Estuary of North West England, PhD thesis, University of Liverpool.

Moore, R. D., Wolf, J., Souza, A. J. and Flint, S. S. (2009), 'Morphological evolution of the Dee Estuary, Eastern Irish Sea, UK: A tidal asymmetry approach', *Geomorphology* 103(4), 588–596.

Mosher, D. C. and Thomson, R. E. (2000), Massive submarine sand dunes in the eastern Juan de Fuca Strait, British Columbia, *in* A. Trentesaux and T. Garlan, eds, 'Marine Sandwave Dynamics, International Workshop, March 23-24 2000, University of Lille 1, France.'.

Myrhaug, D. and Slaatelid, F. G. (1989), 'A rational approach to wave friction coefficients for rough, smooth and transitional turbulent flow', *Coastal Engineering* 13, 11–21.

Narahari, R. K., Narasimna, R. and Badri Narayanan, M. A. (1971), 'The 'bursting' phenomenon in a turbulent boundary layer', *Journal of Fluid Mechanics* 50, 133.

Nielsen, P. (1981), 'Dynamics and geometry of wave generated ripples', *Journal of Geophysical Research* 86, 6467–6472.

Nielsen, P. (1992), 'Coastal Bottom Boundary Layers and Sediment Transport. Advanced series on ocean engineering', *World Scientific* 4, 324.

Nieto Borge, J. C. and Reichert, K. (2005), The marine radar, *in* D. Hauser, K. Kahma, H. E. Krogstad, S. Lehner, J. A. J. Monbaliu and L. R. Wyatt, eds, 'Measuring and analysing the directional spectrum of ocean waves', European COST Action 714, pp. 128–137.

Nieto-Borge, J. C., Reichert, K. and Dittmer, J. (1999), 'Use of marine radar as a wave monitoring instrument', *Coastal Engineering* 37, 331–342.

Olds, S. and Davison, A. (2009), Port of Mostyn Breakwater Quay Development Environmental Statement, Technical report, Port of Mostyn Ltd.

Pethick, J. S. (1994), Estuaries and wetlands: function and form, in 'Wetland Management', Thomas Telford, London, p. 12.

Pingree, R. D. and Griffiths, D. K. (1979), 'Sand transport paths around the British Isles resulting from M2 and M4 tidal interactions', *Journal of the Marine Biology Association* **59**, 497–513.

Plant, N. G. and Holman, R. A. (1997), 'Intertidal beach profile estimation using video images', *Marine Geology* **140**, 1–24.

Prandle, D. (1992), 'Dynamics and exchanges in estuaries and in the coastal zone', *American Geophysical union, Washington DC* p. 647.

Press, W. H., Teukolsky, S. A., Vetterling, W. T. and Flannery, B. P. (1992), *Numerical Recipes in C âĂŞ The Art of Scientific Computing*, second edi edn, Cambridge University Press.

Pye, K. and Neal, A. (1994), 'Coastal dune erosion at Formby Point, north Merseyside, England: causes and mechanisms', *Marine Geology* **119**, 39–56.

Raudkivi, A. J. (1963), 'Study of sediment ripple formation', *Journal of the Hydraulics Division* **89**, 15–33.

RDI (1996), *Acoustic Doppler Current Profiler: Principles of Operation A Practical Primer*, RD Instruments.

Ribberink, J. S. (1998), 'Bed load transport for steady and unsteady oscillatory flow.', *Coastal Engineering* **34**, 59–82.

Ris, R. C., Holthuijsen, L. H. and Booij, N. (1999), 'A third-generation wave model for coastal regions: 2. Verification', *Journal of Geophysical Research* **104**(C4), 7667.

Robins, P. E. and Davies, A. G. (2010), 'Morphological controls in sandy estuaries : the influence of tidal flats and bathymetry on sediment transport', *Ocean Dynamics* **60**, 503–517.

Ruessink, B., Bell, P., van Enckevort, I. and Aarninkhof, S. (2002), 'Nearshore bar crest location quantified from time-averaged X-band radar images', *Coastal Engineering* **45**(1), 19–32.

Ryu, J.-H., Kim, C.-H., Lee, Y.-K., Won, J.-S., Chun, S.-S. and Lee, S. (2008), 'Detecting the intertidal morphologic change using satellite data', *Estuarine, Coastal and Shelf Science* **78**(4), 623–632.

Scott, T. R. and Mason, D. C. (2007), 'Data assimilation for a coastal area morphodynamic model: Morcambe Bay', *Coastal Engineering* **54**, 91–109.

Skolnik, M. I. (1970), *Radar Handbook*, McGraw Hill.

Sleath, J. F. A. (1984), *Sea Bed Mechanics*, Wiley, New York.

Sly, P. (1966), Marine geological studies in the eastern Irish Sea and adjacent estuaries, with special reference to sedimentation in Liverpool Bay and River Mersey, PhD thesis, University of Liverpool, UK.

Small, C. and Nicholls, R. J. (2003), 'A global analtsis of human settlement in coastal zones', *Journal of Coastal Research* **19**, 584–599.

Soulsby, R. (1983), *The bottom boundary layer of shelf seas in physical oceanography of coastal shelf seas,*, Elsivier, Amsterdam.

Soulsby, R. (1997), *Dynamics of marine sands.*, Thomas Telford, London.

Soulsby, R. and Clarke, S. (2005), 'Bed shear stresses under combined waves and currents on smooth and rough beds', *HR Wallingford Report TR 137* .

Soulsby, R., Hamm, L., Klopman, G., Myrhaug, D., Simons, R. and Thomas, G. (1993), 'Wave-current interaction within and outside the bottom boundary layer', *Coastal Engineering* 21(1-3), 41–69.

Soulsby, R. L. and Damgaard, J. S. (2005), 'Bedload sediment transport in coastal waters', *Coastal Engineering* 52(8), 673–689.

Soulsby, R. L. and Whitehouse, R. S. J. W. (1997), Threshold of sediment motion in coastal environments, *in* 'Proceeding of the Pacific Coasts and Ports '97 Conference, Christchurch', pp. 149–154.

Soulsby, R. L. and Whitehouse, R. S. J. W. (2005), Prediction of ripple properties in shelf seas, mark 1 predictor, Technical report, Technical Report TR150. HR Wallingford Ltd., UK.

Speer, P. E. and Aubrey, D. G. (1985), 'A study of non-linear tidal propagation in shallow inlet/estuarine systems. Part II: a theory', *Estuarine and Coastal Shelf Science* 21, 207–224.

Stanev, E. V., Floeser, G. and Wolff, J. O. (2003), 'First- and higher-order dynamical controls on water exchanges between tidal basins and the open ocean. A case study for the East Frisian Wadden Sea.', *Ocean Dynamics* 53, 146–165.

Stanev, E. V., Wolff, J. O., Burchard, H., Bolding, K. and Floeser, G. (2003), 'On the circulation in the East Frisian Wadden Sea: numerical modelling and data analysis', *Ocean Dynamics* 53, 27–51.

Stride, A. H. (1963), 'Current swept sea floors near the southern half of Great Britain', *Quarterly Journal of the Geological Society of London* 119, 175–199.

Strive, M. J. F. and De Vriend, H. J. (1994), Shear stress and mean flow in shoaling and breaking waves, *in* 'Proceedings of the 24th International Conference on Coastal Engineering, ASCE, New York', pp. 594–608.

Takewaka, S. (2005), 'Measurements of shoreline position and intertidal foreshore slopes with X-band marine radar system', *Coastal Engineering Journal* 47(2-3), 91–107.

Ten Brinke, W. B. M., Wilbers, A. W. E. and Wesseling, C. (1999), 'Dune growth, decay and migration rates during a large magnitude flood at a sand and mixed sand gravel bed in the Dutch Rhine River system.', *Special Publication International Association of Sedimentology* 28, 15–32.

Thorne, P. D., Hardcastle, P. J. and Soulsby, R. L. (1993), 'Analysis of acoustic measurements of suspended sediments', *Journal of Geophysical Research* 98(C1), 899–910.

Townend, I. H. (2003), *Coastal and estuary behaviour systems*, ABP Marine Environment Research, Southampton, UK.

Tracy, B. A. (2002), Directional characteristics of the 1990 - 1999 Wave Information Studies Gulf of Mexico hindcast, *in* 'Proceedings of the 7th International Workshop on Wave Hindcasting and Forecasting, Meteorological Service of Candada, U.S. Army Engineer Research and Development Center's Coastal and Hydraulics Laboratory, and Fleet Numerical Meteorology and Oceanography', p. 10.

Trizna, D. B. (2001), 'Errors in bathymetric retrievals using linear dispersion in 3-D FFT analysis of marine radar ocean wave imagery', *IEEE Transactions on Geoscience and Remote Sensing* 39(11), 2465–2469.

Trizna, D. B. and Carlson, D. (1996), 'Studies of low grazing angle radar seascatter in nearshore regions.', *IEEE Transactions on Geosciences and Remote Sensing* **34**, 747–757.

Van Den Berg, J. H. (1987), 'Bedform migration and bed-load transport in some rivers and tidal environments', pp. 681–698.

Van Enckevort, I. M. J. and Ruessink, B. G. (2001), 'Effects of hydrodynamics and bathymetry on video estimates of nearshore sandbar position', *Journal of Geophysical Research* **106**, 16969–16979.

Van Kesteren, W. G. M. and Bakker, W. T. (1984), Near bottom velocities in waves with a current; analytical and numerical computations, *in* 'Proceedings of the 19th Conference of Coastal Engineering, Houston, TX', pp. 1161–1171.

Van Landeghem, K. J. J., Baas, J. H., Mitchell, N. C., Wilcockson, D. and Wheeler, A. J. (2012), 'Reversed sediment wave migration in the Irish Sea, NW Europe: A reappraisal of the validity of geometry-based predictive modelling and assumptions', *Marine Geology* **295-298**, 95–112.

Van Rijn, L. C. (1984*a*), 'Sediment transport Part I: Bedload tranpsort', *Journal of Hydraulic Engineering* **110**(10), 1431–1456.

Van Rijn, L. C. (1984*b*), 'Sediment transport Part II: Suspended load transport', *Journal of Hydraulic Engineering* **110**(11), 1613–1641.

Van Rijn, L. C. (1984*c*), 'Sediment transport, Part III: Bed forma and alluvial roughness', *Journal of Hydraulic Engineering* **110**(12), 1733–1754.

Van Rijn, L. C. (1993), *Principles of sediment transport in rivers, estuaries, and coastal seas.*, Aqua Publications, Blokzijl, The Netherlands.

Van Rijn, L. C. (2007*a*), 'Unified View of Sediment Transport by Currents and Waves . I : Initiation of Motion , Bed Roughness , and Bed-Load Transport', *Journal of Hydraulic Engineering* **133**, 649–667.

Van Rijn, L. C. (2007*b*), 'Unified View of Sediment Transport by Currents and Waves. I: Initiation of Motion, Bed Roughness, and Bed-Load Transport', *Journal of Hydraulic Engineering* **133**, 649–667.

Van Rijn, L. C., Grasmeijer, B. T. and Ruessink, B. G. (2000), Measurement errors of instruments for velocity, wave height, sand concentration and bed levels in field conditions, Technical report, University of Utrecht/Delft Hydraulics Report.

Van Rijn, L. C. and Havinga, F. (1995), 'Transport of fne sands by currents and waves.', *J. Waterway, Port, Coastal, Ocean Eng.* **121**, 123–133.

Van Rijn, L. C. and Kroon, A. (1992), Sediment transport by currents and waves, *in* 'Proceedings of Coastal Engineering Conference, Venice, Italy'.

Van Rijn, L. C. and Walstra, D. J. R. (2003), Modelling of sand transport in delft3d, Technical report, WL Delft Hydraulics.

Van Rijn, L., Davies, A., van de Graaff, J. and Ribberink, J. (2001), *SEDMOC: Sediment Transport Modelling in Marine Coastal Environments.*, Aqua Publications, Amsterdam.

Villard, P. V. and Church, M. A. (2003), 'Dunes and associated sand transport in a tidally influenced sand-bed channel', *Canadian Journal of Earth Sciences* **40**, 115–130.

Villaret, C. (2001), 'Intercomparaison des formules de transport solide.', *Programme Biparti* **reports HP**, 47.

Villaret, C. and Davies, A. (2004), 'Numerical modeling of littoral sand transport.', *Proceedings of the 29th International Conference on Coastal Engineering* **Lisbon, Wo**, 1678–1689.

Villaret, C., Huybrechts, N., Davies, A. G. and Way, O. (2011), 'Effect of bed roughness prediction on morphodynamic modelling : Application to the Dee estuary (UK) and to the Gironde estuary (France)', *Proceedings of 34th IAHR World Congress* (1), 1149–1156.

Vincent, C. E. and Hanes, D. M. (2002), 'The accumulation and decay of near-bed suspended concentration due to waves and wave groups', *Continental Shelf Research* **22**(14), 1987–2000.

Walstra, D. J. R., Mocke, G. P. and Smit, F. (1996), Roller contributions as inferred from inverse modelling techniques, *in* 'Proceedings of the 25th International Conference on Coastal Engineering, ASCE, New York', pp. 1205–1218.

Wang, C. H., Wai, W. H., Onyx, Li, Y. S. and Chen, Y. (2006), 'Modelling of the wave-current interaction in the Pearl River Estuary', *Journal of Hydrodynamics* **18**(3), 159–165.

Wang, Z. B., Jeuken, M. C. J. L., Gerritsen, H., De Vriend, H. J. and Kornman, B. A. (2002), 'Morphology and asymmetry of the vertical tide in the Westerschelde estuary', *Continental Shelf Research* **22**, 2599–2609.

Wells, G. P. (1966), 'The lugworm (Arenicola) - a study in adaptation', *Netherlands Journal of Sea Research* **3**, 294–313.

Wills, L. J. (1912), 'glacial and post glacial changes in the lower Dee valley', *Quarterly Journal of the Geological Society of London* **68**, 180.

Wilson, K. C. (1966), 'Bedload transport at high shear stress', *Journal of Hydrological Society* **92**, 49–59.

Wolf, J. (2008*a*), 'Coupled wave and surge modelling and implications for coastal flooding', *Advanced Geoscience* **17**, 19–22.

Wolf, J. (2008*b*), SWAN modelling of Liverpool Bay including Dee, Mersey and Ribble Estuaries, Technical report, Joint Defra/EA Flood and Coastal Erosion Risk Management R&D Programme.

Wolf, J. and Bell, P. S. (2001), 'Waves at Holderness from X-band radar', *Coastal Engineering* **43**, 247–263.

Wolf, J., Brown, J. M. and Howarth, M. J. (2011), 'The wave climate of Liverpool Bay - observations and modelling', *Ocean Dynamcis* **61**, 639–655.

Wolf, J., Osuna, P., Howarth, M. J. and Souza, A. J. (2007), Modelling and measuring waves in coastal waters, *in* 'Proceedings of ICCE 2006, San Diego, Volume 1', pp. 539–551.

Woodroffe, C. D. (2002), *Coasts: Form, processes and evolution*, Cambridge University Press, Cambridge.

Worley, C. R., Lippmann, T. C., Haines, J. W. and Sallenger, A. H. (1997), An aerial video system for rapidly measuring sand bar morphology, *in* 'Proceedings of Coastal Dynamics '97, ASCE', pp. 346–354.

Yalin, M. S. (1997), *Mechanics of sediment Transport*, Pregamon Press, New York.

Young, I. R., Rosenthal, W. and Ziemer, F. (1985), 'A 3-dimensional analysis of marine radar images for the determination of ocean wave directionality and surface currents', *Journal of Geophysical Research Oceans* **90**, 1049–1059.

Appendix I: Publications arising from this study (conference proceedings)

Villaret, C., Huybrechts, N., Davies, A. G., Way, O. G. (2011). Effect of bed roughness prediction on morphodynamic modelling: Application to the Dee Estuary (UK) and to the Gironde Estuary (France). Proceedings of 34th IAHR World Congress, 1, 1149-1156.

Brown, J. M., Chesher, T. J., Beveridge, A. J., Shafiai, S. H., O'Hara Murray, R. B., Smyth, T. A. G., Bricheno, L. M., Way, O. G. (2011). Briefing: Young Coastal Scientists and Engineers Conference 2011. Proceedings of the Institute of Civil Engineers, Maritime Engineering, 165, MA1, 7-20.

Planned publications arising from this study

X-Band and DGPS paper including key results of increased bed form migration with wave height, demonstrating that sand flats are a major sediment input pathway to the Dee Estuary system.

Synthesis paper including the three methods from this study - hydrodynamic modelling (including bed roughness innovations), DGPS and RADAR. What do we learn about the overall dynamics of the system?

Appendix II: Sample steering (cas) files

TELEMAC-2D

/ TELEMAC-2D STEERING FILE
/
TITLE : 'Dee tide 1'
RELEASE : V5P9
PARALLEL PROCESSORS : 2
/
/ COMPUTER INFORMATION
/
GEOMETRY FILE : dee.geo
BOUNDARY CONDITIONS FILE : dee_conlim
FORTRAN FILE : bord.f
COMPUTATION CONTINUED : YES
PREVIOUS COMPUTATION FILE : spinup.res
RESULTS FILE : current.res
INITIAL TIME SET TO ZERO : YES
/
/ GENERAL INFORMATION - OUTPUTS
/
VARIABLES FOR GRAPHIC PRINTOUTS : 'U,V,H,S,B,M,W,X,Y,E'
/
NUMBER OF FIRST TIME STEP FOR GRAPHIC PRINTOUTS : 1
GRAPHIC PRINTOUT PERIOD : 180
LISTING PRINTOUT PERIOD : 180
TIME STEP : 10
NUMBER OF TIME STEPS : 8640 (+30 mins if wave simulation follows)
/
/ INITIAL CONDITIONS
/
INITIAL CONDITIONS : 'CONSTANT ELEVATION'
INITIAL ELEVATION : 3
/
/ BOUNDARY CONDITIONS
/
PRESCRIBED FLOWRATES : 31.0; 1.5; 0.0
PRESCRIBED ELEVATIONS : 0.0; 0.0; 3
OPTION FOR LIQUID BOUNDARIES : 1
/
/ PHYSICAL PARAMETERS

/
LAW OF BOTTOM FRICTION : 5
FRICTION COEFFICIENT : 0.5
TURBULENCE MODEL : 1
DIFFUSION OF VELOCITY : NO
/VELOCITY DIFFUSIVITY : 0.2
/
/ NUMERICAL PARAMETERS
/
TIDAL FLATS : YES
OPTION FOR THE TREATMENT OF TIDAL FLATS : 1
H CLIPPING : YES
MINIMUM VALUE OF DEPTH : 1.E-2
MASS-BALANCE : NO
ADVECTION : YES
TYPE OF ADVECTION : 1;5
ADVECTION OF U AND V :YES
ADVECTION OF H :YES
NUMBER OF SUB-ITERATIONS FOR NON-LINEARITIES :1
SUPG OPTION : 1;2
SOLVER ACCURACY : 1.E-4
DISCRETIZATIONS IN SPACE : 12 ; 11
PROPAGATION : YES
SOLVER : 1
TREATMENT OF THE LINEAR SYSTEM : 2
PRECONDITIONING : 2
MASS-LUMPING ON H : 1
MASS-LUMPING ON VELOCITY : 0
SPHERICAL COORDINATES : NO
IMPLICITATION FOR DEPTH : 0.6
IMPLICITATION FOR VELOCITY : 0.6
BOTTOM SMOOTHINGS : 0
ZERO : 1.E-12
CORIOLIS : YES
CORIOLIS COEFFICIENT : 1.12E-4
AIR PRESSURE : NO
MAXIMUM NUMBER OF ITERATIONS FOR SOLVER : 500
/
/ END OF STEERING FILE
/
& FIN

TOMAWAC

/ PARAMETER STEERING FILE FOR TOMAWAC

TITLE = 'DEE ESTUARY WAVES' RELEASE = V5P9

THIRD GENERATION MODE = YES
/
/ FILES
/
FORTRAN FILE = fortran_OGW.f
GEOMETRY FILE = '../../Telemac2d/dee.geo' BOUNDARY CONDITIONS FILE = dee_tom.conlim
FORMATTED FILE 1 = wavedata.txt
2D RESULTS FILE = waves.r2d
/
/ OUTPUTS
/
VARIABLES FOR 2D GRAPHIC PRINTOUTS = HM0,DMOY,TPR5,ZF,WD,FX,FY,UX,UY,VX,VY
/
/ INITIAL CONDITIONS
/
CONSIDERATION OF TIDE = YES
BINARY TIDAL WATER LEVEL FILE = '../telemac2d/currents.res'
TIDAL WATER LEVEL FILE FORMAT = 2
RANK OF THE WATER LEVEL DATA IN THE TELEMAC FILE = 4
BINARY CURRENTS FILE = '../telemac2d/currents.res'
CURRENTS FILE FORMAT = 3
TIDE REFRESHING PERIOD = 60
/
/ DISCRETISATION
/
FREQUENTIAL RATIO = 1.12
MINIMAL FREQUENCY = 0.05
NUMBER OF FREQUENCIES = 20
NUMBER OF DIRECTIONS = 24
NUMBER OF FIRST ITERATION FOR GRAPHICS PRINTOUTS = 0
PERIOD FOR LISTING PRINTOUTS = 60
PERIOD FOR GRAPHIC PRINTOUTS = 60
TIME STEP = 60
NUMBER OF TIME STEP = 1440
/
/ CONDITIONS INITIALES
/
TYPE OF INITIAL DIRECTIONAL SPECTRUM = 6
INITIAL SIGNIFICANT WAVE HEIGHT = 0.01
INITIAL PEAK FREQUENCY = 0.5
INITIAL PEAK FACTOR = 3.3
INITIAL ANGULAR DISTRIBUTION FUNCTION = 1
INITIAL WEIGHTING FACTOR FOR ADF = 1.0
INITIAL MAIN DIRECTION 1 = 95
INITIAL DIRECTIONAL SPREAD 1 = 32
/
/ CONDITIONS AUX LIMITES
/
TYPE OF BOUNDARY DIRECTIONAL SPECTRUM = 6
BOUNDARY SIGNIFICANT WAVE HEIGHT = 0.01

BOUNDARY PEAK FREQUENCY = 0.5
BOUNDARY PEAK FACTOR = 3.3
BOUNDARY MAIN DIRECTION 1 = 95
BOUNDARY DIRECTIONAL SPREAD 1 = 32
/
/ OPTIONS DU CALCUL
/
MINIMUM WATER DEPTH = 0.05
INFINITE DEPTH = NO
CONSIDERATION OF SOURCE TERMS = YES
/WIND GENERATION = 1
BOTTOM FRICTION DISSIPATION = 1
/BOTTOM FRICTION COEFFICIENT = 0.042
NUMBER OF BREAKING TIME STEPS = 5
/=========== 1 : Battjes et Janssen (1978)
/=========== 2 : Thornton et Guza (1983)
DEPTH-INDUCED BREAKING DISSIPATION = 2
DEPTH-INDUCED BREAKING 2 (TG) WEIGHTING FUNCTION = 2
DEPTH-INDUCED BREAKING 2 (TG) CHARACTERISTIC FREQUENCY = 5
DEPTH-INDUCED BREAKING 2 (TG) COEFFICIENT B = 1.0
DEPTH-INDUCED BREAKING 2 (TG) COEFFICIENT GAMMA = 0.42
/
&FIN

SISYPHE

RELEASE=V5P9
TITLE = 'DEE SEDIMENT TRANSPORT'
/
/ FILE DEFINITION
/
FORTRAN FILE = '../../Ks_feedback/ride.f'
GEOMETRY FILE = '../../Telemac2d/dee.geo'
HYDRODYNAMIC FILE = '../tomawac/waves.r2d'
WAVE FILE = '../tomawac/waves.r2d'
BOUNDARY CONDITIONS FILE = '../../Telemac2d/dee_conlim'
RESULTS FILE =transport2.res
/COMPUTATION CONTINUED =YES
/PREVIOUS SEDIMENTOLOGICAL COMPUTATION FILE=transport1.res

/ /GRAPHICS
/
VARIABLES FOR GRAPHIC PRINTOUTS = U,V,S,H,B,M,N,P,W,X,E,KS,TOB,THETAW
/
LAW OF BOTTOM FRICTION = 1
FRICTION COEFFICIENT = 0.05
MASS-BALANCE = TRUE
STEADY CASE = NO
MASS-LUMPING = NO

SLOPE EFFECT = YES
/ / Numerical parameters
ZERO = 1e-12
TETA = 0.5
WATER DENSITY = 1027
CRITICAL EVOLUTION RATIO = 1
/
/ SEDIMENT TRANSPORT
SUSPENSION = NO (advection diffusion not applied)
/BED LOAD = YES
/IMPOSED INFLOW CONCENTRATION = YES
TETA SUSPENSION = 1
PRECONDITIONING FOR SUSPENSION = 7
TYPE OF ADVECTION = 6
/DISPERSION ALONG THE FLOW = 0
/DISPERSION ACROSS THE FLOW = 0
BED-LOAD TRANSPORT FORMULA = 4 (BIJKER (bed load + suspension))
EFFECT OF WAVES = YES
B VALUE FOR THE BIJKER FORMULA = 5
MEAN DIAMETER OF THE SEDIMENT = 0.00022
COEFFICIENT FUNCTION OF THE POROSITY = 1.67
BETA = 1.3
&ETA

Appendix III: Conlim file and boundary conditions

The following is an example of the boundary condition ('conlim') file used within the Dee Estuary model described in Chapter 4. The conlim file defines the nature of the driving forces at the boundary of the model domain. The first three columns impose the free surface elevation (z_f) and the velocity components (u and v). The eighth column (z_b) allows the free sediment transport and bed evolution to be predicted. These boundary conditions are set with integer numbers where 5 = prescribed value, 4 = free value and 2 = solid boundary. The last two columns represents the grid node number (N) and the corresponding boundary point number (B). The boundary points are consecutively numbered anti-clockwise starting at the bottom left corner of the model domain.

z_f	u	v					z_b				N	B
2	2	2	0.000	0.000	0.000	0.000	2	0.000	0.000	0.000	31	1
2	2	2	0.000	0.000	0.000	0.000	2	0.000	0.000	0.000	55	2
2	2	2	0.000	0.000	0.000	0.000	2	0.000	0.000	0.000	85	3
2	2	2	0.000	0.000	0.000	0.000	2	0.000	0.000	0.000	120	4
2	2	2	0.000	0.000	0.000	0.000	2	0.000	0.000	0.000	158	5
-	-	-	-	-	-	-	-	-	-	-	-	-
2	2	2	0.000	0.000	0.000	0.000	2	0.000	0.000	0.000	119308	316
4	5	5	0.000	0.000	0.000	0.000	4	0.000	0.000	0.000	119347	317
4	5	5	0.000	0.000	0.000	0.000	4	0.000	0.000	0.000	119398	318
4	5	5	0.000	0.000	0.000	0.000	4	0.000	0.000	0.000	119452	319
2	2	2	0.000	0.000	0.000	0.000	2	0.000	0.000	0.000	119446	320
-	-	-	-	-	-	-	-	-	-	-	-	-
2	2	2	0.000	0.000	0.000	0.000	2	0.000	0.000	0.000	117752	677
5	4	4	0.000	0.000	0.000	0.000	2	0.000	0.000	0.000	117905	678
5	4	4	0.000	0.000	0.000	0.000	2	0.000	0.000	0.000	117710	679
5	4	4	0.000	0.000	0.000	0.000	2	0.000	0.000	0.000	116747	680
5	4	4	0.000	0.000	0.000	0.000	2	0.000	0.000	0.000	115744	681

Appendix IV: DGPS survey data and results

The following chapter lists all bathymetry profiles extracted from the DGPS survey data on West Kirby Sands detailed in Chapter 8. Paired bathymetry profiles with volumetric transport derived from the Exner equation applied in 1D are also given.

Profiles extracted from West Kirby Sands DGPS survey

Distance (m) along profile 2
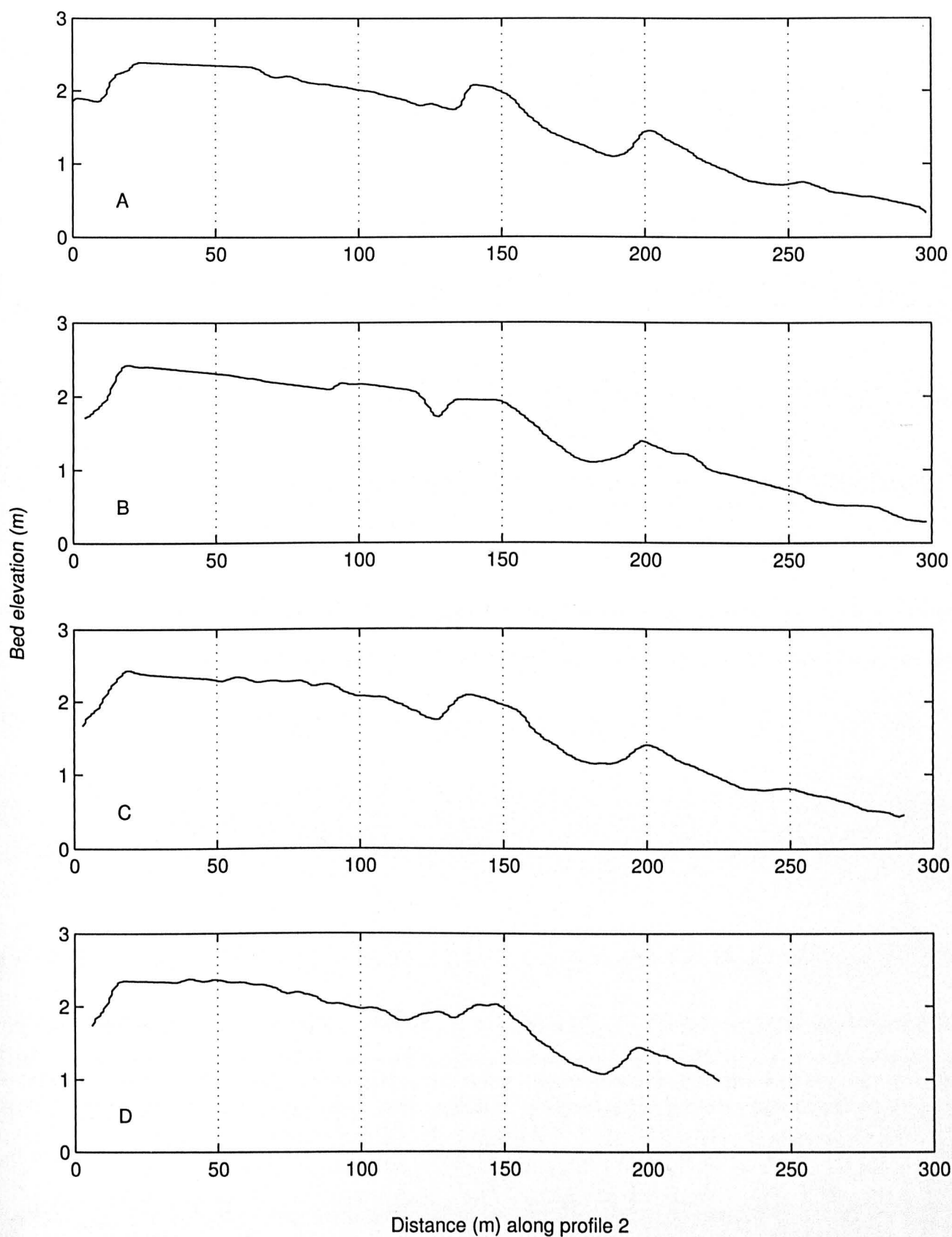
Figure IV.1: Bed elevation profile along profile 2 for all West Kirby Sands survey data A.) 28.01.11 B.) 31.01.11 C.) 08.02.11 D.) 11.02.11.
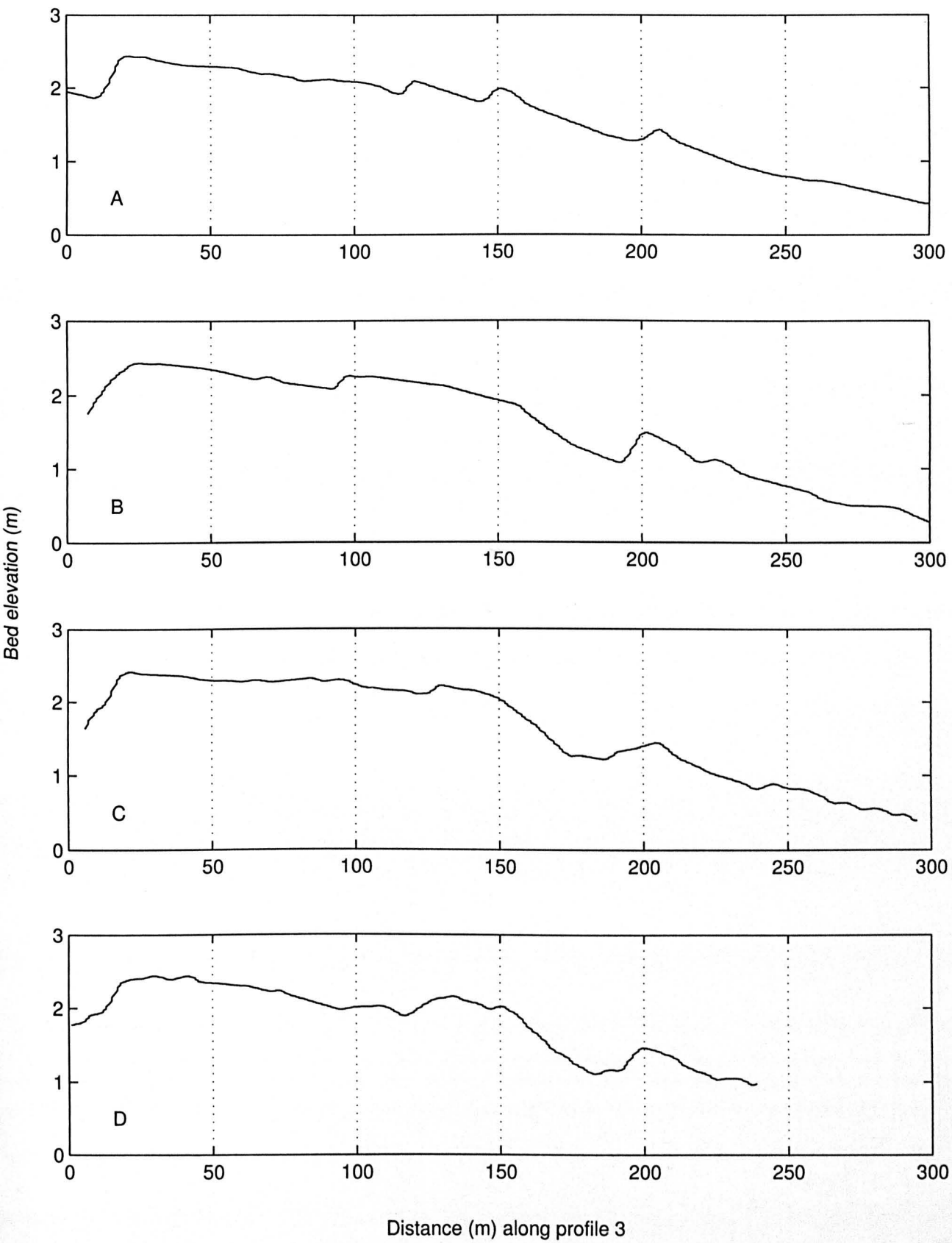
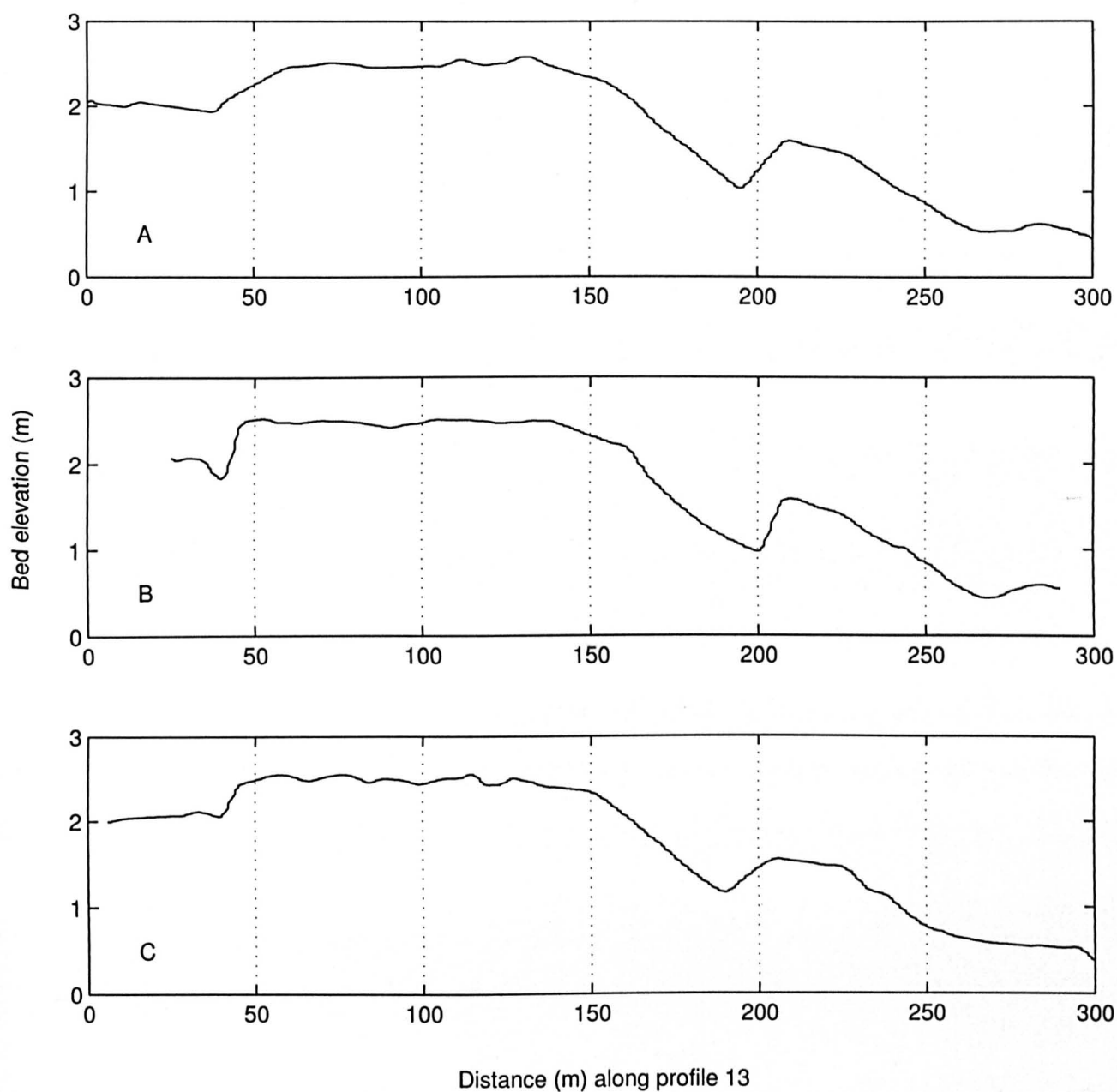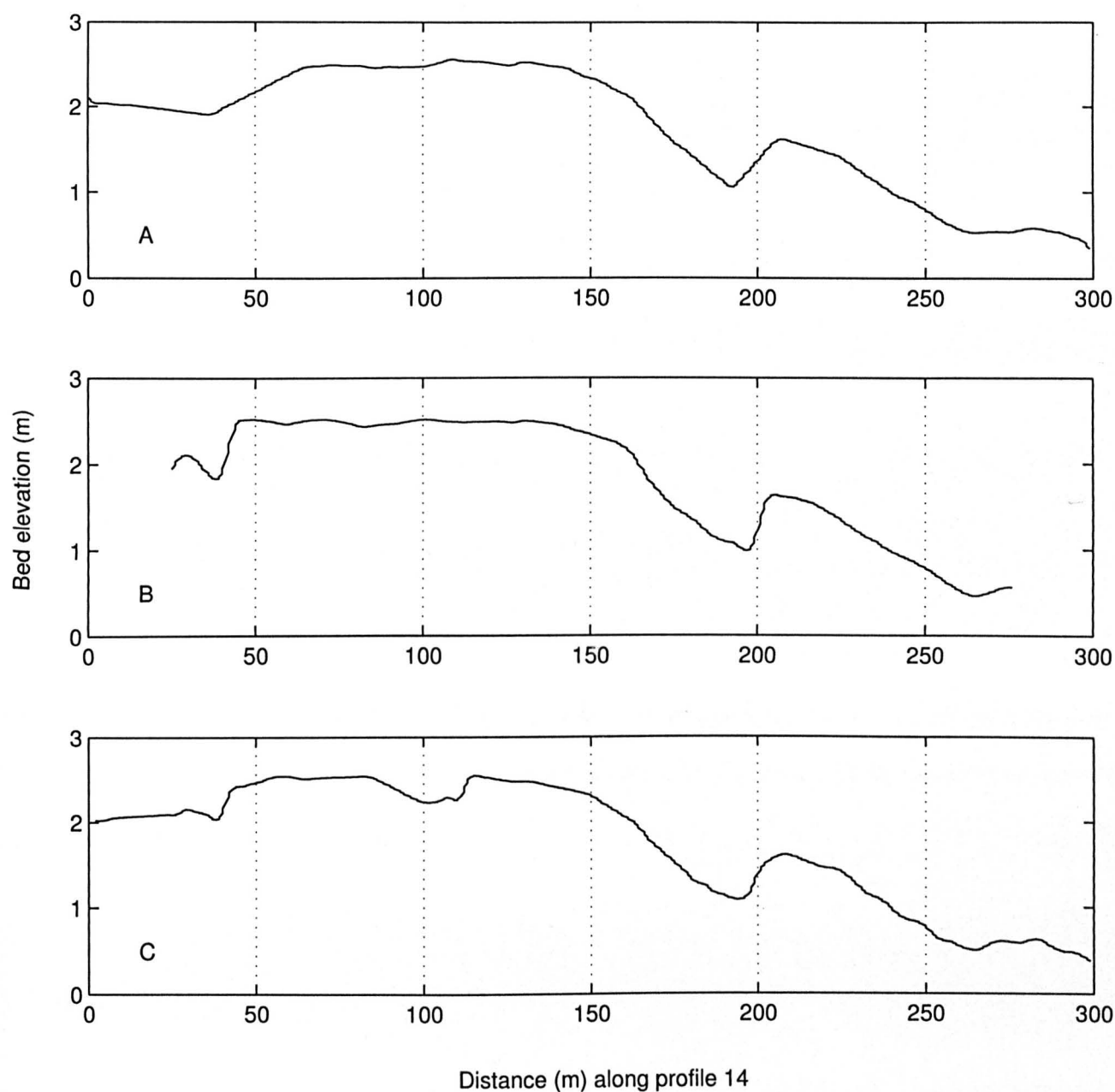Figure IV.2: Bed elevation profile along profile 3 for all West Kirby Sands survey data A.) 28.01.11 B.) 31.01.11 C.) 08.02.11 D.) 11.02.11.
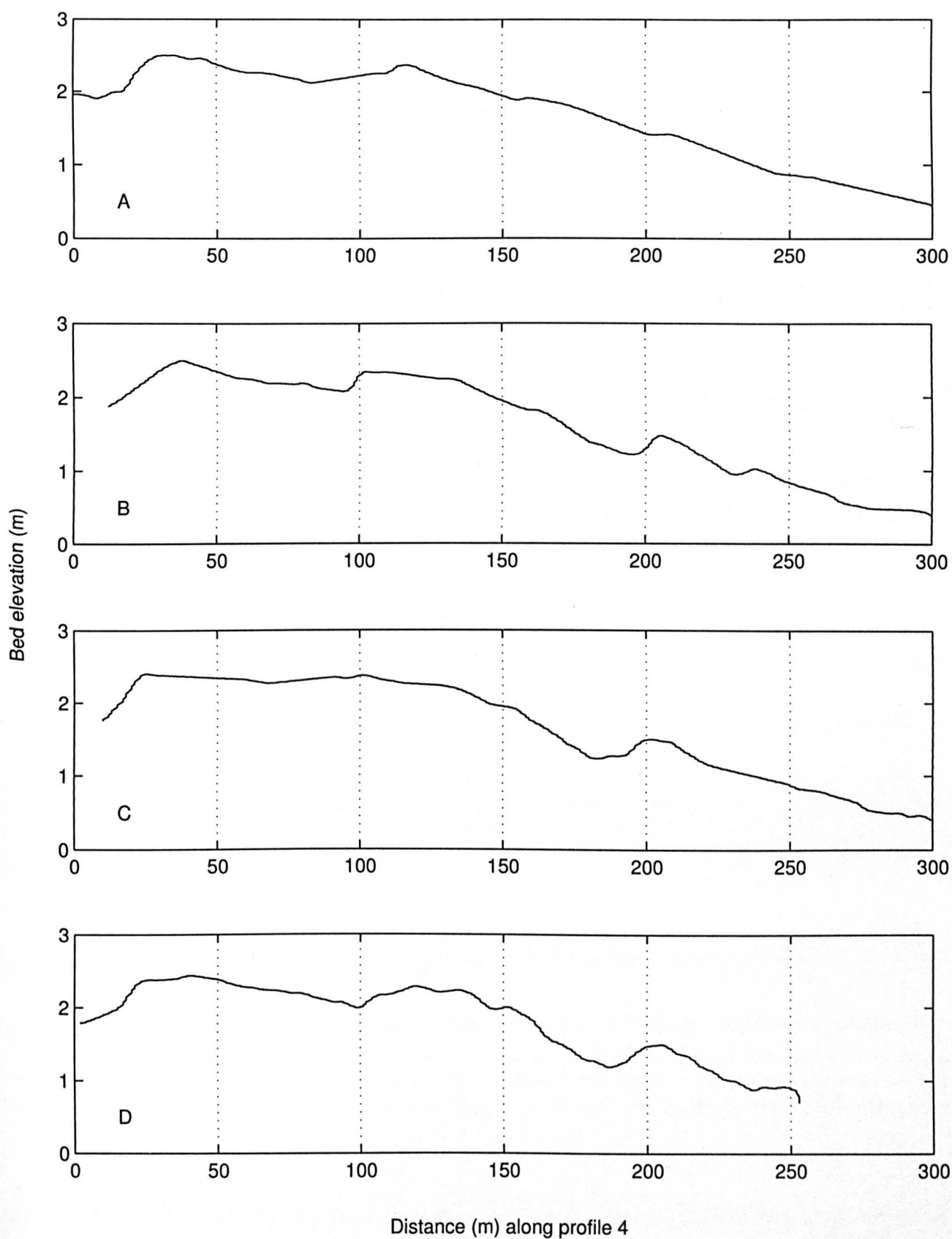
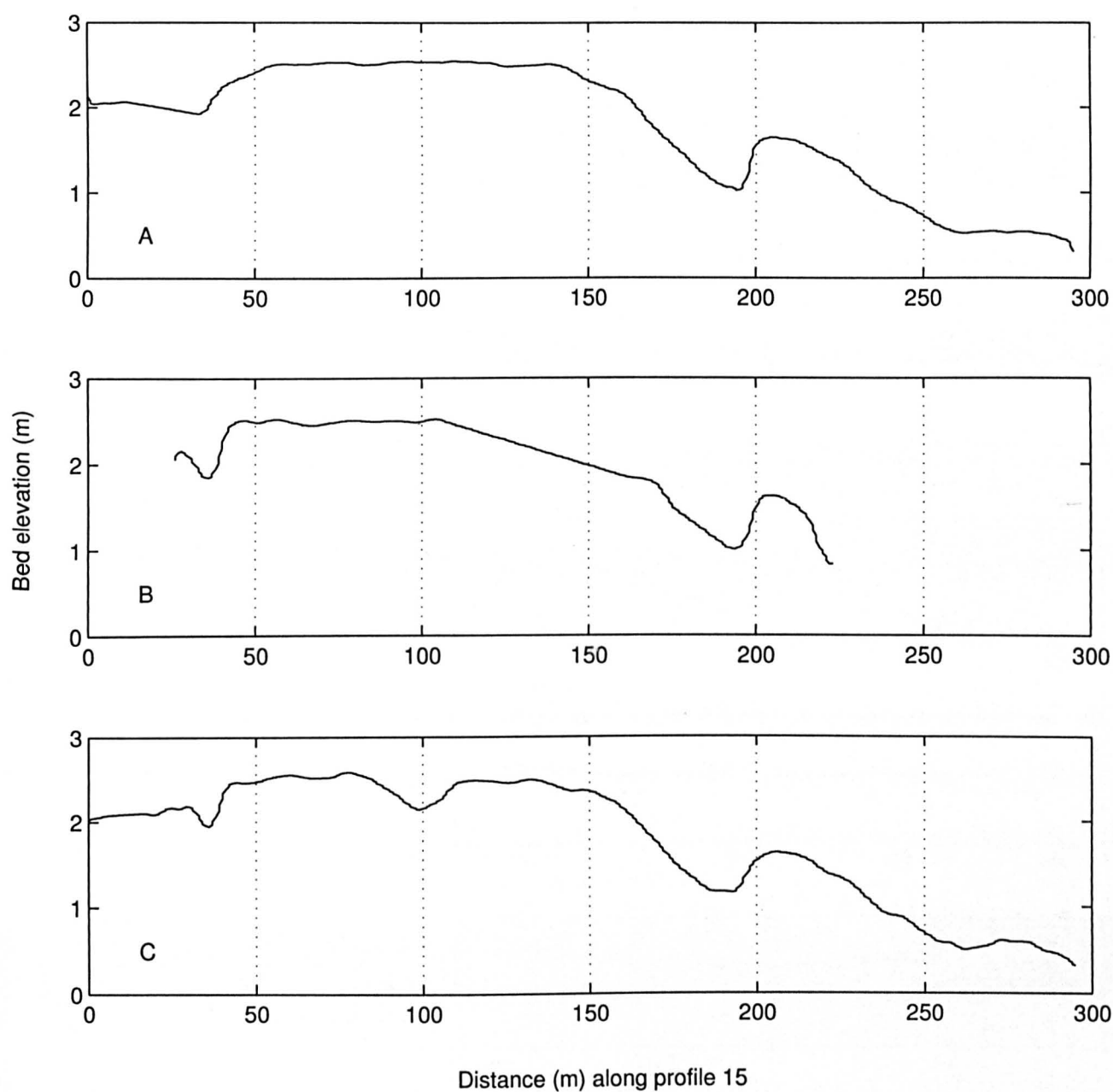Figure IV.3: Bed elevation profile along profile 4 for all West Kirby Sands survey data A.) 28.01.11 B.) 31.01.11 C.) 08.02.11 D.) 11.02.11.

Distance (m) along profile 6
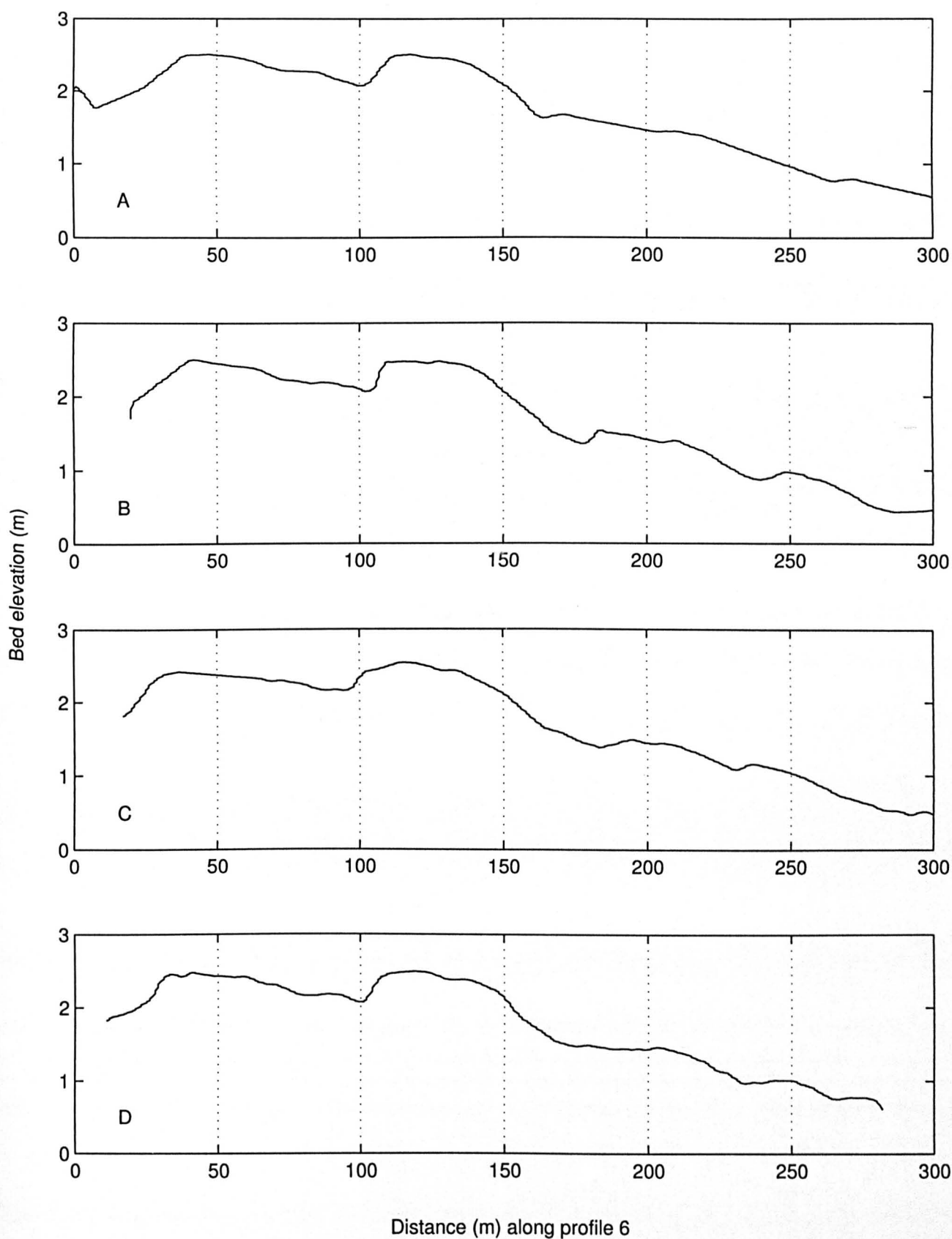
Figure IV.4: Bed elevation profile along profile 6 for all West Kirby Sands survey data A.) 28.01.11 B.) 31.01.11 C.) 08.02.11 D.) 11.02.11.

Distance (m) along profile 7
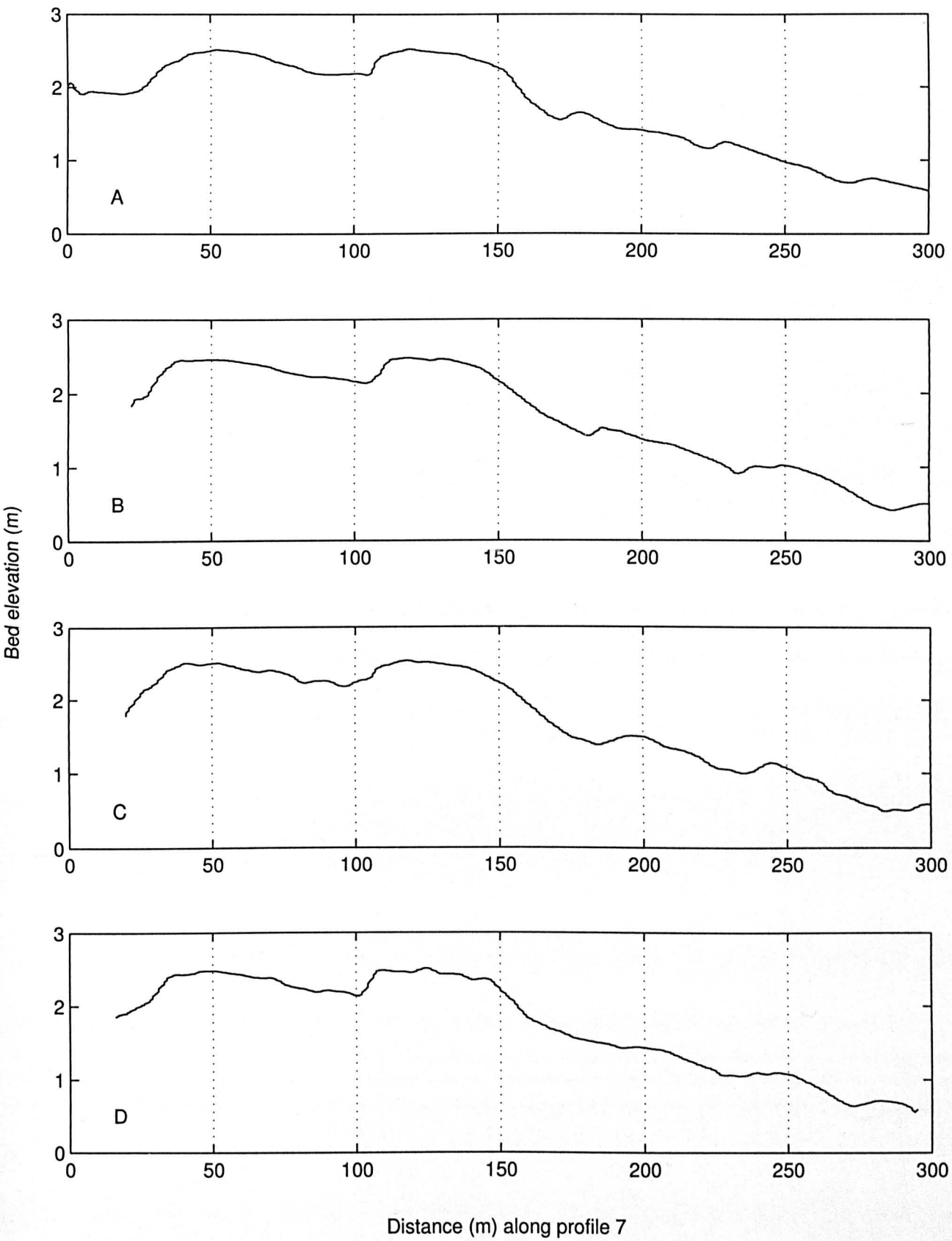
Figure IV.5: Bed elevation profile along profile 7 for all West Kirby Sands survey data A.) 28.01.11 B.) 31.01.11 C.) 08.02.11 D.) 11.02.11.

351
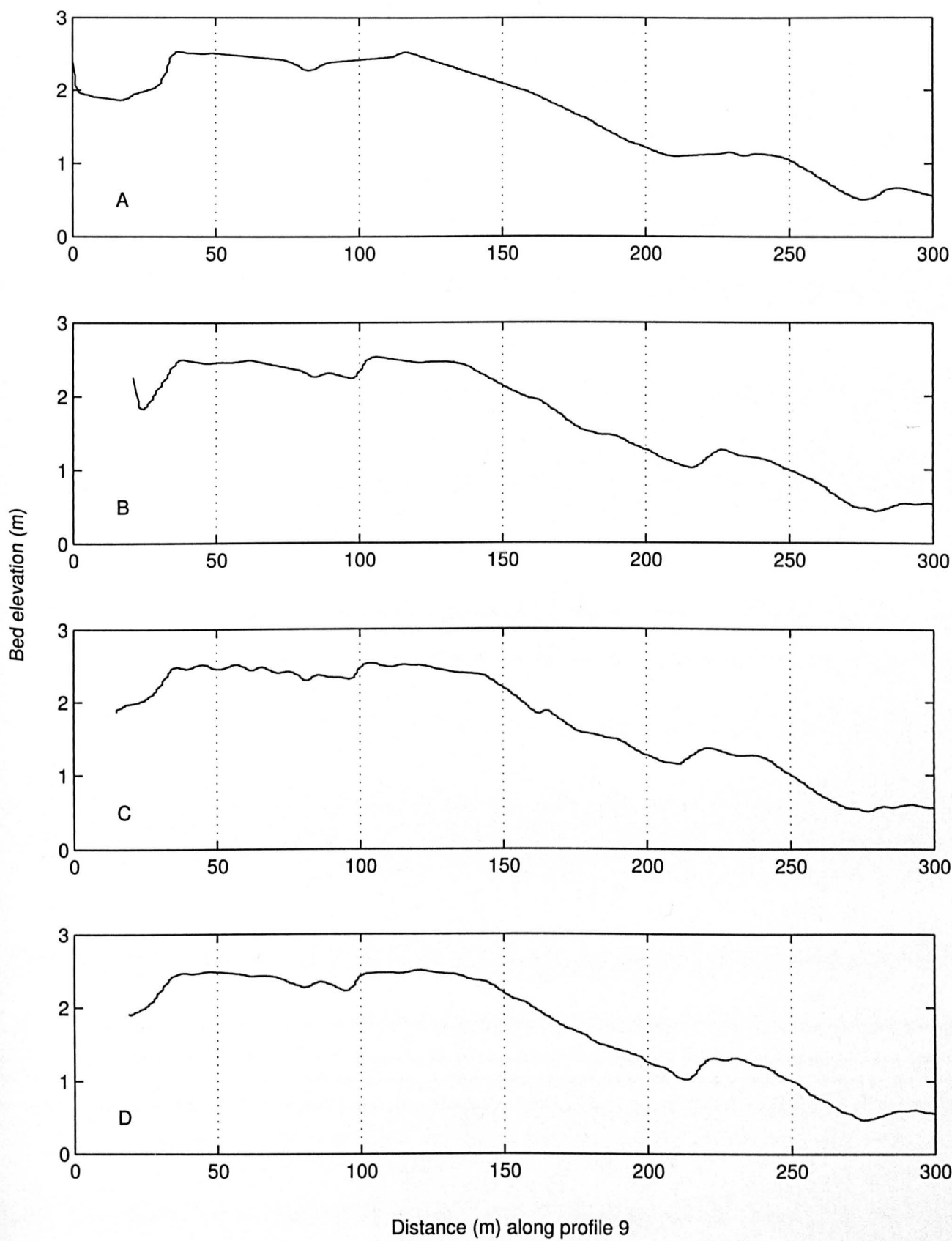
Figure IV.6: Bed elevation profile along profile 9 for all West Kirby Sands survey data A.) 28.01.11 B.) 31.01.11 C.) 08.02.11 D.) 11.02.11.
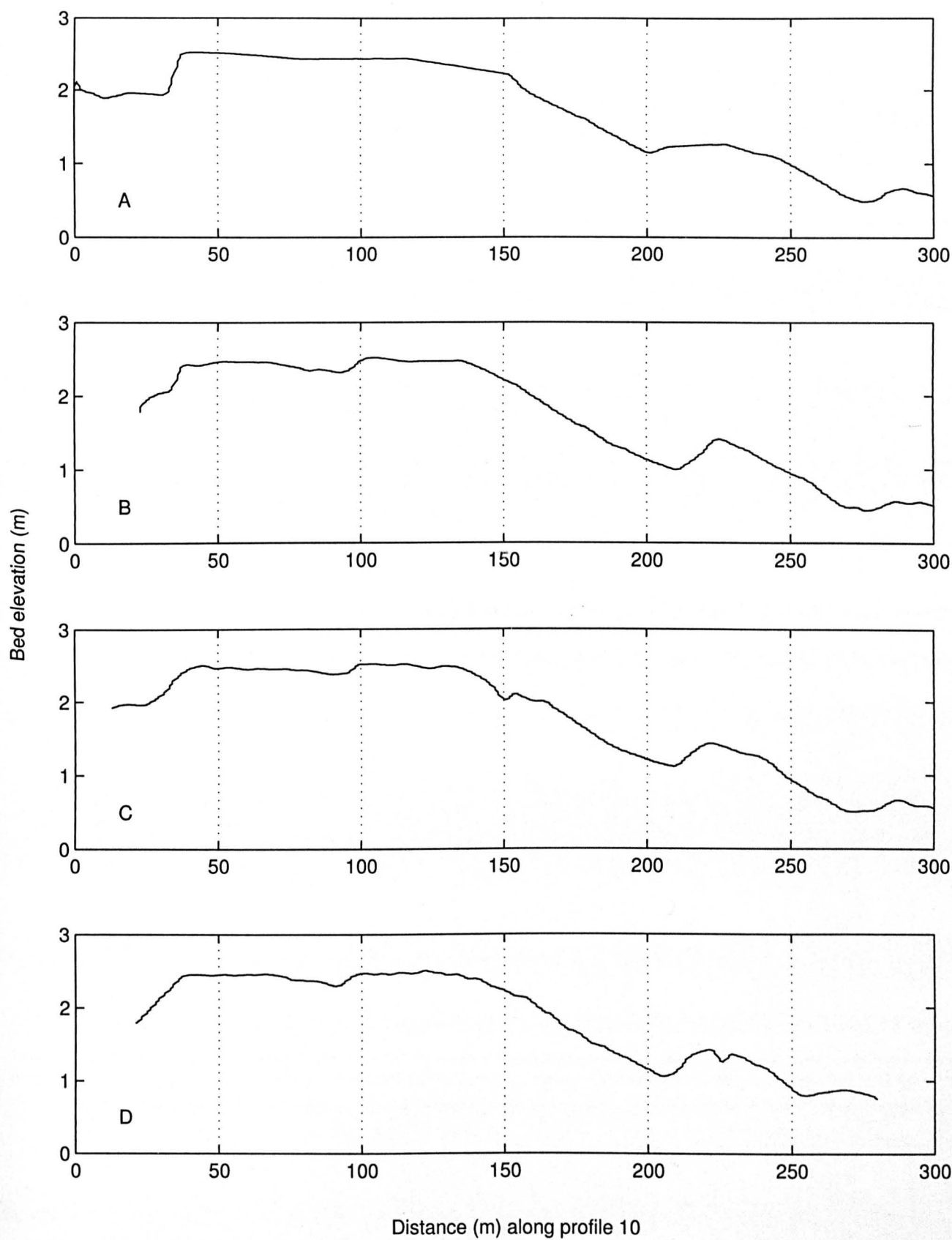
Figure IV.7: Bed elevation profile along profile 10 for all West Kirby Sands survey data A.) 28.01.11 B.) 31.01.11 C.) 08.02.11 D.) 11.02.11.

Distance (m) along profile 11
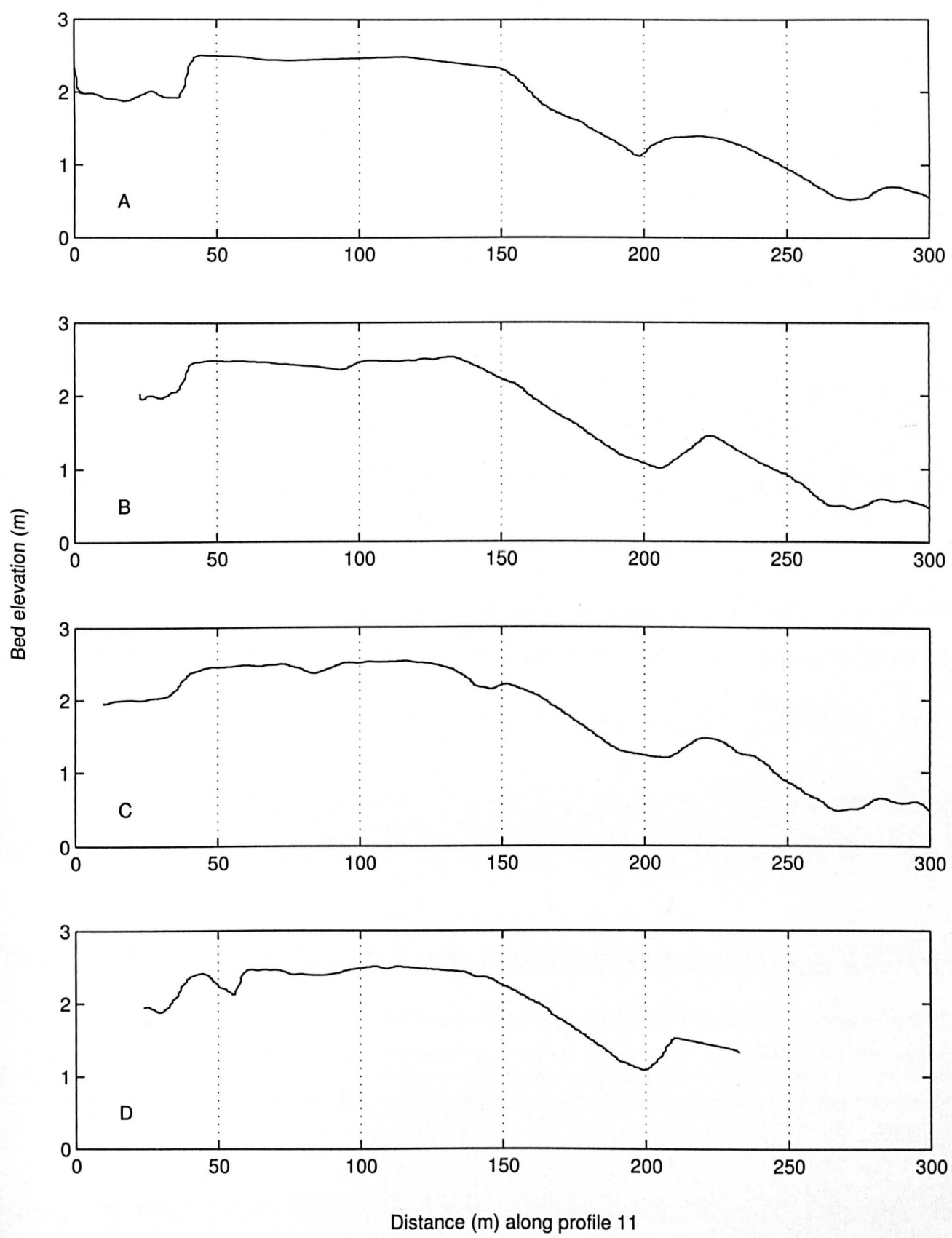
Figure IV.8: Bed elevation profile along profile 11 for all West Kirby Sands survey data A.) 28.01.11 B.) 31.01.11 C.) 08.02.11 D.) 11.02.11.

Distance (m) along profile 12
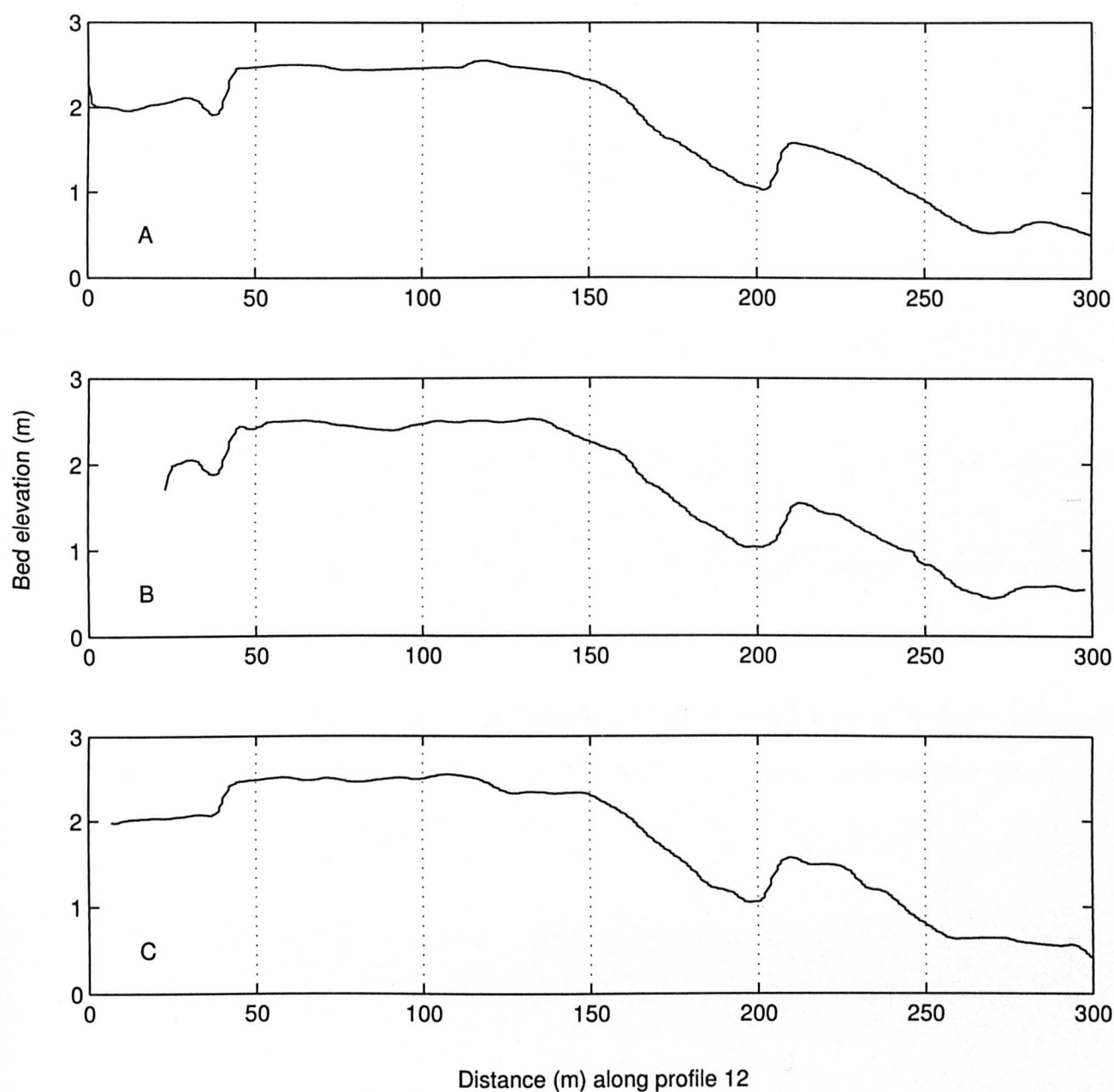
Figure IV.9: Bed elevation profile along profile 12 for West Kirby Sands survey data A.) 28.01.11 B.) 31.01.11 C.) 08.02.11.

Distance (m) along profile 13

Figure IV.10: Bed elevation profile along profile 13 for West Kirby Sands survey data A.) 28.01.11 B.) 31.01.11 C.) 08.02.11.

Distance (m) along profile 14

Figure IV.11: Bed elevation profile along profile 14 for West Kirby Sands survey data A.) 28.01.11 B.) 31.01.11 C.) 08.02.11.

Figure IV.12: Bed elevation profile along profile 15 for West Kirby Sands survey data A.) 28.01.11 B.) 31.01.11 C.) 08.02.11.

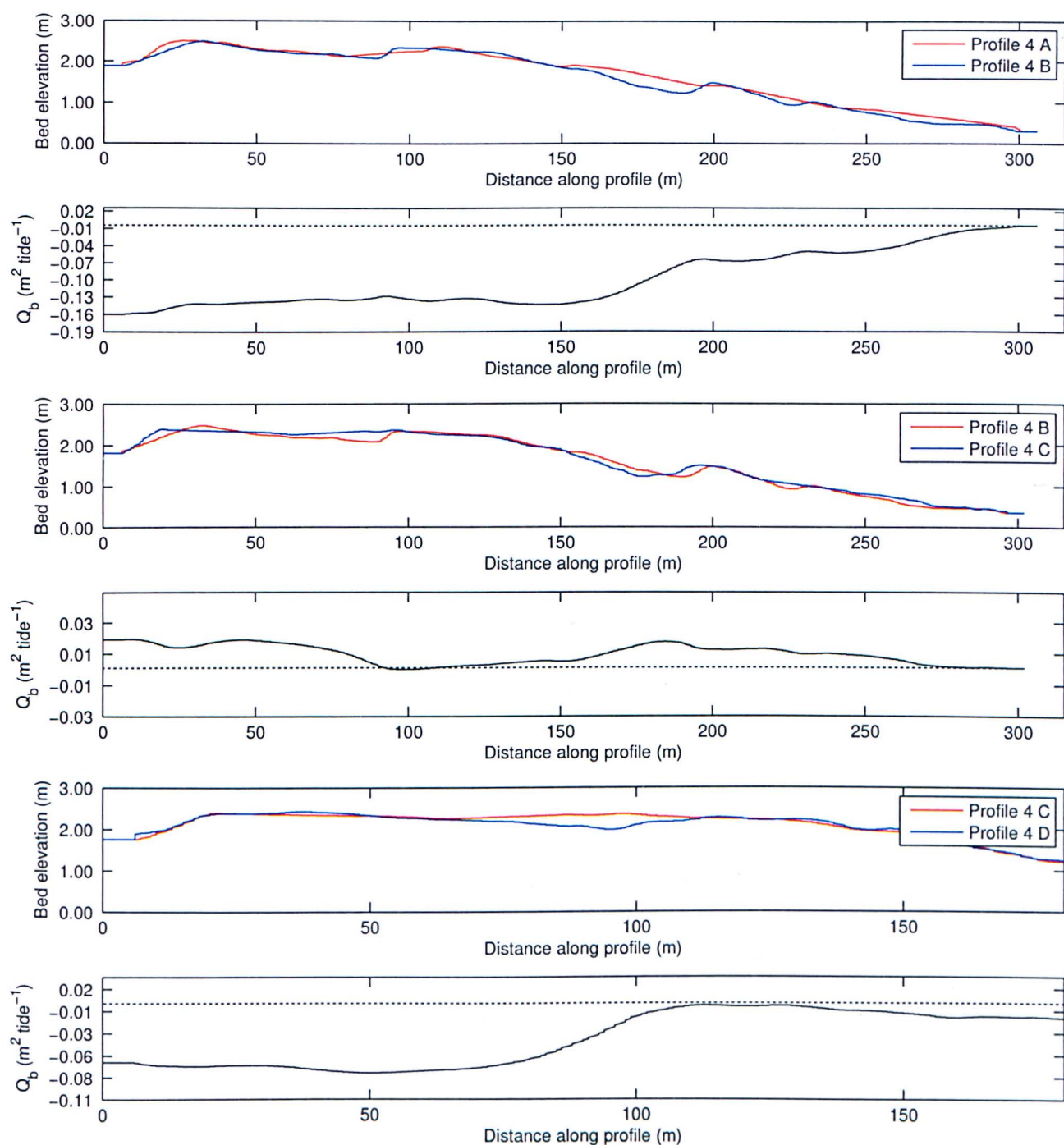# Sediment continuity from paired survey profiles
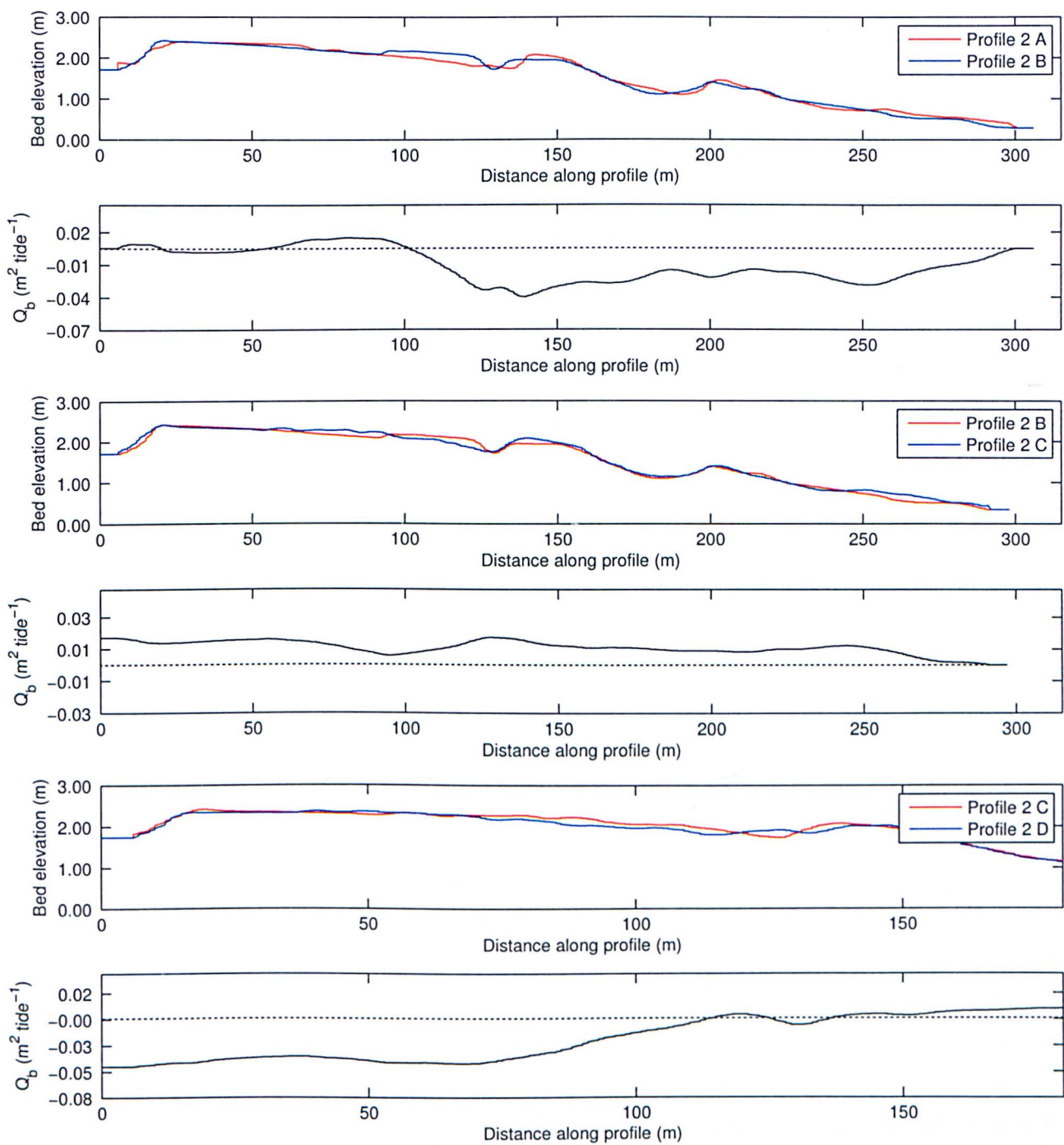
Figure IV.13: Bed elevation for paired profiles (profile 2) for A) 28.01.11, B) 31.01.11, C) 08.02.11 and D) 11.02.11 survey data. The respective profiles pairs have elevations set to the minimum value at both ends and profile lengths are equal as explained in the text. The volumetric transport rate (m^2 tide^{-1}) is calculated by integrating the bed continuity equation (equation 8.8) from the right of the figure (open sea boundary) to the left (sand flats).
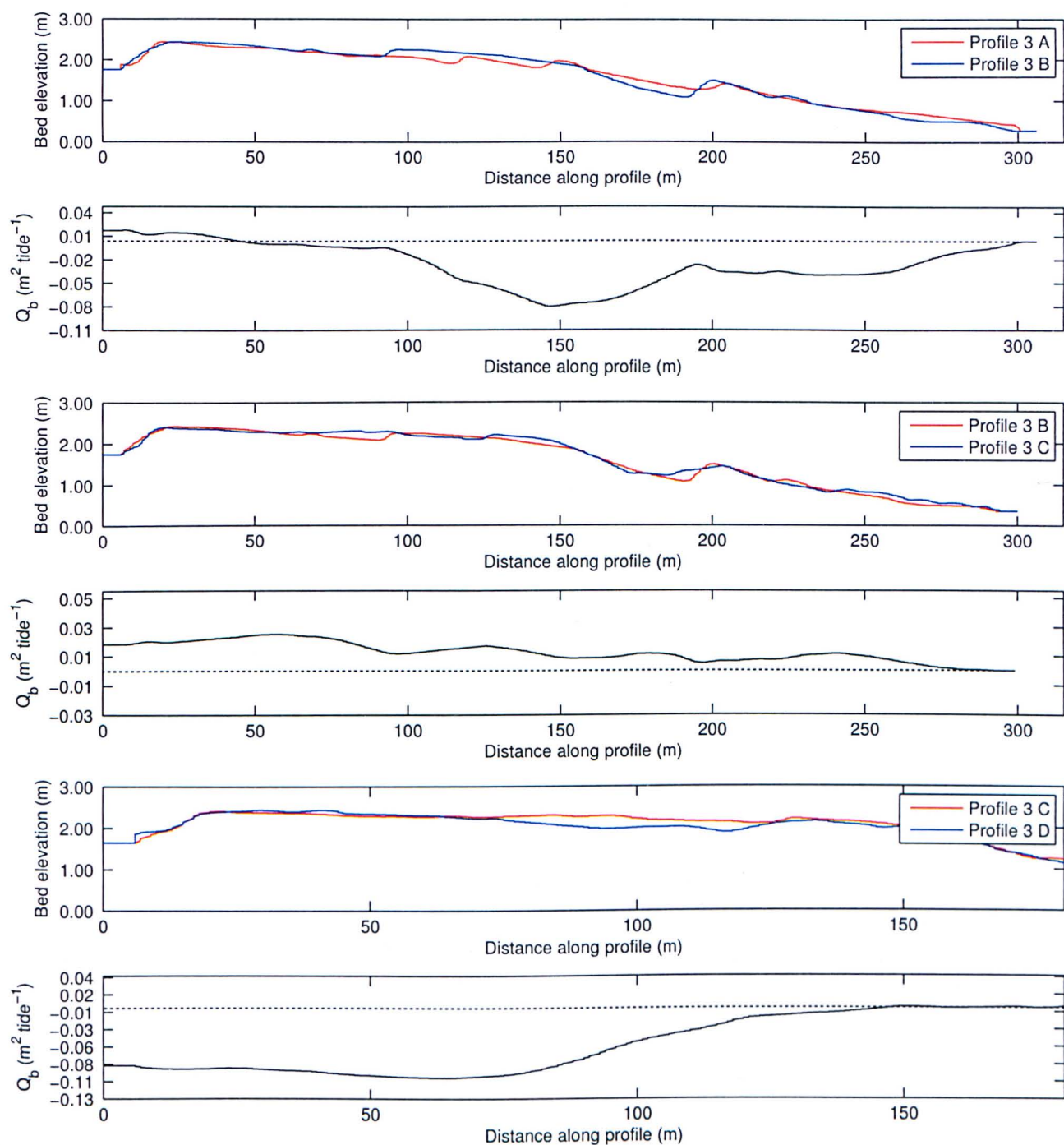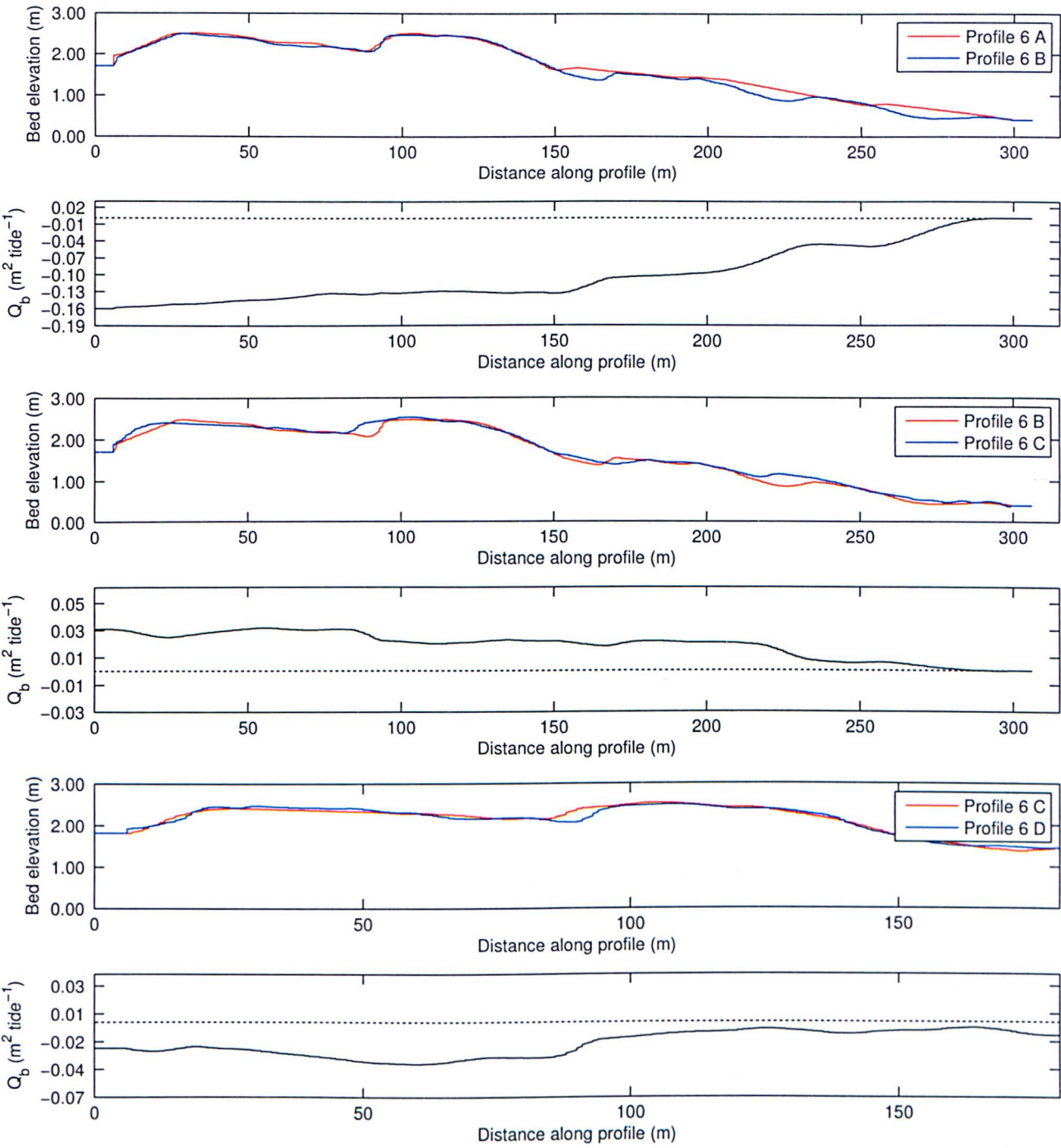
Figure IV.14: Bed elevation for paired profiles (profile 3) for A) 28.01.11, B) 31.01.11, C) 08.02.11 and D) 11.02.11 survey data. The respective profiles pairs have elevations set to the minimum value at both ends and profile lengths are equal as explained in the text. The volumetric transport rate (m^2 tide^{-1}) is calculated by integrating the bed continuity equation (equation 8.8) from the right of the figure (open sea boundary) to the left (sand flats).
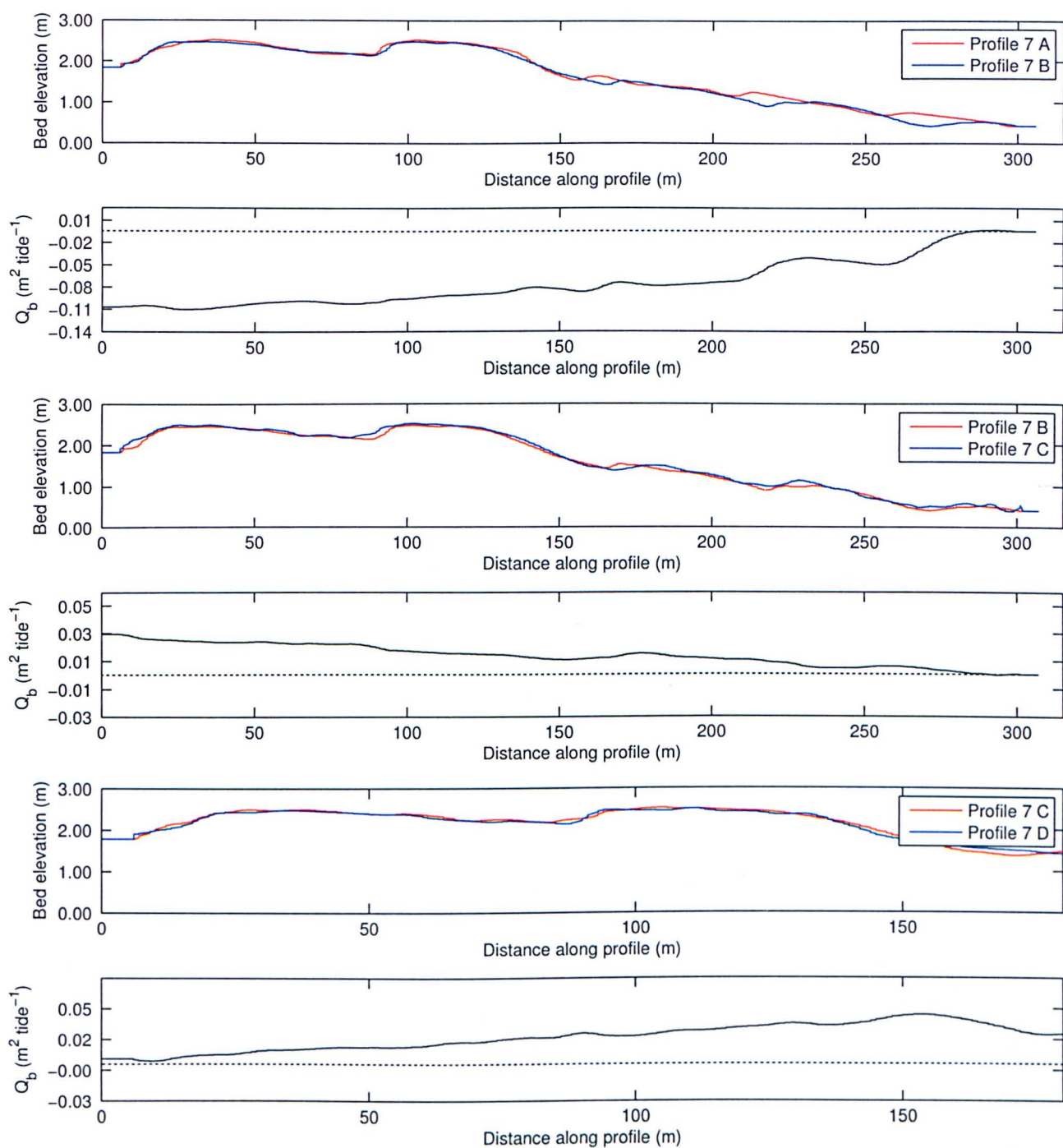
Figure IV.15: Bed elevation for paired profiles (profile 4) for A) 28.01.11, B) 31.01.11, C) 08.02.11 and D) 11.02.11 survey data. The respective profiles pairs have elevations set to the minimum value at both ends and profile lengths are equal as explained in the text. The volumetric transport rate (m^2 tide^{-1}) is calculated by integrating the bed continuity equation (equation 8.8) from the right of the figure (open sea boundary) to the left (sand flats).

Figure IV.16: Bed elevation for paired profiles (profile 6) for A) 28.01.11, B) 31.01.11, C) 08.02.11 and D) 11.02.11 survey data. The respective profiles pairs have elevations set to the minimum value at both ends and profile lengths are equal as explained in the text. The volumetric transport rate (m² tide⁻¹) is calculated by integrating the bed continuity equation (equation 8.8) from the right of the figure (open sea boundary) to the left (sand flats).
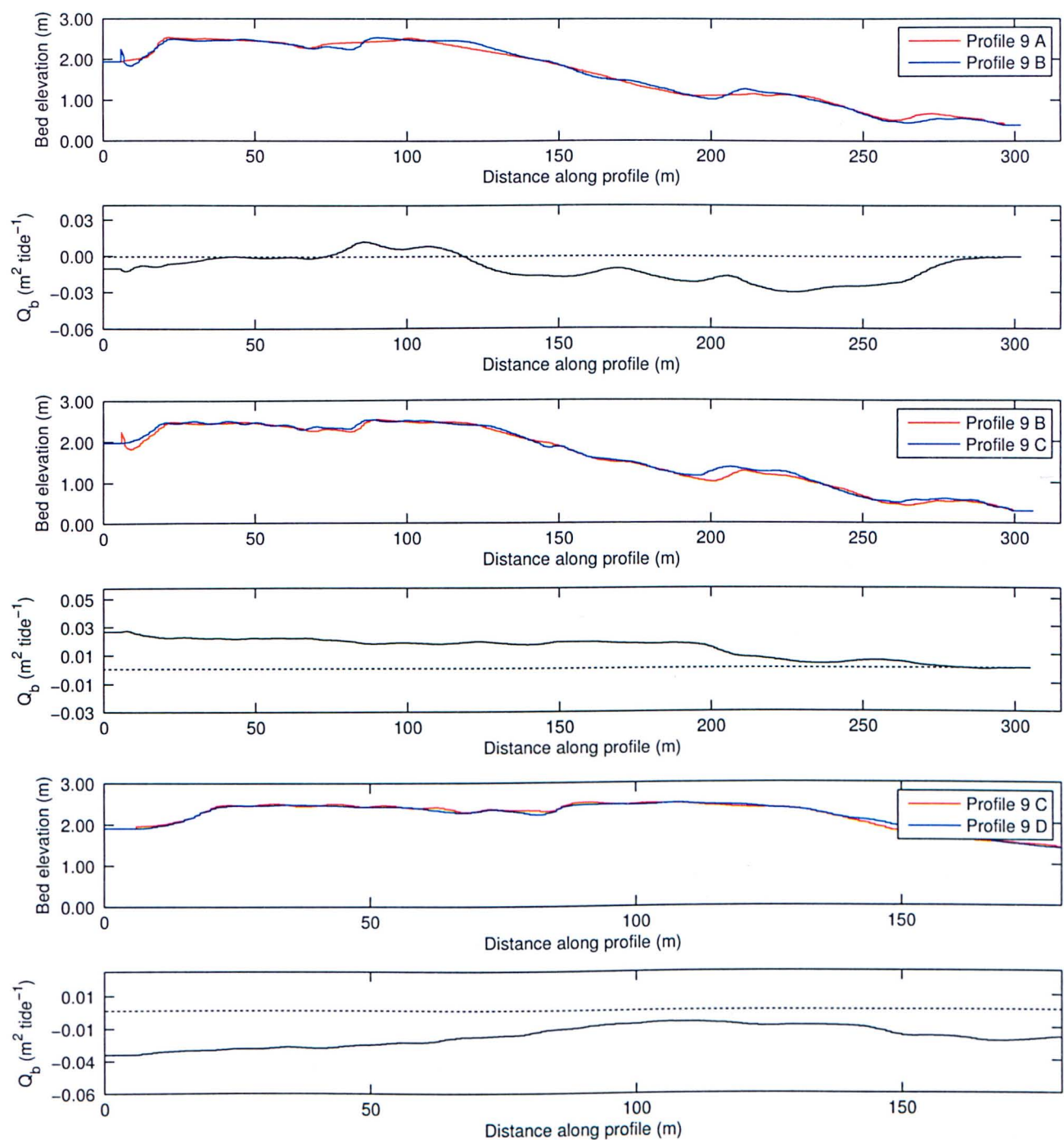
Figure IV.17: Bed elevation for paired profiles (profile 7) for A) 28.01.11, B) 31.01.11, C) 08.02.11 and D) 11.02.11 survey data. The respective profiles pairs have elevations set to the minimum value at both ends and profile lengths are equal as explained in the text. The volumetric transport rate (m^2 $tide^{-1}$) is calculated by integrating the bed continuity equation (equation 8.8) from the right of the figure (open sea boundary) to the left (sand flats).
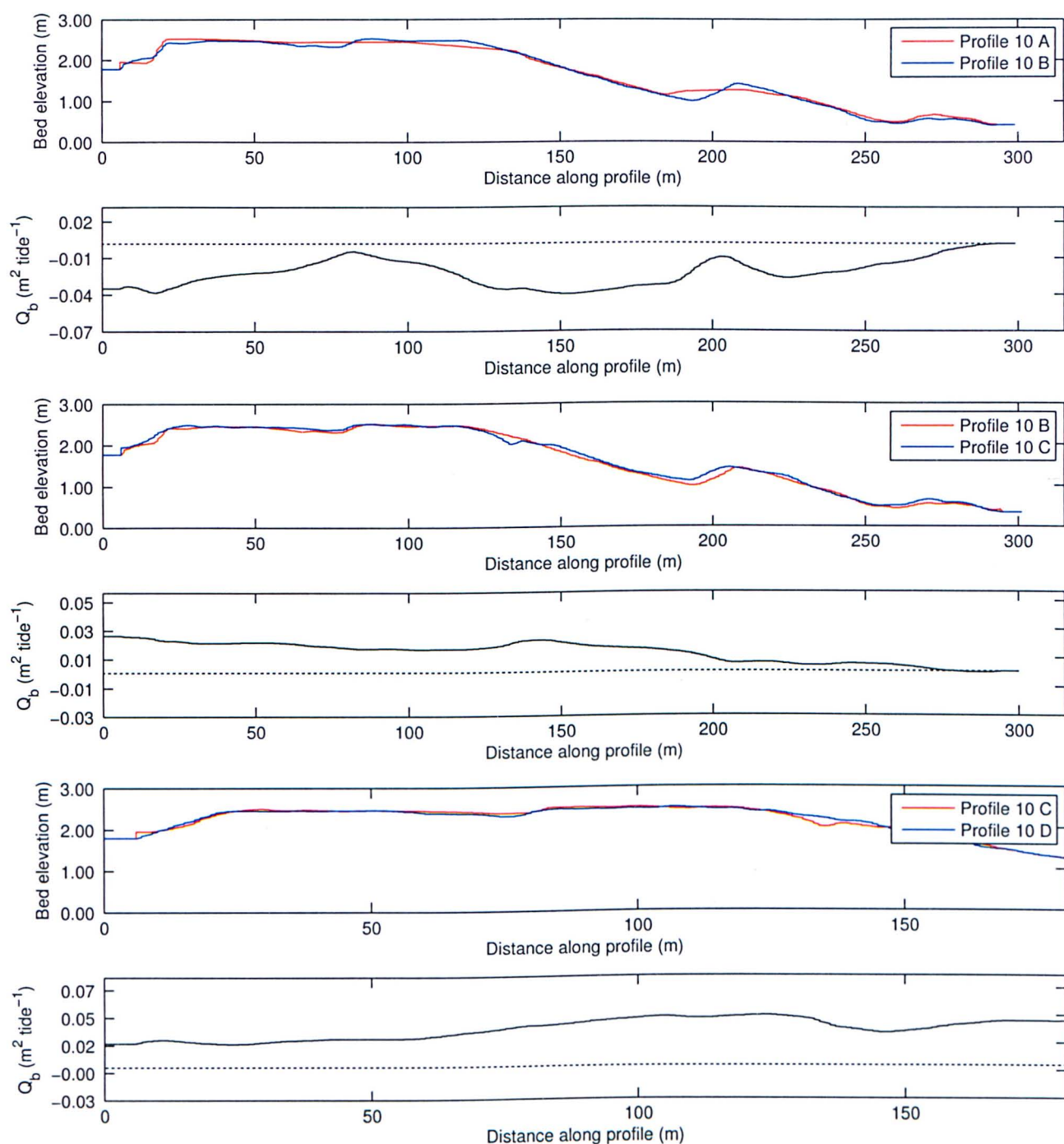
Figure IV.18: Bed elevation for paired profiles (profile 9) for A) 28.01.11, B) 31.01.11, C) 08.02.11 and D) 11.02.11 survey data. The respective profiles pairs have elevations set to the minimum value at both ends and profile lengths are equal as explained in the text. The volumetric transport rate (m^2 $tide^{-1}$) is calculated by integrating the bed continuity equation (equation 8.8) from the right of the figure (open sea boundary) to the left (sand flats).
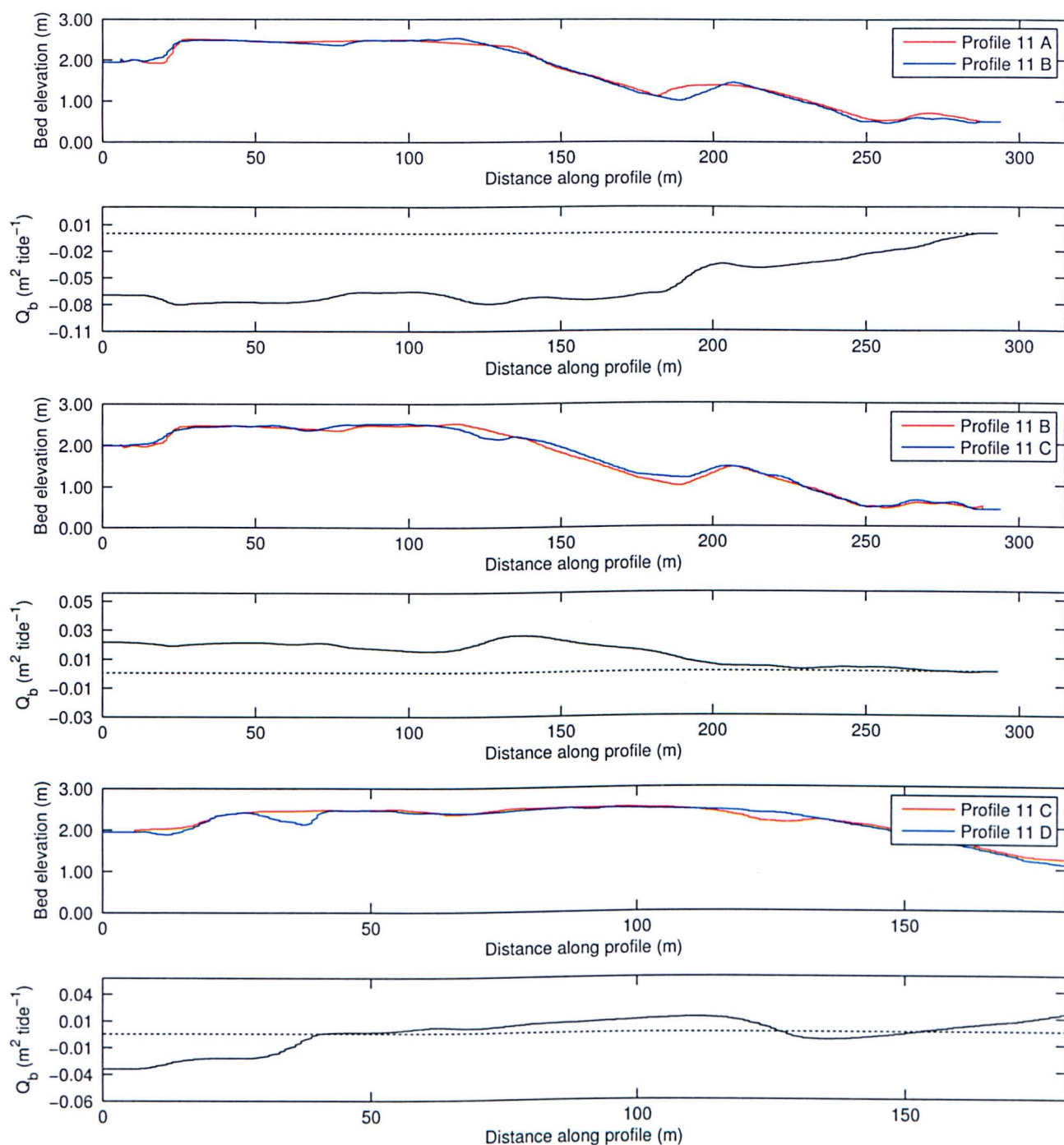
Figure IV.19: Bed elevation for paired profiles (profile 10) for A) 28.01.11, B) 31.01.11, C) 08.02.11 and D) 11.02.11 survey data. The respective profiles pairs have elevations set to the minimum value at both ends and profile lengths are equal as explained in the text. The volumetric transport rate (m^2 $tide^{-1}$) is calculated by integrating the bed continuity equation (equation 8.8) from the right of the figure (open sea boundary) to the left (sand flats).
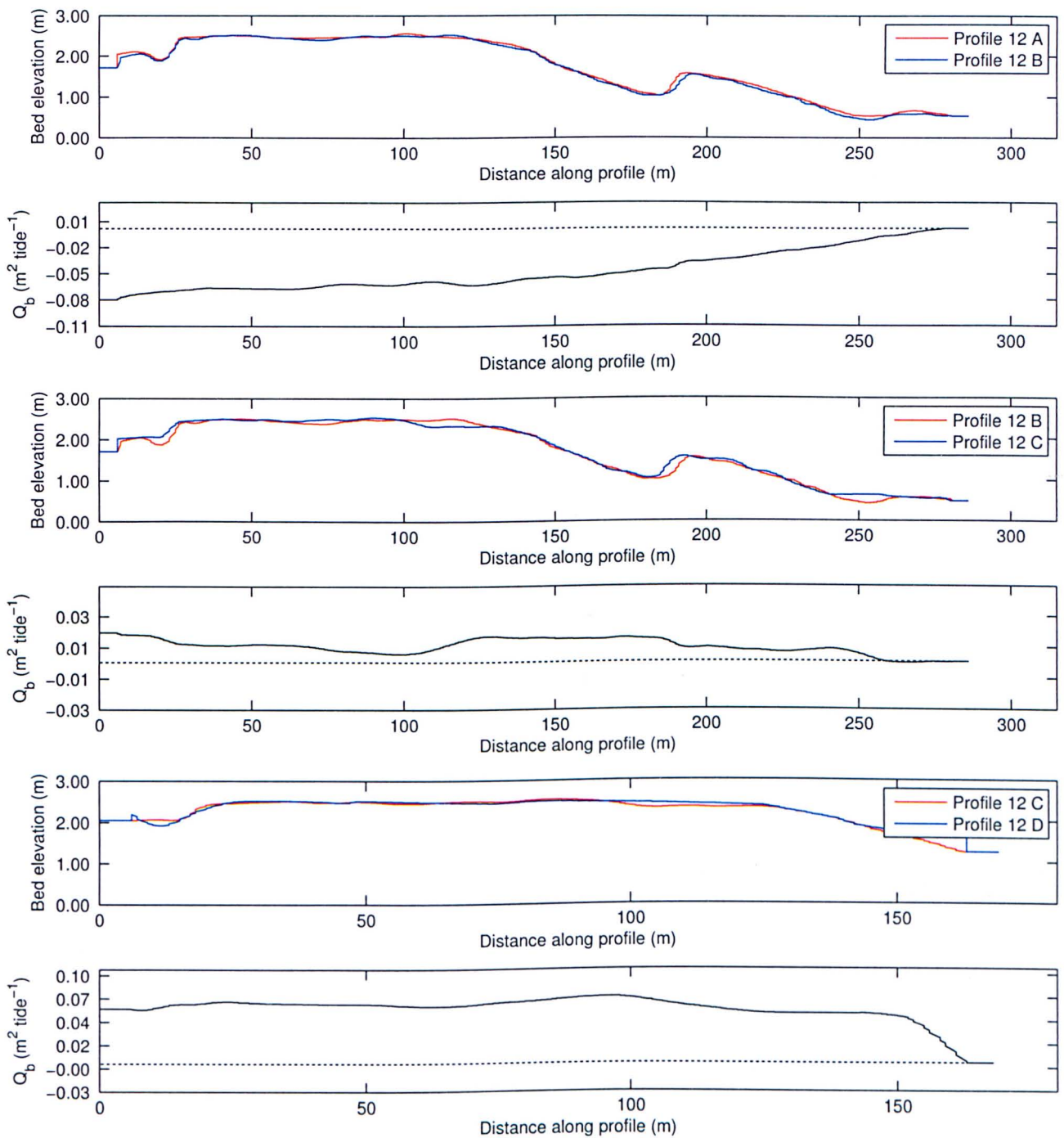
Figure IV.20: Bed elevation for paired profiles (profile 11) for A) 28.01.11, B) 31.01.11, C) 08.02.11 and D) 11.02.11 survey data. The respective profiles pairs have elevations set to the minimum value at both ends and profile lengths are equal as explained in the text. The volumetric transport rate (m^2 tide^{-1}) is calculated by integrating the bed continuity equation (equation 8.8) from the right of the figure (open sea boundary) to the left (sand flats).

Figure IV.21: Bed elevation for paired profiles (profile 12) for A) 28.01.11, B) 31.01.11, C) 08.02.11 and D) 11.02.11 survey data. The respective profiles pairs have elevations set to the minimum value at both ends and profile lengths are equal as explained in the text. The volumetric transport rate (m^2 $tide^{-1}$) is calculated by integrating the bed continuity equation (equation 8.8) from the right of the figure (open sea boundary) to the left (sand flats).
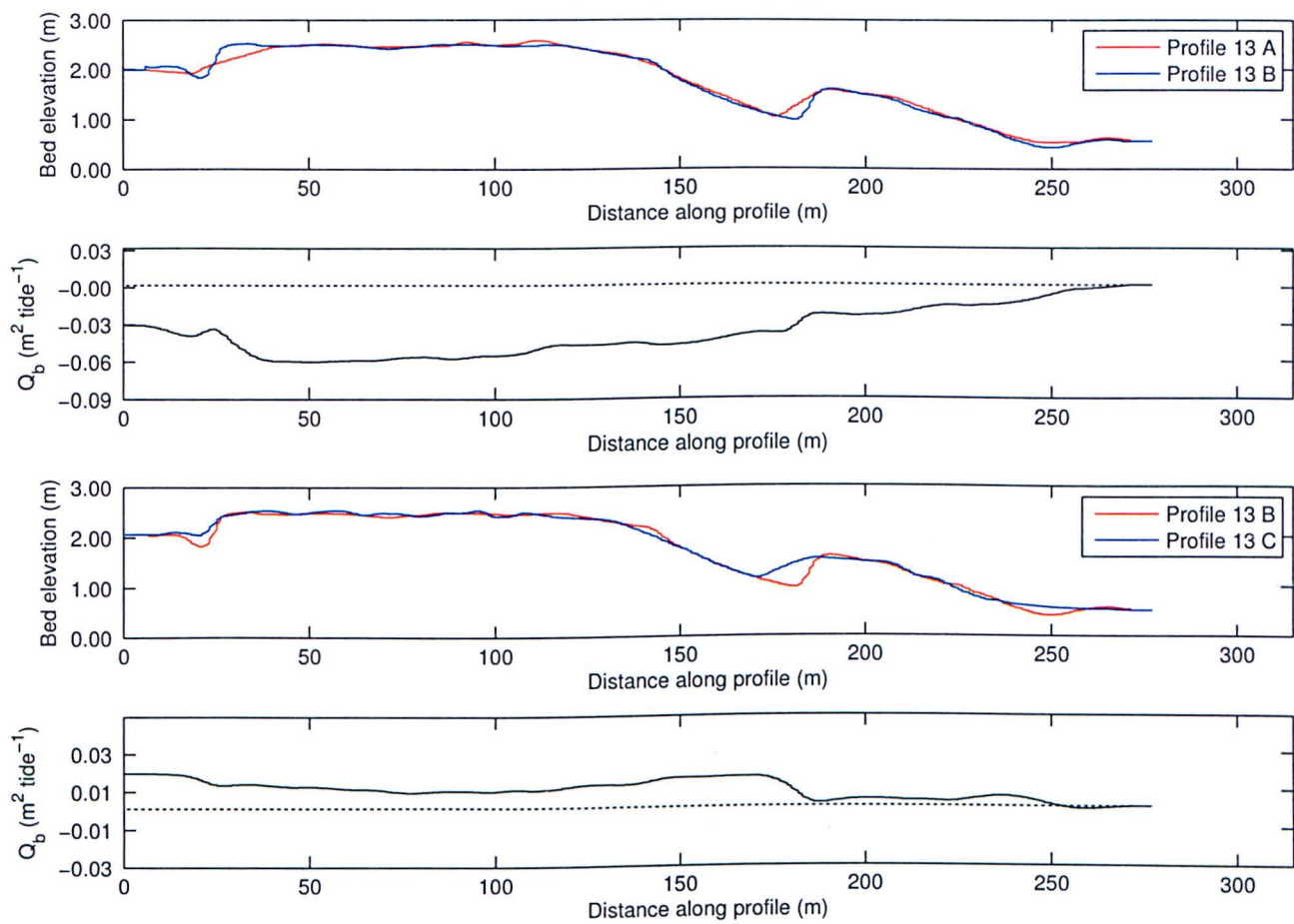
Figure IV.22: Bed elevation for paired profiles (profile 13) for A) 28.01.11, B) 31.01.11, C) 08.02.11 survey data. The respective profiles pairs have elevations set to the minimum value at both ends and profile lengths are equal as explained in the text. The volumetric transport rate (m^2 tide^{-1}) is calculated by integrating the bed continuity equation (equation 8.8) from the right of the figure (open sea boundary) to the left (sand flats).
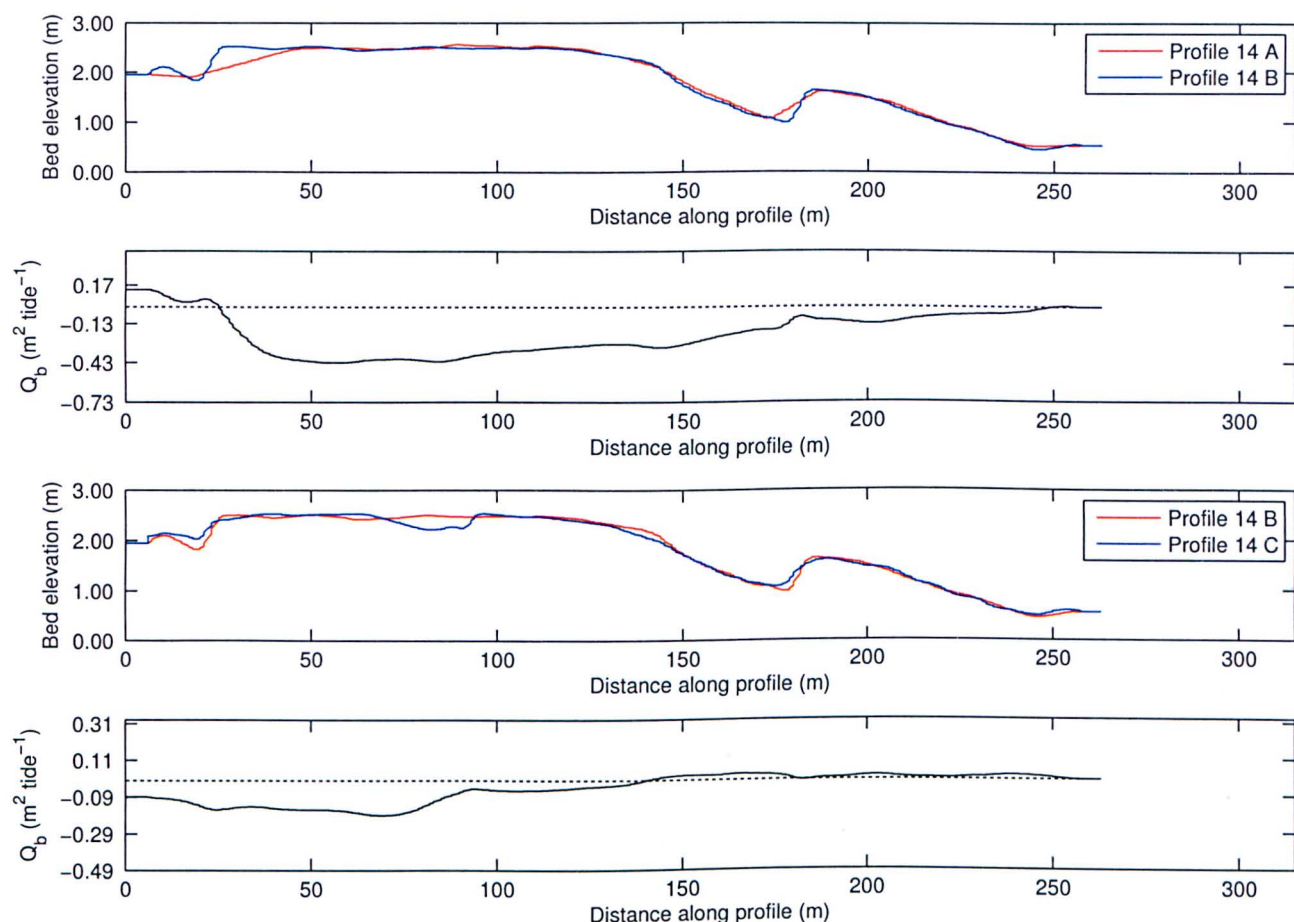
Figure IV.23: Bed elevation for paired profiles (profile 14) for A) 28.01.11, B) 31.01.11, C) 08.02.11 survey data. The respective profiles pairs have elevations set to the minimum value at both ends and profile lengths are equal as explained in the text. The volumetric transport rate (m² tide⁻¹) is calculated by integrating the bed continuity equation (equation 8.8) from the right of the figure (open sea boundary) to the left (sand flats).
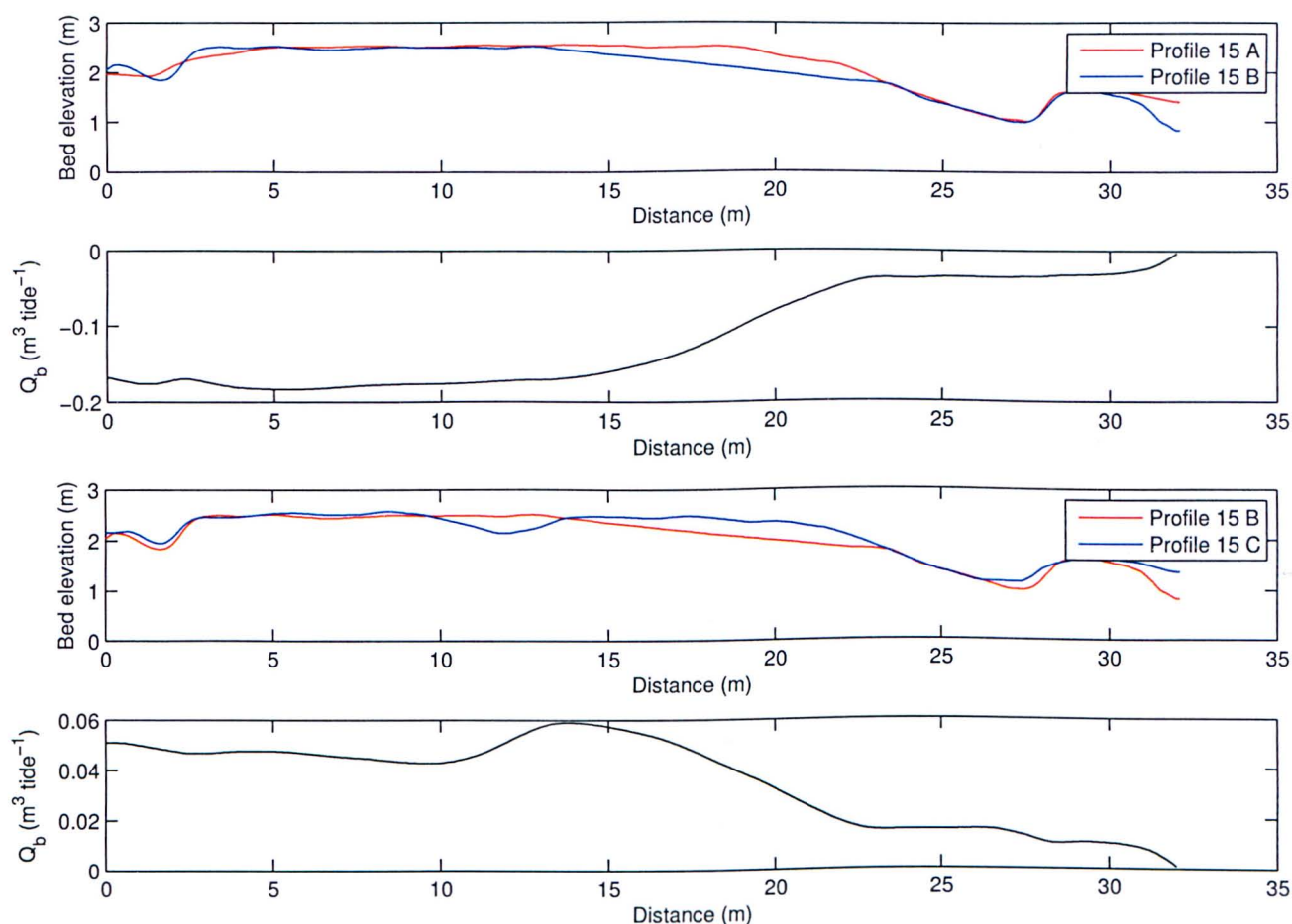
Figure IV.24: Bed elevation for paired profiles (profile 15) for A) 28.01.11, B) 31.01.11, C) 08.02.11 survey data. The respective profiles pairs have elevations set to the minimum value at both ends and profile lengths are equal as explained in the text. The volumetric transport rate (m^2 tide^{-1}) is calculated by integrating the bed continuity equation (equation 8.8) from the right of the figure (open sea boundary) to the left (sand flats).